UNIVERSIDAD COMPLUTENSE DE MADRID
FACULTAD DE CIENICAS QUÍMICAS
Departamento de Química Física I

TESIS DOCTORAL

Estrategias de síntesis de nanopartículas magnéticas Mono-Núcleo y Multi-Núcleo de óxidos de hierro para aplicaciones en biomedicina

MEMORIA PARA OPTAR AL GRADO DE DOCTOR

PRESENTADA POR

Helena Gavilán Rubio

Directores

María del Puerto Morales Herrero
Lucía Gutiérrez Marruedo

Madrid, 2018

Universidad Complutense de Madrid
Facultad de Ciencias Químicas
Departamento de Química Física I

Estrategias de Síntesis de Nanopartículas Magnéticas Mono-Núcleo y Multi-Núcleo de Óxidos de Hierro para Aplicaciones en Biomedicina

Memoria para optar al grado de Doctora presentado por

Helena Gavilán Rubio

Bajo la dirección de
Dr. María del Puerto Morales Herrero
Dr. Lucía Gutiérrez Marruedo

Tutor Académico
Dr. Andrés Guerrero Martínez

Madrid 2017

Synthesis Strategies of Single-Core and Multi-Core Iron Oxide Magnetic Nanoparticles for Biomedical Applications

PhD Thesis

Helena Gavilán Rubio

Supervisors
Dr. María del Puerto Morales Herrero
Dr. Lucía Gutiérrez Marruedo

Tutor
Dr. Andrés Guerrero Martínez

Group of Nanocrystals and Chemistry
Institute of Materials Sciences of Madrid

Madrid 2017

Nature!...She is the only artist; working-up the most uniform material into utter opposites; arriving, without a trace of effor, at perfection, at the most exact precision, though always veiled under a certain softness.

Johann Wolfgang von Goethe

Agradecimientos

Me gustaría dedicar este trabajo a las personas que de alguna manera me han inspirado, motivado y animado a realizar una tesis doctoral en química avanzada y, más importantemente, a aquellas personas que me han ayudado a nivel profesional y a nivel personal todo este tiempo.

En primer lugar quiero nombrar al Prof. José Vicente Heras Castelló, profesor de Química Inorgánica I en la Facultad de Ciencias Químicas de la UCM. Él fue quien, cada día, levantaba mi pasión por la ciencia, en especial por la química inorgánica. Con qué energía y pasión nos hablaba de los compuestos inorgánicos, su estructura y sus propiedades.

De la facultad tampoco me olvido del Dr. Andrés Guerrero Martínez, con quien investigué por primera vez acerca de la síntesis de nanopartículas, y por lo tanto quien me introdujó en el mundo de la nanotecnología. Gracias a é conocí a mi actual directora de tesis. Me gustaré mencionar también al recién doctor, Guille, con quien he tenido un montón de charlas acerca la tesis y de la ciencia en general, y también ha sido un apoyo para mí.

Quiero agradecer de forma especial a mis directoras de tesis la posibilidad de realizar la tesis doctoral bajo su supervisión: a la Dra. María del Puerto Morales Herrero y a la Dra. Lucía Gutiérrez Marruedo. A Puerto, le agradezco la posibilidad de hacer la tesis en el grupo de investigación de Nanocristales y Química, dentro del Instituto de Ciencia de Materiales de Madrid (ICMM). Quiero agradecerle su disposición y empeño en enseñarme todo cuanto sabe, y en querer formarme como científica durante toda mi tesis. A Lucía quiero agradecerle su confianza, cercanía, dedicación y disponibilidad, practicamente las 24 h del día, aunque se encuentre en Zaragoza y no en Madrid. Quiero destacar el buen equipo que han hecho en la dirección de mi tesis. ¡Muchas gracias por todo!.

Esta tesis no sólo se explica con esfuerzo personal, si no que, por suerte, he contado con el apoyo de científicos que me han ayudado en la elaboración de las medidas que se muestran, y en el anális de los resultados. Quiero agradecer, por tanto, al "equipo" NanoMag, el servicio técnico del ICMM y

de la UAM y especialmente, quiero dar las gracias a los doctores Uwe Steinhoff, Oliver Posth, Lara K. Borgart y Balachandran Jehadevan, con quien tuve la suerte de hacer estancias durante mi tesis y quienes me abrieron las puertas a sus laboratorios, me ayudaron con la tesis y me enseñaron más acerca del magnetismo, sin duda.

Hay mucha gente del ICMM con la que he tenido la suerte de trabajar estos últimos tres años. En especial quiero mencionar a Nieves López. No puedo imaginar una mejor compañera de despacho ni amiga. Las dos hemos compartido momentos mejores y peores juntas, días de resultados buenos y malos, y me sorprende que, teniendo en cuenta todas las charlas y las bromas diarias, nuestra productividad juntas aumenta exponencialmente. Gracias a ella he podido compilar este documento. Además quiero dar las gracias a todo el apoyo de mis compaẽros del laboratorio, al Prof. Carlos Serna y a la Dra. Teresita González-Carreño. En especial también quiero mencionar al Dr. Sabino Veintemillas-Verdaguer. Es un gran científico que ha tratado de solucionar cualquier problema que ha surgido en el laboratorio. Le agradezco por tanto su ayuda, su contínua aportación de ideas, y por supuesto sus bromas, que sin duda dan vida al laboratorio. Finalmente, del ICMM me gustaría nombrar al grupo de teatro. ¡Vaya Diciembres hemos pasado preparando bailes y escenas para la obra de teatro de la fiesta de navidad! Nunca olvidaré los ensayos de las diferentes escenas y bailes en los pasillos del sótano, ni los propios días de las obras. Muchas gracias a todos por los buenos momentos. Tampoco me olvido de Celia, José, Leandro, Conchi, Joao, Lupita, de los fotónicos y los magnéticos, ¡Gracias a todos por los buenos momentos en el ICMM!

Realizar una tesis doctoral implica invertir un gran tiempo diario, entre semana y muchos fines de semana. Independientemente del esfuerzo personal, a veces los resultados son buenos y otras son malos. Por ello, todo este tiempo tanto mi familia como mis amigos han sido muy importantes para mi y han hecho que, en las malar rachas donde todo parece que va cuesta arriba, haya podido desconectar un poco. Primero quiero mencional a mis compañeros de piso: Inés, Laura, Lucas y Mati, quienes me han apoyado como los que más todo este tiempo. También quiero mencionar a Lucá, Aaron, Kamilia, Alex, Fito, Sergio y Enrique, todos los fines de semana que hemos compartido cocinando, paseando, o tapeando por Madrid. Quiero agradeceros cuando habéis estado ahí en momentos no tan divertidos.

Por supuesto, quiero agradecer de todo corazón a mi mayor apoyo todo este tiempo, que ha sido mi pilar, la persona que me ha dado calma siempre, Iker, sin él, en muchos momentos en los que faltan ganas de seguir, no se que hubiera hecho.

Además, no me olvido de mis hermanos, María y Kiko, quienes no importa la hora del día, el trabajo que tengan o lo ocupados que estén, hacen tiempo para vernos, para hablar por teléfono o skype, o lo que haga falta. ¡Siempre estaís ahí!

Finalmente, quiero agradecer y dedicar esta tesis a las dos mejores personas que conozco y que más se han dejado la piel por mí, a mis padres. Jamás habría llegado hasta aquí sin vosotros.

Foreword and scope of the Thesis

This thesis work has been carried out in the framework of the European project “NanoMag” (grant agreement n^{o} 604448), whose purposes are to standardize, improve and redefine analysing methods of magnetic nanoparticles and to develop reference samples for biomedical applications.

More specifically, the thesis was oriented toward several aspects: i) synthesis of uniform iron oxide nanoparticles controlling their size, shape, internal structure, assembly and consequently, tailoring their magnetic features; ii) comprehensive characterisation of the nanomaterials shedding light on the relationship between structure and properties iii) functionalisation with molecules/polymers suitable for the interaction with a biological system, iv) assessment of the toxicity of the magnetic nanoparticles and quantification in a biological system.

In order to achieve such tasks, the thesis was divided in three distinctive but complementary parts. Attending to the obtained nanoparticles, which can be classified as individual cores (single-core) or assembled cores forming a nanoparticle with a fixed size (multi-core), these parts are:

- Optimisation of the synthesis of single-core anisometric magnetic nanoparticles (Chapter 2).
- Optimisation and study of the self-assembly processes to obtain multi-core flower-shaped magnetic nanoparticles (Chapters 3 and 4).
- Uptake and toxicity studies of single-core and multi-core magnetic nanoparticles in two cell lines and an animal model (Chapter 5).

The thesis is presented in the format of published papers following the UCM regulations, which can be checked on the website http://pendientedemigracion.ucm.es/bouc/pdf/900.pdf. As a result, the thesis was structured into five chapters, which are briefly outlined in what follows:

Chapter 1 is an introduction that provides the basis of the issues under discussion in the following chapters. It introduces concepts of fine particles and colloid science, and focuses on magnetic nanomaterials, more specifically on the synthesis of iron oxide magnetic nanoparticles. A complete description of the recent progress on synthesis of magnetite and maghemite nanoparticles suitable for biomedical applications can be found on Appendix 1, which is a published chapter that belongs to a book of magnetic nanoparticles. **Chapter 2** describes the preparation of anisometric single-core magnetite nanoparticles (included among these are discs, needles and rhombohedra), based on the synthesis of antiferromagnetic precursors and its reduction. **Chapter 3** illustrates synthesis strategies to produce flower-shaped multi-core maghemite nanoparticles, based on the polyol-mediated synthesis, the partial oxidation of Fe(II) in aqueous media or the reduction of Fe(acac)$_3$ by NaBH$_4$. The structure of these assemblies, in terms of core and particle size and the magnetic interactiosn present in the colloids are calculated, analysed and modelled by structural and magnetic means. **Chapter 4** selects the polyol-mediated synthesis and studies it rigorously in order to understand the key parameters governing the self-assembly and the formation mechanism of the flower-shaped nanoparticles. The heating capacities of the magnetic colloids are evaluated. **Chapter 5** describes the functionalization of some selected samples with biocompatible coatings (dimercaptosuccinic acid, DMSA; citric acid and polyethylene glycol, PEG) and the study of the uptake and toxicity in-vitro (in Hep G2, human hepatocellular carcinoma, and Caco-2, human colorectal adenocarcinoma, cell lines) and in-vivo (in a Xenopus Laevis amphibian model).

The following are the Appendices containing the supporting information of each Chapter. Then, the main conclusions of this thesis are depicted and finally, a summary of this work in English and Spanish, and a list of publications generated in the framework of this thesis, with copy of each publication, can be found.

The experimental part was carried out at the Institute of Material Science of Madrid (ICMM), belonging to the Spanish national research council (CSIC), in the group of Nanocrystals and Chemistry. Additionally, part of the results of the characterisation, arise from external collaborations within the frame of the “NanoMag” project that invariably contributed to enhance the quality of the research. The synthesis of the nanoparticles have been conducted following standard operation procedures and the characterisation of the magnetic colloids have been performed following standardized protocols.

The thesis aims to move forward in the synthesis and self-assembly of different magnetic nanostructures with the potential of being used for biomedical applications. Furthermore, it pursues to establish a relationship between structure and magnetic properties, moving towards the creation of a reference sample.

Table of contents

Nomenclature

χ	Magnetic susceptibility
δ, IS	Isomer shift
η	Viscosity
γ	Interfacial energy
τ_B	Brownian relaxation time
τ_N	Néel relaxation time
E_g	Energy of the gravitational field
A	Surface area
AC	Alternating Current
ACS	AC Susceptibility
B	Magnetic field
B_{hf}	Hyperfine field
BF	Bright field
CA	Contrast Agent
D_h	Hydrodynamic size
D_{SD}	Single-domain diameter

DC	Direct Current
DF	Dark field
DIW	Distilled water
DLS	Dynamic Light Scattering
DLVO Theory	Derjaguin-Landau-Verwey-Overbeek Theory
E_i	Internal Energy
E_s	Surface Energy
E_T	Thermal energy
E_{tot}	Total Energy
ELISA	Enzyme-linked immunosorbent assay
f	Frequency
FC	Field cooling
FM	Ferro/ferri-magnetic
FTIR	Fourier transform infra-red spectroscopy
H	Field strength
H_c	Coercive field
HF	Hyperfine splitting
Hmox1	Heme oxygenase 1
HR-TEM	High Resolution Transmission Electron Microscopy
HS	Hollow Sphere
ICP-OES	Inductively Couple Plasm-optical emission spectroscopy
ILP	Intrinsic Loss Power
IRP	Iron regulatory protein
LO	Longitudinal Optical
M	Magnetisation

M v H	Isothermal magnetisation
M v T	Magnetisation versus Temperature
M_r	Remanent magnetization
M_s	Saturation magnetization
MC	Multi-Core
MFH	Magnetic Fluid Hyperthermia
MNPs	Magnetic Nanoparticles
MRI	Magnetic Resonance Imaging
MS	Mössbauer Spectroscopy
MTT assay	methyl thiazol tetrazolium bromide assay
NF	Nanoflower
NMR	Nuclear Magnetic Resonance
NPs	Nanoparticles
QS	Quadrupole splitting
r_1	Longitudinal relaxation time
r_2	Transversal relaxation time
RCF	Relative Centrifugal Field
rpm	Revolutions per minute
RT	Room temperature
SAED	Selected area electron diffraction
SAR	Specific Absorption Rate
SC	Single-Core
SEM	Scanning Electron Mcroscopy
SP	Superparamagnetic
T_B	Blocking temperature

T_C	Curie Temperature
TEM	Transmission Electron Microscopy
TGA	Thermogravimetric analysis
TO	Transversal Optical
V_H	Hydrodynamic volume
VSM	Vibrating Sample Magnetometer
XRD	X-Ray Diffraction
ZFC	Zero field cooling
ZP	Zeta-Potential
V	Volume

Part A

Introduction

1

General Introduction

1.1 Fine particles, colloids and their characteristics in the nanometric scale

Materials with structure at the nanoscale have gained tremendous interest in research in the last six decades, since they often have unique optical, electronic, magnetic or mechanical properties that differ from their corresponding bulk material.[1] This notion was brought in 1959 by Richard Feynman, a physicist who introduced this particular "universe" in his lecture: “There’s plenty of room at the bottom”.[2] Suddenly, a new and unexplored scale was shown. The understanding and control of the unique properties at the nanoscale have been investigated, not only for fundamental studies, but more importantly for their potential technological exploitation.

Nanostructured materials are one of the main products of nanotechnologies and are defined as a material with one, two or three external dimensions in the nanoscale (“Vocabulary-Part 4: Nanostructured materials” ISO/TS 80004-4:2011). Some of the most commonly studied nanomaterials are synthetic nanoenzymes, fullerenes, graphene nanostructures and inorganic nanoparticles. The importance of nanomaterials rely on the possibility of interacting with biological entities such as proteins, antibodies, viruses, genes, bacteria, etc., due to its small size (Figure 1.1).

Some technologies require the nanomaterials to be used in the form of powder and some others in the form of colloidal suspensions. For its part, although colloids are now known to be involved in a wide range of phenomena (platelet and cell adhesion, membrane transport, phagocytosis, blood rheology, immunology, bone regeneration, photosynthesis, etc.) they remained largely unrecognised until about a century and a half ago,[3] as they are an intermediate class of materials lying between bulk and molecularly dispersed systems. There are different kinds of colloids: in the form of emulsions, sols, aerosols, gels and foams. In all of them, one component is finely dispersed in another but the degree of subdivision does not approach that in simple molecular mixtures.[4] In the last three decades colloids

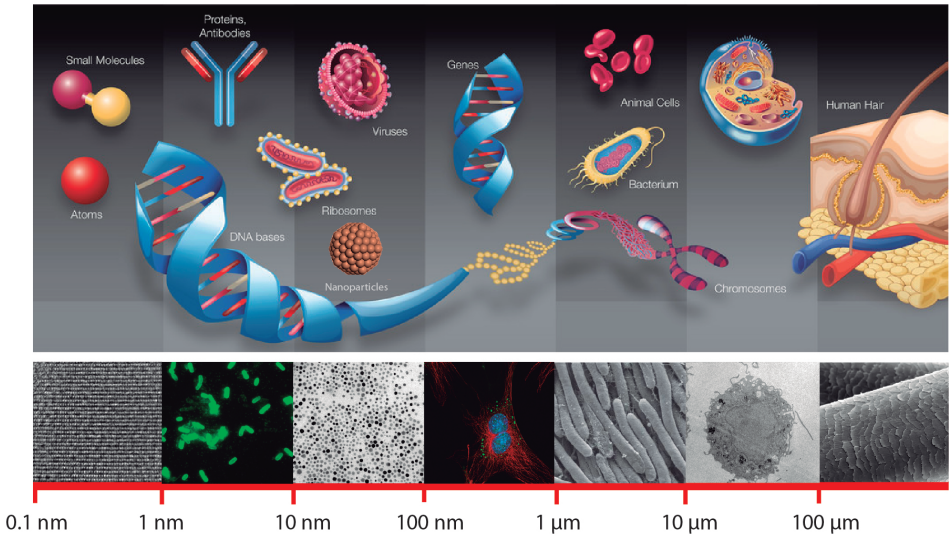

Figure 1.1: From the micro to the nanoscale: sketch of some entities that are nanostructured, and their corresponding electron microscopy images.

of nanomaterials have been developed and explored.

In the particular case of inorganic nanoparticles, when forming a colloid, they are the dispersed phase (or discontinuous phase), and are distributed uniformly in a finely divided state in a dispersion medium (or continuous phase). Faraday prepared the famous gold sols of different colour as early as 1857 and understood their particulate nature.[5] Since then, scientists engaged in colloid research were fascinated with “monodispersed” systems. The synthesis of many different uniform dispersions of elements (sulfur, selenium, silver, etc.)[6] or compounds (silica, tungstic acid, barium sulfate, etc.)[7] was reported in the literature over those years. All these preparations were based on the “trial and error,” with no common underlying scientific principles. The only exception were polymer colloids, traditionally known as latexes, which had been produced in large quantities as exceedingly uniform spherical particles by emulsion or dispersion polymerization. In view of the interest in such systems, much effort has been invested in developing processes and techniques that would yield well-defined colloidal dispersions,[8] by drawing on principles which include physical, chemical or combined physical-chemical approaches.

The effort placed on developing techniques to prepare dispersions of different shapes and chemical composition, consisting of particles of narrow size distributions[9] is because the properties of partic-

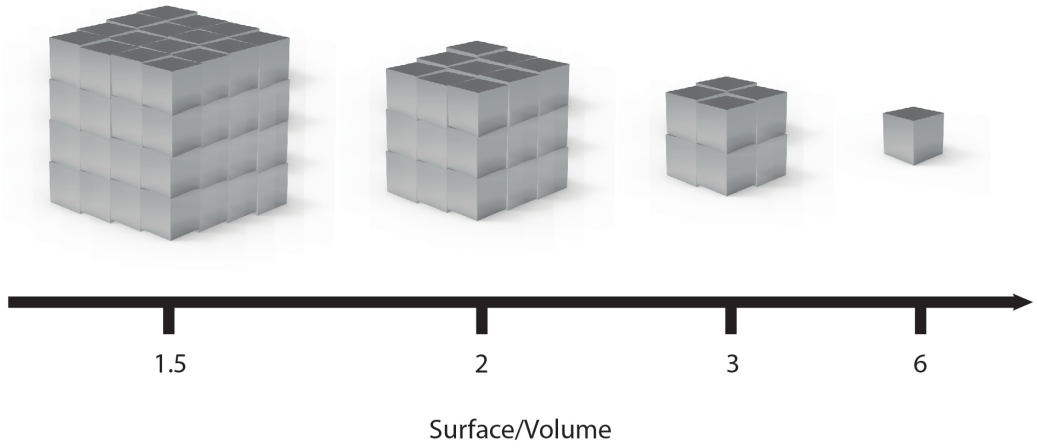

Figure 1.2: Change of surface-to-volume (A/V) ratio associated with the decrease in size: from a cube with a volume of 64 l^3 to a cube of a volume of 1 l^3, there is an increase of the surface-to-volume ratio of the 75 $\%$.

ulate materials are critically determined by their mean size, size distribution, external shape, internal structure, and chemical composition.[10]

The first critical property is the size, since many characteristics of a material are dramatically affected by varying its dimensions.[9] Generally, this can be readily understood from a simple consideration. The total energy of any system, (E_{tot}), consists of two contributions, the internal energy, E_i, and the surface energy, E_s.

$$E_{tot} = E_i + E_s \tag{1.1}$$

$$E_{tot} = e_i V + \gamma A \tag{1.2}$$

E_{tot} can be written as in Eq. 1.2, where e_i is internal energy per unit volume, and γ is the interfacial energy per unit surface area, while V and A are the total volume and area of the dispersed matter, respectively. The contributions of the two terms are not always equal; depending on the conditions, one or the other may prevail. It is easily seen that the dominance of these contributions depend on the geometric factor. The above quation 1.2 expressed per unit volume, reads

$$E_{tot} = e_i + \gamma \frac{A}{V} \tag{1.3}$$

Since e_i and γ are intrinsic properties of a material, the only variable quantity is A/V. If this ratio is large, the second term becomes significant (e.g., A/V $\sim 10^4$ – 10^7 cm^{-1}). The properties of a material

are greatly affected by the surface energy contribution to the total energy of the system. It is obvious that the large value of A/V can be achieved by decreasing the size of a material (Figure 1.2), having one, two or three dimensions rather small, resulting in films, fibres, and fine particles.

The second critical parameter to consider is shape. This parameter is associated with the mechanisms of solid phase transformation and particle growth.[11] Various processes involving interfaces can be explained by the geometry of a solid, such as absorption, adhesion, (hetero)-coagulation, corrosion, and catalysis, to mention a few. Besides influencing many chemical processes, the variation of the geometry of a nanomaterial has accounted for a variation of its physical properties in different aspects: in terms of interaction with electromagnetic radiation (one good example are the surface plasmon polaritons of gold nanorods[12]), the magnetisation dynamics in the presence of an external magnetic field (one good example are maghemite spindles used for magnetic recording since this material provides enhanced coercivity[13]), etc. Finally, other important parameters such as internal structure and chemical composition are also relevant for most applications and depend on a great extent on the precursors and the chosen synthesis route.[14]

In summary, the synthesis of particulate materials and control of the up above mentioned characteristics may constitute the background for the essential development of colloid science and pertinent industries. Scientists aim to learn how to fabricate “monodispersed” fine particles that form systems of exact and reproducible characteristics for a variety of uses. These achievements are especially important in the manufacture of high-quality products requiring stringent specifications of properties. [15]

1.2 Magnetic Nanoparticles

Hereinafter, magnetic nanoparticles are the case of study. This nanomaterial presents some interesting features and advantages that arise from its chemical composition and atomic structure. First, the most important feature is that magnetic nanoparticles obey Coulomb’s law,[16] and this means that they can be manipulated by an external magnetic field gradient. Moreover, magnetic nanoparticles can be made to resonantly respond to a time-varying magnetic field, with advantageous results related to the transfer of energy from the exciting field to the nanoparticle.[17] Finally, magnetic nanoparticles affect the relaxivity of surrounding protons. Based on these features, magnetic nanoparticles are emerging functional materials in material science industry and biomedicine.

As follows, the origin of magnetism in materials and the types of magnetism are depicted. Then, it is described how the magnetic properties of a particle are affected by its size, shape and the magnetic interaction with other particles (interparticle interaction). After, magnetic colloids are presented: the forces that come into play in solution and how to achieve stability and the types of colloids (single-core and multi-core). Finally, the characterisation methods of magnetic nanoparticles are listed, focusing on Mössbauer spectroscopy and AC Susceptibility, as they can be useful characterisation techniques to obtain information about the nature of the iron oxide and other magnetic NPs, and it allows their study

in complex matrixes, respectively.

1.2.1 What is the origin of magnetism in materials?

The fundamental source of magnetic behaviour in a material is the magnetic moment of the electrons of atoms forming molecules and crystals.[18] O, Cr, Fe, Mn, Co, Ni, and some rare earth elements show magnetic ordering. Compounds are diamagnetic when they contain no unpaired electrons. Free ions or molecular compounds that contain one or more unpaired electrons are paramagnetic. Exchange interaction among magnetic moments can occur in clusters and infinite lattices, resulting in ferromagnetism, antiferromagnetism or ferrimagnetism depending on the relative orientations of the individual spins. If a magnetic material is placed in a magnetic field of strength H, it is magnetised according to Maxwell's equations:

$$B = \mu_0(H + V) \tag{1.4}$$

This, defines the relationship between B, H and M. Note that μ_0 is the permeability of free space, and the magnetization $M = m/V$ is the magnetic moment per unit volume, where m is the magnetic moment on a volume V of the material. All materials are magnetic to some extent, with their response depending on temperature and, as above introduced, on their atomic structure. They may be conveniently classified in terms of their volumetric magnetic susceptibility, χ, which describes the magnetisation induced in a material by H. In SI units volumetric χ is dimensionless and both M and H are expressed in A·m^{-1}.

$$M = \chi H \tag{1.5}$$

Thereby magnetic materials can be divided into diamagnetic, paramagnetic, ferro/ferrimagnetic and antiferromagnetic. Figure 1.3 summarises the field dependence magnetization and temperature dependence susceptibility for the different types of magnetism. For diamagnets, χ does not depend on the temperature and it lies in the range of -10^{-6}-10^{-3} and is always negative. For paramagnets, χ has low values. The diamagnetic and paramagnetic materials have zero magnetization at any temperature in the absence of the external magnetic field.

Zero-field (spontaneous) magnetization takes place only in "strong" magnetic materials below the Curie (or N/'eel) temperature, or temperature at which certain materials lose their permanent magnetic properties, due to long-range ordering of magnetic moments. This is the case of ferri and ferromagnetism and its origin lies in the quantum mechanical exchange forces. While ferromagnetism has only one magnetic lattice composed of parallel dipoles (Figure 1.3), ferrimagnetism arises from the considered as superposition of two oppositely directed magnetic sublattices. In the case of ferromagnets, a spontaneous magnetization can be explained by the net magnetization that exists inside a uniformly

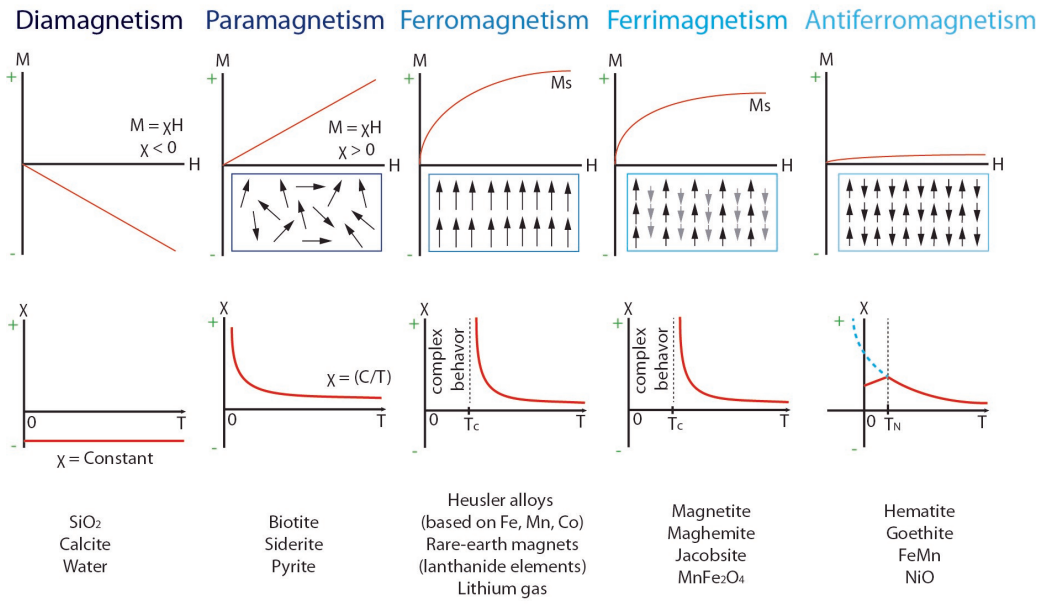

Figure 1.3: Field dependence of magnetization and temperature dependence of susceptibility for the different types of magnetic materials. Inset, the atomic structure of each material is found.

magnetized microscopic volume in the absence of a field. The magnitude of this magnetization, at 0 K, is dependent on the spin magnetic moments of electrons. A related term is the saturation magnetization (M_s) which we can measure in the laboratory. The saturation magnetization is the maximum induced magnetic moment that can be obtained in a magnetic field (see ferro and ferrimagnetism M v H graphs at Figure 1.3); beyond this field no further increase in magnetisation occurs. Saturation magnetisation is an intrinsic property dependent on temperature. Even though electronic exchange forces in ferromagnets are very large, thermal energy eventually overcomes the exchange and produces a randomizing effect. This, as mentioned above, occurs at a particular temperature called the Curie temperature (T_C). Below the Curie temperature, the ferromagnet is ordered and above it, disordered. The saturation magnetization goes to zero at the Curie temperature.

In addition to the Curie temperature and saturation magnetization, ferromagnetic and ferrimagnetic materials can retain a memory of the applied field once it is removed, as observed in Figure 1.4. This behaviour is called hysteresis and a plot of the variation of magnetization with magnetic field (field dependence magnetization) is called a hysteresis loop, which is an irreversibility in the magnetization process that is related to: the pinning of magnetic domain walls at impurities, grain boundaries within the material as well as to intrinsic effects such as the magnetic anisotropy of the crystalline lattice. An example of a hysteresis curve is given in Figure 1.4. In the absence of an applied magnetic field, the demagnetized state is the stable state in large ferromagnetic crystals. At extremely high applied fields,

the magnetization approaches the saturation magnetization value M_s. When the field is decreased, the magnetization does not follow the initial magnetization curve and at zero field a non-zero (remanent) magnetization M_r prevails. If the field is applied in the reverse direction, the magnetization is equal to zero at a characteristic coercive field (-H_C). When the negative field increases still further, the magnetization reaches the saturation value again.[19] Ferro and ferrimagnetic specimens should have very large total magnetic moment even in the absence of an external magnetic field. Actually, this is not the case. The reason is the so-called domain structure of ferromagnets, as explained by Landau and Lifshitz, due to in magnetic field energy.[20]

Lastly, antiferromagnets are a form of identical oppositely directed magnetic sublattices. As a result, their total magnetic moment vanishes. However, slight deviations from ideal antiferromagnetism can exist if the anti-parallelism is not exact. If neighbouring spins are slightly tilted ($<1^\circ$) or canted, a very small net magnetization can be produced. This is called canted antiferromagnetism and hematite is a well-known example. In antiferromagnets, a small positive susceptibility varies in a peculiar way with temperature. Generally, antiferromagnetic order may exist at sufficiently low temperatures, vanishing at and above a certain temperature, the Néel temperature.

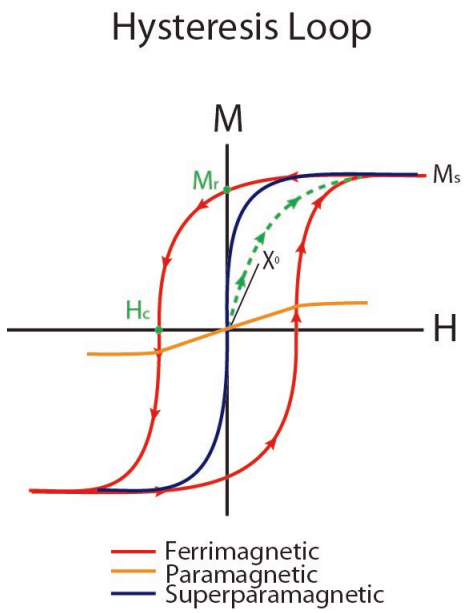

Figure 1.4: Field dependence of magnetization curve of the different types of magnetic materials.

Lastly, magnetite phase has another magnetic feature, the Verwey transition. Due to the strong interaction between electrons, charges are localized on different sites leading to a disproportionation and an ordered superlattice. The charge order transition is accompanied by symmetry breaking and may

lead to ferroelectricity. It is often found in close proximity to superconductivity and colossal magnetoresistance. This long range order phenomena was first discovered in magnetite by Verwey in 1939.[21] He observed an increase of the electrical resistivity by two orders of magnitude at low temperature (T = 125 K), suggesting a phase transition which is now well known as the Verwey transition. The charge ordered structure of magnetite was solved in 2011 by a group led by Paul Attfield.[22] These changes in its magnetic, electrical, and thermal properties are due to crystal lattice changes from a monoclinic structure to the cubic inverse spinel structure that persists at room temperature.[23] The phenomenon is associated with magnetocrystalline anisotropy constant changes in sign, from positive to negative. The temperature and physical expression of the Verwey transition are highly sensitive to the stress state of magnetite and the stoichiometry. Non-stoichiometry in the form of metal cation-substitution or partial oxidation can lower the transition temperature or suppress it entirely.[24] This is considered as a fingerprint of highly crystalline, at least close to stoichiometric, magnetite particles, since maghemite phase does not display this feature.

1.2.2 Size effect

Bulk ferromagnetic specimens consist of a number of small regions, each spontaneously magnetized to saturation. These regions are called "domains". The boundaries between domains are called domain walls. The domain walls must not be regarded as infinitely thin surfaces but rather as zones of transition of finite thickness in which the magnetization rotates coherently from the direction in one domain to that in the next domain.[25] The domain structure can be favorable energetically depending on the balance of magnetostatic energy and the exchange energy relating to domain walls and the magnetization.

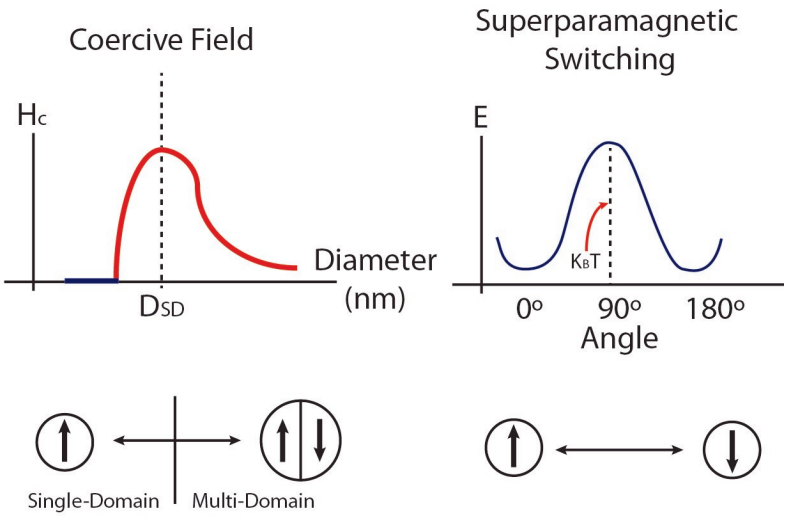

Figure 1.5: Size effect on magnetic nanoparticles: coercive field (left) and relaxation time (right).

The reason for the formation of domain walls relies on the internal energy, which is reduced by dividing a ferromagnetic material into magnetic domains. The magnetization directions of domains are determined mainly by the so-called crystalline anisotropy. The atoms energy in crystals depends on the orientation of the magnetic moment with respect to crystallographic axis. The directions for which the energy has minimum/maximum value are called directions/axes of easy/hard magnetization.

As the dimensions of the specimen are diminished, the relative contributions of the various energy terms to the total energy of ferromagnetic specimen are changed, and the energy of domain walls becomes more important than the magnetostatic volume energy. There is a specimen critical size D_{SD}, at which it is favorable energetically to eliminate the domain boundaries.[26] This is termed as a single magnetic domain (so-called single-domain particle). Particles with size below this critical value D_{SD} have decreased coercive force with decreasing particle size (Figure 1.5 left). When it reaches a zero value, the specimen is in the superparamagnetic regime. Superparamagnetism is a form of magnetism, which appears in small ferromagnetic or ferrimagnetic nanoparticles. In sufficiently small nanoparticles, magnetization can randomly flip direction under the influence of temperature. The typical time between two flips is called the Néel relaxation time and it is defined as:

$$\tau_N = \tau_0 exp \frac{KV}{k_B T} \tag{1.6}$$

where τ_N is thus the average length of time that it takes for the nanoparticle's magnetization to randomly flip as a result of thermal fluctuations. τ_0 is a length of time, characteristic of the material, called the attempt time or attempt period (its reciprocal is called the attempt frequency); its typical value is 10^{-9}–10^{-12} second for non-interacting NPs.[27] K is the nanoparticle's magnetic anisotropy energy density and V its volume. KV is therefore the energy barrier associated with the magnetization moving from its initial easy axis direction, through a "hard plane", to the other easy axis direction. k_B is the Boltzmann constant. T is the temperature. This length of time can be anywhere from a few nanoseconds to years or much longer. In particular, it can be seen that the Néel relaxation time is an exponential function of the grain volume, which explains why the flipping probability becomes rapidly negligible for bulk materials or large nanoparticles.

In the absence of an external magnetic field, when the time used to measure the magnetization of the nanoparticles is much longer than the Néel relaxation time, their magnetization appears to be in average zero: they are said to be in the superparamagnetic state. In this state, an external magnetic field is able to magnetize the nanoparticles, similarly to a paramagnet. However, their magnetic susceptibility is much larger than that of paramagnets (Figure 1.5). Normally, any ferromagnetic or ferrimagnetic material undergoes a transition to a paramagnetic state above its Curie temperature. Superparamagnetism is different from this standard transition since it occurs below the Curie temperature of the material. Blocked state occurs when the time used to measure the magnetization is equal to Néel relaxation time. In several experiments, the measurement time is kept constant but the temperature is

varied, so the transition between superparamagnetism and blocked state is seen as a function of the temperature. This temperature is called the blocking temperature and reads as:

$$T_B = \frac{KV}{k_B ln \frac{\tau_m}{\tau_0}} \tag{1.7}$$

The superparamagnetic blocking temperature (T_B) is defined as the temperature at which the superparamagnetic relaxation time equals the timescale of the experimental technique used for the study of the magnetic properties. Above T_B, superparamagnetic relaxation can be considered negligible, but the magnetization direction may still fluctuate in directions close to the easy axes at θ = 0° and θ = 180°. In other words, in that point, the magnetocrystalline anisotropy energy, E = K V becomes small and comparable to the thermal energy $E_T = k_B T$ (where k_B is the Boltzmann constant), the magnetization oscillates by thermal excitations and easy directions vanish. A simplified graphical model is shown in Figure 1.5 right.

Superparamagnetism occurs in nanoparticles which are single-domain, i.e. composed of a single magnetic domain. This is possible when their diameter is in the range of 3–65 nm,[28] depending on the materials. In this condition, it is considered that the magnetization of the nanoparticles is the sum of all the individual magnetic moments carried by the atoms of the nanoparticle. Because of the nanoparticle's magnetic anisotropy, the magnetic moment has usually only two stable orientations antiparallel to each other, separated by an energy barrier. The stable orientations define the nanoparticle's so called "easy axis". At finite temperature, there is a finite probability for the magnetization to flip and reverse its direction.

Lastly, it must be noted that when dispersed in a carrier liquid, the particle magnetic moment can be decoupled from the physical particle rotation in the liquid. This is the case of Néel relaxation (described in Eq. 1.5), when only stochastic rotation of the magnetic moment occurs. On the other hand, the particle moment can be physically blocked in a specific particle direction. If so, the magnetic relaxation occurs at the same rate as the particle rotation in the liquid (Brownian relaxation). The Brownian relaxation time (stochastic rotation of the total particle) can be expressed by:

$$\tau_B = \frac{3V_H \eta}{k_B T} \tag{1.8}$$

with the particle hydrodynamic volume V_H and the viscosity of the carrier liquid η. The parameters that determine whether we have Néel or Brownian relaxation of a nanoparticle system dispersed in the carrier liquid at given temperature, are the sizes and shapes of the nanoparticles, the magnetic material properties (through the magnetic anisotropy) and the viscous properties of the liquid.

1.2.3 Shape effect

Distortions of particle shape can induce additional anisotropy, stabilizing (or destabilizing) the single-domain state. Small deviations from uniformity in the magnetization field within the nanoparticles can play an essential role in determining its magnetic properties (susceptibility, anisotropy, hysteresis features, etc.).[29] Moreover, the surface effects can be also shape-dependent since the relative number of surface atoms depends on the particle shape.[30] The configuration of the magnetization (inside a single-domain particle) depends strongly on the magnetic anisotropy and particle's shape. On the one hand, if the ferromagnetic ellipsoidal (or spherical) particle has a negligibly small crystalline anisotropy, the atomic magnetic moment may be expected to point along closed rings,[31] so that total magnetic moment of the particle is equal to zero. On the other hand, if the crystalline anisotropy is relatively large most of the atomic magnetic moments may be expected to lie along easy directions. For example, in case of the strong uniaxial anisotropy, the single-domain ellipsoidal particle has uniform magnetization (along unique easy axis) and can act as a permanent magnet.

1.2.4 Interparticle interaction effects

In nanostructured magnetic materials, interactions between nanoparticles often play an important role. Interparticle interaction effects greatly depend on the distance between the magnetic nanoparticles. For long distances (assuming therefore a non-interacting NPs system), the magnetic behaviour is determined by the superparamagnetic relaxation at finite temperatures (Figure 1.6 a). However, those cases when the distance between the magnetic NPs is shorter, the superparamagnetic relaxation can be altered by magnetic dipole interactions and by exchange interactions between particles.[32]

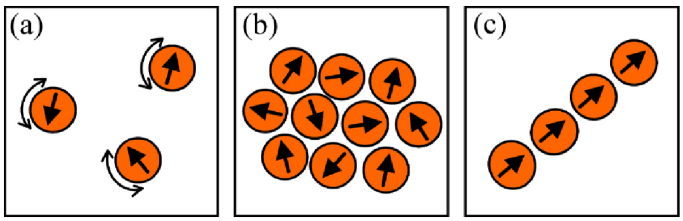

Figure 1.6: Interparticle interactions: (a) Isolated nanoparticles dominated by superparamagnetic relaxation. (b) Interacting nanoparticles dipole moments without alignment. (c) Nanoparticles forming a chain with aligned dipole moments.

The dipole–dipole interaction is the most important type of magnetic interactions in nanoparticle systems due to two main features: long-range character and rather large value of the typical magnetic moment of an individual nanoparticle. In samples with high concentrations of magnetic nanoparticles, which would be superparamagnetic if they were non-interacting, magnetic dipole interactions can result in ordering of the magnetic moments of the nanoparticles below a critical temperature.[33] Dipolar

interactions are markedly anisotropic and promote the formation of aggregates (Figure 1.6 b) or can favour ferromagnetic or antiferromagnetic alignments of the magnetic moments (Figure 1.6 c). When interparticle interactions are sufficiently strong, the blocking processes (related to individual particles) are no longer independent and not the energy barrier coming from the anisotropy contributions of each particle, but the total energy of the assembly must be considered. Consequently, an increase in the blocking temperature is expected.[34, 35]

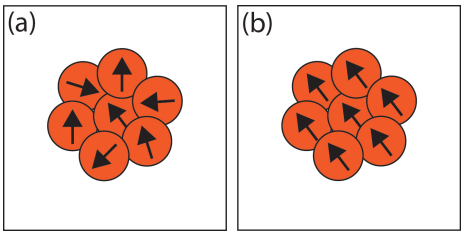

Figure 1.7: Interparticle interactions: exchange interaction (a) randomly oriented and (b) commonly orientated.

If there is close contact between surface atoms of neighboring particles, the exchange interactions are pronounced also. For superparamagnetic nanoparticles in ferrofluids or solid polymer matrix, where there is not direct contact between the particles, exchange interaction mechanisms can be discarded. In some cases, the crystals may have close contact and be attached without (Figure 1.7 a) or with (Figure 1.7 b) a common orientation, and in the latter case, both the crystallographic and the magnetic order continue across the interface. [36] This would imply magnetic correlation length in the direction of the attachment, extended over several particles, obtaining larger particle size (i.e., the magnetic and the crystallographic correlation).[32]

1.2.5 Magnetic colloids and their stabilisation

Controlling a liquid by an external magnetic field was a challenging idea which implied numerous possibilities in basic research and in many practical uses. However, usual liquid materials are diamagnetic and, in the best case, if their atoms possess unpaired electrons (such as transition metals or stable organic ion radicals) they are paramagnetic, whose typical magnetic susceptibility is low. These small susceptibilities imply that the response of the liquid system to an applied magnetic field is weak even if very high field strength is used. Therefore, ferro- or ferrimagnets should be selected for the control of a liquid. This is why there has been a development of suspensions of nanosized magnetic particles[37] in appropriate carrier liquids.

In order to synthesize a ferrofluid, some major problems must be solved. They must be superparamagnetic (with typical diameters of around 10 nm) and be magnetically stable, e.g. no transition from ferro- or ferrimagnetic state to an antiferromagnetic state must appear due, for instance, to oxidation.

Lastly, magnetic particles have to be brought into a stable solution and the suspended particles require a high overall magnetic moment. This former aspect means that the particles have to stay homogenously distributed over the sample even for long times.[13]

The main hindrance for a long-term stability is sedimentation of the particles. The sedimentation can either be driven by the difference between the magnetic particles and the carrier liquid or by magnetic field gradients attracting the magnetic particles and accelerating them relative to the carrier liquid. A stable solution is achieved if the thermal energy of the particles is able to keep them distributed. That means that the thermal energy E_T = k_B T (k_B Boltzmann's constant, T: absolute temperature) has to be greater than their energy in the gravitational field or in a magnetic gradient respectively. The energy of the particles in the gravitational field is given by:

$$E_g = \Delta\rho g V h \tag{1.9}$$

where Δ ρ denotes the density difference between the particles and the carrier liquid, g is the gravitational acceleration, h a typical dimension of the sample and V = $\pi d^3/6$ is the volume of the magnetic particle with d being the diameter. Comparing the thermal and gravitational energy of the particles one obtains an upper limit for the particle size by:

$$d \geq \sqrt[3]{\frac{6k_BT}{\pi\Delta\rho g h}} \tag{1.10}$$

Assuming magnetite particles in water ($\Delta\rho \approx$ 4 x 10^{-3} kg·m^{-3}) and typical height of the sample of h = 0.1 m (g = 9.81 ms^{-2}, T = 300 K) one finds that particles with a diameter less than approximately 12 nm are stable against sedimentation in the earth's gravitational field.

The second drawback in magnetic particles stability in solution is agglomeration. Interparticle forces would lead to a growth of the particle size, which would thus destabilize the suspension and sedimentation would be likely to take place. Agglomeration processes in colloidal suspensions of magnetic particles can be either driven by magnetic particle-particle interactions or by Van der Waals interaction. The latter is a distance-dependent interaction, which is more susceptible of being perturbed. Van der Waals forces quickly vanish at longer distances. Hence, stability is achieved when the thermal energy of two particles is larger than their maximal magnetic interaction energy in contact. This energy diverges for interacting particles with a normalized surface-surface distance l = $2\delta/d$. Although Van der Waals forces described by Fritz London are applicable to atoms, several scientists soon realised that his definition could be extended from the interaction of two molecules or particles. The extended theory is named after H. C. Hamaker who derived the interaction between two spheres.[38] The Hamaker constant represents the magnitude of Van del Waals interaction and depends on the number densities of the two interacting kinds of particles and the coefficient in the particle–particle pair interaction. Works have shown that many inorganic systems are characterised by relatively high Hamaker constants,[39, 40]

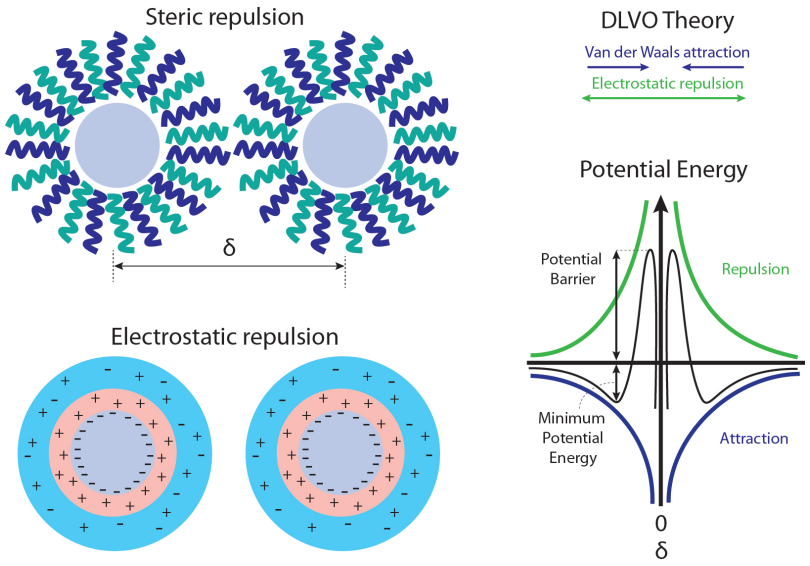

Figure 1.8: Stability of colloids: steric and electrostatic repulsion and DLVO theory, in which the forces that take place between two charged surfaces interacting through a liquid medium are described.

hence making this interaction of significant importance.

Therefore, colloidal stability of a ferrofluids requires that the particles are protected from coming into contact. This is achieved by: i) steric repulsion and ii) electrostatic repulsion (Figure 1.8). The former protection is provided by surfacting the particles with molecules. If the particle surface distance δ falls below two times the thickness of the surfactant layer, a steric repulsion will appear. The electrostatic repulsion is the second way of stabilizing a colloid and it is based on the electrical double layer surrounding the surface of two bodies. Surfaces may become electrically charged by a variety of mechanism, to name a few, ionisation of surface groups, differential solution of ions from the surface of a sparingly soluble crystal, isomorphous substitution, charged crystal surfaces, specific ion adsorption, etc.[3] This ionic atmosphere which is developed around a charged colloid particle is called electrical double layer. The charge on the particle surface is distributed over its surface and is just balanced by the total charge in the double layer in which there is an excess of oppositely charged ions (counter-ions). In this case, when two similarly charged colloid particles, with their associated double layer, move towards one other they will begin to “feel” on another’s presence as soon as any appreciable overlap of interaction will develop steadily as they approach.

Thus, the total potential energy of the system is described by the DLVO theory[41, 42] (Figure 1.8 right) and it is the sum of the attraction potential and the repulsion potential. When two particles approach each other, electrostatic repulsion increases and the interference between their electrical double layers increases. Meanwhile, the Van der Waals attraction increases as they get closer. At each dis-

tance, the net potential energy of the smaller value is subtracted from the larger value. The combination of these forces results in a deep attractive well, which is referred to as the primary minimum. At larger distances, the energy profile goes through a maximum energy barrier, and subsequently passes through a shallow minimum, which is referred to as the secondary minimum. At maximum energy barrier, repulsion is greater than attraction. Particles rebound after interparticle contact, and remain dispersed throughout the medium. The maximum energy needs to be greater than the thermal energy. Otherwise, particles will aggregate due to the attraction potential.

In the particular case of iron oxides surface, it contains structural and functional groups (sites) which interact with gaseous and soluble species, and could interact with molecules in order to prevent them from agglomeration by any type of repulsion (steric or electrostatic). The number of available reactive sites per unit mass solid depends on the specific surface area of the sample.[14] This property influences the reactivity of the oxide, particularly its dissolution and dehydroxylation behaviour, adsorption interactions and phase interactions and even its thermodynamic stability.

1.2.6 Single-core and multi-core magnetic nanoparticles

Magnetic nanoparticle colloids have been recently divided into single-core nanoparticles (with only one magnetic core per particle) and multi-core nanoparticles (with several magnetic cores per particle). Single-core particles are usually coated by some chemical or biochemical active surface layer that help to have the particles isolated. On the contrary, multi-core nanoparticles have a matrix that binds the magnetic cores together to form the final particle, and they are usually coated by a surface layer. Above the superparamagnetic regime, the nanoparticles will have a permanent magnetic moment even at RT, which usually implies some degree of agglomeration. This agglomeration, unlike multi-core particles, can be temporarily reversed (e.g. by mechanical stirring or sonication), however the agglomeration is only avoided when steric or electrostatic repulsion is successfully achieved. These types of magnetic colloids are schematised in Figure 1.9.

Depending on the synthesis route to produce magnetic nanoparticles and to stabilize them, the nanoparticles can be single-core, aggregated single-core or multi-core. The structure of a colloid of magnetic particles, applicable to other type of inorganic nanoparticles, is composed of a magnetic core (monocrystalline or polycrystalline) that is fixed in a matrix and may have a coating (chemical, biochemical or an active surface layer), which all together form the particle size. In addition, the particle has a hydration layer in solution, forming the final hydrodynamic size (Figure 1.10). In the case of multi-core NPs, the structure of the colloid is different, since an initial aggregate exist. Note that the cores might be in direct contact or might by separated by the matrix.

These two types of colloids show different magnetic properties, derived from their distinct structure. On the one hand, for single-core NPs, increasing packing density (decreasing distance between particles) leads to decreasing coercivity, remanence, and hysteresis losses of the single particle. These

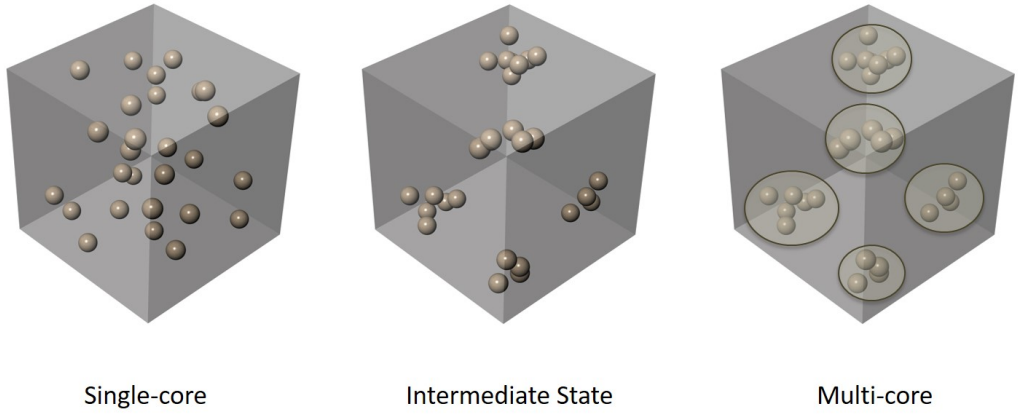

Figure 1.9: Types of magnetic nanoparticle colloids.

decreases are due to increasing dipole–dipole interactions which disturb the energy landscape by occurrence of local energy minima.[43] On the other hand, for superparamagnetic particles, which show weak dipole–dipole interactions, at higher concentrations, a stronger tendency to form agglomerates can be observed due to exchange interactions instead. These particles behave like a particle with an effective volume larger than the single core showing ferri/ferromagnetic behaviour with hysteresis. The resulting multicore NPs are a special type of particles with behaviour that cannot be described in the classical sense by superparamagnetic or ferrimagnetic theory.

Particles consisting of a number of superparamagnetic cores (i.e. around 10 nm) each which forms clusters a few tens of nanometers large,[44, 45] have overall ferrimagnetic behaviour, but coercivity and remanence are significantly lower than for single core particles of comparable size.

1.2.7 Characterisation of magnetic nanoparticles

One of the greatest challenges in materials science is determining how best to characterize the increasing numbers of complex structures and materials being created by scientists. Without agreed upon methods of characterization, both reproducibility and quality control are rendered impossible, and the impact of the entire field is endangered by the inability to replicate data, syntheses, and properties. Moreover, when physical parameters determined through characterisation are to be applied in energy conversion, elsewhere, or modelled and understood with theory and simulation, having standards of characterisation would enable better connections between laboratories, and better understanding of the synthesis and application of the generated materials. Due to the larger variety of nanomaterials, there is not one single characterisation method for all materials[15, 46] and often more than one technique is needed to describe the properties displayed by a nanomaterial. Notably, there is also not only

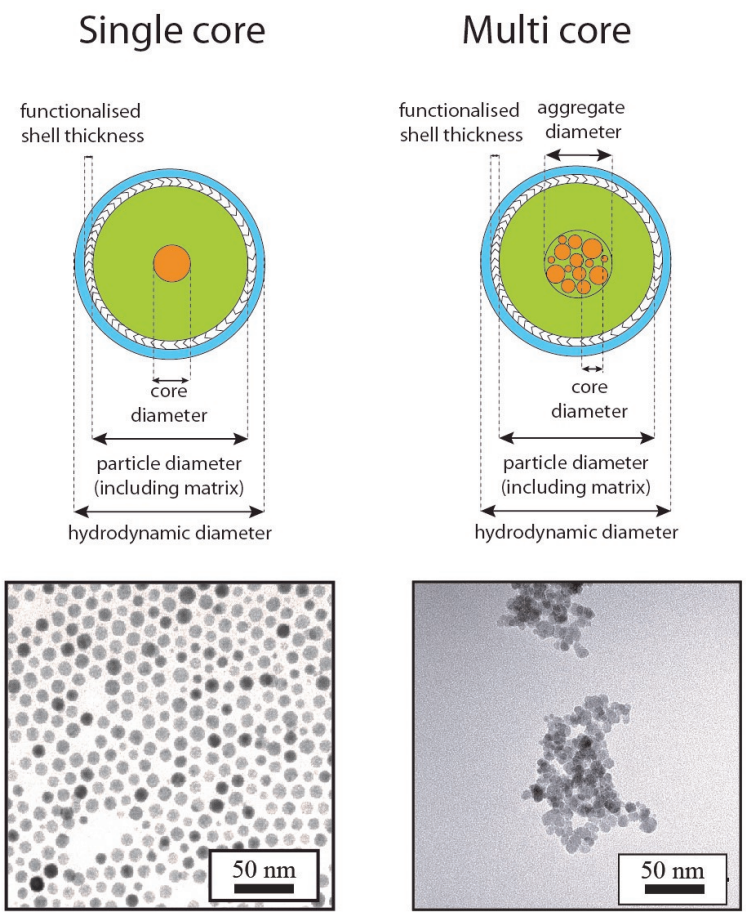

Figure 1.10: Structure of magnetic nanoparticle colloids and representative examples that exist in the literature: Single-core NPs are represented by oleic acid coated magnetite NPs synthesized by high T thermal decomposition. Multi-core NPs are represented by co-precipitation NPs post-coated with citric acid.

one “size” for nanomaterials, but different methods will lead to different “types” of sizes.[47] The objectives of the EU financed NanoMag project (http://www.nanomag-project.eu/) are to standardize, improve and redefine analysing methods of magnetic nanoparticles, focusing on magnetic iron oxides. Using a multitude of characterisation techniques, specific properties have been analyzed, focusing on both structural as well as magnetic properties. Bringing the results together gives a self-consistent picture which describes how structural and magnetic properties are interrelated.

These results have helped developing standard operating procedures (SOP) for the reliable measurement of specific physical parameters. This is a step towards standardization of magnetic colloids, which is an important concern and demand nowadays. SOPs include the following points: i) Acces-

sible physical parameters, ii) assumptions and additional input parameters needed, iii) uncertainties of the method, iv) interrelations with other methods that provide additional input data or to verify the assumptions made, and v) models.

The frequent analysis methods of magnetic colloids or their freeze-dried powders can be divided in structural and magnetic (Table 1.1). This thesis is focused on Electron Microscopy, X-Ray diffraction, Dynamic Light Scattering, Zeta Potential, Inductively Couple Plasm-Mass Spectrometry, Thermogravimetric analysis, Mössbauer Spectroscopy, DC magnetometry and Temperature and Frequency dependent AC susceptibility characterisation methods. All those methods will be briefly described (Infrared Spectroscopy will be included as well, since it is a basic technique that appears throughout this thesis), but there will be a focus on Mössbauer spectroscopy and AC susceptibility since they are useful and relevant techniques in this work.

Regarding the structural characterisation, electron microscopy is based on the interaction of a high-energy electron beam with a specimen, which produces various effects and results in a range of emitted signals. Electron microscopy is utilised for direct observation of crystal size, morphology, phase composition, and domain structure of the specimen. X-ray diffraction involves interaction of electromagnetic radiation with a wavelength of around 0.1 nm, with the atoms in the solid. As the distances between the atoms in a crystal structure are comparable with the wavelength of the radiation, crystals can diffract X-rays. In certain distances (angles of incidence) the elastically scattered rays interfere constructively, thus leading to enhanced intensity. From these patterns, the following parameters can be deduced: angle positions, width and intensity from which the nature of the oxide, its quantity (in a mixture), its unit cell parameters, and its crystallinity (crystal size and order). Dynamic Light Scattering involves a monochromatic light source that hits the magnetic particles, the light scatters in all directions (Rayleigh scattering) as long as the particles are small compared to the wavelength (below 250 nm). The scattering intensity fluctuates over time due to small molecules in solutions undergoing Brownian motion, and so the distance between the scatterers in the solution is constantly changing with time. This scattered light then undergoes either constructive or destructive interference by the surrounding particles, and within this intensity fluctuation, information is contained about the time scale of movement of the scatterers. This results in a particles size distribution, in this case, of the magnetic nanoparticles or the aggregate that they may form. IR spectroscopy arises as a result of interaction of iron oxides with electromagnetic radiation (photons) in the IR wavelength range. These interactions involve the excitation of vibrations or rotation of molecules in their ground electronic state and are associated with stretching deformations of the interatomic bonds and bending deformations of the interbond angles. The frequency depends on the rotational energy levels and the force constants of the interatomic bonds. Both the iron oxide nature and the coating material surrounding the inorganic core can be determined through this technique.

Inductively coupled plasma optical emission spectrometry (ICP-OES) is an analytical technique used for the detection of trace metals. This is achieved by ionizing the sample with inductively coupled plasma

Table 1.1: Characterisation methods of magnetic colloids or their freeze-dried powders

Structural characterisation		**Magnetic characterisation**	
Method	Acronym	Method	Acronym
X-Ray Diffraction	**XRD**	Magnetisation versus Temperature	**M v T**
Small-angle neutron X-ray scattering	**SANS**	Isothermal magnetisation	**M v H, DCM**
Small-angle neutron X-ray scattering	**SAXS**	AC Susceptibility versus Temperature	**AC v T**
Electron Microscopy	**EM**	Ferromagnetic Resonance	**FMR**
Dynamic Light Scattering	**DLS**	Magnetorelaxometry	**MRX**
Electrophoretic Light Scattering	**ELS**	Frequency dependent AC-susceptibility	**AC v f, ACS**
Zeta-Potential	**ZP**	Magnetic Particle Spectroscopy	**MPS**
Asymmetric Flow Field Flow Fractionation	**AF4**	Rotating Magnetic Field	**RMF**
Mössbauer Spectroscopy	**MS**		
Inductively Couple Plasm-optical emission spectroscopy	**ICP-OES**		
Thermogravimetric analysis	**TGA**		

and then using an optical emission spectrometer to separate and quantify those ions. For iron oxide magnetic colloids or their freeze-dried powders Fe is the measured ion. Lastly, thermogravimetric analysis is a method in which changes in physical and chemical properties of materials are measured as a function of increasing temperature (with constant heating rate), or as a function of time (with constant temperature and/or constant mass loss). TGA can provide information about physical phenomena, such as second-order phase transitions, including vaporization, sublimation, absorption and desorption. Likewise, TGA can provide information about chemical phenomena including chemisorptions, desolvation (especially dehydration), decomposition, and solid-gas reactions (e.g., oxidation or reduction). This technique allows quantifying the organic percentage of the samples as well as temperature dependent phase transformations of iron oxides (depending on the selected atmosphere, i.e. oxygen or nitrogen).

Regarding the magnetic characterisation, DC magnetometry measures the magnetisation, direction, strength, or the relative change of a magnetic field at a point of the sample. In isothermal magnetization measurements (M v H) the sample is measured at constant temperature using, e.g. a SQUID magnetometer, VSM (vibrating sample magnetometer), torque magnetometer etc. The external field is varied from positive to negative fields of magnitudes close enough to saturate the sample. The parameters possible to extract from such measurements are, the saturation magnetization (M_s), the remanent magnetization (M_r), the coercive field (H_C), the magnetic moment distribution, and, to some degree, the volume, or anisotropy energy density distribution. Moreover, it is possible to estimate where the sample goes from a nearly pure superparamagnetic state to a blocked one (achievable by measuring the field-dependent magnetization at different temperatures) and may also give an idea of the composition of the material by cooling the sample in an external field above the superparamagnetic blocking temperature and performing a field-cooled measurement, in order to observe shifts (exchange-bias) of the magnetization curves.

Moreover, ZFC/FC magnetisation curves can be conducted. ZFC curve is typically obtained by cooling in zero field from a high temperature where all particles show superparamagnetic behaviour to a low temperature and measuring the magnetisation at step-wise increasing temperatures in a small

applied field. At each temperature measurements are taken after time t_m. The FC magnetisation curve is typically obtained by measuring at stepwise-decreasing temperatures in the same small applied field after waiting t_m at each temperature. This type of measurement can be conducted in order to determine the blocking temperature of the MNPs or to study the up-above mentioned Verwey transition.

1.2.7.1 Mössbauer Spectroscopy

Mössbauer Spectroscopy is based on the magnetic behaviour of (essentially) iron in a crystal structure, and it yields information about charge and coordination of iron nuclear environment. Basically, it involves resonant absorption of γ-radiation ^{57}Fe nuclei in solid iron oxides.

Transmission ^{57}Fe Mössbauer spectra are analysed from fits of the absorption lines for the different iron sites/iron-containing phases. These fits quantify the positions, intensities and widths of the absorption lines. For simple spectra, comprising singlets, doublets and/or sextets, the line positions are determined by the following parameters: (a) the isomer shift, (b) the quadrupole splitting/shift, and (c) the magnetic hyperfine field for each iron site. The isomer shift (IS, δ) is a relative measure describing a shift in the resonance energy of a nucleus due to the transition of electrons within its s orbital (Figure 1.11, blue graph). The quadrupole splitting reflects the interaction between the nuclear energy levels and surrounding electric field gradient. Nuclei with angular quantum number (I) greater than 1/2, produce an asymmetrical electric field (produced by an asymmetric electronic charge distribution or ligand arrangement) which splits the nuclear energy levels. These appear as two specific peaks (or “doublet) in a spectrum (Figure 1.11, red graph). Lastly, hyperfine splitting is a result of the interaction between the nucleus and any surrounding magnetic field. A nucleus with spin I splits into 2I + 1 sub-energy levels in the presence of magnetic field. For example, a nucleus with spin state I = 3/2 will split into 4 non-degenerate sub-states with mI values of +3/2, +1/2, -1/2 and -3/2. Each split is hyperfine, being in the order of 10^{-7} eV. The selection rule of magnetic dipoles means that transitions between the excited state and ground state can only occur where m and I changes by 0 or 1. This gives 6 possible transitions for a 3/2 to 1/2 transition. (Figure 1.11, green graph).

Regarding the accesible physical parameters of though this technique, the most important and commonly used derived quantity is the (quantitative) phase-identification of iron-containing compounds, e.g. maghemite vs. hematite, magnetite, iron metal, iron salts etc. This is typically a “fingerprint” identification due to the technique being sensitive to iron valence, spin state, magnetic order, lattice and electron symmetry. The phase-identification provides a quantitative measure of the relative iron contents and can often be adequately achieved from the recording of a single room temperature spectrum. In the special case where the sample being measured is known to be a magnetic iron oxide, recent work has led some to believe that room temperature Mössbauer spectroscopy can be used to derive the average stoichiometry of magnetite/maghemite mixtures from the mean isomer shift (IS) of the observed spectrum – even in cases when there is no clear demarcation of constituent subspectra.

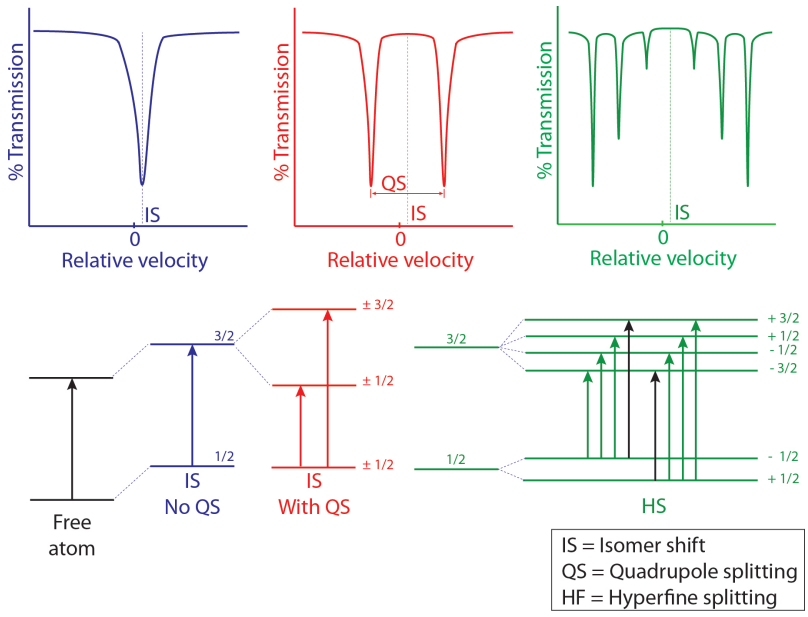

Figure 1.11: Chemical shift and quadrupole splitting of the nuclear energy levels and corresponding Mössbauer spectra. Magnetic splitting of the nuclear energy levels and the corresponding Mössbauer spectrum.

The Mössbauer signature of a blocking transition is typically the superposition of a fast-relaxation doublet and a slow-relaxation sextet. T_B is generally estimated to be the temperature at which the doublet and sextet component assume equal spectral areas. It should be noted that as the measurement time for the Mössbauer nucleus is of order nanoseconds (derived from the Larmor precession time of the nucleus), this Mössbauer T_B is typically much higher than that observed by other techniques such as ZFC magnetisation curves. In some cases more detailed physical quantities can be derived, especially when there is a high degree of knowledge of the sample being studied. These quantities include the magnetic anisotropy energy (KV, K = anisotropy constant, V = particle volume), which can be obtained for particles below T_B from spectra measured at a range of temperatures; and magnetic particle moments (m = MV, m = moment per particle, M = magnetization, V = particle volume), which can be obtained from superparamagnetic particles measured as a function of field. Mössbauer is the best technique for the detection of Fe(II) or Fe(III) and therefore for distinguishing between magnetite and maghemite at the nanoscale which is important because it can be a source of uncertainty of 10% in magnetic parameters normalize to density. Moreover, in the field of biomedicine, insufficient coating of the NPs has led to the release of iron Fe(II) into the cell from particle breakdown[48] that induces the production of hydroxyl radicals (Fenton reaction), which have shown to be toxic.[49, 50] Therefore it is important the quantification of Fe(II), which makes Mössbauer spectroscopy a powerful technique.

1.2.7.2 Temperature and Frequency dependent AC Susceptometry

In the AC susceptometry (ACS) method, an oscillating excitation magnetic field with low field amplitude (usually below about 0.5 mT so the initial susceptibility assumption is valid) is applied to the sample and the dynamic magnetic response from the sample is measured. The magnetic susceptibility (χ) is defined as the response of a material to a magnetic field (Eq. 1.14). In AC magnetic measurements, an AC field is applied to a sample and the resulting magnetic moment is measured. Because the induced samples moment is time-dependent, the AC magnetic susceptibility measurement yields two quantities: the magnitude of the susceptibility, and the phase shift. Thus, the susceptibility is described as having an in-phase, or real component (χ') and an out-of-phase, or imaginary, component (χ'').

The dynamic magnetic response can then be pictured as a complex dynamic susceptibility. The real and imaginary part of the complex susceptibility is recorded as a function of the excitation frequency or the temperature. The excitation field is usually produced by ordinary wound solenoids that physically cover the sample (however also Helmholtz systems can be used if access to the sample is needed). The sensor that records the dynamic magnetic response from the sample can be a differentially coupled induction coil system, fluxgate or SQUID (Superconductor Quantum Interference Device) sensors.

Regarding the accessible physical parameters, from the frequency dependent ACS relaxation spectra it is possible to extract data from the magnetic nanoparticle systems, for instance hydrodynamic size of the particles (if the particles are placed in suspension) and single-domain size if appropriate magnetic parameters (for instance magnetic anisotropy, Néel relaxation time parameters and particle surface layer) and appropriate ACS models are used in order to analyse the experimental data. If the ACS system is correctly calibrated (both in magnitude and phase) the absolute values of the susceptibility can be determined at each measurement frequency, it is also possible to determine the type of relaxation for a given magnetic nanoparticle system (Brownian or Néel relaxation) by observing where the relaxation peak is positioned in frequency, relative width of the relaxation peaks and by measuring on both free and immobilized magnetic nanoparticles.

For temperature dependent AC susceptibility, Figure 1.12 shows the in-phase and out-of-phase signals for materials that may be present in biological matrices. Only superparamagnetic and ferrimagnetic particles show a peak in the out-of-phase component. From the temperature dependent ACS relaxation spectra, T_B can be determined. This depends on the size of the nanoparticles, the crystalline anisotropy and the agglomeration of the particles.[52] Therefore, this technique is sensitive to aggregation and transformation processes. Moreover, this technique has shown to be adequate to study magnetic nanoparticles in a complex matrix, since only the signal of the particles (superparamagnetic) is observed in the out-of-phase susceptobility. Other magnetic contributions coming from a complex biological matrix (as an example, blood gives a paramagnetic signal and tissues give a diamagnetic signal) are not observed.[53] Therefore, it is possible to follow the biodegradation of magnetic nanoparticles in animal models[54, 55] and to quantify the iron content, associated to MNPs.

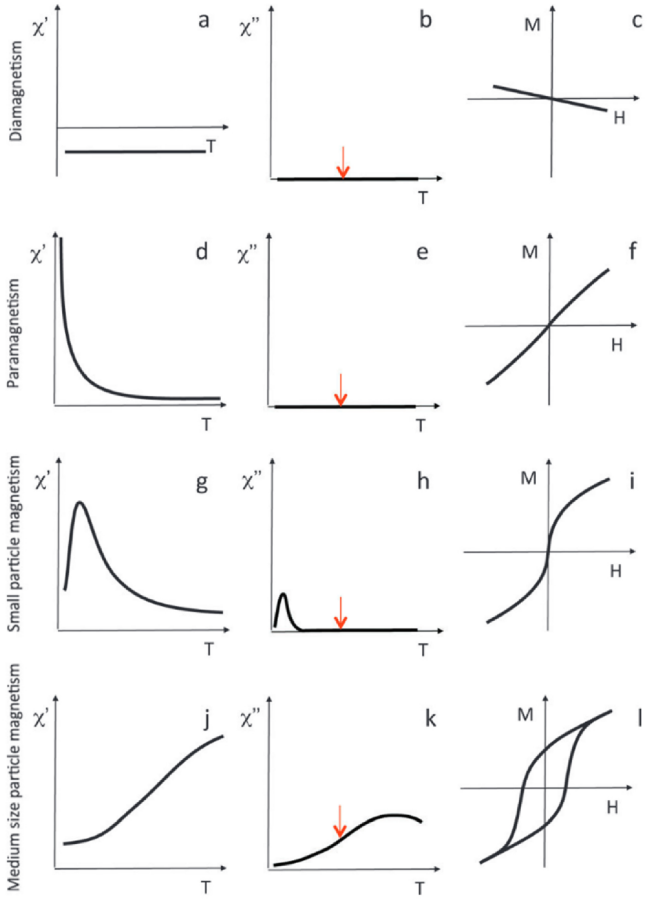

Figure 1.12: Temperature dependence of the in-phase susceptibility, χ'_0(T), (first column), temperature dependence of the out-of-phase susceptibility, χ'(T), (second column) and field dependence of the magnetisation, M(H), (third column) of the typical magnetic species in biological tissues. First row: diamagnetic species as, e.g., water and many organic molecules. Second row: metal-containing paramagnetic molecules as, e.g., deoxy-haemoglobin. Third row: very small mineral magnetic particles, thus superparamagnetic above relatively low temperature, as, e.g., the iron-containing ferritin cores. Fourth row: larger mineral magnetic particles that become magnetically blocked at relatively high temperature as, e.g., some particulate magnetic carriers. The third column M(H) data are supposed to be measured at the temperatures indicated by arrows in the second column; for a given temperature, the nonzero out-of-phase susceptibility and the M(H) hysteresis both reveal the difficulties of the particles magnetic moment to follow the AC magnetic field variations. Images reproduced from literature.[51]

In summary, this technique allows to study the type of relaxation for magnetic nanoparticle system (Brownian or Néel relaxation) by observing where the relaxation peak is positioned in frequency or temperature, the hydrodynamic size of the particles colloids can be determined and the study of

transformation and biodegradation of magnetic particles in a complex matrix. Based on the same concepts, not the degradation but the formation mechanism, in which aggregating nanometric size particles participate, could be explored.

1.3 Iron Oxide Magnetic Nanoparticles

Magnetic iron oxide nanoparticles, which classically refers to magnetite and maghemite, present advantages in comparison to other magnetic nanomaterials. While Ni or Co nanoparticles are highly magnetic, they seem to be relatively toxic[56–58] and are easily oxidized, iron oxide nanoparticles are nontoxic[59] and (at least in the case of maghemite) are stable to oxidation. Furthermore, iron oxide nanoparticles can be cheaply produced and are thus available in large quantities if needed. Because of this, iron oxide magnetic nanoparticles have a wide variety of applications in different technological fields that make them irreplaceable. In the following sections, applications of iron oxide magnetic nanoparticle, emphasizing those in the field of biomedicine, are described. Then, the most common general approaches to synthesize magnetite and maghemite NPs are addressed. After, the coating of the cores is described. This is necessary in order to provide functionality and stability to the magnetic colloid. The sections dedicated to the synthesis and coating have been based on a book chapter entitled “Controlling the size and the shape of uniform magnetic iron oxide nanoparticles for biomedical applications”, which has been included in Appendix 1. Lastly, the current limitations in the fabrication, not only from the synthetic but also from their standardization point of view, are highlighted, which will pave the way for the body of this thesis.

1.3.1 Applications of iron oxide magnetic nanoparticles

Iron oxide magnetic NPs have been developed traditionally for applications such as iron storage or magnetic recording media. However, there are new emerging technologies involving a multidisciplinary field between areas as diverse as geology, biology, chemistry, and medicine where iron oxide magnetic NPs have made impact. Iron oxide magnetic nanoparticles in the form of colloids opened up a wide range of attractive possibilities in biomedicine. This was a direct result of their nanometric features (see subchapter 1.2 magnetic nanoparticles). First, because they are sufficiently small to enable interactions with biological entities, such as receptor molecules, etc. while displaying a size large enough (with a likewise high ratio of surface area to volume) to carry an imaging or therapeutic payload. Moreover, SP magnetic NPs are well suited for biomedical applications as the absence of permanent forces between neighboring nanoparticles (no remnant magnetization) reduces the risk of aggregate formation.[60] Lastly, magnetic NPs display interesting assets as they are able to i) establish a locally perturbing dipolar field in the presence of a magnetic field, ii) be manipulated by an external magnetic field gradient as they experience a magnetic force resulting in magnetophoretic mobility, and iii) generate thermal

energy when exposed to an AMF. From all these outstanding properties derive important biomedical applications such as MRI contrast enhancement, drug and cell targeting and magnetic hyperthermia (in-vivo applications) and magnetic separation (in-vitro application). For the in-vivo applications, the proposed administration have been either the injection to the circulation system or the direct injection on the target area. For the former one, it must be taken into account that below 3 nm, circulating NPs go through the blood system and end in the kidney and the lymphatic system. By exceeding renal clearance threshold (above 3-8 nm and up to 30 nm), IOMNPs circulate longer, which may favour their uptake in leaky vasculature regions such as tumors.[58] Above this size, the fate of the NPs is likely to be the liver.

1.3.1.1 MRI contrast enhancement

Magnetic Resonance Imaging (MRI) is a powerful non-invasive and nonionizing technique that provides anatomical and functional images with high spatial resolution and without depth limitation in the organism.[61] Despite its excellent natural contrast, MRI sometimes requires the use of contrast agents (CA) to better detect pathologies. These CA act through their magnetic effect on mobile water protons: they shorten proton relaxation times.[62] In general, the MRI signal is proportional to the local proton density and is weighted by some function of the longitudinal (T_1) and transverse (T_2 or T_{2*}) relaxation times of the tissues which depend on the actual pulse sequence used to capture the image. The efficacy of CA relies on their efficiency to speed up proton relaxation processes[17] (Figure 1.13 a-b) – defined as relaxivity r_i, according to the following equation:

$$R_i = R_{i0} + r_i[CA], with \quad i = 1, \quad 2 \quad or \quad 2^* \tag{1.11}$$

where $R_i = 1/T_i$ is the relaxation rate observed in presence of CA, R_{i0} is the baseline tissue relaxation rate, r_i is the CA relaxivity, and [CA] is its concentration. This relation applies to both relaxation mechanisms, that is, longitudinal T_1 and transverse, T_2 and T_{2*}. Although the measured MR signal is a complex nonlinear function of the CA concentration, it is thus possible to visualise CA by acquiring appropriately weighted images. In contrast to paramagnetic compounds such as gadolinium chelates that have an r_2/r_1 ratio close to 1 (thus mainly affecting T_1, because R_{10}<R_{20} for most tissues) and providing positive contrast on T_1 weighted images), SP magnetic NPs have generally a high r_2/r_1 ratio, providing a dominant T_2 effect (Figure 1.13 c), which leads to signal voids (negative contrast) on T_2 or T_{2*}-weighted scans.[63] MR relaxivities also depend on the applied magnetic field and the nuclear magnetic resonance dispersion (NMRD) profile. This latter one is a complex function of both the local environment (diffusion time of proton depending on viscosity, temperature, and structural properties of the tissue; accessibility of protons to CA) and of the static and dynamic magnetic properties of CAs. Therefore, the relaxivities of iron oxide NPs can be optimized by modulating the magnetic size, the hydrodynamic size, the magnetization, and the magnetic anisotropy as well as the geometrical arrangement of NPs and the

surrounding matrix (or coating).[64, 65]

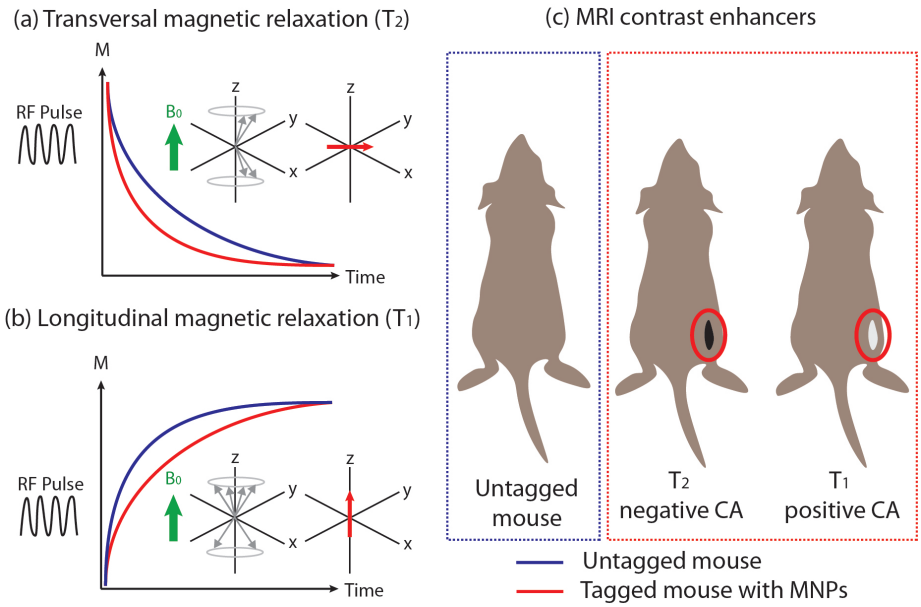

Figure 1.13: Application of magnetic nanoparticles: Magnetic Resonance Imaging. (a) Effect of magnetic nanoparticles on the transversal (T_2), and (b) longitudinal (T_1) relaxation time of water protons in living tissue. (c) Types of imaging contrast enhancers in tissues.

Resovist®, with a particle size of about 60 nm, is a clinically approved superparamagnetic iron oxide MRI contras agent, whose principal effect of is on T_{2*} relaxation and thus MR imaging is usually performed using T_2/T_{2*}-weighted sequences specifically for MRI of the liver. It has a T_2 relaxivity of 282.4 s^{-1}·mM^{-1}.[66] However, in the literature, different clusters of $\gamma^{\smile}Fe_2O_3$ or Fe_3O_4 cores[67] already exceeded a T_2 relaxivity of 500 s^{-1}·mM^{-1}. Core-shell structures of special compositions of ferrite particles with a higher saturation magnetization than pure iron oxide led to even higher relaxivities and have shown to be promising as T_2 CA.[68] However, T_2 pulse sequences are difficult to use for the diagnosis of many pathologies due to the possibility of endogenous negative contrast, which may be produced by calcium depositions, bleeding, or the presence of other metals.[69] This has led to a recent and intense research for the production of iron oxide nanoparticles for T_1 MRI. In this sense, ultrasmall iron oxide NPs have shown synthesized through microwave assisted route have shown to be promising materials as T1 CA achieving r_2/r_1 ratios of 4.7. [70]

1.3.1.2 Magnetic fluid hyperthermia

The possibility of treating cancer by magnetically induced hyperthermia (MFH) has led to the development of many different devices designed to heat malignant cells while sparing surrounding healthy

tissue.[71] In broad terms, the procedure involves dispersing magnetic particles throughout the target tissue, and then applying an AC magnetic field of sufficient strength and frequency to cause the particles to heat. This heat conducts into the immediately surrounding diseased tissue whereby, if the temperature can be maintained above the therapeutic threshold of 42 °C for 30 min or more, the tumour cells are destroyed. Nanoparticles are considered small enough to enable effective delivery to the tumour site, either via encapsulation in a larger moiety or suspension in some sort of carrier fluid. Furthermore, nanoparticles can be coupled with antibodies to facilitate targeting on an individual cell basis.

Candidate materials are divided into two main classes: ferromagnetic or ferrimagnetic (FM) or SP particles. The heat generating mechanisms associated with each class are quite different: For FM particles the amount of heat generated per unit volume is given by the frequency multiplied by the area of the hysteresis loop:

$$P_{FM} = \mu_0 f \oint H dM \tag{1.12}$$

This formula does not take into account other possible mechanisms for magnetically induced heating such as eddy current heating and ferromagnetic resonance, but these are generally irrelevant in the present context. The particles used for magnetic hyperthermia are too small and the AC field frequencies too low for the generation of any substantial eddy currents. P_{FM} can be readily determined from quasi-static measurements of the hysteresis loop using, for example, a VSM or SQUID magnetometer. For SP nanoparticles, when the external field is removed, its magnetization relaxes back to zero due to the ambient thermal energy of its environment by either the physical rotation of the particles themselves within the fluid, or the rotation of the atomic magnetic moments within each particle. Rotation of the particles is referred to as "Brownian rotation" while rotation of the moment within each particle is known as "Néel relaxation". Each of these processes is characterized by a relaxation time (see subchapter 1.2 magnetic nanoparticles). This is determined by the magnetic anisotropy energy of the SP particles relative to the thermal energy. Both Brownian and Néel processes may be present in a ferrofluid, whereas only τ_N is relevant in fixed SP nanoparticles where no physical rotation of the particle is possible. The relaxation times τ_B and τ_N depend differently on particle size. Losses due to Brownian rotation are generally maximized at a lower frequency than are those due to Néel relaxation for a given size.

In order to measure the heat generated by the magnetic NPs in suspension, calorimetric methods must be applied. Usually, the specific absorption rate (SAR) or its equivalents, specific loss power (SLP) or specific heating power (SHP), are calculated. Therefore, MNPs are placed in the centre of a coil (Figure 1.14 a) that produces an AMF, the magnetic NPs absorb energy from the field which is subsequently transformed into heat. If the field is strong enough, and also thermal losses are small enough, the generated heat rises the sample temperature. SAR is calculated from the temperature

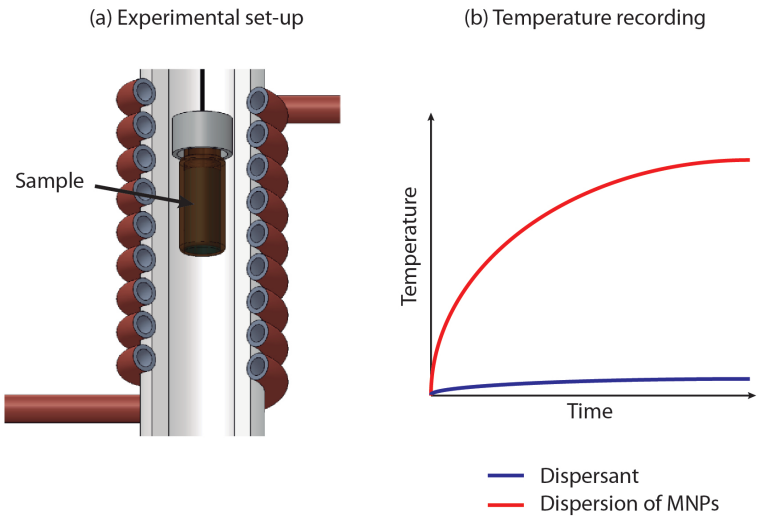

Figure 1.14: Application of magnetic nanoparticles: Magnetic Fluid Hyperthermia. (a) Experimental set-up to apply an AMF to the magnetic colloid. (b) Sample temperature recording and calculation of SAR. Adapted image from literature.[72]

derivative over time at instant t=0 as:

$$SAR = \frac{c_{p,s}}{m_{MNPs}} |\frac{dT}{dt}|_{t=0} \tag{1.13}$$

where $C_{p,s}$,s is the heat capacity of the sample and m_{MNPs} is the mass of the MNPs present in the sample. When MNPs are dispersed in a medium, $C_{p,s}$ in Eq. 1.11 is related to the specific heat capacity of the dispersion medium and the specific heat capacity of the MNPs themselves. If the time evolution of sample temperature is recorded (Figure 1.14 b), the time derivative of temperature at t = 0 can be obtained. Thereafter, the SAR value of the sample can finally be determined by means of Equation 1.13.

In order to be able to measure de temperature rise properly, adiabatic conditions must be achieved and thus, complex isolating systems are required. Natividad et al.[73] developed an adiabatic magneto-thermal setup, Mendo et al. achieved adiabatic conditions with natural cork as insulating material,[74] etc. Furthermore, the SLP parameter is not an intrinsic property of a given system, as it is dependent on the field amplitude and frequency.[75] Using the intrinsic loss power (ILP) parameter (Eq. 1.12), which is a constant in the clinically relevant region where the power generated by magnetic hyperthermia scales linearly with f and quadratically with H, allows comparisons to be made between measurements carried out under different f and H conditions.

$$ILP = \frac{SAR}{H^2 f} \tag{1.14}$$

It must be noted that the product of H·f must be kept below 4.85 x 10^8 kA/m·s, which is mandatory for avoiding nonspecific eddy heating in tissues,[76] affecting patient comfort and leading to side effects such as pain and blisters.

When introduced the colloids in cellular environments, however, large amount of heating power is rarely obtained due to several limitations: the low concentration of magnetic material in injectable doses and restrictions concerning the application of high frequencies and magnetic fields, in order to avoid nonspecific heating of healthy tissues. Considering such limitations, some efforts have been devoted to the optimization of the hyperthermia setup. This heating optimization has been usually performed through novel nanomaterial designs, modifying geometry, and composition of the nanomaterials in suspension, which lead, thus, to a modification of their magnetic anisotropy and with it their time relaxation mechanisms. This means that the heat power capability per particle unit of mass should be as high as possible. Some years ago, the SAR values of iron oxide NPs were typically in the range of 100–200 W·g^{-1}. Then, improved heat generation has been obtained with newly designed nanoparticles: bacterial magnetosomes,[77] synthetic nanocubes,[78] core–shell structures,[79] or multigrain assemblies (nanoflowers)[80] exhibited high values of SLP exceeding 1000 W·g^{-1}. Importantly, Néel and Brownian relaxation times are impacted after interacting with cells, contributing to the slowing of the magnetic moment rotation process, especially in those materials that in suspension are dominated by Brownian relaxation mechanisms, where a significant immobilization of nanoparticles occurs in cellular environment. In this case, the SLP of most efficient materials in solution strongly falls, dividing its value by several orders of magnitude, when placed in cellular environment. So, it should be also highlighted the importance of the complexity of the biological environment, which does not only impact the particles because of the cellular compartment but is also affected by noncellular structures (i.e., the collagenous tumoral matrix, throughout which the particles may be distributed) and biological processes that occur in vivo and reduce the heating (i.e., blood circulation, which may act as a cooling circuit). Therefore, particle size, size distribution, shape, stability, and magnetic anisotropy must be controlled and explored through new ways of synthesis to elaborate better magnetic nanoparticles with high heat performance.[81]

1.3.1.3 Magnetic drug targeting

Magnetic drug targeting is emerging as a promising biomedical application. A major shortcoming related to drug administration is the difficulty to target the site of interest. As a result, drugs tend to distribute in the organism in a process that is governed by physicochemical properties of the molecule. In the attempt to reach drug concentration at therapeutic levels in the site of interest, large amounts of the drug must be administered.[82] In addition, the drug excess may cause toxic side effects at non target organs.[83] Drug targeting strategies aim to reverse this trend via the selective delivery of the therapeutic agent at the site of interest by means of a drug carrier that recognizes and accumulates at

the target. Carriers, such as nanoparticles, liposomes, and micelles, are engineered to recognize the target by means of attached specific ligands in order to selectively bind moieties overexpressed on the target.[84] Alternatively, the carrier-mediated drug delivery at the target may be prompted by internal stimuli such as the presence of specific enzymes or pH changes at the target site or externally triggered by light, ultrasound, or magnetic field.[85] Magnetic drug targeting refers to the localized magnetically assisted delivery of drugs at the site of interest. In overall, the objectives are twofold: (i) to limit the systemic distribution of the cytotoxic drug, thus sparing healthy tissues from off-target side effects and (ii) to reduce the drug dosage required for treatment by enhancing local drug concentration at the target.[17]

1.3.1.4 Others applications

Besides the up-above mentioned applications, magnetic NPs are currently under study for tissue engineering. The ability to insert the NPs inside living cells opens up a new approach to bioengineering: the use of “magnetized” cells as basic building blocks for replacement tissues.[86] Other application whose progress is crucial and aimed is water treatment.[87] Contamination is a major international problem caused by industrial, domestic, and environmental influences. Conceptually the key properties required for the use of any engineered NPs for in situ remediation of polluted groundwater are i) high reactivity for contaminant removal, ii) high mobility within porous media, iii) reactive longevity, and iv) low toxicity. Thus, the material must be manufactured and deployed at a cost that is competitive.

1.3.2 Synthesis of iron oxide magnetic nanoparticles

First, it must be mentioned that iron oxides are ubiquitous in nature. They can be found in geological settings as different as the surface of Mars (where they mostly account for the colour of the red planet), interstellar space, meteorites or the acidic mine drainage on Earth. Moreover, different types of iron oxides can also be biomineralized by organisms.[88] The geomagnetic navigational aids in all migratory birds, fishes and other animals contain magnetic nanoparticles.

In fact, there are 16 iron oxides, hydroxides, or oxihydroxide recognized so far, all called in short iron oxides. Most of them were discovered and described at the beginning of the nineteenth century. Table 1.3 shows the complexity and variety of these phases, since they have different crystal systems, ratio of Fe(III)-Fe(II), which makes that some of them have ferri-, ferromagnetic or antiferromagnetic behaviour. Especially complex is the case of ferrihydrite, since the usual low crystallinity of this phase makes difficult to determine its magnetic behaviour. Recently a ferrimagnetic structure has been described for ferrihydrite nanoparticles synthesised in the presence of organic media that could explain several finding such as the origin of the magnetic component of the Mediterranean soils.[89, 90] In the case of hematite particles, in the nanoscale they can suffer spin canting (see subchapter 1.2 Magnetic properties). Consequently, at low temperatures they can have a weakly ferromagnetic behaviour. Also, “Green rust” phase is highly unstable and tend to get oxidized, which difficults the study of its magnetism.

Table 1.3: Iron oxide, oxyhydroxide and hydroxide phases that exist and type of magnetism they present.

	Mineral Name	Formula	Types of Cations	Type of Magnetism	Crystal Symmetry
Iron Oxide	Magnetite	Fe_3O_4	Fe(II)-Fe(III)	Ferrimagnetic	Cubic
	Hematite	α-Fe_2O_3	Fe(III)	Antiferromagneticc)	Hexagonal
	Maghemite a)	β-Fe_2O_3	Fe(III)	Ferrimagnetic	Cubic Tetragonal
	Maghemite a)	δ-Fe_2O_3	Fe(III)	Ferrimagnetic	Cubic Tetragonal
	Maghemite a)	ε-Fe_2O_3	Fe(III)	Ferrimagnetic	Cubic Tetragonal
	Maghemite	γ-Fe_2O_3	Fe(III)	Ferrimagnetic	Cubic Tetragonal
	Würstite	FeO	Fe(II)	Antiferromagnetic	Cubic
Iron Oxyhydroxide	Green Rust	$[Fe_2^{+4}Fe_3^{+2}(OH)_{12}][CO_3]3H_2O$	Fe(II)-Fe(III)	Under discussion[d)]	-
	Ferrihydrite	$5Fe_2O_39H_2O$	Fe(III)	Under discussion[d)]	Hexagonal
	Goethite	α-FeOOH	Fe(III)	Antiferromagnetic	Orthorhombic
	Akaganeite	β-FeOOH	Fe(III)	Antiferromagnetic	Monoclinic
	Lepidocrocite	γ-FeOOH	Fe(III)	Antiferromagnetic	Orthorhombic
	Feroxyhyte	δ-FeOOHFeOOH	Fe(III)	Ferrimagnetic	Hexagonal
	Schwertmannite	$Fe_8O_8(OH)_6$	Fe(III)	Antiferromagnetic	Tetragonal
Iron Hydroxide	Bernalite	$Fe(OH)_3$	Fe(III)	-	Orthorhombic
	White Rust[b)]	$Fe(OH)_2$	Fe(II)	Under discussion[d)]	Hexagonal

Note: a) These compounds are synthetic. b) This compound has not been found in the nature in the form of mineral. c) Small hematite nanoparticles can have a weakly ferromagnetic behaviour due to spin cantin. d) The magnetic behaviour of these phases is still under discussion since they are not stable and rapidly oxidize.

A characteristic of the iron oxide systems is the variety of possible interconversions between the different phases.[91] Under the appropriate conditions, almost every iron oxide can be converted into at least two others. Under air atmosphere, goethite and hematite are thermodynamically the most stable compounds in this system and are, therefore, the end members of many transformation routes. These interconnections do not only have an important role in corrosion processes and in the process occurring in various natural environments, but they also take place in most of the chemical approaches in the lab to synthesize iron oxide nanoparticles. Generally, dehydration and dehydroxylation reactions occur between two minerals of the same crystal symmetry (ferrihydrite to hematite or goethite to hematite), whereas higher temperature or dissolution and reprecipitation are generally needed to induce a hexagonal to cubic (e.g., goethite to maghemite) or vice versa (maghemite to hematite) alteration.

In order to exploit the magnetic properties of these materials, the phases of maghemite and magnetite, which are ferrimagnetic, are aimed. Paying attention to the precursors, the transformations which yield magnetite or maghemite are schematised in Figure 1.15 and, as will be seen below, all the common synthesis approaches are based on these transformations.

Due to the fact that the properties of iron oxides are highly dependent on the internal structure, particle size and shape, the preparation method should be chosen to give the material required for a needed application. Figure 1.16 shows the synthesis processes to achieve magnetite or maghemite nanoparticles. Traditional Massart's method of co-precipitation[92] is based on the mixture of Fe(III) and Fe(II) (usually, the initial precursors are $FeCl_3$ and $FeCl_2$) in aqueous alkaline conditions. This route achieves sizes in the range of 2-15 nm and normally yields quasi-spherical NPs (the morphology is poorly defined) with broad size distributions. The crystallinity can be poor and generally the as-synthesized particles present some degree of agglomeration. Inspite of that, this is the only commercially available magnetic colloids used for biomedical purposes, since it offers many advantages.

It is conducted in aqueous media (environmentally friendly) and it has shown to be a rapid scalable low-cost process. Indeed, the size and the shape of the nanoparticle can be affected by the type of base and pH,[93] ionic strength and temperature,[94] iron concentration and aging time[95] and nature of the counter anion.[96]

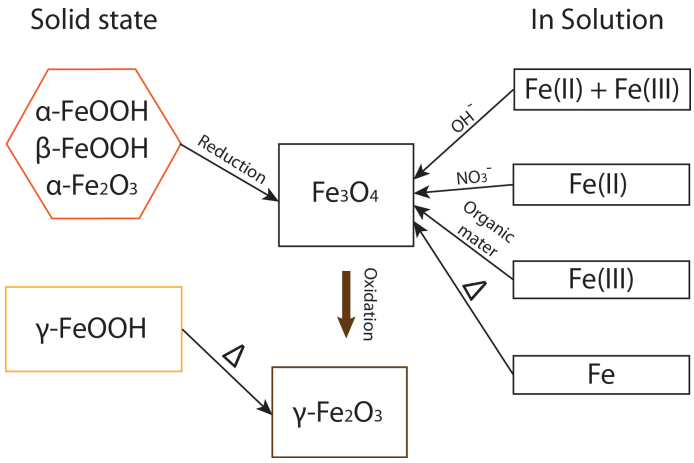

Figure 1.15: Transformations that yield maghemite or magnetite.

The next synthesis route is high temperature thermal decomposition of Fe(III) organic precursors, a route developed by Alivisatos[97] and Hyeon.[98] Usually, the initial precursor was $Fe(CO)_5$ (it has practically fallen into disuse due to its toxicity), and now $Fe(acac)_3$ (iron (III) acetylacetonate) and $Fe(oleate)_3$, are often used. One procedure is the injection of organometallic compounds into a hot surfactant solution, which results in the formation of nuclei almost instantaneously. The other option is the controlled heating of organometallic compounds in a surfactant solution to generate the nuclei. Once the nucleation has occurred, particles grow at high temperature. Finally, through a rapid decrease of the reaction temperature, the growth of the NPs can be stopped.[99] This route achieves narrow size distributions and the obtained nanoparticles are hydrophobic.

This route allow sizes in the range of 2-60 nm and normally yields nanoparticles with well-defined morphology: mostly quasi-spherical, as in Figure 1.16, or cubical, by introducing in the reaction an amount of sodium oleate,[100] as in Figure 1.17 b. The adhesion of specific molecules on crystal facets have allowed to grow rhombohedra nanoparticles[101] (Figure 1.17 a). This route achieves high crystallinity (even at the surface of the nanoparticles), due to the high temperatures and the as-synthesized nanoparticles are well dispersed in the media, as this reaction is conducted in the presence of an extra additive, generally oleic acid or oleylamine, which are surfactants that in-situ coat the NPs. The size and morphology of the nanoparticles can be tuned by controlling the reaction times and the temperature but also the concentration and ratios of the reactants, nature of the solvent, precursors, complexing strength, and addition of seeds. However, this type of process must be improved to be

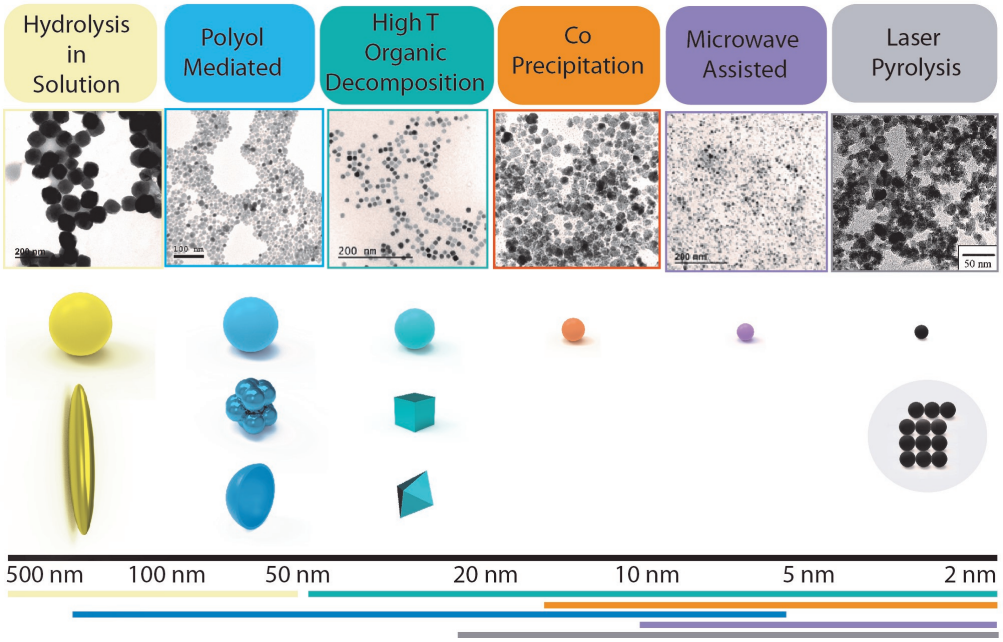

Figure 1.16: Synthesis processes to obtain magnetite/maghemite nanoparticles. Below, the usual sizes and morphologies obtained through each approach.

suitable for industrial preparation, especially in terms of the obtained quantities, safety of the reactants and the high temperatures required.[102]

The polyol process, developed by F. Fievet, Lagier and Figlarzwhich,[103] which can be understood as a sol-gel method, is a versatile chemical approach for the synthesis of nano- and microparticles with well-defined shapes and controlled sizes. In this reaction, polyols (for example, polyethylene glycol, PEG) are used as solvents and they offer interesting properties: owing to their high dielectric constants, they act as solvents able to dissolve inorganic compounds, and owing to their relatively high boiling points, they offer a wide operating-temperature range (from 25 °C to their boiling point, which for example, in the case of TREG is 325 °C).[104] Polyols also serve as reducing agents as well as stabilizers to control particle growth and prevent interparticle aggregation. The metal precursor becomes solubilized in the diol, forms an intermediate, which is then reduced to form metal nuclei that will then nucleate and form metal particles. Cai and Wan[105] developed an easy method to directly produce non-aggregated magnetite nanoparticles below 20 nm using TREG, a long chain polyol. Lastly, Caruntu and coworkers[106] developed another approach, using a mixture $FeCl_2$ and $FeCl_3$, NaOH and N-methyl diethanolamine (NMDEA), (Figure 1.16) since this reagent has chelating properties, it has different donor properties of diethylene glycol and affect the rate of hydrolysis and crystallization. Moreover, it has higher viscosity and boiling point. They could obtain uniform quasi-spherical NPs

closer to 20 nm, and when mixed DEG and NMDEA at the initial phase of synthesis, they could obtain agglomerates of a regular size, called thereupon nanoflowers (Figure 1.17 e). The use of long-chain polyols (DEG) and high pressures have also accounted for this type of flower structure (Figure 1.17 f), which upon aging time and the use of a base, such as sodium acetate, evolves to hollow spheres (Figure 1.17 d).

Hydrothermal syntheses of Fe_3O_4 nanoparticles and ultrafine powders is another traditional synthesis route performed in aqueous media in reactors or autoclaves where the pressure can be higher than 2000 psi and the temperature can be above 200 °C. There are two main routes for the formation of ferrites via hydrothermal conditions: hydrolysis and oxidation or neutralization of mixed metal hydroxides. These two reactions are very similar, except that ferrous salts are used in the first method.[107] In this process, the reaction conditions, such as solvent, temperature, and time, usually have important effects on the products. Particle size can be increased with a prolonged reaction time and higher water content results in precipitation of larger Fe_3O_4 particles (Figure 1.16). In the hydrothermal process, the particle size in crystallization is controlled mainly through the rate processes of nucleation and grain growth, which compete for the species. Their rates depend on the reaction temperature, with other conditions held constant. Nucleation might be faster than grain growth at higher temperatures and results in a decrease in particle size. However although the obtained particles have well-defined morphology, this approach yields particles well above 100 nm with broad size distributions (Figure 1.17 c).

The syntheses described above are all conducted under the presence of a heating source (except from co-precipitation, which can be carried out at RT) based on the heat transfer (either by conduction or radiation). However, other synthesis approaches have been developed based on non-classical heating: These are laser pyrolysis and microwave-assisted synthesis. In the case of laser pyrolysis, the laser source (traditionally, a CO_2 laser that produces a beam of infrared light with the principal wavelength bands centered on 9.4 and 10.6 μm) excites and heats a carrier gas (ethylene), which absorbs the radiation and transmits the heat to the rest of the reagents (the iron precursor, such as iron pentacarbonyl, etc.) by the normal means.[109] As a result, the flowing mixture of gas produces small nanoparticles with narrow size distribution. When the pyrolysis experimental conditions are adjusted, the crystal size of maghemite nanoparticles is varied in the range from 2 to 13 nm (Figure 1.16). This technology is attractive because it allows continuous chemical processes with high rate production. Although low saturation magnetization values are obtained, NPs have very high coercivities at low temperature due to the increase in surface and structural disorder.[110–112] The obtained NPs form generally aggregates that cannot be broken.

Apart from that, microwave assisted synthesis was first reported by Gedye and Giguere[113, 114] and it is based on the dielectric heating ability of some compounds. The preparation of transition-metal oxide nanocrystals and in particular iron oxide NPs rely in the use of non-aqueous[115–117] and aqueous[118] solvents. The obtained NPs have sizes ranging around 2-8 nm (Figure 1.16) and depending on the solvent and temperature ramp it can be up to 15 nm. This is associated with the ultra-

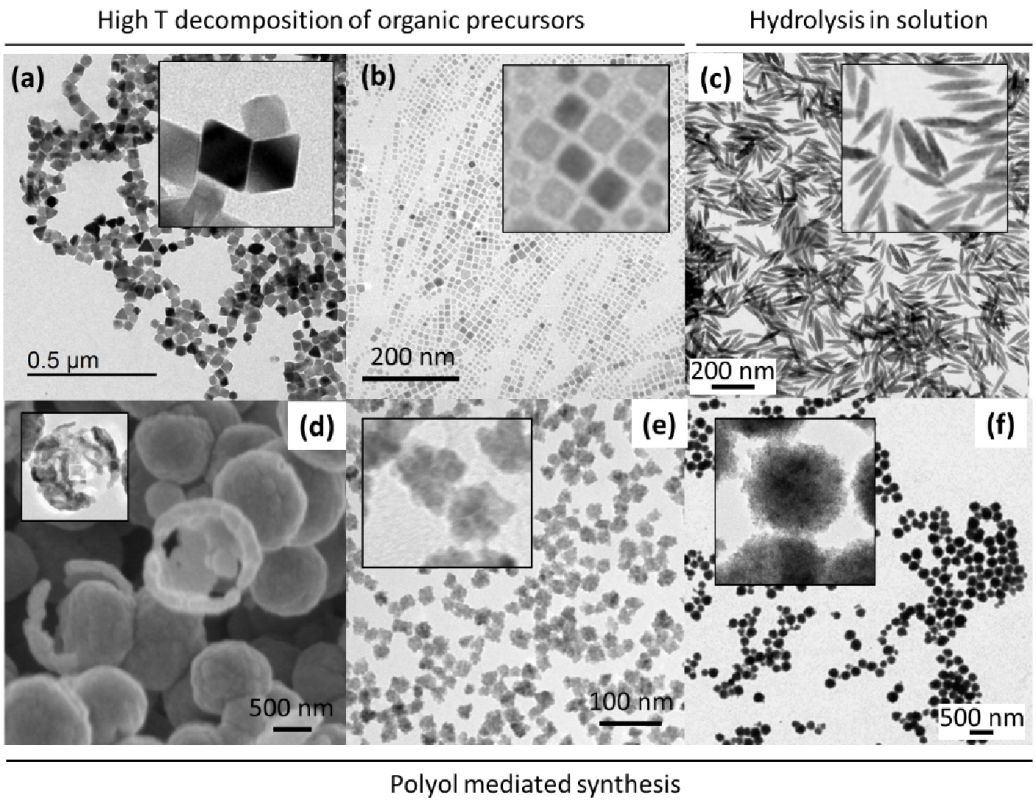

Figure 1.17: Other morphologies of magnetite/maghemite nanoparticles achieved by high T thermal decomposition of organic precursors, polyol mediated synthesis and hydrolysis in solution. Picture (d) is reproduced from literature.[108]

fast heating produced by the microwave which swiftly and massively creates initial nuclei (in contrast to heat transfer that produces less amount of initial nuclei that are able to grow and increase their size by means of metal ions in the media). This method has shown reduction in synthesis time (from hours to minutes), and allows high reproducibility. The main drawback at this moment for this approach is the small batches obtained.

In general, cost-effective, environmental friendly and large-scale synthesis methods have been pursued keeping good control of size, shape, and composition of MNPs, considering that the difference of only few nanometers in particle size means huge differences in volume resulting in a functional or failed product.[119] Reproducibility of current synthetic methods, which are able to manufacture high quality MNPs in large scale, is still a major challenge.

Regarding thermal decomposition method, it has superior structural properties in terms of controlling the size, size distribution and crystallinity. It uses organic iron precursors that decompose at high temperatures in an organic medium containing surfactant stabilizers. This method yields hydrophobic

particles stabilized by the surfactants that need further treatments to make them hydrophilic. The polyol method, likewise, utilizes high-boiling compounds such as ethylene glycol, diethylene glycol or triethylene glycol, and obtains water dispersible, monodisperse magnetite NPs. Therefore, all these methods require extreme conditions in comparison with other non-mentioned approaches, such as biomineralization (see Appendix 1) that occurs at ambient conditions. Moreover, in several cases, harmful organic additives or solvents are used. Finally, dispersion and stabilization of MNPs in water using non-toxic coatings are important issues and have been the subject of numerous publications,[120]as described below.

1.3.3 Coating of iron oxide magnetic nanoparticles

Typically, magnetic NPs for different applications need to be composed of, not only the magnetic core, but also a spacer that protects the core, prevents it from aggregation when forming a colloid,[102] or acts as a platform for extra functionality for specific applications. This spacer can have inorganic or organic nature. Furthermore, in addition to the inorganic/organic coating, which usually serves as a linker, more complex molecules or biomolecules should be bound on the surface of the particle, in order to provide a real activity (Figure 1.18). The first point to consider is that in naked iron oxides, the iron atoms surface act as Lewis acids and coordinate with molecules that donate lone pair of electrons. Therefore, in aqueous solutions, the Fe atoms coordinate with water, which dissociates readily, leaving the iron oxide surface hydroxyl functionalized. These hydroxyl groups are amphoteric and may react with acids or bases.[121] Carboxyl, sulfates, silicates, phosphates, polyethers, and to a lesser extent, alcohols, diols and amines, are groups that have shown to have affinity to the naked surface of iron oxides.[122] Depending on the pH of the solution, the surface of the magnetite will be positive or negative. The isoelectric point (point of zero charge) is observed at pH 6.8.[123] Around this point, the surface charge density is too small and the particles are no longer stable in water and flocculate.

By both electrostatic and steric stabilization stable iron oxide nanoparticles colloids are achievable. Once the naked surface of the particles is coated, in order to bind molecules or biomolecules, different strategies can be followed: i) Sol-gel processes that involve the conversion of monomers into a colloidal solution (sol), which acts as the precursor for an integrated network (or gel). Typical precursors are alkoxides. ii) Layer by layer (LbL) deposition which is formed by depositing alternating layers of oppositely charged materials on the surface of the nanoparticles with wash steps in between. iii) "Click" chemistry, a class of biocompatible reactions intended primarily to join covalently substrates of choice with specific biomolecules. Most frequently in these reactions are included the cycloaddition, thiolene, Diels-Alder and inverse electron demand Diels-Alder reactions, as well as nucleophilic substitutions, carbonyl-chemistry-like formation and, more importantly, addition reactions to carbon-carbon double bonds like dihydroxylation or the alkynes.[102] Importantly, If the NPs are stabilized in non-polar solvents, an extra coating step is needed, in order to transfer them to aqueous media. To do so, the

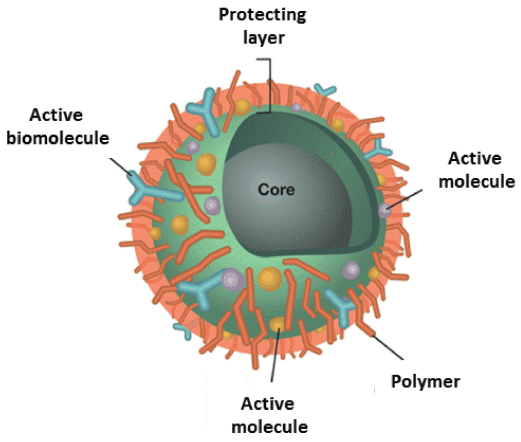

Figure 1.18: Structure of a functional magnetic nanoparticle: it is composed of a magnetic core coated by a protective layer. In order to bind an active molecule, an organic linker is often used.

following approaches can be used: i) Reverse microemulsions, that are liquid mixtures of oil, water and surfactant ("oil" may actually be a complex mixture of different hydrocarbons and olefins) are used as nano-reactors to grow in a controlled way a shell on the surface of a nanoparticle (normally silica). ii) Ligand exchange, iii) Crosslinking, iv) Oxidation or v) Encapsulation.

Furthermore, for the case of biomedical purposes, the NPs must be modified by a biocompatible material.[124] The surface modification of magnetic NPs in aqueous media is crucial to obtain magnetic ferrofluids that are stable against aggregation in biological media and under the action of external magnetic fields.[17] Regarding inorganic spacers, iron oxide nanoparticles can be coated with silica,[125] titania,[126] alumina,[127] or gold.[128] These coatings provide stability to the nanoparticles in solution and also help in binding various biological ligands to the nanoparticle surface. These nanoparticles have an inner iron oxide core with an outer metallic shell or inorganic materials.

Regarding organic spacers, if biomedical applications are pursued, the most common biocompatible polymers are polyethylene glycol (PEG),[129] dextran,[130] chitosan,[131] polyethylenimine (PEI),[132] phospholipids,[133] and polyvinylpyrrolidone (PVP).[134] Such coatings stabilize the NPs under physiological conditions. PEG, dextran and chitosan are particularly interesting because they are nontoxic, biocompatible and can prolong NPs lifetime in blood.[124]

Lastly, some used biomolecules that have shown to present some advantages[135] and to add functionality to the NPs. These include, among others: transferrin (protein widely applied as a targeting ligand in the active targeting of anticancer agents, proteins and genes to primary proliferating cells)[136], lactoferrin (it acts as an anti-infective agent, a modulator of the inflammatory response and iron absorption and an immuno-regulatory protein),[137] transforming growth factor-α(TGF-α) (it promotes proliferation and differentiation of cells and may be important for normal wound healing),[138]

Insulin (a hormone that regulates blood glucose levels),[139] Ceruloplasmin (it plays an important role in iron homeostasis and is also an effective anti-oxidant for a variety of free radicals),[139] albumin (it is the major serum protein, which binds a wide variety of lipophilic compounds including steroids, etc.)[140] and folic acid (it targets preferentially cancer cells, is poorly immunogenic and the folate receptor facilitates internalization of particles).[141] Moreover, antibodies have the advantage of specificity, since they can specifically target cells expressing high levels of a certain protein.[142] Lastly, cadherin is a biomolecule often conjugated to magnetic nanoparticles. It is a transmembrane protein that plays an important role in cell adhesion, forming adherens junctions to bind cells within tissues together.[143]

It must be mentioned that coating is critical in a biomaterial, since the interaction with the biological entity depends on the coating nature and its charge. These parameters have demonstrated to influence the fate, rate of biotransformation (leading to appearance of ferritin) and degradation of the NPs.[144]

1.3.4 Limitations and challenges in the synthesis and coating

As seen in subsection 1.2.5, colloids of magnetic nanoparticles have been classified in single-core and multi-core. But how can this feature be controlled? Ideally, by controlling the growth mechanism and the coating process.

In this sense, as-synthesized single-cores have been obtained through thermal decomposition and polyol process. It is necessary that a simple burst nucleation occurs at critical supersaturation point, generating initial nuclei that grow in a controlled way, in the diffusion growth regime.[145] This model of nucleation is explained by the LaMer theory.[146, 147] In addition, there must be a reagent (oleic acid/oleylamine or a polyol of certain length in the case of thermal decomposition of organic precursors and polyol-mediated synthesis, respectively) that acts as a surfactant controlling the distance between the nuclei and limiting the growth. Many factors that are interplay are responsible for the formation of single core particles and to control them keeping the monodispersity is a challenge. In terms of the shape of magnetite nanoparticles, spherical, cubical and rhombohedral morphologies are commonly obtained, but the rest of the morphologies are not covered by the traditional-direct methodologies. The synthesis of a precursor and its transformation to the magnetite phase is required preserving the nanoparticle morphology and it is not an easy task. In addition, the use of magnetic colloids for biomedical purposes, requires the NPs to be disperse in aqueous media, and those single-cores obtained organic media require further steps in order to transfer them to water. Moreover, there is a limitation on the coating of single-core nanoparticles. As inter-particle interactions become more important with increased sizes of the magnetic core, individual coating is not achieved above the superparamagnetic regime, usually coating big agglomerates of particles that have large hydrodynamic sizes. Aggregated single-cores have been obtained by means of hydrolysis in solution, co-precipitation and laser pyrolysis, in the absence, generally, of such extra additive, allowing the contact between nuclei.

Lastly, multi-core systems have been obtained in two ways: by the in-situ addition of certain poly-

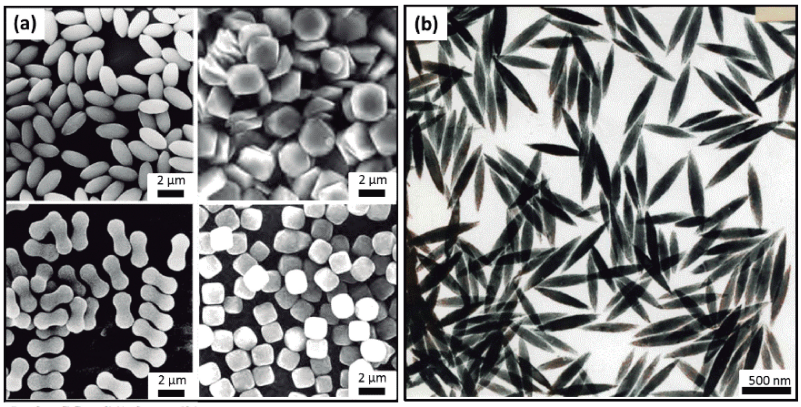

Figure 1.19: Iron oxide anisometric nanoparticles. (a) Adapted image of α-Fe_2O_3 nanoparticles synthesized by T. Sugimoto with different shapes. (b) γ-Fe_2O_3 spindles[148] used in magnetic recording media.

mers causing a reduction in surface charge density of the growing nuclei promoting its approach and clustering, and achieving the oriented aggregation of small subunits in an assembly process, based on monomer-by-monomer addition growth model,[149] driven by the presence of specific molecules or under the action of an external field. However, there is a lack of control over the number of cores per particles and the interaction between them, thus it is aimed to obtain highly regular structures.

1.3.4.1 Controlling the shape of iron oxide magnetic nanoparticles

Anisometric fine iron oxide particles, mostly antiferromagnetic phases such as goethite or hematite, were obtained in the last four decades by E. Matijévic[150–152] and T. Sugimoto in a size range of 1-6 μm (Figure 1.19 a). These particles were defined as "fine" due to its well-defined shape and uniform size (see subchapter 1.1. Colloids, fine particles and their characteristics in the nanoscale). Hematite and goethite have shown to be the most versatile phases in terms of shape: ellipsoids, peanut-like shape, platelets, cubes and many more (spheres, rhombohedra, stars, etc.) are some of the reported morphologies, whose size range is in the micron scale.

However, due to their large size, well above the nanoscale, the particles are polycrystalline. Remarkably, maghemite spindles above 500 nm (Figure 1.19 b) were obtained by reduction-oxidation in the solid state of a precursor (hematite).[153] The characteristics of the resulting powder in terms of particle size and shape, internal inhomogeneities, surface roughness, porosity, impurities, etc., depended on the precursor, since the transformation from any of the mentioned oxide-hydroxide to γ-Fe_2O_3 is a topotactic reaction without important morphological changes. This material was used in the industry for magnetic media recording, exploiting the enhanced coercivity induced by the shape anisotropy.

Although this synthesis approach has fallen into disuse, probably because it involves an extra step in

order to transform the antiferromagnetic phase to the ferrimagnetic phase, it has many advantage that could overcome the current limitations in the synthesis of single-core nanoparticles. First, this approach has the advantage of low inter-particle interactions of as-synthesized antiferromagnetic nanoparticles. Moreover, it covers different size ranges and allows to obtain different morphologies, that antiferromagnetic materials exhibit. This opens up new possibilities and interesting magnetic behaviour, since different geometric shape leads to distinct shape anisotropy. For a practical use, the challenge lies on the decrease of the particle size from the micron to the nanoscale. It must be noted that in these last three decades hematite and goethite nanoparticles have been successfully synthesized. Consequently, this approach is likely to be promising for the development of novel magnetic colloids.

1.3.4.2 Controlling the packing and assembly of iron oxide magnetic nanoparticles

Aggregation is a process that, as mentioned in subsection 1.1 is common in nanometric particles, as a consequence of their surface area, but for magnetic nanocrystals this is even more recurrent, due to additional forces that arise as a consequence of their magnetic moment. As a result, there is a dependency of magnetic properties on particle packing density (aggregation), as explained in subsection 1.2.4 (single-core and multi-core magnetic nanoparticles).

In fact, aggregation is relevant in particle formation and now it is recognized as a common growth phenomenon of many monodisperse iron oxide nanoparticles. As an example, it was demonstrated that β-FeOOH nanorods formed by hydrothermal synthesis suffer oriented aggregation and they transform into monodisperse micron-sized α-Fe_2O_3 spindles.[156] However, the effect of the key primary NP properties (size, saturation magnetization, and magnetic anisotropy) on colloidal stability, assembly, and the emergent collective magnetic properties is still unknown in most cases[157] and often, there is no predictive description of the ensemble behaviour or the origin of the forces driving aggregation.[149, 158]

The first point to consider is, how to achieve self-assembly? On the one hand, self-assembly mediated by Van der Waals forces and hydrophobic interactions generally leads primarily to close-packed structures in the bulk fluid, and to particle clusters when the assembly process is confined to the inferior of an emulsion droplet or to a liquid-liquid interface.[159] Ionic interactions between oppositely charged colloidal particles have also been used to assemble various crystalline lattices.[160] On the other hand, dipole-dipole interactions can be used to create superstructures when attractive or repulsive interactions, respectively, are induced by an external field. In fact, in solution, just by increasing the packing fraction of a magnetic colloid (Figure 1.20 a) dipolar chains and flux closure,[161] dimers, trimers, etc, can appear. Moreover, in nature, the chain formation for relatively large particles (about 30 nm diameter) is well known from magnetotactic bacteria synthesising fine magnetite crystals.[162]

The second point to consider is, how the magnetic properties are expected to change for assembled magnetic cores? Dipole-dipole interactions generally leads to decreasing coercivity, remanence, and

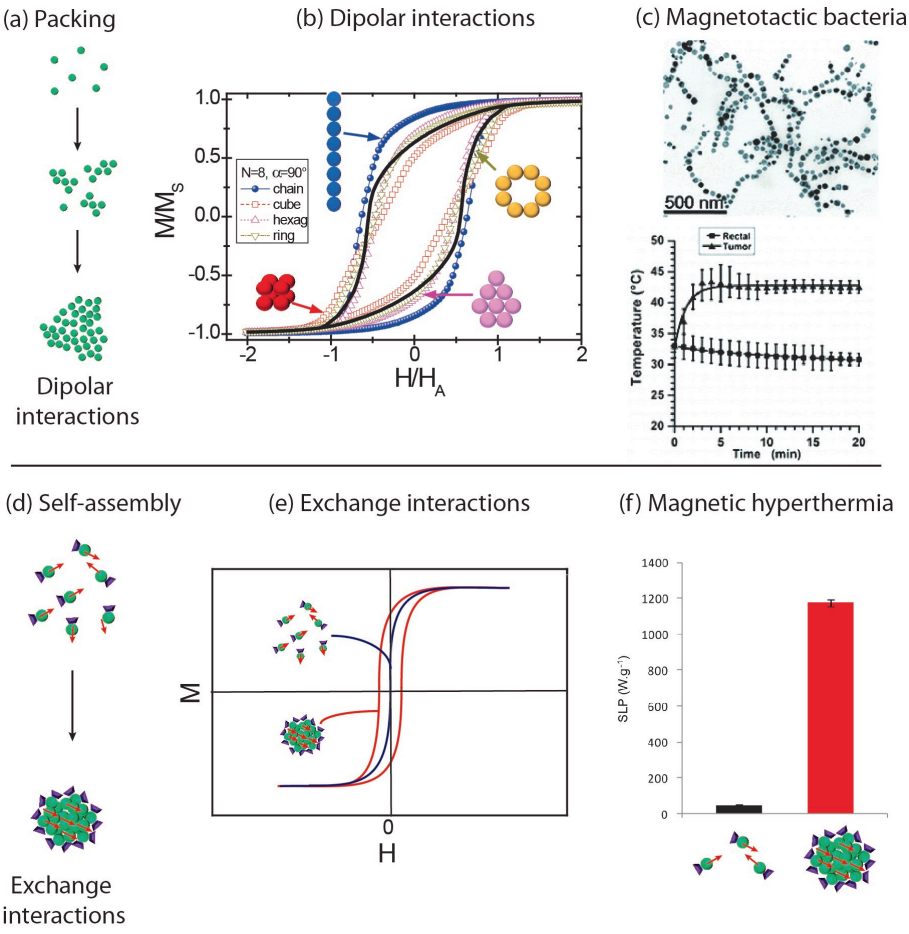

Figure 1.20: Packing (a) of magnetic crystals resulting in dipolar interactions (b). M(H) hysteresis curves corresponding to different dipolar-coupled magnetic nanoparticle assemblies (bidimensional chain, hexagonal lattice, and ring; 3D cube) of the same amount of particles, N = 8, and for the easy anisotropy axes randomly distributed into a cone of angle α = 90°. The black line stands for the case of non-interacting particles. Image adapted from literature.[154] (c) Magnetic heating performance of magnetotactic bacterial. Image adapted from literature.[155] Self-assembly (d) of magnetic crystals resulting in exchange interactions and their influence in the hysteresis (e). Magnetic heating performance of self-assembled structures in comparison with their individual counterparts. Image adapted from literature.[80]

hysteresis losses of the single particle, which leads, for instance, to worsen magnetic hyperthermia efficacy.[163, 164] As shown in Figure 1.20 b, this is theoretically demonstrated for different dipolar-coupled magnetic nanoparticle assemblies. The hysteresis area of all assemblies was diminished in comparison with the non-interacting case (black continuous curve). Only in the chain array the area is greater. The authors explained why chain-like arrangements biomimicking magnetotactic bacteria

has the superior heating performance, increasing more than 5 times in comparison with the randomly distributed system.[154] Moreover, it was also shown that this natural material is promising for cancer therapy, since when isolated and exposed to an alternative magnetic field in a suspension containing breast cancer cells (Figure 1.20 c), cell destruction occurred.[155]

SP nanoparticles show weak dipole–dipole interactions. However, their self-assembly leads to agglomerates that have accounted for exchange interactions instead (Figure 1.20 d), behaving like a particle with an effective volume larger than the single core showing ferromagnetic behaviour with hysteresis. Interestingly, this type of interaction has accounted for increasing coercivity and heating power (Figure 1.19 e).[165] Surprisingly, the heating power of multicore nanoparticles is higher than that of single core particles of comparable coercivity. Multicore particles consisting of a controlled number of superparamagnetic cores of around 10 nm that share crystalline alignment, forming a cluster a few tens of nanometers large, have shown coercivity and remanence significantly lower than for single core particles of comparable size and enhanced hyperthermia efficacy, due to exchange interaction between cores (Figure 1.20 f).[80]

In view of this, it is important to understand the self-assembly processes of magnetic nanocrystals into regular structures. These materials, in which exchange interactions have been induced by forcing the approaching between magnetic cores, seem to be quite promising since they possess some advantages from their individual crystals and interesting collective magnetic properties arising from their assembled structure.

To conclude this section: Nanotechnology is expected to provide groundbreaking solutions to many challenges that threaten our future, and iron oxide magnetic nanoparticles are one of the proposed nanomaterials to do so. There are limitations and challenges in its synthesis and corresponding analysis, which are still to be dealt in order to standardise their production and use. In this thesis, those limitations related with the controlled shape and the assembly of iron oxide magnetic nanoparticles, are addressed in the following chapters.

Bibliography

[1] Society, R. & Engineering, R. A. o. Nanoscience and nanotechnologies: opportunities and uncertainties (2004).

[2] Feynman, R. P. There's plenty of room at the bottom. *Engineering and science* **23**, 22–36 (1960).

[3] Everett, D. H. *Basic principles of colloid science* (Royal Society of Chemistry, 1988).

[4] Ostwald, C. W. W. *An Introduction to Theoretical and Applied Colloid Chemistry," the World of Neglected Dimensions,"* (John Wiley & Sons, Incorporated, 1922).

[5] Faraday, M. The bakerian lecture: experimental relations of gold (and other metals) to light. *Philosophical Transactions of the Royal Society of London* **147**, 145–181 (1857).

[6] Sondi, I., Goia, D. V. & Matijević, E. Preparation of highly concentrated stable dispersions of uniform silver nanoparticles. *Journal of colloid and interface science* **260**, 75–81 (2003).

[7] Stober, W., Fink, A. & Bohn, E. Controlled growth of monodisperse silica spheres in the micron size range. *Journal of colloid and interface science* **26**, 62–69 (1968).

[8] Matijevic, E. Preparation and properties of uniform size colloids. *Chemistry of materials* **5**, 412–426 (1993).

[9] Matijević, E. Fine particles: Science and technology. *MRS bulletin* **14**, 18–22 (1989).

[10] Sugimoto, T. *Fine particles: synthesis, characterization, and mechanisms of growth*, vol. 92 (CRC Press, 2000).

[11] Salas, G., Costo, R. & Morales, M. P. Synthesis of inorganic nanoparticles. *Frontiers in Nanoscience* **4**, 35–79 (2012).

[12] Aizpurua, J. & Hillenbrand, R. *Localized surface plasmons: basics and applications in field-enhanced spectroscopy*, 151–176 (Springer, 2012).

[13] Buschow, K. H. J. *Handbook of magnetic materials*, vol. 15 (Elsevier, 2003).

[14] Cornell, R. & Schwertmann, U. The iron oxides. *Structure, properties* (2001).

[15] Hühn, J. *et al.* Selected standard protocols for the synthesis, phase transfer, and characterization of inorganic colloidal nanoparticles. *Chemistry of Materials* (2016).

[16] Coulomb, C. A. *Premier-[troisième] memoire sur l'electricite et le magnetisme* (Academie Royale des sciences, 1785).

[17] Pankhurst, Q. A., Connolly, J., Jones, S. K. & Dobson, J. Applications of magnetic nanoparticles in biomedicine. *Journal of physics D: Applied physics* **36**, R167 (2003).

[18] Cullity, B. D. & Graham, C. D. *Introduction to magnetic materials* (John Wiley & Sons, 2011).

[19] Bertotti, G. *Hysteresis in magnetism: for physicists, materials scientists, and engineers* (Academic press, 1998).

[20] Landau, L. & Lifshitz, E. On the theory of the dispersion of magnetic permeability in ferromagnetic bodies. *Phys. Z. Sowjetunion* **8**, 101–114 (1935).

[21] Verwey, E. Electronic conduction of magnetite (fe_3o_4) and its transition point at low temperatures. *Nature* **144**, 327–328 (1939).

[22] Senn, M. S., Wright, J. P. & Attfield, J. P. Charge order and three-site distortions in the verwey structure of magnetite. *Nature* **481**, 173–176 (2012).

[23] Walz, F. The verwey transition-a topical review. *Journal of Physics: Condensed Matter* **14**, R285 (2002).

[24] Aragón, R., Buttrey, D. J., Shepherd, J. P. & Honig, J. M. Influence of nonstoichiometry on the verwey transition. *Physical Review B* **31**, 430 (1985).

[25] Neel, L. Some theoretical aspects of rock-magnetism. *Advances in physics* **4**, 191–243 (1955).

[26] Frenkel, J. & Dorfman, J. Spontaneous and induced magnetisation in ferromagnetic bodies. *Nature* **126**, 274–275 (1930).

[27] Garcia-Palacios, J. On the statics and dynamics of magnetoanisotropic nanoparticles. *Advances in Chemical Physics* **112**, 1–210 (2000).

[28] Dunlop, D. Superparamagnetic and single-domain threshold sizes in magnetite. *Journal of Geophysical Research* **78**, 1780–1793 (1973).

[29] Cowburn, R. Property variation with shape in magnetic nanoelements. *Journal of Physics D: Applied Physics* **33**, R1 (2000).

[30] Qi, W., Wang, M. & Liu, Q. Shape factor of nonspherical nanoparticles. *Journal of materials science* **40**, 2737–2739 (2005).

[31] Morrish, A. The physical principles of magnetism, 1965 (1968).

[32] Mørup, S., Hansen, M. F. & Frandsen, C. Magnetic interactions between nanoparticles. *Beilstein journal of nanotechnology* **1**, 182–190 (2010).

[33] Hansen, M. F. & Mørup, S. Models for the dynamics of interacting magnetic nanoparticles. *Journal of Magnetism and Magnetic Materials* **184**, L262–274 (1998).

[34] Lou, W., Nagel, S. & Rosenbaum, T. R. e. rosensweig. *Phys. Rev. Lett* **67**, 2721 (1991).

[35] Luis, F. *et al.* Magnetic relaxation of interacting co clusters: Crossover from two-to three-dimensional lattices. *Physical review letters* **88**, 217205 (2002).

[36] Frandsen, C. *et al.* Oriented attachment and exchange coupling of α-fe$_2$o$_3$ nanoparticles. *Physical Review B* **72**, 214406 (2005).

[37] Faber Jr, O. & Papell, S. On the influence of nonuniform magnetic fields on ferromagnetic colloidal sols (1968).

[38] Hamaker, H. The london—van der waals attraction between spherical particles. *physica* **4**, 1058–1072 (1937).

[39] Bergstrom, L., Meurk, A., Arwin, H. & Rowcliffe, D. J. Estimation of hamaker constants of ceramic materials from optical data using lifshitz theory. *Journal of the American Ceramic Society* **79**, 339–348 (1996).

[40] French, R., Cannon, R., DeNoyer, L. & Chiang, Y.-M. Full spectral calculation of non-retarded hamaker constants for ceramic systems from interband transition strengths. *Solid State Ionics* **75**, 13–33 (1995).

[41] Derjaguin, B. Theory of the stability of strongly charged lyophobic sols and the adhesion of strongly charged particles in solutions of electrolytes. *Acta Physicochim. USSR* **14**, 633–662 (1941).

[42] Verwey, E. & Overbeek, J. T. G. Theory of the stability of lyophobic colloids. *Journal of Colloid Science* **10**, 224–225 (1955).

[43] Grubbs, R. B. Nanoparticle assembly: solvent-tuned structures. *Nature materials* **6**, 553–555 (2007).

[44] Das, S. *et al.* Dual-responsive nanoparticles and their self-assembly. *Advanced Materials* **25**, 422–426 (2013).

[45] Kundu, P. K. *et al.* Light-controlled self-assembly of non-photoresponsive nanoparticles. *Nature chemistry* **7**, 646–652 (2015).

[46] Mulvaney, P., Parak, W. J., Caruso, F. & Weiss, P. S. Standardizing nanomaterials (2016).

[47] Sperling, R. *et al.* Size determination of (bio) conjugated water-soluble colloidal nanoparticles: a comparison of different techniques. *The Journal of Physical Chemistry C* **111**, 11552–11559 (2007).

[48] Connell, J. J., Patrick, P. S., Yu, Y., Lythgoe, M. F. & Kalber, T. L. Advanced cell therapies: targeting, tracking and actuation of cells with magnetic particles. *Regenerative medicine* **10**, 757–772 (2015).

[49] Lewinski, N., Colvin, V. & Drezek, R. Cytotoxicity of nanoparticles. *small* **4**, 26–49 (2008).

[50] Voinov, M. A., Pagan, J. O. S., Morrison, E., Smirnova, T. I. & Smirnov, A. I. Surface-mediated production of hydroxyl radicals as a mechanism of iron oxide nanoparticle biotoxicity. *Journal of the American Chemical Society* **133**, 35–41 (2010).

[51] Gutierrez, L., Morales, M. P. & Lazaro, F. J. Prospects for magnetic nanoparticles in systemic administration: synthesis and quantitative detection. *Physical Chemistry Chemical Physics* **16**, 4456–4464 (2014).

[52] López, A., Gutierrez, L. & Lazaro, F. J. The role of dipolar interaction in the quantitative determination of particulate magnetic carriers in biological tissues. *Physics in medicine and biology* **52**, 5043 (2007).

[53] Lazaro, F. J., Gutierrez, L., Abadía, A. R., Romero, M. S. & López, A. Biological tissue magnetism in the frame of iron overload diseases. *Journal of magnetism and magnetic materials* **316**, 126–131 (2007).

[54] Gutierrez, L. *et al.* Bioinorganic transformations of liver iron deposits observed by tissue magnetic characterisation in a rat model. *Journal of inorganic biochemistry* **100**, 1790–1799 (2006).

[55] Lazaro, F. J. *et al.* Whole tissue ac susceptibility after superparamagnetic iron oxide contrast agent administration in a rat model. *Journal of Magnetism and Magnetic Materials* **311**, 460–463 (2007).

[56] Kim, B., Rutka, J. T. & Chan, W. C. Nanomedicine. *The New England Journal of Medicine* **2010**, 2434–2443 (2010).

[57] Lewis, D. R., Kamisoglu, K., York, A. W. & Moghe, P. V. Polymer-based therapeutics: nanoassemblies and nanoparticles for management of atherosclerosis. *Wiley Interdisciplinary Reviews: Nanomedicine and Nanobiotechnology* **3**, 400–420 (2011).

[58] Torchilin, V. Tumor delivery of macromolecular drugs based on the epr effect. *Advanced drug delivery reviews* **63**, 131–135 (2011).

[59] Liu, Z., Jiao, Y., Wang, Y., Zhou, C. & Zhang, Z. Polysaccharides-based nanoparticles as drug delivery systems. *Advanced drug delivery reviews* **60**, 1650–1662 (2008).

[60] Lu, A., Salabas, E. e. & Schüth, F. Magnetic nanoparticles: synthesis, protection, functionalization, and application. *Angewandte Chemie International Edition* **46**, 1222–1244 (2007).

[61] Faivre, D. *Iron Oxides: From Nature to Applications* (John Wiley & Sons, 2016).

[62] Vuong, Q. L., Berret, J., Fresnais, J., Gossuin, Y. & Sandre, O. A universal scaling law to predict the efficiency of magnetic nanoparticles as mri t2-contrast agents. *Advanced healthcare materials* **1**, 502–512 (2012).

[63] Roch, A., Muller, R. N. & Gillis, P. Theory of proton relaxation induced by superparamagnetic particles. *The Journal of chemical physics* **110**, 5403–5411 (1999).

[64] Levy, M. *et al.* Revisiting mri contrast properties of nanoparticles: beyond the superparamagnetic regime. *The Journal of Physical Chemistry C* **117**, 15369–15374 (2013).

[65] Gossuin, Y., Gillis, P., Hocq, A., Vuong, Q. L. & Roch, A. Magnetic resonance relaxation properties of superparamagnetic particles. *Wiley Interdisciplinary Reviews: Nanomedicine and Nanobiotechnology* **1**, 299–310 (2009).

[66] Wang, Y.-X. J. Superparamagnetic iron oxide based mri contrast agents: current status of clinical application. *Quantitative imaging in medicine and surgery* **1**, 35–40 (2011).

[67] Wang, Y. *et al.* Formulation of superparamagnetic iron oxides by nanoparticles of biodegradable polymers for magnetic resonance imaging. *Advanced Functional Materials* **18**, 308–318 (2008).

[68] Jang, J. *et al.* Critical enhancements of mri contrast and hyperthermic effects by dopant-controlled magnetic nanoparticles. *Angewandte Chemie* **121**, 1260–1264 (2009).

[69] Bhavesh, R., Lechuga-Vieco, A. V., Ruiz-Cabello, J. & Herranz, F. T1-mri fluorescent iron oxide nanoparticles by microwave assisted synthesis. *Nanomaterials* **5**, 1880–1890 (2015).

[70] Hu, F. & Zhao, Y. S. Inorganic nanoparticle-based t 1 and t 1/t 2 magnetic resonance contrast probes. *Nanoscale* **4**, 6235–6243 (2012).

[71] Van der Zee, J. Heating the patient: a promising approach? *Annals of oncology* **13**, 1173–1184 (2002).

[72] Perigo, E. A. *et al.* Fundamentals and advances in magnetic hyperthermia. *Applied Physics Reviews* **2**, 041302 (2015).

[73] Natividad, E. *et al.* New insights into the heating mechanisms and self-regulating abilities of manganite perovskite nanoparticles suitable for magnetic fluid hyperthermia. *Nanoscale* **4**, 3954–3962 (2012).

[74] Mendo, S. G. *et al.* Hyperthermia studies of ferrite nanoparticles synthesized in the presence of cotton. *New Journal of Chemistry* **39**, 7182–7193 (2015).

[75] Blanco-Andujar, C., Ortega, D., Southern, P., Pankhurst, Q. & Thanh, N. High performance multi-core iron oxide nanoparticles for magnetic hyperthermia: microwave synthesis, and the role of core-to-core interactions. *Nanoscale* **7**, 1768–1775 (2015).

[76] Atkinson, W. J., Brezovich, I. A. & Chakraborty, D. P. Usable frequencies in hyperthermia with thermal seeds. *IEEE Transactions on Biomedical Engineering* 70–75 (1984).

[77] Hergt, R. *et al.* Magnetic properties of bacterial magnetosomes as potential diagnostic and therapeutic tools. *Journal of Magnetism and Magnetic Materials* **293**, 80–86 (2005).

[78] Guardia, P. *et al.* Water-soluble iron oxide nanocubes with high values of specific absorption rate for cancer cell hyperthermia treatment. *ACS nano* **6**, 3080–3091 (2012).

[79] Lee, J.-H. *et al.* Exchange-coupled magnetic nanoparticles for efficient heat induction. *Nature nanotechnology* **6**, 418–422 (2011).

[80] Lartigue, L. *et al.* Cooperative organization in iron oxide multi-core nanoparticles potentiates their efficiency as heating mediators and mri contrast agents. *ACS nano* **6**, 10935–10949 (2012).

[81] Henn, K. W. & Waddill, D. W. Utilization of nanoscale zero-valent iron for source remediation—a case study. *Remediation Journal* **16**, 57–77 (2006).

[82] Torchilin, V. P. Drug targeting. *European Journal of Pharmaceutical Sciences* **11**, S81–S91 (2000).

[83] A Silva, A., Silva, E., Carrico, A. & T Egito, E. Magnetic carriers: a promising device for targeting drugs into the human body. *Current pharmaceutical design* **13**, 1179–1185 (2007).

[84] Pirollo, K. F. & Chang, E. H. Does a targeting ligand influence nanoparticle tumor localization or uptake? *Trends in biotechnology* **26**, 552–558 (2008).

[85] Owen, J., Pankhurst, Q. & Stride, E. Magnetic targeting and ultrasound mediated drug delivery: Benefits, limitations and combination. *International Journal of Hyperthermia* **28**, 362–373 (2012).

[86] Norotte, C., Marga, F. S., Niklason, L. E. & Forgacs, G. Scaffold-free vascular tissue engineering using bioprinting. *Biomaterials* **30**, 5910–5917 (2009).

[87] Zhang, W.-x. Nanoscale iron particles for environmental remediation: an overview. *Journal of nanoparticle Research* **5**, 323–332 (2003).

[88] Kirschvink, J. L., Kobayashi-Kirschvink, A. & Woodford, B. J. Magnetite biomineralization in the human brain. *Proceedings of the National Academy of Sciences* **89**, 7683–7687 (1992).

[89] Michel, F. M. *et al.* Ordered ferrimagnetic form of ferrihydrite reveals links among structure, composition, and magnetism. *Proceedings of the National Academy of Sciences* **107**, 2787–2792 (2010).

[90] Gutierrez, L. *et al.* Detailed magnetic monitoring of the enhanced magnetism of ferrihydrite along its progressive transformation into hematite. *Journal of Geophysical Research: Solid Earth* **121**, 4118–4129 (2016).

[91] Navrotsky, A., Mazeina, L. & Majzlan, J. Size-driven structural and thermodynamic complexity in iron oxides. *Science* **319**, 1635–1638 (2008).

[92] Massart, R. Preparation of aqueous magnetic liquids in alkaline and acidic media. *IEEE transactions on magnetics* **17**, 1247–1248 (1981).

[93] Gribanov, N., Bibik, E., Buzunov, O. & Naumov, V. Physico-chemical regularities of obtaining highly dispersed magnetite by the method of chemical condensation. *Journal of Magnetism and Magnetic Materials* **85**, 7–10 (1990).

[94] Qiu, X. Synthesis and characterization of magnetic nano particles. *Chinese Journal of Chemistry* **18**, 834–837 (2000).

[95] Martínez-Mera, I., Espinosa-Pesqueira, M., Perez-Hernandez, R. & Arenas-Alatorre, J. Synthesis of magnetite (fe_3o_4) nanoparticles without surfactants at room temperature. *Materials Letters* **61**, 4447–4451 (2007).

[96] Iwasaki, T., Mizutani, N., Watano, S., Yanagida, T. & Kawai, T. Size control of magnetite nanoparticles by organic solvent-free chemical coprecipitation at room temperature. *Journal of Experimental Nanoscience* **5**, 251–262 (2010).

[97] Rockenberger, J., Scher, E. C. & Alivisatos, A. P. A new nonhydrolytic single-precursor approach to surfactant-capped nanocrystals of transition metal oxides. *Journal of the American Chemical Society* **121**, 11595–11596 (1999).

[98] Hyeon, T., Lee, S. S., Park, J., Chung, Y. & Na, H. B. Synthesis of highly crystalline and monodisperse maghemite nanocrystallites without a size-selection process. *Journal of the American Chemical Society* **123**, 12798–12801 (2001).

[99] Kwon, S. G. & Hyeon, T. Formation mechanisms of uniform nanocrystals via hot-injection and heat-up methods. *Small* **7**, 2685–2702 (2011).

[100] Wetterskog, E. *et al.* Precise control over shape and size of iron oxide nanocrystals suitable for assembly into ordered particle arrays. *Science and Technology of Advanced Materials* **15**, 055010 (2014).

[101] Vita, F. *et al.* Tuning morphology and magnetism of magnetite nanoparticles by calix [8] arene-induced oriented aggregation. *CrystEngComm* **18**, 8591–8598 (2016).

[102] Laurent, S. *et al.* Magnetic iron oxide nanoparticles: synthesis, stabilization, vectorization, physicochemical characterizations, and biological applications. *Chemical reviews* **108**, 2064–2110 (2008).

[103] Fievet, F., Lagier, J., Blin, B., Beaudoin, B. & Figlarz, M. Homogeneous and heterogeneous nucleations in the polyol process for the preparation of micron and submicron size metal particles. *Solid State Ionics* **32**, 198–205 (1989).

[104] Jezequel, D., Guenot, J., Jouini, N. & Fievet, F. Submicrometer zinc oxide particles: Elaboration in polyol medium and morphological characteristics. *Journal of Materials Research* **10**, 77–83 (1995).

[105] Cai, W. & Wan, J. Facile synthesis of superparamagnetic magnetite nanoparticles in liquid polyols. *Journal of colloid and interface science* **305**, 366–370 (2007).

[106] Caruntu, D. *et al.* Synthesis of variable-sized nanocrystals of fe_3o_4 with high surface reactivity. *Chemistry of materials* **16**, 5527–5534 (2004).

[107] Willard, M., Kurihara, L., Carpenter, E., Calvin, S. & Harris, V. Chemically prepared magnetic nanoparticles. *International Materials Reviews* **49**, 125–170 (2004).

[108] Guan, N., Wang, Y., Sun, D. & Xu, J. A simple one-pot synthesis of single-crystalline magnetite hollow spheres from a single iron precursor. *Nanotechnology* **20**, 105603 (2009).

[109] Veintemillas-Verdaguer, S., Morales, M. P. & Serna, C. Continuous production of γ-fe$_2$o$_3$ ultrafine powders by laser pyrolysis. *Materials letters* **35**, 227–231 (1998).

[110] Morales, M. P., Veintemillas-Verdaguer, S. & Serna, C. Magnetic properties of uniform γ-fe$_2$o$_3$ nanoparticles smaller than 5 nm prepared by laser pyrolysis. *Journal of materials research* **14**, 3066–3072 (1999).

[111] Morales, M. P. *et al.* Surface and internal spin canting in γ-fe$_2$o$_3$ nanoparticles. *Chemistry of Materials* **11**, 3058–3064 (1999).

[112] Morales, M. P., Andres-Verges, M., Veintemillas-Verdaguer, S., Montero, M. & Serna, C. Structural effects on the magnetic properties of γ-fe$_2$o$_3$ nanoparticles. *Journal of Magnetism and Magnetic Materials* **203**, 146–148 (1999).

[113] Gedye, R. *et al.* The use of microwave ovens for rapid organic synthesis. *Tetrahedron letters* **27**, 279–282 (1986).

[114] Giguere, R. J., Bray, T. L., Duncan, S. M. & Majetich, G. Application of commercial microwave ovens to organic synthesis. *Tetrahedron letters* **27**, 4945–4948 (1986).

[115] Niederberger, M. & Pinna, N. *Metal oxide nanoparticles in organic solvents: synthesis, formation, assembly and application* (Springer Science & Business Media, 2009).

[116] Carenza, E. *et al.* Rapid synthesis of water-dispersible superparamagnetic iron oxide nanoparticles by a microwave-assisted route for safe labeling of endothelial progenitor cells. *Acta biomaterialia* **10**, 3775–3785 (2014).

[117] Bühler, G. & Feldmann, C. Microwave-assisted synthesis of luminescent lapo4: Ce, tb nanocrystals in ionic liquids. *Angewandte Chemie International Edition* **45**, 4864–4867 (2006).

[118] Zheng, B., Zhang, M., Xiao, D., Jin, Y. & Choi, M. M. Fast microwave synthesis of fe$_3$o$_4$ and fe$_3$o$_4$/ag magnetic nanoparticles using fe^{2+} as precursor. *Inorganic Materials* **46**, 1106–1111 (2010).

[119] Salas, G., Veintemillas-Verdaguer, S. & Morales, M. P. Relationship between physico-chemical properties of magnetic fluids and their heating capacity. *International journal of hyperthermia* **29**, 768–776 (2013).

[120] Kharisov, B. I. *et al.* Solubilization, dispersion and stabilization of magnetic nanoparticles in water and non-aqueous solvents: recent trends. *RSC Advances* **4**, 45354–45381 (2014).

[121] Lefebure, S., Dubois, E., Cabuil, V., Neveu, S. & Massart, R. Monodisperse magnetic nanoparticles: preparation and dispersion in water and oils. *Journal of Materials Research* **13**, 2975–2981 (1998).

[122] Bohara, R. A., Thorat, N. D. & Pawar, S. H. Role of functionalization: strategies to explore potential nano-bio applications of magnetic nanoparticles. *RSC Advances* **6**, 43989–44012 (2016).

[123] Bacri, J.-C., Perzynski, R., Salin, D., Cabuil, V. & Massart, R. Ionic ferrofluids: a crossing of chemistry and physics. *Journal of Magnetism and Magnetic Materials* **85**, 27–32 (1990).

[124] Zahraei, M. *et al.* Versatile theranostics agents designed by coating ferrite nanoparticles with biocompatible polymers. *Nanotechnology* **27**, 255702 (2016).

[125] Tartaj, P., Gonzalez-Carreno, T. & Serna, C. J. Single-step nanoengineering of silica coated maghemite hollow spheres with tunable magnetic properties. *Advanced Materials* **13**, 1620–1624 (2001).

[126] Li, Y. *et al.* Novel approach for the synthesis of fe$_3$o$_4$@ tio$_2$ core–shell microspheres and their application to the highly specific capture of phosphopeptides for maldi-tof ms analysis. *Chemical Communications* 564–566 (2008).

[127] Hlavay, J. & Polyak, K. Determination of surface properties of iron hydroxide-coated alumina adsorbent prepared for removal of arsenic from drinking water. *Journal of Colloid and Interface Science* **284**, 71–77 (2005).

[128] Chen, M., Yamamuro, S., Farrell, D. & Majetich, S. A. Gold-coated iron nanoparticles for biomedical applications. *Journal of applied physics* **93**, 7551–7553 (2003).

[129] Ruiz, A. *et al.* Short-chain peg molecules strongly bound to magnetic nanoparticle for mri long circulating agents. *Acta biomaterialia* **9**, 6421–6430 (2013).

[130] Creixell, M. *et al.* The effect of grafting method on the colloidal stability and in vitro cytotoxicity of carboxymethyl dextran coated magnetic nanoparticles. *Journal of Materials Chemistry* **20**, 8539–8547 (2010).

[131] Qu, J., Liu, G., Wang, Y. & Hong, R. Preparation of fe$_3$o$_4$–chitosan nanoparticles used for hyperthermia. *Advanced Powder Technology* **21**, 461–467 (2010).

[132] Mulens-Arias, V., Rojas, J. M., Perez-Yagüe, S., Morales, M. P. & Barber, D. F. Polyethylenimine-coated spion exhibits potential intrinsic anti-metastatic properties inhibiting migration and invasion of pancreatic tumor cells. *Journal of Controlled Release* **216**, 78–92 (2015).

[133] Cintra, E. *et al.* Nanoparticle agglomerates in magnetoliposomes. *Nanotechnology* **20**, 045103 (2008).

[134] D'Souza, A. J. M., Schowen, R. L. & Topp, E. M. Polyvinylpyrrolidone–drug conjugate: synthesis and release mechanism. *Journal of Controlled Release* **94**, 91–100 (2004).

[135] Gupta, A. K. & Gupta, M. Synthesis and surface engineering of iron oxide nanoparticles for biomedical applications. *Biomaterials* **26**, 3995–4021 (2005).

[136] Qian, Z. M., Li, H., Sun, H. & Ho, K. Targeted drug delivery via the transferrin receptor-mediated endocytosis pathway. *Pharmacological reviews* **54**, 561–587 (2002).

[137] Gupta, A. K. & Curtis, A. S. Lactoferrin and ceruloplasmin derivatized superparamagnetic iron oxide nanoparticles for targeting cell surface receptors. *Biomaterials* **25**, 3029–3040 (2004).

[138] Kralj, S., Rojnik, M., Kos, J. & Makovec, D. Targeting egfr-overexpressed a431 cells with egf-labeled silica-coated magnetic nanoparticles. *Journal of nanoparticle research* **15**, 1666 (2013).

[139] Gupta, A. K., Berry, C., Gupta, M. & Curtis, A. Receptor-mediated targeting of magnetic nanoparticles using insulin as a surface ligand to prevent endocytosis. *IEEE transactions on nanobioscience* **2**, 255–261 (2003).

[140] Baker, M. E. Albumin's role in steroid hormone action and the origins of vertebrates: is albumin an essential protein? *FEBS letters* **439**, 9–12 (1998).

[141] Zhang, Y., Kohler, N. & Zhang, M. Surface modification of superparamagnetic magnetite nanoparticles and their intracellular uptake. *Biomaterials* **23**, 1553–1561 (2002).

[142] Tsourkas, A. *et al.* In vivo imaging of activated endothelium using an anti-vcam-1 magnetooptical probe. *Bioconjugate chemistry* **16**, 576–581 (2005).

[143] Shimizu, K. *et al.* Bone tissue engineering with human mesenchymal stem cell sheets constructed using magnetite nanoparticles and magnetic force. *Journal of Biomedical Materials Research Part B: Applied Biomaterials* **82**, 471–480 (2007).

[144] Ruiz, A. *et al.* Biotransformation of magnetic nanoparticles as a function of coating in a rat model. *Nanoscale* **7**, 16321–16329 (2015).

[145] Thanh, N. T., Maclean, N. & Mahiddine, S. Mechanisms of nucleation and growth of nanoparticles in solution. *Chemical reviews* **114**, 7610–7630 (2014).

[146] LaMer, V. K. & Dinegar, R. H. Theory, production and mechanism of formation of monodispersed hydrosols. *Journal of the American Chemical Society* **72**, 4847–4854 (1950).

[147] Mer, V. K. L. Nucleation in phase transitions. *Industrial & Engineering Chemistry* **44**, 1270–1277 (1952).

[148] Morales, M. P., Pecharroman, C., Carreño, T. G. & Serna, C. Structural characteristics of uniform γ-fe$_2$o$_3$ particles with different axial (length/width) ratios. *Journal of Solid State Chemistry* **108**, 158–163 (1994).

[149] De Yoreo, J. J. *et al.* Crystallization by particle attachment in synthetic, biogenic, and geologic environments. *Science* **349**, aaa6760 (2015).

[150] Matijević, E. & Scheiner, P. Ferric hydrous oxide sols: Iii. preparation of uniform particles by hydrolysis of fe (iii)-chloride,-nitrate, and-perchlorate solutions. *Journal of Colloid and Interface Science* **63**, 509–524 (1978).

[151] Ozaki, M., Kratohvil, S. & Matijević, E. Formation of monodispersed spindle-type hematite particles. *Journal of colloid and interface science* **102**, 146–151 (1984).

[152] Ishikawa, T. & Matijevic, E. Formation of monodispersed pure and coated spindle-type iron particles. *Langmuir* **4**, 26–31 (1988).

[153] Morales, M. P., Gonzalez-Carreno, T. & Serna, C. The formation of α–fe$_2$o$_3$ monodispersed particles in solution. *Journal of Materials Research* **7**, 2538–2545 (1992).

[154] Serantes, D. *et al.* Multiplying magnetic hyperthermia response by nanoparticle assembling. *The Journal of Physical Chemistry C* **118**, 5927–5934 (2014).

[155] Alphandery, E., Faure, S., Seksek, O., Guyot, F. & Chebbi, I. Chains of magnetosomes extracted from amb-1 magnetotactic bacteria for application in alternative magnetic field cancer therapy. *ACS Nano* **5**, 6279–6296 (2011).

[156] Frandsen, C. *et al.* Aggregation-induced growth and transformation of β-feooh nanorods to micron-sized α-fe$_2$o$_3$ spindles. *CrystEngComm* **16**, 1451–1458 (2014).

[157] Stolarczyk, J. K., Deak, A. & Brougham, D. F. Nanoparticle clusters: assembly and control over internal order, current capabilities, and future potential. *Advanced Materials* **28**, 5400–5424 (2016).

[158] Nie, Z., Petukhova, A. & Kumacheva, E. Properties and emerging applications of self-assembled structures made from inorganic nanoparticles. *Nature nanotechnology* **5**, 15–25 (2010).

[159] Erb, R. M., Son, H. S., Samanta, B., Rotello, V. M. & Yellen, B. B. Magnetic assembly of colloidal superstructures with multipole symmetry. *Nature* **457**, 999–1002 (2009).

[160] Shevchenko, E. V., Talapin, D. V., Kotov, N. A., O'brien, S. & Murray, C. B. Structural diversity in binary nanoparticle superlattices. *Nature* **439**, 55–59 (2006).

[161] Chantrell, R., Bradbury, A., Popplewell, J. & Charles, S. Particle cluster configuration in magnetic fluids. *Journal of Physics D: Applied Physics* **13**, L119 (1980).

[162] Dunin-Borkowski, R. E. *et al.* Off-axis electron holography of magnetotactic bacteria. *European Journal of Mineralogy* **13**, 671–684 (2001).

[163] Dutz, S. & Hergt, R. The role of interactions in systems of single domain ferrimagnetic iron oxide nanoparticles. *Journal of Nano-and Electronic Physics* **4**, 2010–1 (2012).

[164] Coral, D. F. *et al.* Effect of nanoclustering and dipolar interactions in heat generation for magnetic hyperthermia. *Langmuir* **32**, 1201–1213 (2016).

[165] Eggeman, A. S., Majetich, S. A., Farrell, D. & Pankhurst, Q. A. Size and concentration effects on high frequency hysteresis of iron oxide nanoparticles. *IEEE transactions on magnetics* **43**, 2451–2453 (2007).

Part B

Single-core nanoparticles

2

How shape and internal structure affect the magnetic properties of anisometric magnetite nanoparticles

Summary

A three-step aqueous approach to obtain large ($>$ 50 nm) magnetite single-core particles has been developed. The steps are a) synthesis of antiferromagnetic nanoparticles, b) particle coating and c) subsequent reduction of the core material to magnetite. By variation of precursor material and process conditions, the synthesis yielded rhombohedra, discs or needles below 200 nm. A combination of X-ray diffraction, ^{57}Fe Mössbauer spectroscopy and infrared spectroscopy confirmed magnetite to be the dominant final core material. From transmission electron microscopy, we identified porous structures after the reduction. Magnetic characterization of the different magnetic nanopaticles revealed strikingly different magnetic behaviour depending on their shape, internal structure and reduction process. We conclude that each of these parameters have to be considered in further characterization of large magnetite nanoparticles.

2.1 Introduction

In the last years, iron oxide magnetic nanoparticles (MNPs) have been widely used for biomedical applications. Examples of these applications include new ways of cancer treatment such as magnetic drug targeting [1] and magnetic hyperthermia [2], or the use of MNPs as contrast agents or tracers in Magnetic Resonance Imaging[3] and Magnetic Particle Imaging[4]. Each application requires MNPs with customized structural and magnetic properties, which are strongly dependent upon both particle size and shape [5]. As an example, ultra-small superparamagnetic MNPs with magnetic core sizes below 10 nm were suitable for the exploration of tumour permeability [6]. However, the uptake of MNPs by macrophages was most effective for MNPs with a core size of 10–30 nm, while for magnetic hyperthermia, maximum heating rate is obtained at the transition from multidomain to single domain magnetic behaviour occurring in a relatively broad size range at about 30 nm with a change of transition of magnetic energy into thermal energy (Néel or Brown) [7]. Moreover, if collective magnetic behaviour of the cores exists originating from interactions within a nanoparticle, heating rates can go up to one order of magnitude higher than for single-domain nanoparticles [8, 9].

Nanoparticle shape can also have significant impact on the magnetic behaviour of MNPs in applications. Firstly, the magnetic shape anisotropy of the MNPs can assume much larger values than the magnetocrystalline anisotropy and thus can strongly affect the orientation of magnetic moments inside the particles. In addition, dipolar interactions between MNPs also depend on the particle shape and will influence the structural agglomerate formation leading to, for example, chain-like arrangements biomimicking magnetotactic bacteria [10] or hollow spheres consisting of oriented aggregates of nanocrystals [11, 12].

One of the current challenges in nanoparticle research is the production of particles [13] comprising a large magnetite core that is well-controlled in size and shape, with a large magnetic moment and long term colloidal stability. Over the past decades, direct syntheses of magnetite NPs with different sizes and morphologies have been reported, including nano- spheres [13], cubes [14, 15], wires [16], rods [17], octahedral [18], plates [19] and prisms [20]. Synthesis of each of these shapes was performed out in organic media, so that, in general, nanocrystal shape control was achieved by selective adhesion of surfactant to a particular crystal facet and this subsequent slow growth along this direction. Without surfactants, nanoparticles can aggregate into dense or hollow micrometre spheres.[11, 12] Synthesis in organic media is limited by the small particle batches that require further steps to be transferred to water, which results in low yields.

In the present paper, we describe an alternative aqueous-based approach to produce single-core magnetite MNPs with different morphologies and core sizes above 25 nm, which could be scalable for large production. Magnetic iron oxide nanorods were already produced by a similar method and showed interesting magnetic properties and tuneable surface functionality [21]. We propose a three-step process (Figure 2.1) from which uniform rhombohedra, discs and elongated MNPs can easily be

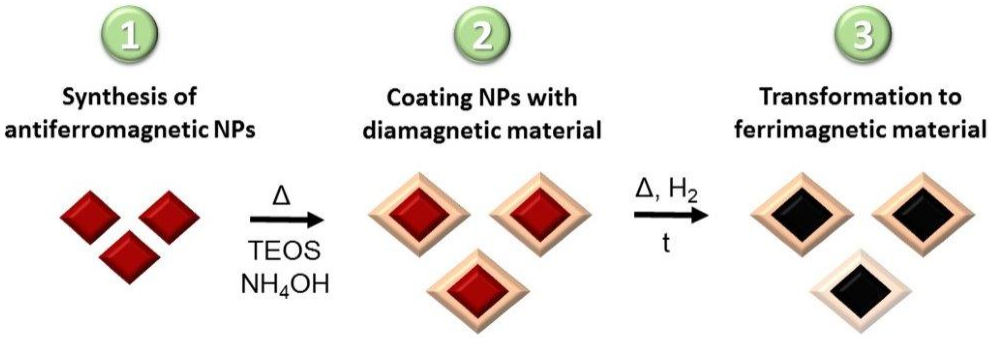

Figure 2.1: General scheme for the synthesis of single-core MNPs.

obtained. First, an aqueous synthesis route is followed to obtain uniform antiferromagnetic precursors such as goethite or hematite, whose size and shape can be tuned by changing the synthesis conditions including temperature, pressure, and nature and concentration of the salts used [22]. Then, the antiferromagnetic precursor particles are coated by a silica layer that prevents their aggregation [23, 24]. Finally, the silica coated antiferromagnetic particles are reduced to magnetite. This is either performed on particles in powder form (dry-reduction), by exposing them to a hydrogen atmosphere at a certain partial pressure [25], or in liquid form, using oleic acid and an organic solvent (wet-reduction). In both processes, the hydrogen and oleic acid act as the reducing agents [26, 27]. Transformation of these antiferromagnetic phases into magnetite particles requires the full control of key parameters including temperature, atmosphere and pressure to produce pure single phases and avoid core sintering.

The products are physicochemically characterized by electron microscopy, X-ray diffraction, ^{57}Fe Mössbauer spectroscopy and infrared spectroscopy. Their magnetic behaviour is analysed by field and temperature dependent magnetization measurements. This characterization allows for comparing the products of dry reduction and wet reduction.

2.2 Experimental section

Synthesis of the precursors: The preparation of uniform and nanometer precursor particles requires slight modifications of reported synthetic routes for hematite [26] and goethite [28] to obtain particle sizes below 200 nm and keep the uniformity.

(i) Hematite: The synthesis of hematite (α-Fe_2O_3) nano-sized rhombohedra and discs was carried out in a glass bottle dissolving $FeCl_3 \cdot 6H_2O$ in 50 mL of pure ethanol and 10 mL or 1 mL of water for rhombohedra or discs respectively under vigorous magnetic stirring. Then sodium acetate was added while magnetically stirring and the solution was homogenized by sonication for 10 minutes. The final solution had a concentration of $FeCl_3$ of 0.082 and 0.096 M for rhombohedra and discs, respectively. The concentration of sodium acetate was 0.49 and 0.58 M for rhombohedra and discs, respectively. The mixtures were sealed in a teflon-lined autoclave (125 mL) and maintained at 180°C for 12 h for solvothermal crystallization. After natural cooling to ambient temperature, the resulting red solid product was washed with distilled water, filtered and finally dried overnight in an oven at 50°C.

(ii) Goethite: The synthesis of goethite (α-FeOOH) nano-sized needles was performed by precipitation of a Fe(II) sulfate 0.15 M aqueous solution by the addition of a 0.225 M solution of sodium carbonate. The resulting dispersion was then oxidized at constant temperature. The concentration ratio of the reagents [CO^{3-}]/[Fe(II)] is 1.5. These processes were carried out according to the following procedure. Oxygen was first removed from the distilled water by N_2 bubbling to prevent Fe(II) oxidation during the dissolution of $FeSO_4$. The Fe(II) and sodium carbonate solutions 125 mL, each) were prepared with the desired concentrations. The sodium carbonate solution was then introduced into a thermostatic water bath at 44°C under moderate stirring and the Fe(II) solution was added applying a constant air flow with a rate of 2 L·min^{-1} through the resulting suspension. Particles of goethite are then formed by aerial oxidation. After 180 min of reaction, the resulting precipitate was cooled, centrifuged and washed several times with distilled water. Finally, the powdered solid was collected by filtration and dried overnight at 50°C.

Coating and reduction to magnetite: Silica coating and subsequent reduction of the precursor particles were carried out by optimizing procedures described elsewhere [25–27]. Silica coating ensures both, steric and electrostatic protection and it acts as dispersing agent of many electrostatic colloids. These advantages render silica an ideal, low-cost material to tailor surface properties. Additionally, this coating should endow the cores with several beneficial properties, such as the biocompatibility and the possibility of subsequent functionalization by connecting the silanol groups on the surface with other organic molecular agents [29]. For the silica coating, 100 mg of the precursor particles in powder form were dispersed in a 2-propanol/H_2O 2:1 v/v solution of 300 mL. NH_4OH 28 % v/v and tetraethyl orthosilicate (TEOS) were added during sonication and the reaction was allowed to continue for 15 min. The final volume was 320.2 mL and the final concentration of the reagents was: [NH_4OH] = 4.5 x 10^{4-} M, [TEOS] = 2.8 x 10^{-6} M. The product was washed twice with 2-propanol. The solution was filtered

and dried overnight at 50°C.

(i) Wet reduction: For the reduction to magnetite in liquid, 50 mg of the silica coated precursor nanoparticles and 35 mL of trioctylamine were mixed by sonication for 30 min and subsequently 2.2 mL oleic acid were added. The mixture was transferred into a three-necked flask and heated at 350°C under H_2 flow of 0.486 L·min^{-1} for 1 h until the colour changed to dark. After cooling to ambient temperature, the black product was collected by centrifugation and washed 3 times with toluene. Finally, the product was dried overnight at 50°C.

(ii) Dry reduction: For dry reduction, 50 mg of the silica coated precursor nanoparticles in powder form were treated at 360°C for 2 h in vacuum to remove moisture. The reduction was performed under H_2 atmosphere with a partial gas pressure of 61 kPa for 3.5 h refreshing the H_2 atmosphere after 1 h. The sample was then cooled down to ambient temperature.

Nanoparticle characterization: The size of the iron oxide cores in both the precursors and the final products was determined by transmission electron microscopy (TEM) with a JEM1010 microscope (JEOL, Peabody, USA) operating at 100 kV. TEM samples were prepared by placing a drop of the particles suspended in water onto a carbon coated copper grid and allowing it to dry at room temperature. The size distribution was determined by manual measurement of more than 100 particles using the public domain ImageJ software (http://imagej.nih.gov/). High-resolution TEM (HRTEM) was performed in a JEM-3100F microscope (JEOL, Peabody, USA) operating at 300 kV. The particle morphology was determined from scanning electron microscopy (SEM) with a Philips XL30 microscope operating at 10 kV. The sample preparation is identical to the preparation for the TEM analysis.

The crystal structure of the antiferromagnetic precursors and the reduced particles was identified using a combination of X-ray diffraction (XRD), Fourier transform infra-red spectroscopy (FTIR) and room temperature ^{57}Fe Mössbauer spectroscopy. XRD was performed in a Bruker D8 Advance diffractometer with a graphite monochromator using CuK_α radiation (λ = 1.5406). The patterns were collected within 10° and 70° in 2θ at a scan rate of 0.2 (2θ)/min. The core crystalline size was calculated via the Scherrer equation (XRD size), using was obtained from the broadening (104) and (110) X-ray diffraction lines for the precursors, hematite and goethite, respectively and from (311) X-ray diffraction line for the resulting magnetite. FTIR was performed in a Bruker IFS 66V-S apparatus, in the range of 2000-250 cm$_{-1}$. The samples were prepared for FTIR by diluting the dried powder in KBr at 2 $\%$ by weight and pressing it into a pellet.

Room temperature ^{57}Fe Mössbauer spectroscopy was used to determine the resulting iron oxide phase after reduction of the precursors. Approximately 50 mg of each sample was mixed with ca. 200 mg sucrose in a pestle and mortar to form a paste, and then flattened within a coin shaped absorber. Spectra were recorded at room temperature in transmission geometry using a ^{57}Co source in a R_h matrix, using a W302 spectrometer and W202 detector, both from SEECo (Minneapolis, USA).

For the magnetic characterization, the samples were measured in powder form after drying in an inox coated oven at 50°C for 24 h. The powder was filled into polycarbonate capsules after accurately

weighing. The sample mass was determined to be between 1 and 4 mg. Finally, the powder was immobilized in gelatin. The magnetization measurements have been performed in a Magnetic Property Measurement System (Quantum Design, USA) allowing the detection of the sample magnetic moment as a function of applied magnetic field and temperature.

In the field dependent measurements the magnetic field varied between -5 T and 5 T. The amplitude of consecutive field steps was changed logarithmically to ensure a sufficient number of measurements at low fields. The time between consecutive magnetization measurements was about 3 min to guarantee quasi-static conditions. Hysteresis loops were measured at 295 K and at 5 K. In the temperature dependent measurements the sample was first cooled down to 5 K in zero magnetic field (zero field cooling, ZFC). Then, a magnetic field of 5 mT was applied and the magnetic moment of the sample was measured with increasing temperature. After reaching 295 K, the magnetic moment was measured with decreasing temperature under the presence of the magnetic field of 5 mT (field cooling, FC). Hysteresis loops were also measured in a vibrating sample magnetometer (MLVSM9, MagLab 9T, Oxford Instruments, UK) at room temperature and at 5 K after saturating the sample in a 5 T (-5 T) field and recording the complete magnetization curves at a field change rate of 0.3 T·min^{-1}.

2.3 Results and discussion

Structural characterisation of the precursor:

A general scheme of the synthesis strategy followed in this work is presented in Figure 1. After the synthesis of the precursors and before the particles were coated, their morphology has been investigated by SEM. The scanning electron micrographs of the precursors (Figure 2.2) show the three different morphologies obtained: (A) rhombohedra, (B) hexagonal discs and (C) needles. Image S1 of SI confirms the morphology of the rhombohedra, where the typical square bipyramids of this polyhedron is observed, in any of the orthogonal orientations of the nanoparticle. Both the size and the shape of the nanoparticles are highly homogeneous.

Transformation of the precursors to magnetite:

Figure 3 shows TEM images of the precursor and the obtained MNPs where the core material has been transformed to magnetite by dry and wet reduction methods. The precursor has been successfully coated with a uniform silica shell around single cores or double-triple cores (75%), although a fraction of multi-cores (5-10 cores coated) (25%) cannot be discarded. TEOS condensation occurs only on the surface of the NPs and no colloidal silica nanoparticles have been observed.

The core size after reduction of the precursor was determined from the TEM images. The rhombohedra have an average core diameter of 67 nm, the discs are 140 nm in diameter and 22 nm thick and finally the needles are 183 nm in length and 33 nm thick. All samples have a standard deviation lower

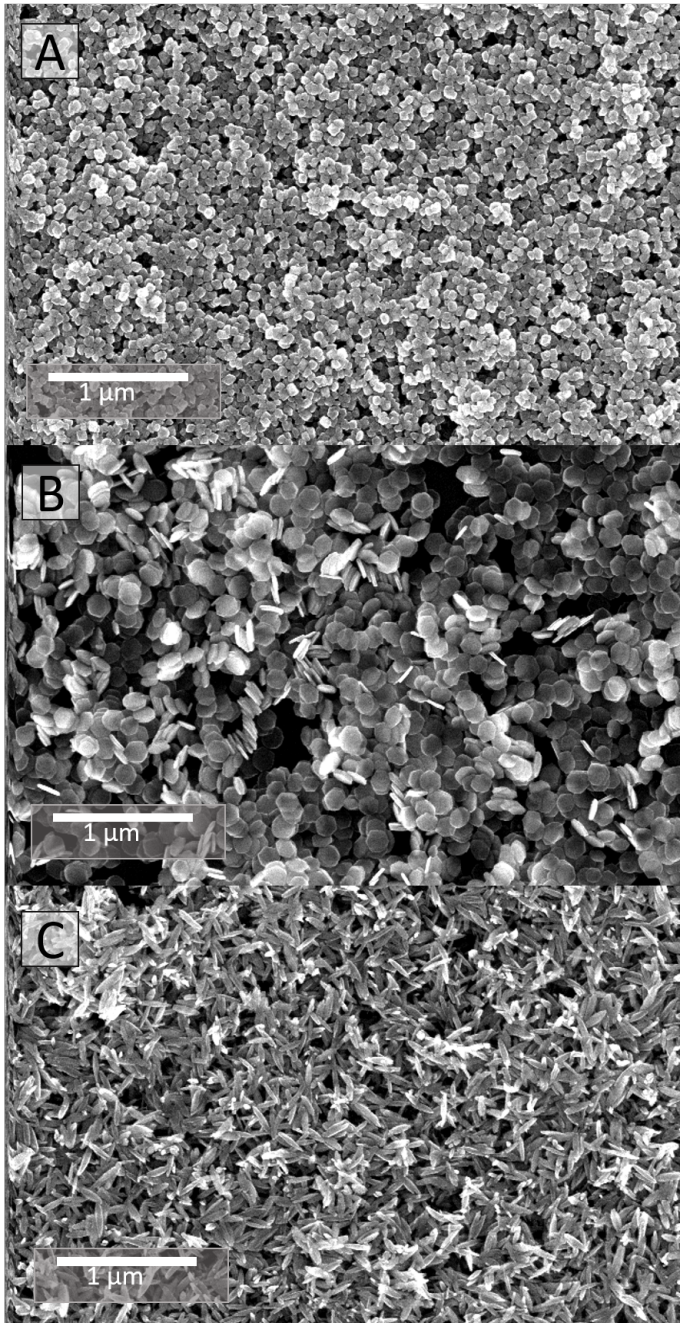

Figure 2.2: SEM images of the precursor material (A) rhombohedra, (B) discs and (C) needles.

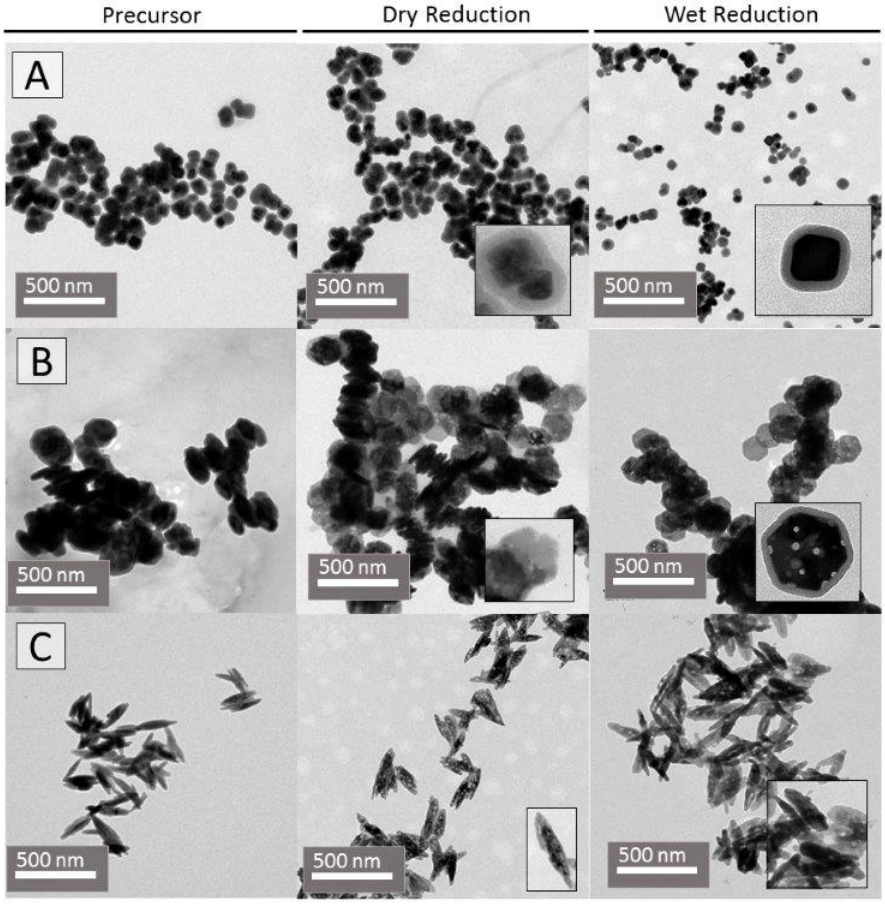

Figure 2.3: TEM images of the precursors and the magnetic nanoparticles obtained by dry and wet reduction. (A) rhombohedra, (B) discs, (C) needles.

than 20% (see Table 1). By comparing the images before and after reduction we see that the particle size and morphology are conserved which is due to the silica coating of approximately 10 nm. We also observe pores within the core structure after the reduction to magnetite, which is a consequence of the phase transformation from goethite in the case of the needles (Figure 2.3 C), or hematite, in the case of the discs (Figure 2.3 B) and the rhombohedra (Figure 2.3 A).

When the silica coated goethite nanoparticles (either in powder or in solution) are heated up above 350°C, dehydration firstly occurs forming directly hematite:

$$2FeOOH \longrightarrow Fe_2O_3 + H_2O \tag{2.1}$$

The conversion of goethite to hematite is facilitated by the common anion structure shared by these

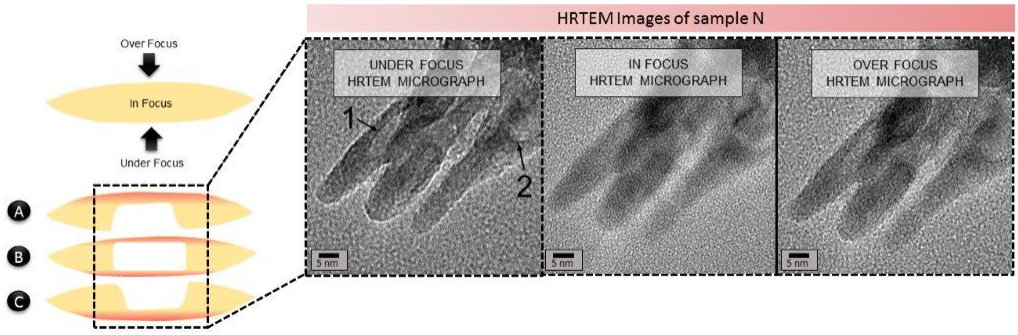

Figure 2.4: Reconstruction of the internal structure of the needles after dehydration process. Dark contrast differences observed in TEM images might be explained by: (A), (C) External cavities/surface roughness/discontinuous thickness along the needle; (B) Internal cavities along the needle. The red areas on the left represent the observed areas when images are taken under, over and in-focus.

two compounds. Three unit cells of goethite form one unit cell of hematite leading to contraction of the volume by a fraction of 0.62 [30]. The nanoparticles develop porosities within the structure due to the expulsion of water [22], occurring along the central axis of the needles, often merging with a single, elongated defect running along the entire length of the crystallite [31]. Pores along the c-axis were also reported [32] in good agreement with our observations. High resolution TEM images of the needles after the dehydration show contrast differences. These might be explained by either discontinuities of the thickness along the nanoparticle (surface roughness) or by discontinuities in the density of the nanoparticle (internal cavities). In order to elucidate the structure of the needles, a combination of under, over and in-focus high resolution TEM images have been taken. In doing this we are able to observe a certain degree of surface roughness, but more interestingly a porous internal structure has been evidenced (Figure 2.4). In spite of the porosity, a continuous single-crystalline structure corresponding to a monocrystal has been demonstrated for the needles. After the dehydration, the nanoparticles are reduced to magnetite without interparticle sintering and this is because of both the silica shell and the mild temperatures used for reduction (below 600°C).

TEM images obtained in this manner reveal the presence of pores for all particle morphologies, synthesised from both types of precursor. For hematite precursors, we observe pores in both the magnetite discs and rhombohedra that are randomly distributed within the structure (Figure 3), as previously observed by Edwards et al. [33]. The reduction itself is associated with the formation of tunnels by the removal of oxygen. Magnetite is formed in the surrounding areas parallel to the tunnel generation, which yields an overall crystal structure of magnetite with such pores [34].

High-resolution TEM (HR-TEM) images of the needles and rhombohedra after both the wet and dry reduction are shown in Figure S2-S4 (Appendix 2). For the rhombohedra, Fourier transformation of the HR-TEM image yields a diffraction pattern that corresponds to a monocrystal and demonstrates that

even with such pores, each particle has a single crystal structure. It is particularly striking in the case of needles (Figure S3, Appendix 2) after the dehydration and reduction process, that a continuous single-crystal structure corresponding to a monocrystal has been likewise demonstrated, despite the porosity along the c-axis. However, when lower reduction temperatures and shorter times were used, nanorods consisting of clusters of maghemite embedded in an aniferromagnetic hematite matrix were obtained [35].

Identification of iron oxide phase and measurement of core size

XRD patterns confirm that the precursor used to synthesise the rhombohedra and discs is indeed hematite, whilst the diffraction pattern of the precursor used to synthesize needles corresponds to goethite (Figure 2.5). The X-ray diffractograms of nanoparticles produced via wet and dry reduction methods indicate a single iron oxide phase, which we attribute to the inverse spinel structure of either magnetite or maghemite. We have used the Scherrer equation on the most intense diffraction peak to calculate the average core crystalline size of each of the precursors; this corresponds to the (110) reflection for hematite and the (111) reflection for goethite. XRD patterns confirm that the cores of both the hematite rhombohedra and discs are single crystal structures and have similar average sizes, in good agreement with that measured via TEM. For the goethite needles, the core crystalline size obtained using the (111) reflection is closer to the smallest TEM dimension, and is in agreement with the goethite crystals being elongated along the (100) direction [22]. Table 1 shows core sizes determined by TEM and crystal sizes obtained by XRD measurements.

FTIR spectra of the hematite precursors (Figure S5 in supporting information) show bands at 355 cm^{-1} and 477 cm^{-1} which are attributed to the parallel and transverse vibrations (E_u), and bands at 575 cm^{-1} and 381 cm^{-1} attributed to the longitudinal vibration (A_{2u}). For the goethite precursor, a band at 409 cm-1 can be attributed to the Fe-O antisymmetric stretch parallel to the c-axis and bands at 628, 790, 886 cm^{-1} can be attributed to the Fe-O symmetric stretch parallel to the a-axis. The transformation of the antiferromagnetic precursors to the magnetic phase was monitored using a combination of XRD - via the (311) reflection for the obtained magnetite nanoparticles - and FTIR. It should be mentioned that there are two main features contributing to the X-ray broadening, the crystal order and the particle shape, which makes such an analysis via XRD difficult.

The crystallite sizes obtained from the (311) reflection for the resulting magnetite needles, which is at 30° of the longest particle dimension, indicates a slightly increase with respect to the crystalline size calculated for the precursor, indicating a somewhat better crystal order after the reduction. By comparing XRD values for both reduction techniques, it seems that the dry reduction provides particles with a slightly larger crystallite size or less defects than the wet reduction.

Infra-red (IR) spectra measured after both wet and dry reduction, show bands that correspond to the silica coating of the nanoparticles and bands corresponding to magnetite, together with the band at

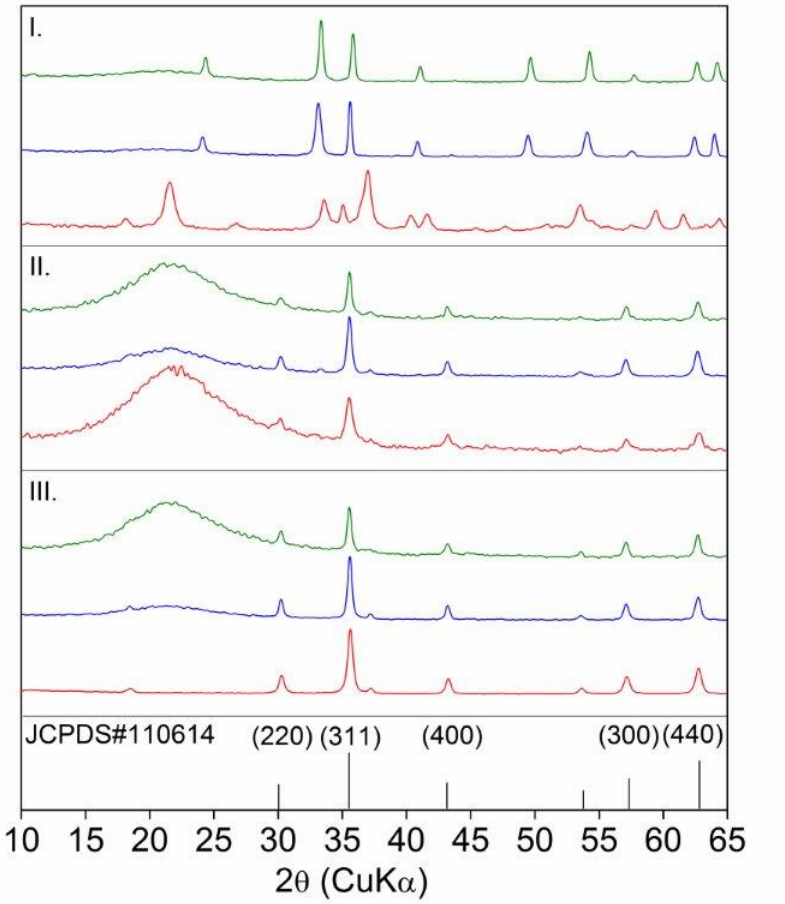

Figure 2.5: X-ray powder diffractograms of the precursor (I) and products obtained by wet (II) and dry reduction (III). A single phase, whose Bragg peaks are attributed to magnetite or maghemite, is obtained through both reduction techniques for all morphologies: rhombohedra (green), discs (blue) and needles (red).

Table 2.1: TEM core size vs. X-ray crystallite size of the hematite/goethite precursor and the obtained MNPs by wet and dry reduction. P: Antiferromagnetic Precursor, W.R.: Wet Reduction, D.R.: Dry Reduction.

	Antiferromagnetic precursor			**After reduction**		
Sample	Iron Oxide	D_{TEM} (nm), (%)	$D_{XRD,P}$ (nm)	Iron Oxide	$D_{XRD,W.R}$ (nm)	$D_{XRD,D.R}$ (nm)
Rhombohedra	α-Fe_2O_3	67, σ=18	69	Fe_3O_4	47	48
Discs	α-Fe_2O_3	140 x 22, σ=10.4	121	Fe_3O_4	34	42
Needles	α-FeO(OH)	183 x 33, σ=18.7	17	Fe_3O_4	19	27

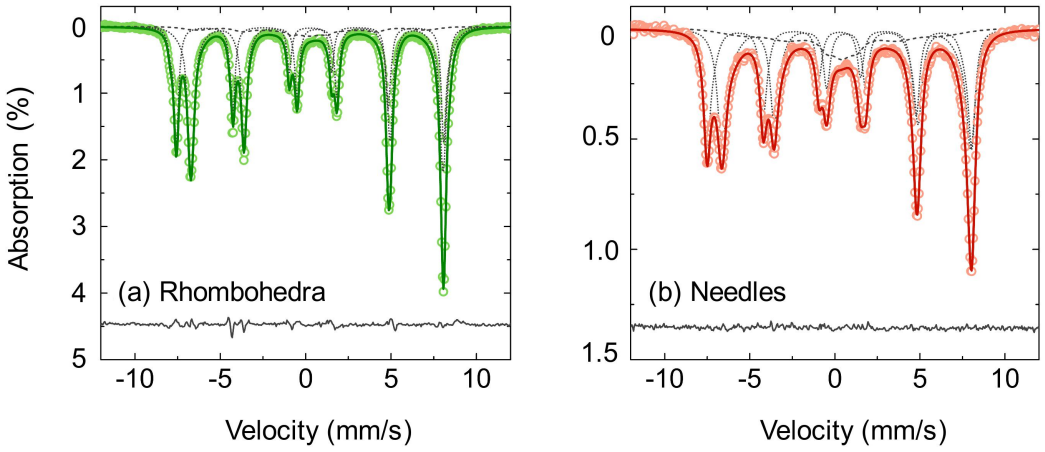

Figure 2.6: Comparison of room temperature Mössbauer spectra for (a) rombohedra and (b) needles after reduction. For each, points are the observed counts, the solid line is the modelled best fit to the data, and the dotted liens are the Voigtian sub spectra The quality of fit is indicated by the reduced χ^2 and the residual, given by I_{obs}-I_{cal}.

1632 cm^{-1} due to the stretching and bending vibration of H_2O molecules. The very strong and broad IR band at 1111 cm^{-1} with a shoulder at 1188 cm^{-1} is usually assigned to the transversal optical (TO) and longitudinal optical (LO) modes of the Si-O-Si asymmetric stretching vibrations, the band at 956 cm^{-1} is assigned to silanol groups and the one at 800 cm^{-1} is assigned to Si-O-Si symmetric stretching vibrations. Lastly, in the Fe-O range IR bands at 568 cm^{-1} and 357 cm^{-1} are attributable to magnetite [22], (Figure S5). The presence of maghemite is not evident due to the absence of small shoulders around these two main bands in the low frequency range which are particularly sharp for the needles.

Room temperature Mössbauer spectra of rhombohedra and needles reduced via dry powder methods are shown in Figure 2.6. For the rhombohedra, the spectrum is a sharp six-line pattern comprising two sub-spectra and is reminiscent of stoichiometric magnetite. The best fit spectra comprise a superposition of three Voigtian sextets, two of which have isomer shifts close to 0.26 $mm{\cdot}s^{-1}$ and 0.67 $mm{\cdot}s^{-1}$, and associated hyperfine fields close to 49 T and 46 T, respectively, which are indicative of the tetra and octahedral sites within magnetite.

The third sub-component comprises less than 8% of the spectral area and is a broad sextet, with an isomer shift of 0.26 $mm{\cdot}s^{-1}$ and is likely to come from Fe atoms around pore structures in the rhombohedra. We surmise that majority of the sample is well crystallised, stoichiometric magnetite.

Whilst we see that the Mössbauer spectrum of the needles (Figure 2.6 (b)) also comprises a 6-line pattern, here we see that the absorption lines are broader and also slightly asymmetric. The best fit is also obtained using a superposition of three Voigtian sextets, two of which have isomer shifts and hyperfine fields reminiscent of magnetite as seen for the rhombohedra. The third sub-component comprises

ca.18% of the spectral area and results in the slight 'hanging' of the spectra at v = 0. The isomer shift of this component is 0.41 mm·s^{-1} and cannot be attributed to either Fe^{3+} on the A site of $Fe^{2+,3+}$ on the B site. We attribute this component to the highly porous structure disrupting the crystalline structure experienced by Fe nuclei in the needles. The mean isomer shift of the spectra is 0.48 mm·s^{-1} and 0.49 mm·s^{-1}, respectively, which are close to the value of 0.53 mm·s^{-1} for stoichiometric magnetite [36, 37].

Magnetic characterisation of the magnetite particles

The field and temperature dependent magnetization measurements on all samples are shown in Figure 2.7. For each sample system, the field dependent measurements performed at 5 K and 295 K are plotted in one graph. The insets show the magnetization behaviour in the low field regime at $\pm$ 300 kA/m.

All magnetization curves show similar behaviour for different shapes and different reduction techniques. The samples exhibit non-zero remanence and coercivity indicating that the particles are magnetically blocked at room temperatures and below.

Looking into the details, it can be seen that the rhombohedra and needles obtained by wet reduction present a so-called wasp-waisted hysteresis loop, which is not observed in the materials produced by dry reduction. Roberts et al. explained the occurrence of a wasp-waisted hysteresis loop by a mixture of single- and multi-domain remanence states within the particles [38]. Since the samples prepared by dry reduction do not show the wasp-waisted hysteresis behaviour, it seems that this reduction technique produces particles with a more uniform magnetization state compared to the particles synthesised by wet reduction. This is in good agreement with the findings on the crystallite size measured by XRD, because defects and pores are usually responsible for the pinning and nucleation sites for magnetic domains, and obviously these defects and pores are less pronounced for dry reduced MNPs.

The saturation magnetization of the different samples is determined at 5 T where nearly all magnetic moments are aligned in field direction and thus dipolar interactions between the particle's magnetic moments are negligible. The saturation magnetization increases with decreasing temperature and the values of the saturation magnetization at room temperature are smaller than the 130 Am^2/kg(Fe) found for bulk magnetite [39]. The reduced magnetization for fine-particle systems by finite-size effects is well known in literature [40]. Magnetite nanocrystals obtained directly by the polyol process and aggregated in dense or hollow spheres show similar saturation magnetisation values (110 Am^2/ kg(Fe)) and a coercive field of (11 kA/m) at room temperature [11].

The saturation magnetization MS and coercive field H_C have been extracted from the magnetization data and summarized in Table 2.2. The value of M_s is largest for the rhombohedra while the discs exhibit the lowest saturation magnetization and that can be traced back to influences of the particles size. Interestingly, the saturation magnetization is considerably lower for the wet reduced particles than for dry reduction indicating again a significant effect of the reduction process and the presence of pores

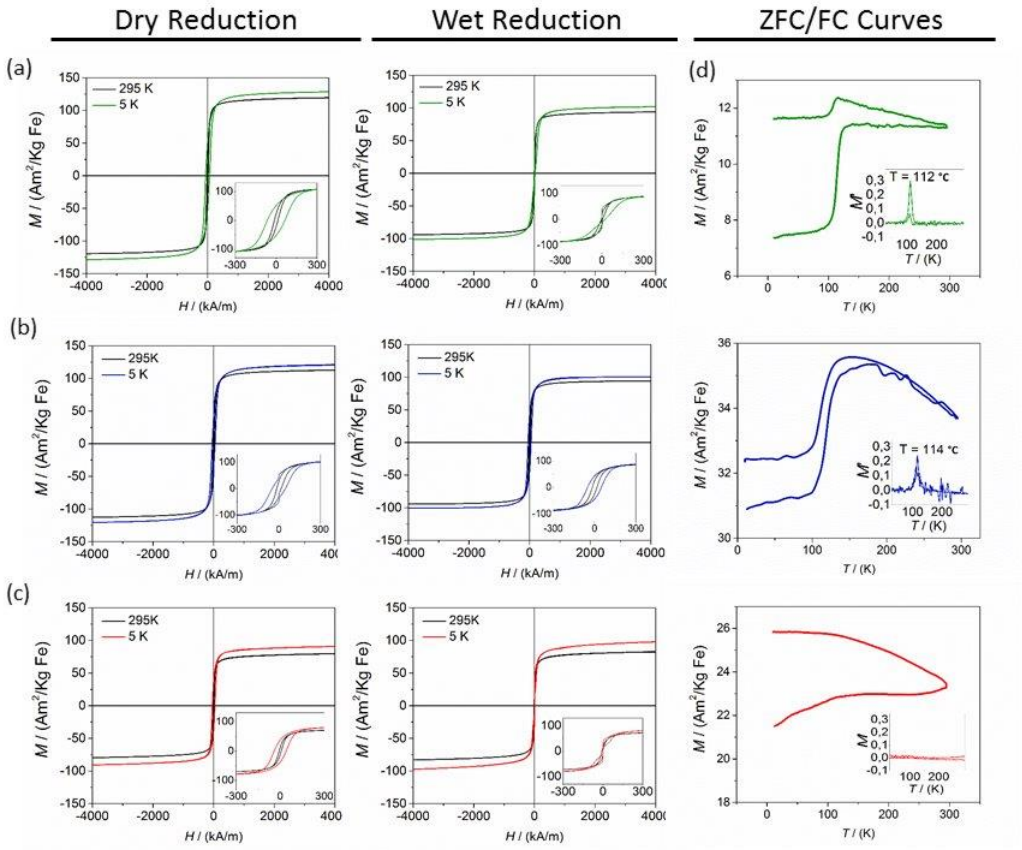

Figure 2.7: Hysteresis cycles at 295 and 5 K for all particle morphologies (green=rhombohedra, blue=disks, red=needles), comparing wet and dry reduction. Inset: the hysteresis cycles at low field regime ($\pm$ 300 kA/m) are shown. In addition, ZFC/FC curves (measured at 5 mT) of samples reduced in liquid are presented with the inset showing the first derivative of the magnetization with respect to temperature.

on the magnetic properties of the material. For the disc shaped particles the coercivity is identical in the wet and in the dry reduced samples. The coercivity of the rhombohedra and the needles cannot be compared due to the wasp-waisted hysteresis behaviour in case of wet reduction.

Field dependent magnetization curves recorded at higher field sweeping rates for the rhombohedra and needles are shown in Figure 2.8. Here the wasp-waisted hysteresis curve as observed in quasi-static magnetization measurements has vanished. The fact that the hysteresis curve depends on the field change rate indicates that the wasp-waisted hysteresis curves originate from domain formation within the particles, since the nucleation of domain wall and its movement are time dependent [41].

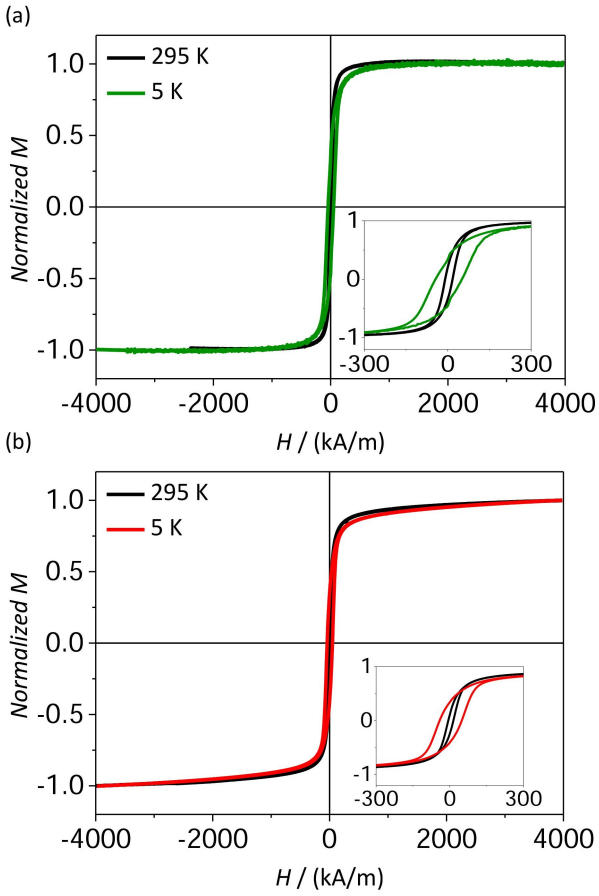

Figure 2.8: Magnetisation curves between $\pm$ 5 T measured with a field sweep of 0.3 T/min for magnetite rhombohedra (green) and needles (red) obtained by wet reduction.

Zero-field cooled/field cooled (ZFC/FC) magnetization curves of all products obtained from wet reduction are shown in (Figure 7). A clear Verwey transition [42] is observed in the case of rhombohedra

Table 2.2: Comparison of the values of saturation magnetization (MS) of magnetite particles after wet and dry reduction, and coercivity (H_C) at 5 and 295 K. (R) indicates the rhombohedra, (D) the discs and (N) the needles particles.

	Wer reduction				**Dry reduction**			
	M_s (Am^2/kg(Fe))		H_C(kA/m)		M_s (Am^2/kg(Fe))		H_C(kA/m)	
Sample	5 K	295 K	5 K	295 K	5 K	295 K	5 K	295 K
Rhombohedra	102	94	11	4	128	119	62	12
Discs	100	94	50	50	121	113	50	15
Needles	98	83	0	0	126	113	62	16

and discs at 112-114 K (obtained from a hematite precursor). However, the transition in case of the discs is less sharp than for the rhombohedra. In case of the needles (obtained from a goethite precursor) the Verwey transition is almost invisible.

Small degrees of non-stoichiometry or impurities in magnetite can reduce the Verwey transition temperature [43], located at 125 K for stoichiometric magnetite [44] and that could explain the different Verwey temperature observed for rhombohedra and discs. However, our XRD and Mössbauer studies confirm the magnetite nature of the particles. In fact, the reason for the shifted Verwey transition could be the crystal size, as discussed in [42, 45], where the state change during the transition and its temperature reduces with decreasing crystal size. The fact that almost no transition is observed in the needles could be associated to the smaller crystal size as determined by XRD for this sample (Table 2.1) and the observation of a porous structure within a single particle by HRTEM (Figure 5 and S2 in supporting information). Mössbauer spectra support this conclusion showing broader lines and a central singlet for the needles suggesting poorer crystallinity, which would explain the loss of the Verwey transition, against sharp absorption lines for rhombohedra corresponding to pure stoichiometric magnetite.

The shape of the Verwey transition for the different morphologies, especially for the smeared out transition of the discs, could be traced back to the existence of pores inside the particles and therefore a less-ordered crystal structure.

2.4 Conclusions

In this work, an alternative route to produce a library of iron oxide magnetic nanoparticles in a core size range of 50-100 nm and three different shapes has been successfully demonstrated. Here the goethite and hematite precursors are coated with silica to avoid sintering and to conserve the particle shape in the subsequent reduction of the precursor material to magnetite. Two different reduction methods have been successfully applied yielding a single iron oxide phase of magnetite.

The magnetite phase has been verified by X-ray diffractograms and ZFC/FC magnetization curves. Magnetite nanoparticles coming from hematite precursor show a very clear Verwey transition at slightly

lower temperatures than the reported ones for pure magnetite, probably due to small impurities or pores in the particles. The hysteresis parameters revealed that there is a difference between the magnetic material obtained by wet and dry reduction with higher values of saturation magnetization after dry reduction. However, rhombohedra and needle shaped samples show, in the case of the wet reduction, interesting magnetic properties with a wasp-shaped hysteresis curve and a very low coercive field at room temperature originated probably from the domain formation within the particles.

In addition, the approach for the reduction of the precursors has an influence on the magnetic behaviour of the final magnetite particles. MNPs that have been produced by dry reduction show fewer defects in the crystal structure. The possibility of generating a discontinuous structure within a particle by forcing the pore formation may be an interesting strategy to develop new materials with tuned magnetic properties for biomedical applications.

In conclusion, we demonstrate the production of large (> 25 nm) magnetite MNPs where shape and internal structure could be varied by the synthesis parameters. We demonstrate that both MNPs shape and internal MNPs structure affect strongly the magnetic behaviour of the MNPs. In future characterization of magnetite MNPs systems, these parameters should always be taken into account.

Bibliography

[1] Mejías, R. *et al.* Dimercaptosuccinic acid-coated magnetite nanoparticles for magnetically guided in vivo delivery of interferon gamma for cancer immunotherapy. *Biomaterials* **32**, 2938–2952 (2011).

[2] Maier-Hauff, K. *et al.* Efficacy and safety of intratumoral thermotherapy using magnetic iron-oxide nanoparticles combined with external beam radiotherapy on patients with recurrent glioblastoma multiforme. *Journal of Neuro-Oncology* **103**, 317–324 (2011).

[3] Shin, T.-H., Choi, Y., Kim, S. & Cheon, J. Recent advances in magnetic nanoparticle-based multi-modal imaging. *Chemical Society Reviews* **44**, 4501–4516 (2015).

[4] Khandhar, A., Ferguson, R., Arami, H. & Krishnan, K. Monodisperse magnetite nanoparticle tracers for in vivo magnetic particle imaging. *Biomaterials* **34**, 3837–3845 (2013).

[5] Hilger, I. & Kaiser, W. Iron oxide-based nanostructures for mri and magnetic hyperthermia. *Nanomedicine* **7**, 1443–1459 (2012).

[6] Wáng, Y., Idée, J.-M. & Corot, C. Scientific and industrial challenges of developing nanoparticle-based theranostics and multiple-modality contrast agents for clinical application. *Nanoscale* **7**, 16146–16150 (2015).

[7] Dutz, S. & Hergt, R. Magnetic particle hyperthermia - a promising tumour therapy? *Nanotechnology* **25** (2014).

[8] Lartigue, L. *et al.* Cooperative organization in iron oxide multi-core nanoparticles potentiates their efficiency as heating mediators and mri contrast agents. *ACS Nano* **6**, 10935–10949 (2012).

[9] Dutz, S. Are magnetic multicore nanoparticles promising candidates for biomedical applications? *IEEE Transactions on Magnetics* **52** (2016).

[10] Serantes, D. *et al.* Multiplying magnetic hyperthermia response by nanoparticle assembling. *Journal of Physical Chemistry C* **118**, 5927–5934 (2014).

[11] Guan, N., Wang, Y., Sun, D. & Xu, J. A simple one-pot synthesis of single-crystalline magnetite hollow spheres from a single iron precursor. *Nanotechnology* **20** (2009).

[12] Jia, B. & Gao, L. Morphological transformation of fe3o4 spherical aggregates from solid to hollow and their self-assembly under an external magnetic field. *Journal of Physical Chemistry C* **112**, 666–671 (2008).

[13] Salas, G. *et al.* Controlled synthesis of uniform magnetite nanocrystals with high-quality properties for biomedical applications. *Journal of Materials Chemistry* **22**, 21065–21075 (2012).

[14] Kim, D. *et al.* Synthesis of uniform ferrimagnetic magnetite nanocubes. *Journal of the American Chemical Society* **131**, 454–455 (2009).

[15] Kovalenko, M. *et al.* Fatty acid salts as stabilizers in size- and shape-controlled nanocrystal synthesis: The case of inverse spinel iron oxide. *Journal of the American Chemical Society* **129**, 6352–6353 (2007).

[16] Palchoudhury, S. *et al.* Synthesis and growth mechanism of iron oxide nanowhiskers. *Nano Letters* **11**, 1141–1146 (2011).

[17] Sun, H. *et al.* Solvothermal synthesis of tunable electroactive magnetite nanorods by controlling the side reaction. *Journal of Physical Chemistry C* **116**, 5476–5481 (2012).

[18] Zhang, L., Wu, J., Liao, H., Hou, Y. & Gao, S. Octahedral fe_3o_4 nanoparticles and their assembled structures. *Chemical Communications* 4378–4380 (2009).

[19] Lu, J., Jiao, X., Chen, D. & Li, W. Solvothermal synthesis and characterization of fe_3o_4 and γ-fe_2o_3 nanoplates. *J. Phys. Chem. C* **113**, 4012–4017 (2009).

[20] Zeng, Y., Hao, R., Xing, B., Hou, Y. & Xu, Z. One-pot synthesis of fe_3o_4 nanoprisms with controlled electrochemical properties. *Chemical Communications* **46**, 3920–3922 (2010).

[21] Rebolledo, A., Bomatí-Miguel, O., Marco, J. & Tartaj, P. A facile synthetic route for the preparation of superparamagnetic iron oxide nanorods and nanorices with tunable surface functionality. *Advanced Materials* **20**, 1760–1765 (2008).

[22] Cornell, R. & Schwertmann, U. *The Iron Oxides: Structure, Properties, Reactions, Occurrence and Uses* (1996).

[23] Graf, C., Vossen, D., Imhof, A. & Van Blaaderen, A. A general method to coat colloidal particles with silica. *Langmuir* **19**, 6693–6700 (2003).

[24] Stöber, W., Fink, A. & Bohn, E. Controlled growth of monodisperse silica spheres in the micron size range. *Journal of Colloid And Interface Science* **26**, 62–69 (1968).

[25] Morales, M. P., Pecharroman, C., Carreño, T. & Serna, C. Structural characteristics of uniform γ-fe$_2$o$_3$ particles with different axial (length/width) ratios. *Journal of Solid State Chemistry* **108**, 158–163 (1994).

[26] Yang, Y. *et al.* Orientation mediated enhancement on magnetic hyperthermia of fe$_3$o$_4$ nanodisc. *Advanced Functional Materials* **25**, 812–820 (2015).

[27] Yang, Y., Liu, X. & Ding, J. Synthesis of α-fe$_2$o$_3$ templates via hydrothermal route and fe$_3$o$_4$ particles through subsequent chemical reduction. *Science of Advanced Materials* **5**, 1199–1207 (2013).

[28] Pozas, R., Ocaña, M., Morales, M. P. & Serna, C. Uniform nanosized goethite particles obtained by aerial oxidation in the feso$_4$-na$_2$co$_3$ system. *Journal of Colloid and Interface Science* **254**, 87–94 (2002).

[29] Liz-Marzán, L. & Mulvaney, P. The assembly of coated nanocrystals. *Journal of Physical Chemistry B* **107**, 7312–7326 (2003).

[30] Naono, H., Nakai, K., Sueyoshi, T. & Yagi, H. Porous texture in hematite derived from goethite: Mechanism of thermal decomposition of geothite. *Journal of Colloid And Interface Science* **120**, 439–450 (1987).

[31] Baker, A. *et al.* A structural study of haematite samples prepared from sulfated goethite precursors: The generation of axial mesoporous voids. *Journal of Materials Chemistry* **10**, 761–766 (2000).

[32] Morales, M. P., Tirado, J. & Macias, M. Changes in crystallite size and microstrains of hematite derived from the thermal decomposition of synthetic akaganeite. *Journal of Solid State Chemistry* **53**, 303–312 (1984).

[33] Brill-Edwards, H., Daniell, B. & Samuel, R. Structural changes accompanying the reduction of polycrystalline heamatite. *J. Iron Steel Inst.* **203** (1965).

[34] Swann, P. & Tighe, N. High voltage microscopy of the reduction of hematite to magnetite. *Metallurgical Transactions B* **8**, 479–487 (1977).

[35] Rebolledo, A. *et al.* Iron oxide nanosized clusters embedded in porous nanorods: A new colloidal design to enhance capabilities of mri contrast agents. *ACS Nano* **4**, 2095–2103 (2010).

[36] Da Costa, G., Blanco-Andujar, C., De Grave, E. & Pankhurst, Q. Magnetic nanoparticles for in vivo use: A critical assessment of their composition. *Journal of Physical Chemistry B* **118**, 11738–11746 (2014).

[37] Santoyo Salazar, J. *et al.* Magnetic iron oxide nanoparticles in 10-40 nm range: Composition in terms of magnetite/maghemite ratio and effect on the magnetic properties. *Chemistry of Materials* **23**, 1379–1386 (2011).

[38] Roberts, A., Cui, Y. & Verosub, K. Wasp-waisted hysteresis loops: mineral magnetic characteristics and discrimination of components in mixed magnetic systems. *Journal of Geophysical Research* **100**, 17,909–17,924 (1995).

[39] O'Handley, R. *Modern Magnetic Materials* (2000).

[40] Batlle, X. & Labarta, A. Finite-size effects in fine particles: Magnetic and transport properties. *Journal of Physics D: Applied Physics* **35**, R15–R42 (2002).

[41] Hillebrands, B. & Ounadjela, K. *Spin Dynamics in Confined Magnetic Structures* (2002).

[42] Goya, G., Berquó, T., Fonseca, F. & Morales, M. P. Static and dynamic magnetic properties of spherical magnetite nanoparticles. *Journal of Applied Physics* **94**, 3520–3528 (2003).

[43] Aragan, R., Buttrey, D., Shepherd, J. & Honig, J. Influence of nonstoichiometry on the verwey transition. *Physical Review B* **31**, 430–436 (1985).

[44] Friedrich, W. The verwey transition - a topical review. *J. Phys. Condens. Matter* **14** (2002).

[45] Snow, C., Shi, Q., Boerio-Goates, J. & Woodfield, B. Heat capacity studies of nanocrystalline magnetite (fe_3o_4). *Journal of Physical Chemistry C* **114**, 21100–21108 (2010).

Part C

Multi-Core nanoparticles

3

Colloidal Flower-shaped Iron Oxide Nanoparticles: Synthesis Strategies and Coatings

Summary

The assembly of magnetic cores into regular structures may notably influence the properties displayed by a magnetic colloid. In this work, key synthesis parameters driving the self-assembly process capable of organizing colloidal magnetic cores into highly regular and reproducible multi-core nanoparticles are determined. In addition, a self-consistent picture that explains the collective magnetic properties exhibited by these complex assemblies is achieved through structural, colloidal and magnetic means. For this purpose, different strategies to obtain flower-shaped iron oxide assemblies in the size range 25-100 nm are examined. The routes are based on the partial oxidation of $Fe(OH)_2$, polyol mediated synthesis or the reduction of iron acetylacetonate. The nanoparticles are functionalized either with dextran, citric acid or alternatively embedded in polystyrene and their long-term stability is assessed. The core size is measured, calculated and modelled using both structural and magnetic means while the Debye model and multi-core extended model have been used to study inter-particle interactions. This is the first step towards standardized protocols of synthesis and characterization of flower-shaped nanoparticles.

3.1 Introduction

Despite the progress in colloidal self-assembly of organic[1] or inorganic[2, 3] building blocks to form close-packed structures such as colloidal crystals,[4] there are only a few reports of controlled assembly of ordered nanoparticles in suspension.[5] In this matter, many fundamental aspects remain unknown and often, there is no predictive description of the ensemble behaviour or the origin of the forces driving aggregation.[6, 7] Nonetheless, aggregation is a general mechanism of particle formation now recognized as a common growth phenomenon for many different monodisperse nanoparticles,[8–12]in contrast to the monomer by monomer addition that is described in classical models.

In absence of templates, interfaces or external fields, the self-assembly process in solution is governed by the balance of attractive and repulsive forces. Magnetic nano-particles (MNPs) are - a priori - different due to additional forces that arise as a consequence of their magnetic moment. These interactions can be either intraparticle ex-change interactions, or long-range magnetostatic dipolar forces between particles. Exchange interactions between cores of a multi-core particle may lead to the so-called “superferrimagnetic” behaviour,[13] exhibiting large magnetic moment and weak remanence in zero field, and thus, having low tendency to form agglomerates. On the other hand, dipolar interactions between particles with sufficient high moment account for the formation of configurations such as chains, which may change strongly the magnetic properties of the colloid.[14]

As a consequence, the assembly of MNPs in multi-core structures can, in some cases, give rise to collective magnetic properties, which yields microscopic magnetic behaviour that is very different from single-core nanoparticles or bulk materials.[15, 16] Such multi-core nanoparticles are currently of great interest in many different areas such as catalysis,[17] ferrofluids and rheology,[18] as well as bioapplications, which are mainly focused on iron oxide nanoparticles (magnetite or maghemite) because of their low toxicity.[19] Colloids made of magnetic multi-core nanoparticles show high NMR relaxivity (r_2),[20] high MPI signals,[21] high specific absorption rate of AC field (SAR),[22–24] high magnetic moment when manipulated with an external magnet[25] and enhanced performance as theranostic agents.[26–28]

Herein, we analyse the key synthesis parameters driving the self-assembly process capable of organizing colloidal magnetic cores into highly regular and reproducible multi-core nanoparticles showing the so called “superferrimagnetic state” due to exchange interactions. For that purpose we have conducted a comparison of four different synthesis of colloidal magnetic multi-core structures called flower-shaped nanoparticles (Figure 3.1), consisting of iron oxide cores that are aggregated to form isometric 3D arrangements. Out of the numerous synthesis strategies re-ported in the literature,[5] we have focused our investigation on those that either produce multi-core particles in the single-domain region, i.e. smaller than 50 nm, or above the multi-domain limit, i.e. larger than 100 nm. In this work, some used approaches describe the in situ formation of MNPs and assembly in the presence of molecules or polymers, while others describe first the assembly of the formed MNPs and its further polymer coating,

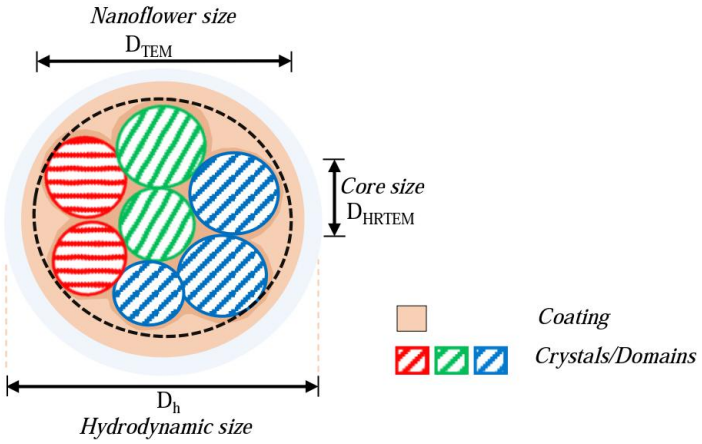

Figure 3.1: Flower-shaped multi-core nanoparticle: Nanoflower and core size have been determined through TEM and HRTEM, respectively, and has a final hydrodynamic size in solution. The term crystal/domain is designated as cores that share crystal alignment.

encapsulation or embedment. By comparing synthesis approaches we have been able to gain a better understanding into the nature of this self-assembly process that lead to multi-core magnetic nanoparticles with controllable size, shape and collective behaviour. Moreover, we have been able to determine to which extent the systems can be tuned by choice of synthesis conditions yielding core aggregation and colloidal stability.

Comprehensive structural and magnetic characterisation of colloidal dispersions and freeze-dried powders has been performed following standardized protocols that have facilitated the comparison of these structures.[29] This is the first step towards standardization of synthesis and characterization of these nanoparticles, which is an important concern and demand nowadays.[30] First, we analyse the core arrangement within the particle and secondly we analyse interparticle interactions. A key parameter to understand the behaviour of the colloid is the degree of fusion of the cores within the nanoflowers, specifically whether they are in direct contact and if so, if they share crystalline alignment.[31] Secondly, we analyse the inter-particle interactions,[32] which are minimized by steric and/or electrostatic repulsion due to the surface coatings (dextran, citric acid) or alternatively by embedding the cores on surfactant stabilized polystyrene beads. Surface modification of the flower-shaped nanoparticles provides colloidal stability in water and specific functionalization, which is of utmost importance for their successful application in the nano-bio area.[33]

3.2 Experimental section

Synthesis of flower-shaped nanoparticles:

- Sample NF1: Dextran coated iron oxide nanoparticles were synthesized by partial oxidation of $Fe(OH)_2$ and green rust. Typically, KNO_3 2 M, NaOH 2 M and dextran solution (5 mL) were added to MilliQ water (25 mL) and degassed by bubbling with nitrogen.[34] Under stirring, $FeSO_4 \cdot 7H_2O$ 0.3 M (8.3 mL) were slowly added to the initial solution resulting in the precipitation of gel-like $Fe(OH)_2$ and green rust. To accelerate the oxidation process the solution was heated to 90 °C for 4 hours. Finally, the particles were purified by dialysis and centrifugation resulting in a stable colloidal dispersion.

- Sample NF2: Dextran coated γ-Fe_2O_3 NPs were synthesized by a polyol method adapted from Lartigue et al.[24] In a typical procedure of $FeCl_3 \cdot 6H_2O$ (4 mmol) and $FeCl_2 \cdot 4H_2O$ (2 mmol) were dissolved in diethylene glycol (DEG) and N-methyldiethanolamine (NMDEA) (1:1 v/v, 80 g) at room temperature. The solution was stirred for 1h. Separately, NaOH (16 mmol) was dissolved in the polyol mixture (40 g) and subsequently added to the iron chlorides solution. The mixture was then stirred for 3 hours at room temperature. The temperature of the solution was then elevated to 210 °C using a ramp temperature of 2 °C/min. Once the temperature reached 210 °C, the solution was stirred for 12 h at the same conditions. Then the mixture was cooled down to room temperature. The nanoparticles were separated magnetically and washed four times with a mixture of ethanol and ethyl acetate (1:1, v/v) and once with 10% nitric acid. Then, a, aqueous solution (20 mL) containing iron (III) nitrate (8.25 g) was added to the NPs, and the mixture was heated to 80 °C for 45 minutes. After cooling down to room temperature, the nanoparticles were washed again, once with 10% nitric acid, once with ethanol and once with acetone. The sediment was dried for 2 h at 40 °C. Finally, the particles were re-dispersed in water (20 mL). Coating with dextran was carried out by high-pressure homogenization process.[35]

- Sample NF3:Sample NF3:γ-Fe_2O_3 NPs were synthesized by a polyol mediated method previously reported by Liu J et al.[36] Typically, iron chloride (2.702 g) was dissolved in ethylene glycol (EG, 47 mL) under magnetic stirring. Then trisodium citrate (Na_3Cit) and sodium acetate (NaAc) was gradually added under mild heating and magnetic stirring. The final concentration of the reagents is: [$FeCl_3$] = 0.21 M, [Na_3Cit] = 0.05 M, and [NaAc] = 0.76 M. The mixture was stirred vigorously for 30 min and then sealed in a Teflon-lined Aluminium autoclave (125 mL capacity) and maintained at 200 °C for 10 h. After cooling down to room temperature, the black product was washed 3 times with distilled water by centrifugation.

- Sample NF4: Iron oxide nanoparticles were produced by a reduction method that was based on reports in the literature.[37, 38] In brief, iron acetylacetonate (9.43 g) and sodium borohydride

(5.04 g) were added to a mixture of H_2O and THF (400 mL), as detailed in the literature report. The mixture was stirred overnight at 150 rpm. The black precipitates were collected by centrifugation and rinsed with deionized water. A solution consisting oleic acid (67 mL) in THF (533 mL) was added to the suspension and shaken for 2 hours. The nanoparticles were precipitated with ethanol and collected by centrifugation, followed by redispersion in chloroform (10 mL). In solution 1, the particle solution (6.25 ml) was added gently to chloroform (20.25 g). In the case of sample NF4, poly (styrene) (500 mg) is previously dissolved in the chloroform) in a 25 ml glass vial; In solution 2, poly (styrene-alt-maleic acid)-sodium salt solution (13.96 g) and sodium lauryl sulphate (3.35 g) solution is added to DIW (1 L). Solution 1 is added to solution 2 (53 mL) in a 100 mL Erlenmeyer flask by ultra sonication for 15 min with ultrasonic probe Amplitude 40% in an ice bath. Chloroform was evaporated under reduced pressure. The solution is centrifuged 2000 rpm for 5 min. The supernatant is collected and the precipitate is discarded.

Characterization: TEM Analysis. A FEI Tecani G2 T20 transmission electron microscope (TEM) equipped with LaB_6 electron gun and operated at 200 kV was used in this study. TEM sample preparation was done by putting a droplet of the diluted suspension in water on holey carbon film coated TEM Cu grid, and then letting it dry in air at room temperature. Images were acquired in bright field (BF) imaging mode and evaluated using DigtalMicrograph software. The method used for measuring the diameter of both the multicore particles and iron oxide nanocrystals is described as follows. First, a circle was drawn on the image in DigitalMicrograph. Then the circle was adjusted so that its size is as small as possible but still covers a single particle or nanocrystal to be measured. The diameter of this circle is subsequently taken as the diameter of the particle. Structure of individual flower particles were also analysed by selected area electron diffraction (SAED), bright field and dark field (DF) imaging and high resolution transmission electron microscopy (HRTEM) imaging.

X-ray Powder Diffraction Analysis. Chemical composition and core crystal structure were confirmed along with the determination of crystal size by X-ray powder diffraction (XRD) experiments performed at room temperature (RT) in a D8 Advance diffractometer, using a Cu K_α radiation with Bragg-Brentano geometry. The samples in solution were freeze-dried for the subsequent XRD measurement, which were placed on a Si single-crystal low background sample holder that was rotated at 15 rpm to improve random orientation of crystallites, while minimizing the effect of preferred orientations within the sample. The acquired data were analysed through the Rietveld refinement method using the FullProf Suite software.[39] To describe the peak profiles, a Thompson-Cox-Hastings function was chosen to guarantee a good description of the width excess to extract the average crystal size (D) of the samples. The figures of merit are acceptable for fine particle systems. To fully account for peak broadening, it is necessary to include some lattice strain contribution (ε). These ε values lie around 50 0/000 and it is a sign of crystal defects, especially on particle surfaces.

Mössbauer Spectroscopy. The iron oxide phase was identified using room temperature ^{57}Fe Mössbauer spectroscopy. Approximately 50 mg of each sample was mixed with ca. 200 mg sucrose in a

pestle and mortar to form a paste, and then flattened within a coin shaped absorber. Spectra were recorded at room temperature in transmission geometry using a ^{57}Co source in a Rh matrix, using a W302 spectrometer and W202 detector, both from SEECo (Minneapolis, USA). Low temperature Mössbauer measurements were recorded also in transmission geometry with a source of ^{57}Co in Rh, but using a close cycle helium refrigerator from APD Cryogenics and a spectrometer from Wissel GmbH operated in the constant acceleration mode. Best fits to the spectra have been obtained using a model independent analysis to obtain the best fit (lowest χ^2) to the observed spectra as described by Fock et al.[40, 41] In this way, spectra have been fit using Voigtian lineshapes to represent a Gaussian distribution of Lorentzian hyper-fine fields, which we have used to account for a distribution of particle volumes and shapes as well as reduced hyperfine fields related to relaxation effects.

Infrared Spectroscopy. FTIR was used to detect and identify the presence of coating on the nanoparticle surface using a Bruker IFS 66V-S in the range of 2000-250 cm^{-1}. The samples were prepared by diluting the dried powder in KBr at 2% by weight and pressing it into a pellet. DLS Analysis. Colloidal properties were analysed by DLS. Measurements were carried out in an instrument NICOMP Submicron Particle Sizer Model 370. The measured angle was 90°, a wavelength of 632.8 nm was used, the temperature was set to 30 °C and the sample was diluted with MilliQ water to 5 mM iron. Then, 300 μL of the diluted sample were measured three times using a run time of 5 min each. The data analysis was performed with the 2nd cumulant method, and the Gaussian distributions are intensity-weighted. For the Z-potential measurements, a Zetasizernano ZS, Malvern instrument was used and data were evaluated by the Smoluchowski model. The measurements were recorded at 25 °C. 700 μL of each dilution (which was likewise diluted to 5 mM iron with MilliQ water) was pipetted into a folded capillary cell (DTS 1062) and then measured two times with 20 runs per measurement.

DC Magnetometry Measurements. DC magnetization measurements have been performed at 300 K on liquid samples using a Magnetic Property Measurement System (MPMS)-XL from Quantum Design (USA). 30 μL of the suspensions were filled into a polycarbonate (PC) capsule. The measurement system was demagnetized before measurement and the magnetic moment was recorded within a magnetic field range of $\pm$ 4.9 T. Data evaluation was performed by subtracting the empty sample holder signal (measured in a previous measurement) and the water contribution (using the susceptibility χ_{water} = -9 x 10^{-6}). The sample magnetization M′ was calculated using the measured magnetic moment and the suspension volume M′=(Magn. moment)/V, and with the iron concentration c_{Fe}, the magnetization M=M′/c_{Fe} in terms of A·m^2/kg(Fe) was obtained. Fitting the virgin curve by a bimodal model (see section 4 of SI) provides magnetic core size.

AC Susceptibility measurements. The altering current susceptibility (ACS) measurements on nanoflower samples were performed at room temperature utilizing two custom-built susceptometers by Technische Universität Braunschweig.[42] The frequency was swept from 10 Hz – 10 kHz and from 200 Hz – 1 MHz in logarithmical steps. The amplitudes of the excitation field amounted to 567 μT and 90 μT, respectively. Measurements have been carried out on suspensions of original and 10-fold diluted concentration

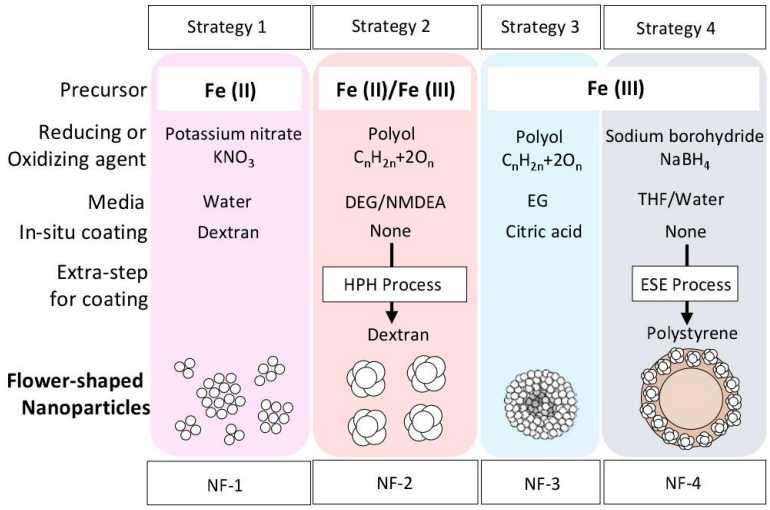

Figure 3.2: Strategies followed to obtain flower-shaped nanoparticles. N-methyl diethanolamine, HPH process stands for high-pressure homogenization coating and ESE process stands for emulsion solvent evaporation.

and on freeze-dried reference samples, i.e. samples with immobilized nanoparticles of original concentration with a sample volume of 150 μL each. A blank measurement was performed prior to the sample measurement and subtracted from the acquired spectra of the sample. The systems are calibrated with a Dy_2O_3 powder sample with defined volume susceptibility. We also used two AC susceptometers at Acreo, the first one is the commercially available DynoMag system with excitation frequencies up to 500 kHz and a prototype high frequency AC susceptometer with excitation frequencies up to 10 MHz. In the DynoMag system the excitation field is 5 mT and 30 μT in the high frequency AC susceptometer. Also in these AC susceptometers the calibration was performed using the paramagnetic Dy_2O_3 material.

3.3 Results and discussion

Key parameters controlling self-assembly :

Strategy 1 (Figure 3.2) involves the oxidative aging of an $Fe(OH)_2$ intermediate in water in the presence of dextran (90 °C/4 h), to yield NF1. Table 3.1 includes the mean size of the particle and core determined through transmission electron microscopy (TEM) and high-resolution transmission electron microscopy (HRTEM), respectively. Nanoflowers produced in this way have a mean diameter of 46 nm and they are composed of 7 nm cores that are loosely packed together (Figure 3.3).

HRTEM images suggest that the cores share the same crystallographic orientation in some areas of

Table 3.1: Flower-shaped nanoparticles (D_{TEM}), core (D_{HRTEM}), crystal (D_{XRD}) and hydrodynamic ($D_{h,DLS}$) sizes estimated through structural characterisation.

Sample	D_{TEM} (nm)	D_{HRTEM} (nm)	D_{XRD} (nm)	$D_{h,DLS}$ (nm)
NF1	46 ± 27	7	9 ± 1	192 ± 84
NF2	47 ± 17	15	15 ± 1	51 ± 15
NF3	110 ± 13	4	8 ± 1	158 ± 53
NF4	$24 \pm 7^{a)}$	$10^{b)}$	10 ± 1	250 ± 46
	172 ± 70			

Note: TEM size in this system means size of the nanoflower, and the polymer sphere embedding the flowers. b) HRTEM size in this system means core size of the nanoflower.

the particle but not throughout the whole particle. It has previously been reported that for this reaction the excess of OH^- or Fe^{2+} in the media defines the mechanism of particle growth and therefore the formation of single or multi-core particles.[43, 44] In our approach, an excess of OH^- was used to move the pH away from the magnetite isoelectric point ($\approx$ 6.5),[45] thus charging the surface of the initial growing nuclei keeping them apart and resulting in single-core particles.[44, 46, 47] The use of in situ dextran coating, however, causes a reduction in surface charge density of the growing nuclei promoting its approach and aggregation. We observe that flower-shaped nanoparticles produced in this way have a poorly defined size, shape and broad size distribution (relative standard deviation $>$50%), probably due to the poor capping effect of dextran hydroxyl groups, which are attached through hydrogen bonds to the iron oxide particle surface.[48]

Samples NF2 and NF3 were obtained using polyol media (Figure 3.2) at elevated temperatures (220 °C/12 h and 200 °C/10 h, respectively) and while NF2 is coated with dextran in a second step, NF3 is in situ coated with citric acid. Figure 3 shows that NF2 is composed of monodisperse 47 nm nanoflowers with a well defined size (Table 3.1) and shape. HRTEM images reveal cores of approximately 15 nm that are densely packed with essentially the same crystal orientation across the entire particle. Similarly, nanoflowers in NF3 are composed of spherical 110 nm nanoparticles (more than twice that of NF2) with a well-defined size and shape. HRTEM reveals that NF3 consists of very small randomly orientated cores of approximately 4 nm. It has been reported that polyols play an important role in the reaction and act as solvent, surfactant and reductant.[49] Here, we have used polyols of short chain length (diethylene glycol, DEG, in NF2 and ethylene glycol, EG, in NF3), which enable clustering of the cores to obtain desired multicore structures. For NF2, sodium hydroxide was added to a stoichiometric mixture of iron (II) and iron (III) salts to control the precursor hydrolysis,[50] initiating a burst nucleation followed by the uniform growth of the single cores (LaMer growth). Also, the heating was prolonged for 12 h to promote clustering and subsequent coalescence of the cores leading to flower-shaped nanoparticles.[51, 52] Interestingly, if either the heating time is limited to 2-3 h under these conditions, or if polyols of longer

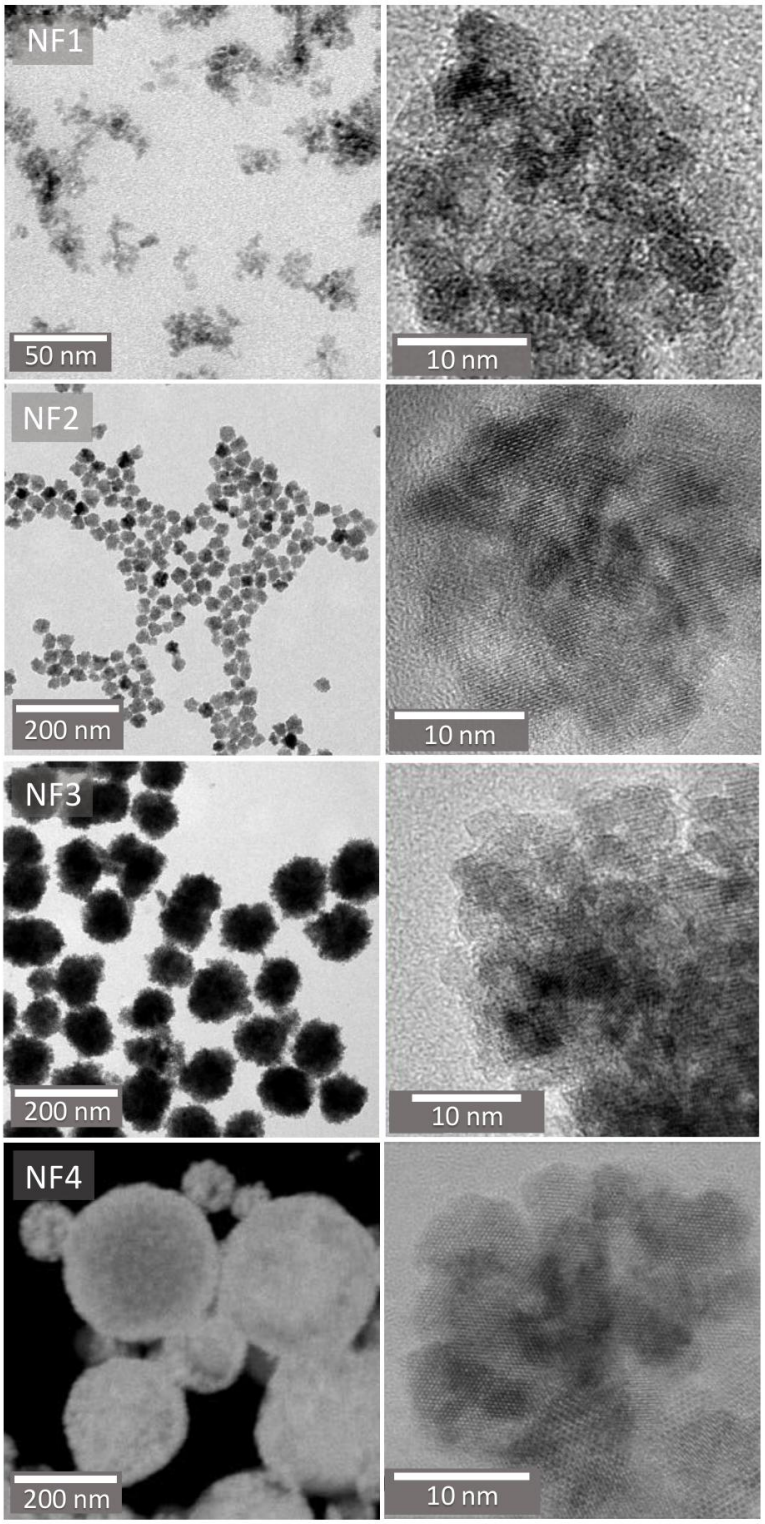

Figure 3.3: TEM (NF1-NF3), STEM (NF4) (left), and HRTEM images (right) of the different flower-shaped nanoparticles.

chain length are used, such as triethylene glycol[53] or 1,2-hexadecanediol,[54] then, only single-core nanoparticles are obtained.

Regarding NF3, we observe three key parameters that allow the formation of the multi-core structure: the control of temperature and pressure by using an autoclave as reactor, the concentration of the precipitator (sodium acetate, NaAc) that promotes the hydrolysis of the Fe^{+3} ions and thereby controlling the phase transformation and the particle morphology, and finally, the addition of an extra stabilizer (sodium citrate, Na_3Cit) that acts as capping agent. High concentrations of NaAc, as those used in NF3, led to flower-shaped nanoparticles composed of uniform cores in size that self-assemble into solid spheres to reduce the surface energy and suffer the so-called recrystallization process.[36] Lower concentrations of NaAc led to the formation of 200 nm magnetite hollow spheres composed of cores with different sizes. The dissolution of inner small cores and growth of the larger ones on the surface, leads to the formation of such voids that are not observed in this work, by the Ostwald ripening process.[55] NF3 have such small core size of 4 nm (Figure 3.1), due to the presence of sodium citrate (Na_3Cit). This extra stabilizer acts as capping agent, significantly suppresses the nuclei growth (in a comparable way to the dextran in NF1 synthesis) and facilitates the final dispersion of the flower-shaped nanoparticles in aqueous media. Carboxyl groups of citric acid coordinate to the iron oxide particle surface via one or two of the carboxylate functionalities, depending upon steric necessity and the curvature of the surface. [56] Alternatively, the use of other additives such as polyacrylic acid (PAA) or polyvinylpyrrolidone (PVP) instead of Na_3Cit have been reported to account for different particle size (30-250 nm). [55, 57, 58]

As HRTEM images of NF2 and NF3 reveal a different degree of crystallographic orientation texture between the cores (also termed “domains”) we have used dark field (DF) imaging analysis to further investigate the nature of the alignment, as is summarized in Figure 3.4. The bright areas in the DF images contribute to the diffraction spots marked by white arrows in the corresponding selected area electron diffraction (SAED) patterns. In all acquired DF images only part of the nanoflower becomes bright, which clearly illustrates that there is no obvious common crystallographic orientation of the cores. In the case of NF2, for example, we observe that a much larger area becomes bright, indicating orientated assembly of the cores forming the nanoflowers. Interestingly, we observe in the case of NF3 that these domains are much smaller than for NF2.

Finally, in strategy 4 (Figure 3.2) nanoflowers were obtained by means of sodium borohydride, which acts as reducing agent and iron (III) acetylacetonate ($Fe(acac)_3$), which acts as an iron source. [37, 38] In this case we obtain monodisperse 24 nm nanoflowers composed of cores of approximately 10 nm (Figure 3.1 right). HRTEM imaging suggests that there is a continuous crystallinity through the nanoflower, although contrast differences within a single nanoflower were also clearly visible (Figure S1). For this reduction reaction, it was reported that higher $NaBH_4$/$Fe(acac)_3$ molar ratios lead to smaller particles. Molar ratios of 10, 25 and 40 yielded 8, 6 and 5 nm single-core particles respectively, since $NaBH_4$ increases burst nucleation and decreases the diffusional growth.[52] It was also reported that by elevating the temperature, the crystal size increased.[59] We propose that the key parameter

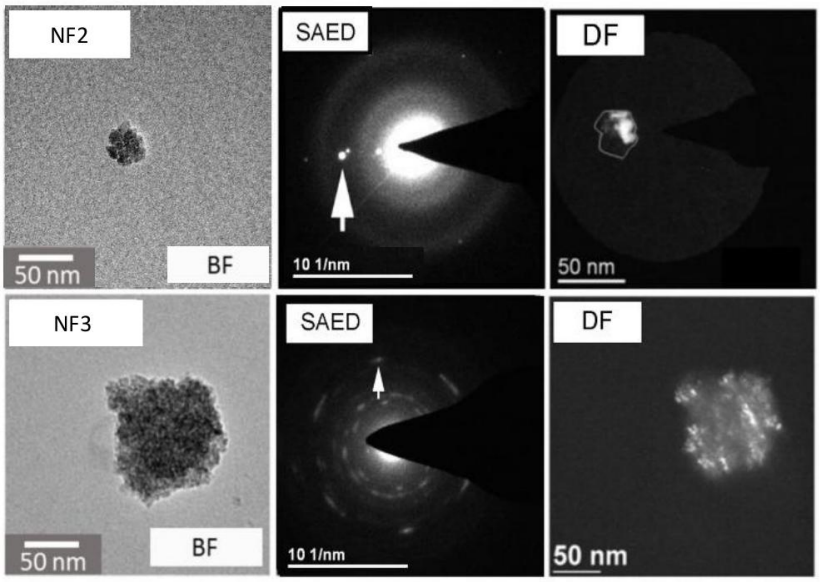

Figure 3.4: Bright (BF) and Dark Field (DF) analysis of samples NF2 and NF3.

governing the formation of complex nanoflower structures is the molar ratio of $NaBH_4$ to iron precursor; we selected a ratio of around 5, which is relatively low in comparison to other reports. [38] Additionally, the use of prolonged time period (overnight) for the synthesis, also contributes to the formation of this multi-core structure. Nanoflowers synthesized by this route were embedded on polystyrene spheres (Figure S2) via the emulsion solvent evaporation (ESE) process, described in detail elsewhere. [37, 38] The final NF4 samples has an average diameter of 172 nm and a standard deviation of 69 nm, as observed in the STEM image at low magnification (Figure 3.3).

Long term stability of the colloids:

Hydrodynamic size (D_h) was measured using dynamic light scattering (DLS) (Table 3.1). Whilst D_h varies between 50 nm (NF2) and 250 nm (NF4), colloidal stability was maintained for more than 200 days for samples NF1, 2 and 3 (Figure 3.5). There are mainly two mechanisms for colloidal stability: electrostatic repulsion (if zeta-potential values at a given pH are higher than 20 mV or lower than -20 mV) and steric repulsion (for the cases where polymeric or macromolecular surfactants and molecules, i.e. dextran or polystyrene coating). NF1 shows a nearly neutral surface (+2.9 mV), whilst NF2 is highly positively charged (+23 mV) and NF3 is highly negatively charged (-40 mV). Although NF4 has a surface charge of -62 mV we observe an increase in its hydrodynamic size overtime (Figure 5), which is probably due to aggregation phenomena because of its large particle size.

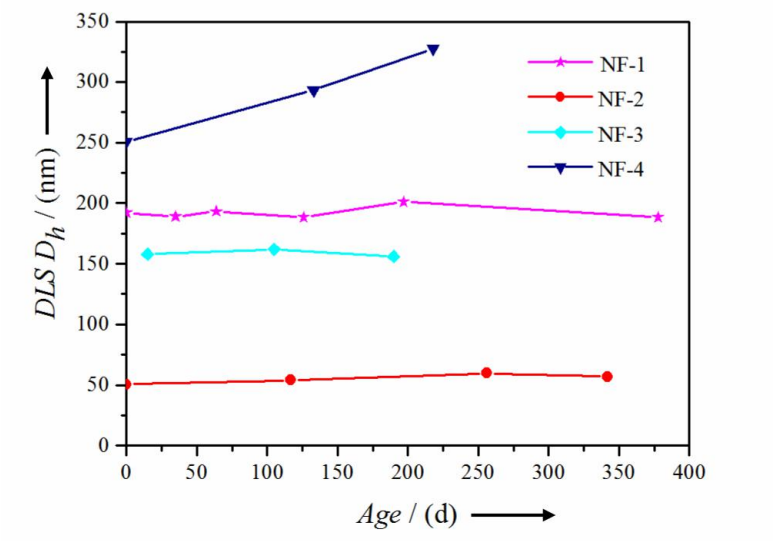

Figure 3.5: Hydrodynamic size measured throughout time for the different flower-shaped nanoparticles.

Core arrangement within the nanoflower and inter-particle interactions:

The crystal structure of all nanoflowers was identified as a mixture of magnetite (Fe_3O_4) and maghemite (γ-Fe_2O_3) using X- ray diffraction (XRD) and ^{57}Fe Mössbauer spectroscopy (Figure 3.6 and 3.7, respectively). The acquired XRD data were analyzed through the Rietveld refinement method (Figure S3). All the reflections were accounted with the Fd-3m space group with no sign of any spurious phase within the ($<$5 %) uncertainty inherent in XRD. Calculated values of lattice parameters are in the range of 8.35-8.37 , which lie between the bulk value reported $\sim$8.39 and $\sim$8.34 for magnetite[60] and maghemite,[61] respectively (Table S1 and S2). This indicates that all samples are at least partially oxidized to maghemite; this is in particularly notable for NF2, which was subjected to an oxidation treatment with iron nitrate prior to dextran coating. Bulk magnetite and maghemite can be distinguished by their different lattice parameter, but in nanosized materials, the combination of peak broadening and variation of the lattice parameters make this challenging. In addition, whereas the space group of magnetite is well established to be Fd-3m, maghemite may be present in different space groups depending of the vacancy ordering, Fd-3m being one of the possibilities.[62]

The crystal sizes, previously described (Figure 3.1), were calculated from the XRD data and are summarized in Table 3.1, along with core sizes measured by HRTEM (the term core is likewise described in Scheme 1). XRD sizes range from 8 (1) to 15 (1) nm. Differences in terms of crystal size allow us to categorize the nanoflowers into three regimes, that is below, equal or larger than 10 nm. NF3 has the largest nanoflower size (110 nm) and is composed of crystals of less than 8 nm, whereas NF2

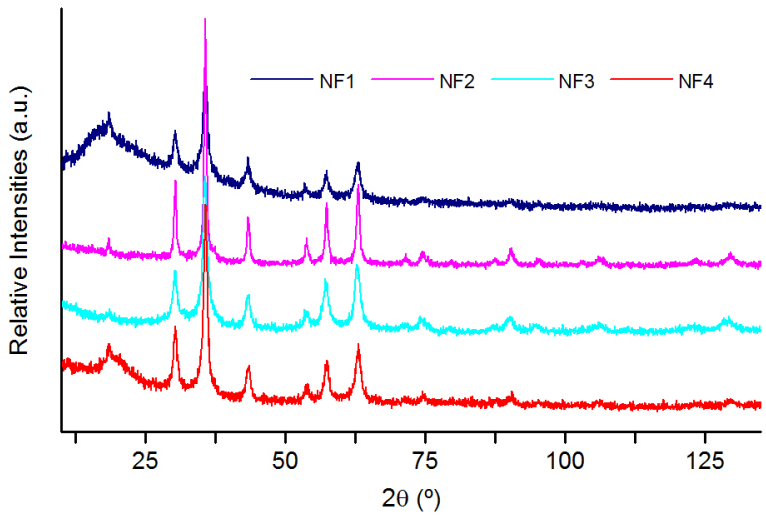

Figure 3.6: Room-temperature X-ray diffraction patterns of the different flower-shaped nanoparticles. The hump observed at low angles (below 25°) in NF1 and NF4 samples results from their amorphous organic content.

with much smaller nanoflowers (47 nm), has crystals of 15 nm, the largest in this series of nanoflowers. These results are in very good agreement with the observations in both, HRTEM and DF images. Lastly, both NF1and NF4 are intermediate systems with crystal sizes of 9 and 10 nm, respectively.

^{57}Fe Mössbauer spectroscopy measurements highlight their crystalline nature and shed light on the influence of the size and structural arrangement of the cores on the magnetic properties. Room temperature (RT) spectra are shown in Figure 3.7. All four samples comprise magnetically split spectra but with different degrees of magnetic relaxation due to their crystallinity (seen as line broadening, and partially collapsed or 'hanging' sextets). In all four spectra, more than half of the spectral area is magnetically split and we surmise that, despite such relaxation effects, the samples are all below their superparamagnetic blocking temperature at room temperature on the time scale of Mössbauer spectroscopy ($\sim$1 ns).

Magnetic relaxation effects are most pronounced in the NF1-spectrum (Figure 3.7 a), which is a superposition of a superparamagnetic doublet (13%) and a sextet with broad lines. Relaxation effects are least pronounced in the NF2-spectrum (Figure 3.7 b), which features a sextet with relatively sharp lines. It is noticeable that samples NF1 and NF2, which have similar TEM particle sizes, show very different magnetic relaxation. The longer magnetic relaxation times of NF2 are likely to be a consequence of the core arrangement within the nanoflowers (showing crystalline correlation length of ca. XRD size=15 nm) compared to NF1 (9 nm) and is in agreement with previous observations that ex-

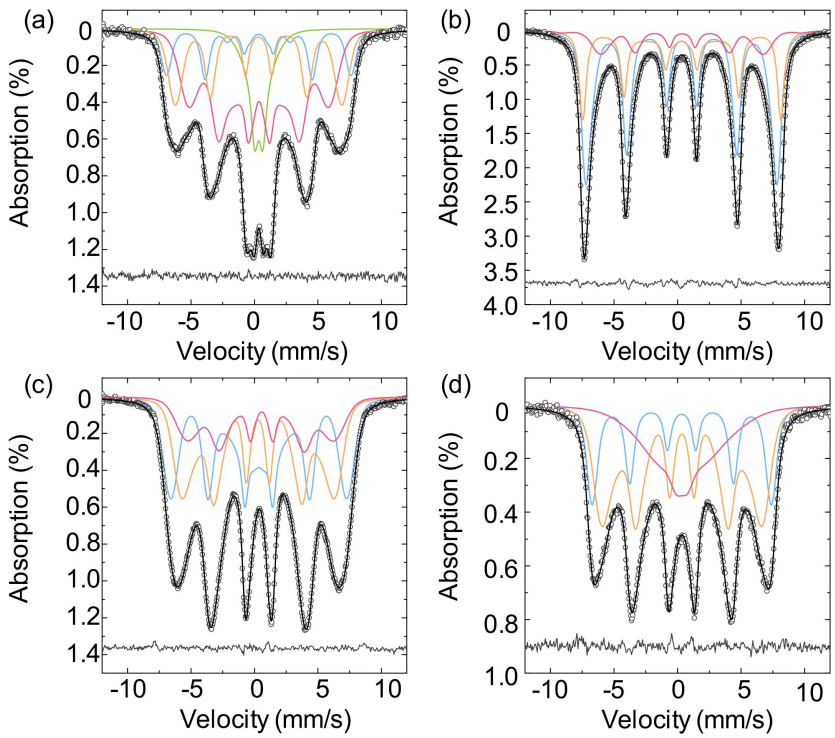

Figure 3.7: Room-temperature ^{57}Fe Mössbauer Spectroscopy spectra of: (a) NF1, (b) NF2, (c) NF3 and (d) NF4. All spectra have been fitted according to Fock et al 2016 using Voigitan line shapes. Total fit is shown by solid black line (Voigtian sub-spectra in grey). The quality of each fit is indicated by the residual - the difference between observed and fitted intensities – shown beneath each spectrum.

change interaction between surface atoms of aggregated nano-scale cores tends to suppress superparamagnetic relaxation.[62] NF3 and NF4 display almost identical relaxation (Figure 3.7 c-d), which is especially interesting as they are comprised of quite different core and nanoflower sizes. This suggests the presence of much stronger interactions between the cores in the particle in NF3 compared to the larger polystyrene-embedded NF4 nanoflowers. Furthermore, the smaller cores in NF3 seem to interact more strongly than the larger cores in NF1. These results perfectly match our previous observations by HRTEM of cores densely packed in a solid sphere in NF3, compared to the loosely packed cores in NF1 (Figure 1). RT Mössbauer spectra support the hypothesis that flower-shaped nanoparticles of larger core size show reduced relaxation, and that an increased density of cores within the nanoflowers suppresses magnetic relaxation.

The mean isomer shift (“centre”) of the Mössbauer spectra relative to α-Fe is sensitive to the oxidation state of iron and allows for the quantification of the magnetite-maghemite content in the samples via the method described by Fock $\&$ Bogart et al.[40] The method is applicable to room-temperature

Table 3.2: Parameters determined through magnetic characterisation: Saturation magnetisation (M_s) and magnetic size ($d_{c,1}$ and $d_{c,2}$) by DC Magnetometry[a)], Hydrodynamic size (ACS $D_{h,1}$ and ACS $D_{h,2}$) by ACS versus frequency (Debye model and Multi-Core extended model, respectively)[b)] and anisotropy constant (KACvT) by ACS versus temperature.[c)]

Sample	M_s / (Am^2/kg Fe) σ	$d_{c,1}$ / (nm) σ	$d_{c,2}$ / (nm) σ	β[d)]	ACS $D_{h,1}$ / (nm) σ	ACS $D_{h,2}$ / (nm)	K_{ACvT}/ (x 10^4 J/m^3)
NF1	93 (3)	4.3 (0.52)	18.7 (0.24)	0.44	251 (116)	180	2.5 (2)
NF2	112 (3)	2 (0.8)	24.7 (0.08)	0.74	54 (11)	45	2.3 (2)
NF3	103 (3)	-	16 (0.1)	-	247 (5)	175	1.8 (2)
NF4	119 (4)	2.5 (0.56)	13.6 (0.03)	0.69	-	-	4.0 (3)

Note: a) Measurements performed in the dried samples (powder form). b) Measurements performed in both colloidal dispersion and immobilized samples. c) Measurements performed in the colloidal dispersion. d) β is the normalized fraction of the larger particle size distribution.

spectra, but in case of spectra obtained at low temperature (18 and 80 K) (see Figure S4), where relaxation effects are negligible and hence spectral lines sharper, the mean isomer shift can be obtained with less uncertainty (see Table S3). [40] From this, we find that the percentages of Fe atoms in the form of magnetite in the samples are, 9 $\pm$ 2, 5 $\pm$ 3, 5 $\pm$ 2, and 3 $\pm$ 2 for NF1, NF2, NF3 and NF4 respectively, i.e. the samples are essentially maghemite. This means that the differences found in XRD lattice parameters are related to differences in the degree of structural order rather than to variation in magnetite/maghemite content. Indeed, the largest lattice parameters correspond to NF1 and NF3, which also have the smallest core sizes and therefore larger fraction of surface atoms. Samples NF1 and NF3 were synthesized in the presence of dextran and citric acid that absorb on the core surface hampering the contact between adjacent cores.

The static magnetic properties were evaluated for all samples in liquid suspensions by DC magnetometry measurements at 300 K (Figure 3.8 a). The effective magnetic size of the nanoflowers was obtained by modelling the M(H) curve using the classical superparamagnetic Langevin function (see SI). These results are presented in Table 3.2. The magnetization curve of NF3 was fitted by a monomodal size distribution indicating that the cores have a uniform size with a single effective magnetic diameter of 16 nm. In the case of NF2, we observe a better fit to the experimentally measured M(H) curve when our Langevin fit uses a bimodal size distribution. This gives two effective magnetic sizes; the first size of 25 nm has a very narrow size distribution of 0.1 while the second distribution has a much smaller size of 2 nm. In addition, this sample has high saturation magnetization value and high initial susceptibility, both of which are due to the high fraction of particles with large magnetic sizes.

Likewise, for NF1 and NF4, the M(H) curves are better fitted with a bimodal size distribution. Both samples consist magnetically of two particle fractions with different magnetic diameters although inspection of the initial magnetization slope at low fields suggests that NF4 contains a larger fraction of larger sizes, which justifies the larger saturation magnetization. It should be noted that in many cases

the derived effective magnetic sizes cannot directly be compared with the particle size determined by TEM or the crystal sizes determined by XRD.

The effective magnetic size modelled by the Langevin function is further a distribution of magnetic moments projected on a sphere. This sphere is usually smaller than the TEM size due to the surface dead layer.[63] For the special case of flower-shaped nanoparticles consisting of packed cores forming a multi-core structure, this sphere is smaller than the flower TEM sizes but larger than the core size for all the systems in this work. The interactions between the cores can lead to magnetic sizes that are larger than the crystal sizes measured by XRD. DC magnetometry data indicates that the nanoflowers are, in general, better fitted using a bimodal size distribution and indicates that size and shape of the cores varies across the nanoflower, as revealed by DF images (Figure 3.4). However, for NF3, whose cores are smaller and randomly distributed, the best fit of the magnetization curve is with a monomodal distribution.

Dynamic magnetic properties of the nanoflowers were characterized by AC susceptibility (ACS) vs frequency and temperature. These measurements were conducted on samples in both dispersed and immobilized states (See Figure 3.8 b and SI). An ACS hydrodynamic diameter was calculated using the generalized Debye model (ACS $D_{h,1}$)[64] and the multi-core extended model (ACS $D_{h,2}$)[65] as summarized in Table 3.2.

NF1 shows a weak maximum of the imaginary part at $\sim$80 Hz caused by Brownian rotation. The gradual decay of the real part of both dispersed and immobilized particles (Figure S5) indicates a wide distribution of relaxation times. This is further supported by the constant imaginary part of the sample with immobilized nanoparticles, which is superimposed by the weak Brownian relaxation peak for the dispersed sample, which indicates that the majority of particles relax via the internal Néel mechanism. Using the generalized Debye model we obtain an average hydrodynamic diameter of 251 nm whilst this value decreases to 180 nm using the multi-core extended model, which is comparable to the value measured by DLS (192 nm).

However, for NF2, a pronounced peak in the imaginary part at 5 kHz clearly indicates Brownian rotation with a Néel contribution of 10-20%. The linear decay of the real part of the immobilized sample when plotted vs. ln(f) indicates a wide distribution of Néel relaxation times, i.e. anisotropy energies.[66] Modelling these data using the generalized Debye model yields a mean hydrodynamic diameter of 54 nm and 45 nm using the Debye and multi-core extended model, respectively, both of which are in good agreement with the value measured in DLS measurements (51 nm).

For NF3, the Brownian relaxation peak in the out-of-phase component of the AC susceptibility is at about 50 Hz with a shallow shoulder towards low frequencies indicating agglomeration. The low frequency relaxation disappears when the nanoparticles are diluted. The real part levels off at high frequencies together with a nearly zero imaginary part which can be caused by intra-potential-well contributions[67–69] and by nanoparticles that follow the excitation field via the internal Néel mechanism with relaxation times well below 1 μs, i.e. moments can follow the sinusoidal excitation field without

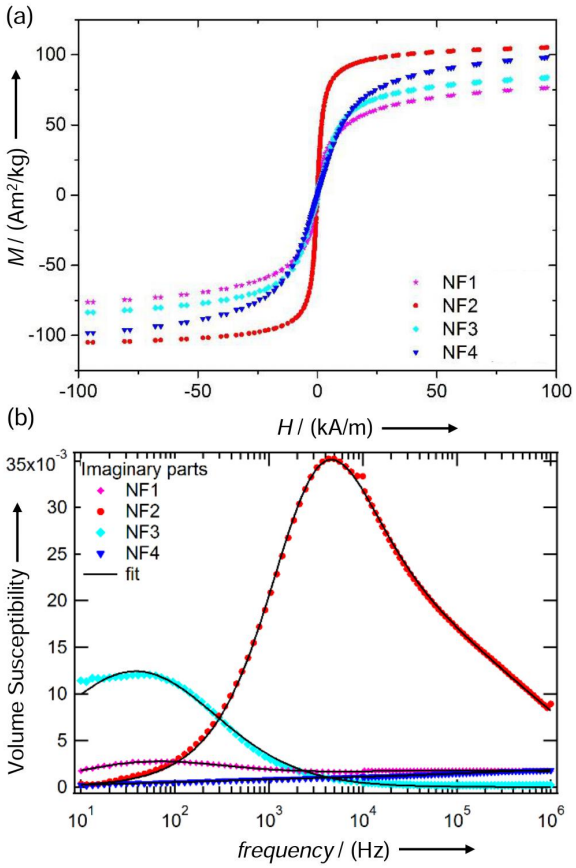

Figure 3.8: Magnetic characterization at 300 K. (a) DC Magnetization curves and (b) AC susceptibility vs frequency (imaginary part) of all flower-shaped nanoparticles in suspension (The solid line shows best fit with generalized Debye model).

phase lag up to at least 1 MHz frequency. In this case, the values of average hydrodynamic diameters are 247 nm using the generalized Debye model and 175 nm using the multi-core model, the latter being more comparable to the value measured by DLS (158 nm).

Interestingly, for NF4, we observed almost no difference between immobilized and dispersed particles (Figure S5), which is typical for a nanoparticle system that undergoes 100 % Néel relaxation. The Néel relaxation peak in the out-of-phase component is in the range of several MHz, i.e. outside the measurement window: since the MNP dynamics are dominated by the Néel mechanism, no information can be obtained on their hydrodynamic size.

ACS vs temperature was performed at low temperature (5-260 K) to derive an effective anisotropy constant for the nanoflowers that is presented in Table 3.2. The in-phase component ($\chi\prime$) of the AC susceptibility approaches a frequency independent value as T$\longrightarrow$ 0, corresponding to the intra-potential-

well response of the particle moments.[69] Using the low-T χ ′-values, we determined the effective anisotropy constant values (K) of: 2.5 (2), 2.3 (2), 1.8 (2) and 4.0 (3) (x10^4 J/m^3) for NF1, 2, 3 and 4 respectively (see Figure S5 and Table S6 in SI for details). Interestingly, we find that the nanoflower system with the largest anisotropy constant (NF4), is also the only system for which blocking temperature is close to room temperature (see Figure S5 b). This implies that the embedded nanoflowers might also display some order on the poly (styrene) sphere, as described for some magnetic nanocrystals forming close-packed structures, which showed an increase in anisotropy.[70] Conversely, NF1-3 are clearly blocked in the temperature range 5 – 390 K for f $<$ 1000 Hz.

Description of the structure of a nanoflower:

The results obtained for the core and particle size for each flower-shaped system through different characterization techniques are summarised in Figure 3.9. The size of the cores range from 4 to 15 nm and the size of the particle range from 50 to 250 nm. Differences in both, core and particle size reflect the complicated nature of these materials. In general, the size calculated via XRD (D_{XRD}) is larger than that estimated via HRTEM (D_{HRTEM}). This reflects the multi-core nature of the samples, whose cores are fused to a greater or lesser degree to form flower-shaped structures.

In those cases with high values of $D_{XRD} \approx D_{HRTEM} >$ 10 nm (NF2 and NF4), significant coalescence of the cores is detected, which justifies the highest Ms values displayed by those samples. For all cases, the magnetic size deduced from our Langevin based modelling ($d_{c,2}$) is larger than both D_{HRTEM} and D_{XRD} suggesting the presence of interactions between cores and thus shedding light on the collective behaviour within the nanoflowers. For samples that possess larger effective magnetic size, such as NF2, we observe both an increase in χ_0 in the RT magnetization curve and an increase in magnetic relaxation times, as demonstrated by a ^{57}Fe Mössbauer spectrum sextet with relatively sharp lines at RT. Samples with a more reduced effective magnetic size (NF1, NF3 and NF4) have a visibly smaller χ_0 in the magnetization curve and also have reduced relaxation, i.e. less MMössbauer spectral area within the sextet. We surmise that when there is a close contact between cores within a particle, the continuity of the crystal orientation is ensured favouring magnetic ordering across the interfaces. This is indeed the case of the structures previously called nanoflower that showed one order of magnitude higher heating rates than the specific absorption rate (SAR) reported for conventional 11 nm maghemite nanoparticles in the same field exposure conditions.[51]

Regarding the particle size, samples in which DLS $D_h \gg D_{TEM}$ either contain a large amount of coating and water hydration on their surface or have collective behaviour between the particles (interparticle interactions, i.e. dipolar interactions). The former can be detected by IR spectroscopy and quantified by thermogravimetric analysis (See Figure S7). This is the case of NF1 and NF2 that have similar D_{TEM} particles sizes and therefore similar surface-area-to-volume ratios but they have very different organic content (80% for NF1 and 20% for NF2). Consequently, DLS D_h size of NF1 is much

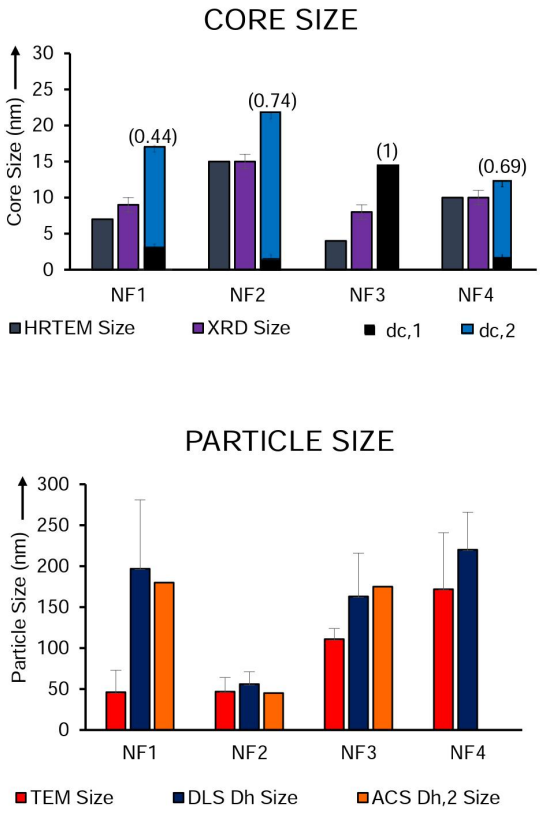

Figure 3.9: Core (above) and particle size (below) of the flower-shaped nanoparticles as determined by structural and magnetic means, according to Table 3.1 and 3.2. Between brackets, β is included, the normalized fraction of the larger particle size distribution as determined by DC magnetometry.

larger than D_{TEM} and hence indicates a larger amount of dextran present on the nanoparticles surface compared to NF2. The existence of organic component is already supported by the XRD data displayed in Figure 3.4, where the hump that appears for NF1 at low angles (below 25 °) is consequence of such contribution. The collective behaviour that is related to interparticle interactions can be detected by AC susceptibility. All samples have comparable hydrodynamic sizes obtained by both DLS D_h and ACS $D_{h,2}$ (modelled by the extended multi-core function), confirming that dipolar interactions between particles are minimized in these colloids and explaining the observed long-term stability. In the case of NF3, dipolar interactions between particles may cause the formation of chains and explain the observed change in AC spectrum with sample dilution.

Comparing core and particle size from the magnetic measurements, i.e. effective magnetic size

($d_{c,2}$) and hydrodynamic size ACS $D_{h,2}$, we have identified three different flower-shaped multi-core systems. For NF2, the effective magnetic size tends to approach the nanoflower size (ACS $D_{h,2}$ / $d_{c,2} \sim$ 1.8) indicating strong magnetic interactions between cores within a particle. Cores inside the nanoflower are not only oriented but also in close contact leading to exchange interactions, and therefore collective magnetic behaviour. For NF1 and NF3, the effective magnetic size is much smaller than the flower size (ACS $D_{h,2}$ / $d_{c,2} \sim$ 10) indicating less contact between cores, which in NF1 may be loosely packed within the flower. Much more complicated is the case of NF4, where nanoflowers were embedded onto polymeric spheres creating a superstructure. The relatively small nanoflower size, high anisotropy constant, but low blocking temperature of NF4 suggests that the finite size of the nanoflower systems is one of the key parameters that dictates their Néel relaxation properties.

Towards the standardization: comparison of the nanoflower synthesis:

Differences between the systems (NF1-4) are directly related to the various synthetic routes (Strategy 1-4), in terms of formation mechanism (clustering and coalescence, clustering and recrystallization or Ostwald ripening) and free energy involved in the process and experimental conditions (pH, surface charge, temperature, pressure and time). Table 3.3 provides a comparison of the key parameters determining the core assembly and their implication on the resulting unique colloidal and magnetic properties. Additionally, from the synthesis standardization point of view, the advantages and disadvantages of each strategy are highlighted.

NF1 offers the possibility of large production and allows the synthesis of larger batches in aqueous media. The nanoflowers are directly stabilized by the presence of dextran in the reaction media and present long-term stability for at least 500 days (Figure 3.5). The use of polyol media provides great control over core aggregation, which yields multi-core structures that consist of cores in more or less contact (NF2 and NF3) depending on the synthesis conditions. Furthermore, polyol media allows the use of higher reaction temperatures (200 °C) leading to fused cores within a particle e.g. NF2. However, in NF3, the use of an extra additive (sodium citrate) to facilitate the final dispersion of the particles in aqueous media hampers the aggregation of the cores in a similar way to dextran in the synthesis of NF1. Aqueous suspensions of these systems present long-term stability for at least 200 days (Figure 3.5). However, it should be taken into account that high temperatures over long time as applied in the synthesis of NF2 and NF3 (10-12 h) generally lead to high-energy consumption (costs). Moreover, one-pot syntheses such as those followed to obtain NF1 and NF3 have advantages compared to the conventional step-wise reactions as used for NF2 and NF4.

Table 3.3: Comparison resulting from the analysis of the synthesis and characterization of the flower-shaped iron oxide nanoparticles.

General comparison		**NF1**	**NF2**	**NF3**	**NF4**
Synthesis strategies	Reaction	One step	Multistep	One step	Multistep
	Production Yield	Large	Moderate	Moderate	Low
	Mechanism	Clustering	Clustering + Recrystallisation	Clustering + Coalescence	Clustering + Coalescence + Embedment
Colloids Flower-shaped magnetic nanoparticles	Interactions between cores	Low	High	Moderate-high	Moderate
	Interaction between particles	Low	Low	Moderate	High
Advantages		Long term colloidal stability	Large saturation magnetisation and large susceptibility	Large magnetic moment per particle	Magnetic superstructure with high anisotropy
Disadvantages		Wide particle size distribution	High energy consuming synthesis		Reduced long term colloidal stability

3.4 Conclusions

Analysis of the self-assembly process conducted in this work leads to the formation of flower-shaped nanoparticles with properties and possible applications that differ strongly from single-core particles of similar size and corresponding bulk material. Synthesis reagents and experimental conditions are key factors to control the core and particle sizes, as well as intra- and interparticle interactions, i.e. between cores and particles in suspensions. The results obtained from different characterisation techniques have been brought together to obtain a self-consistent picture that describes how structural and magnetic properties are interrelated in those systems. Controlling self-assembly of magnetic multi-core nanoparticles allow the design of optimal magnetic properties of the colloids as a function of its specific application.

Bibliography

[1] Xing, P. & Zhao, Y. Multifunctional nanoparticles self-assembled from small organic building blocks for biomedicine. *Advanced Materials* (2016).

[2] Pan, S., He, L., Peng, J., Qiu, F. & Lin, Z. Chemical-bonding-directed hierarchical assembly of nanoribbon-shaped nanocomposites of gold nanorods and poly (3-hexylthiophene). *Angewandte Chemie* (2016).

[3] Volkmann, M., Meyns, M., Lesyuk, R., Lehmann, H. & Klinke, C. Attachment of colloidal nanoparticles to boron nitride nanotubes. *Chemistry of Materials* (2016).

[4] Sayevich, V. *et al.* 3d assembly of all-inorganic colloidal nanocrystals into gels and aerogels. *Angewandte Chemie International Edition* **55**, 6334–6338 (2016).

[5] Stolarczyk, J. K., Deak, A. & Brougham, D. F. Nanoparticle clusters: Assembly and control over internal order, current capabilities, and future potential. *Advanced Materials* (2016).

[6] Nie, Z., Petukhova, A. & Kumacheva, E. Properties and emerging applications of self-assembled structures made from inorganic nanoparticles. *Nature nanotechnology* **5**, 15–25 (2010).

[7] De Yoreo, J. J. *et al.* Crystallization by particle attachment in synthetic, biogenic, and geologic environments. *Science* **349**, aaa6760 (2015).

[8] Ocaña, M., Rodriguez-Clemente, R. & Serna, C. J. Uniform colloidal particles in solution: Formation mechanisms. *Advanced Materials* **7**, 212–216 (1995).

[9] Raju, M., Van Duin, A. C. & Fichthorn, K. A. Mechanisms of oriented attachment of tio2 nanocrystals in vacuum and humid environments: reactive molecular dynamics. *Nano letters* **14**, 1836–1842 (2014).

[10] Frandsen, C. *et al.* Aggregation-induced growth and transformation of β-feooh nanorods to micron-sized α-fe$_2$o$_3$ spindles. *CrystEngComm* **16**, 1451–1458 (2014).

[11] Bannwarth, M. B. *et al.* Well-defined nanofibers with tunable morphology from spherical colloidal building blocks. *Angewandte Chemie International Edition* **52**, 10107–10111 (2013).

[12] Ingham, B. *et al.* How nanoparticles coalesce: an in situ study of au nanoparticle aggregation and grain growth. *Chemistry of Materials* **23**, 3312–3317 (2011).

[13] Dutz, S. Are magnetic multicore nanoparticles promising candidates for biomedical applications? *IEEE Transactions on Magnetics* **52**, 1–3 (2016).

[14] Serantes, D. *et al.* Multiplying magnetic hyperthermia response by nanoparticle assembling. *The Journal of Physical Chemistry C* **118**, 5927–5934 (2014).

[15] Jeong, U., Teng, X., Wang, Y., Yang, H. & Xia, Y. Superparamagnetic colloids: controlled synthesis and niche applications. *Advanced Materials* **19**, 33–60 (2007).

[16] Gutierrez, L. *et al.* Synthesis methods to prepare single-and multi-core iron oxide nanoparticles for biomedical applications. *Dalton Transactions* **44**, 2943–2952 (2015).

[17] Gijs, M. A., Lacharme, F. & Lehmann, U. Microfluidic applications of magnetic particles for biological analysis and catalysis. *Chemical reviews* **110**, 1518–1563 (2009).

[18] Nowak, J., Wiekhorst, F., Trahms, L. & Odenbach, S. The influence of hydrodynamic diameter and core composition on the magnetoviscous effect of biocompatible ferrofluids. *Journal of Physics: Condensed Matter* **26**, 176004 (2014). URL `http://stacks.iop.org/0953-8984/26/i=17/a=176004`.

[19] Mahmoudi, M., Hofmann, H., Rothen-Rutishauser, B. & Petri-Fink, A. Assessing the in vitro and in vivo toxicity of superparamagnetic iron oxide nanoparticles. *Chemical reviews* **112**, 2323–2338 (2011).

[20] Laurent, S. *et al.* Magnetic iron oxide nanoparticles: Synthesis, stabilization, vectorization, physicochemical characterizations, and biological applications. *Chemical Reviews* **108**, 2064–2110 (2008). URL `http://dx.doi.org/10.1021/cr068445e`.

[21] Eberbeck, D. *et al.* Multicore magnetic nanoparticles for magnetic particle imaging. *IEEE Transactions on Magnetics* **49**, 269–274 (2013).

[22] Grüttner, C., Müller, K., Teller, J. & Westphal, F. Synthesis and functionalisation of magnetic nanoparticles for hyperthermia applications. *International Journal of Hyperthermia* **29**, 777–789 (2013).

[23] Dutz, S., Kettering, M., Hilger, I., Müller, R. & Zeisberger, M. Magnetic multicore nanoparticles for hyperthermia—influence of particle immobilization in tumour tissue on magnetic properties. *Nanotechnology* **22**, 265102 (2011).

[24] Hugounenq, P. *et al.* Iron oxide monocrystalline nanoflowers for highly efficient magnetic hyperthermia. *The Journal of Physical Chemistry C* **116**, 15702–15712 (2012).

[25] Alexiou, C. *et al.* Locoregional cancer treatment with magnetic drug targeting. *Cancer research* **60**, 6641–6648 (2000).

[26] Bigall, N. C. *et al.* Colloidal ordered assemblies in a polymer shell: A novel type of magnetic nanobeads for theranostic applications. *Chemistry of Materials* **25**, 1055–1062 (2013).

[27] Zoppellaro, G. *et al.* Theranostics of epitaxially condensed colloidal nanocrystal clusters, through a soft biomineralization route. *Chemistry of Materials* **26**, 2062–2074 (2014).

[28] Mazuel, F. *et al.* Magneto-thermal metrics can mirror the long-term intracellular fate of magneto-plasmonic nanohybrids and reveal the remarkable shielding effect of gold. *Advanced Functional Materials* (2017).

[29] Ludwig, F. *et al.* Magnetic, structural, and particle size analysis of single-and multi-core magnetic nanoparticles. *IEEE Transactions on Magnetics* **50**, 1–4 (2014).

[30] Mulvaney, P., Parak, W. J., Caruso, F. & Weiss, P. S. Standardizing nanomaterials (2016).

[31] Schaller, V., Wahnström, G., Sanz-Velasco, A., Enoksson, P. & Johansson, C. Determination of nanocrystal size distribution in magnetic multicore particles including dipole-dipole interactions and magnetic anisotropy: a monte carlo study. In *AIP Conference Proceedings*, vol. 1311, 42–50.

[32] Frankamp, B. L., Boal, A. K., Tuominen, M. T. & Rotello, V. M. Direct control of the magnetic interaction between iron oxide nanoparticles through dendrimer-mediated self-assembly. *Journal of the American Chemical Society* **127**, 9731–9735 (2005).

[33] Bohara, R. A., Thorat, N. D. & Pawar, S. H. Role of functionalization: strategies to explore potential nano-bio applications of magnetic nanoparticles. *RSC Advances* **6**, 43989–44012 (2016).

[34] Gehrke, N. *et al.* Magnetic characterization of clustered core magnetic nanoparticles for mpi. *IEEE Transactions on Magnetics* **51**, 1–4 (2015).

[35] Wabler, M. *et al.* Magnetic resonance imaging contrast of iron oxide nanoparticles developed for hyperthermia is dominated by iron content. *International Journal of Hyperthermia* **30**, 192–200 (2014).

[36] Liu, J. *et al.* Highly water-dispersible biocompatible magnetite particles with low cytotoxicity stabilized by citrate groups. *Angewandte Chemie* **121**, 5989–5993 (2009).

[37] Sommertune, J. *et al.* Polymer/iron oxide nanoparticle composites—a straight forward and scalable synthesis approach. *International journal of molecular sciences* **16**, 19752–19768 (2015).

[38] Yathindranath, V. *et al.* A versatile method for the reductive, one-pot synthesis of bare, hydrophilic and hydrophobic magnetite nanoparticles. *Advanced Functional Materials* **21**, 1457–1464 (2011).

[39] Rodriguez-Carvajal, J. Recent developments of the program fullprof. *Commission on powder diffraction (IUCr). Newsletter* **26**, 12–19 (2001).

[40] Fock, J. *et al.* Uncertainty budget for determinations of mean isomer shift from mössbauer spectra. *Hyperfine Interactions* **237**, 1–11 (2016).

[41] Fock, J. *et al.* On the 'center of gravity' method for measuring the composition of magnetite/maghemite mixtures, or the stoichiometry of magnetite-maghemite solid solutions, via ^{57}fe mössbauer spectroscopy in preparation. *(In preparation)* .

[42] Ludwig, F., Guillaume, A., Schilling, M., Frickel, N. & Schmidt, A. Determination of core and hydrodynamic size distributions of cofe$_2$o$_4$ nanoparticle suspensions using ac susceptibility measurements. *Journal of Applied Physics* **108**, 033918 (2010).

[43] Sugimoto, T. & Matijević, E. Formation of uniform spherical magnetite particles by crystallization from ferrous hydroxide gels. *Journal of Colloid and Interface Science* **74**, 227–243 (1980).

[44] Vereda, F., de Vicente, J., Morales, M. P., Rull, F. & Hidalgo-Alvarez, R. Synthesis and characterization of single-domain monocrystalline magnetite particles by oxidative aging of fe(oh)$_2$. *The Journal of Physical Chemistry C* **112**, 5843–5849 (2008).

[45] Parks, G. A. The isoelectric points of solid oxides, solid hydroxides, and aqueous hydroxo complex systems. *Chemical Reviews* **65**, 177–198 (1965).

[46] Verges, M. A. *et al.* Uniform and water stable magnetite nanoparticles with diameters around the monodomain–multidomain limit. *Journal of Physics D: Applied Physics* **41**, 134003 (2008).

[47] Luengo, Y., Morales, M. P., Gutierrez, L. & Veintemillas-Verdaguer, S. Counterion and solvent effects on the size of magnetite nanocrystals obtained by oxidative precipitation. *Journal of Materials Chemistry C* **4**, 9482–9488 (2016).

[48] Bautista, M. *et al.* Comparative study of ferrofluids based on dextran-coated iron oxide and metal nanoparticles for contrast agents in magnetic resonance imaging. *Nanotechnology* **15**, S154 (2004).

[49] Dong, H., Chen, Y.-C. & Feldmann, C. Polyol synthesis of nanoparticles: status and options regarding metals, oxides, chalcogenides, and non-metal elements. *Green Chemistry* **17**, 4107–4132 (2015).

[50] Caruntu, D., Caruntu, G. & O'Connor, C. J. Magnetic properties of variable-sized fe$_3$o$_4$ nanoparticles synthesized from non-aqueous homogeneous solutions of polyols. *Journal of physics D: Applied physics* **40**, 5801 (2007).

[51] Ge, J., Hu, Y., Biasini, M., Beyermann, W. P. & Yin, Y. Superparamagnetic magnetite colloidal nanocrystal clusters. *Angewandte Chemie International Edition* **46**, 4342–4345 (2007).

[52] Lartigue, L. *et al.* Cooperative organization in iron oxide multi-core nanoparticles potentiates their efficiency as heating mediators and mri contrast agents. *ACS nano* **6**, 10935–10949 (2012).

[53] Cai, W. & Wan, J. Facile synthesis of superparamagnetic magnetite nanoparticles in liquid polyols. *Journal of colloid and interface science* **305**, 366–370 (2007).

[54] Liu, H.-L. *et al.* One-pot polyol synthesis of monosize pvp-coated sub-5nm fe$_3$o$_4$ nanoparticles for biomedical applications. *Journal of Magnetism and Magnetic Materials* **310**, e815–e817 (2007).

[55] Sun, Q., Ren, Z., Wang, R., Chen, W. & Chen, C. Magnetite hollow spheres: solution synthesis, phase formation and magnetic property. *Journal of Nanoparticle Research* **13**, 213–220 (2011).

[56] Sahoo, Y. *et al.* Aqueous ferrofluid of magnetite nanoparticles: fluorescence labeling and magnetophoretic control. *The Journal of Physical Chemistry B* **109**, 3879–3885 (2005).

[57] Vereda, F., Morales, M. P., Rodriguez-Gonzalez, B., de Vicente, J. & Hidalgo-Alvarez, R. Control of surface morphology and internal structure in magnetite microparticles: from smooth single crystals to rough polycrystals. *CrystEngComm* **15**, 5236–5244 (2013).

[58] Cheng, C., Xu, F. & Gu, H. Facile synthesis and morphology evolution of magnetic iron oxide nanoparticles in different polyol processes. *New Journal of Chemistry* **35**, 1072–1079 (2011).

[59] Yonezawa, T., Kamoshita, K., Tanaka, M. & Kinoshita, T. Easy preparation of stable iron oxide nanoparticles using gelatin as stabilizing molecules. *Japanese Journal of Applied Physics* **47**, 1389 (2008).

[60] Okudera, H., Kihara, K. & Matsumoto, T. Temperature dependence of structure parameters in natural magnetite: single crystal x-ray studies from 126 to 773 k. *Acta Crystallographica Section B: Structural Science* **52**, 450–457 (1996).

[61] Pecharroman, C., Gonzalez-Carreno, T. & Iglesias, J. E. The infrared dielectric properties of maghemite, γ-fe$_2$o$_3$, from reflectance measurement on pressed powders. *Physics and Chemistry of Minerals* **22**, 21–29 (1995).

[62] Frandsen, C. & Mørup, S. Spin rotation in α-fe$_2$o$_3$ nanoparticles by interparticle interactions. *Physical review letters* **94**, 027202 (2005).

[63] Morales, M. P. *et al.* Surface and internal spin canting in γ-fe$_2$o$_3$ nanoparticles. *Chemistry of Materials* **11**, 3058–3064 (1999).

[64] Chung, S.-H. *et al.* Biological sensing with magnetic nanoparticles using brownian relaxation. *Journal of applied physics* **97**, 10R101 (2005).

[65] Bogren, S. *et al.* Classification of magnetic nanoparticle systems—synthesis, standardization and analysis methods in the nanomag project. *International journal of molecular sciences* **16**, 20308–20325 (2015).

[66] Ludwig, F. *et al.* Optimization of magnetic nanoparticles for magnetic particle imaging. *IEEE Transactions on Magnetics* **48**, 3780–3783 (2012).

[67] Shliomis, M. & Stepanov, V. Theory of the dynamic susceptibility of magnetic fluids. *Advances in Chemical Physics* **87**, 32 (1994).

[68] Ahrentorp, F. *et al.* Sensitive high frequency ac susceptometry in magnetic nanoparticle applications. In *Aip Conference Proceedings*, vol. 1311, 213.

[69] Svedlindh, P., Jonsson, T. & Garcia-Palacios, J. Intra-potential-well contribution to the ac susceptibility of a noninteracting nano-sized magnetic particle system. *Journal of magnetism and magnetic materials* **169**, 323–334 (1997).

[70] Parker, D., Lisiecki, I. & Pileni, M. Do 8 nm co nanocrystals in long-range-ordered face-centered cubic (fcc) supracrystals show superspin glass behavior? *The Journal of Physical Chemistry Letters* **1**, 1139–1142 (2010).

4

Formation mechanism of maghemite nanoflowers synthesized by polyol mediated process

Summary

Magnetic nanoparticles are being developed as structural and functional materials for use in diverse areas, including biomedical applications. Here, we report the synthesis of maghemite (γ-Fe_2O_3) nanoparticles with distinct morphologies: single-core and multi-core, including hollow spheres and nanoflowers, prepared by the polyol process. We have used sodium acetate (NaAc) to control the nucleation and assembly process to obtain the different particle morphologies. Moreover, from samples obtained at different time steps during the synthesis, we have elucidated the formation mechanism of the nanoflowers: The initial phases of the reaction present a lepidocrocite (γ-FeOOH) structure, which suffers a fast dehydroxylation, transforming to an intermediate "undescribed" phase - possibly partly dehydroxylated lepidocrocite - that after some incubation time evolves to maghemite nanoflowers. Once the nanoflowers have been formed, a crystallization process takes place where the γ-Fe_2O_3 crystallites within the nanoflowers grow in size (from $\sim$ 11 to 23 nm), but the particle size of the flower remains essentially unchanged ($\sim$ 60 nm). Samples with different morphologies were coated with citric acid and their heating capacity in an alternating magnetic field was evaluated. We observe that nanoflowers with large cores (23 nm, controlled by annealing) densely packed (tuned by low NaAc concentration) offer five times enhanced heating capacity compared to the nanoflowers with smaller core sizes (15 nm), 4 times heating effect compared to the hollow spheres and 1.5 times compared to single-core nanoparticles (36 nm) used in this work.

4.1 Introduction

Through the polyol-mediated synthesis developed by F. Fievet, Lagier and Figlarz,[1] the formation of both noble metals and metal oxide nanocrystals has been widely reported, obtaining monodisperse systems thanks to the polyol acting as the surfactant of the as-synthesized particles, reducer and reaction media.[2] The first advantage of this procedure is that it allows the synthesis of hydrophilic particles that remain stable in aqueous media[3] and other polar solvents within one-step,[4] avoiding further coating steps required by other synthesis routes such us thermal decomposition of organometallic precursors. In addition, owing to the high dielectric constants of the polyols,[5] they are able to dissolve inorganic compounds used as reactants, and due to their relatively high boiling points, great crystallinity of the particles can be achieved.

Several examples of the synthesis of metal nanoparticles achieved by this procedure exist in the literature. Among others, functional materials such as Au–Pd colloidal nanoparticles for catalysis purposes[6] and Co nanorods for the development of new permanent magnets[7] have been recently synthetized. Besides noble metals, both the synthesis of single-core and multi-core iron oxide magnetic nanoparticles[8] have been reported through polyol reduction, organizing colloidal magnetic cores into highly regular nanoparticles with tuned properties.

Of special interest are iron oxide multi-core nanoparticles assembled in flower-shaped structures synthesized by polyols.[9, 10] In comparison with the single-core counterparts, these flower-like nanoparticles have shown enhanced longitudinal and transverse relaxivities for magnetic resonance imaging (MRI) contrast generation[11] and enhanced specific absorption rate (SAR) values for magnetic hyperthermia due to hysteresis heating.[12] The interest on magnetite (Fe_3O_4) and maghemite (γ-Fe_2O_3) nanoparticles for biomedical applications, both in diagnosis[13] and therapy,[14, 15] relies on its biocompatibility[11, 16] and non-toxicity,[17] its chemical stability, and the strong response when exposed to an external magnetic field.[18]

Assembly process and particle and core sizes are crucial characteristics that determine the magnetic properties of the colloid and therefore its optimal use for a given application.[19, 20] In the present work, we have analysed the assembly process that leads to the formation of single-core and multi-core hollow and flower-like maghemite nanoparticles through the polyol process. We have also determined the experimental parameters that allow control of the core sizes within the nanoflowers. In detail, we have analysed the role of specific experimental conditions in the synthesis such as the presence of a precipitator (sodium acetate, NaAc) and an extra stabilizer (polyvinylpyrrolidone, PVP), and the aging time. Then, the consequences of the different morphologies and core sizes on the magnetic cooperative behaviour have been studied. Finally, some selected samples were coated with citric acid and the possible use of these particles for magnetic hyperthermia applications has been evaluated through specific loss power (SLP) measurements.

4.2 Experimental section

Materials and methods

Materials: Comercial reagents were used without further purification. Ferric chloride hexahydrate ($FeCl_3 \cdot 6H_2O$,$\geq$ 98%, Sigma Aldrich), polyvinylpyrrolidone (PVP40, Sigma Aldrich), sodium acetate trihydrate ($NaAc \cdot 3H_2O$, $\geq$ 99%, Sigma Aldrich), ethylene glycol (EG, $\geq$ 99.5 %, Fluka) and citric acid ($C_6H_8O_7$, $\geq$ 99.5%, Sigma Aldrich) were obtained and used without any further treatment.

Synthesis of nanoparticles: The synthesis of iron oxide nanoparticles has been based on a previous work described in the literature,[14] but the experimental procedure and the concentration of NaAc and PVP have been varied. Typically, 2.62 mmol $FeCl_3 \cdot 6H_2O$ were dissolved with ultrasound in 109 mL ethylene glycol. Then, 140 mmol PVP40 were added slowly under vigorously magnetic stirring ($>$ 1000 rpm) and mild heating until completely dissolved. Then, 15.8–36.5 mmol of $NaAc \cdot 3H_2O$ were added to the solution. The mixture was sealed in a Teflon-lined autoclave (125 mL) and maintained at 200 °C for 0.5 – 48 h for solvothermal crystallization, following cooling inside oven. The precipitated solid product was washed with ethanol and distilled water through centrifugation several times.

Surface coating: For citric acid coating a standard procedure was used.[8, 21] First, sample volume equivalent to 20 mg of Fe was adjusted to pH 2 and then dispersed in 13 mL of a solution of citric acid 0.1 M. Afterwards, the mixture was heated at 80 °C for 30 min. The solution was centrifuged and washed with distilled water. Finally the pH was adjusted first to 11 with KOH 1M and then to 7 with HNO_3 0.01 M.

Characterization: The particle sizes and morphologies were determined by transmission electron microscopy (TEM) with a JEM1010 microscope (JEOL, Peabody, USA) operating at 100 kV. Samples were prepared by placing a drop of the uncoated particles suspended in water onto a carbon coated copper grid and allowing it to dry at room temperature. The size distributions were determined by manual measurement of more than 100 particles using the public domain software ImageJ.

The crystal structure was identified by X-ray diffraction (XRD) performed on freeze-dried powders in an X'pert PRO diffractometer from Panalytical with a Johansson monochromator and using Cu K_α radiation (λ = 1.5406). The patterns were collected within a 2θ-range of 10° - 90° at a scan rate of 0.04° /min. The crystallite size, d_{XRD}, of the maghemite samples was determined by Scherrer's formula, using the (311) diffraction line.

The presence of the coating and the phase evolution was also confirmed by Fourier transform infrared spectroscopy (FTIR) in the range of 4000-250 cm^{-1} by use of a Bruker (USA) IFS 66VS. The samples for FTIR were prepared diluting the dried powder in KBr at 2% by weight and pressing it into a pellet. Colloidal properties were studied in a Zetasizer Nano S, from Malvern Instruments (UK). The hydrodynamic size, D_h, was determined by Dynamic Light Scattering (DLS) and the zeta potential was measured as a function of pH at 25 °C, using HNO_3 and KOH to change the pH of the suspensions. D_h is given as the intensity-weighted and number-weighted mean values to compare to the TEM mean

values.

For the magnetic characterization, the samples were measured in powder form after drying in an inox-coated oven at 50 °C. After accurately weighing a mass of $\approx$ 10 mg, the powder was filled into polycarbonate capsules and immobilized with cotton wool. Hysteresis loops were measured in a Vibrating Sample Magnetometer (MLVSM9, MagLab 9T, Oxford Instruments, UK) at 5 and 290 K in fields up to 4000 kA/m at a field change rate of 240 kA/(m·min) after saturating the sample in a 4000 kA/m field. AC susceptibility measurements were performed in a Quantum Design (USA) MPMS-XL SQUID magnetometer using the same capsules described above. Data was collected in the temperature range between 2 and 300 K using magnetic field amplitude of 326 A/m and frequency of 11 Hz. Additional measurements at 0.11 and 110 Hz were performed in selected samples.

In order to further elucidate the composition of the samples and their magnetic properties, ^{57}Fe Mössbauer spectra were obtained in transmission geometry on freeze-dried samples at 18, 80 and 295 K, using a constant acceleration spectrometer from Wissel GmbH and a flux-closed helium refrigerator from APD Cryogenics. Spectra have been fit using Lorentzian-shaped lines. Isomer shifts are given relative to that of α-Fe.

The evaluation of heat generation was determined by a commercial AC-field applicator (DM100, Nanoscale Biomagnetics, Spain). 1 ml of sample was placed in a closed container centered in the inductive coil and the AC-field was applied for 5 minutes. The applied field amplitude was H = 24 kA/m and the applied frequencies were 419, 542 and 710 kHz. The temperature of the sample was recorded by an optic fiber sensor incorporated in the equipment.

4.3 Results and discussion

Some relevant parameters were initially fixed to assure the formation of monodispersed colloids with particle sizes below 200 nm, which is a key issue to guarantee colloidal stability and to make this suspension potentially more suitable for biomedical applications.

The first parameter is the choice of polyol and especially its length, which has been shown to influence the size and the assembly of the magnetic cores.[22] In this work, ethylene glycol (EG) has been selected, as it is a short polyol that allows clustering such that multi-core particles can be obtained. Polyols with longer chains generally lead to single-core nanoparticles[4, 23] (depending on the rest of the reagents present in the reaction vessel). The second parameter is the addition of PVP, which has been shown to provide extra stability, since it acts as capping agent. The third parameter is the iron/PVP concentration, which determines the particle size. Polyol-based synthesis of iron (III) salts in an autoclave using polyols of short chain and stabilizers such as PVP or polyethylene glycol (PEG) usually leads to uniform particles of around 300 nm.[14, 24, 25] The use of a base, namely sodium hydroxide (NaOH)[25] or urea[26] has accounted for a further reduction of size. In this work, the iron/PVP concentration was fixed to achieve particles smaller than 200 nm.

Table 4.1: Sodium acetate optimization: Experimental conditions, TEM size distribution and XRD size of maghemite nanoparticles with different morphologies including single-core (SC), hollow spheres (HS) and nanoflowers (NF).

Sample	**[NaAc] (mmol)**	**Time(h)**	**d**$_{TEM}$ **(nm)**	**d**$_{XRD}$ **(nm)**
SC	36.5	16	35 ± 8	36.2 ± 0.1
HS	26.2	16	170 ± 30	27.4 ± 0.2
NF	15.8	16	63 ± 13	22.9 ± 0.2

This section is divided in three parts. First, the role of NaAc on the growth and assembly process is evaluated. Then, the formation mechanism of the nanoflowers is analysed. Last, four samples with different morphologies (different assembly configurations) and crystallite sizes are selected and functionalized with citric acid, such that they form stable magnetic colloids, and their different potential for magnetic hyperthermia treatments is evaluated.

The Role of Sodium Acetate on the Assembly Process:

The amount of NaAc·3H_2O was varied from 15.8 to 36.5 mmol (Table 4.1), while maintaining the rest of the reactants and conditions. Figure 4.1 shows the normalized log-normal size distributions of the samples, obtained by manual measurement of the particle diameter through Image J software and further data fitting using Origin software.

In all cases monodisperse systems with narrow size distributions were achieved thanks to the presence of PVP (the standard deviation was below 25%). Figure S1 shows the particles obtained in the absence of PVP with irregular morphology (means size of 200 nm and standard deviation of 48%). We found that the variation of NaAc concentration leads to nanoparticles with distinctly different structures (Figure 4.1). The highest concentration of NaAc (36.5 mmol) produced single-core nanoparticles of 35 nm (sample SC, Figure 4.1 a).

These particles appear under the TEM randomly distributed and somewhat aggregated (possibly as a consequence of their magnetic character and the drying process on the TEM grid), but no specific assembly of the single-core particles was observed. However, when decreasing the NaAc concentration to 26.2 mmol, spherical hollow multi-core nanoparticles about 170 nm in diameter were formed (sample HS, Figure 4.1 b). TEM images reveals lower material density in the inner part which is attributed to hollow structure.[14] Figure S2 further supports the existence of voids within the spheres (again due to contrast between the darker edges of the particle and the brighter centers). The lowest amount of NaAc (15.8 mmol) yielded multi-core particles with flower-like structure (sample NF, Figure 4.1 c). In this case, the cores ($<$ 20 nm) are densely packed forming a nanoflower particle with a characteristic size of $\sim$ 60 nm.

Figure 4.2 shows the XRD patterns of samples SC, HS and NF, which correspond to a ferrite spinel structure attributed to γ-Fe_2O_3 (JCPDS # 110614). An increase in the broadening of the Bragg peaks,

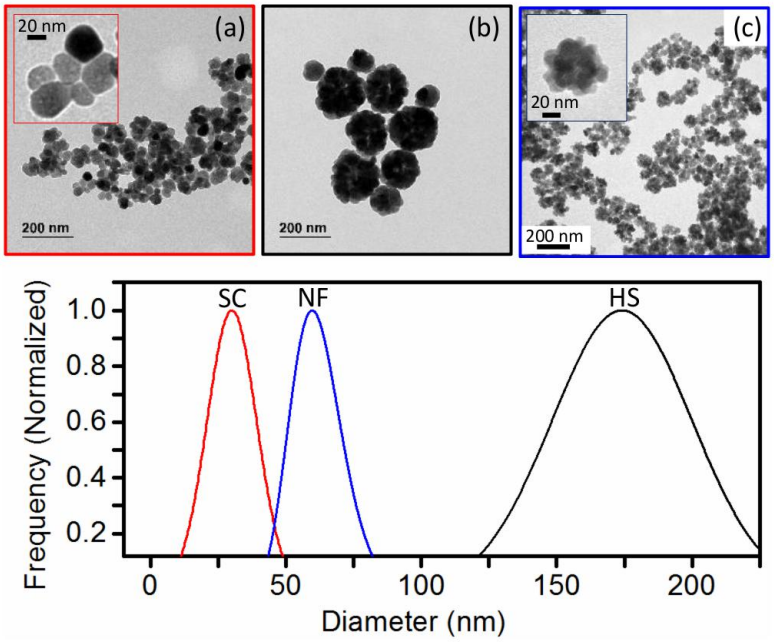

Figure 4.1: TEM images of the different structures obtained when varying the NaAc amount: (a) Single-core particles (SC), 36.5 mmol, (b) hollow spheres (HS), 26.2 mmol, (c) nanoflowers (NF), 15.8 mmol. Below, normalized log-normal TEM size distributions of the samples.

which indicates a decreasing crystallite size, is observed from SC, to HS, and again to NF. The crystal sizes d_{XRD} (Table 4.1) determined by Scherrer's equation agrees well with d_{TEM} in the case of single-core particles (SC) (d_{XRD} = 36 nm), but in case of NF and HS, d_{XRD} is significantly smaller d_{TEM}. This discrepancy reflects the multi-core nature of these samples.[19] From TEM and XRD, it is clear that decreasing the amount of NaAc leads to more densely packed assemblies with smaller core sizes.

Figure 4.3 shows the field dependence of magnetisation of the three different particle morphologies: SC, HS and NF, at 290 K and 5 K. The insets in Figure 4.3 show the hysteresis loops in the low field regime, and Table 4.2 summarizes the saturation magnetization (M_s), initial mass susceptibility at low fields (χ_0), squareness (M_r/M_s ratio) and coercivity (H_C). Please, note that M_s obtained in this work is formally the magnetic moment per unit mass (the volume magnetization is divided by the samples mass, which is equal to the density. This is generally termed as the specific magnetization, σ) and that χ_0 is calculated through the numerical field derivative of M. The samples have M_s values between 80–90 Am^2/kg at room temperature and go up to 100 Am^2/kg at 5 K. As with XRD, saturation magnetisation is larger for sample SC, than samples HS and NF. Enlargement of the low field sections of the curves are shown in the insets, in order to get a more accurate view of hysteresis effects.

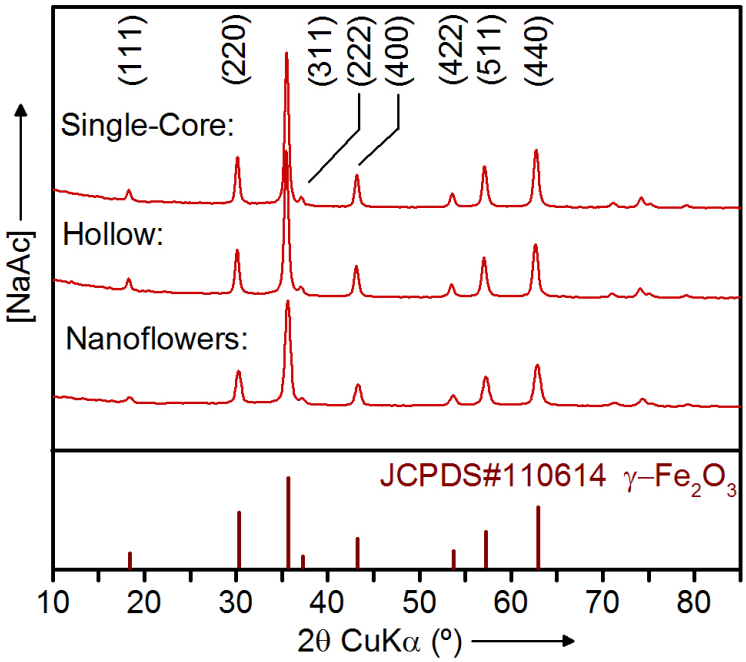

Figure 4.2: X-ray diffractogram of single-core particles (SC), hollow spheres (HS) and nanoflowers (NF).

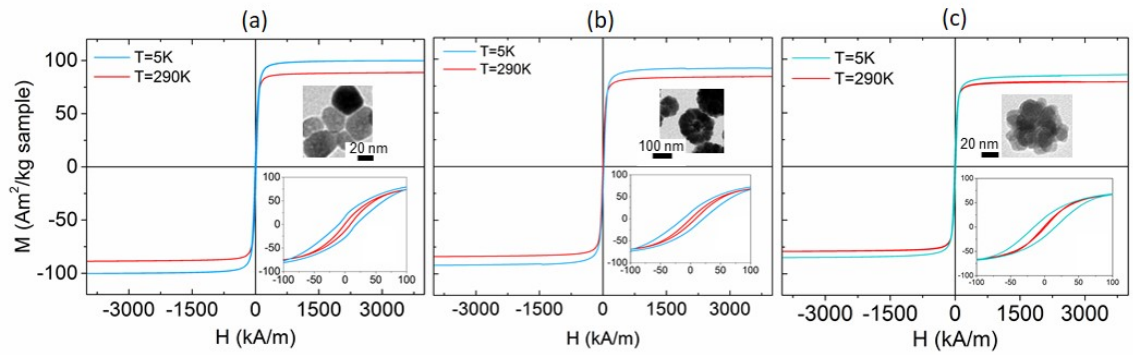

Figure 4.3: Magnetization curves for single-core particles (SC) (a), hollow spheres (HS) (b) and nanoflowers (NF) (c) at 5 and 290 K.

Samples SC and HS show larger coercivity values of 4.5 and 4 kA/m, respectively, at 290 K, in contrast to sample NF that shows nearly zero coercivity and remanence at 290 K. All samples, regardless of their structure, have coercivity values between 14 and 17 kA/m at low temperature, which is of the same order of magnitude that the coercivity reported for magnetite-maghemite nanoparticles with

Table 4.2: Hysteresis parameters at room temperature and 5 K for samples SC, HS, and NF.

Sample	RT			5 K		
	M_s	H_C	χ_0	M_s	M_r/M_s	H_C
	(Am^2/kg)	(kA/m)	(m^3/kg)	(Am^2/kg)		(kA/m)
SC	90.2 ± 0.1	4	1.70 ± 0.02	100.3 ± 0.1	0.23 ± 0.1	14
HS	84.3 ± 0.1	4	1.31 ± 0.01	92.5 ± 0.1	0.21 ± 0.1	17
NF	79.7 ± 0.1	1	1.60 ± 0.02	85.5 ± 0.1	0.22 ± 0.1	16

only magnetocrystalline anisotropy.[27] Also, the initial mass susceptibility (1.31–1.70 m^3/kg) at room temperature and the low squareness ratio (0.21–0.23) at 5 K are comparable for the three materials.

The above results show the fundamental role of NaAc in this synthesis route, since it directly defines the core size and morphology of the samples, and in turn leads to nanoparticles with different magnetic behavior. The reason underlies in the chemical process taking place. It is known that both NaAc and water need to be present in the reaction to modify the reduction potential of the polyol, that otherwise is not able to reduce the iron reactants.[28] Moreover, its concentration defines the self-assembly process. Thus, for the highest acetate concentration (0.3 M), massive nucleation and uniform growth by diffusion takes place, resulting in single-core particles. When the amount of acetate is reduced ($\sim$ 0.25 M), the initial nuclei seem to grow by partial aggregation in hollow spheres.

Other studies have reported the formation of similar hollow spheres by dissolution of inner small cores and growth of the larger ones on the surface by Ostwald ripening process.[14] Further reduction in acetate ($<$ 0.2 M) leads to smaller nuclei that strongly aggregate to produce the final flower-like particles. In absence of NaAc, no precipitation occurred, as previously reported.[29]

Formation Mechanism of Multi-Core Nanoflowers:

In order to study the formation mechanism and magnetic properties of multi-core nanoflowers, the NaAc concentration (15.8 mmol) was fixed and the heating time was varied from 0.5 to 48 h. All NF samples are named according to their heating time (measured in hours). For this series of samples,

NF–16 is equivalent to sample NF studied above. First, electron microscopy was used to study the evolution of nanoflower formation. Figure 4.4 shows the as-synthesized product at the different reaction times. At short reaction times ($<$ 30 min), a reddish colloidal suspension is observed, consisting of primary nuclei of 2-3 nm unstable under the TEM electron beam. After 1.8 h, there is a reddish-brown precipitate, which corresponds with nuclei that rarely approach and form aggregates poorly defined (as distinctly observed in the inset image of Figure 4.4). After 2 h of aging time, the primary nuclei seem to be transformed into a material with a laminar habit (sheets that have lower contrast than the nanoflowers) and the first nanoflowers (60 nm in size) are observed. The laminar phase disappears

Table 4.3: TEM and XRD sizes during the formation of nanoflower particles. For all these syntheses, [NaAc] was kept at 15.8 mmol.

Sample	Time (h)	d_{TEM} (nm)	d_{XRD} (nm)
NF-0.5	0.5	-	-
NF-1	1	-	-
NF-1.8	1.8	-	-
NF-2	2	60 ± 11	11.3 ± 0.3
NF-4	4	56 ± 13	14.8 ± 0.3
NF-8	8	61 ± 16	19.2 ± 0.2
NF-16	16	63 ± 13	22.9 ± 0.2
NF-48	48	58 ± 11	23.7 ± 0.2

after 4 h. The nanoflower size is preserved ($d_{XRD} \approx 60$ nm) between 2 and 48 h, see Table 4.3, but a clear increase of the core size is observed over time.

Thus, TEM images reveal two different stages in the mechanism of flower formation. The first one is an initial stage ($<$ 2 h of heating time) where several intermediate phases may coexist. The second one (2-48 h) comprises the growth of the cores within a nanoflower, which does not change in its total size ($\approx$ 60 nm). Figure S3 shows the histograms obtained from TEM measurements of the nanoflower sizes. This data was fitted to a log-normal size distribution (Figure S4) and it seems that the size distribution gets narrower after longer periods of heating time. This is in good agreement with a two-stage mechanism of nanoparticle formation by self-assembly of diffusing aggregating nanocrystalline subunits, which are in turn formed by burst nucleation in a supersaturated solution, followed by coarsening.[30] A detailed analysis of both stages is provided in the following sections.

Initial stages of the flower formation ($<$ 2 h):

In order to identify the different phases that appear during these initial stages, the composition of samples NF-0.5-2 were evaluated by XRD (Table 4.3). For all these syntheses, [NaAc] was kept at 15.8 mmol. Figure 4.5 shows the X-ray diffraction pattern of the NF samples. At t = 0.5 h, the pattern clearly matches that of lepidocrocite (γ-FeOOH) (2-θ angles of 27, 36, 47 and 60°). A different pattern is observed at 1 and 1.8 h reaction time. These patterns do not correspond with any of the well-known iron oxide or oxyhydroxide phases.

As the patterns are quite distinct we speculate that they may represent the formation of an unknown intermediate phase. At 2 h of reaction time, most of the XRD peaks can be indexed to maghemite (γ-$Fe_2 2O_3$), whose typical XRD profile is shown in red below the diffractograms). Additionally, there are two small and narrow peaks (at 24.6° and 47.2°) that reveal some remain of the intermediated phase (in correspondence with the observations by TEM). Figure S5 shows the XRD patters of those samples collected after 6 months of storage. It is noteworthy that while sample NF-0.5 is unstable and tends to evolve to ferroxyhyte (FeOOH JCPDS#220353) and that the unknown intermediate phase (NF–1 and

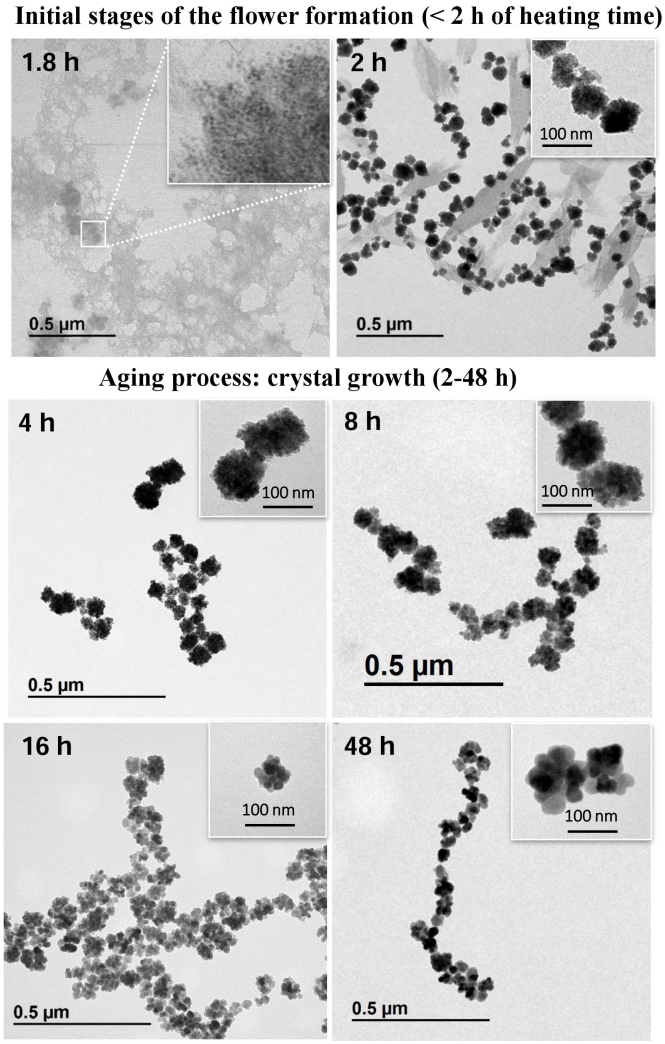

Figure 4.4: TEM images of NF samples prepared with 15.8 mmol of NaAc at different reaction times: 1.8, 2, 4, 8, 16 and 48 h. Insets show a detailed image of a single nanoflower.

NF–1.8) remains stable after 6 months.

Figure 4.6 shows the Mössbauer spectra of NF powders in the initial stages, t = 0.5–2 h. The spectra of all four samples are magnetically split at 18 K and have been fitted with 2 or 3 sextets with an isomer shift, δ, around 0.50 mm/s, indicating that the samples consist of ferric phases. At 80 K and room temperature, doublets dominate the spectra. Again, the isomer shift of the doublets ($\sim$ 0.45 mm/s at 80 K and $\sim$ 0.37 mm/s at room temperature) as well as their quadrupole splittings ($\varepsilon \sim$ 0.6 mm/s), indicate

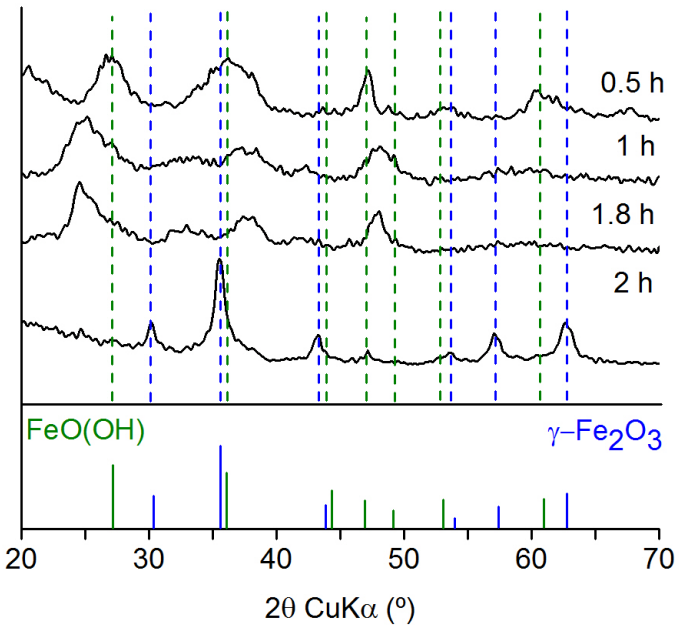

Figure 4.5: Formation mechanism of nanoflowers followed by X-ray diffraction of the powders collected after 0.5, 1, 1.8 and 2 h of aging time. Expected peak positions of lepidocrocite (γ-FeOOH, green) and maghemite (γ-Fe_2O_3, blue) are shown.

only ferric phases in all four powder samples.

The spectrum of NF–0.5 obtained at 18 K has been fitted with 3 sextets. The most dominating sextet (shown in dark blue color) has broad lines, a hyperfine field, B_{hf}, around 45 T, and ε around 0.0 mm/s. This sextet is most likely due to the presence of lepidocrocite, in agreement with the XRD and TEM results. The Néel temperature of lepidocrocite is 77 K,[31] but there appears to be quite a lot of magnetic relaxation of lepidocrocite already at low temperature, indicated by the broad lines and the blue sextet with lower hyperfine field. At 80 K and room temperature, lepidocrocite is paramagnetic and hence seen as a doublet. The third sextet (orange) in the spectrum of sample NF–0.5 has sharp lines, a hyperfine field B_{hf} of $\sim$50.6 T and a quadrupole shift, ε, of -0.13 mm/s. The hyperfine parameters of this component match those of goethite, although this (probably nanocrystalline) phase was not detected by X-ray. At 80 K a ferric (goethite) sextet (B_{hf} = 48.0 T, ε = 0.12 mm/s) with broad lines remains, while the room temperature spectrum features no goethite sextet, presumably due to superparamagnetic relaxation.This goethite component occupies about 7 % of the spectral area of NF–0.5 and is not seen in the other samples.

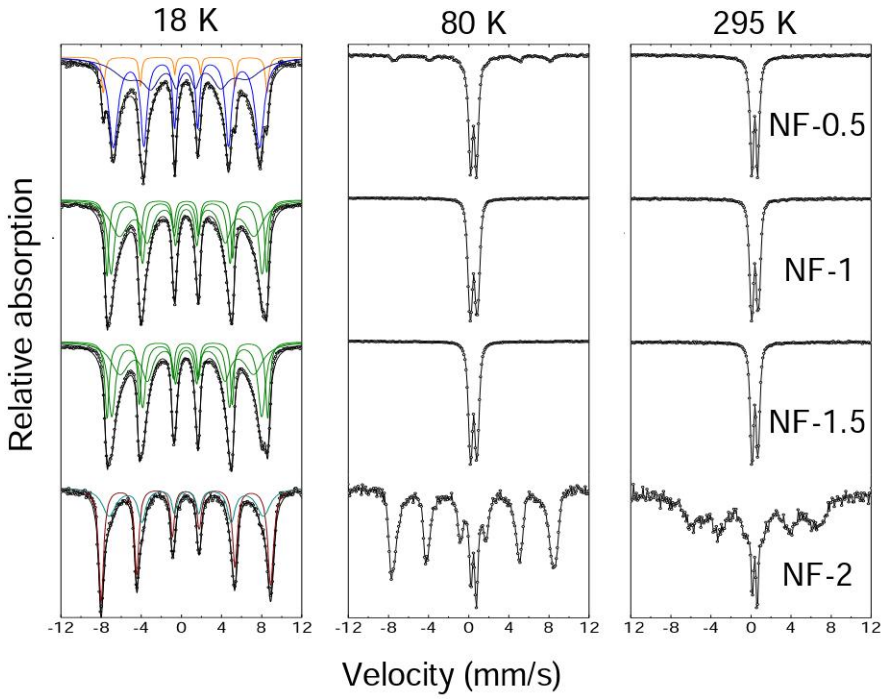

Figure 4.6: Formation mechanism of nanoflowers followed by Mössbauer spectroscopy at 18, 80 and 295 K for samples collected after 0.5, 1, 1.5 and 2 h of aging time.

The Mössbauer spectra of NF-1 and NF–1.5 are very similar to each other (in agreement with the XRD patterns of NF-1 and NF-1.8). These Mossbauer spectra, where the outer sextets have $B_{hf} \sim$ 46.2-49.6 T, $\delta \sim$ 0.5 mm/s, $\varepsilon \sim$ 0.0 mm/s, could be assigned to ferrihydrite, or magnetically relaxing maghemite, but such assignment does not match the XRD patterns, whose main peaks are not found to match an existing phase (explicitly not ferrihydrite or maghemite).

The Mössbauer parameters match well with a (new) undescribed intemediate phase in-between that of lepidocrocite and maghemite, i.e. a phase that is dehydroxylated lepidocrocite (or “maghemite with hydroxylgroups”). Mössbauer spectra obtained at 80 K in an applied field of 0.5 T show no magnetic splitting, indicating that this phase is paramagnetic at 80 K. Recent studies have shown the presence of new intermediate phases that occur during the transformation between iron oxides/oxyhydroxides that may not be stable enough to be easily characterised. For example, an intermediate phase has been identified in the transformation between 2-line ferrihydrite and hematite, which was termed as “hydromaghemite” or “ferriferrihydrite”.[32] Although this phase has similar B_{hf} and δ values to the intermediate phase observed in this work, the X-ray patterns do not mach, which means that we have captured a different “intermediate” phase.

The 18 K spectrum of NF-2 is dominated by a maghemite sextet (shown in wine red) with B_{hf} =52.6.0 T, ε = 0.01 mm/s, $\delta \sim$ 0.5 mm/s. The asymmetry of this sextet (between lines 1 and 6) and its isomer shift strongly indicate that it is ferric, i.e. almost pure maghemite. At 80 K, part of the spectrum ($\sim$ 20 %) is relaxed into a doublet, but the majority of the spectrum is a sextet with relatively sharp lines. Measurements obtained within an applied field (data not shown), show that the relaxed part is paramagnetic, i.e presumably due to the lepidocrocite or the "intermediate" phase. At room temperature, the sextet contribution remains most of its spectral area but has very broad lines. From this relaxation behavior, a mixture of phases is assumed (in agreement with XRD), i.e. part of the sample is paramagnetic already at 80 K (lepidocrocite), while the remaining part of the sample (maghemite) show slow relaxation even at room temperature.

Figure 4.7 shows the AC magnetic measurements performed in the primary stages of the reaction, in order to follow the particle formation, especially at the initial stage of 0.5 h where sample is unstable under the TEM beam. For NF-0.5, the in-phase susceptibility presents Curie-like behaviour down to 25 K, with a magnetic effective moment of about 2.6 μB (Bohr magnetons), calculated by assuming, e.g., the formula of lepidocrocite. The deviation of the in-phase susceptibility from the Curie law behaviour at low temperatures, together with the rise of the out-of-phase component suggests that magnetic blocking of very small nanoparticles takes place below $\sim$ 20 K.

For NF-1.8, the maximum of the in-phase component together with the out-of-phase component step at $\sim$ 150 K indicates magnetic blocking of nanoparticles up to this temperature. The location of these maxima, which are at higher temperatures than in the case of NF–0.5 h, indicates the growth of the nanoparticles at these early stages. Given that at this temperature lepidocrocite (and the "intermediate" phase of NF–1 and NF–1.5 should be paramagnetic, this feature may be caused by particles with considerable magnetisation, possibly being made of the undescribed intermediate phase in its advance stage (1.8 h).

For NF–2, the appearance of both components of the AC susceptibility is typical of particles magnetically blocked well above room temperature, displaying susceptibility maxima at temperatures above the measured range, in agreement with the observation of maghemite flowers (60 nm) by TEM.

The results of TEM, XRD, MMössbauer spectroscopy and AC susceptibility support that, prior to formation of maghemite nanoflowers, lepidocrocite with laminar habit is formed which transforms to maghemite through an intermediate phase, probably dehydroxylated lepidocrocite. Consequently, the formation mechanism can occur as follows at this initial stage:

$$COO^- + H_2O \longrightarrow CH_3COOH + OH^- \tag{4.1}$$

$$Fe^{3+} + 3OH^- \longrightarrow Fe(OH)_3 \tag{4.2}$$

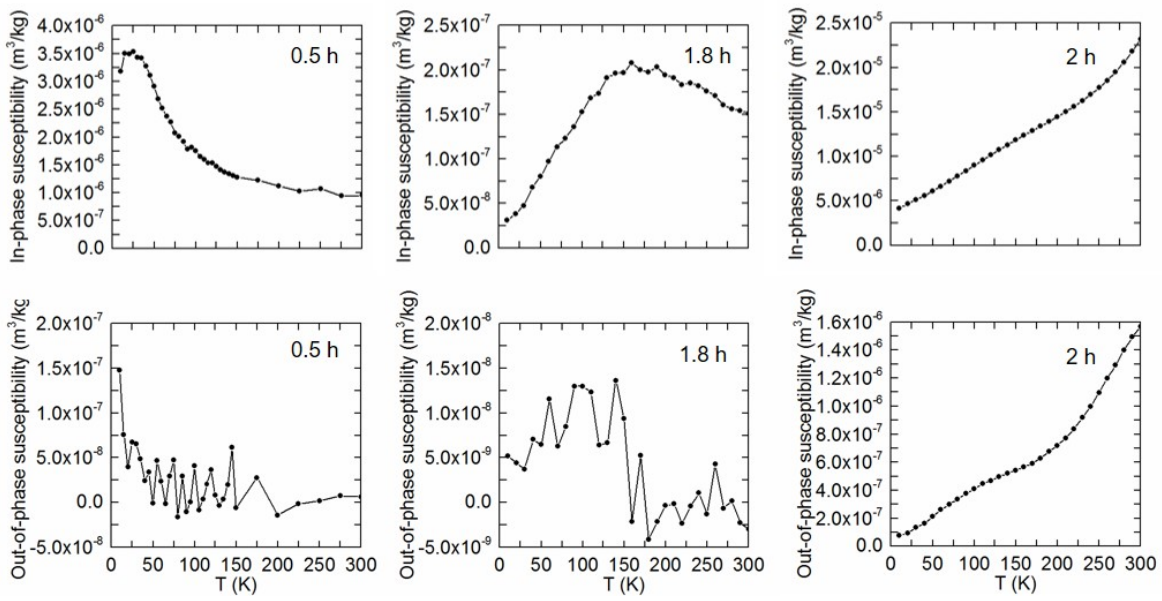

Figure 4.7: Temperature dependence of the low field mass AC susceptibility at 11 Hz, for the initial stages (heating times 0.5, 1.45 and 2 hours) of the nanoflower formation. Please, note the different susceptibility scales in each plot.

$$2Fe(OH)_3 \longrightarrow \gamma - FeOOH + H_2O \tag{4.3}$$

$$CH_2OH - CH_2OH \longrightarrow CH_2OH - CHO + H_2O \tag{4.4}$$

First, NaAc causes a weak hydrolyzation (Equation 4.1), which controls the release rate of OH^-. It has been reported that iron ions could coordinate to the acetate anion (CH_3COO^-) forming a coordination compound that could evolve to magnetite directly in the presence of EG that is oxidized to glycolaldehyde (Equation 4.4), a reductant capable of reducing most noble metal ions.[33] However, in our case, since lepidocrocite and dehydroxylated lepidocrocite have been suggested through XRD and Mössbauer spectroscopy as intermediate phases (samples NF-0.5, 1 and 1.8), we propose that the mechanism follows a sol-gel reaction, where the initial γ-FeOOH nuclei are formed thanks to the sodium acetate releasing OH^- (Equations 4.2-4.3).The high temperatures, pressure and the action of sodium acetate allows the formation of lepidocrocite by a burst type nucleation,[34, 35] which in this case seems to occur rapidly (< 0.5 h). After nucleation, there is phase transformation (via dehydrolyzation) and aggregation leading to maghemite nanoflowers with a fixed size.

To figure out whether the immediate product is magnetite or maghemite is by no means a trivial is-

sue. On the one hand, a reduction process (Equation 4.4) can occur during the solvent mediated transformation to magnetite[2]), which is easily oxidized maghemite. On the other hand, it has been demonstrated by Navrotsky et al.[36] that a direct size driven transformation of lepidrocrocite to maghemite is thermodinamically possible . Our results seem to support the thermodynamic considerations stated by Navrotsky and we conclude that this oxy-hydroxide transforms directly to maghemite,[37] but we could not exclude the initial presence of small amounts of Fe^{+2} in our samples that will remain undetectable by further oxidation during the characterisation process.

Aging process: crystal growth (2 - 48 h):

Once the maghemite nanoflowers have formed, after 2 h of reaction time, an aging process starts. This process has been studied through TEM, XRD and magnetic measurements. Figure 4.8 a shows the XRD patterns collected for NF-2-48. After 4 h, only maghemite is detected. The diffraction peaks become narrower throughout the aging process and the crystal size obtained from the width of the diffraction peaks by use of the Scherrer's formula show that the nanoflowers undertake a crystallization process, increasing its mean crystal size d_{XRD} from 11 to 23 nm (Figure 4.8 b). Similar trend is observed by TEM, where the cores of the particles are seen to grow over time (Figure 4.8 c). Throughout time the organic content of the samples is reduced, as seen in the thermogravimetric analyses (TGA) in Figure S7), from 12 to 4%.

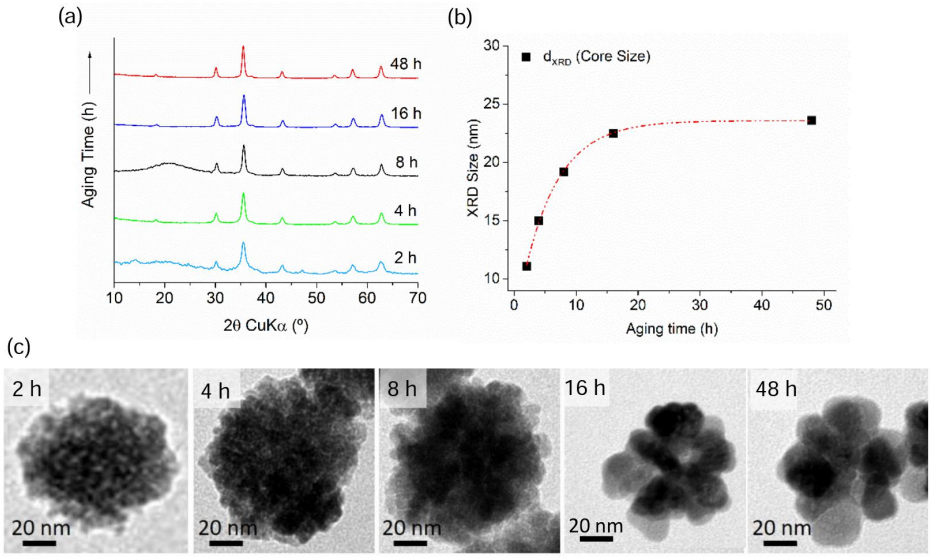

Figure 4.8: Structure of the NF along at t = 2-48 h: (a) XRD patters. (b) Crystallite size calculated by Scherrer's equation. (d) Representative TEM images of the growing cores.

Figure 4.9a illustrates the whole progress of formation mechanism and crystallization of NF samples, which can be linked to Equations 4.1-4.4, where laminar lepidocrocite is formed and then transformed to maghemite nanoflowers. The magnetic properties of the flowers during the aging steps 2-48 h were evaluated in detail (Figure 4.9 b-e). By prolonging the aging time (4, 8, 16 and 48 h), the nanoflowers saturation magnetization is increased from 48 to 90 Am^2/kg at 290 K (Figure 4.9 b), which implies quite a significant enhancement. The samples also show increasing coercivity values ($\sim$ 0.5-2 kA/m at RT and 8-19 kA/m at 5 K) with aging. The initial mass susceptibility at low fields (χ_0) was calculated for all samples through DC magnetometry from the numerical field derivative of the magnetization (Figure 4.9 c) (as χ_0 calculated in Table 4.2). Samples NF-4, NF–8 and NF–48 have χ0 values of 2.3–2.5 m3/kg, which is higher than SC and HS nanoparticles (χ_0 for these samples is 1.7 and 1.35 m^3/kg, respectively). This enhancement on the magnetic susceptibility has been previously linked to a magnetic cooperative effect due to aggregation of cores forming densely packed nanoflowers.[12] The magnetic behaviour of the progressively aged nanoflowers has also been investigated by means of AC susceptibility (see Figure 4.9 d-e).

The results can be interpreted by considering three contributions: i) a positive in-phase susceptibility level at room temperature due to the presence of rather large magnetic entities with permanent magnetism, ii) a wide and rounded out-of-phase maximum very likely indicating the blocking of magnetic entities of intermediate size and iii) a low temperature step in the in-phase component accompanied by a rather sharp peak in the out-of-phase below $\sim$ 50 K. The major contribution corresponds to the particles magnetically blocked well above room temperature, already detected in sample NF-2, although from t=4 h up to t=48 h the magnitude of the resulting in-phase susceptibility is significantly higher since paramagnetic lepidocrocite dissolves in favour of other strongly magnetic phases. These samples present much higher signal per mass of sample than NF–2 (Figure 4.7) in agreement with the disappearance of the lepidocrocite or the intermediate phases observed by TEM and XRD at the longest reaction times.

For NF-4, NF-8 and NF-48, the magnitude of the room temperature in-phase component decreases for increasing aging time. This result well agrees with the field derivative of magnetization shown in Figure 4.9 c. We believe this value mostly results from the contribution of the large magnetic entities. The magnetic dynamics of the lower temperature anomalies have been investigated to interpret their nature (detailed discussion, Figure S8 and Table S1 from the Supporting Information). The relative sharpness of the lowest temperature peaks, their pre-exponential factors of the Arrhenius law, their regular dependence with the aging time, and the occurrence also in iron oxide nanoparticles prepared by completely different methods[38, 39] point to some phenomenon intrinsic to maghemite or to some usually appearing intermediate phase, although no rigorous interpretation of this phenomenon can be offered yet. In summary, the analysis of the samples with longest reaction times indicates that lepidocrocite and the “undescribed” intermediate phase have disappeared. Interestingly, increasing reaction times give rise to a significant increase of the core sizes but not of the flower size.

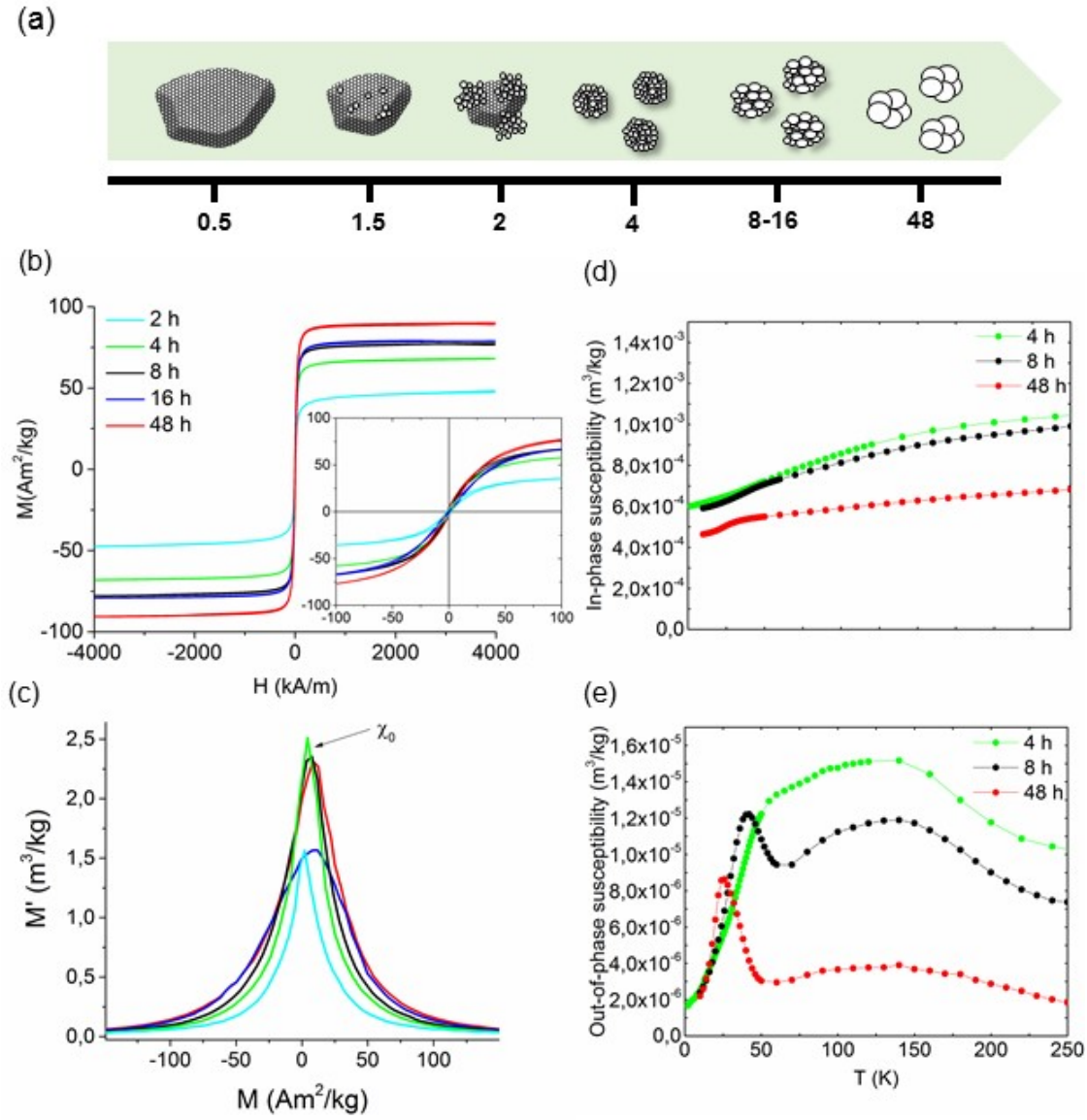

Figure 4.9: Formation mechanism of maghemite nanoflowers: (a) Sketch of particle evolution thoughout the aging process. (b) DC magnetization curves at 290 K of samples NF-2-48, (c) mass initial susceptibility (χ_0) of samples NF–2–48 and (d-e) Temperature dependence of the low field AC susceptibility at 11 Hz, along the formation of nanoflowers at 4, 8 and 48 hours of aging time.

Biomedical Applications:

We here evaluate aspects relevant for biomedical applicability (especially colloidal stability and heating potential for magnetic hyperthermia) of four selected samples: SC, HS and NF–4 and NF–48, as these

Table 4.4: Colloidal properties of maghemite nanoparticles with the different morphologies: Single-core (SC), hollow spheres (HS) and nanoflowers at different aging time (NF-4 and NF-28) coated with citric acid (CIT).

	As-synthesized			**Citric acid coating**		
Sample	D_h (nm)	PdI	IEP	D_h (nm)	PdI	IEP
SC-CIT	896	0.28	5.5	161	0.26	5.0
HS-CIT	705	0.31	5.7	298	0.25	5.1
NF-4-CIT	331	0.27	6.6	109	0.14	4.9
NF-48-CIT	965	0.23	6.0	102	0.11	4.0

samples represent distinct different morphologies (tuned by the NaAc concentration) and hold different core sizes. The surface charge and the colloidal stability of samples SC, HS, NF-4 and NF-48 were enhanced by citric acid coating. Infrared spectroscopy confirms the successful citric acid coating from the absorption bands typical of the carboxyl at 1384 and 1022 cm^{-1} (Figure S6 of SI).

The hydrodynamic size (D_h), polydispersity index (PdI) and isoelectric point (IEP) of as-synthesized and coated particles are summarized in Table 4.4. The hydrodynamic sizes are smaller for the coated samples than for the as-synthesized particles due to an increase in the surface charge, as the shift of the IEP to lower pHs confirms (the NPs have increased surface charge at pH 7). Figure 4.10 a shows the change in hydrodynamic size after the coating for sample NF–4. Dh for NF–4 changes from a polydisperse distribution to a narrow monomodal distribution centered at $\sim$100 nm after the coating, which is closer to the average particle size determined by TEM (Table 4.1). Furthermore, number-weighted D_h values for NF samples (50–70 nm) do approach d_{TEM}, as this is number weighted. Similarly, a change to a more well-dispersed system is also seen for sample NF-48 when coated with citric acid. For samples SC and HS the hydrodynamic size after coating is 161 and 298 nm, respectively, which is much larger than d_{TEM} for sample SC and relatively larger than d_{TEM} for sample HS suggesting a certain degree of agglomeration of the particles in suspension.

Figure 4.10 b shows the measured zeta potential curve for sample NF-4. The citric acid coating promotes the stabilization by repulsive forces,[40] since there is an increase of the surface charge from -10 mV up to -40 mV at pH 7, assuring long-term stability at physiological pH. We observe a similar increase of surface charge for samples SC, HS and NF–48. Moreover, there is, for all samples, a shift of the isoelectric point (zero zeta potential) to lower pH values that confirms the successful coating with carboxyl groups for sample NF–4. This shift is larger in the nanoflowers, probably due to the higher surface-to-volume ratio in comparison with the single-core particles (SC) and the hollow spheres (HS).

The heating capacity of the coated materials in water at physiological pH was evaluated in order to study the differences in terms of sample morphology and crystallinity. Therefore, MNPs are placed in the centre of a coil that produces an AMF, the magnetic NPs absorb energy from the field which is

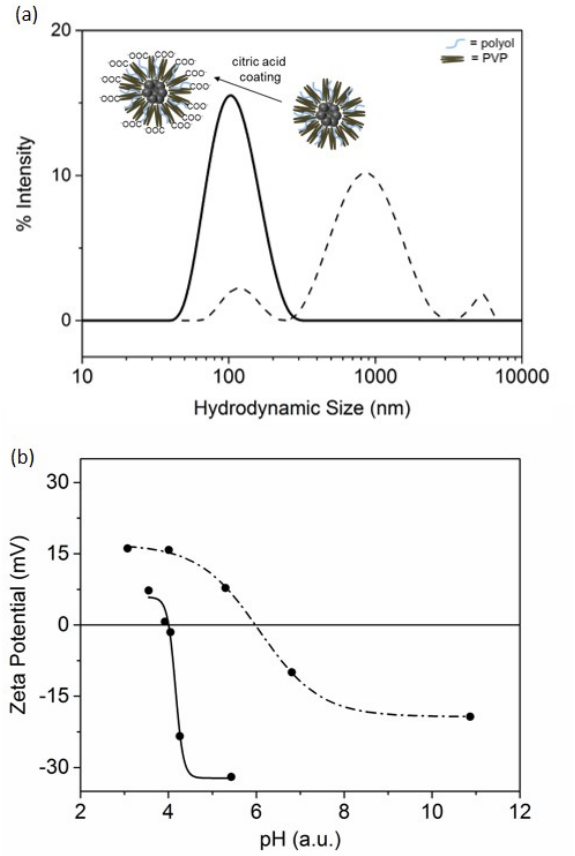

Figure 4.10: Effect of the citric acid coating on sample NF–4: (a) DLS measurement and inset scheme of the coating and (b) Zeta Potential curves fitted to a Boltzmann sigmoidal function. Dashed line connects data points for as-synthesized sample. Continuous line connects data points for citric acid coating.

subsequently transformed into heat. The specific loss power is found as:

$$SLP(W/g_{Fe}) = c\frac{Mass_{Sample}}{Mass_{Fe}}\frac{\Delta T}{\Delta t} \tag{4.5}$$

where c is the capacity of the suspension (typically assumed to be the heat capacity of the suspension medium for low concentrations of MNPs).[41]

Figure 4.11 shows the different specific loss power (SLP) values calculated through “the slope method” (change of temperature over time ΔT/Δt) for different frequencies: 419, 542 and 710 KHz, for samples SC, HS, NF–4 and NF–48. Nanoflowers with a core size of 23 nm (NF–48) have the highest SLP values e.g. yielding 1131.2 W/g Fe for a frequency of 710 KHz. This sample displays SLP

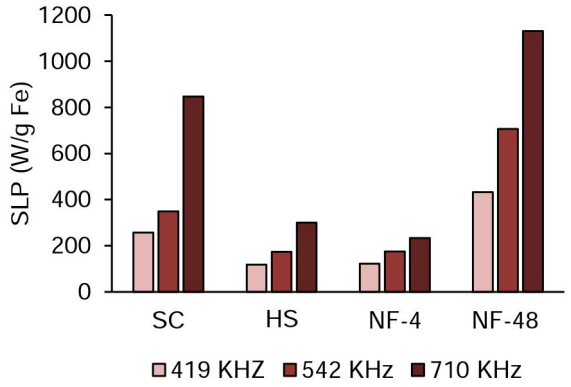

Figure 4.11: SLP values of samples SC, HS, NF-4 and NF-48. SLP values of different samples calculated by the "slope method". Field amplitud was 23.8 kA/m and three different frequencies were applied: 419, 542 and 710 KHz.

values nearly 5 times larger than nanoflowers with crystal size of 15 nm (NF–4), nearly 4 times larger than hollow spheres and 1.5 times larger than single-core nanoparticles, although these two latter samples (HS and SC) have bigger core sizes of 27 and 36 nm, respectively. This demonstrates that both core sizes and the packing of the cores have decisive influence on the heating capacity. Specifically, we observe that nanoflowers with large cores (controlled by annealing) and densely packed cores (tuned by NaAc concentration) offer enhanced heating capacity compared with nanoflowers with smaller crystallite sizes, hollow spheres, and single-core nanoparticles used in this work.

Given the heterogeneity in the conditions (field and frequency) used to measure SLP by different research groups, and the multiple possibilities of the materials characterized (with different particle size, shape, structure (single-core or multi-core), crystalline structure, composition, etc.), it is complicated to find the most appropriate examples in the literature to compare our data. For example, 30 nm single-core magnetite nanoparticles, obtained by $FeSO_4$ precipitation and subsequent ageing had a SLP value of 95 W/g (field amplitude 10 kA/m and frequency of 249 kHz).[42] Our SC sample, with similar particle size, presents a higher SLP value (257 W/g) with the lowest amplitude and frequency (22.8 kA/m and 419 kHz, respectively), however, the measurement conditions are not exactly the same. Regarding hollow structures, liposomes (120 nm) encapsulating magnetite particles (10 nm core size) presented a SLP value of 210 W/g.[15] With the same conditions, sample HS has a similar SLP value of 301 W/g, although the core size and the particle size are not exactly the same. In the frame of multi-core structures, materials obtained by coprecipitation of ferric and ferrous chloride in a microwave, with crystal size of 13 nm and hydrodynamic sizes of 123 nm, similar to sample NF–4, had a SLP value of 190 W/g (field amplitude 10.5 kA/m and frequency of 950 kHz).[43] These values are similar to the

ones obtained for sample NF-4 at the most similar conditions measured in our case (232 W/g with field amplitude 24 kA/m and frequency of 700 kHz). Measurements in the same field and frequency conditions for a material similar to sample NF-48 (magnetite nanoflowers of 22 nm obtained by the polyol-mediated synthesis) yielded similar SLP data (1130 W/g for NF-48 and 1180 W/g for the 22 nm nanoflowers).

The obtained SLP data for our materials envisages a possible use for magnetic fluid hyperthermia treatment of cancer, however, the lack of standardized measurement conditions makes complicated to compare the data with other existing materials. The intrinsic loss power (ILP) of the samples was calculated from Equation 4.6

$$ILP = \frac{SAR}{H^2 f} \tag{4.6}$$

It ranges from 0.5–0.6 (in the case of samples NF–4 and HS, respectively), 1.9 (sample SC) up to 2.6 (sample NF–48). Lastly, it must be noted that the product of H·f was kept for all combinations below 4.85 x 10^8 kA/m·s, which is mandatory for avoiding nonspecific eddy heating in tissues.[44]

4.4 Conclusions

The polyol-mediated synthesis has been explored and developed for the preparation of well-controlled magnetic nanoparticles with different core size and arrangement to form the final single-core and multi-core particles. The particles are formed by burst nucleation and growth processes that determine the final nanostructure going from single-core to hollow spheres and nanoflowers, with high crystallinity, due to the selected polyol synthesis route that uses high temperature over long periods of times.

Sodium acetate is found to be a key parameter governing the self-assembly process. In this reaction, it has a double role: the particle formation, and the nucleation and growth. For higher acetate concentration, massive nucleation and growth by diffusion takes place, resulting in single-core particles. As the amount of acetate is reduced, the initial nanocrystalline subunits seem to grow by partial aggregation in hollow spheres. Further reduction in acetate leads to initial nanocrystalline nuclei that strongly aggregate to produce the final flower-like particles.

The synthesis of magnetic nanoflowers occurs via burst nucleation, growth by aggregation and recrystallization that takes place over time. The initial stages of the reaction are composed of lepidocrocite, which suffers a fast dehydroxylation, transforming to an intermediate “undescribed” phase – possibly a partly dehydroxylated lepidocrocite – that evolves to maghemite nanoflowers. A prolonged heating of the flowers leads to nanoflower particles with larger cores with interesting magnetic and colloidal properties and consequently high heating capacities, being sample NF-48 the one that displays the highest ILP value.

In the future, the transferred energy from an exciting magnetic field to nanoparticles, leading to a

dissipation of heat in targeted bodies such as tumors, is likely to be explored much further. Taking advantage of this physical phenomenon, magnetic nanoparticles are by many also considered as potential chemotherapy and radiotherapy enhancement agents, where a limited heat dissipation dose increases the effectiveness in cell destruction. Our studies have outlined possible ways to control the formation of distinct structures via polyol synthesis, specifically core sizes and arrangement have been tuned. This indicates ways to tailor and optimize magnetic properties for specific applications. On the one hand, the most well-crystalline nanoflowers (NF-48) has the highest heating capacity. On the other hand, nanoflowers with core size above 15 nm (NF-4) combine high saturation magnetization and initial susceptibility, while conserving low remanence at room temperature, which can be suitable for specific biomedical applications and also applications such as magnetic separation.

Bibliography

[1] Fievet, F., Lagier, J., Blin, B., Beaudoin, B. & Figlarz, M. Homogeneous and heterogeneous nucleations in the polyol process for the preparation of micron and submicron size metal particles. *Solid State Ionics* **32**, 198–205 (1989).

[2] Dong, H., Chen, Y.-C. & Feldmann, C. Polyol synthesis of nanoparticles: status and options regarding metals, oxides, chalcogenides, and non-metal elements. *Green Chemistry* **17**, 4107–4132 (2015).

[3] Qu, H., Caruntu, D., Liu, H. & O'Connor, C. J. Water-dispersible iron oxide magnetic nanoparticles with versatile surface functionalities. *Langmuir* **27**, 2271–2278 (2011).

[4] Cai, W. & Wan, J. Facile synthesis of superparamagnetic magnetite nanoparticles in liquid polyols. *Journal of colloid and interface science* **305**, 366–370 (2007).

[5] Haynes, W. & Lide, D. Crc handbook of chemistry and physics, crc handbook of chemistry and physics (2012).

[6] Zhang, H., Watanabe, T., Okumura, M., Haruta, M. & Toshima, N. Catalytically highly active top gold atom on palladium nanocluster. *Nature materials* **11**, 49–52 (2012).

[7] Soumare, Y. *et al.* Kinetically controlled synthesis of hexagonally close-packed cobalt nanorods with high magnetic coercivity. *Advanced Functional Materials* **19**, 1971–1977 (2009).

[8] Gutiérrez, L. *et al.* Synthesis methods to prepare single-and multi-core iron oxide nanoparticles for biomedical applications. *Dalton Transactions* **44**, 2943–2952 (2015).

[9] Cheng, C., Xu, F. & Gu, H. Facile synthesis and morphology evolution of magnetic iron oxide nanoparticles in different polyol processes. *New Journal of Chemistry* **35**, 1072–1079 (2011).

[10] Caruntu, D. *et al.* Synthesis of variable-sized nanocrystals of fe_3o_4 with high surface reactivity. *Chemistry of materials* **16**, 5527–5534 (2004).

[11] Laurent, S. *et al.* Magnetic iron oxide nanoparticles: synthesis, stabilization, vectorization, physicochemical characterizations, and biological applications. *Chemical reviews* **108**, 2064–2110 (2008).

[12] Lartigue, L. *et al.* Cooperative organization in iron oxide multi-core nanoparticles potentiates their efficiency as heating mediators and mri contrast agents. *ACS nano* **6**, 10935–10949 (2012).

[13] Kim, B. H. *et al.* Large-scale synthesis of uniform and extremely small-sized iron oxide nanoparticles for high-resolution t 1 magnetic resonance imaging contrast agents. *Journal of the American Chemical Society* **133**, 12624–12631 (2011).

[14] Sun, Q., Ren, Z., Wang, R., Chen, W. & Chen, C. Magnetite hollow spheres: solution synthesis, phase formation and magnetic property. *Journal of Nanoparticle Research* **13**, 213–220 (2011).

[15] Di Corato, R. *et al.* Magnetic hyperthermia efficiency in the cellular environment for different nanoparticle designs. *Biomaterials* **35**, 6400–6411 (2014).

[16] Mahmoudi, M., Hofmann, H., Rothen-Rutishauser, B. & Petri-Fink, A. Assessing the in vitro and in vivo toxicity of superparamagnetic iron oxide nanoparticles. *Chemical reviews* **112**, 2323–2338 (2011).

[17] Weissleder, R. a. *et al.* Superparamagnetic iron oxide: pharmacokinetics and toxicity. *American Journal of Roentgenology* **152**, 167–173 (1989).

[18] Pankhurst, Q. A., Connolly, J., Jones, S. & Dobson, J. Applications of magnetic nanoparticles in biomedicine. *Journal of physics D: Applied physics* **36**, R167 (2003).

[19] Gavilán, H. *et al.* Colloidal flower-shaped iron oxide nanoparticles: Synthesis strategies and coatings. *Particle & Particle Systems Characterization* (2017).

[20] Gavilán, H. *et al.* How shape and internal structure affect the magnetic properties of anisometric magnetite nanoparticles. *Acta Materialia* **125**, 416–424 (2017).

[21] Martina, M.-S. *et al.* Generation of superparamagnetic liposomes revealed as highly efficient mri contrast agents for in vivo imaging. *J. Am. Chem. Soc* **127**, 10676–10685 (2005).

[22] Hachani, R. *et al.* Polyol synthesis, functionalisation, and biocompatibility studies of superparamagnetic iron oxide nanoparticles as potential mri contrast agents. *Nanoscale* **8**, 3278–3287 (2016).

[23] Caruntu, D., Caruntu, G. & O'Connor, C. J. Magnetic properties of variable-sized fe_3o_4 nanoparticles synthesized from non-aqueous homogeneous solutions of polyols. *Journal of Physics D: Applied Physics* **40**, 5801 (2007).

[24] Jia, B. & Gao, L. Morphological transformation of fe_3o_4 spherical aggregates from solid to hollow and their self-assembly under an external magnetic field. *The Journal of Physical Chemistry C* **112**, 666–671 (2008).

[25] Ge, J., Hu, Y., Biasini, M., Beyermann, W. P. & Yin, Y. Superparamagnetic magnetite colloidal nanocrystal clusters. *Angewandte Chemie International Edition* **46**, 4342–4345 (2007).

[26] Xu, F., Cheng, C., Chen, D.-X. & Gu, H. Magnetite nanocrystal clusters with ultra-high sensitivity in magnetic resonance imaging. *ChemPhysChem* **13**, 336–341 (2012).

[27] Cullity, B. D. & Graham, C. D. *Introduction to magnetic materials* (John Wiley & Sons, 2011).

[28] Gerischer, H. Elektrodenpotentiale: Tables of standard electrode potentials. hrsg. von g. milazzo und s. caroli. john wiley & sons, chichester, new york 1978. xvi, 421 s., geb.£ 17, 50. *Nachrichten aus der Chemie* **26**, 661–661 (1978).

[29] Poul, L., Ammar, S., Jouini, N., Fievet, F. & Villain, F. Synthesis of inorganic compounds (metal, oxide and hydroxide) in polyol medium: A versatile route related to the sol-gel process. *Journal of Sol-Gel Science and Technology* **26**, 261–265 (2003).

[30] Privman, V. Diffusional nucleation of nanocrystals and their self-assembly into uniform colloids. *arXiv preprint arXiv:0806.4644* (2008).

[31] Cornell, R. M. & Schwertmann, U. *The iron oxides: structure, properties, reactions, occurrences and uses* (John Wiley & Sons, 2003).

[32] Barrón, V., Torrent, J. & De Grave, E. Hydromaghemite, an intermediate in the hydrothermal transformation of 2-line ferrihydrite into hematite. *American Mineralogist* **88**, 1679–1688 (2003).

[33] Skrabalak, S. E., Wiley, B. J., Kim, M., Formo, E. V. & Xia, Y. On the polyol synthesis of silver nanostructures: glycolaldehyde as a reducing agent. *Nano letters* **8**, 2077–2081 (2008).

[34] Baronov, A., Bufkin, K., Shaw, D. W., Johnson, B. L. & Patrick, D. L. A simple model of burst nucleation. *Physical Chemistry Chemical Physics* **17**, 20846–20852 (2015).

[35] Thanh, N. T., Maclean, N. & Mahiddine, S. Mechanisms of nucleation and growth of nanoparticles in solution. *Chemical reviews* **114**, 7610–7630 (2014).

[36] Navrotsky, A., Mazeina, L. & Majzlan, J. Size-driven structural and thermodynamic complexity in iron oxides. *Science* **319**, 1635–1638 (2008).

[37] Serna, C. & Morales, M. P. Maghemite (γ-fe$_2$o$_3$): a versatile magnetic colloidal material. *Surface and colloid science* 27–81 (2004).

[38] Kostopoulou, A. *et al.* Assembly-mediated interplay of dipolar interactions and surface spin disorder in colloidal maghemite nanoclusters. *Nanoscale* **6**, 3764–3776 (2014).

[39] Kuchkina, N. V. *et al.* Hydrophobic periphery tails of polyphenylenepyridyl dendrons control nanoparticle formation and catalytic properties. *Chemistry of Materials* **26**, 5654–5663 (2014).

[40] Liu, J. *et al.* Highly water-dispersible biocompatible magnetite particles with low cytotoxicity stabilized by citrate groups. *Angewandte Chemie* **121**, 5989–5993 (2009).

[41] Kozissnik, B., Bohorquez, A. C., Dobson, J. & Rinaldi, C. Magnetic fluid hyperthermia: advances, challenges, and opportunity. *International Journal of Hyperthermia* **29**, 706–714 (2013).

[42] Vergés, M. A. *et al.* Uniform and water stable magnetite nanoparticles with diameters around the monodomain–multidomain limit. *Journal of Physics D: Applied Physics* **41**, 134003 (2008).

[43] Blanco-Andujar, C., Ortega, D., Southern, P., Pankhurst, Q. & Thanh, N. High performance multicore iron oxide nanoparticles for magnetic hyperthermia: microwave synthesis, and the role of core-to-core interactions. *Nanoscale* **7**, 1768–1775 (2015).

[44] Atkinson, W. J., Brezovich, I. A. & Chakraborty, D. P. Usable frequencies in hyperthermia with thermal seeds. *IEEE Transactions on Biomedical Engineering* 70–75 (1984).

Part D

Absorption and Metabolisation in-vitro and in-vivo

5

Unravelling the mechanisms that determine absorption and metabolization of magnetic single and multi-core nanoparticles in-vitro and in a Xenopus laevis model

Summary

Multi-core superparamagnetic nanoparticles have been proposed as ideal tools for some biomedical applications because of its high magnetic moment per particle, high specific surface area and long term colloidal stability. Controlling aggregation and packing of the cores it is possible to obtain not only single-core but also multi-core and hollow spheres having internal voids. In this work we compare toxicological properties of single and multi-core nanoparticles. Both types of particles showed moderate in vitro toxicity (MTT assay) tested in Hep G2 (human hepatocellular carcinoma) and Caco-2 (human colorectal adenocarcinoma) cells. The influence of surface chemistry in their biological behaviour was also studied after functionalization with O,O'-bis(2-aminoethyl)PEG, (2000 Da). These nanoparticles were evaluated in a Xenopus laevis model, studied their toxicity and described how they trigger iron metabolism. The results also highlight the potential of Xenopus laevis model bridging the gap between in vitro cell-based assays and rodent models for toxicity assessment to develop effective nanoparticles for biomedical applications.

5.1 Introduction

Iron oxide magnetic nanoparticles (IOMNPs) have recently rised as potential materials for biomedical applications.[1, 2] Their surface chemistry can be modified, adding functionality to the material and enabling their use for gene therapy, tissue regeneration and drug delivery, to specifically target tumors using external magnetic fields. Their magnetic properties can be exploited for magnetic resonance imaging and magnetic-fluid hyperthermia, which raised hope for improved imaging techniques[3] and cancer treatment.[4, 5] However, in spite of their potential, few of these biomaterials have reached the clinical practice[6].

A crucial issue for magnetic nanoparticle safe utilization in biomedicine and their approval by regulatory agencies lies in their biotransformation and toxicity. On one hand, the course and fate of the nanoparticles once they fullfil their mission needs to be studied. On the other hand, the safety metabolization of the by-products must be assessed and assured. Since iron is involved in diverse vital processes, organisms display mechanisms to transport and store iron in non-toxic forms.[7] Therefore, IOMNPs are predicted to be safely incorporated in biological systems. Increasing evidence demonstrates that iron oxide MNPs trigger iron-coping mechanisms in cells and that the degradation products of these materials are incorporated into normal iron metabolic routes.[8–14] However, nanoparticle coating has been shown to be determinant on the IOMNPs uptake, degradation and fate.[15, 16] In order to establish solid conclusions about IOMNPs toxicity the study of IOMNPs toxicity and biodistribution, and its cellular effects, it would be ideal to have biologically pertinent models.

In this sense, Xenopus laevis is an amphibian model ideal to study the course and fate of the nanoparticles since it allows flexible bioassay for evaluating vertebrate embryology development, basic cell and molecular biology, genomics, neurobiology and toxicology.[17] Though this model, the risk of exposure to contaminated water was reported. The contaminants were metal oxide-based nanomaterials (γ-Fe_2O_3, TiO_2, ZnO and CuO) and the mortality, malformations and growth inhibition were studied,[18] confirming that γ-Fe_2O_3 did not pose risks to amphibian populations. Furthermore, it was pointed that NPs sizes above 200 nm had toxic effects.[19] Despite this literature available on the effects of many compounds on the larval development of X. laevis in environmental studies, there are no reports evaluating nanoparticles designed for bioapplications bridging the safety assessment of NPs in cell-based assays with data generated from rodent in vivo systems. Rat animal models have proven to be suitable models for the study of anaemia oral treatment with IOMNPs.[20]

In this work, we report the effect of γ-Fe_2O_3 magnetic single and multi-core nanoparticles suitable for bioapplications on X. laevis embryos. The particles have uniform size in the nanoscale and are coated with biocompatible shells. MNPs colloids used in this work can be classified as single-core (with only one magnetic core per particle) and multi-core (with several magnetic cores per particle).[21] While single-core superparamagnetic nanoparticles have been proposed as ideal tools in biomedicine, since they circulate longer after injection in an animal,[22] which may favour their uptake in leaky vas-

culature regions such as tumors,[23] for some medical applications, such as bioseparation or magnetic fluid hyperthermia, it can be advantageous to use larger multi-core particles that have large magnetic moment per particle.[24] However, few in vitro and in vivo studies have been dedicated to the comparison of single-core and multi-core nanoparticles[25] and there is a lack of knowledge still on how the aggregation of magnetic cores forming multi-core nanoparticles affects the nanoparticle uptake and transformation, and thus its toxicity and biodistribution.

AC magnetic susceptibility measurements will be used here to characterize the IOMNPs once they are internalised in biological systems. This technique has proven to be an excellent tool to study magnetic nanoparticles in complex matrices, since the diamagnetic signal coming from tissues does not interfere with the superparamagnetic signal of the NPs.[26] This way it was possible to follow the signal of the magnetic nanoparticles in animal models[27, 28] and to quantify the iron content. This is one of the greatest challenges in the nanomaterials area nowadays, i.e. determining how best to characterize the nanopaticles and follow its transformation/degradation.[29] The study of in vivo fate of IOMNPs is imperative to develop successful biomedical applications . In this work, it is presented for the first time, the study, by means of AC magnetic susceptibility measurements, of the intake of iron-containing particles in X. laevis embryos.

5.2 Experimental section

Materials and Methods:

Materials: Iron(III) chloride hexahydrate ($FeCl_3 \cdot 6H_2O$, $>$98%, Sigma-Aldrich), sodium oleate ($>$82%, Riedel-de Haen), oleic acid (90%, Sigma-Aldrich), oleylamine (70%, Sigma-Aldrich), meso-2,3dimercap tosuccinic acid (DMSA, 98% Sigma-Aldrich), 1-octadecene (90%, Sigma-Aldrich), n-hexane (99%, Scharlau), toluene (99.8%, Sigma-Aldrich), dimethyl sulfoxide ($>$99.5%, Sigma-Aldrich), O,O'-bis(2-aminoethyl)PEG, 2000 Da (Sigma Aldrich), ethyl-3-(3-dimethylaminopropyl)-carbodiimide ($\geqslant$ 98%, Fluka, EDS) polyvinylpyrrolidone (PVP40, Sigma-Aldrich), sodium acetate trihydrated ($NaAc \cdot 3H_2O$, $\geqslant$ 99%, Sigma-Aldrich), ethylene glycol (EG, $\geqslant$ 99.5 %, Fluka), citric acid ($C_6H_8O_7$, $\geqslant$ 99.5%, Sigma-Aldrich) and ethanol (96%, Panreac). Dialysis tubing cellulose membranes were purchased from Sigma and washed prior to use.

Nanoparticles synthesis:

- Synthesis of iron oxide single-core nanoparticles (SC). The synthesis of iron oxide nanoparticles has been based on a previous work described in the literature.[30] The reaction was carried out under nitrogen. In a round-bottomed flask (500 mL), and it was equipped with a mechanical stirrer (glass stirrer shaft), thermometer, entry for nitrogen flow and reflux condenser. Iron(III) oleate (4.54 g, 5 mmol) was mixed with oleic acid (0.724 g, 2.6 mmol) in 1-octadecene (50 mL). The mixture was stirred (100 rpm) and slowly heated (5 $^\circ$C$\cdot$min^{-1} for T$<$ 100^{o}C, and 2°C$\cdot$min^{-1}

for T$>$ 100°C) until reflux (325°C) with a heating mantle. The heating mantle was withdrawn and the system was allowed to cool down to room temperature. The resulting black mixture was washed with ethanol several times by centrifugation (RCF = 7500) and magnetic decantation (the particles were separated with the aid of a magnet). The resulting dried black solid (the solid was dried under nitrogen flux) was redispersed in hexane. The as-synthesized nanoparticles are coated with oleic acid.

- Synthesis of iron oxide multi-core nanoparticles (MC). The synthesis of multi-core iron oxide nanoparticles has been based on a previous work described in the literature[31] but the experimental procedure and the concentration of NaAc have been varied. Typically, 2.62 mmol iron(III) chloride were dissolved with ultrasound in 109 mL of ethylene glycol. Secondly,, 140 mmol PVP40 were added slowly under vigorously magnetic stirring (>1000 rpm) and mild heating until completely dissolved. Then, 26.2 mmol of NaAc·3H_2O were added to the solution. The mixture was sealed in a Teflon-lined autoclave (125 mL) and maintained at 200 °C for 16 h for solvothermal crystallization, following cooling inside oven. The precipitated solid product was washed with ethanol and distilled water through centrifugation (RCF = 7500) several times. The as-synthesized nanoparticles are coated with the polyol and the PVP.

Surface modification:

- Ligand exchange with dimercaptosuccinic acid on single-core NPs (SC@DMSA). For DMSA ligand exchange, a standard procedure was used.[32] In a typical experiment, ethanol (20 mL) was added to a volume of SC dispersed in hexane containing a mass of NPs of 50 mg. The mixture was sonicated and then placed on a magnet to separate the liquid from the black solid residue of nanoparticles. The residue was washed with more ethanol (5 X 10 mL) following the same procedure, until the discarded liquid had a clean appearance. The remaining black residue was dispersed in toluene (20 mL) and the dispersion added to a solution of DMSA (90 mg) in dimethyl sulfoxide (5 mL). The resulting black suspension was then shaken in a laboratory tube rotator. After 2 days, SC@DMSA nanoparticles were precipitated as a black powder stuck to the glass tube and the liquid phase was transparent and pale yellow. The liquid was discarded and the nanoparticles were washed with ethanol (4 X 10 mL), sonicating and centrifuging (RCF = 7500). The final black solid was air dried and redispersed in distilled water. KOH 1 M was added to increase the pH to 10 and HNO_3 0.01 M was used to lower the pH to 7. The dispersion was then placed in a cellulose membrane and dialyzed for 5 days in distilled water, to remove any excess of unreacted DMSA and any other small impurities that may be present in the dispersion without being attached to the nanoparticles.

- Surface coating with citric acid on multi-core NPs (MC@CIT). For citric acid coating a standard procedure was used.[21, 33] First, sample volume equivalent to 20 mg of Fe was adjusted to pH 2

and then dispersed in 13 mL of a solution of citric acid 0.1 M. Afterwards, the mixture was heated at 80 °C for 30 min. The solution was centrifuged and washed with distilled water. Finally the pH was adjusted first to 11 with KOH 1M and then to 7 with HNO_3 0.01 M.

- Surface coating with polyethylene glycol (SC@DMSA@PEG and MC@CIT@PEG). PEG conjugation reaction has been based on a previous work described in the literature.[34] Amine-functionalized PEG was attached to SC@DMSA or MC@CIT via an ethyl-3-(3-dimethylaminopropyl)-carbodiimide (EDC)-mediated coupling reaction using the polymer O,O'-bis(2-aminoethyl)PEG, 2000 Da. PEGylation reaction was carried out in a refrigerated ultrasonic bath; an aqueous solution containing 10 mg SC@DMSA or MC@CIT was mixed with the PEG derivative (4 mg). The total amount of EDC (1 mg) was divided into five aliquots, one of which was added every 1 h, and the fifth 4 h after the previous addition. The molar ratio of COOH groups/amine groups/EDC was 1:1.5:1; pH was adjusted to 6, and the mixture was sonicated (4 h, 25 °C), followed by extensive dialysis.

Nanoparticle structural characterization : The particle sizes and morphologies were determined by transmission electron microscopy (TEM) with a JEM1010 microscope (JEOL, Peabody, USA) operating at 100 kV. Samples were prepared by placing a drop of the uncoated particles suspended in water onto a carbon coated copper grid and allowing it to dry at room temperature. The size distributions were determined by manual measurement of more than 100 particles using the public domain software ImageJ.

The presence of the coating and the washing process was also confirmed and studied by Fourier transform infrared spectroscopy (FTIR) in the range of 4000-250 cm^{-1} by use of a Bruker (USA) IFS 66VS. The samples for FTIR were prepared diluting the dried powder in KBr at 2% by weight and pressing it into a pellet.

The presence of the coating was also studied by thermogravimetric analyses (TGA). They were performed in a Seiko TG/DTA 320U thermobalance, whose temperature scanning range is from room temperature up to 900 °C. For this work, samples were heated from room temperature to 700 °C at 10 °C/min under an air flow of 100 mL·min^{-1}. Platinum pans were used and α-Al_2O_3 was used as reference.

Colloidal properties were studied in a Zetasizer Nano S, from Malvern Instruments (UK). The hydrodynamic size was determined by Dynamic Light Scattering (DLS) and the zeta potential was measured as a function of pH at 25 °C, using HNO_3 and KOH to change the pH of the suspensions. Hydrodynamic size is given as the intensity-weighted mean.

Cell culture: Hep G2 (human hepatocellular carcinoma) and Caco-2 (human colorectal adenocarcinoma) cells were cultured as mono-layers in Dulbecco's modified Eagle medium supplemented with 2% penicillin-streptomycin and 10% fetal bovine serum, in a humidified incubator (37°C, 5% CO_2). For toxicity experiments, cells were seeded in 96-well plates at 50,000 cells/cm^2 (approximately 1.6 x 10^4

cells/well, 150 μL/well).

For iron uptake experiments, Caco-2 cells between passages 30-36 were seeded onto collagen-coated 12-well plates (Bio-Greiner, UK) at a density of 2 x 10^5 cells/well suspended in 1 mL of supplemented DMEM which was replaced every 2 days. Cells were used on confluence at days 13-15 post-seeding. In order to ensure a low basal media iron levels, 24 hours prior to the initiation of the nanoparticles treatments, the DMEM medium was replaced by Eagle's minimum essential medium (MEM) without foetal bovine serum supplemented with 10 mmol/L PIPES [piperazine-N, N' –bis-(2-ethanesulfonic acid)], 26.1 mM $NaHCO_3$, 19.4 mmol/L glucose, 1% antibiotic-antimycotic solution, 11 μmol/L hydrocortisone, 0.87 μmol/L insulin, 0.02 μmol/L sodium selenite (Na_2SeO_3), 0.05 μmol/L triiodothyronine and 20 μg/L epidermal growth factor.[35] The day of the experiment, the nanoparticles were diluted in the low-iron MEM to obtain a 250 μM final iron concentration and subsequently Caco-2 cells were exposed for 24 hours with the treatments.

Cytotoxicity assay (MTT): In order to determine the Cell viability a (MTT) assay 24 h after exposure to NP was conducted. Therefore, a standard 3-(4,5-dimethylthiazol-2-yl)-2,5-diphenyl tetrazolium bromide was used. Cells were seeded in 96-well plates at 50,000 cells/cm^2 (approximately 1.6 x 10^4 cells/well, 150 μL/well). In total 60 wells were seeded per plate (6 rows x 10 columns) as the outer wells were left empty to avoid errors due to evaporation. Each row was used as a replicate (3 wells/condition) and serial dilutions went across the columns of the plate. Cells were left to grow until 70-80 % confluency. NP-containing medium was removed after 24 h, cells were rinsed three times with PBS, and MTT solution in medium (final MTT concentration 50 μg·mL^{-1}) was added and incubated (2 h, 37 °C). The MTT solution was removed without disturbing cells, 0.2 mL $well^{-1}$ of DMSO and 0.025 mL $well^{-1}$ of Sorensen buffer were added, the plates were shaken gently to dissolve formazan crystals, and the absorbance was read on a microplate reader at 550 nm. Cell viability ($\%$) was calculated as [(A - B)/A 100], where A and B are the absorbance of control and treated cells, respectively. Values represent mean $\pm$ SD (n=3).

In vivo test: For the Xenopus laevis embryo toxicity model, adult females were primed with PMSG (Pregnant Mare's Serum Gonadotropin) four days before the experiment and induced with Chorulon (contains Human Chorionic Gonadotrophin, HCG) the day before. Eggs were obtained by squeeze and fertilized in a petri dish by adding male sperm (male testis incubated with 2ml 1xMMR (Marc's modified ringers) and 8 mL FBS). Then the eggs were washed with 0.1xMMR to remove the sperm (20 min) and left 7 min in L-cysteine (10g into 500mL 1xMMR pH 8.0). Finally 2 washes were performed with 1xMMR, and the eggs were plated in BSA-coated petri dishes covered with 0.1xMMR. Embryos were left at 23°C until they reached stage 38, and then plated at 24-well plates (7 embryos/well) in 0.1xMMR media containing the nanoparticles and incubated at 23°C. Non-treated embryos were used as control. The mortality and the morphological changes of the embryos were recorded every 24h until embryos reached stage 45.

Histological evaluation: When the embryos reach the appropiate stage, they where fixed in

MEMFA (3.7% Formaldehyde, 1X MEM salts and DEPC H_2O) overnight at 4°C. Samples were washed in PBS, dehydratated and kept in 100% ethanol. To embeed embryos in wax, they were directly washed in histoclear, 1:1 histoclear:wax and finally wax and placed in moulds. Embryos were sectioned using a microtome generating 10um slices. Slices were then hydrated and dryed to be analysed by Scanning electron microscopy.

Iron content analysis: Groups of 7 embryos were pooled. Animals were weighed and lyophilized 72 hours in a Telstar lyoquest lyophilizer (Spain), and the iron content was measured by Inductively Coupled Plasma-Optical Emission Spectrometry (ICP-OES) in an Optima 2100 DV from PerkinElmer, after acid digestion, with HNO_3 ($\geq$ 65%) during 1 h, or kept freeze-dried for magnetic characterization, respectively. The sample manipulation was performed using disposable plastic material to avoid ferromagnetic contamination.

Magnetic characterization: The resulting freeze-dried samples were placed into gelatin capsules for their magnetic characterization in a Quantum Design MPMS-XL SQUID magnetometer with an AC susceptibility option. The measurements were performed with AC amplitude of 0.41 Oe, in the temperature range between 1.8 and 300 K and at a frequency of 11 Hz.

RNA extraction and quantitative PCR: Gropus of 7 embryos were snap frozen in liquid nitrogen. RNA was extracted using High Pure RNA isolation kit (Roche) and 1 ug of RNA was taken to synthetise cDNA using Maxima First Strand cDNA synthesis kit (Thermofisher). RT-PCR was perfored using SYBER Green detection method. Primers were designed targeting both copies of X.laevis genes. Dmt1$_F$: cagaggatgaaacgcactca, Dmn1$_R$: atcctgccactgatccagac; Fth1$_F$: tggagtaacaccctggaagc, Fth1$_R$: aggatcaaccttgtcggatg; Tf$_F$: agaaagggcaagtgggtttt, Tf_R: tctggcaaagtgacaacagc; hepcidin$_F$: aaatcaaccccaatctgctg, hepcidin$_R$: gtttgttgattgccgaaggt; hmox1$_F$: ggagacctctcaggtggaca, hmox1$_R$: atggagttcatacgggaacg; gpx1$_F$: ttccccctctttgagaaggt, gpx1$_R$: atgatgctcttgggatcctg; sod2$_F$: tgtgcaggctcagtgtttgt, sod2$_R$: gctgcagagcaccataatca; gsr$_F$: gcaaagaggagaaggtggtg, gsr$_R$: cggaggaagtcggatgaata.

5.3 Results and discussion

Nanoparticles synthesis and characterization

Two different types of iron oxide nanoparticles were synthesized in this work. Single core nanoparticles (SC) were obtained by thermal decomposition of the iron(III) oleate precursor in 1-octadecene (Figure 5.1 a-b). Particles were 13 $\pm$ 1 nm in diameter, uniform in size (Figure 5.1 c), relatively spherical and well dispersed, owing to the presence of oleic acid around the particles. In a different approach multi-core nanoparticles (MC) were obtained by polyol mediated reduction of iron(III) chloride. MC are composed of spherical 142 $\pm$ 23 nm nanoparticles with a well-defined size and shape. These MC nanoparticles consist of smaller cores of approximately 10 nm. HRTEM and X-ray diffraction patterns have already been reported.[36]

Table 5.1: Colloidal properties of aqueous suspensions of the nanoparticles at pH 7. Hydrodynamic sizes, PDI (=standard deviation/mean size) and surface charge of single and multi-core nanoparticles after PEG conjugation.

Sample	**Hydrodynamic size (nm)**	**PDI**	**ζ-Potential (mV)**
SC@DMSA	34.2	0.054	-38 $\pm$ 12
SC@DMSA@PEG	65.2	0.084	-24 $\pm$ 7
MC@Cit	181.0	0.201	-25 $\pm$ 9
MC@Cit@PEG	183.1	0.225	-18 $\pm$ 9

Particle structure and size were selected intentionally, since they are two key parameters that directly influence in vivo biological behaviour. The size of intravenously injected nanoparticles greatly affects their in vivo biodistribution, e.g. particles from 60 to 150 nm in size are taken up by the reticuloendothelial system leading to rapid uptake in the liver and spleen. Intravenously injected nanoparticles with diameters of 10–40 nm allow longer blood circulation and can cross capillary walls, and they are often phagocytosed by macrophages which traffic to lymph nodes and bone marrow.[37] However, how these parameters affect the greater picture of toxicity and biodegradability mechanisms is still poorly understood.

Iron oxide nanoparticles obtained by thermal decomposition are hydrophobic. To make them suitable for biological applications, oleic acid on the surface of the nanoparticle was removed with DMSA via ligand exchange reaction (SC@DMSA). Polyol mediated process render hydrophilic nanoparticles along with polyvinylpyrrolidone (PVP40), present in the reaction, however an extra capping agent like citric acid enhance the electrostatic repulsion and facilitates the final dispersion of the MC nanoparticles in aqueous media (MC@Cit). Hydrodynamic sizes are always higher than sizes measured by TEM, indicating the presence of the coating or some degree of agglomeration after surface modification, but both types of particles remains below 200 nm (34 and 181 nm were obtained for SC@DMSA and MC@Cit), an important requirement for biomedical applications. Both particles have high negative surface charge at pH 7 (Z-potential equal to -38 and -25 mV for SC@DMSA and MC@Cit, respectively). In order to evaluate the influence of the surface charge in particle absorption and biodegradation we conjugated covalently a diamine PEG derivative to the carboxylic groups (from both DMSA and citric acid) in the surface of the nanoparticles. After PEG conjugation, average hydrodynamic size at pH 7 increased from 34 to 65 nm and from 181 to 183 nm for SC@DMSA and MC@CIT, respectively (SC@DMSA@PEG and MC@Cit@PEG) and net surface charge decreased from approximately -38 to -24 mV for SC@DMSA@PEG samples and from -25 to -18 mV for MC@Cit@PEG. Colloidal properties of aqueous suspensions of the nanoparticles at pH 7 are summarized in Table 5.1.

Nanoparticle surface modification was also confirmed by FTIR (Figure 5.2 a-b). For all the samples the typical bands of metal skeleton vibration (Fe-O) in the region of 550-600 cm^{-1} and a broad peak between 3000 and 3500 cm^{-1} due to surface -OH groups are observed. After PEG conjuga-

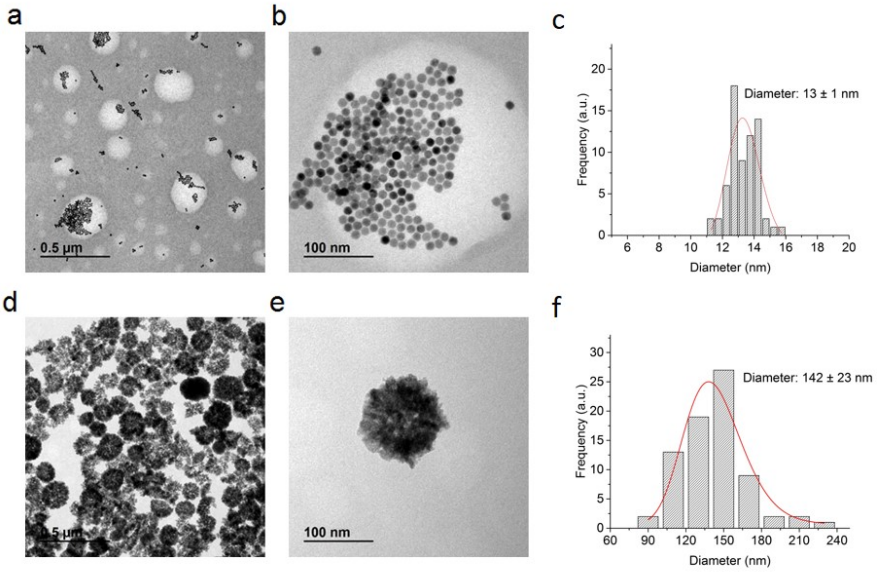

Figure 5.1: Transmission electron microscopy (TEM) images of single and multi-core nanoparticles. (a,b) SC@DMSA; (d,e) MC@Cit; (c,f) Size distribution histograms. Red lines indicate the log-normal fitting function of TEM particle size data.

tion, some peaks appeared at 1354 and 1102 cm^{-1}, indicating asymmetric and symmetric stretching of C–O–C, and out-of-plane bending of the –CH of the PEG chains at 956 cm^{-1}. TGA of the unconjugated nanoparticles reveals a weight loss of $\sim$15% and 8% for SC@DMSA and MC@CIT, respectively, due to the removal of physical and chemical water and capping molecules (DMSA or citric acid). Particles modified with diamine PEG nonetheless showed a larger amount of conjugated polymer ($\sim$20% in the case of SC@DMSA@PEG and 13% for MC@Cit@PEG) which indicates greater reaction efficiency. In all cases, weight loss took place between 200 and 400°C, associated with polymer burning.

Toxicity in-vitro

Figure 5.3 shows in vitro toxicological characterization of the nanoparticles, evaluated through the degree of cell survival by means of the standard methyl thiazol tetrazolium bromide (MTT assay). The analysis of cytotoxicity after incubation with Hep G2 and Caco-2 cells with the nanoparticles showed that viability of cell culture is not significantly affected by the presence of the nanoparticles up to 1000 μM Fe concentration after 24 h of treatment (80–100% viability compared with the control). At iron concentrations higher than 1000 μM, SC decrease the viability of both cell lines down to values of 20%. In the case of MC, viability percentage of both cell lines is in the range of 60-80 %, indicating lower toxicity even at high iron concentrations. Differences in toxicity profile at higher doses could be related to

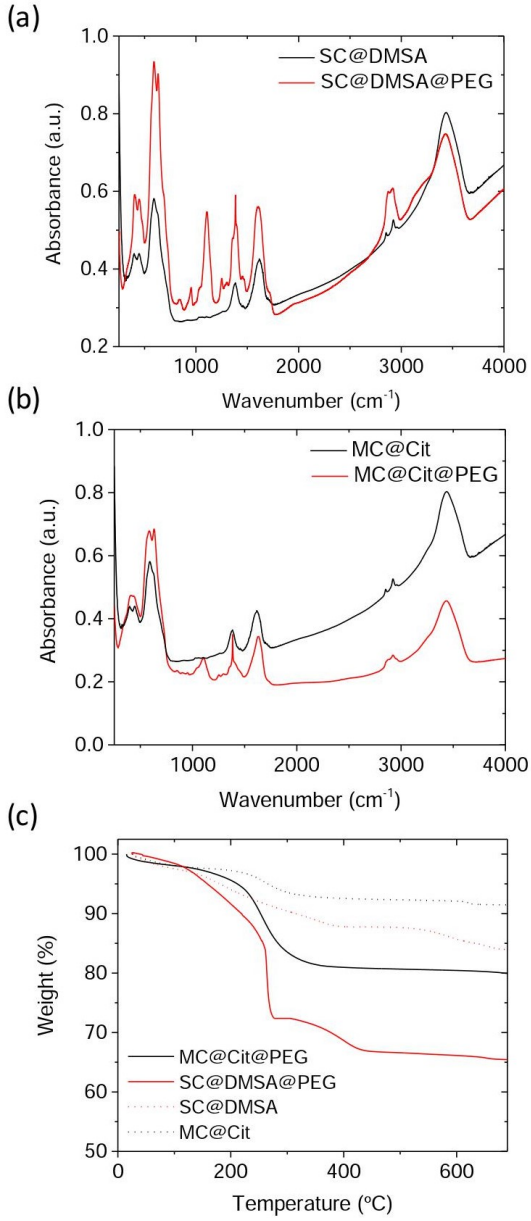

Figure 5.2: FTIR spectra of uncoated/coated with PEG nanoparticles (a) Single-core nanoparticles; (b); Multi-core nanoparticles (c) TGA curves.

different sensitivity of both cell lines used in the treatment with nanoparticles. The effect of PEG coating is not very clear at high iron concentration. In the case of Hep G2 cells PEG functionalization improves

the cytotoxicity for SC while in Caco-2 has no effect. For MC, PEG functionalization reduces the viability down to 60 % in Caco-2 cells. Even when this method needs further refinement and standardization for toxicity evaluation of nanoparticles it offers an inexpensive and high-throughput alternative to perform in vitro cytotoxicity screenings.[38]

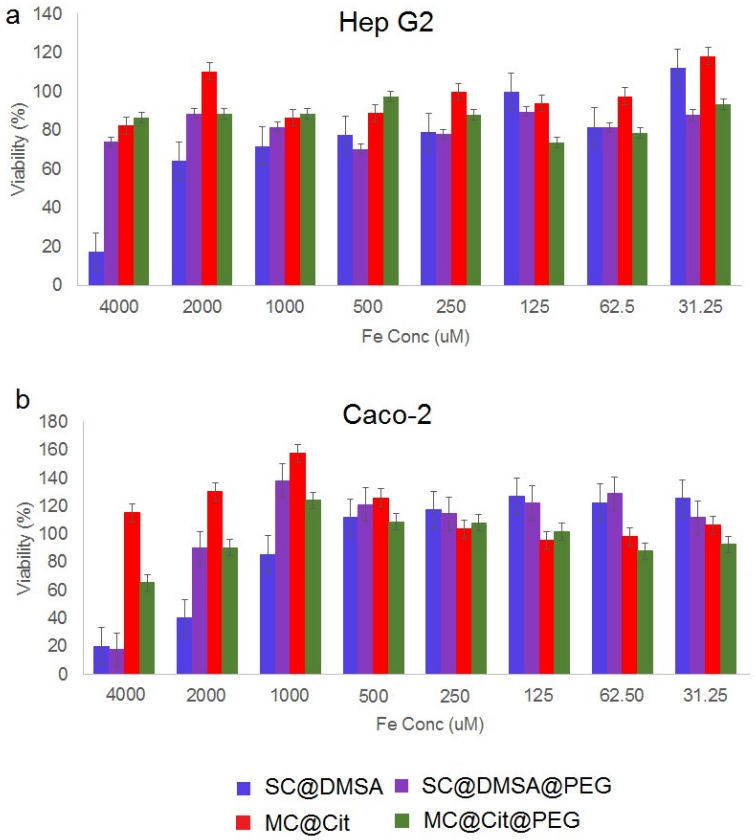

Figure 5.3: Evaluation of cell viability by MTT assay of (a) Hep G2 cells and (b) Caco-2 cells after 24 h treatment with the nanoparticles. Values indicated mean $\pm$ SD (n=3).

In-vivo iron evaluation of nanoparticles

The use of this model has advantages with respect to other animal models. First, embryos develop externally, allowing experiments to be performed prior to, or directly following fertilization. They have a rapid embryo growth and development within 48 hours (Figure 5.4), a tadpole has a fully functional set of organs, and it can be examined to determine if any experimental intervention (in this case a solution containing nanoparticles) has had an effect. In this experiment, nanoparticles were added at

stage 38 (late tailbud) and survival was evaluated every 24 h until embryos reach stage 45 (tadpole), approximately 72 h of exposure. In order to optimise the dose for the following experiments, embryos were treated with four different concentrations, 0.25 mg/mL, 0.5 mg/mL, 0.75 mg/mL and 1 mg/mL. None of the conditions were found lethal for the embryos (Figure 5.5), therefore we decided to perform the rest of the experiments comparing a low and a high dose of nanoparticles (0.5 and 1 mg/mL).

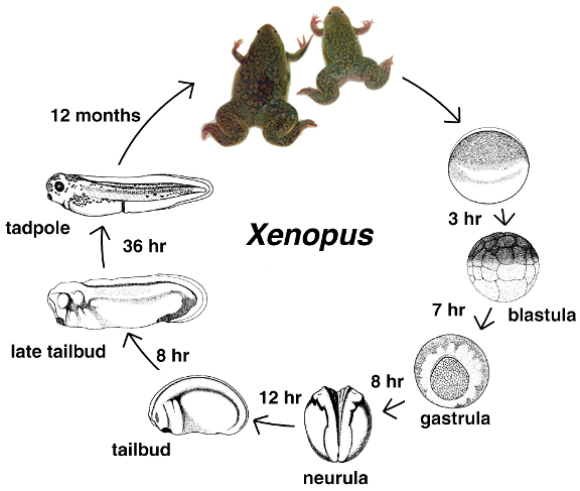

Figure 5.4: Life cycle of X. laevis. Frog embryos develop externally. The embryo growth takes place fast and a tadpole with fully functional set of organs is formed within 48 h. The growth to adult takes place within 12 months. Image from http://www.xenbase.org/anatomy/intro.do.

The transparency of Xenopus embryos allows the visualization of the nanoparticles as they are being swallowed, which takes place mainly for the SC@DMSA, suggesting that this nanoparticles are massively absorbed by the organisms.

All embryos displayed a general body toxicity when treated with NPs at 1 mg/mL characterised by defects in embryo body shape, tail bending and developmental delay. In the case of embryos treated with 0.5 mg/mL, defects were more subtile (Figure 5.6). This result suggested a dose-dependant uptake of the NPs by the embryos. As the main organs involved in NPs' absorption and biotransformation are the gut and liver, we evaluate the morphology of these organs. For SC-treated embryos, the intestine coiled structure is preserved although is visible enlarged when embryos are treated at 1 mg/mL.

The MC-treated embryos displayed a dramatic effect in the morphology of the intestine. The organ is not mantained or not well formed, as we are unable to see the intestine loops (as marked by red arrows in Figure 5.6). Interestingly, at lower dosis of SC or MC, where the general toxic effects of the embryo are visibly reduced, the damage in the gut is absent in the treatment with PEG functionalized nanoparticles compared with the uncoated ones.

Electron microscopy images of pharynx sections (Figure 5.7), taken from different embryos, have allowed us to localize the particles in the organisms. The presence of the NPs in the tissue sample

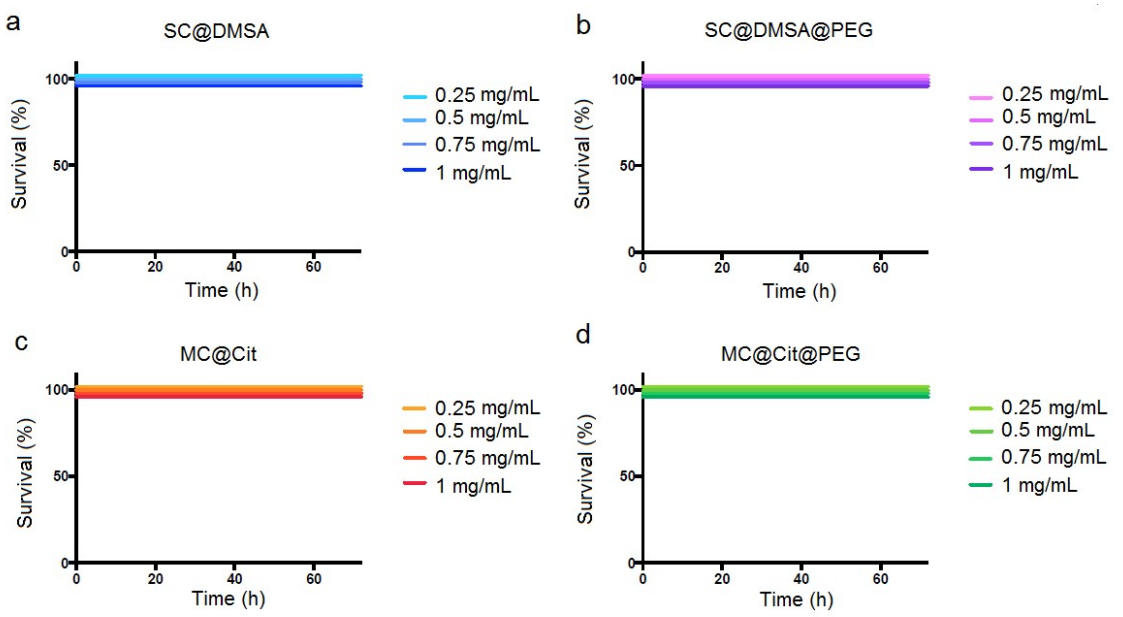

Figure 5.5: Survival curves of X. laevis exposed to different particle concentrations (n=7 per group).

is evidenced by the Energy Dispersive X-ray (EDS) elemental mapping. Those spots with brighter contrast, due to the higher Z atomic number of iron, confirmed that only at the dose of 1 mg/mL, SC@DMSA and MC@Cit, could be detected in the upper body tissue sections, in contrast with the control. PEGylated nanoparticles (SC or MC) were no detected in any sample.

Iron quantification – AC magnetic susceptibility and ICP-OES

IOMNPs intake is visibly detected in the images of pharynx sections of the embryos because the EDS spectra clearly showed K electron shell (K-α and K-β lines) of iron, whereas in the case of control these peaks are absent. In order to quantify the iron present in the samples through these technique, the application of quantitative correction procedures are needed, which are sometimes referred to as matrix corrections.[39] As SEM only provides local information, the quantitative analysis of nanoparticles' intake, was performed through magnetic characterization and iron elemental analysis. Moreover, these techniques allow the comparison of the accumulation depending on the coating and the surface charge (DMSA, citric acid, and PEG functionalization).

In order to evaluate the accumulation of the nanoparticles in the animals, we performed AC susceptibility of pools of seven animals. Magnetic measurements, especially AC magnetic susceptibility, are extremely sensitive being able to distinguish the contribution from the magnetic nanoparticles from that of other endogenous iron-containing species, usually present in a bigger concentration but with weaker

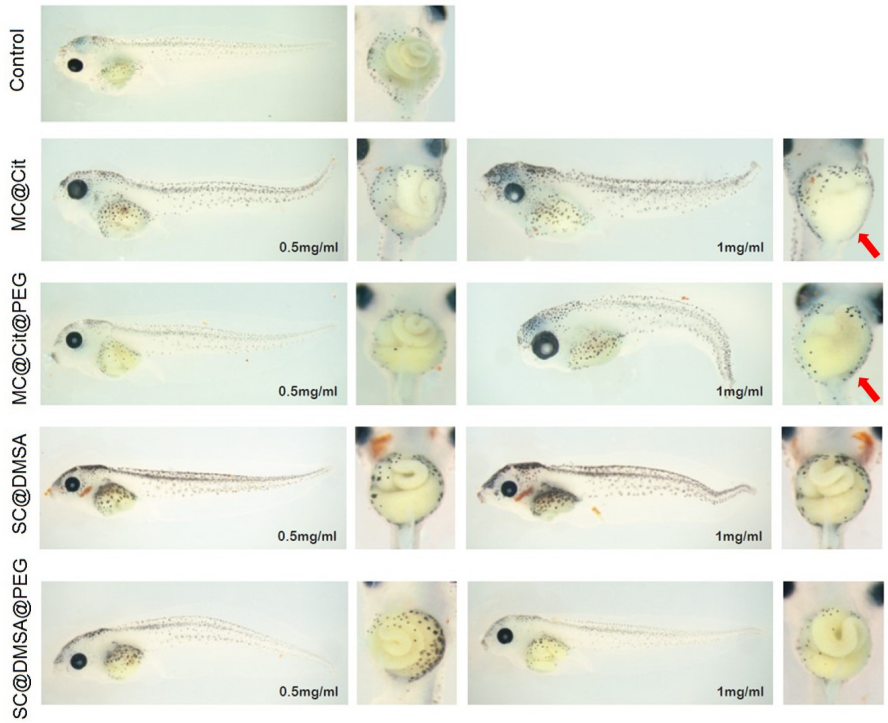

Figure 5.6: Representative images from X. laevis exposed to 0.5 and 1 mg/mL of nanoparticles. (n=7 per group). Red arrows highlight those intestines in which the effect of treatment was dramatic, modifying their coiled structure.

magnetic signal than the nanoparticles. The presence of magnetic nanoparticles can be identified by a maximum in the in-phase magnetic susceptibility (χ') accompanied by a maximum at slightly lower temperatures in the out-of-phase susceptibility (χ''). The temperature location of the maxima depends on the nanoparticle (material, size, aggregation degree, etc). The height of the maxima is a surrogate measurement of the concentration of nanoparticles.

In our case, a dose-dependent amount of nanoparticles is observed in the animals treated with particles without PEG coating (Figure 5.7), independently if they are SC or MC. Interestingly PEG coated nanoparticles, both SC and MC, were not detected, or at least they are under the detection limits of the technique. These results are in agreement with what we observed by EDX-SEM. In this work, the presence of ferritin, the iron storage protein with an out-of-phase susceptibility maxima located at around 10 K, has not been observed. The absence of a substantial paramagnetic contribution, usually observed at the lowest temperatures, indicates that the presence of free iron atoms that could come from a degradation process is very low.

Thought AC magnetic susceptibility, dose-dependent amount of nanoparticles (SC@DMSA and

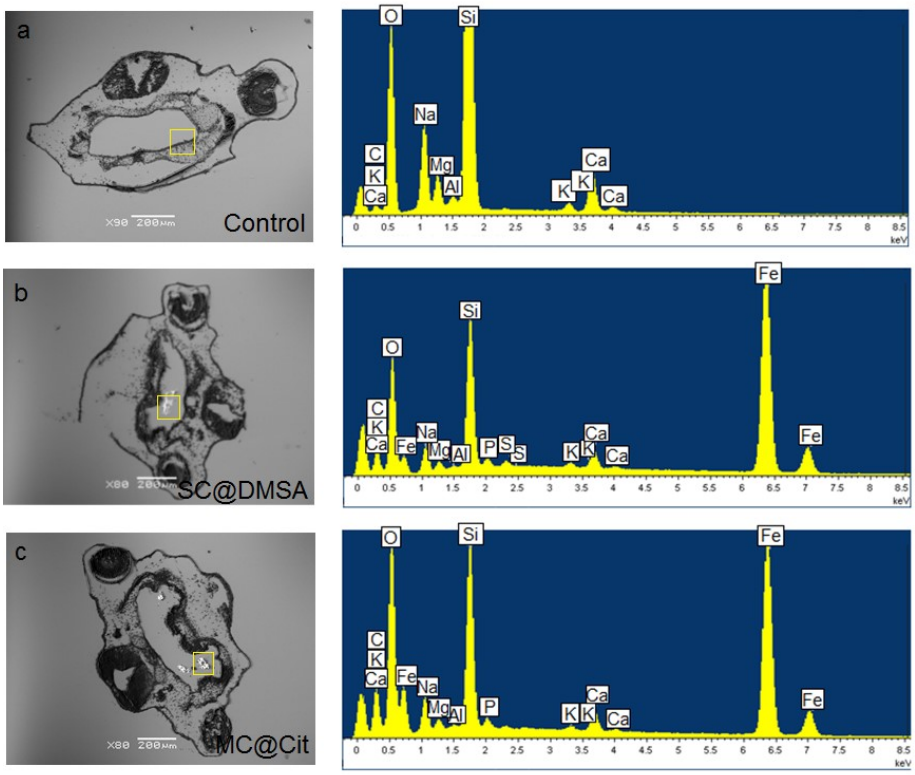

Figure 5.7: Scanning electron microscopy (SEM) images of pharynx sections from different embryos: (a) Control, (b) Embryos exposed to SC@DMSA nanoparticles, (c) Embryos exposed to MC@Cit nanoparticles. Right panel shows elemental analysis of selected areas in the images obtained by Energy Dispersive X-ray Spectrometry (SEM-EDS).

MC@Cit) has been detected. However, a quantitative analysis of NPs' intake was performed by ICP-OES. Data is summarized in Figure 5.8. Elemental analysis results are in agreement with the iron content detected by AC magnetic susceptibility, observing a dose-dependent iron absorption. The massive absorption of SC@DMSA detected in the embryos has been confirmed by ICP-OES, a two or five-fold increase in comparison with MC@Cit for iron concentrations of 0.5 and 1 mg/mL, respectively. Interestingly, the iron content in the animals treated with PEGylated NPs is comparable to the control.

One possible explanation for the visual disturbance of the intestine structure of the embryos treated with MC@Cit@PEG, could be that the particles are rapidly excreted by the organism and therefore the iron content in these animals is so low. PEG functionalization reduces net surface charge of the particles and this effect could reduce the absorption of the particles in the gut favouring their excretion. Another possible explanation for the morphological alterations observed at higher doses in the treatment

with the nanoparticles could be the presence of residual chemicals used during the MC synthesis non-associated to the iron cores.

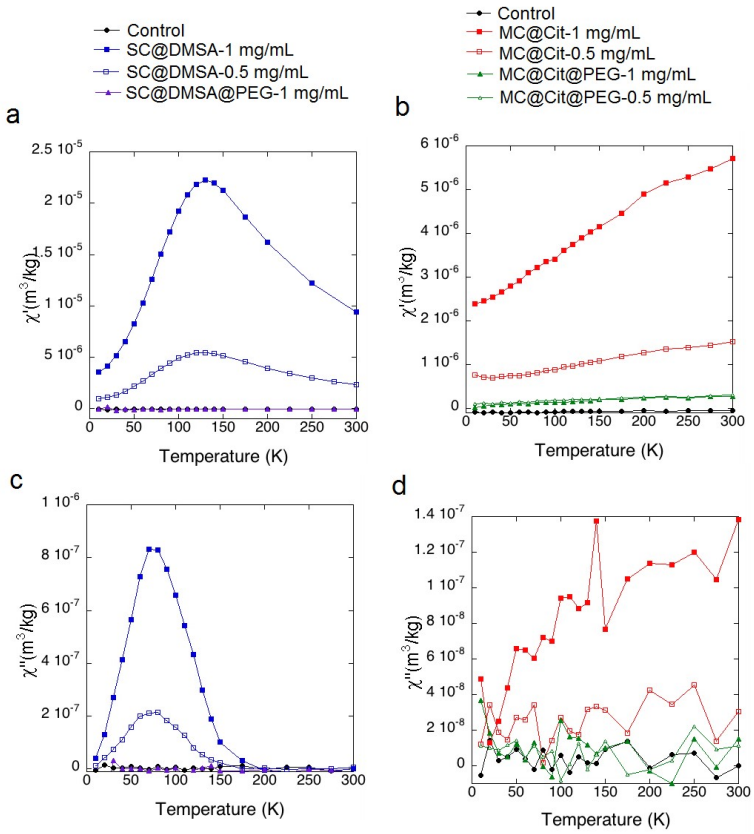

Figure 5.8: Tissue characterization by AC magnetic susceptibility. In-phase (χ'(T)) and out-of-phase (χ''(T)) components of the magnetic susceptibility, per mass of sample, corresponding to freeze-dried tissues from different embryos: (a, c) Embryos exposed to SC nanoparticles, (b, d) Embryos exposed to MC nanoparticles. (n=7 per group).

Iron metabolism

The study of in vivo fate of NPs is imperative to develop successful biomedical applications. The safety assessment of nanoparticles should include different nanotoxicological tests after nanoparticles exposure, but also monitoring the material biodegradation and integration in the metabolic pathways. Since iron resulting from NPs' degradation is predicted to be processed by iron metabolic pathways, we next studied the expression of different genes involved in iron metabolism and oxidative stress. The ex-

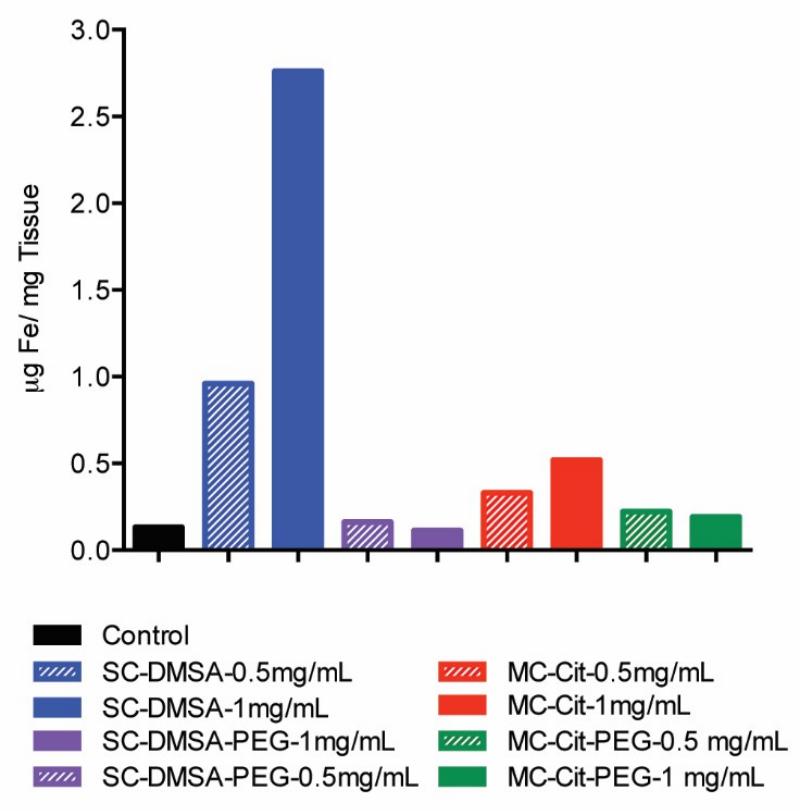

Figure 5.9: Iron quantification though ICP-OES of the freeze-dried tissues from different embryos: On the left treated an iron concentrations of 0.5 mg/mL, and on the right of 1 mg/mL.

pression of genes linked to iron metabolism was assessed by real-time quantitative PCR (RT-qPCR) in embryos treated with SC@DMSA and MC@Cit after 72 h of treatment with the nanoparticles at 1 mg/mL.

In the SC@DMSA treated embryos, there is an increase of dmt1 1.9 times higher than the control coupled with a downregulation of hepcidin of 0.3 times. The levels of transferrin are also increased 2.6 compared with the control. Contrary, the MC@Cit treated embryos do not seem to have an increase in the levels of dmt1 and transferrin. In both cases the expression of ferritin is increased after nanoparticle treatment, 2.9 fold change for SC@DMSA and 1.9 fold change for MC@Cit treated embryos.

From this data we can describe differences in the metabolization speed of single core or multicore nanoparticles. After iron ingestion, ferrous ions (Fe^{2+}) are absorbed in the enterocytes through the divalent metal transporter^{-1} (DMT1). In the apical membrane of the enterocytes, the duodenal cytochrome B (Dcytb) facilitates the reduction of ferric to ferrous ions enabling the absorption of iron. In the basolateral membrane of the enterocytes the ferroportin transporter is located together with hepcidin, which

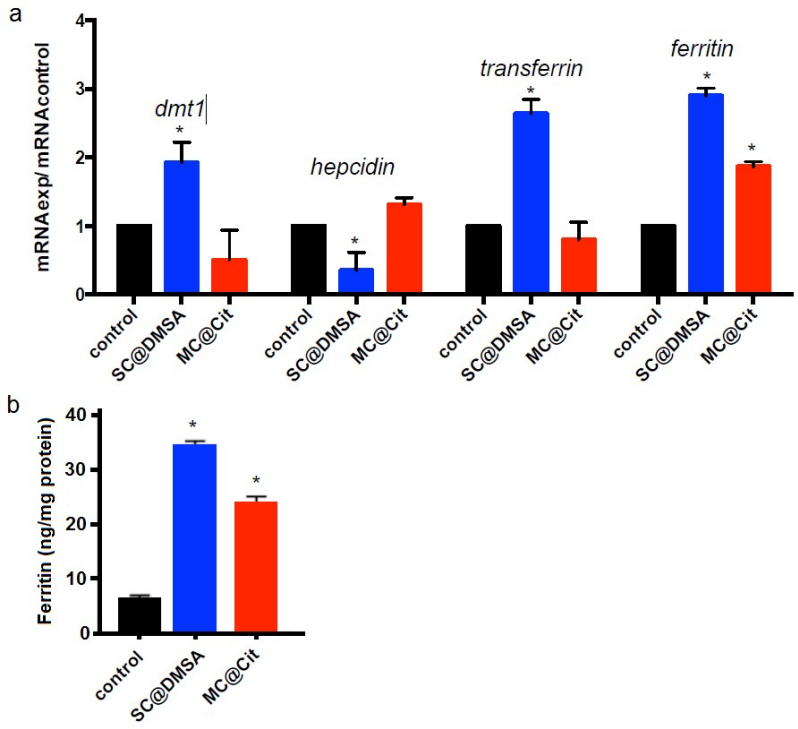

Figure 5.10: (a) Effect on the expression of different genes involved in iron metabolism in X. laevis embryos exposed to SC@DMSA or MC@Cit. (n=7 per group). * shows statistically-significance compared with the control ($p<0.05$) (b) Ferritin formation in Caco-2 cells exposed to 250 μM of single or multi-core nanoparticles. Cells were exposed for 24 hours with the different nanoparticles treatments. Data represent means $\pm$ SD (n=3).

regulates the entry of iron into circulation through inhibiting ferroportin. In the bloodstream, transferrin is capable to bind iron exported by ferroportin and carry it through the different organs. Ferritin is the most important protein involved in iron storage within cells, and the levels of Fe^{2+} present in the organism regulates its expression.[40]

From magnetic measurements and elemental analysis we detected a higher absorption of SC@DMSA compared with MC@Cit. Depending on the amount of internalized particles, the embryos will trigger iron metabolic pathway with different speed. In the case of SC@DMSA treated embryos; dmt-1, transferrin and ferritin have the highest levels of expression. Hepcidin is already downregulated, which implies a saturation of the metabolic pathway of iron. In the case of MC@Cit only ferritin and hepcidin are upregulated corroborating a slower activation of the iron metabolic pathway depending on the amount of internalized particles after 72 h of treatment.

Although when in cell culture experiments we cannot observe the complex interactions around the

mechanism of NPs' degradation, we can describe some cellular aspects. In order to determine whether the iron released by the nanoparticles is bioavailable to the cells, we analysed ferritin formation in Caco-2 cells as a measure of cell iron uptake. Single core nanoparticles seems to be internalized by the cells more efficiently than multicore nanoparticles. This increase in the content of ferritin in the cells, measured by ELISA, is in agreement with the increase in the gene expression observed in Xenopus.

Oxidative stress

It has been described in macrophages treated with iron oxide hybrids nanomaterials, an increase in transcript levels of hmox1.[41] Hmox1 is induced after oxidative stress, reactive oxygen species or heavy metals, thus degrading haem group to form biliverdin and Fe^{2+}. The production of Fe^{2+} leads to the activation of iron regulatory protein (IRP) which is able to control the translation of iron sensitive protein like ferritin. In the absence of iron, IRP binds to ferritin mRNA and inhibits its translation. However, when iron ions are available, they bind to IRP and release it from ferritin mRNA, thus allowing its translation.[42] The increase in Fe^{2+} in the embryos 72 h after the treatment, activates iron response proteins, which activates the translation of proteins involved in iron metabolism such as ferritin. For the first time we are observing in vivo the activation by Hmox-1 of iron regulatory proteins and their effect in the transcription of ferritin mRNA associated to the treatment with iron oxide nanoparticles.

The rest of the genes studied (sod, catalase and gsr) showed an increase in the expression of enzymes involved in the attenuation of oxidative stress in the case of embryos treated with SC@DMSA compared with MC@Cit. These results suggest the activation of protective mechanisms depending on NPs' intake in order to reduce reactive oxygen species (ROS) generated during the biodegradation process. This is the early response of the organism when nanoparticle clearance induces the formation of ROS. However we are not in the presence of an acute state of oxidative stress when a general decrease of antioxidant enzymes takes place.[43]

5.4 Conclusions

In this work, the uptake and toxicity effects of DMSA, citric acid and PEG coated single-core and multi-core iron oxide magnetic nanoparticles has been studied in Hep G2 (human hepatocellular carcinoma) and Caco-2 (human colorectal adenocarcinoma) cell lines and in an amphibian animal model during its embryo development.

The viability of both cell lines is preserved in all cases when treated with the nanoparticles up to an iron concentration of 1000 μM. Above that concentration, DMSA and PEGylated nanoparticles caused toxicity on HepG2 and Caco-2 cell lines, respectively. In the case of the in-vivo viability, none of the single-core nor multi-core coated nanoparticles were found lethal for the embryos. However, at high iron concentration (1 mg/mL) the embryos showed defects in their body shape, especially in the intestine,

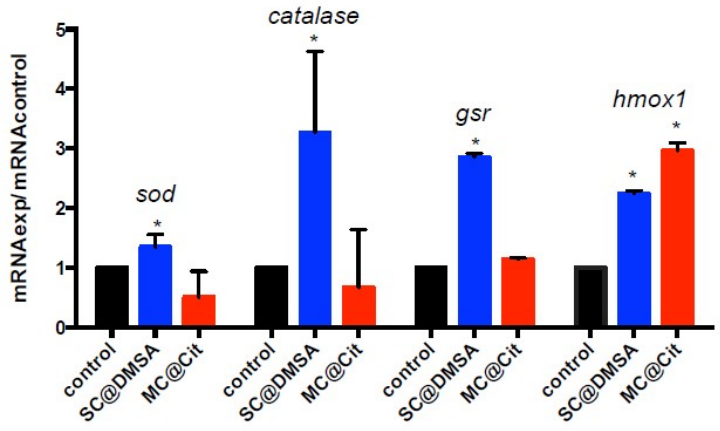

Figure 5.11: Effect on the expression of different genes involved in oxidative stress in X. laevis embryos exposed to single or multi-core nanoparticles. (n = 7 per group). * shows statistically-significance compared with the control ($p<0.05$).

tail bending and developmental delay. Furthermore, single-core nanoparticles are massively absorbed in comparison with multi-core nanoparticles. Non-accumulation of the NPs occurs when the surface charge is lower, i.e. in the case of PEGylated nanoparticles. For this system, the nanoparticles seem to be excreted. In order to confirm this, the iron content of the animal's faeces and the medium should be analysed. With the rise in production of nanoparticles for diagnostic or therapeutic purposes, the only way to reach the clinical practice is understanding the nano-biodegration of the particles.[44] Besides, at the present a dedicated regulatory framework for testing nanomedicines does not yet exist and cell based assays are the most current method of choice to describe nanomaterial biotransformation.[14, 15] With all these results, we provide evidence that an early developmental vertebrate models such as Xenopus laevis is a rapid and inexpensive systems for NPs toxicity assessment, compared with adult mammalian models. Because most theranostic applications need nanoparticles to be taken up by the cells, intracellular nano-biodegradation in an in vitro model needs to correlate with in vivo observations. In the case of IONPs degradation in vitro and their biodisponibility by the cells traduced in the increase of ferritin levels, should correlate with the corresponding activation of the iron metabolic pathway like we observed in this work.

Here, we demonstrated for the first time, the study, by means of AC magnetic susceptibility measurements, of the intake of iron-containing particles in X. laevis embryos. We can consider Xenopus as the bridge between cell-based assays and mammalian models taking into account that the activation of the iron metabolic pathway, especially with SC@DMSA, correlates with the previous results of the group in different murine models tracking IONPs biodegradation.[16, 34]

Bibliography

[1] Roger, J., Pons, J., Massart, R., Halbreich, A. & Bacri, J. Some biomedical applications of ferrofluids. *The European Physical Journal Applied Physics* **5**, 321–325 (1999).

[2] Schütt, W. *et al.* Applications of magnetic targeting in diagnosis and therapy—possibilities and limitations: a mini-review. *Hybridoma* **16**, 109–117 (1997).

[3] Laurent, S. *et al.* Magnetic iron oxide nanoparticles: synthesis, stabilization, vectorization, physicochemical characterizations, and biological applications. *Chemical reviews* **108**, 2064–2110 (2008).

[4] Alexiou, C. *et al.* Locoregional cancer treatment with magnetic drug targeting. *Cancer research* **60**, 6641–6648 (2000).

[5] Jordan, A., Scholz, R., Wust, P., Fähling, H. & Felix, R. Magnetic fluid hyperthermia (mfh): Cancer treatment with ac magnetic field induced excitation of biocompatible superparamagnetic nanoparticles. *Journal of Magnetism and Magnetic Materials* **201**, 413–419 (1999).

[6] Weissleder, R., Nahrendorf, M. & Pittet, M. J. Imaging macrophages with nanoparticles. *Nature materials* **13**, 125–138 (2014).

[7] Crichton, R. R. & Boelaert, J. R. *Inorganic biochemistry of iron metabolism: from molecular mechanisms to clinical consequences* (John Wiley & Sons, 2001).

[8] Balakumaran, A. *et al.* Superparamagnetic iron oxide nanoparticles labeling of bone marrow stromal (mesenchymal) cells does not affect their “stemness”. *PloS one* **5**, e11462 (2010).

[9] Geppert, M., Hohnholt, M. C., Nürnberger, S. & Dringen, R. Ferritin up-regulation and transient ros production in cultured brain astrocytes after loading with iron oxide nanoparticles. *Acta biomaterialia* **8**, 3832–3839 (2012).

[10] Hohnholt, M. C., Geppert, M. & Dringen, R. Treatment with iron oxide nanoparticles induces ferritin synthesis but not oxidative stress in oligodendroglial cells. *Acta biomaterialia* **7**, 3946–3954 (2011).

[11] Gu, J. *et al.* The internalization pathway, metabolic fate and biological effect of superparamagnetic iron oxide nanoparticles in the macrophage-like raw264. 7 cell. *Science China Life Sciences* **54**, 793–805 (2011).

[12] Rojas, J. M. *et al.* Superparamagnetic iron oxide nanoparticle uptake alters m2 macrophage phenotype, iron metabolism, migration and invasion. *Nanomedicine: Nanotechnology, Biology and Medicine* **12**, 1127–1138 (2016).

[13] Mulens-Arias, V., Rojas, J. M., Pérez-Yagüe, S., Morales, M. P. & Barber, D. F. Polyethylenimine-coated spions trigger macrophage activation through tlr-4 signaling and ros production and modulate podosome dynamics. *Biomaterials* **52**, 494–506 (2015).

[14] Mazuel, F. *et al.* Massive intracellular biodegradation of iron oxide nanoparticles evidenced magnetically at single-endosome and tissue levels. *ACS nano* **10**, 7627–7638 (2016).

[15] Rojas, J. M. *et al.* Time-course assessment of the aggregation and metabolization of magnetic nanoparticles. *Acta Biomaterialia (In Press* (2017).

[16] Ruiz, A. *et al.* Biotransformation of magnetic nanoparticles as a function of coating in a rat model. *Nanoscale* **7**, 16321–16329 (2015).

[17] James-Zorn, C. *et al.* Xenbase: Core features, data acquisition, and data processing. *genesis* **53**, 486–497 (2015).

[18] Nations, S. *et al.* Acute effects of fe_2o_3, tio_2, zno and cuo nanomaterials on xenopus laevis. *Chemosphere* **83**, 1053–1061 (2011).

[19] Nations, S. *et al.* Effects of zno nanomaterials on xenopus laevis growth and development. *Ecotoxicology and environmental safety* **74**, 203–210 (2011).

[20] Martín, M. *et al.* Magnetic study on biodistribution and biodegradation of oral magnetic nanostructures in the rat gastrointestinal tract. *Nanoscale* **8**, 15041–15047 (2016).

[21] Gutiérrez, L. *et al.* Synthesis methods to prepare single-and multi-core iron oxide nanoparticles for biomedical applications. *Dalton Transactions* **44**, 2943–2952 (2015).

[22] Faivre, D. *Iron Oxides: From Nature to Applications* (John Wiley & Sons, 2016).

[23] Torchilin, V. Tumor delivery of macromolecular drugs based on the epr effect. *Advanced drug delivery reviews* **63**, 131–135 (2011).

[24] Dutz, S., Kettering, M., Hilger, I., Müller, R. & Zeisberger, M. Magnetic multicore nanoparticles for hyperthermia—influence of particle immobilization in tumour tissue on magnetic properties. *Nanotechnology* **22**, 265102 (2011).

[25] Espinosa, A. *et al.* Duality of iron oxide nanoparticles in cancer therapy: amplification of heating efficiency by magnetic hyperthermia and photothermal bimodal treatment. *ACS nano* **10**, 2436–2446 (2016).

[26] Mulvaney, P., Parak, W. J., Caruso, F. & Weiss, P. S. Standardizing nanomaterials (2016).

[27] Lázaro, F. J., Gutiérrez, L., Abadía, A. R., Romero, M. S. & López, A. Biological tissue magnetism in the frame of iron overload diseases. *Journal of magnetism and magnetic materials* **316**, 126–131 (2007).

[28] Gutiérrez, L. *et al.* Bioinorganic transformations of liver iron deposits observed by tissue magnetic characterisation in a rat model. *Journal of inorganic biochemistry* **100**, 1790–1799 (2006).

[29] Lázaro, F. J. *et al.* Whole tissue ac susceptibility after superparamagnetic iron oxide contrast agent administration in a rat model. *Journal of Magnetism and Magnetic Materials* **311**, 460–463 (2007).

[30] Salas, G. *et al.* Controlled synthesis of uniform magnetite nanocrystals with high-quality properties for biomedical applications. *Journal of Materials Chemistry* **22**, 21065–21075 (2012).

[31] Sun, Q., Ren, Z., Wang, R., Chen, W. & Chen, C. Magnetite hollow spheres: solution synthesis, phase formation and magnetic property. *Journal of Nanoparticle Research* **13**, 213–220 (2011).

[32] Huh, Y.-M. *et al.* In vivo magnetic resonance detection of cancer by using multifunctional magnetic nanocrystals. *Journal of the American Chemical Society* **127**, 12387–12391 (2005).

[33] Martina, M.-S. *et al.* Generation of superparamagnetic liposomes revealed as highly efficient mri contrast agents for in vivo imaging. *J. Am. Chem. Soc* **127**, 10676–10685 (2005).

[34] Ruiz, A. *et al.* Short-chain peg molecules strongly bound to magnetic nanoparticle for mri long circulating agents. *Acta biomaterialia* **9**, 6421–6430 (2013).

[35] Glahn, R. P., Lee, O. A., Yeung, A., Goldman, M. I. & Miller, D. D. Caco-2 cell ferritin formation predicts nonradiolabeled food iron availability in an in vitro digestion/caco-2 cell culture model. *The Journal of nutrition* **128**, 1555–1561 (1998).

[36] Jia, B. & Gao, L. Morphological transformation of fe_3o_4 spherical aggregates from solid to hollow and their self-assembly under an external magnetic field. *The Journal of Physical Chemistry C* **112**, 666–671 (2008).

[37] Corot, C., Robert, P., Idée, J.-M. & Port, M. Recent advances in iron oxide nanocrystal technology for medical imaging. *Advanced drug delivery reviews* **58**, 1471–1504 (2006).

[38] Mahmoudi, M., Hofmann, H., Rothen-Rutishauser, B. & Petri-Fink, A. Assessing the in vitro and in vivo toxicity of superparamagnetic iron oxide nanoparticles. *Chemical reviews* **112**, 2323–2338 (2011).

[39] Goldstein, J. *et al. Scanning electron microscopy and X-ray microanalysis: a text for biologists, materials scientists, and geologists* (Springer Science & Business Media, 2012).

[40] Waldvogel-Abramowski, S. *et al.* Physiology of iron metabolism. *Transfusion Medicine and Hemotherapy* **41**, 213–221 (2014).

[41] Elgrabli, D. *et al.* Intracellular degradation of functionalized carbon nanotube/iron oxide hybrids is modulated by iron via nrf2 pathway. *Scientific reports* **7** (2017).

[42] Eisenstein, R. & Munro, H. Translational regulation of ferritin synthesis by iron. *Enzyme* **44**, 42–58 (1990).

[43] Radu, M. *et al.* Exposure to iron oxide nanoparticles coated with phospholipid-based polymeric micelles induces biochemical and histopathological pulmonary changes in mice. *International journal of molecular sciences* **16**, 29417–29435 (2015).

[44] Bouwmeester, H. *et al.* Minimal analytical characterization of engineered nanomaterials needed for hazard assessment in biological matrices. *Nanotoxicology* **5**, 1–11 (2011).

Part E

Conclusions

Conclusions

The main conclusions of Chapter 2 are:

- This route has allowed to produce a library of iron oxide magnetic nanoparticles in a core size range of 50-100 nm (in its minor axis) and three different shapes has been successfully demonstrated: rhombohedral, elongated and hexagonal discs.
- Both reduction methods were successfully applied, yielding a single iron oxide phase of magnetite. The magnetite phase has been verified by X-ray diffractograms, Mössbauer spectra and ZFC/FC magnetization curves.
- Magnetite nanoparticles coming from hematite precursor show a very clear Verwey transition at slightly lower temperatures than the reported ones for pure magnetite, probably due to small impurities or pores in the particles.
- The hysteresis (H_c) and saturation magnetization (M_s) parameters revealed that there is a difference between the magnetic material obtained by wet and dry reduction with higher values of both H_C and M_s in the case of dry reduction.
- Rhombohedra and needle shaped samples show, in the case of the wet reduction, interesting magnetic properties with a wasp-shaped hysteresis curve and a very low coercive field at room temperature originated probably from the domain formation within the particles.
- The approach for the reduction of the precursors has an influence on the magnetic behaviour of the final magnetite particles. MNPs that have been produced by dry reduction show fewer defects in the internal structure.

The main conclusions of Chapter 3 are:

- Structural differences between the assemblies of maghemite cores are directly related to their formation mechanism (clustering and coalescence, clustering and recrystallization or Ostwald ripening), free energy involved in the process and experimental conditions (pH, surface charge, temperature, pressure and time).
- Large values of crystal size (calculated from XRD or estimated by HRTEM) $>$ 10 nm indicates significant coalescence of the cores, displaying higher M_s values.
- The magnetic size deduced from our Langevin based modeling ($d_{c,2}$) is larger than calculated from XRD or estimated by HRTEM suggesting the presence of interactions between cores and thus shedding light on the collective behaviour within the nanoflowers.

- When there is a close contact between cores within a particle and continuity of the crystal orientation, magnetic ordering across the interfaces is favored. This is reflected in less pronounced relaxation effects (detected by Mössbauer spectroscopy) and higher χ_0 in the magnetization curve.
- Hydrodynamic sizes modelled by the extended multi-core function (ACS $D_{h,2}$) confirm that dipolar interactions between particles can be minimized in these colloids.
- If this modelled hydrodynamic size (ACS $D_{h,2}$) tends to approach the effective magnetic size ($d_{c,2}$) is due to exchange interactions, displaying collective magnetic behaviour. In this case, cores inside the nanoflower are not only oriented but also in close contact.

The main conclusions of Chapter 4 are:

- Sodium acetate is found to be a key parameter governing the self-assembly process. In this reaction, it has a double role: the particle formation, and the nucleation and growth. For higher acetate concentration, single-core particles are obtained. As the amount of acetate is reduced, the initial nanocrystalline subunits grow by partial aggregation in hollow spheres. Further reduction in acetate leads to initial nanocrystalline nuclei that strongly aggregate to produce the final nanoflowers.
- The synthesis of magnetic nanoflowers occurs via burst nucleation, growth by aggregation and recrystallization that takes place over time.
- The initial stages of the reaction are composed of lepidocrocite, which suffers a fast dehydroxylation, transforming to an intermediate “undescribed” phase - possibly a partly dehydroxylated lepidocrocite – that evolves to maghemite nanoflowers.
- Prolonged heating times of the raction lead to nanoflowers with increasing core size. The samples have increased saturation magnetisation and coercivity, and display increasing ILP values.

The main conclusions of Chapter 5 are:

- The use of cell lines and simplified animal models that are easy to handle, allow to select optimised samples and to study them, decreasing the number of tests in rodents.
- The viability of both cell lines is preserved in all cases when treated with the nanoparticles up to an iron concentration of 1000 μM. Above that concentration, DMSA and PEGylated nanoparticles caused toxicity on HepG2 and Caco-2 cell lines, respectively.
- In the case of the in-vivo viability, none of the single-core nor multi-core coated nanoparticles were found lethal for the embryos. However, at high iron concentration the embryos showed defects in their body shape, especially in the intestine, tail bending and developmental delay.

- Single-core nanoparticles are massively absorbed in comparison with multi-core nanoparticles and non-accumulation of the nanoparticles occurs when the surface charge is lower, i.e. in the case of PEGylated nanoparticles. For these systems, the nanoparticles seem to be excreted. In order to confirm this, the iron content of the animal's faeces and the medium should be analysed.
- The degradation of iron oxide nanoparticles in vitro and their biodisponibility by the cells is traduced in an increase of ferritin levels, which is in agreement with the corresponding activation of the iron metabolic pathway. Intracellular nano-biodegradation in vitro correlates with in vivo observations.

Part F

Summary

Summary

Introduction

In this thesis, iron oxides nanoparticles has been the case of study (more specifically magnetite and maghemite iron oxide phases), since this nanomaterial presents some interesting features and advantages that arise from its chemical composition and atomic structure. First, the most important feature is that magnetic nanoparticles obey Coulomb's law,[1] and this means that they can be manipulated by an external magnetic field gradient. Moreover, magnetic nanoparticles can be made to resonantly respond to a time-varying magnetic field, with advantageous results related to the transfer of energy from the exciting field to the nanoparticle.[2] Finally, magnetic nanoparticles affect the relaxivity of surrounding protons. Based on these features, magnetic nanoparticles are emerging functional materials in material science industry and biomedicine.

Thus, both systems of ferrimagnetic (FM) and superparamagnetic (SP) magnetic nanoparticles have been studied. The magnetic behaviour that they exhibit has been modulated by modifying: their size, shape and interactions. As follows, how these parameters affect such behaviour are described:

- Particles with size below a critical value D_{SD} (Single-domain diameter) have decreased coercive force with decreasing particle size. When it reaches a zero value, the specimen is in the superparamagnetic regime. Superparamagnetism is a form of magnetism, which appears in small ferromagnetic or ferrimagnetic nanoparticles. In sufficiently small nanoparticles, magnetization can randomly flip direction under the influence of temperature, and after being exposed to an external magnetic, since they have zero coercive field, the measured magnetization will average to zero. In this state, an external magnetic field is able to magnetize the nanoparticles, similarly to a paramagnet. However, their magnetic susceptibility is much larger than that of paramagnets. This is why this type of magnetic material has been proposed as ideal material for biomedical

applications.

- Distortions of particle shape can induce additional anisotropy (directional dependence of a material's magnetic properties), stabilizing (or destabilizing) the single-domain state. Small deviations from uniformity in the magnetization field within the nanoparticles can play an essential role in determining its magnetic properties (susceptibility, anisotropy, hysteresis features, etc.).[3]

- In nanostructured magnetic materials, interactions between nanoparticles often play an important role. Interparticle interaction effects greatly depend on the distance between the magnetic nanoparticles. For long distances (assuming therefore a non-interacting NPs system), the magnetic behaviour is determined by the superparamagnetic state at finite temperatures. However, for cases when the distance between the magnetic NPs is shorter, the superparamagnetic state can be altered by magnetic dipole interactions and by exchange interactions between particles.[4] As a result, increasing dipole–dipole interactions disturb the energy landscape by occurrence of local energy minima[5] and leads to decreasing coercivity and remanence. On the other hand, exchange interactions in SP NPs can lead to ferri/ferromagnetic behaviour with hysteresis.

Thus, controlling such parameters allow the design and fabrication of nanomagnetic systems with predefined magnetic properties.

Paying attention to the structure of magnetic nanoparticle in solution, they have been recently divided in the literature into single-core nanoparticles (with only one magnetic core per particle) and multi-core nanoparticles (with several magnetic cores per particle) (Figure 1). Single-core particles are usually coated by some chemical or biochemical active surface layer that help to have the particles isolated. On the contrary, multi-core nanoparticles have a matrix that binds the magnetic cores together to form the final particle, and they are usually coated by a surface layer. Moreover, above the superparamagnetic regime, the nanoparticles will have a permanent magnetic moment even at RT, which usually implies some degree of agglomeration. This agglomeration, unlike multi-core particles, can be temporarily reversed (e.g. by mechanical stirring or sonication), however the agglomeration is only avoided when steric or electrostatic repulsion is successfully achieved. But how can this colloid feature be controlled? Ideally, by controlling the growth mechanism and the coating process of the magnetic nanoparticles.

Therefore, the first point to consider is the synthesis of iron oxide magnetic nanoparticles. In this sense, as-synthesized single-cores have been obtained through high temperature thermal decomposition of organic precursors and by the polyol-mediated process. It is necessary that a simple burst nucleation occurs at critical supersaturation point, generating initial nuclei that grow in a controlled way, in the diffusion growth regime.[6] This model of nucleation is explained by the LaMer theory.[7, 8] In addition, there must be a reagent (oleic acid/oleylamine or a polyol of certain length in the case of thermal decomposition of organic precursors and polyol-mediated synthesis, respectively) that acts as a surfactant controlling the distance between the nuclei and limiting the growth. Many factors that

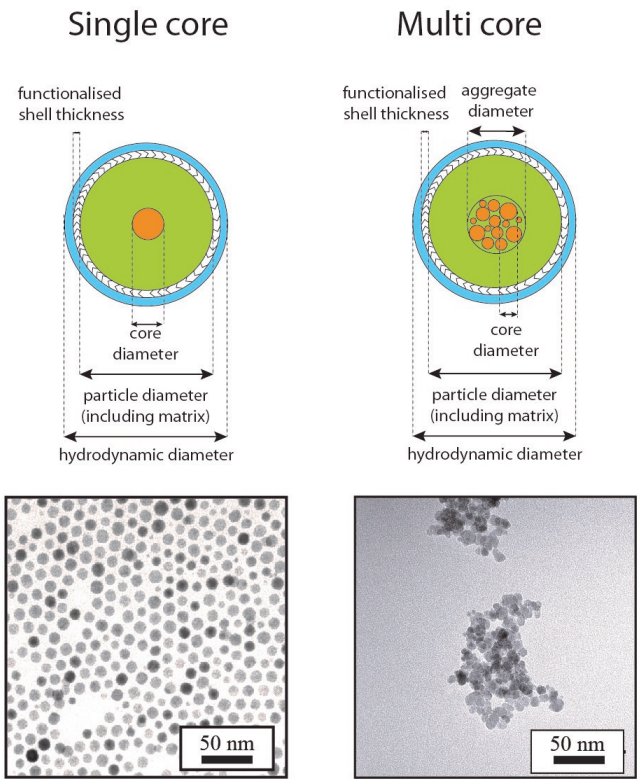

Figure 1: Structure of magnetic nanoparticle colloids and representative examples that exist in the literature: Single-core NPs are represented by oleic acid coated magnetite NPs synthesized by high T thermal decomposition. Multi-core NPs are represented by co-precipitation NPs post-coated with citric acid.

are interplay are responsible for the formation of single core particles and to control them keeping the monodispersity is a challenge. In terms of the shape of magnetite nanoparticles, spherical, cubical and rhombohedral morphologies are commonly obtained, but the rest of the morphologies are not covered by the traditional-direct methodologies. The synthesis of a precursor and its transformation to the magnetite phase is required preserving the nanoparticle morphology and it is not an easy task. In addition, the use of magnetic colloids for biomedical purposes, requires the NPs to be disperse in aqueous media, and those single-cores obtained organic media require further steps in order to transfer them to water.

On the other hand, multi-core systems have been obtained in two ways: by the in-situ addition of certain polymers causing a reduction in surface charge density of the growing nuclei promoting its approach and clustering, and achieving the oriented aggregation of small subunits in an assembly process, based on monomer-by-monomer addition growth model,[9] or driven by the presence of specific

molecules or under the action of an external field. However, there is a lack of control over the number of cores per particles and the interaction between them, thus it is aimed to obtain highly regular structures.

Once designed the magnetic colloid. What's the next step to fabricate a functional material? Typically, magnetic NPs for different applications need to be composed of not only the magnetic core, but also a spacer that protects the core, prevents it from aggregation when forming a colloid,[10] or that acts as a platform for extra functionality for specific applications. This spacer can have inorganic or organic nature. Furthermore, in addition to the inorganic/organic coating, which usually serves as a linker, more complex molecules or biomolecules should be bind on the surface of the particle, in order to provide a real activity (Figure 2).

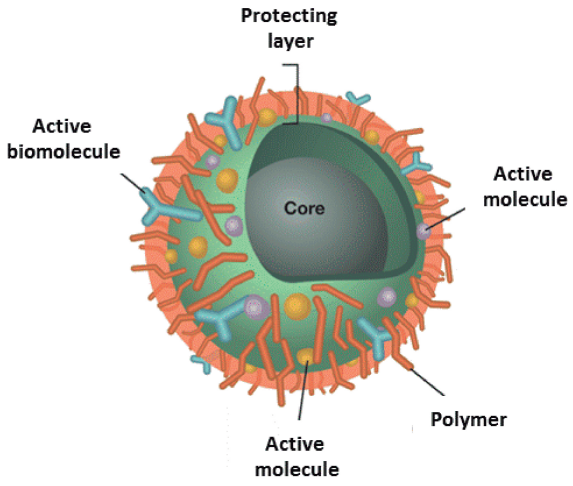

Figure 2: Structure of a functional magnetic nanoparticle: it is composed of a magnetic core coated by a protective layer. In order to bind an active molecule, an organic linker is often used.

Lastly, iron oxide magnetic nanoparticles in the form of colloids opened up a wide range of attractive possibilities in biomedicine. This was a direct result of their nanometric features. First, because they are sufficiently small to enable interactions with biological entities, such as receptor molecules, etc. while displaying a size large enough (with a likewise high ratio of surface area to volume) to carry an imaging or therapeutic payload. Magnetic NPs display interesting assets as they are able to i) establish a locally perturbing dipolar field in the presence of a magnetic field, ii) be manipulated by an external magnetic field gradient as they experience a magnetic force resulting in magnetophoretic mobility, and iii) generate thermal energy when exposed to an AMF. From all these outstanding properties derive important biomedical applications such as MRI contrast enhancement, drug and cell targeting and magnetic hyperthermia (in-vivo applications) and magnetic separation (in-vitro application). In particular, the possibility of treating cancer by magnetically induced hyperthermia has led to the development of many different devices designed to heat malignant cells while sparing surrounding healthy tissue.[11]

In broad terms, the procedure involves dispersing magnetic particles throughout the target tissue, and then applying an AC magnetic field of sufficient strength and frequency to cause the particles to heat. This heat conducts into the immediately surrounding diseased tissue whereby, if the temperature can be maintained above the therapeutic threshold of 42° C for 30 min or more, the tumour cells die.

However, prior use of IOMNPs in the field of biomedicine, there is a demand in the standardisation of their synthesis and analysis methods. This would ensure the reproducibility in the fabrication of these nanoparterials and would serve to define and constrain some characteristics (of their structure and magnetic nature) important in their safe use in biomedicine. Apart from that, it is necessary to study and assess the biotransformation and toxicity of IOMNPs in animal models. If these demands were met, magnetic nanoparticles produced in the laboratories could be transferred to clinic.

In conclusion, this summarised introduction presents the advantages of magnetic nanoparticles and clarifies why iron oxides have been proposed as ideal nanomaterials for emergent biomedical applications. Their magnetic behaviour depends strongly on their size, shape and interactions, and in this Thesis work, these latter two parameters have been modulated, always keeping the size in the nanoscale.

Objectives

This Thesis work has been carried out in the framework of the European project “NanoMag” (grant agreement n° 604448), whose objectives are to standardize, improve and redefine analysing methods of magnetic nanoparticles and to develop reference samples for biomedical applications.

Thus, it was oriented toward general tasks:

- Synthesis of uniform iron oxide nanoparticles controlling their size, shape, internal structure, assembly and consequently, tailoring their magnetic features.
- Comprehensive characterisation of the nanomaterials shedding light on the relationship between structure and properties.
- Functionalisation with molecules/polymers suitable for the interaction with a biological system.
- Assessment of the toxicity of the magnetic nanoparticles and quantification in a biological system.

Attending to the structure of a magnetic nanoparticles (single-core or multi-core), the specific objectives of this thesis are:

- Optimisation of the synthesis of single-core anisometric magnetic nanoparticles.
- Optimisation and study of the self-assembly processes to obtain multi-core flower-shaped magnetic nanoparticles. Analysis of the size (core and particle) effects on their magnetic properties.
- Study of the toxicity, accumulation and detection of single-core and multi-core magnetic nanoparticles in-vitro and in a novel simplified animal model easy to handle.

Results

Chapter 2. How shape and internal structure affect the magnetic properties of anisometric magnetite nanoparticles

The up-above mentioned applications of magnetic MNPs require MNPs with customized structural and magnetic properties, which are strongly dependent on both particle size and shape [12]. For magnetic hyperthermia, maximum heating rate is obtained at the transition from multidomain to single domain magnetic behaviour occurring in a relatively broad size range at about 30 nm with a change of transition of magnetic energy into thermal energy (Néel or Brown) [13]. Furthermore, nanoparticle shape can also have significant impact on the magnetic behaviour of MNPs in applications. Firstly, because the magnetic shape anisotropy of the MNPs can assume much larger values than the magnetocrystalline anisotropy and thus can strongly affect the orientation of magnetic moments inside the particles. In addition, dipolar interactions between MNPs also depend on the particle shape and will influence the structural agglomerate formation leading to, for example, chain-like arrangements biomimicking magnetotactic bacteria [14] or hollow spheres consisting of oriented aggregates of nanocrystals [15, 16].

In Chapter 2, we describe an alternative aqueous-based approach to produce single-core magnetite MNPs with different morphologies and core sizes above 25 nm, which could be scalable for large production. Magnetic iron oxide nanorods were already produced by a similar method and showed interesting magnetic properties and tuneable surface functionality [17].

We propose a three-step process from which uniform rhombohedra, discs and elongated MNPs can easily be obtained. First, an aqueous synthesis route is followed to obtain uniform antiferromagnetic precursors such as goethite or hematite, whose size and shape can be tuned by changing the synthesis conditions including temperature, pressure, and nature and concentration of the salts used [18]. Then, the antiferromagnetic precursor particles are coated by a silica layer that prevents their aggregation [19, 20]. Finally, the silica coated antiferromagnetic particles are reduced to magnetite. This is either performed on particles in powder form (dry-reduction), by exposing them to a hydrogen atmosphere at a certain partial pressure [21], or in liquid form, using oleic acid and an organic solvent (wet-reduction).

After the synthesis of the precursors and before the particles were coated, their morphology has been investigated by SEM. The scanning electron micrographs of the precursors (Figure 3) show the three different morphologies obtained: (A) rhombohedra, (B) hexagonal discs and (C) needles. Both the size and the shape of the nanoparticles are highly homogeneous.

After the synthesis of the precursors the nanoparticles are coated with a silica shell and they were transformed to magnetite by a dry or a wet reduction method. As a result, the precursor has been successfully coated with a uniform silica shell around single cores or double-triple cores ($\sim$ 75%), although a fraction of multi-cores (5-10 cores coated) ($\sim$ 25%) cannot be discarded. TEOS condensation occurs only on the surface of the NPs and no colloidal silica nanoparticles have been observed.

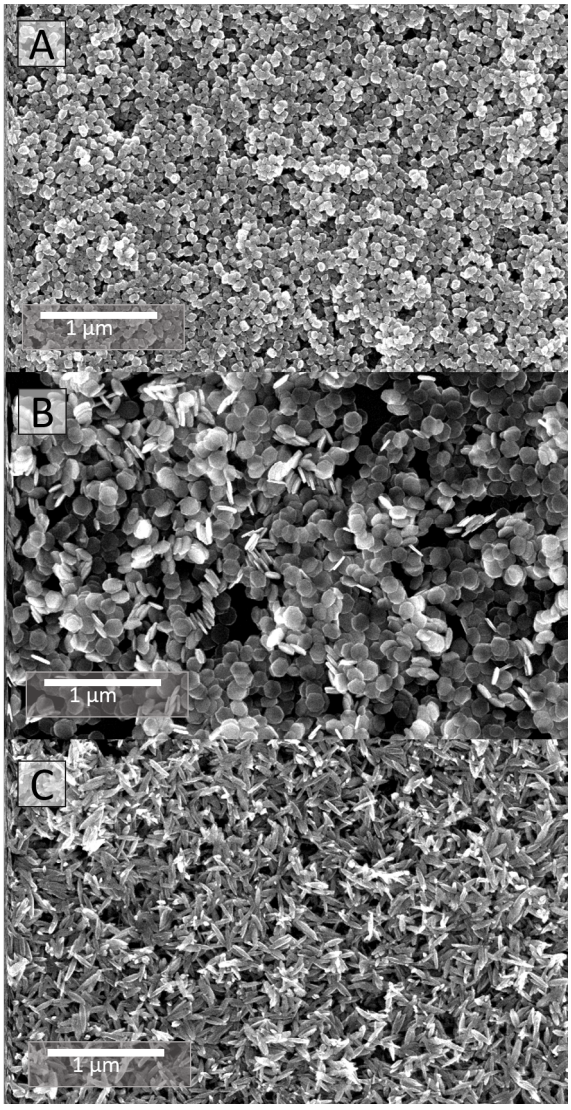

Figure 3: SEM images of the precursor material (A) rhombohedra, (B) discs and (C) needles.

When the silica coated goethite nanoparticles (either in powder or in solution) are heated up above 350° C, dehydration firstly occurs forming directly hematite. The nanoparticles develop porosities within the structure due to the expulsion of water [18], occurring along the central axis of the needles, often merging with a single, elongated defect running along the entire length of the crystallite [22]. Pores along the c-axis were also reported [23] in good agreement with our observations. In spite of the porosity, a continuous single-crystalline structure corresponding to a monocrystal has been demonstrated for the needles. After the dehydration, the nanoparticles are reduced to magnetite without interparticle sintering and this is because of both the silica shell and the mild temperatures used for reduction (below 600°C).

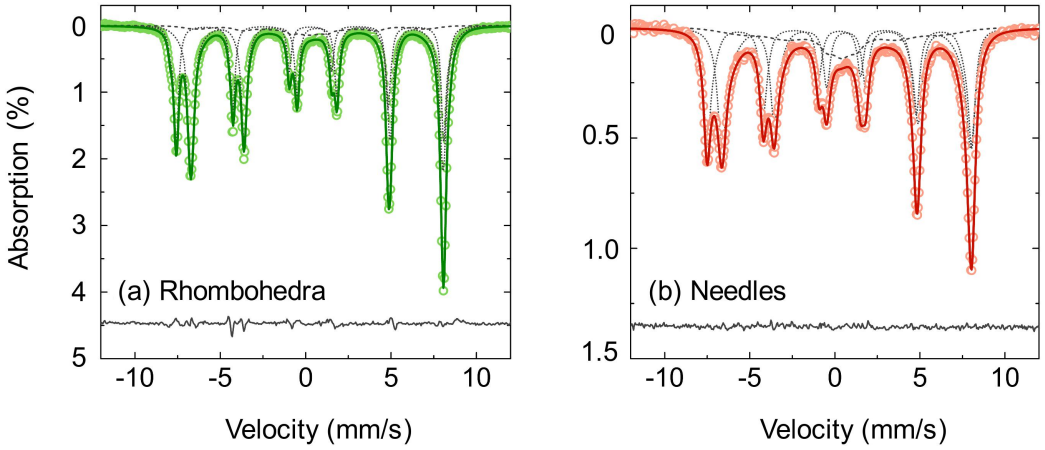

Figure 4: Comparison of room temperature Mössbauer spectra for (a) rombohedra and (b) needles after reduction. For each, points are the observed counts, the solid line is the modelled best fit to the data, and the dotted liens are the Voigtian sub spectra The quality of fit is indicated by the reduced χ^2 and the residual, given by I_{obs}-I_{cal}.

Room temperature Mössbauer spectra (Figure 4), along with X-ray Diffraction and FTIR spectroscopy confirm the correct transformation to magnetite and though MS, the tetra and octahedral sites within magnetite are detected.

The magnetization curves of the samples (Figure 5) show similar behaviour for different shapes and different reduction techniques. The samples exhibit non-zero remanence and coercivity indicating that the particles are magnetically blocked at room temperatures and below. Looking into the details, it can be seen that the rhombohedra and needles obtained by wet reduction present a so-called wasp-waisted hysteresis loop, which is not observed in the materials produced by dry reduction. Roberts et al. explained the occurrence of a wasp-waisted hysteresis loop by a mixture of single- and multi-domain remanence states within the particles [24].

Since the samples prepared by dry reduction do not show the wasp-waisted hysteresis behaviour, it seems that this reduction technique produces particles with a more uniform magnetization state com-

pared to the particles synthesised by wet reduction. This is in good agreement with the findings on the crystallite size measured by XRD, because defects and pores are usually responsible for the pinning and nucleation sites for magnetic domains, and obviously these defects and pores are less pronounced for dry reduced MNPs.

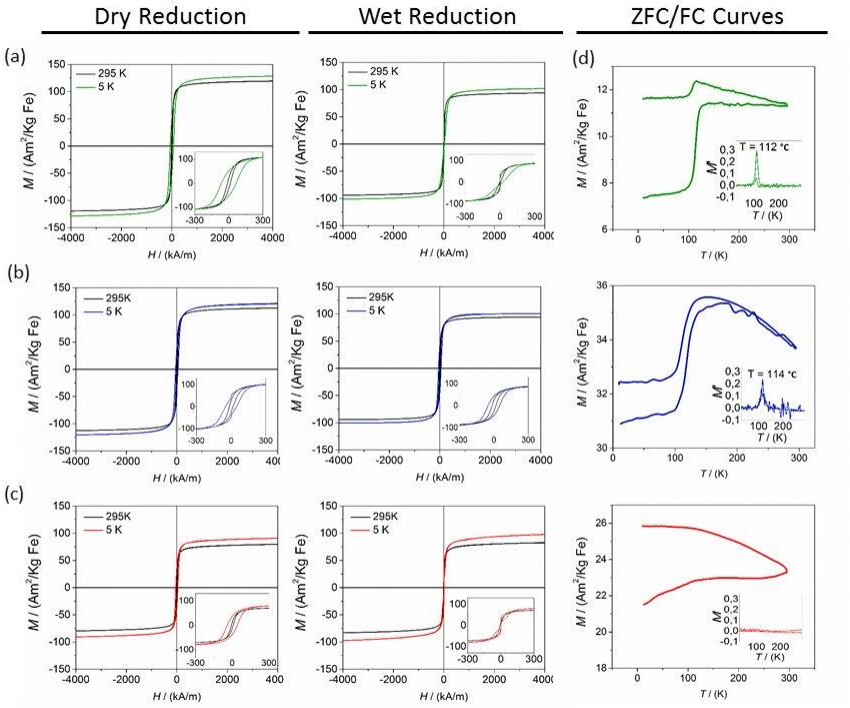

Figure 5: Hysteresis cycles at 295 and 5 K for all particle morphologies (green=rhombohedra, blue=disks, red=needles), comparing wet and dry reduction. Inset: the hysteresis cycles at low field regime ($\pm$ 300 kA/m) are shown. In addition, ZFC/FC curves (measured at 5 mT) of samples reduced in liquid are presented with the inset showing the first derivative of the magnetization with respect to temperature.

The value of M_s is largest for the rhombohedra while the discs exhibit the lowest saturation magnetization and that can be traced back to influences of the particles size. Interestingly, the saturation magnetization is considerably lower for the wet reduced particles than for dry reduction indicating again a significant effect of the reduction process and the presence of pores on the magnetic properties of the material. For the disc shaped particles the coercivity is identical in the wet and in the dry reduced samples. The coercivity of the rhombohedra and the needles cannot be compared due to the wasp-waisted hysteresis behaviour in case of wet reduction.

Field dependent magnetization curves recorded at higher field sweeping rates for the rhombohedra

and needles are shown in Figure 5. Here the wasp-waisted hysteresis curve as observed in quasi-static magnetization measurements has vanished. The fact that the hysteresis curve depends on the field change rate indicates that the wasp-waisted hysteresis curves originate from domain formation within the particles, since the nucleation of domain wall and its movement are time dependent [25].

Zero-field cooled/field cooled (ZFC/FC) magnetization curves of all products obtained from wet reduction are shown in (Figure 5). A clear Verwey transition [26] is observed in the case of rhombohedra and discs at 112-114 K (obtained from a hematite precursor). However, the transition in case of the discs is less sharp than for the rhombohedra. In case of the needles (obtained from a goethite precursor) the Verwey transition is almost invisible.

The fact that almost no transition is observed in the needles could be associated to the smaller crystal size as determined by XRD for this sample and the observation of a porous structure within a single particle by HRTEM. Mössbauer spectra support this conclusion showing broader lines and a central singlet for the needles suggesting poorer crystallinity, which would explain the loss of the Verwey transition. The shape of the Verwey transition for the different morphologies, especially for the smeared out transition of the discs, could be traced back to the existence of pores inside the particles and therefore a less-ordered crystal structure.

Chapter 3. Colloidal Flower-shaped Iron Oxide Nanoparticles: Synthesis Strategies and Coatings

Despite the progress in colloidal self-assembly of organic[27] or inorganic[28, 29] building blocks to form close-packed structures such as colloidal crystals,[30] there are only a few reports of controlled assembly of ordered nanoparticles in suspension.[31] Aggregation is a general mechanism of particle formation now recognized as a common growth phenomenon for many different monodisperse nanoparticles,[32–36] in contrast to the monomer by monomer addition that is described in classical models. In the case of magnetic nano-particles (MNPs), this is - a priori - different due to additional forces that arise as a consequence of their magnetic moment. These interactions can be either intraparticle ex-change interactions, or long-range magnetostatic dipolar forces between particles. Exchange interactions between cores of a multi-core particle may lead to the so-called “superferrimagnetic” behaviour,[37] exhibiting large magnetic moment and weak remanence in zero field, and thus, having low tendency to form agglomerates. On the other hand, dipolar interactions between particles with sufficient high moment account for the formation of configurations such as chains, which may change strongly the magnetic properties of the colloid.[38]

As a consequence, the assembly of MNPs in multi-core structures can, in some cases, give rise to collective magnetic properties, which yields microscopic magnetic behaviour that is very different from single-core nanoparticles or bulk materials.[39, 40] Such multi-core nanoparticles are currently of great interest in many different areas such as catalysis,[41] ferrofluids and rheology,[42] as well as bioapplications, which are mainly focused on iron oxide nanoparticles (magnetite or maghemite) because of their low toxicity.[43] Colloids made of magnetic multi-core nanoparticles show high NMR relaxivity (r_2),[10] high MPI signals,[44] high specific absorption rate of AC field (SAR),[45–47] high magnetic moment when manipulated with an external magnet[48] and enhanced performance as theranostic agents.[49–51]

In Chapter 3, we analyse the key synthesis parameters driving the self-assembly process capable of organizing colloidal magnetic cores into highly regular and reproducible multi-core nanoparticles showing the so called “superferrimagnetic state” due to exchange interactions. For that purpose we have conducted a comparison of four different synthesis of colloidal magnetic multi-core structures called flower-shaped nanoparticles (Figure 6), consisting of iron oxide cores that are aggregated to form isometric 3D arrangements.

Comprehensive structural and magnetic characterisation of colloidal dispersions and freeze-dried powders were performed following standardized protocols to facilitate comparison of these structures.[52] This is the first step towards standardization of synthesis and characterization of these nanoparticles, which is an important concern and demand nowadays.[53] First, we analysed the core size through HR-TEM, XRD and M v H curves (by means of the Langevin function). Secondly, we studied the core arrangement within the particle and the interparticle interactions. Therefore, the particle size is calculated

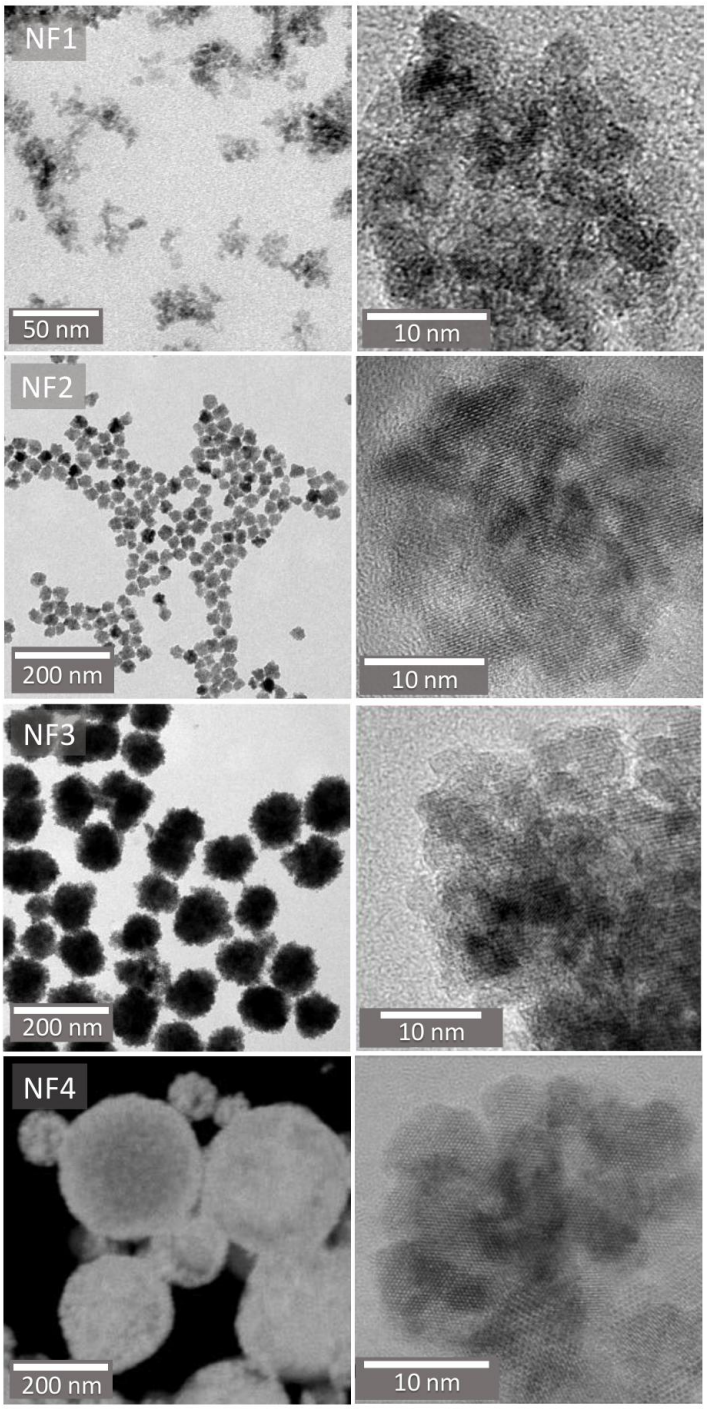

Figure 6: TEM (NF1-NF3), STEM (NF4) (left), and HRTEM images (right) of the different flower-shaped nanoparticles.

through TEM, DLS and ACS v f (by means of the Debye model and the Multi-core extended model). Each technique gave a characteristic core/particle size that allowed us to determine key parameters driving the magnetic behaviour of the colloids of flower-shaped nanoparticles, and are summarised in Figure 7. The size of the cores range from 4 to 15 nm and the size of the particle range from 50 to 250 nm. Differences in both, core and particle size reflect the complicated nature of these materials. In general, the size calculated via XRD (D_{XRD}) is larger than that estimated via HRTEM (D_{HRTEM}). This reflects the multi-core nature of the samples, whose cores are fused to a greater or lesser degree to form flower-shaped structures.

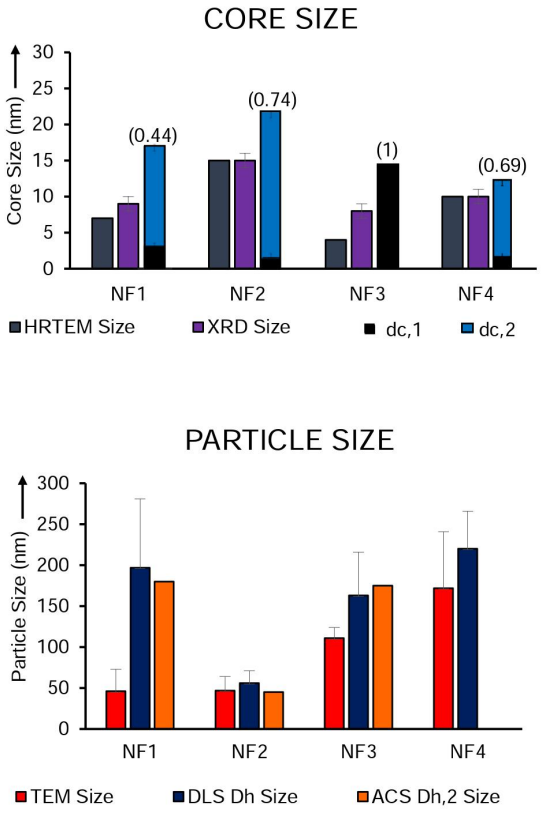

Figure 7: Core (above) and particle size (below) of the flower-shaped nanoparticles as determined by structural and magnetic means, according to Table 3.1 and 3.2. Between brackets, β is included, the normalized fraction of the larger particle size distribution as determined by DC magnetometry.

In those cases with high values of $D_{XRD} \approx D_{HRTEM} > 10$ nm (NF2 and NF4), significant coalescence of the cores is detected, which justifies the highest M_s values displayed by those samples.

For all cases, the magnetic size deduced from our Langevin based modelling ($d_{c,2}$) is larger than both D_{HRTEM} and D_{XRD} suggesting the presence of interactions between cores and thus shedding light on the collective behaviour within the nanoflowers. We surmise that when there is a close contact between cores within a particle, the continuity of the crystal orientation is ensured favouring magnetic ordering across the interfaces. This is indeed the case of the structures previously called nanoflower that showed one order of magnitude higher heating rates than the specific absorption rate (SAR) reported for conventional 11 nm maghemite nanoparticles in the same field exposure conditions.[54]

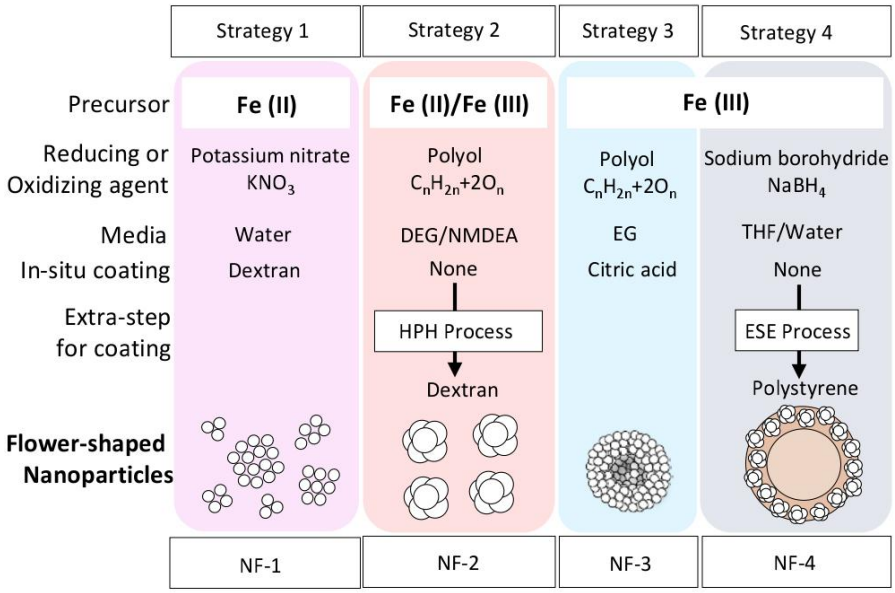

Figure 8: Strategies followed to obtain flower-shaped nanoparticles. N-methyl diethanolamine, HPH process stands for high-pressure homogenization coating and ESE process stands for emulsion solvent evaporation.

Regarding the particle size, samples in which DLS $D_h \gg D_{TEM}$ either contain a large amount of coating and water hydration on their surface or have collective behaviour between the particles (interparticle interactions, i.e. dipolar interactions). The former can be detected by IR spectroscopy and quantified by thermogravimetric analysis (See Figure S7). This is the case of NF1 and NF2 that have similar D_{TEM} particles sizes and therefore similar surface-area-to-volume ratios but they have very different organic content (80% for NF1 and 20% for NF2). Consequently, DLS D_h size of NF1 is much larger than D_{TEM} and hence indicates a larger amount of dextran present on the nanoparticles surface compared to NF2.

The collective behaviour that is related to interparticle interactions can be detected by AC susceptibility. All samples have comparable hydrodynamic sizes obtained by both DLS D_h and ACS $D_{h,2}$

(modelled by the extended multi-core function), confirming that dipolar interactions between particles are minimized in these colloids and explaining the observed long-term stability. In the case of NF3, dipolar interactions between particles may cause the formation of chains and explain the observed change in AC spectrum with sample dilution.

Comparing core and particle size from the magnetic measurements, i.e. effective magnetic size ($d_{c,2}$) and hydrodynamic size ACS $D_{h,2}$, we have identified three different flower-shaped multi-core systems. For NF2, the effective magnetic size tends to approach the nanoflower size (ACS $D_{h,2}$ / $d_{c,2} \sim$ 1.8) indicating strong magnetic interactions between cores within a particle. Cores inside the nanoflower are not only oriented but also in close contact leading to exchange interactions, and therefore collective magnetic behaviour. For NF1 and NF3, the effective magnetic size is much smaller than the flower size (ACS $D_{h,2}$ / $d_{c,2} \sim$ 10) indicating less contact between cores, which in NF1 may be loosely packed within the flower. Much more complicated is the case of NF4, where nanoflowers were embedded onto polymeric spheres creating a superstructure. The relatively small nanoflower size, high anisotropy constant, but low blocking temperature of NF4 suggests that the finite size of the nanoflower systems is one of the key parameters that dictates their Néel relaxation properties.

Differences between the systems (NF1-4) are directly related to the various synthetic routes (Strategy 1-4, Figure 8), in terms of formation mechanism (clustering and coalescence, clustering and recrystallization or Ostwald ripening) and free energy involved in the process and experimental conditions (pH, surface charge, temperature, pressure and time). NF1 offers the possibility of large production and allows the synthesis of larger batches in aqueous media. The use of polyol media provides great control over core aggregation, which yields multi-core structures that consist of cores in more or less contact (NF2 and NF3) depending on the synthesis conditions. Furthermore, polyol media allows the use of higher reaction temperatures (200 °C) leading to fused cores within a particle e.g. NF2. However, in NF3, the use of an extra additive (sodium citrate) to facilitate the final dispersion of the particles in aqueous media hampers the aggregation of the cores in a similar way to dextran in the synthesis of NF1. However, it should be taken into account that high temperatures over long time as applied in the synthesis of NF2 and NF3 (10-12 h) generally lead to high-energy consumption (costs). Moreover, one-pot syntheses such as those followed to obtain NF1 and NF3 have advantages compared to the conventional step-wise reactions as used for NF2 and NF4.

This is the first step towards standardized protocols of synthesis and characterization of flower-shaped nanoparticles.

Chapter 4. Formation mechanism of maghemite nanoflowers synthesized by polyol mediated process

Through the polyol-mediated process, the iron oxide multi-core nanoparticles assembled in flower-shaped structures has been reported.[55, 56] In comparison with the single-core counterparts, these flower-like nanoparticles have shown enhanced longitudinal and transverse relaxivities for magnetic resonance imaging (MRI) contrast generation[57] and enhanced specific absorption rate (SAR) values for magnetic hyperthermia due to hysteresis heating.[58]

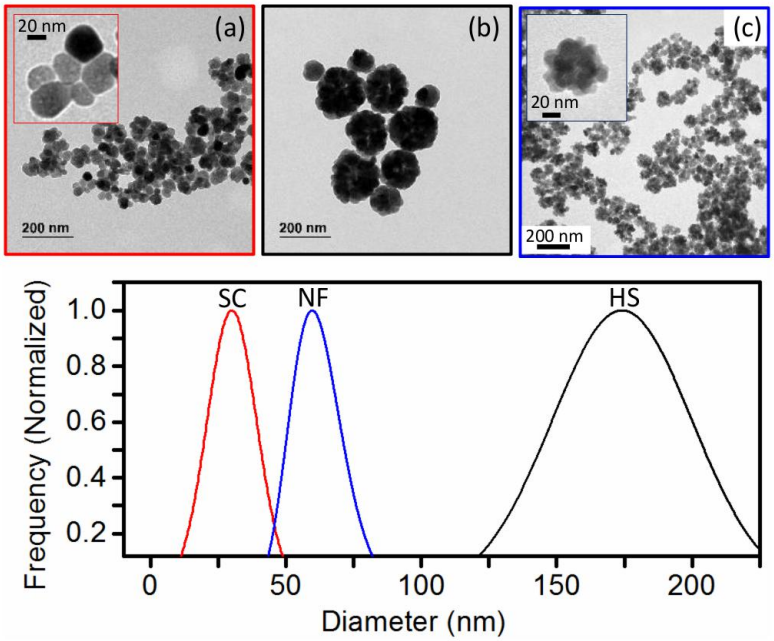

Figure 9: TEM images of the different structures obtained when varying the NaAc amount: (a) Single-core particles (SC), 36.5 mmol, (b) hollow spheres (HS), 26.2 mmol, (c) nanoflowers (NF), 15.8 mmol. Below, normalized log-normal TEM size distributions of the samples.

Assembly process and particle and core sizes are crucial characteristics that determine the magnetic properties of the colloid and therefore its optimal use for a given application.[59, 60]

In Chapter 4, we have analysed the assembly process that leads to the formation of single-core and multi-core hollow and flower-like maghemite nanoparticles through the polyol process. We have also determined the experimental parameters that allow control of the core sizes within the nanoflowers. In detail, we have analysed the role of specific experimental conditions in the synthesis such as the presence of a precipitator (sodium acetate, NaAc) and an extra stabilizer (polyvinylpyrrolidone, PVP), and the aging time. Then, the consequences of the different morphologies and core sizes on the

magnetic cooperative behaviour have been studied. Finally, some selected samples were coated with citric acid and the possible use of these particles for magnetic hyperthermia applications has been evaluated through specific loss power (SLP) measurements.

First, the amount of NaAc·3H_2O was varied from 15.8 to 36.5 mmol, while maintaining the rest of the reactants and conditions. Figure 9 shows TEM images of each sample and their normalized log-normal size distributions, obtained by manual measurement of the particle diameter through Image J software and further data fitting using Origin software.

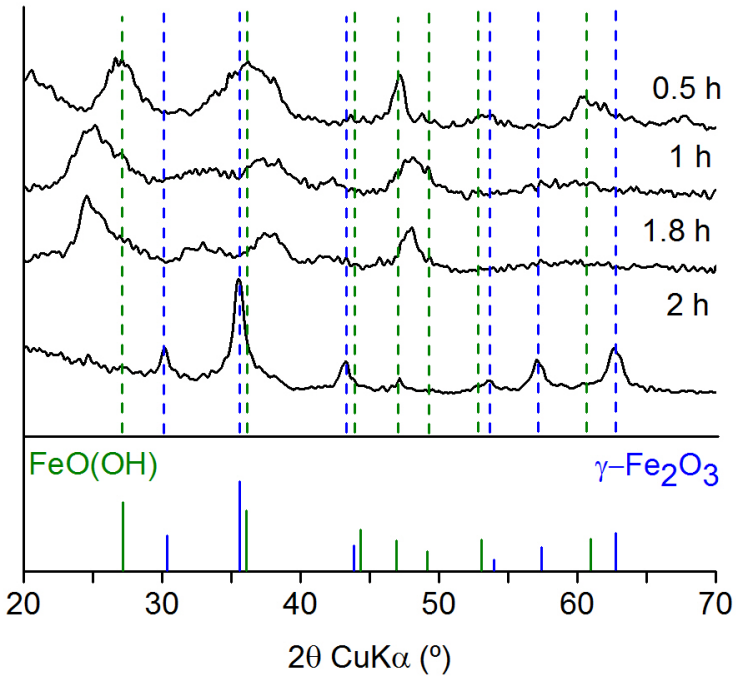

Figure 10: Formation mechanism of nanoflowers followed by X-ray diffraction of the powders collected after 0.5, 1, 1.8 and 2 h of aging time. Expected peak positions of lepidocrocite (γ-FeOOH, green) and maghemite (γ-$Fe_2 2O_3$, blue) are shown.

We found that the variation of NaAc concentration leads to nanoparticles with distinctly different structures (Figure 9). The highest concentration of NaAc (36.5 mmol) produced single-core nanoparticles of 35 nm (sample SC, Figure 9 a). However, when decreasing the NaAc concentration to 26.2 mmol, spherical hollow multi-core nanoparticles about 170 nm in diameter were formed (sample HS, Figure 9 b). The lowest amount of NaAc (15.8 mmol) yielded multi-core particles with flower-like structure (sample NF, Figure 9 c). In this case, the cores ($<$ 20 nm) are densely packed forming a nanoflower

particle with a characteristic size of $\sim$ 60 nm.

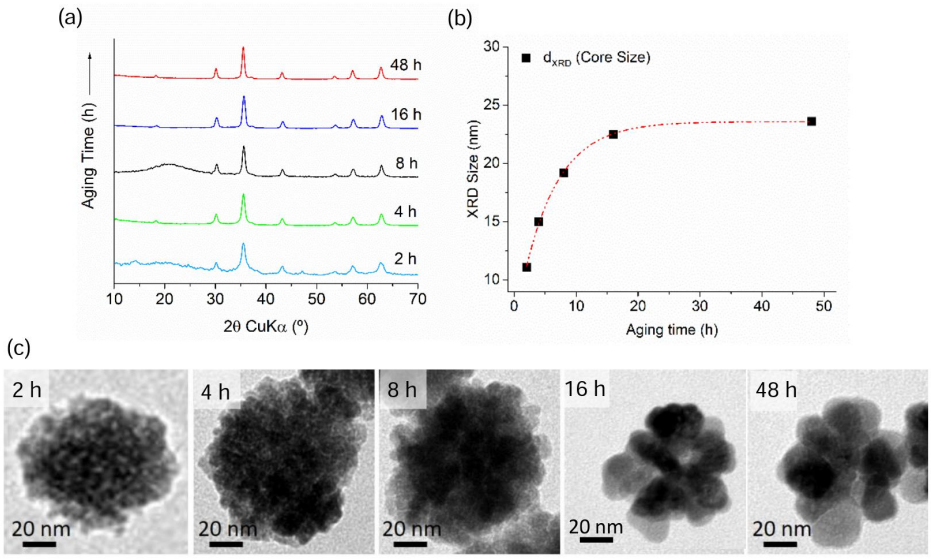

Figure 11: Structure of the NF along at t = 2-48 h: (a) XRD patters. (b) Crystallite size calculated by Scherrer's equation. (d) Representative TEM images of the growing cores.

In order to study the formation mechanism and magnetic properties of multi-core nanoflowers, the NaAc concentration (15.8 mmol) was fixed and the heating time was varied from 0.5 to 48 h. Figure 10 shows the X-ray diffraction pattern of the NF samples. At t = 0.5 h, the pattern clearly matches that of lepidocrocite (γ-FeOOH) (2-θ angles of 27, 36, 47 and 60°). A different pattern is observed at 1 and 1.8 h reaction time. These patterns do not correspond with any of the well-known iron oxide or oxyhydroxide phases. As the patterns are quite distinct we speculate that they may represent the formation of an unknown intermediate phase. At 2 h of reaction time, most of the XRD peaks can be indexed to maghemite (γ-$Fe_2 2O_3$), whose typical XRD profile is shown in red below the diffractograms). Additionally, there are two small and narrow peaks (at 24.6° and 47.2°) that reveal some remain of the intermediated phase (in correspondence with the observations by TEM). Moreover, XRD conducted on the unknown intermediate phase shows that this phase remains stable. This proposed formation mechanism has been further confirmed by means of ACS v T and Mössbauer spectroscopy.

Once the maghemite nanoflowers have formed, after 2 h of reaction time, an aging process starts. This process has been studied through TEM, XRD and magnetic measurements. Figure 11 a shows the XRD patterns collected for NF-2-48. After 4 h, only maghemite is detected. The diffraction peaks become narrower throughout the aging process and the crystal size obtained from the width of the diffraction peaks by use of the Scherrer's formula show that the nanoflowers undertake a crystallization process, increasing its mean crystal size d_{XRD} from 11 to 23 nm (Figure 11 b). Similar trend is observed

by TEM, where the cores of the particles are seen to grow over time (Figure 11 c).

DC magnetometry measurements were conducted on the nanoflowers which undertook a crystallization process. By prolonging the aging time (4, 8, 16 and 48 h), the nanoflowers saturation magnetization is increased from 48 to 90 Am^2/kg at 290 K (Figure 9b), which implies quite a significant enhancement. The samples also show increasing coercivity values ($\sim$ 0.5-2 kA/m at RT and 8-19 kA/m at 5 K) with aging. The magnetic behaviour of the progressively aged nanoflowers has also been investigated by means of AC susceptibility v T. The results suggest that that the major contribution corresponds to the particles magnetically blocked well above room temperature, but at longer aging times, magnetic dynamics anomalies at the lower temperature appear, that we attribute to some phenomenon intrinsic to maghemite or to some usually appearing intermediate phase, although no rigorous interpretation of this phenomenon can be offered yet.

Lastly, in Chapter 4, the colloidal stability and heating potential for magnetic hyperthermia of four selected samples (2 nanoflowers with distincs core size, single-core NPs and hollow spheres) was studied. Therefore, the surface charge and the colloidal stability were enhanced by citric acid coating. Infrared spectroscopy confirms the successful citric acid coating, DLS and Zeta Potential analysis confirm this functionalisation. The nanoflowers show narrow monomodal DLS hydrodynamic distribution centered at $\sim$100 nm after the coating. Samples single-core and hollow spheres have a hydrodynamic size after coating of 161 and 298 nm, respectively. The heating capacity of the coated materials in water at physiological pH was evaluated in order to study the differences in terms of sample morphology and crystallinity. Nanoflowers with a core size of 23 nm (NF–48) have the highest SLP values e.g. yielding 1131.2 W/g Fe for a frequency of 710 KHz. This sample displays SLP values nearly 5 times larger than nanoflowers with crystal size of 15 nm (NF–4), nearly 4 times larger than hollow spheres and 1.5 times larger than single-core nanoparticles, although these two latter samples (HS and SC) have bigger core sizes of 27 and 36 nm, respectively. This demonstrates that both core sizes and the packing of the cores have decisive influence on the heating capacity. Specifically, we observe that nanoflowers with large cores (controlled by annealing) and densely packed cores (tuned by NaAc concentration) offer enhanced heating capacity compared with nanoflowers with smaller crystallite sizes, hollow spheres, and single-core nanoparticles used in this work.

Chapter 5.Unravelling the mechanisms that determine absorption and metabolization of magnetic single and multi-core nanoparticles in-vitro and in-vivo

A crucial issue for magnetic nanoparticle safe utilization in biomedicine and their approval by regulatory agencies lies in their biotransformation and toxicity. On one hand, the course and fate of the nanoparticles once they fullfil their mission needs to be studied. On the other hand, the safety metabolization of the by-products must be assessed and assured. Since iron is involved in diverse vital processes, organisms display mechanisms to transport and store iron in non-toxic forms.[61] Therefore, IOMNPs are predicted to be safely incorporated in biological systems. Increasing evidence demonstrates that iron oxide MNPs trigger iron-coping mechanisms in cells and that the degradation products of these materials are incorporated into normal iron metabolic routes.[62–68] However, nanoparticle coating has been shown to be determinant on the IOMNPs uptake, degradation and fate.[69, 70] In order to establish solid conclusions about IOMNPs toxicity the study of IOMNPs toxicity and biodistribution, and its cellular effects, it would be ideal to have biologically pertinent models.

In chapter 5, we report the effect of γ-Fe_2O_3 magnetic single and multi-core nanoparticles suitable for bioapplications in Hep G2 (human hepatocellular carcinoma), Caco-2 (human colorectal adenocarcinoma) cells (in-vitro) and in a Xenopus laevis, an amphibian model ideal to study the course and fate of the nanoparticles since it allows flexible bioassay for evaluating vertebrate embryology development, basic cell and molecular biology, genomics, neurobiology and toxicology.[71]

Single core nanoparticles (SC) were obtained by thermal decomposition of the iron(III) oleate precursor in 1-octadecene (Figure 5.1 a-b). Particles are 13 $\pm$ 1 nm in diameter, uniform in size (Figure 12 c), relatively spherical and well dispersed, owing to the presence of oleic acid around the particles. In a different approach multi-core nanoparticles (MC) were obtained by polyol mediated reduction of iron(III) chloride. MC are composed of spherical 142 $\pm$ 23 nm nanoparticles with a well-defined size and shape. Iron oxide nanoparticles obtained by thermal decomposition are hydrophobic. To make them suitable for biological applications, oleic acid on the surface of the nanoparticle was removed with DMSA via ligand exchange reaction (SC@DMSA). Polyol mediated process render hydrophilic nanoparticles along with polyvinylpyrrolidone (PVP40), present in the reaction, however an extra capping agent like citric acid enhance the electrostatic repulsion and facilitates the final dispersion of the MC nanoparticles in aqueous media (MC@Cit). Both samples were conjugated PEG, slightly increasing their hydrodynamic size and lowering their surface charge. The presence of the coating was studied also through FTIR and TGA.

Figure 12 shows in vitro toxicological characterization of the nanoparticles, evaluated through the degree of cell survival by means of the standard methyl thiazol tetrazolium bromide (MTT assay). The analysis of cytotoxicity after incubation with Hep G2 and Caco-2 cells with the nanoparticles showed that viability of cell culture is not significantly affected by the presence of the nanoparticles up to 1000 μM Fe concentration after 24 h of treatment (80–100% viability compared with the control). At iron

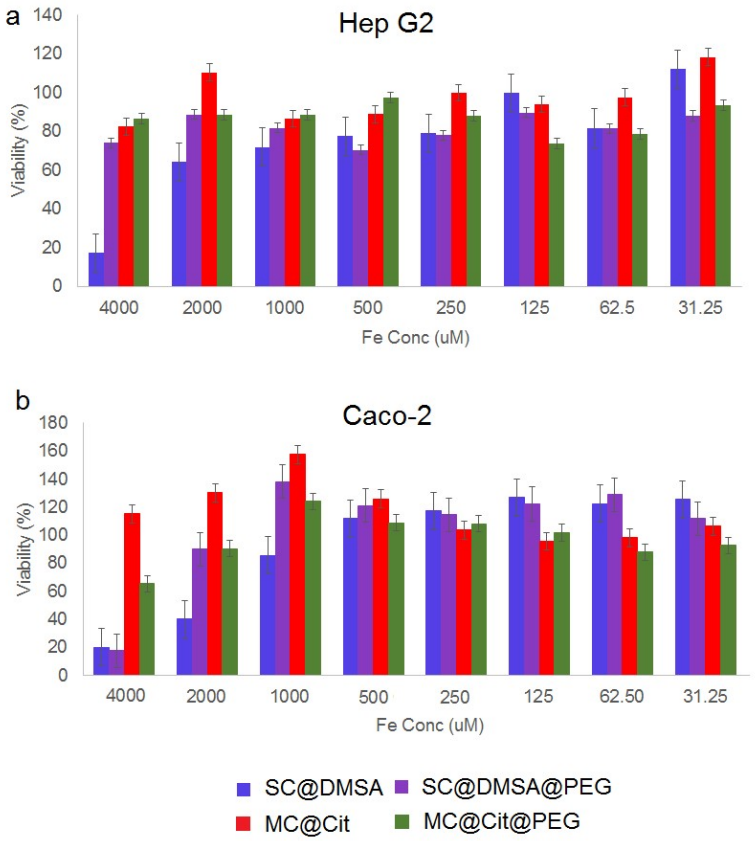

Figure 12: Evaluation of cell viability by MTT assay of (a) Hep G2 cells and (b) Caco-2 cells after 24 h treatment with the nanoparticles. Values indicated mean $\pm$ SD (n=3).

concentrations higher than 1000 μM, SC decrease the viability of both cell lines down to values of 20%. In the case of MC, viability percentage of both cell lines is in the range of 60-80 %, indicating lower toxicity even at high iron concentrations. Differences in toxicity profile at higher doses could be related to different sensitivity of both cell lines used in the treatment with nanoparticles. The effect of PEG coating is not very clear at high iron concentration. In the case of Hep G2 cells PEG functionalization improves the cytotoxicity for SC while in Caco-2 has no effect. For MC, PEG functionalization reduces the viability down to 60 % in Caco-2 cells.

The use of Xenopus laevis model has the advantages rapid embryo growth and development within 48 hours, which has allowed us to study the effect of the different types of IOMNPs in tadpoles with fully functional set of organs. The embryos were treated with four different concentrations, 0.25 mg/mL, 0.5 mg/mL, 0.75 mg/mL and 1 mg/mL. None of the conditions were found lethal for the embryos. The second advantage of this model is that it has allowed us the direct visualization of the nanoparticles as

they are being swallowed. The embryos body toxicity was evaluated at 0.5 and 1 mg Fe/mL.

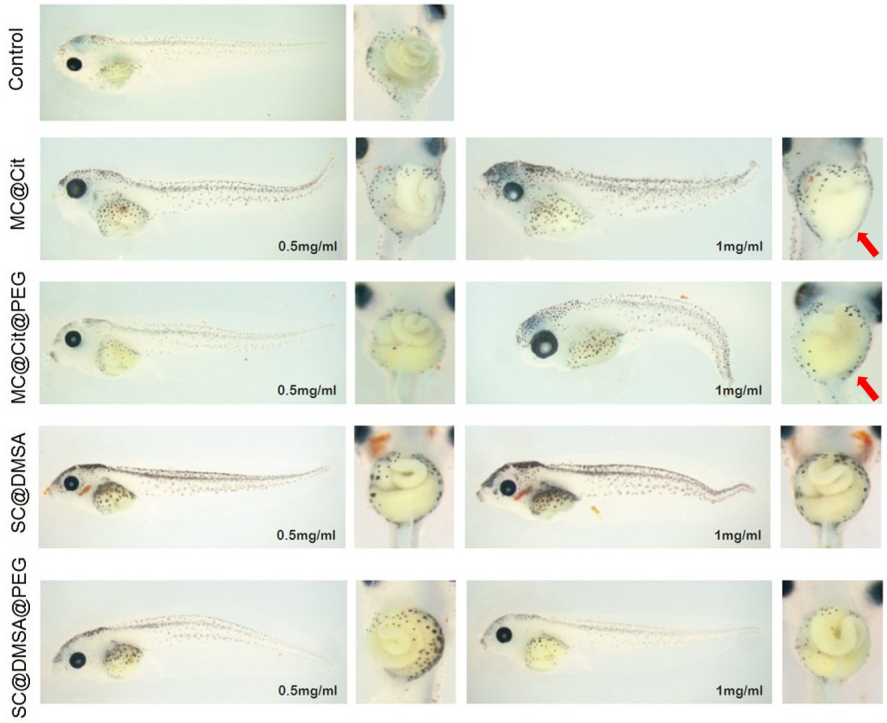

Figure 13: Representative images from X. laevis exposed to 0.5 and 1 mg/mL of nanoparticles. (n=7 per group). Red arrows highlight those intestines in which the effect of treatment was dramatic, modifying their coiled structure.

Figure 13 suggest that uptake has taken place mainly for the SC@DMSA and that nanoparticles have been massively absorbed by the organisms. All embryos displayed a general body toxicity when treated with NPs at 1 mg/mL characterised by defects in embryo body shape, tail bending and developmental delay. In the case of embryos treated with 0.5 mg/mL, defects were more subtile (Figure 13). This result suggested a dose-dependant uptake of the NPs by the embryos. As the main organs involved in NPs' absortion and biotransformation are the gut and liver, we evaluate the morphology of these organs. For SC-treated embryos, the intestine coiled structure is preserved although is visible enlarged when embryos are treated at 1 mg/mL. The MC-treated embryos displayed a dramatic effect in the morphology of the intestine. The organ is not mantained or not well formed, as we are unable to see the intestine loops (as marked by red arrows in Figure 13). Interestingly, at lower dosis of SC or MC, where the general toxic effects of the embryo are visibly reduced, the damage in the gut is absent in the treatment with PEG functionalized nanoparticles compared with the uncoated ones.

In order to evaluate the accumulation of the nanoparticles in the animals, we performed AC sus-

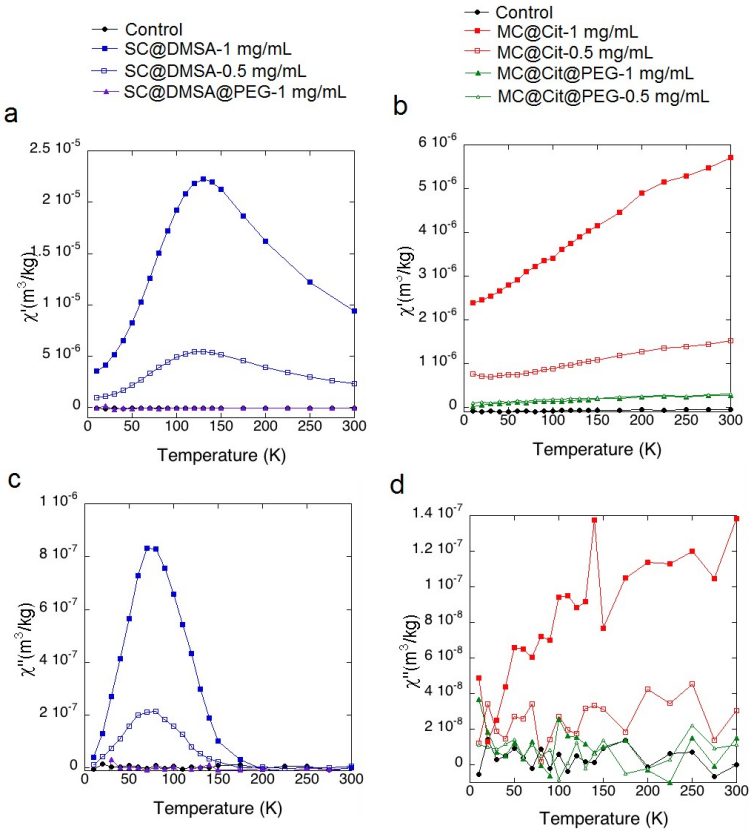

Figure 14: Tissue characterization by AC magnetic susceptibility. In-phase (χ'(T)) and out-of-phase (χ''(T)) components of the magnetic susceptibility, per mass of sample, corresponding to freeze-dried tissues from different embryos: (a, c) Embryos exposed to SC nanoparticles, (b, d) Embryos exposed to MC nanoparticles. (n=7 per group).

ceptibility of pools of seven animals. The presence of magnetic nanoparticles can be identified by a maximum in the in-phase magnetic susceptibility (χ') accompanied by a maximum at slightly lower temperatures in the out-of-phase susceptibility (χ''). The temperature location of the maxima depends on the nanoparticle (material, size, aggregation degree, etc). The height of the maxima is a surrogate measurement of the concentration of nanoparticles. In our case, a dose-dependent amount of nanoparticles is observed in the animals treated with particles without PEG coating (Figure 14), independently if they are SC or MC. Interestingly PEG coated nanoparticles, both SC and MC, were not detected, or at least they are under the detection limits of the technique. The absence of a substantial paramagnetic contribution, usually observed at the lowest temperatures, indicates that the presence of free iron atoms that could come from a degradation process is very low. These results are in agreement with what we

observed by EDX-SEM and determined by ICP-OES. There was massive absorption of SC@DMSA, a two or five-fold increase in comparison with MC@Cit for iron concentrations of 0.5 and 1 mg/mL, respectively. Interestingly, the iron content in the animals treated with PEGylated NPs is comparable to the control. One possible explanation for the visual disturbance of the intestine structure of the embryos treated with MC@Cit@PEG, could be that the particles are rapidly excreted by the organism and therefore the iron content in these animals is so low. PEG functionalization reduces net surface charge of the particles and this effect could reduce the absorption of the particles in the gut favouring their excretion.

Since iron resulting from NPs' degradation is predicted to be processed by iron metabolic pathways, in Chapter 5 we next studied the expression of different genes involved in iron metabolism and oxidative stress by real-time quantitative PCR (RT-qPCR). We detected an increase of ferritine, dmt1 and hepcidin. The levels of transferrin are also increased. However, the MC@Cit treated embryos do not seem to have an increase in the levels of dmt1 and transferrin. From this data we can describe differences in the metabolization speed of single core or multicore nanoparticles. After iron ingestion, ferrous ions (Fe^{2+}) are absorbed in the enterocytes through the divalent metal transporter^{-1} (DMT1). In the apical membrane of the enterocytes, the duodenal cytochrome B (Dcytb) facilitates the reduction of ferric to ferrous ions enabling the absorption of iron. In the basolateral membrane of the enterocytes the ferroportin transporter is located together with hepcidin, which regulates the entry of iron into circulation through inhibiting ferroportin. In the bloodstream, transferrin is capable to bind iron exported by ferroportin and carry it through the different organs. Ferritin is the most important protein involved in iron storage within cells, and the levels of Fe^{2+} present in the organism regulates its expression.[72]

The increase in Fe^{2+} in the embryos 72 h after the treatment, activates iron response proteins, which activates the translation of proteins involved in iron metabolism such as ferritin. For the first time we are observing in vivo the activation by Hmox-1 of iron regulatory proteins and their effect in the transcription of ferritin mRNA associated to the treatment with iron oxide nanoparticles.

The rest of the genes studied (sod, catalase and gsr) showed an increase in the expression of enzymes involved in the attenuation of oxidative stress in the case of embryos treated with SC@DMSA compared with MC@Cit. These results suggest the activation of protective mechanisms depending on NPs' intake but we are not in the presence of an acute state of oxidative stress when a general decrease of antioxidant enzymes takes place.[73]

Conclusions

The main conclusions of this thesis are:

- By means of the synthesis of antiferromagnetic nanoparticles, their coating with a silica shell, and their reduction to magnetite, we have produced a library of iron oxide magnetic nanoparticles in a core size range of 50-100 nm (in its minor axis) and three different shapes has been successfully demonstrated: rhombohedral, elongated and hexagonal discs. We have yielded a single iron oxide phase of magnetite (as verified by X-ray diffractograms, Mössbauer spectra and ZFC/FC magnetization curves) and due to the effect of pores and deffects in their crystalline structure, inherent to the transformation to magnetite, some samples show a very clear Verwey transition at slightly lower temperatures and some samples present a "wasp-shaped" hysteresis curve and a very low coercive field at room temperature.

- Assemblies of maghemite nanocrystals with flower-shaped structure have been synthesized by 4 strategies. Structural differences between the assemblies of maghemite cores are directly related to their formation mechanism (clustering and coalescence, clustering and recrystallization or Ostwald ripening), free energy involved in the process and experimental conditions (pH, surface charge, temperature, pressure and time). Through structural and magnetic means, the flower-shaped structure of the assemblies has been described and modelled. We have demonstrated that the key parameters driving the magnetic collective properties of these samples are: the contact between the cores within a particle, and the continuity in the crystal alignment, which favours the magnetic orderbetween the interfases. This is reflected in less pronounced relaxation effects (detected by Mössbauer spectroscopy) and higher χ_0 in the magnetization curve. AC magnetic susceptibility measurements have allowed us to model the particle size in solution of the nanoflowers.

- In the polyol mediated synthesis, the addition of sodium acetate is found to be a key parameter governing the self-assembly process. In this reaction, it has a double role: the particle formation, and the nucleation and growth. For higher acetate concentration, single-core particles are obtained. As the amount of acetate is reduced, the initial nanocrystalline subunits seem to grow by partial aggregation in hollow spheres. Further reduction in acetate leads to initial nanocrystalline nuclei that strongly aggregate to produce the final nanoflowers. In the case of the synthesis of the nanoflowers, the initial stages of the reaction are composed of lepidocrocite, which suffers a fast dehydroxylation, transforming to an intermediate “undescribed” phase - possibly a partly dehydroxylated lepidocrocite – that evolves to maghemite nanoflowers. This formation mechanism has been followed by AC magnetic suscetibility. Prolonged heating times of the raction lead to nanoflowers with increasing core size. The samples have increased saturation magnetisation and coercivity, and display increasing ILP values.

- The toxicity in-vitro (in 2 cell lines) and in-vivo (in a X. Laevis amphibian model) has been studied in a MC system (hollow spheres) and a SC system (NPs synthesized by high termperature decomposition). Therefore the samples were coated with different biocompatibles molecules and polymers. The viability of both cell lines is preserved in all cases when treated with the nanoparticles up to an iron concentration of 1000 μM. In the case of the in-vivo viability, none of the single-core nor multi-core coated nanoparticles were found lethal for the embryos. However, at high iron concentration the embryos showed defects in their body shape, especially in the intestine, tail bending and developmental delay. SC nanoparticles are massively absorbed in comparison with MC nanoparticles and non-accumulation of the nanoparticles occurs when the surface charge is lower (in the case of PEGylated nanoparticles). The accumulation of the NPs in-vivo was studied thanks to AC magnetic susceptibility. The degradation of iron oxide nanoparticles in vitro and their biodisponibility by the cells is traduced in an increase of ferritin levels, which is in agreement with the corresponding activation of the iron metabolic pathway. Intracellular nano-biodegradation in vitro correlates with in vivo observations.

Fundamental contributions of this thesis work

This thesis presents significant advancements in the synthesis and self-assembly of different magnetic nanostructures with the potential of being used for biomedical applications.

Both the shape and the assembly of the magnetic cores have been modulated in this work, and it has been analysed how these affect the magnetic properties of the obtained material. The possibilities of generating a discontinuous structure within a single-core nanoparticle (Chapter 2) may be an interesting strategy to develop new materials with tuned magnetic properties. Moreover, the possibilities of inducing magnetic exchange interactions by self-assembly and approaching of the magnetic cores (Chapter 3) leads multi-core structures with collective properties and enhanced heating performance (Chapter 4).

Thus, this thesis provides a complete and detailed characterisation of the presented structures. Therefore, this work opens new ways for controllable synthesis with well-defined size and shape and interesting collective properties. Moreover, the presented samples could serve as SC and MC reference samples and will contribute as a basis to make reliable comparisons with these types of materials in the future.

Lastly, the use of AC magnetic susceptibility has been implemented, making use of this technique throughout this Thesis in order to: i) model a structural parameter, the hydrodynamic size (Chapter 3), ii) follow the formation mechanism of magnetic nanoparticles (Chapter 4) and iii) follow the accumulation and degradation of magnetic nanoparticles in-vivo in complex biological matrices.

Bibliography

[1] de Coulomb, C. Premiere memoire sur l'electricite et le magnetism. second memoire sur l'electricite et le magnetism. troisieme memoire sur l'electricite et le magnetism. *Histoire de l'Académie Royal des Sciences* 569–638 (1785).

[2] Pankhurst, Q. A., Connolly, J., Jones, S. & Dobson, J. Applications of magnetic nanoparticles in biomedicine. *Journal of physics D: Applied physics* **36**, R167 (2003).

[3] Cowburn, R. Property variation with shape in magnetic nanoelements. *Journal of Physics D: Applied Physics* **33**, R1 (2000).

[4] Mørup, S., Hansen, M. F. & Frandsen, C. Magnetic interactions between nanoparticles. *Beilstein journal of nanotechnology* **1**, 182 (2010).

[5] Grubbs, R. B. Nanoparticle assembly: solvent-tuned structures. *Nature materials* **6**, 553–555 (2007).

[6] Thanh, N. T., Maclean, N. & Mahiddine, S. Mechanisms of nucleation and growth of nanoparticles in solution. *Chemical reviews* **114**, 7610–7630 (2014).

[7] LaMer, V. K. & Dinegar, R. H. Theory, production and mechanism of formation of monodispersed hydrosols. *Journal of the American Chemical Society* **72**, 4847–4854 (1950).

[8] Mer, V. K. L. Nucleation in phase transitions. *Industrial & Engineering Chemistry* **44**, 1270–1277 (1952).

[9] De Yoreo, J. J. *et al.* Crystallization by particle attachment in synthetic, biogenic, and geologic environments. *Science* **349**, aaa6760 (2015).

[10] Laurent, S. *et al.* Magnetic iron oxide nanoparticles: synthesis, stabilization, vectorization, physicochemical characterizations, and biological applications. *Chemical reviews* **108**, 2064–2110 (2008).

[11] Van der Zee, J. Heating the patient: a promising approach? *Annals of oncology* **13**, 1173–1184 (2002).

[12] Hilger, I. & Kaiser, W. Iron oxide-based nanostructures for mri and magnetic hyperthermia. *Nanomedicine* **7**, 1443–1459 (2012).

[13] Dutz, S. & Hergt, R. Magnetic particle hyperthermia - a promising tumour therapy? *Nanotechnology* **25** (2014).

[14] Serantes, D. *et al.* Multiplying magnetic hyperthermia response by nanoparticle assembling. *Journal of Physical Chemistry C* **118**, 5927–5934 (2014).

[15] Guan, N., Wang, Y., Sun, D. & Xu, J. A simple one-pot synthesis of single-crystalline magnetite hollow spheres from a single iron precursor. *Nanotechnology* **20** (2009).

[16] Jia, B. & Gao, L. Morphological transformation of fe3o4 spherical aggregates from solid to hollow and their self-assembly under an external magnetic field. *Journal of Physical Chemistry C* **112**, 666–671 (2008).

[17] Rebolledo, A., Bomatí-Miguel, O., Marco, J. & Tartaj, P. A facile synthetic route for the preparation of superparamagnetic iron oxide nanorods and nanorices with tunable surface functionality. *Advanced Materials* **20**, 1760–1765 (2008).

[18] Cornell, R. & Schwertmann, U. *The Iron Oxides: Structure, Properties, Reactions, Occurrence and Uses* (1996).

[19] Graf, C., Vossen, D., Imhof, A. & Van Blaaderen, A. A general method to coat colloidal particles with silica. *Langmuir* **19**, 6693–6700 (2003).

[20] Stöber, W., Fink, A. & Bohn, E. Controlled growth of monodisperse silica spheres in the micron size range. *Journal of Colloid And Interface Science* **26**, 62–69 (1968).

[21] Morales, M., Pecharroman, C., Carreñ, T. & Serna, C. Structural characteristics of uniform γ-fe2o3 particles with different axial (length/width) ratios. *Journal of Solid State Chemistry* **108**, 158–163 (1994).

[22] Baker, A. *et al.* A structural study of haematite samples prepared from sulfated goethite precursors: The generation of axial mesoporous voids. *Journal of Materials Chemistry* **10**, 761–766 (2000).

[23] Morales, J., Tirado, J. & Macias, M. Changes in crystallite size and microstrains of hematite derived from the thermal decomposition of synthetic akaganeite. *Journal of Solid State Chemistry* **53**, 303–312 (1984).

[24] Roberts, A., Cui, Y. & Verosub, K. Wasp-waisted hysteresis loops: mineral magnetic characteristics and discrimination of components in mixed magnetic systems. *Journal of Geophysical Research* **100**, 17,909–17,924 (1995).

[25] Hillebrands, B. & Ounadjela, K. *Spin Dynamics in Confined Magnetic Structures* (2002).

[26] Goya, G., Berquó, T., Fonseca, F. & Morales, M. Static and dynamic magnetic properties of spherical magnetite nanoparticles. *Journal of Applied Physics* **94**, 3520–3528 (2003).

[27] Xing, P. & Zhao, Y. Multifunctional nanoparticles self-assembled from small organic building blocks for biomedicine. *Advanced Materials* (2016).

[28] Pan, S., He, L., Peng, J., Qiu, F. & Lin, Z. Chemical-bonding-directed hierarchical assembly of nanoribbon-shaped nanocomposites of gold nanorods and poly (3-hexylthiophene). *Angewandte Chemie* (2016).

[29] Volkmann, M., Meyns, M., Lesyuk, R., Lehmann, H. & Klinke, C. Attachment of colloidal nanoparticles to boron nitride nanotubes. *Chemistry of Materials* (2016).

[30] Sayevich, V. *et al.* 3d assembly of all-inorganic colloidal nanocrystals into gels and aerogels. *Angewandte Chemie International Edition* **55**, 6334–6338 (2016).

[31] Stolarczyk, J. K., Deak, A. & Brougham, D. F. Nanoparticle clusters: Assembly and control over internal order, current capabilities, and future potential. *Advanced Materials* (2016).

[32] Ocaña, M., Rodriguez-Clemente, R. & Serna, C. J. Uniform colloidal particles in solution: Formation mechanisms. *Advanced Materials* **7**, 212–216 (1995).

[33] Raju, M., Van Duin, A. C. & Fichthorn, K. A. Mechanisms of oriented attachment of tio2 nanocrystals in vacuum and humid environments: reactive molecular dynamics. *Nano letters* **14**, 1836–1842 (2014).

[34] Frandsen, C. *et al.* Aggregation-induced growth and transformation of β-feooh nanorods to micron-sized α-fe2o3 spindles. *CrystEngComm* **16**, 1451–1458 (2014).

[35] Bannwarth, M. B. *et al.* Well-defined nanofibers with tunable morphology from spherical colloidal building blocks. *Angewandte Chemie International Edition* **52**, 10107–10111 (2013).

[36] Ingham, B. *et al.* How nanoparticles coalesce: an in situ study of au nanoparticle aggregation and grain growth. *Chemistry of Materials* **23**, 3312–3317 (2011).

[37] Dutz, S. Are magnetic multicore nanoparticles promising candidates for biomedical applications? *IEEE Transactions on Magnetics* **52**, 1–3 (2016).

[38] Serantes, D. *et al.* Multiplying magnetic hyperthermia response by nanoparticle assembling. *The Journal of Physical Chemistry C* **118**, 5927–5934 (2014).

[39] Jeong, U., Teng, X., Wang, Y., Yang, H. & Xia, Y. Superparamagnetic colloids: controlled synthesis and niche applications. *Advanced Materials* **19**, 33–60 (2007).

[40] Gutierrez, L. *et al.* Synthesis methods to prepare single-and multi-core iron oxide nanoparticles for biomedical applications. *Dalton Transactions* **44**, 2943–2952 (2015).

[41] Gijs, M. A., Lacharme, F. & Lehmann, U. Microfluidic applications of magnetic particles for biological analysis and catalysis. *Chemical reviews* **110**, 1518–1563 (2009).

[42] Nowak, J., Wiekhorst, F., Trahms, L. & Odenbach, S. The influence of hydrodynamic diameter and core composition on the magnetoviscous effect of biocompatible ferrofluids. *Journal of Physics: Condensed Matter* **26**, 176004 (2014). URL `http://stacks.iop.org/0953-8984/26/i=17/a=176004`.

[43] Mahmoudi, M., Hofmann, H., Rothen-Rutishauser, B. & Petri-Fink, A. Assessing the in vitro and in vivo toxicity of superparamagnetic iron oxide nanoparticles. *Chemical reviews* **112**, 2323–2338 (2011).

[44] Eberbeck, D. *et al.* Multicore magnetic nanoparticles for magnetic particle imaging. *IEEE Transactions on Magnetics* **49**, 269–274 (2013).

[45] Grüttner, C., Müller, K., Teller, J. & Westphal, F. Synthesis and functionalisation of magnetic nanoparticles for hyperthermia applications. *International Journal of Hyperthermia* **29**, 777–789 (2013).

[46] Dutz, S., Kettering, M., Hilger, I., Müller, R. & Zeisberger, M. Magnetic multicore nanoparticles for hyperthermia—influence of particle immobilization in tumour tissue on magnetic properties. *Nanotechnology* **22**, 265102 (2011).

[47] Hugounenq, P. *et al.* Iron oxide monocrystalline nanoflowers for highly efficient magnetic hyperthermia. *The Journal of Physical Chemistry C* **116**, 15702–15712 (2012).

[48] Alexiou, C. *et al.* Locoregional cancer treatment with magnetic drug targeting. *Cancer research* **60**, 6641–6648 (2000).

[49] Bigall, N. C. *et al.* Colloidal ordered assemblies in a polymer shell: A novel type of magnetic nanobeads for theranostic applications. *Chemistry of Materials* **25**, 1055–1062 (2013).

[50] Zoppellaro, G. *et al.* Theranostics of epitaxially condensed colloidal nanocrystal clusters, through a soft biomineralization route. *Chemistry of Materials* **26**, 2062–2074 (2014).

[51] Mazuel, F. *et al.* Magneto-thermal metrics can mirror the long-term intracellular fate of magneto-plasmonic nanohybrids and reveal the remarkable shielding effect of gold. *Advanced Functional Materials* (2017).

[52] Ludwig, F. *et al.* Magnetic, structural, and particle size analysis of single-and multi-core magnetic nanoparticles. *IEEE Transactions on Magnetics* **50**, 1–4 (2014).

[53] Mulvaney, P., Parak, W. J., Caruso, F. & Weiss, P. S. Standardizing nanomaterials (2016).

[54] Ge, J., Hu, Y., Biasini, M., Beyermann, W. P. & Yin, Y. Superparamagnetic magnetite colloidal nanocrystal clusters. *Angewandte Chemie International Edition* **46**, 4342–4345 (2007).

[55] Cheng, C., Xu, F. & Gu, H. Facile synthesis and morphology evolution of magnetic iron oxide nanoparticles in different polyol processes. *New Journal of Chemistry* **35**, 1072–1079 (2011).

[56] Caruntu, D. *et al.* Synthesis of variable-sized nanocrystals of fe3o4 with high surface reactivity. *Chemistry of materials* **16**, 5527–5534 (2004).

[57] Kim, B. H. *et al.* Large-scale synthesis of uniform and extremely small-sized iron oxide nanoparticles for high-resolution t 1 magnetic resonance imaging contrast agents. *Journal of the American Chemical Society* **133**, 12624–12631 (2011).

[58] Lartigue, L. *et al.* Cooperative organization in iron oxide multi-core nanoparticles potentiates their efficiency as heating mediators and mri contrast agents. *ACS Nano* **6**, 10935–10949 (2012).

[59] Gavilán, H. *et al.* Colloidal flower-shaped iron oxide nanoparticles: Synthesis strategies and coatings. *Particle & Particle Systems Characterization* (2017).

[60] Gavilán, H. *et al.* How shape and internal structure affect the magnetic properties of anisometric magnetite nanoparticles. *Acta Materialia* **125**, 416–424 (2017).

[61] Crichton, R. R. & Boelaert, J. R. *Inorganic biochemistry of iron metabolism: from molecular mechanisms to clinical consequences* (John Wiley & Sons, 2001).

[62] Balakumaran, A. *et al.* Superparamagnetic iron oxide nanoparticles labeling of bone marrow stromal (mesenchymal) cells does not affect their “stemness”. *PloS one* **5**, e11462 (2010).

[63] Geppert, M., Hohnholt, M. C., Nürnberger, S. & Dringen, R. Ferritin up-regulation and transient ros production in cultured brain astrocytes after loading with iron oxide nanoparticles. *Acta biomaterialia* **8**, 3832–3839 (2012).

[64] Hohnholt, M. C., Geppert, M. & Dringen, R. Treatment with iron oxide nanoparticles induces ferritin synthesis but not oxidative stress in oligodendroglial cells. *Acta biomaterialia* **7**, 3946–3954 (2011).

[65] Gu, J. *et al.* The internalization pathway, metabolic fate and biological effect of superparamagnetic iron oxide nanoparticles in the macrophage-like raw264. 7 cell. *Science China Life Sciences* **54**, 793–805 (2011).

[66] Rojas, J. M. *et al.* Superparamagnetic iron oxide nanoparticle uptake alters m2 macrophage phenotype, iron metabolism, migration and invasion. *Nanomedicine: Nanotechnology, Biology and Medicine* **12**, 1127–1138 (2016).

[67] Mulens-Arias, V., Rojas, J. M., Pérez-Yagüe, S., Morales, M. P. & Barber, D. F. Polyethylenimine-coated spions trigger macrophage activation through tlr-4 signaling and ros production and modulate podosome dynamics. *Biomaterials* **52**, 494–506 (2015).

[68] Mazuel, F. *et al.* Massive intracellular biodegradation of iron oxide nanoparticles evidenced magnetically at single-endosome and tissue levels. *ACS nano* **10**, 7627–7638 (2016).

[69] Rojas, J. M. *et al.* Time-course assessment of the aggregation and metabolization of magnetic nanoparticles. *Acta Biomaterialia (In Press* (2017).

[70] Ruiz, A. *et al.* Biotransformation of magnetic nanoparticles as a function of coating in a rat model. *Nanoscale* **7**, 16321–16329 (2015).

[71] James-Zorn, C. *et al.* Xenbase: Core features, data acquisition, and data processing. *genesis* **53**, 486–497 (2015).

[72] Waldvogel-Abramowski, S. *et al.* Physiology of iron metabolism. *Transfusion Medicine and Hemotherapy* **41**, 213–221 (2014).

[73] Radu, M. *et al.* Exposure to iron oxide nanoparticles coated with phospholipid-based polymeric micelles induces biochemical and histopathological pulmonary changes in mice. *International journal of molecular sciences* **16**, 29417–29435 (2015).

Part G

Appendices

APPENDIX 1

CONTROLLING THE SIZE AND THE SHAPE OF UNIFORM MAGNETIC IRON OXIDE NANOPARTICLES FOR BIOMEDICAL APPLICATIONS

Chapter 1: Controlling the size and the shape of uniform magnetic iron oxide nanoparticles for biomedical applications.

Helena Gavilán, María Eugenia Fortes Brollo, Lucía Gutiérrez, Sabino Veintemillas-Verdaguer and María del Puerto Morales
Instituto de Ciencia de Materiales de Madrid, Sor Juana Inés de la Cruz 3, 28049 Madrid, Spain

CONTENTS

ABSTRACT

In this chapter, an update of recent advances in the synthesis of iron oxide magnetic nanoparticles, consisting of uniform magnetic cores stabilized in water forming biocompatible aqueous colloids is presented. Aqueous synthetic routes granting nanoparticle shape control by the synthesis of antiferromagnetic precursors or highly ordered magnetic nanostructures by biomineralization are presented. Alternative synthetic routes in organic and polyols media allowing nanoparticle size and aggregation control, and surface functionality tuning are also included. Finally, other routes such as microwave assisted methods, and electrochemistry or plasma techniques are discussed. Special attention has been paid to determine the reproducibility of the synthetic routes, the possibilities of large production and the mechanism of nanoparticle formation and self-assembling processes that could be a powerful tool to control the dimensions and morphology of NPs, essential for the optimization of their properties.

1.1 STATE OF THE ART: SIZE, SHAPE CONTROL AND SELF-ASSEMBLY PROCESSES

In the last decade, there have been huge advances in the synthesis of magnetic nanoparticles (MNPs) for biomedical applications encompassing the requirements in terms of size, surface and colloidal stability under physiological conditions intrinsic to each particular application.[1-4] Numerous studies have reached the clinical use of MNPs as magnetic resonance imaging (MRI) contrast agents. Nevertheless, for other applications such as hyperthermia treatments, tissue regeneration, magnetically driven transfection of stem cells or delivery of genetic materials, nanoparticles' use in an efficient and biocompatible manner remains to be assessed.[5] Scientific and industrial challenges involved in developing MNPs for clinical applications have been recently highlighted[6]. The limitation in many cases comes from the wide size distribution of the nanoparticles (NPs), the lack of aggregation control or the poor/weak functionality of the surface.

Typically, MNPs for biomedical applications are composed of a magnetic core, usually a ferrite and most commonly an iron oxide, modified with a biocompatible material resulting in a core-shell structure[3]. The shell acts not only as a hydrophilic layer to render colloidal stability and avoid aggregation but also as a platform for functionalization for specific applications within the biomedical area. To improve their magnetic properties, other metal ions have been chosen to dope into the ferrite spinel structure such as manganese,[7] zinc and cobalt[8-10]. With the same purpose, metallic NPs[11-12] with higher magnetic moments have also been synthesized and stabilized by different coatings[13,14-16]. However, magnetite and maghemite are still the most popular material for biomedical applications because of its biocompatibility and good magnetic properties when properly synthesized with high crystallinity and free of impurities.

This chapter aims to provide an update of recent advances in the synthesis of iron oxide MNPs, consisting of uniform magnetic cores stabilized in water forming biocompatible aqueous colloids (Figure 1.1).

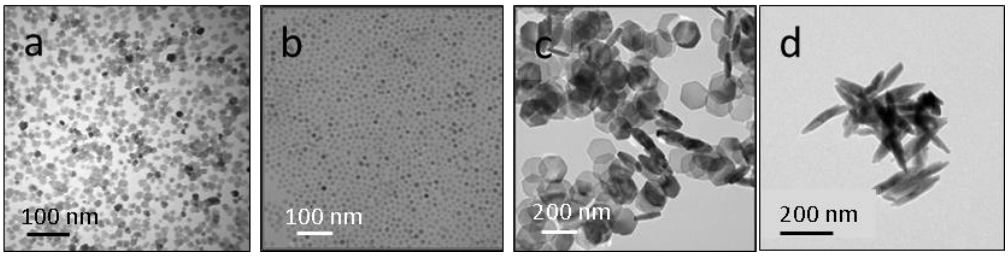

FIGURE 1.1. Transmission electron microscopy (TEM) images of uniform magnetic nanoparticles with well-defined size and shape prepared by different routes: From left to right: a) polyol process, b) decomposition in organic media, and c) and d) reduction of antiferromagnetic precursors synthesized in aqueous media (hematite and goethite).

Some of the methods described in this chapter were already mentioned in Chapter 2 "Synthesis and characterisation of iron oxide ferrite NPs and ferrite-based aqueous fuids" by Etienne Duguet *et al.* in the book "Magnetic nanoparticles: From fabrication to clinical applications, ISBN 9781439869321)[17] but they have been modified to better control the size, shape or distribution of the NPs. In the case of

aqueous synthetic routes, the last advances in the nanoparticle shape control by the synthesis of antiferromagnetic precursors[18] and the biomineralization of highly ordered magnetic nanostructures[19] are presented in section 1.2.1. In sections 1.2.2-1.2.6, alternative synthetic routes to the conventional ones, allowing nanoparticle size and aggregation control, and surface functionality tuning are presented. In these Sections, we include synthetic routes in organic media (Section 1.2.2) that received recently a significant amount of effort, the polyol process (1.2.3), microwave assisted methods (1.2.4) and others such as electrochemistry or plasma techniques (Sections 1.2.5 and 1.2.6).

We will distinguish whether a synthetic route leads to single or multi-core particles, taking into account that the term 'core' describes an individual nanoparticle, and 'multi-core' describes a collection of cores held by a matrix forming a fixed structure[20]. Single- and multi-core particles could further agglomerate as a consequence of weak physical interactions in a reversible process. To differentiate this reversible agglomeration process from stronger irreversible processes, we use the term "aggregate" to refer to the stronger assemblage that occurs in multi-core NPs to generate the discrete entity. These systems may present strong magnetic interactions between the cores, changing the properties of the material if compared to a non-interacting system[21-22]. The need for understanding the different magnetic properties of single-core and multi-core particles underlies the importance of reliable synthetic methods to reproduce nanoparticle size, shape and structural homogeneity[23].

Special attention has also be paid to the mechanism of nanoparticle formation and self-assembling processes that could be a powerful tool to control the dimensions and morphology of NPs, essential for the optimization of their properties. The typical crystal growth pathway by monomer addition is characterized by a free energy, as a function of the crystal size that exhibits a maximum representing the free energy barrier of nucleation, followed by a progressive decrease as the crystal size increases. Alternative, less common mechanisms have been discovered in the recent years, that may lead to crystals, whose morphologies or internal structures can be very different from the thermodynamically stable final phase, *i.e.* the bulk octahedral crystals of magnetite[24]. Some of these alternative growth pathways, in particular those leading to uniform NPs, involve the oriented aggregation of small subunits in an assembly process driven by the presence of specific molecules or under the action of an external field. This leads to the generation of nanostructures with properties different from those of the discrete NPs from which they derive[25-28].

In general, the self-assembly processes on the base of the oriented aggregation mechanism – also indicated as oriented attachment as they are able to generate perfect monocrystals – are difficult to differentiate from the classical growth by molecular incorporation, and there are very few systems in which this mechanism has been unequivocally demonstrated[24, 29-30]. An oriented attachment process has been observed for iron oxides MNPs prepared in water or in polyol and it has been related to the biomineralization process[31-33]. In aqueous media, the pH in which magnetite particle growth takes place determines whether or not aggregation of the growing particles occurs. If the pH of the system is close to the isoelectric point of magnetite (pH = 6-7), aggregation of particles will happen readily, whereas at pH values away from that pH growing particles have a surface charge and electrostatic forces will prevent aggregation. The effect of the

ensemble, *i.e.* the size of the subunits and the degree of orientation on the magnetic behavior of magnetite NPs has also been studied[34-36].

1.2 PROGRESS ON SYNTHESIS ROUTES

1.2.1 AQUEOUS SYNTHESIS

The synthetic routes to obtain magnetite NPs in aqueous media are currently one of the most commonly studied processes due to the high availability lab set-up and low cost of its reagents, the overall ease of scaling-up the process, and the low toxicity associated to this route. Conventionally, there have been processes based on the aqueous precipitation of a mixed Fe(II)/Fe(III) solution, the so-called co-precipitation route, and secondly the partial reduction or oxidation of a Fe(III) or Fe(II) salt, respectively, always in the presence of a base. However, these routes lead to nanoparticle populations with broad core size distribution (generally the size range is below 20 nm) and not well-defined morphology, in comparison with other synthetic routes, *i.e.* high temperature decomposition of organic precursors or polyol-based processes[3, 37-38]. Nevertheless, these conventional routes have recently allowed a thoroughly control over the iron concentration, aging time, counter ions present in the reaction and the presence of extra organic additives, improving the above mentioned limitations of aqueous syntheses.

Alternatively, new strategies have emerged as promising aqueous routes to obtain crystalline, monodisperse and well-defined magnetite crystals. These strategies are based on the use of iron hydroxide (ferrihydrite or white/green rust) and iron oxide (hematite or goethite) NPs as starting precursors to obtain magnetite via biomineralization routes.

1.2.1.1 Co-precipitation of Iron (II) and (III) Salts.

The simplest and most straightforward method to obtain magnetite synthetically is the co-precipitation of Fe(III) and Fe(II) in aqueous alkaline conditions, which can be carried out at room temperature under an inert atmosphere[39]. The introduction of the acidic Fe(III) /Fe(II) mixture into a highly alkaline solution leads to instant magnetite precipitation according to equation 1. This typically results in small NPs with diameters < 20 nm that due to the limited size of the magnetic domain have superparamagnetic properties.

$$2\ Fe^{3+} + Fe^{2+} + 8\ OH^- \rightarrow Fe_3O_4 + 4\ H_2O \qquad (1.1)$$

Unfortunately, the synthetic procedure provides little means of control over the size distribution and morphology. Indeed, it was shown that the size and the shape of the nanoparticle can be affected by the type of base and pH value,[40] ionic strength and temperature,[41] iron concentration and aging time[42] and nature of the counter anion.[43] An optimized chemical protocol consisting of an acid treatment post-synthesis reduces the size distribution width (standard deviation < 0.25) (Figure 1.2) and improves the magnetic properties and colloidal stability of iron oxide MNPs through the reduction of particle surface disorder in the range of sizes below 15 nm mostly[44]. Recent advances in the co-precipitation method led to the scale up of the process with continuous monitoring of the magnetization[45].

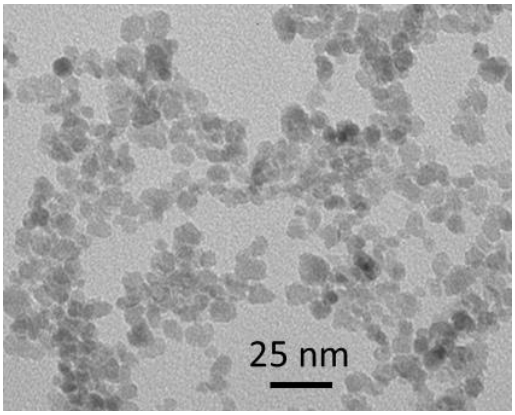

FIGURE 1.2 TEM images of magnetite nanoparticles prepared by the co-precipitation method and subjected to an acid treatment post-synthesis to reduce the size distribution as described in ref [44].

Iron oxide NPs synthesised using the co-precipitation method in the presence of oleic acid have been used to develop a drug delivery system to the gastrointestinal (GI) tract with potential for magnetic targeting and tracking, which can release its payload on demand using localised magnetic hyperthermia to trigger release[46]. Gelatin capsules were dip coated into a dispersion of oleic acid-capped iron oxide NPs in molten eicosane. This renders the capsule impervious to water/acid/base ingress providing a coating that is resistant to the harsh conditions experienced in the GI tract.

An interesting alternative to conventional routes to prepare in one-step hydrophilic magnetite NPs in aqueous media is the hydrothermal route. Recently, a rapid and easily scalable hydrothermal synthesis of single core magnetite NPs[47] and multicore NPs assembled in a unique flower-shaped structure were reported[48]. Furthermore surface modified magnetite NPs were obtained using a one-step continuous hydrothermal process in a counter-current flow reactor[49]. It remains challenging to obtain Fe_3O_4 (magnetite) NP exclusively starting from a mixture of Fe(III)/ Fe(II) under high pressure, temperature, and flow of suspension with controlled shape and a narrow size distribution, avoiding the presence of large particles and therefore ensuring the superparamagnetic nature of the NPs.

Another potential solution to narrow the size distribution was found using bioinspired routes. The basic coprecipitation in a hydrogel network offers diffusion control of nucleation and crystal growth by suppressing convection[50]. Living organisms such as chitons and magnetotactic bacteria are also able to form magnetite crystals with well-controlled sizes and shapes using macromolecular templates. Following the same approach the use of water-soluble (bio)macromolecular control agents, such as magnetosome proteins has become of great interest[51]. The cationic polypeptide poly(-L-arginine) was used in an ultraslow titration co-precipitation reaction which led to the formation of monodisperse stable single-domain magnetite NPs of 35 ± 5 nm[51]. Interestingly, other magnetosome proteins such as MamJ and MtxAD1–24 have significantly different effects on magnetite co-precipitation, since they strongly inhibit magnetite nucleation. Biomacromolecules such as Mms6 have proven to promote well-defined cubic-octahedral magnetite crystals when used as extra additive in the co-precipitation process. This is due to the amphiphilic nature of the magnetosome protein Mms6, that allows to form micelle-like aggregates in aqueous solution[51].

Based on these results the authors concluded that ‘‘in the case of magnetite formation proteins, larger complexes, or membrane components promoting the nucleation *in vivo* are likely to expose positively charged residues to a negatively charged crystal surface’’[52]. Moreover, the limitations on the production of core sizes above 20 nm (up to 60 nm) and different shapes were overcome by conducting slow co-precipitation of magnetite through a ferrihydrite/Fe (II) precursor in mildly alkaline aqueous medium using a NH_3 by the use of different co-polypeptides poly(L-aspartic acid) and poly(L-lysine) with varying co-polypeptides/Fe ratios as additives.

1.2.1.2 Partial Reduction of Iron (III) Salts

Hydrophilic magnetite NP have also been obtained in aqueous media in one-step syntheses by the hydrothermal-reduction of Fe(III) salts in an autoclave. Hydrazine, citrate, sodium borohydride, carbon monoxide and dimethyl-formamide have been used as reductants although they are highly reactive and pose potential environmental risks[53-55]. Other mild and nontoxic reducing agents such as ascorbic acid, tartaric acid, aspartic acid and α-D glucose have also been used for the synthesis of iron oxide NP by hydrothermal-reduction method[56]. Tunable size and narrow size distribution can be achieved by choosing an appropriate mixture of solvents and varying parameters such as temperature, pressure and reaction time. The advantages of using a hydrothermal/solvothermal approach for synthesizing MNP include a high degree of product purity, easy control of the size, high crystallinity and uniform morphology of the NP, relatively lower temperatures (in general < 200 ºC) and the use of non-specialized equipment and simple overall process.

1.2.1.3 Partial Oxidation of Iron (II) Salts.

Partial oxidation of Fe(II) salt solution in alkaline media is summarized in equation 2[57-58]. An intermediate phase (the green rust) is formed owing to the presence of the base and undergoes dehydroxylation steps leading to the formation of magnetite. Sugimoto & Matijevic developed several procedures for the preparation of magnetite particles between 100 and up to 1000 nm using this route[59].

$$3\ FeCl_2 + 6\ NaOH \rightarrow 3\ Fe(OH)_2 + 6\ NaCl$$
$$2\ Fe(OH)_2 + 0.5\ O_2 \rightarrow 2\ FeOOH + H_2O$$
$$2\ FeOOH + Fe(OH)_2 \rightarrow Fe_3O_4 + 2\ H_2O \qquad (1.2)$$

In the latter work, it was pointed out that a dramatic change in mean particle diameter was observed over a very small concentration range of Fe(II) salt due to a sharp pH change[60]. In this case, the Fe(II) salt was kept oxygen-free by bubbling N_2 in a water bath at a fixed temperature. Both the base and the oxidant (KNO_3 instead of air) were added dropwise. The obtained magnetite particles had cubic shape and were monodisperse with a size range of 50-200 nm. In the past decades partial oxidation has been less studied than other synthetic routes. Interestingly, this strategy led to magnetite NPs with a size range of 20-100 nm, well-defined size and shape and with few defects on the surface.

The control of the main parameters of the process (the oxidant, iron concentration, pH and the temperature) following the guidelines stated by Sugimoto & Matijevic,[59] enables the reproducible large scale synthesis of magnetite nanocrystals.[61] Unfortunately, two iron oxides phases are often formed

simultaneously if the conditions are not properly chosen. The origin of such difficulty lies in the complexity of the process that takes place through the gelatinous intermediate (the green rust) that evolves to magnetite by reaction with Fe(II) in solution, or to an oxyhydroxide such as lepidocrocite or goethite, depending mostly on the rate of oxidation. The author´s emphasized that magnetite formation requires the complete dehydroxylation of the precursor (green rust) prior to their oxidation.[62] If oxidation is too fast and precedes dehydroxylation, lepidocrocite is formed in preference to magnetite. MNPs prepared in this way are characterized by very high saturation magnetizations values and have been proved to be useful for biomedical applications such as magnetothermia and magnetically guided drug delivery[61, 63-64].

Among the factors that influence the oxidation rate of green rust, the counterions are presumably relevant because they affect green rust's structure that consists of positively charged octahedral brucite-type Fe(II)-Fe(III) hydroxyl layers linked by anions[62]. Recently, a detailed study on the effect of different counterions along with the use of mixed solvents was carried out[65]. The differential stabilities of green rust modifications as well as the dehydration and oxidation processes of Fe(II) that follow (both facilitated by cosmotropic environments) are responsible for the differences in magnetite particle sizes obtained (Figure 1.3). This is especially relevant because the average particle size of the obtained particles is often close to the superparamagnetic-ferrimagnetic limit of magnetite (close to 20 nm). The range of nanocrystal sizes obtained (20-60 nm) has a profound influence on the magnetic moment per particle.

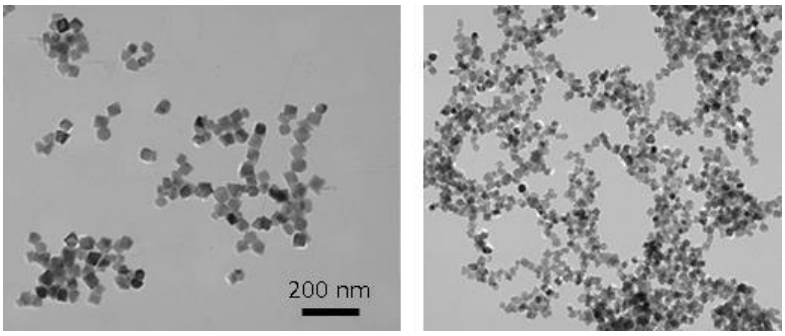

FIGURE 1.3 TEM micrographs at the same magnification of the sodium bearing magnetite nanocrystals obtained by partial oxidation of Fe(II) salts in water (on the left) and ethanol 25% (on the right).

1.2.1.4 Reduction of an Antiferromagnetic Precursor

One of the current challenges in MNPs research is the production of large magnetite cores with well-controlled size and shape, large magnetic moment and long term colloidal stability. An interesting aqueous-based approach to produce single-core magnetite NPs with different morphologies and core sizes above 25 nm using antiferromagnetic precursors has been developed recently. It consists of a three-step process (Figure 1.4) and enables to obtain uniform magnetite rhombohedra, discs and elongated MNPs[66]. Similar procedure was used to obtain magnetite and iron metal nanorods[18, 67].

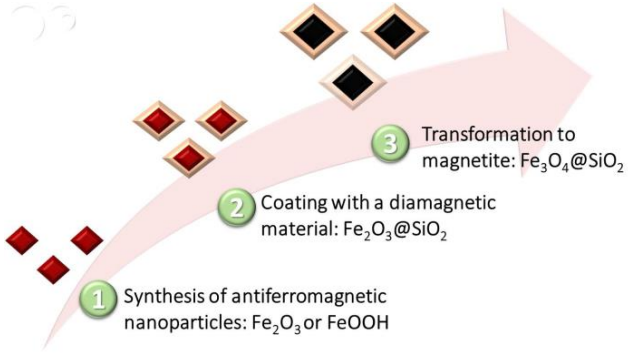

FIGURE 1 4 General scheme for the synthesis of single core NPs with sizes above 25 nm and different morphologies through the reduction of antiferromagnetic nanoparticles.

First, an aqueous synthesis route is followed to obtain uniform antiferromagnetic precursors such as hematite or goethite, whose size and shape can be tuned by changing the synthetic conditions including temperature, pressure, and nature and concentration of the salts used (Figure 1.5)[62]. Furthermore, this route could be scalable for large production. Then, the antiferromagnetic precursor particles are coated by a silica or alumina layer that prevents their aggregation[18, 68]. Finally, the silica coated antiferromagnetic particles are reduced to magnetite. This can be either performed on particles in powder form, by exposing them to a hydrogen atmosphere at a certain partial pressure (dry reduction)[69] or in liquid form, where oleic acid and an organic solvent are used (wet reduction)[70]. In both processes, the hydrogen and oleic acid act as the reducing agents.

As a result, exotic morphologies of magnetite such as rhombohedra (70 nm), discs (140 x 20 nm) and needles (180 x 30 nm) were obtained, and both reduction methods transform completely the starting precursor to a single iron oxide phase of magnetite without morphology changes[66] (Equation 1.3.a and b and Figure 1.5). Powder reduction shows fewer defects in the crystal structure, slightly higher values of saturation magnetization, and a more homogeneous remanent magnetization state. Pores within the core structure were observed, being more pronounced in the case of using goethite precursor as a consequence of the phase transformation (goethite suffers dehydration to hematite prior transformation to magnetite, Equation 1.3.a). Moreover, when lower reduction temperatures and shorter times are used, nanorods consisting of clusters of maghemite embedded in an antiferromagnetic hematite matrix are obtained with very interesting relaxometric properties and potential use as MRI contrast agents[71].

$$2\mathrm{FeOOH} \rightarrow \mathrm{Fe_2O_3} + \mathrm{H_2O} \qquad (1.3.a)$$

$$3\mathrm{Fe_2O_3} + \mathrm{H_2} \rightarrow 2\mathrm{Fe_3O_4} + \mathrm{H_2O} \qquad (1.3.b)$$

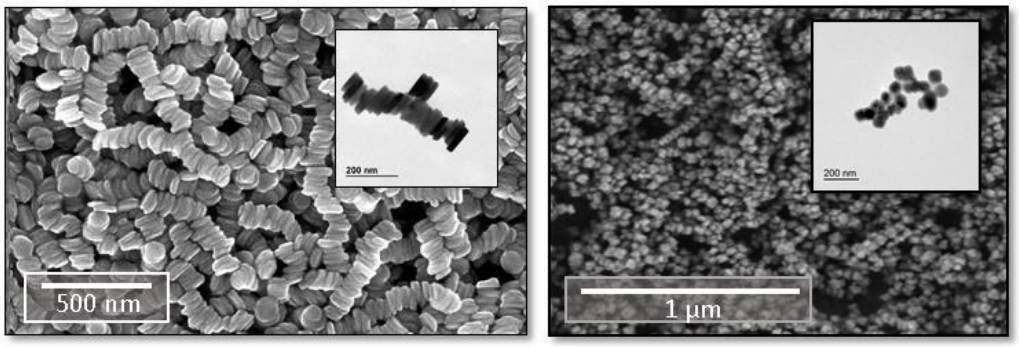

FIGURE 1.5. Scanning electron microscopy (SEM) images of the antiferromagnetic hematite precursors of magnetite nanoparticles with different shape: Discs on the left and rhombohedra on the right.

The possibility of generating a discontinuous structure within a particle by forcing the pore formation as those showed in the magnetite needles after reduction (Figure 1.6),[71] may be an interesting strategy to develop new materials for biomedical applications. Moreover, this method has the advantage of covering different particle size ranges and morphologies, opening up new possibilities and the potential interesting magnetic properties.

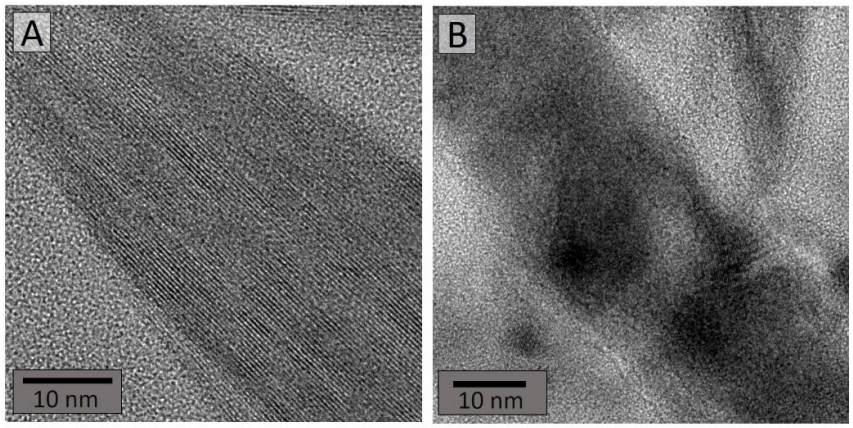

FIGURE 1.6 High resolution TEM images of the goethite precursor (A) and the resulting needle magnetite nanoparticles (B) after reduction, showing pore formation.

1.2.1.5 Biomineralization

Biomineralization in broad sense are all processes that biological systems employ to build the organic–inorganic hybrid materials present in all living systems, with functions ranging from navigation, mechanical support, photonics, to the protection of the soft parts of the bod[72-73]. Often these biominerals have complex shapes and textures, exceptional structural hierarchy, and interesting properties and in general are characterized by the highest observed level of control over composition, structure, size and morphology of the constituent mineral components. Examples of iron-based biominerals are the radula teeth of chitons mollusks that contain crystalline iron oxides such as magnetite (Fe_3O_4) and lepidocrocite (γ-FeO(OH)), and the intracellular chains of magnetite NPs synthesized by magnetotactic bacteria[74].

Researchers have taken inspiration from nature, aiming to apply the key aspects of biomineralization to more sustainable synthetic methods. Indeed, in particular, mimicking the pathways used by magnetotactic bacteria would open the way to aqueous room temperature synthetic methods that still allow control over dimension, structure and, as a consequence, magnetic properties of the magnetite synthesized. Recently, the synthesis of magnetite at ambient conditions was followed by using hexagonal ferrihydrite as a precursor, starting from Fe(III) salt, obtaining a gel-like precursor material identified as 6-line ferrihydrite[75]. The latter transformation of ferrihydrite to magnetite was carried out by the addition of Fe(II) salt under a N_2 atmosphere, and the subsequent increase of the solution pH by NH_3 diffusion. It was observed that the assembly of 1.5–2.0 nm primary particles into aggregates after ~1.5 h reaction time lead 10-20 nm uniform magnetite NPs after >12 hours. This route was conducted in the presence of random copolymer of glutamic acid, lysine and alanine producing magnetite with a less polydispersed size distribution[75].

1.2.2 ORGANIC SYNTHESIS BY THERMAL DECOMPOSITION OF AN ORGANIC PRECURSOR

Thermal decomposition of organometallic compounds is able to produce MNPs with good crystallinity and high monodispersity[76]. This approach offers two routes to control nucleation and growth processes that occur during the particles synthesis. One procedure is the injection of organometallic compounds into a hot surfactant solution, which results in the formation of nuclei almost instantaneously. The other option is the controlled heating of organometallic compounds in a surfactant solution to generate the nuclei. Once the nucleation has occurred, particles grow at high temperature. Finally, through a rapid decrease of the reaction temperature, the growth of the NPs can be stopped[77]. Control of the nanoparticle size, shape and aggregation depends on the number of nuclei initially generated and the presence of surfactant or other molecules hampering the nanoparticle growth process[78]. Direct syntheses of magnetite NPs with different sizes and morphologies have been reported, including nanospheres,[78] nanocubes,[79-81] nanowires,[82] nanorods,[83] nanooctahedra,[84] nanoplates[85] and nanoprisms[86]. Examples of particles obtained by thermal decomposition of organometallic compounds showing very narrow core size distributions can be observed in Figure 1.7. Other materials such as cobalt substituted ferrite NPs[87] and Ag@Fe_3O_4 core-shell NPs[88] can also be prepared by thermal decomposition of organometallic precursors. In the last case, a temperature pause introduced in a simple single-step thermal decomposition of iron precursors, with the presence of silver seeds formed in the same reaction mixture, gives rise to this novel compact heterostructure.

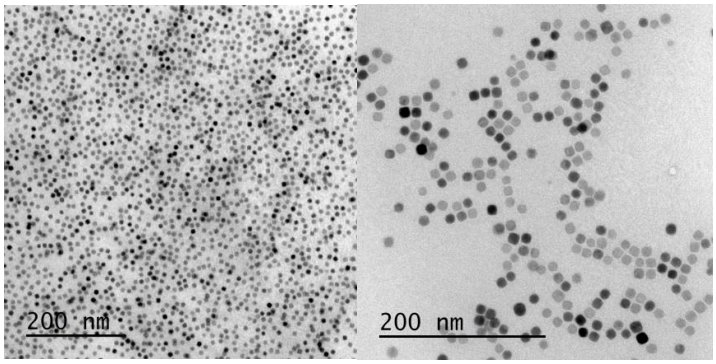

FIGURE 1.7 TEM images of magnetite nanoparticles prepared by thermal decomposition of Fe(III)-oleate complex in 1-octadecene.

The control of particle size could be achieved by the use of an extension of the La-Mer mechanism in combination with a careful addition of reactant[89] or by a seeded-growth technique[90-91]. Most commonly particle sizes can be controlled by varying the precursor concentration, the Fe(III)/oleic acid ratio[92] or the solvents used[93-94]. Single-core iron oxide nanocubes with sizes in the range between 20 nm and 160 nm have been synthetized with Fe(III) acetylacetonate in oleic acid and benzyl ether[79]. Particle shape may be modified from spheres to cubes by adding sodium oleate to the synthesis[95]. Alternative iron precursors include iron pentacarbonyl leading to smallest NPs[96] and iron oleate that allows to obtain very uniform and larger particles[78].

Nanocrystal shape control has been generally achieved by selective adhesion of surfactant to a particular crystal face and its slow growth along this direction. Without surfactants, NPs can suffer an oriented aggregation into dense or hollow micrometer spheres[97-98]. Uniform anisotropic 1-D magnetite nanorods with length of from 63 to 140 nm and diameter of ca. 6.5 nm were prepared by solvothermal reaction with iron pentacarbonyl, oleic acid, and hexadecylamine as raw materials and 1-octanol as solvent. Oleic acid displaces the carbonyl group to form iron oleate, which could be a precursor of iron oxide. Simultaneously the easier thermal decomposition of the residual iron pentacarbonyl supplied the growth sites for the incorporation of the magnetite nucleus generated from the iron oleate by hydrolysis driven by the water released by the condensation between oleic acid and hexadecylamine present in the reaction media. The controlled releasing water promotes the formation of 1-D magnetite nanorods. The length of the nanorods could be tuned by changing reaction time and the amount of hexadecylamine[83]. Calorimetric and AC magnetometry experiments performed for the first time on highly crystalline Fe_3O_4 nanorods consistently show large specific absorption rate (SAR) values (862 W/g for an AC field of 800 Oe and 310 kHz), which are superior to spherical and cubic NPs of similar volume (~140 and ~314 W/g, respectively). Increasing the aspect ratio of the nanorods from 6 to 11 improves the SAR by 1.5 times[99].

In the synthesis of iron oxide NPs by thermal decomposition in organic media, the growth occurs mainly by monomer addition, and the cluster dimension is controlled by the presence of surfactants, usually oleic acid and oleylamine[100]. The importance of the ligands that form the protecting monolayer in controlling the oriented aggregation growth was evidenced by Xue *et. al*[101]. In this frame, the presence of a multidentate ligand on the NPs surface would roughen the growing surface make it prone to aggregation. Good candidates could be calix[n]arenes,

synthetic aromatic macrocycles, extensively employed in the host-guest chemistry as platforms for the construction of very efficient and selective hosts[102]. It is also known that they can chelate Fe(III) ions and are able to act as capping agent for iron oxide NPs [103-104]. The p-tert-butyl calix[8]arene induce oriented aggregation of iron oxide NPs to obtain homogeneous and monocrystalline magnetite 45 nm nano-octahedra. This process allows a high control degree of product morphology. In particular, stopping the reaction before the aggregation process reaches its completion, it is possible to obtain crystals in multi-core state, with interesting magnetic and hyperthermia properties (Figure 1.8)[105]. Application of calixarene derivatives in biotechnology and bio-medical researches has been already reviewed[106].

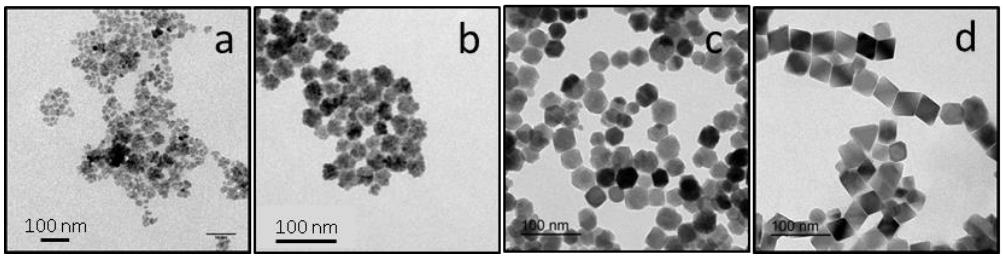

FIGURE 1.8 TEM images showing the evolution of particle aggregation from a) to d) with heating for a mixture of iron(III) acetylacetonate and oleic acid in benzyl ether in the presence of calixarenes. Reproduced with permission of Dr. Vita.

Although thermal decomposition in organic media has been proven to be an effective approach for preparing uniform, single-crystalline, well-defined and phase pure MNPs, some disadvantages remain, such as the required rigorous and more control of the synthetic conditions, including oxygen-free atmosphere, long reaction time and high reaction temperatures. In addition, many of the reactants and by-products are considered to be toxic. More important, the surfactants bind to the nanoparticle surface render them hydrophobic and therefore further steps are needed after the synthesis, to stabilize the particles in aqueous medium for its use in biomedical applications. This transfer to water can lead to irreversible aggregation of the particles.

There are many methods employed to avoid this outcome, and that can successfully transfer particles from non-polar solvents to aqueous media in the form of individual particles using either inorganic or organic coatings (Figure 1.9)[107-110]. In this sense, high binding affinity of poly(ethylene glycol)-gallol (PEG-gallol) has been showed to allow freeze drying and re-dispersion of 9 nm iron oxide cores individually stabilized with approximately 9-nm-thick stealth coatings, yielding particle stability for at least 20 months[111]. PEG-gallol coated iron oxide nanocubes can be remotely activated with an alternating magnetic field and a near-infrared laser achieving a very efficient heat conversion at clinical doses[112].

Also the transfer process to water has benefits that further functionalities to the NPs can be added. For example an amphiphilic polymer, poly(maleic anhydride-alt-1-octadecene) (PMAO) was modified with tetramethylrhodamine 5(6)-carboxamide cadaverine (TAMRA) and used to obtain a fluorescent magnetic nanosystem that after further steps of biofunctionalization offers a great opportunity for the development of active targeting strategies for the early detection and treatment of cancer[113-114]. Using the same approach, different biocompatible tumor cell-targeting ligands were investigated to date, such as

saccharides, that represent promising molecules for the delivery of such nanoprobes[115-118]. By careful choice of a PEG-ylated amphiphilic polymer it was possible to stabilize hydrophobic magnetite NPs of 27 nm in water with hydrodynamic diameters as low as 54 nm. This colloid was successfully used as a tracer for magnetic particle imaging (MPI) with a superior performance to Resovist®[119].

Recently, colloidal inorganic NPs have been coated with a thin, cross-linked, and functionalized shell containing organic and inorganic layers[120]. The synthesis of the hybrid surface layer takes advantage of the adsorption of amphiphilic polymers to the hydrophobic stabilizing ligands on the colloidal nanoparticle surfaces. Commercial poly(styrene-co-maleic anhydride) (PSMA) was adsorbed. Then, the silica precursor, 3-aminopropyltriethoxysilane (TEAPS), was reacted, resulting in a silane being tethered to the polymer. The temperature of the reaction mixture was lowered to further aid this process. The polymerization of the tethered silica precursors occurs (Scheme 1, step C) resulting in particles that are soluble in dimethyl sulfoxide (DMSO), dimethylformamide (DMF), and 0.05 M NaOH.[120]

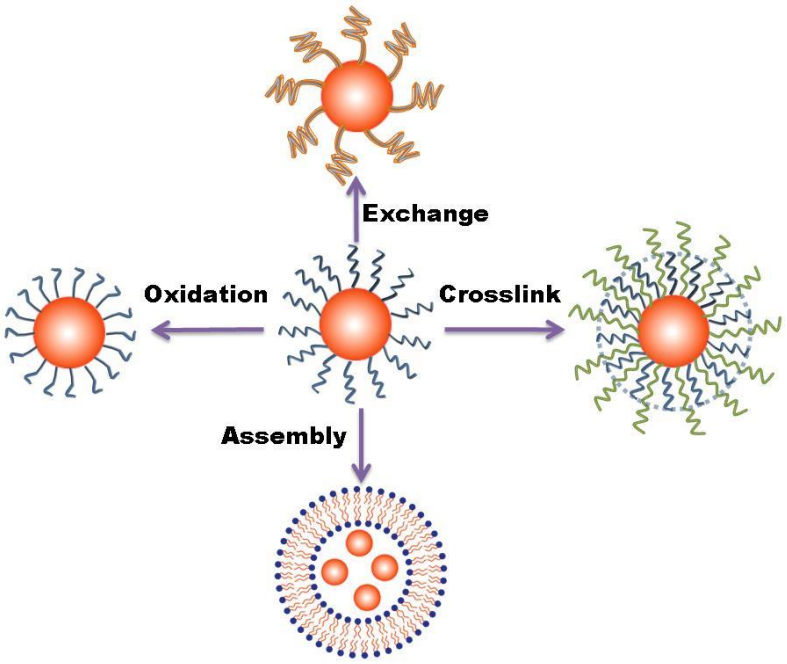

FIGURE 1.9. Different strategies to transfer particles from non-polar solvents to aqueous media.

1. 2.3. POLYOL SYNTHESIS

The synthesis routes to obtain magnetite NPs mediated by polyols (polyhydric alcohols or etherglycols) are at present one of most versatile processes due to the possibility to obtain particles with very different structures and morphologies in the nanometer size range (Figure 1.10) [121-122]. Generally, the polyol is able to dissolve the iron precursor (nitrate, chloride, acetate), due to its high dielectric constant and because its extensive hydrogen-bonds. The solution is heated to a given temperature, which can reach the boiling point of the polyol, for a certain period after which the NPs are formed. Among other advantages, the monodispersity of the obtained particles as well as the functionality that the polyol provides (this

allows them to remain stable in aqueous media and other polar solvents) are highlighted. Furthermore, great crystallinity is achieved owing to the typical high temperatures used during the synthesis.

The polyol-mediated synthesis was described at first as a novel route for preparing metal powders by reducing the metal ions present in the precursor through the polyols[122]. These can be oxidized to their corresponding aldehydes (Equation 1.4) and act as mild reducing agents, being capable of reducing some metals easily, such as copper and noble metals.

$$HOCH_2\text{-}CH_2OH + 2/n\ M^{n+} \rightarrow HOCH_2\text{-}CHO + M^{(0)} \quad (1.4)$$

However, in the case of iron and other less reducible metals, the reaction temperature should reach the boiling point of the polyol, resulting in oxidation to the diacetyl, leading to the reduction of the metal. In order to obtain the corresponding metal oxide instead of the metal with zero oxidation state, the presence of oxygen or a certain amount of water is required. Moreover, polyols such as α-diols, have chelating properties and act as coordinating solvents which can form complexes with many metal cations.

Therefore, they can form reactive intermediate species on one hand, and on the other adsorb onto the surface of the growing particles preventing aggregation. Iron oxide MNPs (such as magnetite Fe_3O_4, or maghemite γ-Fe_2O_3 phase) have been synthesized by the polyol mediated process[35]. This is due to the capability of producing hydrophilic iron oxide NPs with high magnetization values and zero remanence at room temperature within one step. Some of the above mentioned morphologies that the crystals can adopt by optimizing the reaction conditions are: spherical single-core NPs[121, 123], nanocrystal clusters[124], compact microspheres,[125] hollow nanospheres,[126] and flower-like NPs[34]. In Figure 1.9, magnetite single-core particles (a) are obtained by mixing the Fe(II) and Fe(III) salts in a 1 : 1 w/w solution of diethylene glycol (DEG) and N-methyl diethanolamine (NMDEA), the addition of a sodium hydroxide solution and a subsequent thermal treatment. By optimizing the thermal treatment that the initial reactants undergo, multi-core nanoflowers (b) can be produced.

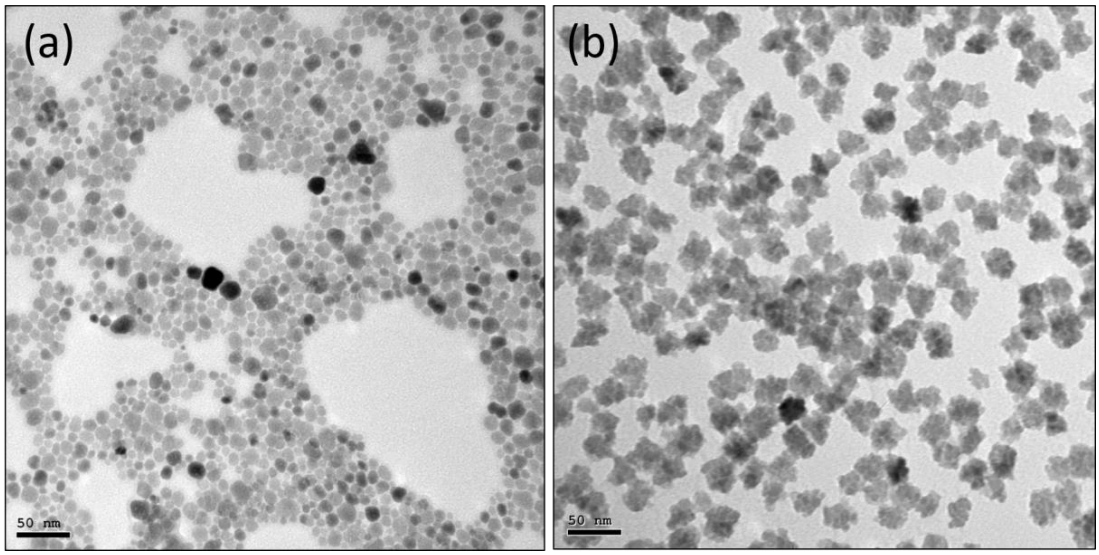

FIGURE 1.10. Representative TEM images of magnetite nanoparticles prepared in a polyol mediated synthesis by mixing the initial Fe(II) and (III) salts in a DEG/NMDEA (1 : 1, w/w). (a) single-core particles. (b) Multi-core nanoflowers.

These Fe_3O_4 multi-core NPs assembled in flower-shape structures have shown enhanced longitudinal and transverse relaxivities for MRI contrast generation and enhanced SAR values for magnetic hyperthermia[35]. Another common polyol-mediated synthesis routes start from an Fe(III) salt and the reaction is performed in an autoclave. In such a way, the reaction solution is held at high temperatures and pressures. This simple route allows obtaining relatively large batches of particles. Water-dispersible iron oxide NPs (6-14 nm) were obtained in such way starting from iron acetylacetonate ($Fe(acac)_3$) and triethylene glycol (TREG)[127]. The particles were subsequently coated with carboxylic acid ligands achieving long term stability and proving to be effective as MRI contrast agents for applications such as stem cell tracking or cancer cell targeted imaging.

Polyols have diverse physico-chemical properties (see table 1) that allow magnetite NPs with different properties to be obtained.

TABLE 1.1 Principal physico-chemical properties of different polyols and their comparison with water and ethanol. Ethylene glycol (EG), propylene glycol (PG), diethylene glycol (DEG), triethylene glycol (TREG), εr = Dielectric constant, μ (D)= Electric dipole moment in Debye units, T_{eb}= Boiling point.

Solvent	Water	EG	PG	DEG	TREG	Ethanol
ε_r	78.50	38.99	32.0	30.03	19.35	24.30
μ (D)	1.85	2.28	-	2.31	-	1.66
T_{eb} (°C)	100	198	189	245	325	36

Ethylene glycol (EG) and propylene glycol (PG) were compared as solvents in the reaction. It was found that the morphology evolutions of iron oxide NPs are significantly different in these two polyol processes. Because of their different reductive ability, the formation and growth rate of NPs is different, achieving more aggregated NPs in the case of PG and resulting in porous single crystals after Ostwald ripening process[127]. Nonetheless, for the cluster formed in EG with a

relatively lower formation rate of NPs, most of NPs have enough time to self-assemble along the same orientation in the cluster with retention of its secondary structure (flower-like cluster), owing to the lower surface energy.

Figure 1.11 (a-f) shows TEM images of flower-shaped magnetite NPs formed by aggregation of primary particles. The TEM images in Figure 1.11 show a reproduced synthesis of magnetite dense and hollow spheres. The hollow spheres (Figure 1.11 c-d) are formed by dissolving ferric chloride, polyvinylpyrrolidone (PVP) and an optimized amount of sodium acetate (NaAc) in ethylene glycol[126]. The mixture is heated in an autoclave and maintained at 200 ºC for 16 h. Nano-sized hollow magnetite has attracted great interest because of its properties such as low density, selective permeability, and large specific area, etc[126]. Dense spheres (Figure 1.11 a-b) of 100 nm were obtained using sodium citrate and not PVP as stabilizer. [124] The rest of experimental conditions and reactants (sodium acetate, EG, and solvothermal crystallization in an autoclave at 200 ºC for 16 h) are very similar to those used in the synthesis of hollow spheres. Finally, Figure 1.11 e-f shows TEM images of a reproduced synthesis of core/shell structure of magnetite/carbon colloidal NPs with average size about 190 nm prepared via a one-step solvothermal process using ferrocene as a single reactant[37, 128].

Improving water stability of magnetic NPs produced by the polyol process have been achieved by coating with different hydrophilic polymers, such as poly(hydroxyethyl methacrylate) and poly(methacrylic acid), using atomic transfer radical polymerization (ATRP)[129]. Similar 150 nm superparamagnetic nanocrystal clusters were synthesized by a modified polyol process in the presence of glucose and poly(vinyl-pyrrolidone). At high concentrations due to the thick and uniform coating and size these systems in presence of magnetic fields form photonic crystals with reflection colours depending on the strength of the magnetic field applied[130].

On the other hand, manganese doped iron oxide nanoparticle clusters have also been synthesized by a similar approach and showed distinct performance as imaging contrast agents and excellent characteristics as heating mediators in magnetic fluid hyperthermia arising from the Mn doping[131].

The superparamagnetic behavior, high magnetization, and high water dispersibility make nanocrystal clusters or flower-shaped NPs below 150 nm ideal candidates for diverse biomedical applications, since they are composed of crystals below 10 nm, and they do not have strong magnetic interactions in dispersion[132-134]. In addition, some of them exhibit low cytotoxicity, a good biocompatibility, and high capacity for efficient and convenient enrichment of trace peptides[134]. This make them promising candidates for bio-applications in various related fields, such as cell imaging and cell sorting, and for sample pre-enrichment to analyze trace peptides or proteins in proteomics, and in particular those related with diseases, and to find biomarkers[124].

The polyol synthesis of MNPs has two main limitations, the restricted reducing power of polyols and the resulting polyol-functionalised particle surface of the as prepared particles.

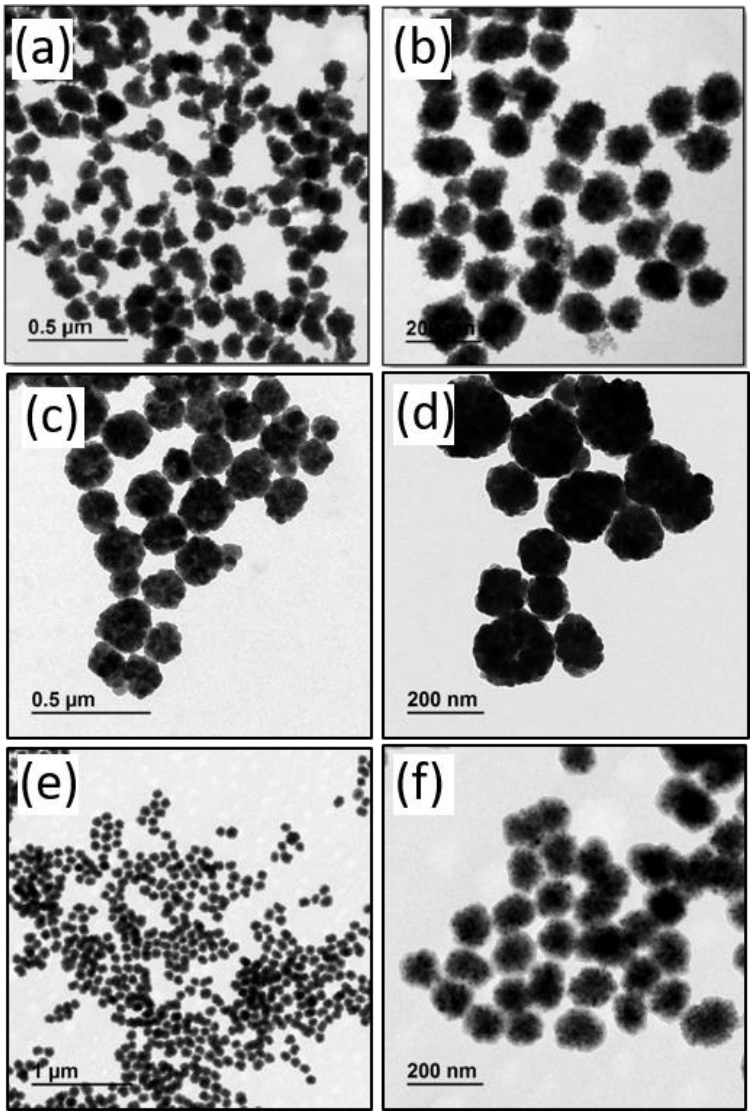

FIGURE 1.11 TEM images of magnetite flower-shaped nanoparticles prepared in a polyol mediated synthesis from iron (III): (a-b) 100 nm solid spheres. (c-d) 200 nm hollow spheres. (e-f) 100 nm carbon encapsulated flower-like nanoparticles obtained by hydrothermal decomposition of ferrocene in acetone in an autoclave.

1.2.4. MICROWAVE ASSISTED SYNTHESIS

In the past two decades, microwave dielectric heating has gained a lot of attention as a new nanoparticle synthesis method. This is due to its versatile nature in different disciplines, such as polymer chemistry, biomedicine, materials science and nanotechnology. This non-classical heating method has shown an impressive reduction in synthesis time (from hours to minutes), an increase in product yield and superior material properties as well as reproducibility when compared to the conventional heating (by heat transfer)[135]. The first reports on microwave heating in chemistry were published in 1986 by the groups of Gedye and Giguere,[136-137] since the first commercial microwave oven for home use was launched in 1954.

Microwaves are electromagnetic energy with low frequency in the range of 300 to 300.000 MHz. When a sample is irradiated with microwave frequencies, the dipoles tend to align in the direction of the applied electric field. As the field

oscillates, the dipoles try to realign along the alternating field streamlines, in such a way energy is lost in the form of heat, through dielectric loss and molecular friction[138]. If the dipole does not have enough time to realign with the applied field, no heating will occur, the same if it reorients too quickly. The frequency of 2450 MHz, corresponding to a wavelength of 12.24 cm, chosen by all commercial systems, is between these two extremes and does not interfere with phone frequencies and telecommunication.

Either the substrate or reagents are likely to be polar, presenting a dielectric property for the reaction, allowing sufficient heating by microwaves. When considering solvents for the microwave reaction, boiling points become less important, than in conventional heating under reflux since the pressurized vessels provide reasonable use of solvents with lower boiling points, but the efficiency of the mixture to couple with an applied microwave field becomes an important factor. It can be found in the literature tables of solvents, classifying them by dielectric constant, tan (δ) and dielectric loss,[138] that gives an idea of which solvent is more appropriate for the required nanoparticle synthesis. Table 1.2 shows some common organic solvents and its respective values for the dissipative factor tan(δ) = ε"/ε' (ε" is the dielectric loss factor related with the energy transformed to heat and ε' is the dielectric constant related with the capacity of the material to store energy in form of electrical potential). If tan (δ) > 0.5, the solvent is classified as high microwave absorbing, if 0.1 < tan(δ) < 0.5 as medium and if tan(δ) < 0.1 as low microwave absorbing.

TABLE 1.2 Dissipative factors of some common organic solvents. Dissipative factor tan(δ) = □"/□' (□" is the dielectric loss factor related with the energy transformed to heat and □' is the dielectric constant related with the capacity of the material to store energy in form of electrical potential.

Solvent	tan(δ)	Solvent	Tan (δ)
Ethylene glycol	1.350	Acetone	0.054
Ethanol	0.941	Dichloromethane	0.042
2-Propanol	0.799	Toluene	0.040
Water	0.123	Hexane	0.020

Preparation routes for transition-metal oxide nanocrystals and in particular iron oxide NPs rely on nonhydrolytic pathways, in non-aqueous solvents[139]. These routes allow a good control over structure, size and shape of the nanocrystals. Alcohols are classified as high tan(δ) solvents, being convenient as reaction media for this non-aqueous microwave-assisted synthesis although other solvents like dibenzyl ether or ethylene glycol have been used.

In organic media, starting from Fe(III)acetylacetonate in benzyl alcohol, Fe_3O_4 nanocrystals of 10 nm were successfully produced, by ultrafast reaction, *i.e.* in just a few minutes at 200 ºC under microwave heating,[140] or at 180 ºC for 10 minutes[141]. Ultrasmall iron oxide NPs of around 3.7 nm with excellent T_1 MRI contrast properties were synthesized using also Fe(III)acetylacetonate in benzyl alcohol but adding oleylamine and 1,2-dodecanediol[142]. The presence of a polymer like PVP also leads to small iron oxide NPs of around 5 nm whose size can be increased up to 7 nm by changing the heating ramp up to 210 ºC for 10 hours[143].

On the contrary, uniform flower-like Fe_3O_4 clusters of a few μm were fabricated in ethylene glycol with $FeCl_3$, sodium acetate and a surfactant, under

microwave irradiation at 160ºC for 15 to 60 min (Figure 1.12)[144]. It was speculated that microwave irradiation set the conditions for creating nanocrystals seeds and accelerated its clustering under assistance of stabilizers. Using a pressurized microwave reactor, particles in the range of 20 to 130 nm were obtained, dissolving $FeCl_3.6H_2O$ in ethylene glycol followed by the addition of ammonium acetate, for 30 min at 220 ºC[145].

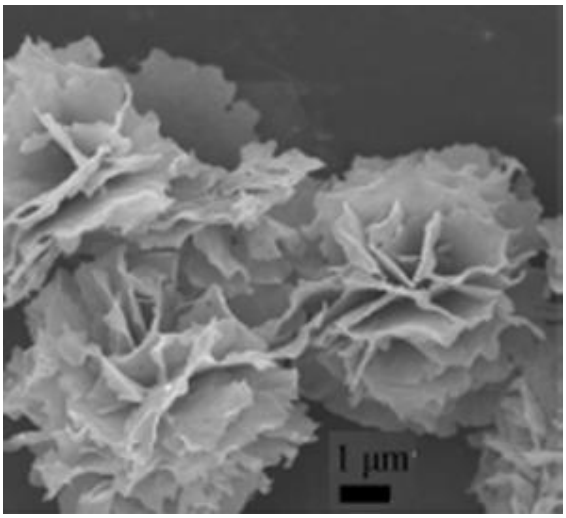

FIGURE 1.12 SEM images of uniform flower-like Fe_3O_4 clusters of a few µm, fabricated in ethylene glycol with $FeCl_3$ by microwave assisted synthesis. Copyright 2010 American Chemical Society. Reproduced with permission[144].

Alternatively, room temperature ionic liquids (such as 1-butyl-3-methylimidazolium tetrafluoroborate ([BMIM][BF_4]) are ideal candidates for making a nonpolar solvent suitable for microwave heating. Ionic liquids have received a great deal of attention in recent years as novel solvent systems for a range of organic reactions due to their polar nature, and attractive properties such as incombustibility, non-volatility, unique phase behavior, and good solubilizing capacity[146-148]. The ionic character of ionic liquids provides excellent coupling capability with microwave irradiation. Although numerous nanomaterials including iron oxide nanocrystals have been prepared by using ionic liquids as solvents or co-solvents[140, 149-150] only a few reports deal with the synthesis of Fe_3O_4 NPs[151]. To combine the high temperature solution-phase reaction in an organic solvent like benzyl ether (boiling point = 297 ºC) and the microwave heating, an ionic liquid [BMIM][BF_4] was used in a small proportion (ionic liquid: dibenzyl ether = 1: 20 v/v) and magnetite NPs of 6 nm up to 10 nm were obtained in 10 min. Benzyl ether is not preferred for use in microwave-assisted high-temperature synthesis due to its substantially lower dielectric constant (e = 3.86). The ionic liquid can be recovered and reused in successive reactions for many times[151].

In aqueous media, NPs with average core size from 13 to 17 nm were sucessfully synthesized by irradiating a mixture of $FeCl_2$ and $FeCl_3$ with sodium carbonate solution, for 10 to 60 min at 60 ºC followed by addition of citric acid solution. The solution was maintained at 60 ºC for further 10 to 60 min[152]. The particles have a multi-core structure with a loose random packing of the constituent core particles. Varying the microwave power from 50 to 300 W or the reaction time from 10 to 60 min does not have a major effect on core size.

However, the post-precipitation addition of a citric acid solution and microwave treatment lead to a decrease in the particle size from around 150 nm to 50 nm (Figure 1.12). Under similar conditions but starting from an Fe(II) salt ($FeSO_4.7H_2O$), spherical NPs with core size of around 80 nm were synthesized in an alkaline medium at pH 11 in a microwave oven at high power for one minute[153]. When starting from $FeCl_3$ and in the presence of citric acid trisodium salt, hydrazine monohydrate is needed. This reaction is allowed to continue in the microwave and stirred at different temperatures from 60 ºC up to 140 ºC at 240 W during 10 min. It was shown that, contrary to other approaches, the citric acid can be incorporated from the beginning to get very small citric acid coated NPs that are well dispersed and possess a good crystallinity. These properties are mandatory requirements for a good T_1-weighted contrast in MRI[154].

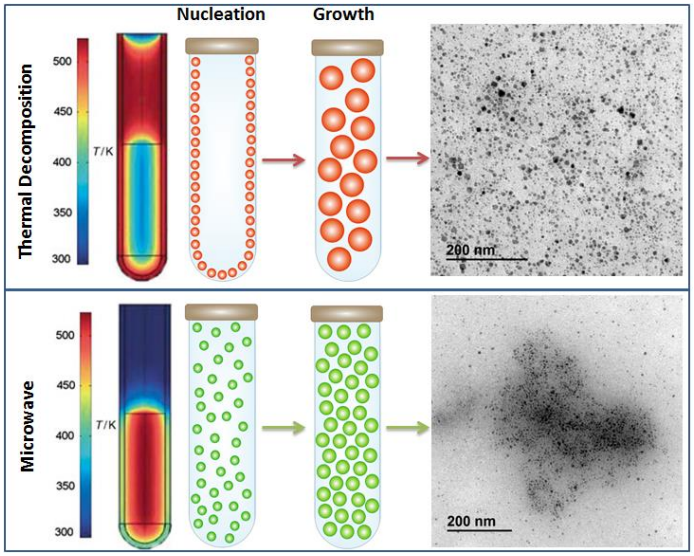

FIGURE 1.13 Different nucleation systems for thermal decomposition and microwave, when the nanocrystals nucleate on the vessel wall first or throughout the entire solution, respectively. The images of TEM show the two syntheses on the same conditions with different heating mechanism, with mean core sizes 6 nm and 5 nm respectively. Temperature gradients in oil-bath heating (up) versus microwave (below) after 1 min of irradiation. The wall temperature in the oil-bath is much higher than the one from microwave, where the whole volume is heated simultaneously[155].

In general a higher quality of the microwave derived NPs was observed in comparison with their convection heated equivalents, regarding increased phase purity, narrower size distribution and lower surface defects. This led to speculation on the so-called ‘specific microwave effects’. Using conventional heating, nanocrystals tend to nucleate on the vessel walls first, given its inhomogeneous heating profile. In contrast, microwave produces efficient internal heating, creating numerous ‘hot spots’, which could trigger multiple nucleation of seeds throughout the solution, leading to a faster nanoparticle development, and increasing the product yield. This different nucleation system could explain why NPs synthesized by microwave are smaller than the ones synthesized by conventional heating, as

shown in Figure 1.13. Microwave effects on the synthesis are still in debate and are subject of controversy. It is uncertain whether the unique outcome of NPs irradiated by microwave derives from genuine effects of the dielectric heating mechanisms or by misinterpretation of experimental evidence[156].

1.2.5. ELECTROCHEMICAL SYNTHESIS

Anodic oxidation of metal salts in solution or sacrificial metal electrodes allows the preparation of nanometric magnetic materials, in particular iron oxides[157]. Synthetic conditions, such as the nature of the electrolyte, its concentration, pH, current density, or potential, play an important role on the powder nature, purity and particle size and distribution. In addition, the synthesis can be carried out in the presence of a surfactant that may provide colloidal stability and active sites at the nanoparticle surface for further functionalization.

The advantages of electrochemical synthesis over other methods are the control of the particle size by adjusting experimental conditions such as the imposed electrooxidation current density or potential and the electrolytes present in the reaction media. The generated particles are hydrophilic and, therefore, their surface could be easily modified with biomolecules of interest. The electrochemical synthesis method is an environmentally friendly approach since it is based on an aqueous medium. The yield of this technique is low at approximately 15% because the applied current is also used in other reactions, such as the anodic oxidation of water[157]. Recent works have reported the electrochemical synthesis of Fe_3O_4, $ZnFe_2O_4$, $MnFe_2O_4$ and $CoFe_2O_4$ NPs of different sizes[158-160]. Moderate size and anisotropy of some of these ferrites ensure higher performances for hyperthermia applications. This is the case of cobalt ferrite[161] and manganese ferrite[159].

Polydopamine coated magnetite NPs were synthesized in one step by electrooxidation of iron in an aqueous medium in the presence of dopamine[162]. The oxidative conditions and alkaline pH involved in the synthesis favor the self-polymerization of dopamine that adheres at the surface of the MNPs in a simultaneous process. It is shown that the size of the magnetite NPs as well as the polydopamine coating can be controlled by varying the synthetic approach that is, adding dopamine at the beginning of the electrosynthesis, in the middle or at the end of the process. The particle size of the cores varies between a few nanometers and 25 nm whilst the shell can reach thicknesses of up to 5 nm[162].

1.2.6 OTHER SYNTHETIC ROUTES

New techniques apart of the chemical routes have been explored for the synthesis of MNPs for biomedicine. In particular, gas aggregation sources offer the possibility to fabricate NPs with controlled size, composition and different structures[163-165]. These nanometric particles are generated in the gas phase and deposited on substrates in vacuum or ultra-high vacuum conditions. A modified gas aggregation approach allows the one-step generation of well-controlled complex NPs. Thus, it is demonstrated that the atoms of the core and shell of the NPs can be easily inverted, avoiding intrinsic constraints of chemical methods. It was also proposed a fabrication route in ultra-high vacuum that is compatible with the subsequent dispersion and functionalization of NPs with PEG in aqueous media in one single step[164]. The result is the formation of NPs with a structure

mainly composed by a metallic iron core and an iron oxide shell, surrounded by a second PEG shell dispersed in aqueous solution. Relaxivity measurements of these PEG functionalized NPs assessed their effectiveness as contrast agents for MRI. Therefore, this new fabrication route is a reliable alternative for the synthesis of NPs for biomedicine, whose toxicity *in vitro and in vivo* needs further study.

Multifunctional core–shell NPs consisting of a single-domain metallic Fe core covered with a biocompatible MgO shell can attain a significant increase in the efficiency of magnetic thermal induction compared to conventional superparamagnetic oxides due to interparticle dipolar interactions' substantial influence. Those NPs can be synthesized directly from the gas phase by using a physical vapor deposition technique under inert argon atmosphere. This process has been developed at PROMES facilities in Odeillo-Font Romeu (France) using reactors operating with concentrated sunlight in a solar furnace apparatus[166]. The solar furnace is constituted of a mobile plane mirror which tracks the sun and reflects the radiation on a 2 kW parabolic concentrator (Ø 2 m). The target-material to be melted is placed onto a water-cooled holder in the center of a glass vacuum chamber. The chamber's pressure is adjusted in the high vacuum region by introducing argon and is maintained by a rotary pump. The target is transferred to the focus of the concentrator and evaporation starts to take place. Shields facilitate the growth rate control by regulating the solar beam. Particles are collected in a cold finger (nano-porous ceramic filter). By this setup, the nanoparticle production rate is about 1 g/h when the beam flux is in the order of 1 kW/m^2. The control of the Fe-to-MgO evaporation ratio and the final particle size was achieved by the variation of the iron-to-magnesium ratio[166].

MNPs produced *via* nanoimprint lithography can change the current paradigm of fabrication processes from chemical "bottom-up" synthesis to "top-down" fabrication. The combination of controlled non-directional magnetron sputtering, ethylene tetrafluoroethylene (ETFE) mold, bilayer lift-off, and dry etching release can control the shape, size, and structure of the fabricated NPs. The resulting MNPs have a novel "sombrero" shape with complex and unique physical/magnetic properties. Particles around 200-300 nm long by 20-50 nm thick are obtained by this technique[167-168].

Pulsed laser ablation in liquids has been employed to obtain polymetallic MNPs using a pulsed Nd-Yag laser and a variety of alloys as targets. Due to the presence of a liquid, the system affords synthesis and coating in a single step. By changing the target and the solvent, a variety of systems could be obtained[169.] The biomedical applications of the ablation materials are still rare due to the complexity of the equipment required and the polydispersity of the samples but terbium doped gadolinium oxide obtained using this technique was employed as a dual contrast agent (fluorescent and T_1 MRI)[170.] For the optimized 1% Tb ion doped samples, Gd_2O_3:Tb ion is capable of optical labeling, efficient for MR imaging, and does not cause significant cytotoxic effects.

1.2 PARTICLES' COATING AND POLYMER ENCAPSULATION.

In common cases the synthetic methods described above result in naked MNPs. If biomedical applications are pursued, NPs must be coated with biocompatible molecules or polymers, such as polyethylene glycol (PEG),[171] dextran,[172] chitosan,[173] polyethylenimine (PEI),[174] and phospholipids[175]. Such coatings stabilize the NPs under physiological conditions. PEG, dextran and

chitosan are particularly interesting because they are nontoxic, biocompatible and can prolong NPs lifetime in blood[176].

Dextran has been widely used to coat superparamagnetic iron oxide NPs because of its polar interactions based on multiple hydrogen bonding that provide high affinity for iron oxide NP surfaces[177]. Many of the commercial ferrofluids are dextran coated NPs. In the literature, different methods to attach dextran to the NP surface are described; however, covalent bonds instead of hydrogen bonding are preferred for their enhanced stability in physiological conditions[61, 172].

PEG is a biocompatible linear synthetic polyether that can be prepared with a wide range of sizes and terminal functional groups. The uncharged, extremely hydrophilic nature of PEG, combined with its low toxicity and low immunogenicity, render these PEG-coated NPs 'invisible' to the immune system making them attractive for biomedical applications[171]. As a result of that, PEG is commonly used in many drug and gene delivery applications.

Chitosan is a unique cationic, hydrophilic polymer that has beneficial properties such as low immunogenicity, excellent biodegradability as well as a high positive charge that easily forms polyelectrolyte complexes with negatively charged entities[178]. Magnetite–chitosan NPs have been obtained by crosslinking chitosan amino groups using glutaraldehyde[176, 179]. The disadvantage of this method is the toxicity of this cross-linker. In contrast, ionic gelation (polyionic coacervation) is an interesting technique that uses non-toxic polyanions, such as sodium tripolyphosphate (TPP) as ionic crosslinker. This procedure is simple and reproducible and NPs are encapsulated in a chitosan shell by ionic interactions.

Various temperature-responsive N-isopropylacrylamide-based (NIPAM) functional copolymers have been used for the stabilization of iron oxide NPs[180]. Although this polymer (pNIPAM) is one of the most popular stimulus-responsive polymers for research, it has been demonstrated that the NIPAM monomer is toxic and needs to be completely removed to assure biocompatibility. Long term experiments proved that pNIPAM-coated surfaces were not cytotoxic under some conditions[181].

When multi-core NPs are desired, a common approach is the use of a polymeric matrix to entrap several magnetic cores. Synthetic methods for polymer/NPs hybrid multi-core particles, where the polymer is not only intended as a stabilizer for NPs, have been reported in literature and can be divided in to three major approaches: (a) the incorporation of NPs into a forming polymer phase, e.g., polymerization in the presence of the NPs; (b) NPs formation from iron salts in an existing polymer particle and (c) the trapping within a precipitating polymer in the so-called emulsion-solvent-evaporation process (ESE). All of these processes have their advantages and disadvantages[182].

The ESE process for magnetic particles was first reported to produce hybrid beads in the size range of 125–250 μm. Hamoudeh *et. al*[183] reported a modified process, yielding magnetite/poly(lactic acid) hybrids in the size range between 320 nm and 1.5 μm, based on earlier poly(caprolactone) (PCL) hybrids between 3 and 23 μm[184]. Smaller 90–180 nm hybrid particles can be achieved based on a solvent diffusion process rather than a solvent evaporation process. The major advantage of the ESE process is the wide choice of polymers. Pre-synthesized polymers can be used, even such that cannot be synthesized in an aqueous environment such as poly(lactic acid) (PLA) and PCL. Multi-core NPs can be synthesised by controlled precipitation within a well-defined oil-in-water emulsion to trap the NPs in a range of polymer matrices of choice, such as poly(styrene), PLA, poly(methyl

methacrylate), and PCL[185]. Multi-core particles were obtained within the size range of 130 to 340 nm (hydrodynamic diameter determined by dynamic light scattering). With the aim to combine the fast room temperature magnetic relaxation of small individual cores with high magnetization of the ensemble, small (<10 nm) core NPs were used. The performed synthesis is highly flexible with respect to the choice of polymer and SPION loading and gives rise to multi-core particles with interesting magnetic properties and MRI contrast efficacy[185].

2 Final remarks

In general, cost-effective, environmental friendly and large-scale synthesis methods have been pursued keeping good control of size, shape, and composition of MNPs, which is a difficult task considering that the difference of only few nanometers in particle size means huge differences in volume resulting in a functional or failed product[63]. Reproducibility of current synthetic methods, which are able to manufacture high quality MNPs in large scale, is still a major challenge. On one hand there is a fundamental and pressing need to develop more sustainable protocols, less toxic nanomaterials in a more efficacious manner[186] On the other hand, uniformity is a critical point in order to establish the relationships between the physicochemical properties of the nanostructures and their behavior *in vitro* and *in vivo*, which is currently poorly understood. This is partly due to the complexity of the phenomena of aggregation or transformation that may take place when particles are injected into the body, interact with blood components and furthermore accumulate in different organs[187-190]. Long-term consequences of NPs on human health need further studies in the coming decades[191]. The other problem is the lack of standardization protocols for the characterization of MNPs aqueous suspensions for biomedical applications that need to be developed and implemented.

For comparison of synthetic approaches to obtain magnetite NPs, in order to have comparable crystallinity and monodispersity of magnetite, elevated temperature and pressure must be applied, *i.e.* hydrothermal syntheses, using a co-precipitation reaction, a reductive process, or an oxidative process. Regarding thermal decomposition method, it has superior structural properties in terms of controlling the size, size distribution and crystallinity. However, organic iron precursors require high temperature in an organic medium containing surfactant stabilizers. This method yields hydrophobic particles stabilized by the surfactants that need further treatments to make them hydrophilic. The polyol method, likewise, utilizes high-boiling compound such as ethylene glycol, diethylene glycol or triethylene glycol, and obtains water dispersible, monodisperse magnetite NPs. Therefore, all these methods require extreme conditions in comparison with biomineralization processes at ambient conditions, and in several cases the use of harmful organic additives or solvents. Finally, dispersion and stabilization of MNPs in water using non-toxic coatings are important issues and have been the subject of numerous publications[192] and will be discussed more in details in Chapter 5 in this book.

Acknowledgements

This work was partially supported by the Spanish Ministry of Economy and Competitiveness (Mago project, Nº MAT2014-52069-R) and by the European Commission Framework Program 7 (NanoMag project, Nº 604448).

REFERENCES

1. Xu, C.; Sun, S., New forms of superparamagnetic nanoparticles for biomedical applications. *Advanced Drug Delivery Reviews* **2013,** *65* (5), 732-743.
2. Bohara, R. A.; Thorat, N. D.; Pawar, S. H., Role of functionalization: Strategies to explore potential nano-bio applications of magnetic nanoparticles. *RSC Advances* **2016,** *6* (50), 43989-44012.
3. Ling, D.; Lee, N.; Hyeon, T., Chemical synthesis and assembly of uniformly sized iron oxide nanoparticles for medical applications. *Accounts of Chemical Research* **2015,** *48* (5), 1276-1285.
4. Blanco-Andujar, C., Aurelie Walter, Geoffrey Cotin, Catalina Bordeianu, Damien Mertz, Delphine Felder-Flesch & Sylvie Begin-Colin, Design of iron oxide-based nanoparticles for MRI and magnetic hyperthermia. *Nanomedicine* **2016,** *11* (14), 1889-1910.
5. Shah, B.; Yin, P. T.; Ghoshal, S.; Lee, K. B., Multimodal magnetic core-shell nanoparticles for effective stem-cell differentiation and imaging. *Angewandte Chemie - International Edition* **2013,** *52* (24), 6190-6195.
6. Wang, Y. X. J.; Idee, J.-M.; Corot, C., Scientific and industrial challenges of developing nanoparticle-based theranostics and multiple-modality contrast agents for clinical application. *Nanoscale* **2015,** *7* (39), 16146-16150.
7. Makridis, A.; Topouridou, K.; Tziomaki, M.; Sakellari, D.; Simeonidis, K.; Angelakeris, M.; Yavropoulou, M. P.; Yovos, J. G.; Kalogirou, O., In vitro application of Mn-ferrite nanoparticles as novel magnetic hyperthermia agents. *Journal of Materials Chemistry B* **2014,** *2* (47), 8390-8398.
8. Lee, J. H.; Huh, Y. M.; Jun, Y. W.; Seo, J. W.; Jang, J. T.; Song, H. T.; Kim, S.; Cho, E. J.; Yoon, H. G.; Suh, J. S.; Cheon, J., Artificially engineered magnetic nanoparticles for ultra-sensitive molecular imaging. *Nature Medicine* **2007,** *13* (1), 95-99.
9. Hao, R.; Xing, R.; Xu, Z.; Hou, Y.; Gao, S.; Sun, S., Synthesis, Functionalization, and Biomedical Applications of Multifunctional Magnetic Nanoparticles. *Advanced Materials* **2010,** *22* (25), 2729-2742.
10. Sanpo, N.; Berndt, C. C.; Wen, C.; Wang, J., Transition metal-substituted cobalt ferrite nanoparticles for biomedical applications. *Acta biomaterialia* **2013,** *9* (3), 5830-5837.
11. Kostevšek, N.; Šturm, S.; Serša, I.; Sepe, A.; Bloemen, M.; Verbiest, T.; Kobe, S.; Rožman, K. Ž., "Single-" and "multi-core" FePt nanoparticles: from controlled synthesis via zwitterionic and silica bio-functionalization to MRI applications. *Journal of Nanoparticle Research* **2015,** *17* (12), 1-15.
12. Lukanov, P.; Anuganti, V. K.; Krupskaya, Y.; Galibert, A. M.; Soula, B.; Tilmaciu, C.; Velders, A. H.; Klingeler, R.; Büchner, B.; Flahaut, E., CCVD Synthesis of Carbon-Encapsulated Cobalt Nanoparticles for Biomedical Applications. *Advanced Functional Materials* **2011,** *21* (18), 3583-3588.
13. Branca, M.; Marciello, M.; Ciuculescu-Pradines, D.; Respaud, M.; Morales, M. P.; Serra, R.; Casanove, M. J.; Amiens, C., Towards MRI T2 contrast agents of increased efficiency. *Journal of Magnetism and Magnetic Materials* **2015,** *377*, 348-353.
14. Bruce, I. J.; Sen, T., Surface Modification of Magnetic Nanoparticles with Alkoxysilanes and Their Application in Magnetic Bioseparations. *Langmuir* **2005,** *21* (15), 7029-7035.

15. Gruar, R. I.; Tighe, C. J.; Southern, P.; Pankhurst, Q. A.; Darr, J. A., A Direct and Continuous Supercritical Water Process for the Synthesis of Surface-Functionalized Nanoparticles. *Industrial & Engineering Chemistry Research* **2015,** *54* (30), 7436-7451.
16. Wei, W.; Zhaohui, W.; Taekyung, Y.; Changzhong, J.; Woo-Sik, K., Recent progress on magnetic iron oxide nanoparticles: synthesis, surface functional strategies and biomedical applications. *Science and Technology of Advanced Materials* **2015,** *16* (2), 023501.
17. Thanh, N. T. K., *Magnetic nanoparticles: from fabrication to clinical applications : theory to therapy, chemistry to clinic, bench to bedside*. CRC: Boca Raton, Fla, London, 2012.18. Rebolledo, A. F.; Bomatí-Miguel, O.; Marco, J. F.; Tartaj, P., A facile synthetic route for the preparation of superparamagnetic iron oxide nanorods and nanorices with tunable surface functionality. *Advanced Materials* **2008,** *20* (9), 1760-1765.
19. Kolinko, I.; Lohße, A.; Borg, S.; Raschdorf, O.; Jogler, C.; Tu, Q.; Pósfai, M.; Tompa, É.; Plitzko, J. M.; Brachmann, A.; Wanner, G.; Müller, R.; Zhang, Y.; Schüler, D., Biosynthesis of magnetic nanostructures in a foreign organism by transfer of bacterial magnetosome gene clusters. *Nature Nanotechnology* **2014,** *9* (3), 193-197.
20. Gutiérrez, L.; Costo, R.; Grüttner, C.; Westphal, F.; Gehrke, N.; Heinke, D.; Fornara, A.; Pankhurst, Q. A.; Johansson, C.; Veintemillas-Verdaguer, S.; Morales, M. P., Synthesis methods to prepare single- and multi-core iron oxide nanoparticles for biomedical applications. *Dalton Transactions* **2015,** *44* (7), 2943-2952.
21. Branquinho, L. C.; Carrião, M. S.; Costa, A. S.; Zufelato, N.; Sousa, M. H.; Miotto, R.; Ivkov, R.; Bakuzis, A. F., Effect of magnetic dipolar interactions on nanoparticle heating efficiency: Implications for cancer hyperthermia. *Scientific Reports* **2013,** *3*, 2887.
22. Orozco-Henao, J. M.; Coral, D. F.; Muraca, D.; Moscoso-Londoño, O.; Mendoza Zélis, P.; Fernandez van Raap, M. B.; Sharma, S. K.; Pirota, K. R.; Knobel, M., Effects of Nanostructure and Dipolar Interactions on Magnetohyperthermia in Iron Oxide Nanoparticles. *The Journal of Physical Chemistry C* **2016,** *120* (23), 12796-12809.
23. Ludwig, F.; Kazakova, O.; Barquín, L. F.; Fornara, A.; Trahms, L.; Steinhoff, U.; Svedlindh, P.; Wetterskog, E.; Pankhurst, Q. A.; Southern, P.; Morales, M. P.; Hansen, M. F.; Frandsen, C.; Olsson, E.; Gustafsson, S.; Gehrke, N.; Lüdtke-Buzug, K.; Grüttner, C.; Jonasson, C.; Johansson, C., Magnetic, structural, and particle size analysis of single- and multi-core magnetic nanoparticles. *IEEE Transactions on Magnetics* **2014,** *50* (11).
24. De Yoreo, J. J.; Gilbert, P. U. P. A.; Sommerdijk, N. A. J. M.; Penn, R. L.; Whitelam, S.; Joester, D.; Zhang, H.; Rimer, J. D.; Navrotsky, A.; Banfield, J. F.; Wallace, A. F.; Michel, F. M.; Meldrum, F. C.; Cölfen, H.; Dove, P. M., Crystallization by particle attachment in synthetic, biogenic, and geologic environments. *Science* **2015,** *349* (6247).
25. Glotzer, S. C.; Solomon, M. J., Anisotropy of building blocks and their assembly into complex structures. *Nature Materials* **2007,** *6* (8), 557-562.
26. Nie, Z.; Petukhova, A.; Kumacheva, E., Properties and emerging applications of self-assembled structures made from inorganic nanoparticles. *Nature Nanotechnology* **2010,** *5* (1), 15-25.

27. Cheng, K.; Chen, Q.; Wu, Z.; Wang, M.; Wang, H., Colloids of superparamagnetic shell: Synthesis and self-assembly into 3D colloidal crystals with anomalous optical properties. *CrystEngComm* **2011,** *13* (17), 5394-5400.
28. Finney, E. E.; Finke, R. G., Nanocluster nucleation and growth kinetic and mechanistic studies: A review emphasizing transition-metal nanoclusters. *Journal of Colloid and Interface Science* **2008,** *317* (2), 351-374.
29. Frandsen, C.; Legg, B. A.; Comolli, L. R.; Zhang, H.; Gilbert, B.; Johnson, E.; Banfield, J. F., Aggregation-induced growth and transformation of β-FeOOH nanorods to micron-sized α-Fe2O3 spindles. *CrystEngComm* **2014,** *16* (8), 1451-1458.
30. Yang, J.; Choi, M. K.; Kim, D. H.; Hyeon, T., Designed Assembly and Integration of Colloidal Nanocrystals for Device Applications. *Advanced Materials* **2016,** *28* (6), 1176-1207.
31. Baumgartner, J.; Dey, A.; Bomans, P. H. H.; Le Coadou, C.; Fratzl, P.; Sommerdijk, N. A. J. M.; Faivre, D., Nucleation and growth of magnetite from solution. *Nature Materials* **2013,** *12* (4), 310-314.
32. Revealed, I.; Yuwono, V. M.; Burrows, N. D.; Soltis, J. A.; Lee Penn, R., Oriented aggregation: Formation and transformation of mesocrystal. *Journal of the American Chemical Society* **2010,** *132* (7), 2163-2165.
33. Vereda, F.; Morales, M. P.; Rodríguez-González, B.; Vicente, J. D.; Hidalgo-Alvarez, R., Control of surface morphology and internal structure in magnetite microparticles: From smooth single crystals to rough polycrystals. *CrystEngComm* **2013,** *15* (26), 5236-5244.
34. Lartigue, L.; Hugounenq, P.; Alloyeau, D.; Clarke, S. P.; Lévy, M.; Bacri, J. C.; Bazzi, R.; Brougham, D. F.; Wilhelm, C.; Gazeau, F., Cooperative organization in iron oxide multi-core nanoparticles potentiates their efficiency as heating mediators and MRI contrast agents. *ACS Nano* **2012,** *6* (12), 10935-10949.
35. Hachani, R.; Lowdell, M.; Birchall, M.; Hervault, A.; Mertz, D.; Begin-Colin, S.; Thanh, N. T. B. D. K., Polyol synthesis, functionalisation, and biocompatibility studies of superparamagnetic iron oxide nanoparticles as potential MRI contrast agents. *Nanoscale* **2016,** *8* (6), 3278-3287.
36. Materia, M. E.; Guardia, P.; Sathya, A.; Pernia Leal, M.; Marotta, R.; Di Corato, R.; Pellegrino, T., Mesoscale Assemblies of Iron Oxide Nanocubes as Heat Mediators and Image Contrast Agents. *Langmuir* **2015,** *31* (2), 808-816.
37. Herman, D. A. J.; Cheong-Tilley, S.; McGrath, A. J.; McVey, B. F. P.; Lein, M.; Tilley, R. D., How to choose a precursor for decomposition solution-phase synthesis: the case of iron nanoparticles. *Nanoscale* **2015,** *7* (14), 5951-5954.
38. Ravikumar, C.; Bandyopadhyaya, R., Mechanistic study on magnetite nanoparticle formation by thermal decomposition and coprecipitation routes. *The Journal of Physical Chemistry C* **2011,** *115* (5), 1380-1387.
39. Massart, R., Preparation of Aqueous Magnetic Liquids in Alkaline and Acidic Media. *IEEE Transactions on Magnetics* **1981,** *17* (2), 1247-1248.
40. Gribanov, N. M.; Bibik, E. E.; Buzunov, O. V.; Naumov, V. N., Physico-chemical regularities of obtaining highly dispersed magnetite by the method of chemical condensation. *Journal of Magnetism and Magnetic Materials* **1990,** *85* (1-3), 7-10.
41. Qiu, X. P., Synthesis and characterization of magnetic nanoparticles. *Chinese Journal of Chemistry* **2000,** *18* (6), 834-837.

42. Martínez-Mera, I.; Espinosa-Pesqueira, M. E.; Pérez-Hernández, R.; Arenas-Alatorre, J., Synthesis of magnetite (Fe3O4) nanoparticles without surfactants at room temperature. *Materials Letters* **2007,** *61* (23-24), 4447-4451.
43. Iwasaki, T.; Mizutani, N.; Watano, S.; Yanagida, T.; Kawai, T., Size control of magnetite nanoparticles by organic solvent-free chemical coprecipitation at room temperature. *Journal of Experimental Nanoscience* **2010,** *5* (3), 251-262.
44. Costo, R.; Bello, V.; Robic, C.; Port, M.; Marco, J. F.; Morales, M.P.; Veintemillas-Verdaguer, S., Ultrasmall iron oxide nanoparticles for biomedical applications: Improving the colloidal and magnetic properties. *Langmuir* **2012,** *28* (1), 178-185.
45. Milosevic, I.; Warmont, F.; Lalatonne, Y.; Motte, L., Magnetic metrology for iron oxide nanoparticle scaled-up synthesis. *RSC Advances* **2014,** *4* (90), 49086-49089.
46. Che Rose, L.; Bear, J. C.; McNaughter, P. D.; Southern, P.; Piggott, R. B.; Parkin, I. P.; Qi, S.; Mayes, A. G., A SPION-eicosane protective coating for water soluble capsules: Evidence for on-demand drug release triggered by magnetic hyperthermia. *Scientific Reports* **2016,** *6*, 20271.
47. Maurizi, L.; Bouyer, F.; Paris, J.; Demoisson, F.; Saviot, L.; Millot, N., One step continuous hydrothermal synthesis of very fine stabilized superparamagnetic nanoparticles of magnetite. *Chemical Communications* **2011,** *47* (42), 11706-11708.
48. Thomas, G.; Demoisson, F.; Chassagnon, R.; Popova, E.; Millot, N., One-step continuous synthesis of functionalized magnetite nanoflowers. *Nanotechnology* **2016,** *27* (13), 135604.
49. Thomas, G.; Demoisson, F.; Boudon, J.; Millot, N., Efficient functionalization of magnetite nanoparticles with phosphonate using a one-step continuous hydrothermal process. *Dalton Transactions* **2016,** *45* (26), 10821-10829.
50. Heinke, D., Diffusion-Controlled Synthesis of Magnetic Nanoparticles *International Journal on Magnetic Particle Imaging* **2016**.
51. Baumgartner, J.; Antonietta Carillo, M.; Eckes, K. M.; Werner, P.; Faivre, D., Biomimetic magnetite formation: From biocombinatorial approaches to mineralization effects. *Langmuir* **2014,** *30* (8), 2129-2136.
52. Lenders, J. J. M.; Zope, H. R.; Yamagishi, A.; Bomans, P. H. H.; Arakaki, A.; Kros, A.; De With, G.; Sommerdijk, N. A. J. M., Bioinspired magnetite crystallization directed by random copolypeptides. *Advanced Functional Materials* **2015,** *25* (5), 711-719.
53. Park, S., Preparation of iron oxides using ammonium iron citrate precursor: Thin films and nanoparticles. *Journal of Solid State Chemistry* **2009,** *182* (9), 2456-2460.
54. Zheng, Y.-h.; Cheng, Y.; Bao, F.; Wang, Y.-s., Synthesis and magnetic properties of Fe 3 O 4 nanoparticles. *Materials research bulletin* **2006,** *41* (3), 525-529.
55. Behdadfar, B.; Kermanpur, A.; Sadeghi-Aliabadi, H.; Morales, M.P.; Mozaffari, M., Synthesis of high intrinsic loss power aqueous ferrofluids of iron oxide nanoparticles by citric acid-assisted hydrothermal-reduction route. *Journal of Solid State Chemistry* **2012,** *187*, 20-26.
56. Qu, X.-F.; Zhou, G.-T.; Yao, Q.-Z.; Fu, S.-Q., Aspartic-Acid-Assisted Hydrothermal Growth and Properties of Magnetite Octahedrons. *The Journal of Physical Chemistry C* **2010,** *114* (1), 284-289.

57. David, I.; Welch, A. J. E., The oxidation of magnetite and related spinels: Constitution of gamma ferric oxide. *Transactions of the Faraday Society* **1956,** *52*, 1642-1650.
58. Sidhu, P. S.; Gilkes, R. J.; Posner, A. M., Mechanism of the low temperature oxidation of synthetic magnetites. *Journal of Inorganic and Nuclear Chemistry* **1977,** *39* (11), 1953-1958.
59. Sugimoto, T.; Matijević, E., Formation of uniform spherical magnetite particles by crystallization from ferrous hydroxide gels. *Journal of Colloid And Interface Science* **1980,** *74* (1), 227-243.
60. Vergés, M. A.; Costo, R.; Roca, A. G.; Marco, J. F.; Goya, G. F.; Serna, C. J.; Morales, M. P., Uniform and water stable magnetite nanoparticles with diameters around the monodomain-multidomain limit. *Journal of Physics D: Applied Physics* **2008,** *41* (13).
61. Marciello, M.; Connord, V.; Veintemillas-Verdaguer, S.; Vergés, M. A.; Carrey, J.; Respaud, M.; Serna, C. J.; Morales, M. P., Large scale production of biocompatible magnetite nanocrystals with high saturation magnetization values through green aqueous synthesis. *Journal of Materials Chemistry B* **2013,** *1* (43), 5995-6004.
62. Cornell, R. M.; Schwertmann, U., *The iron oxides: structure, properties, reactions, occurrences and uses*. John Wiley & Sons: 2003.
63. Salas, G.; Veintemillas-Verdaguer, S.; Morales, M. P., Relationship between physico-chemical properties of magnetic fluids and their heating capacity. *International Journal of Hyperthermia* **2013,** *29* (8), 768-776.
64. González-Fernández, M. A.; Torres, T. E.; Andrés-Vergés, M.; Costo, R.; de la Presa, P.; Serna, C. J.; Morales, M. P.; Marquina, C.; Ibarra, M. R.; Goya, G. F., Magnetic nanoparticles for power absorption: Optimizing size, shape and magnetic properties. *Journal of Solid State Chemistry* **2009,** *182* (10), 2779-2784.
65. Luengo, Y.; Morales, M.P.; Gutiérrez, L.; Veintemillas-Verdaguer, S., Counterion and solvent effects on the size of magnetite nanocrystals obtained by oxidative precipitation. *Journal of Materials Chemistry C* **2016,** *4* (40), 9482-9488.
66. Gavilán, H.; Posth, O.; Bogart, L. K.; Steinhoff, U.; Gutiérrez, L.; Morales, M. P., How shape and internal structure affect the magnetic properties of anisometric magnetite nanoparticles. *Acta Materialia* **2017,** *125*, 416-424.
67. Pozas, R.; Ocãa, M.; Morales, M. P.; Serna, C. J., The influence of protective coatings on the magnetic properties of acicular iron nanoparticles. *Nanotechnology* **2006,** *17* (5), 1421-1427.
68. Graf, C.; Vossen, D. L. J.; Imhof, A.; Van Blaaderen, A., A general method to coat colloidal particles with silica. *Langmuir* **2003,** *19* (17), 6693-6700.
69. Morales, M. P.; Pecharroman, C.; Carreñ, T. G.; Serna, C. J., Structural Characteristics of Uniform γ-Fe2O3 Particles with Different Axial (Length/Width) Ratios. *Journal of Solid State Chemistry* **1994,** *108* (1), 158-163.
70. Yang, Y.; Liu, X.; Ding, J., Synthesis of α-Fe<inf>2</inf>O<inf>3</inf> Templates via Hydrothermal Route and Fe<inf>3</inf>O<inf>4</inf> Particles Through Subsequent Chemical Reduction. *Science of Advanced Materials* **2013,** *5* (9), 1199-1207.
71. Rebolledo, A. F.; Laurent, S.; Calero, M.; Villanueva, A.; Knobel, M.; Marco, J. F.; Tartaj, P., Iron oxide nanosized clusters embedded in porous nanorods: A

new colloidal design to enhance capabilities of MRI contrast agents. *ACS Nano* **2010,** *4* (4), 2095-2103.
72. Mirabello, G.; Lenders, J. J. M.; Sommerdijk, N. A. J. M., Bioinspired synthesis of magnetite nanoparticles. *Chemical Society Reviews* **2016,** *45* (18), 5085-5106.
73. Lenders, J. J. M.; Mirabello, G.; Sommerdijk, N. A. J. M., Bioinspired magnetite synthesis via solid precursor phases. *Chemical Science* **2016,** *7* (9), 5624-5634.
74. Mann, S., *Biomineralization: principles and concepts in bioinorganic materials chemistry*. Oxford University Press on Demand: 2001; Vol. 5.
75. Dey, A.; Lenders, J. J. M.; Sommerdijk, N. A. J. M., Bioinspired magnetite formation from a disordered ferrihydrite-derived precursor. *Faraday Discussions* **2015,** *179*, 215-225.
76. Hyeon, T.; Su Seong, L.; Park, J.; Chung, Y.; Hyon Bin, N., Synthesis of highly crystalline and monodisperse maghemite nanocrystallites without a size-selection process. *Journal of the American Chemical Society* **2001,** *123* (51), 12798-12801.
77. Kwon, S. G.; Hyeon, T., Formation Mechanisms of Uniform Nanocrystals via Hot-Injection and Heat-Up Methods. *Small* **2011,** *7* (19), 2685-2702.
78. Salas, G.; Casado, C.; Teran, F. J.; Miranda, R.; Serna, C. J.; Morales, M. P., Controlled synthesis of uniform magnetite nanocrystals with high-quality properties for biomedical applications. *Journal of Materials Chemistry* **2012,** *22* (39), 21065-21075.
79. Kim, D.; Lee, N.; Park, M.; Kim, B. H.; An, K.; Hyeon, T., Synthesis of uniform ferrimagnetic magnetite nanocubes. *Journal of the American Chemical Society* **2009,** *131* (2), 454-455.
80. Guardia, P.; Di Corato, R.; Lartigue, L.; Wilhelm, C.; Espinosa, A.; Garcia-Hernandez, M.; Gazeau, F.; Manna, L.; Pellegrino, T., Water-soluble iron oxide nanocubes with high values of specific absorption rate for cancer cell hyperthermia treatment. *ACS Nano* **2012,** *6* (4), 3080-3091.
81. Kovalenko, M. V.; Bodnarchuk, M. I.; Lechner, R. T.; Hesser, G.; Schäffler, F.; Heiss, W., Fatty acid salts as stabilizers in size- and shape-controlled nanocrystal synthesis: The case of inverse spinel iron oxide. *Journal of the American Chemical Society* **2007,** *129* (20), 6352-6353.
82. Palchoudhury, S.; An, W.; Xu, Y.; Qin, Y.; Zhang, Z.; Chopra, N.; Holler, R. A.; Turner, C. H.; Bao, Y., Synthesis and growth mechanism of iron oxide nanowhiskers. *Nano Letters* **2011,** *11* (3), 1141-1146.
83. Sun, H.; Chen, B.; Jiao, X.; Jiang, Z.; Qin, Z.; Chen, D., Solvothermal synthesis of tunable electroactive magnetite nanorods by controlling the side reaction. *Journal of Physical Chemistry C* **2012,** *116* (9), 5476-5481.
84. Zhang, L.; Wu, J.; Liao, H.; Hou, Y.; Gao, S., Octahedral Fe3O4 nanoparticles and their assembled structures. *Chemical Communications* **2009,** (29), 4378-4380.
85. Jian, L.; Xiuling, J.; Dairong, C.; Wei, L., Solvothermal synthesis and characterization of Fe3O4 and γ-Fe2O3 nanoplates. *Journal of Physical Chemistry C* **2009,** *113* (10), 4012-4017.
86. Zeng, Y.; Hao, R.; Xing, B.; Hou, Y.; Xu, Z., One-pot synthesis of Fe3O4 nanoprisms with controlled electrochemical properties. *Chemical Communications* **2010,** *46* (22), 3920-3922.

87. Fantechi, E.; Campo, G.; Carta, D.; Corrias, A.; de Julián Fernández, C.; Gatteschi, D.; Innocenti, C.; Pineider, F.; Rugi, F.; Sangregorio, C., Exploring the Effect of Co Doping in Fine Maghemite Nanoparticles. *The Journal of Physical Chemistry C* **2012,** *116* (14), 8261-8270.
88. Brollo, M. E. F.; López-Ruiz, R.; Muraca, D.; Figueroa, S. J. A.; Pirota, K. R.; Knobel, M., Compact Ag@Fe3O4 Core-shell Nanoparticles by Means of Single-step Thermal Decomposition Reaction. *Scientific Reports* **2014,** *4*, 6839.
89. Vreeland, E. C.; Watt, J.; Schober, G. B.; Hance, B. G.; Austin, M. J.; Price, A. D.; Fellows, B. D.; Monson, T. C.; Hudak, N. S.; Maldonado-Camargo, L.; Bohorquez, A. C.; Rinaldi, C.; Huber, D. L., Enhanced Nanoparticle Size Control by Extending LaMer's Mechanism. *Chemistry of Materials* **2015,** *27* (17), 6059-6066.
90. Castellanos-Rubio, I.; Insausti, M.; Garaio, E.; Gil de Muro, I.; Plazaola, F.; Rojo, T.; Lezama, L., Fe3O4 nanoparticles prepared by the seeded-growth route for hyperthermia: electron magnetic resonance as a key tool to evaluate size distribution in magnetic nanoparticles. *Nanoscale* **2014,** *6* (13), 7542-7552.
91. Salado, J.; Insausti, M.; Lezama, L.; Gil de Muro, I.; Goikolea, E.; Rojo, T., Preparation and Characterization of Monodisperse Fe3O4 Nanoparticles: An Electron Magnetic Resonance Study. *Chemistry of Materials* **2011,** *23* (11), 2879-2885.
92. Roca, A. G.; Marco, J. F.; Morales, M. P.; Serna, C. J., Effect of nature and particle size on properties of uniform magnetite and maghemite nanoparticles. *Journal of Physical Chemistry C* **2007,** *111* (50), 18577-18584.
93. Park, J.; Lee, E.; Hwang, N. M.; Kang, M.; Sung, C. K.; Hwang, Y.; Park, J. G.; Noh, H. J.; Kim, J. Y.; Park, J. H.; Hyeon, T., One-nanometer-scale size-controlled synthesis of monodisperse magnetic iron oxide nanoparticles. *Angewandte Chemie - International Edition* **2005,** *44* (19), 2872-2877.
94. Baaziz, W.; Pichon, B. P.; Fleutot, S.; Liu, Y.; Lefevre, C.; Greneche, J. M.; Toumi, M.; Mhiri, T.; Begin-Colin, S., Magnetic iron oxide nanoparticles: Reproducible tuning of the size and nanosized-dependent composition, defects, and spin canting. *Journal of Physical Chemistry C* **2014,** *118* (7), 3795-3810.
95. Wetterskog, E.; Agthe, M.; Mayence, A.; Grins, J.; Wang, D.; Rana, S.; Ahniyaz, A.; Salazar-Alvarez, G.; Bergström, L., Precise control over shape and size of iron oxide nanocrystals suitable for assembly into ordered particle arrays. *Science and Technology of Advanced Materials* **2014,** *15* (5).
96. Kim, B. H.; Hackett, M. J.; Park, J.; Hyeon, T., Synthesis, characterization, and application of ultrasmall nanoparticles. *Chemistry of Materials* **2014,** *26* (1), 59-71.
97. Guan, N.; Wang, Y.; Sun, D.; Xu, J., A simple one-pot synthesis of single-crystalline magnetite hollow spheres from a single iron precursor. *Nanotechnology* **2009,** *20* (10).
98. Jia, B.; Gao, L., Morphological transformation of Fe3O4 spherical aggregates from solid to hollow and their self-assembly under an external magnetic field. *Journal of Physical Chemistry C* **2008,** *112* (3), 666-671.
99. Das, R.; Alonso, J.; Nemati Porshokouh, Z.; Kalappattil, V.; Torres, D.; Phan, M. H.; Garaio, E.; García, J. A.; Sanchez Llamazares, J. L.; Srikanth, H.,

Tunable High Aspect Ratio Iron Oxide Nanorods for Enhanced Hyperthermia. *Journal of Physical Chemistry C* **2016,** *120* (18), 10086-10093.

100. Sun, S.; Zeng, H.; Robinson, D. B.; Raoux, S.; Rice, P. M.; Wang, S. X.; Li, G., Monodisperse MFe<inf>2</inf>O<inf>4</inf> (M = Fe, Co, Mn) Nanoparticles. *Journal of the American Chemical Society* **2004,** *126* (1), 273-279.
101. Xue, X.; Penn, R. L.; Leite, E. R.; Huang, F.; Lin, Z., Crystal growth by oriented attachment: Kinetic models and control factors. *CrystEngComm* **2014,** *16* (8), 1419-1429.
102. Arbaoui, A.; Redshaw, C.; Elsegood, M. R. J.; Wright, V. E.; Yoshizawa, A.; Yamato, T., Iron(III) and Zinc(II) calixarene complexes: Synthesis, structural studies, and use as procatalysts for ε-caprolactone polymerization. *Chemistry - An Asian Journal* **2010,** *5* (3), 621-633.
103. Ben-Ishay, M. L.; Gedanken, A., Difference in the bonding scheme of calix(6)arene and p-sulfonic calix(6)arene to nanoparticles of Fe2O3 and Fe 3O4. *Langmuir* **2007,** *23* (10), 5238-5242.
104. Khan, L. U.; Brito, H. F.; Hölsä, J.; Pirota, K. R.; Muraca, D.; Felinto, M. C. F. C.; Teotonio, E. E. S.; Malta, O. L., Red-Green Emitting and Superparamagnetic Nanomarkers Containing Fe3O4 Functionalized with Calixarene and Rare Earth Complexes. *Inorganic Chemistry* **2014,** *53* (24), 12902-12910.
105. Vita, F. V.; Gavilán, H.; Rossi, F.; De Julian Fernandez, C.; Secchi, A.; Arduini, A.; Albertini, F.; Morales, M.P., Tuning morphology and magnetism of magnetite nanoparticles by calixarene-induced oriented aggregation. CrysEngComm 2016, 18, 8591–8598.
106. Roman, V. R.; Vyacheslav, I. B.; Vitaly, I. K., Calixarenes in Bio-Medical Researches. *Current Medicinal Chemistry* **2009,** *16* (13), 1630-1655.
107. Palma, S. I. C. J.; Marciello, M.; Carvalho, A.; Veintemillas-Verdaguer, S.; Morales, M. P.; Roque, A. C. A., Effects of phase transfer ligands on monodisperse iron oxide magnetic nanoparticles. *Journal of Colloid and Interface Science* **2015,** *437*, 147-155.
108. Roca, A. G.; Carmona, D.; Miguel-Sancho, N.; Bomatí-Miguel, O.; Balas, F.; Piquer, C.; Santamaría, J., Surface functionalization for tailoring the aggregation and magnetic behaviour of silica-coated iron oxide nanostructures. *Nanotechnology* **2012,** *23* (15).
109. Fratila, R. M.; Moros, M.; de la Fuente, J. M., Recent advances in biosensing using magnetic glyconanoparticles. *Analytical and Bioanalytical Chemistry* **2016,** *408* (7), 1783-1803.
110. Branca, M.; Ibrahim, M.; Ciuculescu, D.; Philippot, K.; Amiens, C., Water Transfer of Hydrophobic Nanoparticles: Principles and Methods. In *Handbook of Nanoparticles*, Aliofkhazraei, M., Ed. Springer International Publishing: Cham, 2015; pp 1-26.
111. Amstad, E.; Zurcher, S.; Mashaghi, A.; Wong, J. Y.; Textor, M.; Reimhult, E., Surface functionalization of single superparamagnetic iron oxide nanoparticles for targeted Magnetic resonance imaging. *Small* **2009,** *5* (11), 1334-1342.
112. Espinosa, A.; Di Corato, R.; Kolosnjaj-Tabi, J.; Flaud, P.; Pellegrino, T.; Wilhelm, C., Duality of Iron Oxide Nanoparticles in Cancer Therapy: Amplification of Heating Efficiency by Magnetic Hyperthermia and Photothermal Bimodal Treatment. *ACS Nano* **2016,** *10* (2), 2436-2446.

113. Dias, A. M. G. C.; Hussain, A.; Marcos, A. S.; Roque, A. C. A., A biotechnological perspective on the application of iron oxide magnetic colloids modified with polysaccharides. *Biotechnology Advances* **2011,** *29* (1), 142-155.
114. Moros, M.; Delhaes, F.; Puertas, S.; Saez, B.; de la Fuente, J. M.; Grazú, V.; Feracci, H., Surface engineered magnetic nanoparticles for specific immunotargeting of cadherin expressing cells. *Journal of Physics D: Applied Physics* **2015,** *49* (5), 054003.
115. El-Boubbou, K.; Zhu, D. C.; Vasileiou, C.; Borhan, B.; Prosperi, D.; Li, W.; Huang, X., Magnetic Glyco-Nanoparticles: A Tool To Detect, Differentiate, and Unlock the Glyco-Codes of Cancer via Magnetic Resonance Imaging. *Journal of the American Chemical Society* **2010,** *132* (12), 4490-4499.
116. Lartigue, L.; Oumzil, K.; Guari, Y.; Larionova, J.; Guérin, C.; Montero, J.-L.; Barragan-Montero, V.; Sangregorio, C.; Caneschi, A.; Innocenti, C.; Kalaivani, T.; Arosio, P.; Lascialfari, A., Water-Soluble Rhamnose-Coated Fe3O4 Nanoparticles. *Organic Letters* **2009,** *11* (14), 2992-2995.
117. Lartigue, L.; Innocenti, C.; Kalaivani, T.; Awwad, A.; Sanchez Duque, M. d. M.; Guari, Y.; Larionova, J.; Guérin, C.; Montero, J.-L. G.; Barragan-Montero, V.; Arosio, P.; Lascialfari, A.; Gatteschi, D.; Sangregorio, C., Water-Dispersible Sugar-Coated Iron Oxide Nanoparticles. An Evaluation of their Relaxometric and Magnetic Hyperthermia Properties. *Journal of the American Chemical Society* **2011,** *133* (27), 10459-10472.
118. Palma, S. I. C. J.; Rodrigues, C. A. V.; Carvalho, A.; Morales, M. P.; Freitas, F.; Fernandes, A. R.; Cabral, J. M. S.; Roque, A. C. A., A value-added exopolysaccharide as a coating agent for MRI nanoprobes. *Nanoscale* **2015,** *7* (34), 14272-14283.
119. Ferguson, R. M.; Khandhar, A. P.; Kemp, S. J.; Arami, H.; Saritas, E. U.; Croft, L. R.; Konkle, J.; Goodwill, P. W.; Halkola, A.; Rahmer, J.; Borgert, J.; Conolly, S. M.; Krishnan, K. M., Magnetic Particle Imaging With Tailored Iron Oxide Nanoparticle Tracers. *IEEE Transactions on Medical Imaging* **2015,** *34* (5), 1077-1084.
120. McNaughter, P. D.; Bear, J. C.; Steytler, D. C.; Mayes, A. G.; Nann, T., A Thin Silica–Polymer Shell for Functionalizing Colloidal Inorganic Nanoparticles. *Angewandte Chemie International Edition* **2011,** *50* (44), 10384-10387.
121. Cai, W.; Wan, J., Facile synthesis of superparamagnetic magnetite nanoparticles in liquid polyols. *Journal of Colloid and Interface Science* **2007,** *305* (2), 366-370.
122. Fievet, F.; Lagier, J. P.; Blin, B.; Beaudoin, B.; Figlarz, M., Homogeneous and heterogeneous nucleations in the polyol process for the preparation of micron and submicron size metal particles. *Solid State Ionics* **1989,** *32*, 198-205.
123. Daniela, C.; Gabriel, C.; Charles, J. O. C., Magnetic properties of variable-sized Fe 3 O 4 nanoparticles synthesized from non-aqueous homogeneous solutions of polyols. *Journal of Physics D: Applied Physics* **2007,** *40* (19), 5801.
124. Liu, J.; Sun, Z.; Deng, Y.; Zou, Y.; Li, C.; Guo, X.; Xiong, L.; Gao, Y.; Li, F.; Zhao, D., Highly Water-Dispersible Biocompatible Magnetite Particles with Low Cytotoxicity Stabilized by Citrate Groups. *Angewandte Chemie International Edition* **2009,** *48* (32), 5875-5879.

125. Liang, J.; Ma, H.; Luo, W.; Wang, S., Synthesis of magnetite submicrospheres with tunable size and superparamagnetism by a facile polyol process. *Materials Chemistry and Physics* **2013,** *139* (2–3), 383-388.
126. Sun, Q.; Ren, Z.; Wang, R.; Chen, W.; Chen, C., Magnetite hollow spheres: solution synthesis, phase formation and magnetic property. *Journal of Nanoparticle Research* **2011,** *13* (1), 213-220.
127. Cheng, C.; Xu, F.; Gu, H., Facile synthesis and morphology evolution of magnetic iron oxide nanoparticles in different polyol processes. *New Journal of Chemistry* **2011,** *35* (5), 1072-1079.
128. Wang, H.; Sun, Y.-B.; Chen, Q.-W.; Yu, Y.-F.; Cheng, K., Synthesis of carbon-encapsulated superparamagnetic colloidal nanoparticles with magnetic-responsive photonic crystal property. *Dalton Transactions* **2010,** *39* (40), 9565-9569.
129. Basti, H.; Tahar, L. B.; Smiri, L. S.; Herbst, F.; Nowak, S.; Mangeney, C.; Ammar, S., Surface modification of γ-Fe2O3 nanoparticles by grafting from poly-(hydroxyethylmethacrylate) and poly-(methacrylic acid): Qualitative and quantitative analysis of the polymeric coating. *Colloids and Surfaces A: Physicochemical and Engineering Aspects* **2016,** *490*, 222-231.
130. Luo, W.; Ma, H.; Mou, F.; Zhu, M.; Yan, J.; Guan, J., Steric-repulsion-based magnetically responsive photonic crystals. *Advanced Materials* **2014,** *26* (7), 1058-1064.
131. Casula, M. F.; Conca, E.; Bakaimi, I.; Sathya, A.; Materia, M. E.; Casu, A.; Falqui, A.; Sogne, E.; Pellegrino, T.; Kanaras, A. G., Manganese doped-iron oxide nanoparticle clusters and their potential as agents for magnetic resonance imaging and hyperthermia. *Physical Chemistry Chemical Physics* **2016,** *18* (25), 16848-16855.
132. Park, J.; Joo, J.; Soon, G. K.; Jang, Y.; Hyeon, T., Synthesis of monodisperse spherical nanocrystals. *Angewandte Chemie - International Edition* **2007,** *46* (25), 4630-4660.
133. Gu, H.; Xu, K.; Xu, C.; Xu, B., Biofunctional magnetic nanoparticles for protein separation and pathogen detection. *Chemical Communications* **2006,** (9), 941-949.
134. Jun, Y.-w.; Huh, Y.-M.; Choi, J.-s.; Lee, J.-H.; Song, H.-T.; KimKim; Yoon, S.; Kim, K.-S.; Shin, J.-S.; Suh, J.-S.; Cheon, J., Nanoscale Size Effect of Magnetic Nanocrystals and Their Utilization for Cancer Diagnosis via Magnetic Resonance Imaging. *Journal of the American Chemical Society* **2005,** *127* (16), 5732-5733.
135. Baghbanzadeh, M.; Carbone, L.; Cozzoli, P. D.; Kappe, C. O., Microwave-Assisted Synthesis of Colloidal Inorganic Nanocrystals. *Angewandte Chemie International Edition* **2011,** *50* (48), 11312-11359.
136. Gedye, R.; Smith, F.; Westaway, K.; Ali, H.; Baldisera, L.; Laberge, L.; Rousell, J., The use of microwave ovens for rapid organic synthesis. *Tetrahedron Letters* **1986,** *27* (3), 279-282.
137. Giguere, R. J.; Bray, T. L.; Duncan, S. M.; Majetich, G., Application of commercial microwave ovens to organic synthesis. *Tetrahedron Letters* **1986,** *27* (41), 4945-4948.
138. Rana, K. K.; Rana, S., Microwave Reactors: A Brief Review on Its Fundamental Aspects and Applications. *Open Access Library Journal* **2014,** *1* (06), 1.

139. Niederberger, M.; Pinna, N., *Metal oxide nanoparticles in organic solvents: synthesis, formation, assembly and application*. Springer Science & Business Media: 2009.
140. Bilecka, I.; Djerdj, I.; Niederberger, M., One-minute synthesis of crystalline binary and ternary metal oxide nanoparticles. *Chemical Communications* **2008,** (7), 886-888.
141. Carenza, E.; Barceló, V.; Morancho, A.; Montaner, J.; Rosell, A.; Roig, A., Rapid synthesis of water-dispersible superparamagnetic iron oxide nanoparticles by a microwave-assisted route for safe labeling of endothelial progenitor cells. *Acta Biomaterialia* **2014,** *10* (8), 3775-3785.
142. Pellico, J.; Lechuga-Vieco, A. V.; Benito, M.; García-Segura, J. M.; Fuster, V.; Ruiz-Cabello, J.; Herranz, F., Microwave-driven synthesis of bisphosphonate nanoparticles allows in vivo visualisation of atherosclerotic plaque. *RSC Advances* **2015,** *5* (3), 1661-1665.
143. Yu, S.; Hachtel, J. A.; Chisholm, M. F.; Pantelides, S. T.; Laromaine, A.; Roig, A., Magnetic gold nanotriangles by microwave-assisted polyol synthesis. *Nanoscale* **2015,** *7* (33), 14039-14046.
144. Ai, Z.; Deng, K.; Wan, Q.; Zhang, L.; Lee, S., Facile Microwave-Assisted Synthesis and Magnetic and Gas Sensing Properties of Fe3O4 Nanoroses. *The Journal of Physical Chemistry C* **2010,** *114* (14), 6237-6242.
145. Kozakova, Z.; Kuritka, I.; Kazantseva, N. E.; Babayan, V.; Pastorek, M.; Machovsky, M.; Bazant, P.; Saha, P., The formation mechanism of iron oxide nanoparticles within the microwave-assisted solvothermal synthesis and its correlation with the structural and magnetic properties. *Dalton Transactions* **2015,** *44* (48), 21099-21108.
146. Wilkes, J. S., A short history of ionic liquids-from molten salts to neoteric solvents. *Green Chemistry* **2002,** *4* (2), 73-80.
147. Rogers, R. D.; Seddon, K. R., Ionic Liquids--Solvents of the Future? *Science* **2003,** *302* (5646), 792.
148. Chiappe, C.; Pieraccini, D., Ionic liquids: solvent properties and organic reactivity. *Journal of Physical Organic Chemistry* **2005,** *18* (4), 275-297.
149. Wasserscheid, P.; Keim, W., Ionic Liquids—New “Solutions” for Transition Metal Catalysis. *Angewandte Chemie International Edition* **2000,** *39* (21), 3772-3789.
150. Jacob, D. S.; Bitton, L.; Grinblat, J.; Felner, I.; Koltypin, Y.; Gedanken, A., Are Ionic Liquids Really a Boon for the Synthesis of Inorganic Materials? A General Method for the Fabrication of Nanosized Metal Fluorides. *Chemistry of Materials* **2006,** *18* (13), 3162-3168.
151. Hu, H.; Yang, H.; Huang, P.; Cui, D.; Peng, Y.; Zhang, J.; Lu, F.; Lian, J.; Shi, D., Unique role of ionic liquid in microwave-assisted synthesis of monodisperse magnetite nanoparticles. *Chemical Communications* **2010,** *46* (22), 3866-3868.
152. Blanco-Andujar, C.; Ortega, D.; Southern, P.; Pankhurst, Q. A.; Thanh, N. T. K., High performance multi-core iron oxide nanoparticles for magnetic hyperthermia: microwave synthesis, and the role of core-to-core interactions. *Nanoscale* **2015,** *7* (5), 1768-1775.
153. Zheng, B.; Zhang, M.; Xiao, D.; Jin, Y.; Choi, M. M. F., Fast microwave synthesis of Fe3O4 and Fe3O4/Ag magnetic nanoparticles using Fe2+ as precursor. *Inorganic Materials* **2010,** *46* (10), 1106-1111.

154. Pellico, J.; Ruiz-Cabello, J.; Saiz-Alía, M.; del Rosario, G.; Caja, S.; Montoya, M.; Fernández de Manuel, L.; Morales, M. P.; Gutiérrez, L.; Galiana, B.; Enríquez, J. A.; Herranz, F., Fast synthesis and bioconjugation of 68Ga core-doped extremely small iron oxide nanoparticles for PET/MR imaging. *Contrast Media & Molecular Imaging* **2016,** *11* (3), 203-210.
155. Schanche, J.-S., Microwave synthesis solutions from personal chemistry. *Molecular diversity* **2003,** *7* (2), 291-298.
156. Obermayer, D.; Kappe, C. O., On the importance of simultaneous infrared/fiber-optic temperature monitoring in the microwave-assisted synthesis of ionic liquids. *Organic & Biomolecular Chemistry* **2010,** *8* (1), 114-121.
157. Cabrera, L.; Gutierrez, S.; Menendez, N.; Morales, M. P.; Herrasti, P., Magnetite nanoparticles: Electrochemical synthesis and characterization. *Electrochimica Acta* **2008,** *53* (8), 3436-3441.
158. Mazarío, E.; Herrasti, P.; Morales, M. P.; Menéndez, N., Synthesis and characterization of CoFe 2 O 4 ferrite nanoparticles obtained by an electrochemical method. *Nanotechnology* **2012,** *23* (35), 355708.
159. Mazarío, E.; Sánchez-Marcos, J.; Menéndez, N.; Cañete, M.; Mayoral, A.; Rivera-Fernández, S.; de la Fuente, J. M.; Herrasti, P., High Specific Absorption Rate and Transverse Relaxivity Effects in Manganese Ferrite Nanoparticles Obtained by an Electrochemical Route. *The Journal of Physical Chemistry C* **2015,** *119* (12), 6828-6834.
160. Rivero, M.; del Campo, A.; Mayoral, A.; Mazario, E.; Sanchez-Marcos, J.; Munoz-Bonilla, A., Synthesis and structural characterization of ZnxFe3-xO4 ferrite nanoparticles obtained by an electrochemical method. *RSC Advances* **2016,** *6* (46), 40067-40076.
161. Mazario, E.; Menéndez, N.; Herrasti, P.; Cañete, M.; Connord, V.; Carrey, J., Magnetic Hyperthermia Properties of Electrosynthesized Cobalt Ferrite Nanoparticles. *The Journal of Physical Chemistry C* **2013,** *117* (21), 11405-11411.
162. Mazario, E.; Sanchez-Marcos, J.; Menendez, N.; Herrasti, P.; Garcia-Hernandez, M.; Munoz-Bonilla, A., One-pot electrochemical synthesis of polydopamine coated magnetite nanoparticles. *RSC Advances* **2014,** *4* (89), 48353-48361.
163. Huttel, Y., *Nanoscale* **2014,** *6*, 13483.
164. Oprea, B.; Martínez, L.; Román, E.; Vanea, E.; Simon, S.; Huttel, Y., Dispersion and Functionalization of Nanoparticles Synthesized by Gas Aggregation Source: Opening New Routes Toward the Fabrication of Nanoparticles for Biomedicine. *Langmuir* **2015,** *31* (51), 13813-13820.
165. Llamosa, D.; Ruano, M.; Martinez, L.; Mayoral, A.; Roman, E.; Garcia-Hernandez, M.; Huttel, Y., The ultimate step towards a tailored engineering of core@shell and core@shell@shell nanoparticles. *Nanoscale* **2014,** *6* (22), 13483-13486.
166. Martinez-Boubeta, C.; Simeonidis, K.; Serantes, D.; Conde-Leborán, I.; Kazakis, I.; Stefanou, G.; Peña, L.; Galceran, R.; Balcells, L.; Monty, C.; Baldomir, D.; Mitrakas, M.; Angelakeris, M., Adjustable Hyperthermia Response of Self-Assembled Ferromagnetic Fe-MgO Core–Shell Nanoparticles by Tuning Dipole–Dipole Interactions. *Advanced Functional Materials* **2012,** *22* (17), 3737-3744.

167. Kwon, B. S.; Zhang, W.; Li, Z.; Krishnan, K. M., Direct Release of Sombrero-Shaped Magnetite Nanoparticles via Nanoimprint Lithography. *Advanced Materials Interfaces* **2015,** *2* (3), 1400511-n/a.
168. Hu, W.; Wilson, R. J.; Koh, A.; Fu, A.; Faranesh, A. Z.; Earhart, C. M.; Osterfeld, S. J.; Han, S.-J.; Xu, L.; Guccione, S.; Sinclair, R.; Wang, S. X., High-Moment Antiferromagnetic Nanoparticles with Tunable Magnetic Properties. *Advanced Materials* **2008,** *20* (8), 1479-1483.
169. Wagener, P.; Jakobi, J.; Rehbock, C.; Chakravadhanula, V. S. K.; Thede, C.; Wiedwald, U.; Bartsch, M.; Kienle, L.; Barcikowski, S., Solvent-surface interactions control the phase structure in laser-generated iron-gold core-shell nanoparticles. *Scientific Reports* **2016,** *6*, 23352.
170. Chen, F.; Chen, M.; Yang, C.; Liu, J.; Luo, N.; Yang, G.; Chen, D.; Li, L., Terbium-doped gadolinium oxide nanoparticles prepared by laser ablation in liquid for use as a fluorescence and magnetic resonance imaging dual-modal contrast agent. *Physical Chemistry Chemical Physics* **2015,** *17* (2), 1189-1196.
171. Ruiz, A.; Salas, G.; Calero, M.; Hernández, Y.; Villanueva, A.; Herranz, F.; Veintemillas-Verdaguer, S.; Martínez, E.; Barber, D. F.; Morales, M. P., Short-chain PEG molecules strongly bound to magnetic nanoparticle for MRI long circulating agents. *Acta Biomaterialia* **2013,** *9* (5), 6421-6430.
172. Creixell, M.; Herrera, A. P.; Latorre-Esteves, M.; Ayala, V.; Torres-Lugo, M.; Rinaldi, C., The effect of grafting method on the colloidal stability and in vitro cytotoxicity of carboxymethyl dextran coated magnetic nanoparticles. *Journal of Materials Chemistry* **2010,** *20* (39), 8539-8547.
173. Qu, J.; Liu, G.; Wang, Y.; Hong, R., Preparation of Fe3O4–chitosan nanoparticles used for hyperthermia. *Advanced Powder Technology* **2010,** *21* (4), 461-467.
174. Mulens-Arias, V.; Rojas, J. M.; Pérez-Yagüe, S.; Morales, M. P.; Barber, D. F., Polyethylenimine-coated SPION exhibits potential intrinsic anti-metastatic properties inhibiting migration and invasion of pancreatic tumor cells. *Journal of Controlled Release* **2015,** *216*, 78-92.
175. Cintra, E. R.; Ferreira, F. S.; Junior, J. L. S.; Campello, J. C.; Socolovsky, L. M.; Lima, E. M.; Bakuzis, A. F., Nanoparticle agglomerates in magnetoliposomes. *Nanotechnology* **2009,** *20* (4), 045103.
176. Zahraei, M.; Marciello, M.; Lazaro-Carrillo, A.; Villanueva, A.; Herranz, F.; Talelli, M.; Costo, R.; Monshi, A.; Shahbazi-Gahrouei, D.; Amirnasr, M.; Behdadfar, B.; Morales, M. P., Versatile theranostics agents designed by coating ferrite nanoparticles with biocompatible polymers. *Nanotechnology* **2016,** *27* (25).
177. Veiseh, O.; Gunn, J. W.; Zhang, M., Design and fabrication of magnetic nanoparticles for targeted drug delivery and imaging. *Advanced Drug Delivery Reviews* **2010,** *62* (3), 284-304.
178. Laurent, S.; Forge, D.; Port, M.; Roch, A.; Robic, C.; Vander Elst, L.; Muller, R. N., Magnetic Iron Oxide Nanoparticles: Synthesis, Stabilization, Vectorization, Physicochemical Characterizations, and Biological Applications. *Chemical Reviews* **2008,** *108* (6), 2064-2110.
179. Patil, R. M.; Shete, P. B.; Thorat, N. D.; Otari, S. V.; Barick, K. C.; Prasad, A.; Ningthoujam, R. S.; Tiwale, B. M.; Pawar, S. H., Superparamagnetic iron oxide/chitosan core/shells for hyperthermia application: Improved colloidal

stability and biocompatibility. *Journal of Magnetism and Magnetic Materials* **2014,** *355*, 22-30.
180. Aqil, A.; Vasseur, S.; Duguet, E.; Passirani, C.; Benoit, J. P.; Jerome, R.; Jerome, C., Magnetic nanoparticles coated by temperature responsive copolymers for hyperthermia. *Journal of Materials Chemistry* **2008,** *18* (28), 3352-3360.
181. Cooperstein, M. A.; Canavan, H. E., Assessment of cytotoxicity of (N-isopropyl acrylamide) and Poly(N-isopropyl acrylamide)-coated surfaces. *Biointerphases* **2013,** *8* (1), 19.
182. Rahman, M. M.; Elaissari, A., Organic–Inorganic Hybrid Magnetic Latex. In *Hybrid Latex Particles: Preparation with (Mini)emulsion Polymerization*, van Herk, A. M.; Landfester, K., Eds. Springer Berlin Heidelberg: Berlin, Heidelberg, 2010; pp 237-281.
183. Hamoudeh, M.; Faraj, A. A.; Canet-Soulas, E.; Bessueille, F.; Léonard, D.; Fessi, H., Elaboration of PLLA-based superparamagnetic nanoparticles: Characterization, magnetic behaviour study and in vitro relaxivity evaluation. *International Journal of Pharmaceutics* **2007,** *338* (1–2), 248-257.
184. Hamoudeh, M.; Fessi, H., Preparation, characterization and surface study of poly-epsilon caprolactone magnetic microparticles. *Journal of Colloid and Interface Science* **2006,** *300* (2), 584-590.
185. Sommertune, J.; Sugunan, A.; Ahniyaz, A.; Bejhed, S. R.; Sarwe, A.; Johansson, C.; Balceris, C.; Ludwig, F.; Posth, O.; Fornara, A., Polymer/Iron Oxide Nanoparticle Composites—A Straight Forward and Scalable Synthesis Approach. *International Journal of Molecular Sciences* **2015,** *16* (8).
186. Hyeon, T.; Manna, L.; Wong, S. S., Sustainable nanotechnology. *Chemical Society Reviews* **2015,** *44* (16), 5755-5757.
187. Mejías, R.; Gutiérrez, L.; Salas, G.; Pérez-Yagüe, S.; Zotes, T. M.; Lázaro, F. J.; Morales, M. P.; Barber, D. F., Long term biotransformation and toxicity of dimercaptosuccinic acid-coated magnetic nanoparticles support their use in biomedical applications. *Journal of Controlled Release* **2013,** *171* (2), 225-233.
188. Mazuel, F.; Espinosa, A.; Luciani, N.; Reffay, M.; Le Borgne, R.; Motte, L.; Desboeufs, K.; Michel, A.; Pellegrino, T.; Lalatonne, Y.; Wilhelm, C., Massive Intracellular Biodegradation of Iron Oxide Nanoparticles Evidenced Magnetically at Single-Endosome and Tissue Levels. *ACS Nano* **2016,** *10* (8), 7627-7638.
189. Kolosnjaj-Tabi, J.; Di Corato, R.; Lartigue, L.; Marangon, I.; Guardia, P.; Silva, A. K. A.; Luciani, N.; Clément, O.; Flaud, P.; Singh, J. V.; Decuzzi, P.; Pellegrino, T.; Wilhelm, C.; Gazeau, F., Heat-Generating Iron Oxide Nanocubes: Subtle “Destructurators” of the Tumoral Microenvironment. *ACS Nano* **2014,** *8* (5), 4268-4283.
190. Guardia, P.; Riedinger, A.; Kakwere, H.; Gazeau, F.; Pellegrino, T., Magnetic Nanoparticles for Magnetic Hyperthermia and Controlled Drug Delivery. In *Bio- and Bioinspired Nanomaterials*, Wiley-VCH Verlag GmbH & Co. KGaA: 2014; pp 139-172.
191. Kendall, M.; Lynch, I., Long-term monitoring for nanomedicine implants and drugs. *Nat Nano* **2016,** *11* (3), 206-210.
192. Kharisov, B. I.; Dias, H. V. R.; Kharissova, O. V.; Vazquez, A.; Pena, Y.; Gomez, I., Solubilization, dispersion and stabilization of magnetic nanoparticles in water and non-aqueous solvents: recent trends. *RSC Advances* **2014,** *4* (85), 45354-45381.

APPENDIX 2

How Shape and Internal Structure Affect the Magnetic Properties of Anisometric Magnetite Nanoparticles

1. Scanning Electron Microscopy

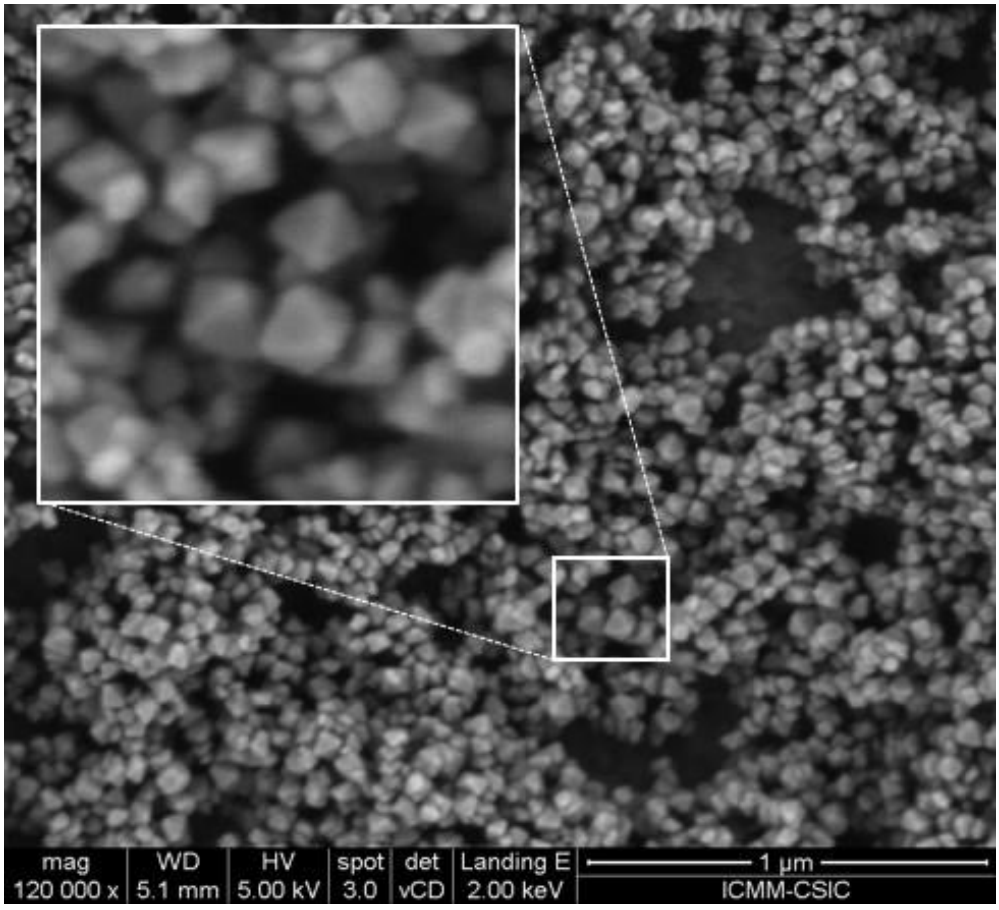

Figure S1: SEM Image of hematite rhombohedra.

2. High-Resolution Transmission Electron Microscopy

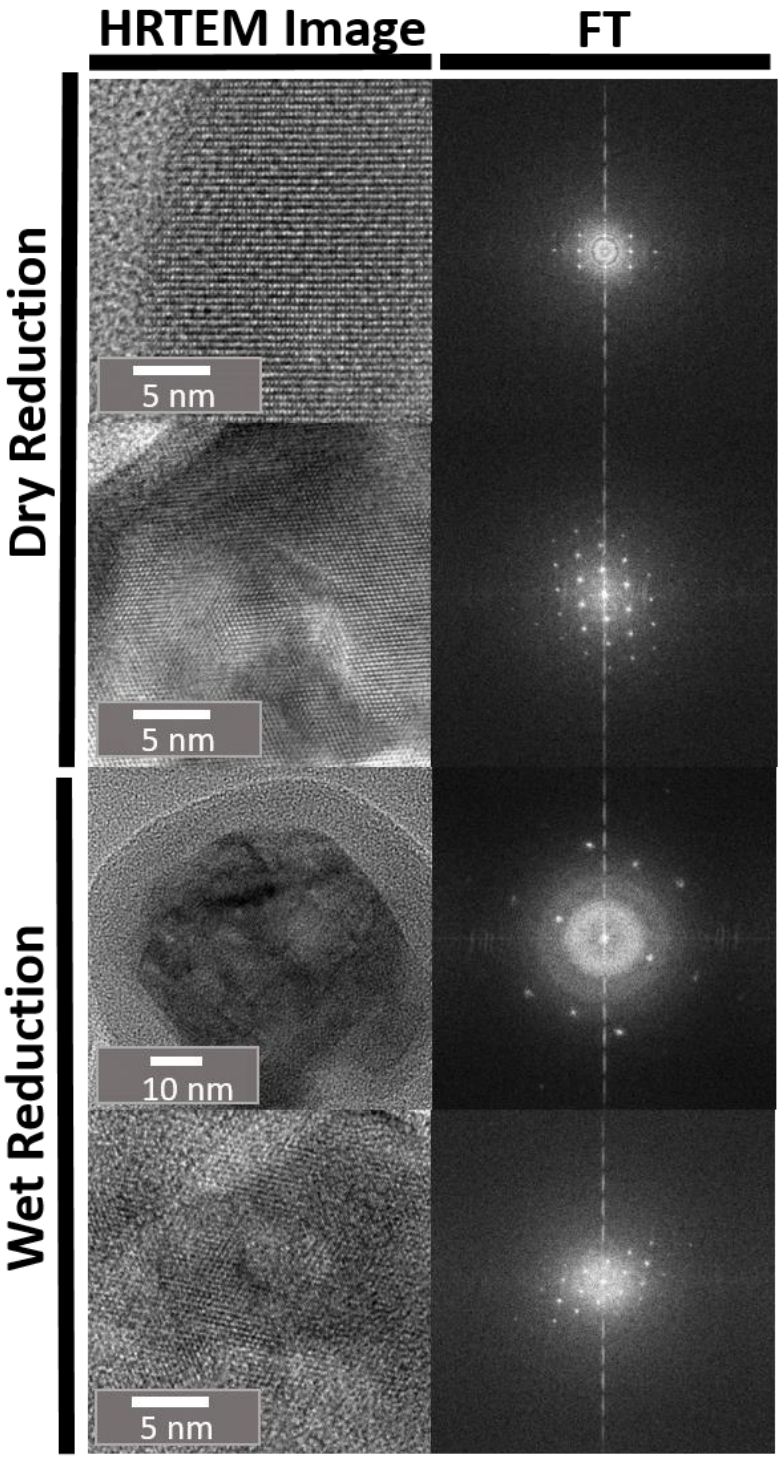

Figure S2: HRTEM Images of rhombohedra reduced in dry and wet showing one particle at different magnification and their corresponding Fourier transform images . Note that the internal porosity is evidenced by dark contrast differences in the images as a consequence of inhomogeneous material density.

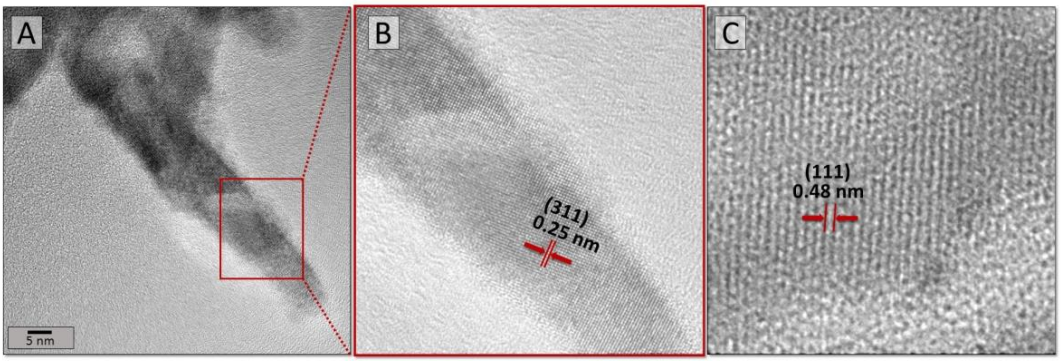

Figure S3: HRTEM Images of: (A) needle MNPs obtained from goethite precursor, (B) Amplification of an area of image A, and (C) higher magnification of magnetite particles after dry reduction. Paralel lines indicate crystal structure exhibiting (311) and (111) lattice sets with measured *d*-spacings of 0.25 and 0.48 nm respectively.

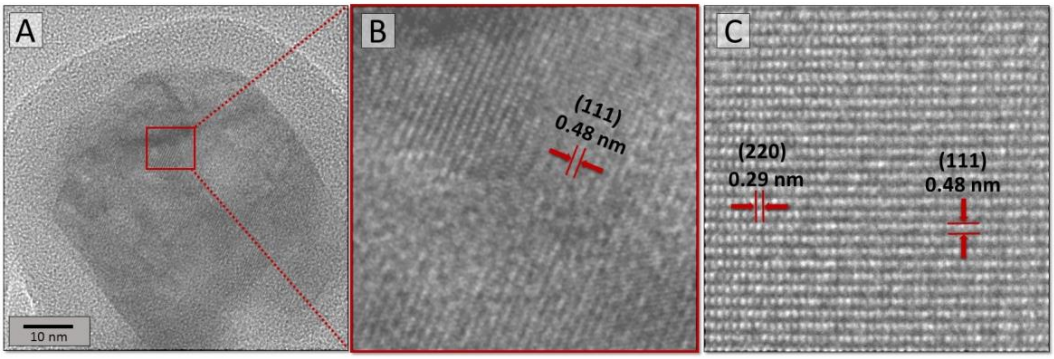

Figure S4: HRTEM images of: (A) rhombohedron MNPs obtained from hematite precursor after dry reduction, (B) Amplification of an area of image A, and (C) higher magnification of magnetite particles after reduction. Paralel lines indicate crystal structure exhibiting (111) and (220) lattice sets with measured *d*-spacings of 0.48 and 0.29 nm respectively.

3. Infrared Spectroscopy

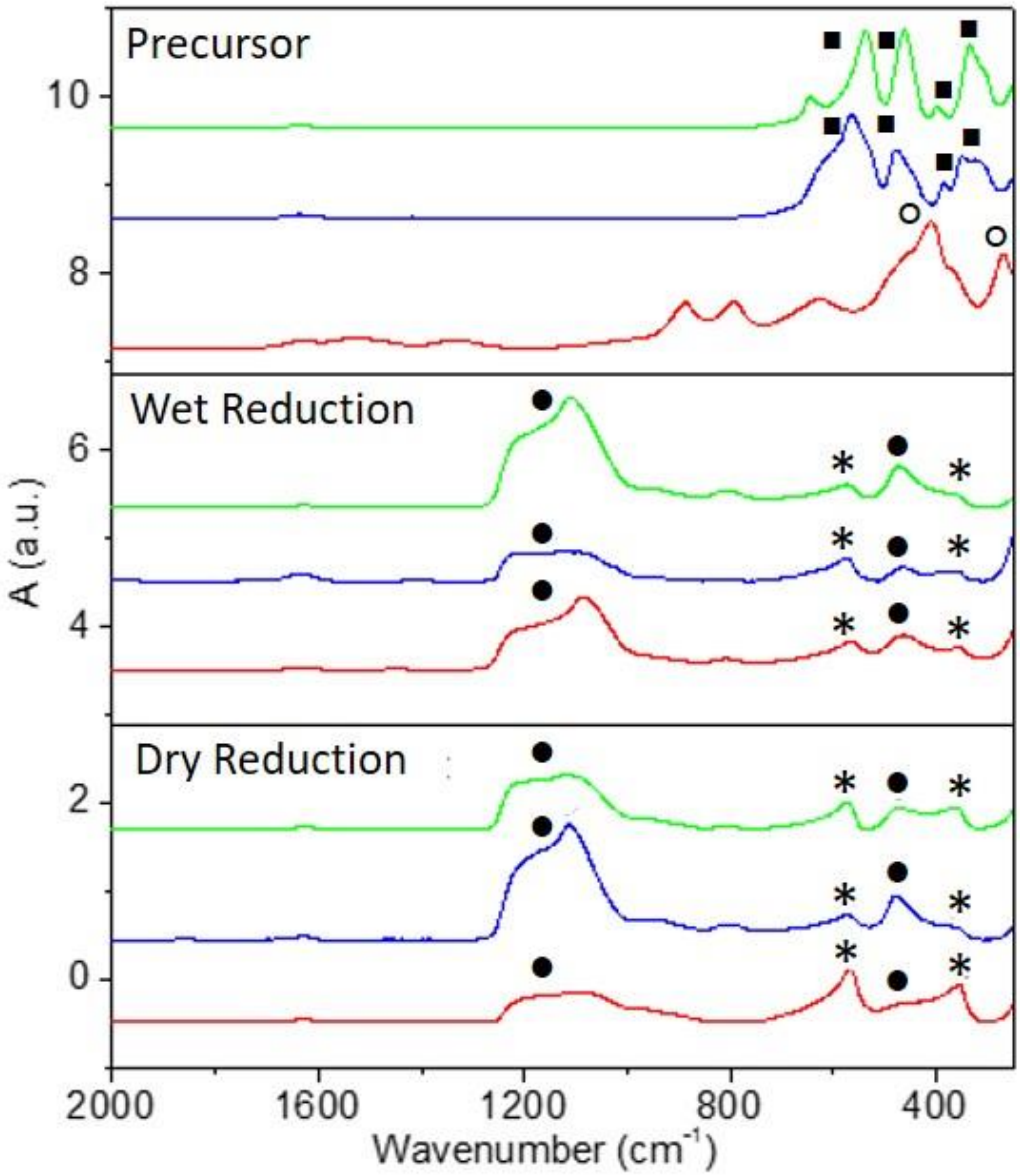

Figure S5: FT-IR spectra of the precursors and the final product obtained by wet and dry reduction. Rhombohedrons (green), discs (blue) and needles (red). (■) Bands attributed to Hematite. (°) Bands attributed to Goethite. (*) Bands attributed to magnetite. (●) Bands attributed to silica.

APPENDIX 3

Colloidal Flower-shaped Iron Oxide Nanoparticles: Synthesis Strategies and Coatings

1. Transmission Electron Microscopy

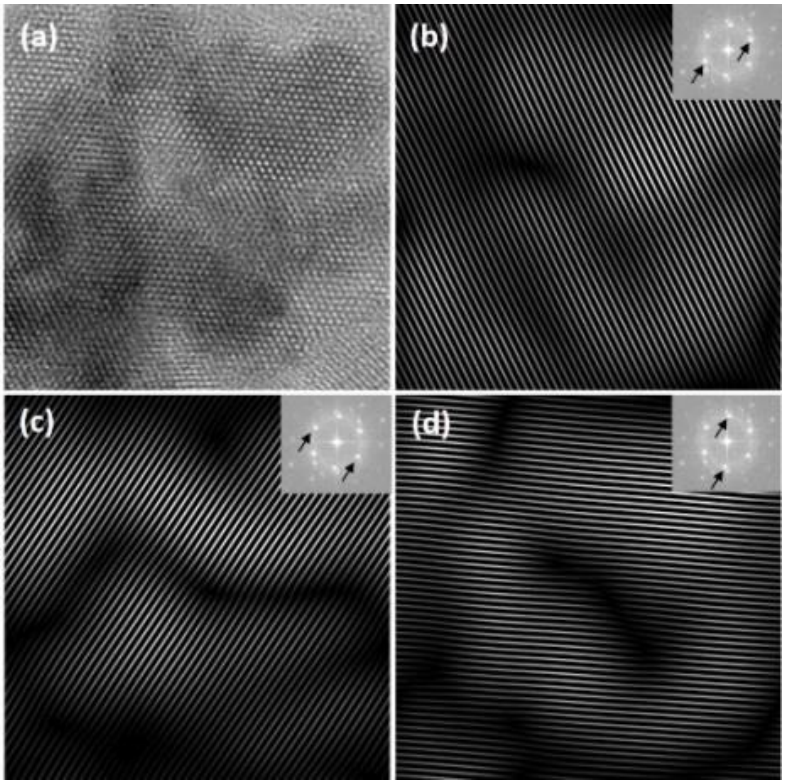

Figure S1. a) HRTEM image of NF4, b-d) Images obtained by selecting 3 specific lattice fringes and performing inverse-FFT. The resultant images showed lattice fringes that were contiguous along the entire nanoparticle.

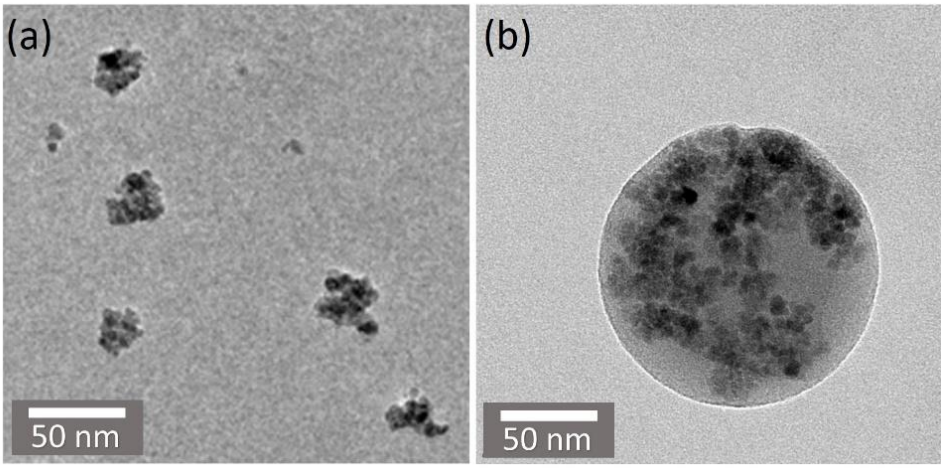

Figure S2. TEM images for the formation of sample NF4: (a) As-synthesized flower-shaped nanoparticles at low magnification. (b) Obtained polymer beads with embedded nanoflowers.

2. X-Ray Diffraction

Rietveld analysis has been performed for a set of iron-oxide nanoparticles (IONP) -nicknamed Nanoflowers due to their peculiar shape - to obtain their crystal-size, among other properties gathered in Table S1. With this aim, it has been assumed a *Fd-3m* space group for the refinement of the IONPs.

Table S1: Crystal Structure for Magnetite.[1,2] Fe_3O_4/ Space Group Fd-3m and the Origin choice 2.

Atom	Wyckoff Position	x	y	z	Occup
O	32 e	1/4	1/4	1/4	1
Fe oct [a]	16 d	0	0	0	1
Fe tet [b]	8 a	3/8	3/8	3/8	1

[a] oct stands for octahedral sites and [b] tet stands for tetrahedral sites.

Regarding the measurement, the instrumental calibration is based on a standard Si sample [3] for the position of the diffraction peaks, and on a LaB6 one [4] for the instrumental contribution to the width of the peaks at several different diffraction angles. All Rietveld refinements within this work have been performed using the FullProf Suite. [5] To describe the peak profiles a Thompson-Cox-Hastings function was selected which assures a good description of the width excess to extract the average crystal size (D) of the samples. The key parameters of the refinements are summarized in Table S2.

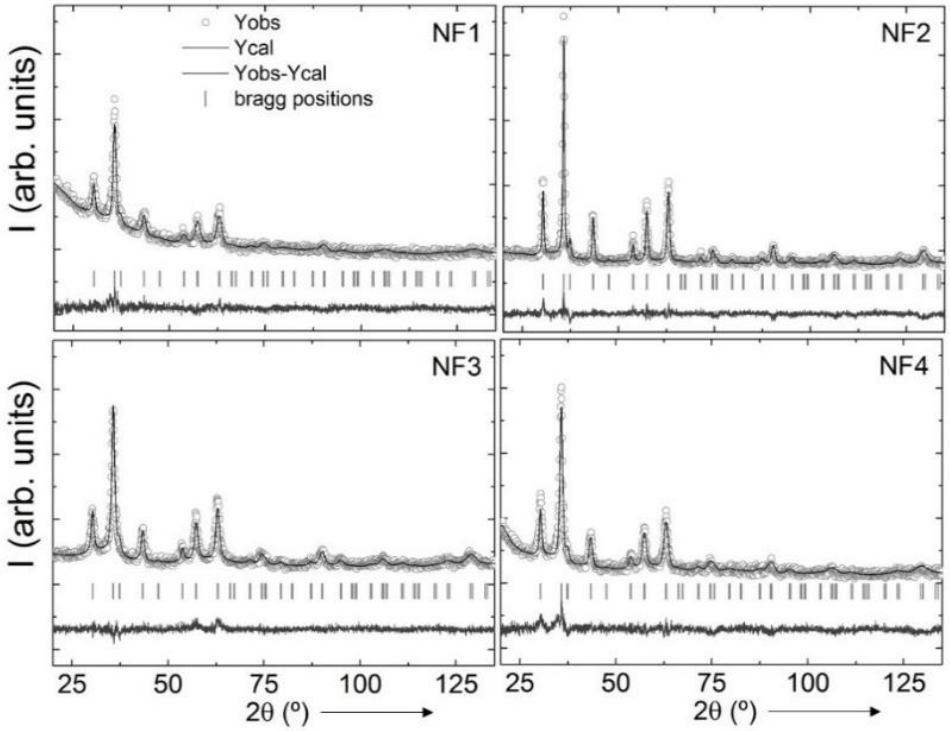

Figure S3. Rietveld refinements of the X-ray diffraction patterns obtained at room temperature in the set of different flower-shaped nanoparticles. The calculated and the residual profiles are represented with solid lines. Vertical tick marks indicate the position of the allowed diffraction peaks.

Table S2. Results of the Rietveld refinement performed with FullProf [7] and assuming a Fd-3m space group for the Magnetite Fe_3O_4.

Parameters	NF1	NF2	NF3	NF4
a (Å)	8.363 (2)	8.3515 (6)	8.370 (1)	8.352 (1)
XRD Diameter (nm)	9 (1)	15 (1)	8 (1)	10 (1)
ε (0/000) [a]	68 (14)	27 (4)	44 (6)	54 (12)
Bragg R-factor	12.4	7.11	7.32	9.41
Rwp	6.45	9.88	7.62	7.80
Chi2	1.16	1.45	1.20	1.50

[a] Parts-per-ten-thousand.

3. Mössbauer spectroscopy

Table S3. Mean isomer shift ($\bar{\delta}$), hyperfine field ($\bar{H}$) and fraction of Fe atoms present in the form of magnetite content for the flower-shaped samples. *assuming all Fe is present in the form of magnetite and maghemite.

Samples	T [K]	$\bar{\delta}$ (mm/s)	$\mu_0\bar{H}$ (T)	α
NF1	295	0.34 ± 0.02	29.4	0.11 ± 0.10
	18	0.452 ± 0.004	51.5	0.09 ± 0.02
NF2	295	0.33 ± 0.01	44.6	0.03 ± 0.05
	80	0.438 ± 0.005	51.4	0.05 ± 0.03
NF3	295	0.36 ± 0.02	34.1	0.17 ± 0.10
	18	0.444 ± 0.004	51.7	0.05± 0.02
NF4	295	0.37 ± 0.02	32.3	0.24± 0.10
	18	0.441 ± 0.004	52.1	0.03± 0.02

The mean isomer shift, $\bar{\delta}$, is given relative to that of α-Fe at room temperature (295 K). The magnetite content, α (fraction of Fe atoms present in the form of magnetite), is determined from $\bar{\delta}$, as described in by Fock et al. [6] The uncertainty in $\bar{\delta}$ and α is higher for spectra obtained at room temperature than at low temperatures (18 or 80 K), due to the broader lines.

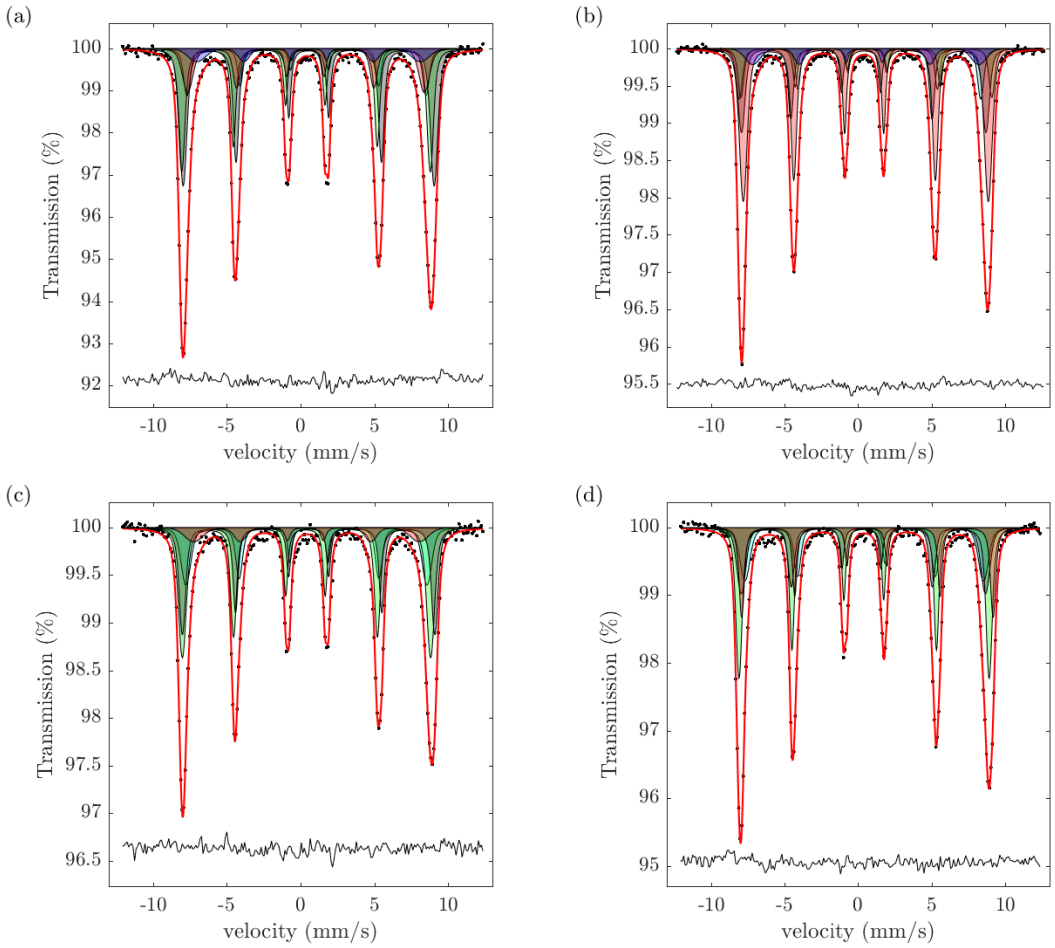

Figure S4: ^{57}Fe Mössbauer Spectroscopy spectra of: (a) NF1 measured at 18 K, (b) NF2 measured at 80 K (c) NF3 measured at 18 K and (d) NF4 measured at 18 K. The spectra show only evidence of Fe atoms present in the form of magnetite or maghemite. All spectra have been fitted using Voigtian lineshapes according to Fock et al. [7] Total fit is shown by solid red line (Voigtian sub-spectra in green). The quality of each fit is indicated by the residual - the difference between observed and fitted intensities – shown beneath each spectrum.

4. DC Magnetometry

The results of the magnetization measurements are summarized in table S4. The saturation magnetization M_S is determined by using the measured magnetic moment at the largest magnetic field of 3.9 MA/m (4.9 T), the suspension volume V and the iron concentrationc_{Fe}. The virgin curve can be modelled by a distribution of magnetic moment, where each moment m follows the Langevin function $L = \coth(\zeta) - 1/\zeta, \zeta = m\mu_0 H/k_B T$. Here, χ_0 is the vacuum permeability, H the magnetic field strength, k_B the Boltzmann constant and T the temperature. By using the saturation magnetization, the magnetic moment can be transferred into an effective core size. The magnetization of the suspension then is described by the median magnetic core diameter d_c and distribution width σ_c, assuming non-interacting MNPs exhibiting log-normal size distribution f. [8]

$$M(H,T) = \frac{M_S}{V \cdot c_{Fe}} \int_{d_c=0}^{d_{max}} f(d_c, \bar{d}_c, \sigma_c) \cdot \frac{\pi}{6} d_c^3 \cdot L(d_c, H, T) dd_c,$$

In a bimodal size distribution the magnetization curve is modelled by a fraction of small particle, which show magnetic saturation at very high fields, and a larger fraction, mostly arising from interactions between the small crystallites, showing a high initial susceptibility and relatively small saturation fields. The bimodal size distribution at isothermal measurements is expressed as:

$$M(H) = (1-\beta)M_1(H) + \beta M_2(H).$$

β is the normalized fraction the larger particle size distribution.

Table S4: Hysteresis parameters and sample properties calculated by fitting the magnetization vs. field curves by a bimodal model. β is the normalized fraction of the larger particle size distribution.

Magnetic parameters	NF1	NF2	NF3	NF4
M_s (3.9 MA/m) / (Am^2/kg_{Fe})	93 (3)	112 (3)	103 (3)	119 (4)
$d_{c,1}$ / nm (σ_c)	4.3 (0.52)	2 (0.8)	16 (0.1)	2.5 (0.56)
$d_{c,2}$ / nm (σ_c)	18.7 (0.24)	24.7 (0.08)	-	13.6 (0.03)
β	0.44	0.74	-	0.69

5. AC Susceptibility versus frequency

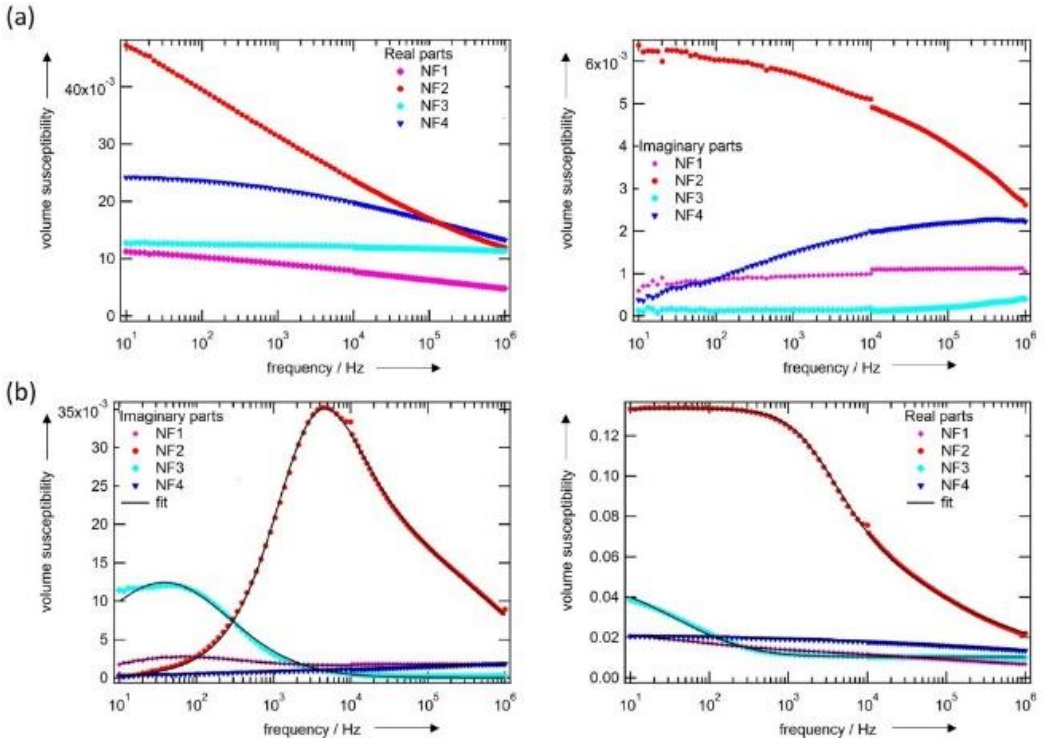

Figure S5: AC-susceptibility versus frequency of flower-shaped nanoparticles of both (a) immobilized and (b) nanoparticles in solution.

The complex (AC) susceptibility of a suspension of magnetic nanoparticles can be described by the Debye model. Generalizing it to multidisperse magnetic nanoparticles (generalized Debye model), exhibiting both a distribution of core $f(d_c)$ and hydrodynamic diameters $f(d_h)$, and assuming spherical particle shape, results in [9,10]

$$\chi'(\omega) = \chi_0^* \int_0^\infty f(d_h) \int_0^\infty \frac{d_c^6 \cdot f(d_c)}{1 + (\omega\tau_{eff})^2} dd_c dd_h + \chi_\infty$$

and

$$\chi''(\omega) = \chi_0^* \int_0^\infty f(d_h) \int_0^\infty \frac{d_c^6 \cdot f(d_c) \cdot \omega\tau_{eff}}{1 + (\omega\tau_{eff})^2} dd_c dd_h$$

With $\chi_0^* = \frac{\mu_0 n M_s^2}{3k_B T} \left(\frac{\pi}{6}\right)^2$.

Here, the effective relaxation time is given by

$$\tau_{eff} = \frac{\tau_B \tau_N}{\tau_B + \tau_N} \text{ With } \tau_B = \frac{\pi \cdot d_h^3 \cdot \eta}{2k_B \cdot T} \text{ and } \tau_N = \tau_0 \exp\left[\frac{K \cdot \pi \cdot d_c^3}{6k_B \cdot T}\right].$$

χ_∞ is caused by particles with very short relaxation times, presumably caused by the Néel mechanism, and by intra-potential-well contributions.

Here it is assumed that all nanoflowers have the same saturation magnetization M_s and anisotropy constants K. Distributions of core $f(d_c)$ and hydrodynamic diameters $f(d_h)$ are supposed to follow a lognormal distribution

$$f(d_i, \bar{d}_i, \sigma_i) = \frac{1}{\sqrt{2\pi} d_i \sigma_i} \exp\left[-\frac{(\ln d_i - \ln \bar{d}_i)^2}{2\sigma_i^2}\right]$$

With i being either c or h. To minimize the number of free parameters when fitting the model to the measured ACS spectra, the core diameter distribution parameters have been taken from fitting static magnetization curves also presented in this paper. The hydrodynamic diameter distribution parameters as well as the anisotropy constant K and the finite value of the real part at high frequencies χ_∞ are taken as free fitting parameters.

Table S5: Fit parameters derived from the analysis of the complex ac susceptibilities of nanoflowers.

Sample	ln ($\bar{d}_c$)	σ_c	ln ($\bar{d}_h$)	σ_h	K/ kJ/m³	χ_∞	$d_{h,mean}$ (nm)	SD (nm)
NF1	2.93	0.25	5.43	0.44	4.35	0.004	251.3	116.2
NF2	3.20	0.15	3.97	0.20	3.87	0.0162	54.1	10.9
NF3	2.78	0.20	5.51	0.02	6.19	0.0106	247.2	4.9
NF4	2.62	0.20	-	-	12.09	0.0103	-	-

We also analyzed the AC susceptibility data using the multi-core extended model. [11] The multi-core extended ACS model is a superposition consisting of a first part due to the Brownian relaxation and a second part due to the Néel relaxation. The second Néel

relaxation part can be omitted if the MNP system contains 100 % Brownian relaxation (multi-core model), according to:

$$\chi(\omega) = \chi_{0_B} \int \frac{1}{(1 + j\omega\tau_B(d_H))} f(d_H) dd_H + \frac{\chi_{0_N}}{1 + (j\omega\tau_N)^{\alpha}}$$

Where χ_{0B} gives the DC susceptibility from the Brownian relaxation and χ_{0N} gives the Néel DC susceptibility contribution. The Néel relaxation contribution to the AC susceptibility is modelled with a Cole-Cole expression where α is the Cole-Cole parameter (determines the degree of distribution of Néel relaxation times, $0 \leq \alpha \leq 1$).

6. AC Susceptibility versus temperature

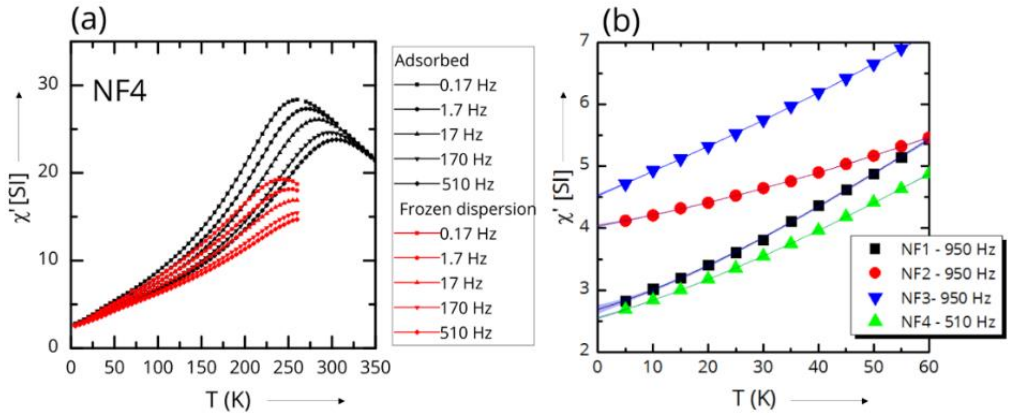

Figure S6: (a) AC-susceptibility versus temperature (χ') of NF4 comparing a frozen dispersion (5-260 K) with a dispersion adsorbed in cotton 5-350 K. (b) Low field susceptibility of the nanoflower samples NF1-4 over the temperature range 5-60 K. The data was fitted to a 3rd order polynomial. The shaded region represents 95% confidence bands.

AC-susceptibility data was measured using a Quantum Design MPMS XL. Example data is shown in Fig. S6 for NF4, the only sample in this series that displays well resolved temperature dependent cusps in the range of 5-390K. In the graph, two sets of curves are shown comparing the AC-properties of a frozen dispersion to that of a dispersion absorbed in cotton fiber. Clearly, the low-field susceptibility is largely independent of the sample preparation technique as the values χ' converge to the same point as T→0, in contrast to the blocking temperatures and high temperature susceptibility that increases slightly in the adsorbed sample. The in-phase component (χ') of the AC-susceptibility should approach a value, which is independent of the frequency as the temperature approaches zero. This corresponds to the intra-potential-well response of the particle moments χ⊥. [12]

$$\chi_{\perp} = \frac{\mu_0 M_S^2(0)}{2K} \langle \sin^2(\theta) \rangle$$

Here K is the uniaxial anisotropy constant, θ is the angle between the magnetic field and the particle easy axis, and the value of $\langle \sin^2(\theta) \rangle$ is averaged over the distribution of easy

axis orientations. In the case of a non-interacting nanoparticle dispersion, it is reasonable to adopt a random distribution of easy axes orientations, i.e. $\langle \sin^2(\theta) \rangle = 2/3$. The low-temperature data was fitted to a 3rd order polynomial.

Table S6. AC Susceptibility. Effective anisotropy calculation.

Samples	$M_s(0)$*	Phase composition $Fe_3O_4/\gamma\text{-}Fe_2O_3$*	$\chi_\perp T \rightarrow 0$, SI units (dimensionless)	Effective anisotropy AC ($\chi_\perp T \rightarrow 0$) 10^4 J/m^3
NF1	114 Am^2/kg$_{Fe}$ 399 kA/m	$\gamma\text{-}Fe_2O_3$	2.69(3)	2.5 (2)
NF2	133 Am^2/kg$_{Fe}$ 466 kA/m	$\gamma\text{-}Fe_2O_3$	4.04(1)	2.3 (2)
NF3	127 Am^2/kg$_{Fe}$ 444 kA/m	$\gamma\text{-}Fe_2O_3$	4.53(1)	1.8 (2)
NF4	141 Am^2/kg$_{Fe}$ 494 kA/m	$\gamma\text{-}Fe_2O_3$	2.55(1)	4.0 (3)

* = An uncertainty of ±3% was assumed.
Assumptions: Phase: $\gamma\text{-}Fe_2O_3$, $\rho \approx 5.0$ g/cm^3, random distributions of easy axes

A quick note on the uncertainty of the estimation of K using the low temperature χ'-data. First, we assume that the uncertainty of the low-temperature moment (M) is 3 % (6 % here since M is squared). The uncertainty of the fit as $T \rightarrow 0$ is < 1 % (see the confidence intervals in the graphs). The maximum uncertainty in the magnetization values when converting the magnetization axis from moment per mass iron (Am^2/kg$_{Fe}$) to A/m (SI) is roughly 10%. The maximum error is obtained if the particles are e.g. pure Fe_3O_4 but that the density and oxygen per iron is assumed to be that of $\gamma\text{-}Fe_3O_4$. In this case, since the particles are quite close to $\gamma\text{-}Fe_3O_4$ as determined by Mössbauer and XRD, 5 % is a reasonable estimate including the uncertainty of the density. Additionally, we there is a 3 % uncertainty from the magnetization value for $\chi_\perp$ (this measurement is separate from the determination of M).
This yields a total uncertainty of 8% for the determination of K from $\chi_\perp$ ($\Delta K = \sqrt{0.06^2 + 0.05^2 + 0.03^2}$).

7. Coating determination and colloidal properties of the suspensions

The final samples are coated by different stabilizers, i.e. dextran, citrate and polystyrene, and were characterized by infrared spectroscopy and thermogravimetric analysis (Fig. S7). In all samples, we can distinguish infrared bands at 3430 and 1630 cm^{-1} due to surface OH groups and bands in the low frequency region (800-300 cm^{-1}) typical from iron oxides. One of the latter is splitted at 630 and 586 cm^{-1} indicating the presence of maghemite in good agreement with Mössbauer spectra.

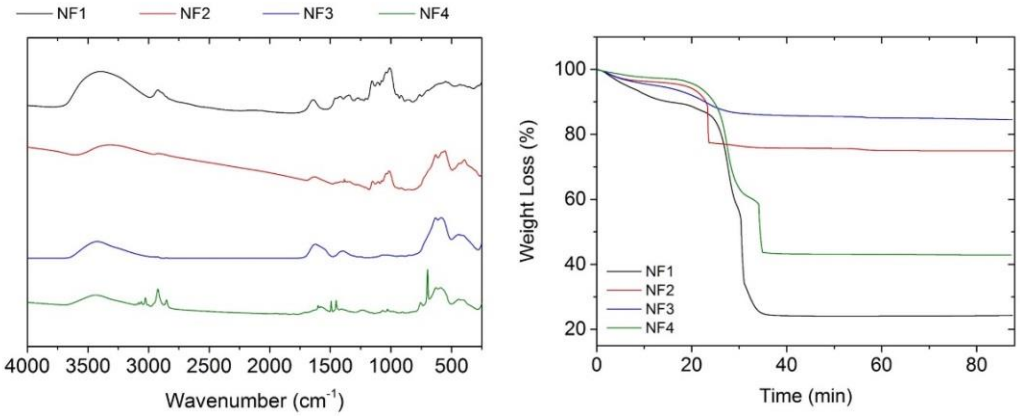

Figure S7: Coating characterisation of flower-shaped nanoparticles: IR-spectra (left). Thermogravimetric curves (right).

Between 1000 and 2000 cm^{-1}, IR spectra show the presence of dextan for samples NF1 and NF2 by the band at 916 cm^{-1} attributed to v (C-C) vibration of dextran and other at 1008cm^{-1} (ρ (CH_3) and v (C-C)), 1043 cm^{-1} (ρ (CH_3)), 1108 cm^{-1} (v (C-OH)) and 1158 cm^{-1} (δ (C-OH). For sample NF3 the band at 1631 cm^{-1} assigned to C=O vibration (symmetric stretching) and at 1397 cm^{-1} from C-O symmetric stretching from the COOH groups confirm the presence of citrate groups. For sample NF4 the polystyrene coating was unambiguously demonstrated by the presence of sharp bands at 697 and 755 cm^{-1} (attributed to aromatic C-H deformation vibration) and at 1451, 1492 and 1600 cm^{-1} (attributed to aromatic C-H stretching).

With respect to the thermogravimetric curves, sample NF2 has a weight loss of 20%, nearly 4 times less than sample NF1. This can be explained by the difference in terms of size between these two samples, which change dramatically the specific surface area. Lastly, sample NF3 has a weight loss of 15%, a reasonable result attending again to the decrease of surface that the flowers of 111 nm (in comparison with the rest of the flowers beside the product of the encapsulation in polystyrene). Sample NF4 has weight loss of nearly 60%, assumed as a loss of polystyrene.

The colloidal properties of the dispersions were studied by DLS and Z-potential measurements. Figure S7 shows the surface charge of the dispersions of nanoclusters.

Table S7. Z-potential of the samples.

Sample	Zeta Potential (mV)
NF1	+ 2.9
NF2	+ 23
NF3	- 40
NF4	- 62

References

1. H. Okudera, K. Kihara and T. Matsumoto, *Acta Crystallographica Section B: Structural Science*, 1996, **52**, 450-457.
2. V. Mazzocchi and C. Parente, *Journal of applied crystallography*, 1998, **31**, 718-725.
3. D. R. Black, D. Windover, A. Henins, J. Filliben and J. P. Cline, *Powder Diffraction*, 2011, **26**, 155-158.
4. D. R. Black, D. Windover, A. Henins, D. Gil, J. Filliben and J. P. Cline, *Powder Diffraction*, 2010, **25**, 187-190.
5. J. Rodríguez-Carvajal, *Commission on powder diffraction (IUCr). Newsletter*, 2001, **26**, 12-19.
6. J. Fock, L. K. Bogart, O. Posth, M. F. Hansen, Q. A. Pankhurst and C. Frandsen, *Hyperfine Interactions*, 2016, **237**, 1-11.
7. J. Fock, L. K. Bogart, D. Gonzalez-Alonzo, J. I. E. Martinez, M. F. Hansen, M. Varon, C. Frandsen and Q. A. Pankhurst, *(In preparation)*.
8. D. Eberbeck, F. Wiekhorst, S. Wagner and L. Trahms, *Applied physics letters*, 2011, **98**, 182502.
9. S.-H. Chung, A. Hoffmann, K. Guslienko, S. Bader, C. Liu, B. Kay, L. Makowski and L. Chen, *Journal of applied physics*, 2005, **97**, 10R101.
10. F. Ludwig, *AIP Conference Proceedings*, 2010, **1311**, 249-254.
11. S. Bogren, A. Fornara, F. Ludwig, M. del Puerto Morales, U. Steinhoff, M. F. Hansen, O. Kazakova and C. Johansson, *International journal of molecular sciences*, 2015, **16**, 20308-20325.
12. P. Svedlindh, T. Jonsson and J. García-Palacios, *Journal of magnetism and magnetic materials*, 1997, **169**, 323-334.

APPENDIX 4

FORMATION MECHANISM OF MAGHEMITE NANOFLOWERS SYNTHESIZED BY POLYOL MEDIATED PROCESS

1. Transmission Electron Microscopy

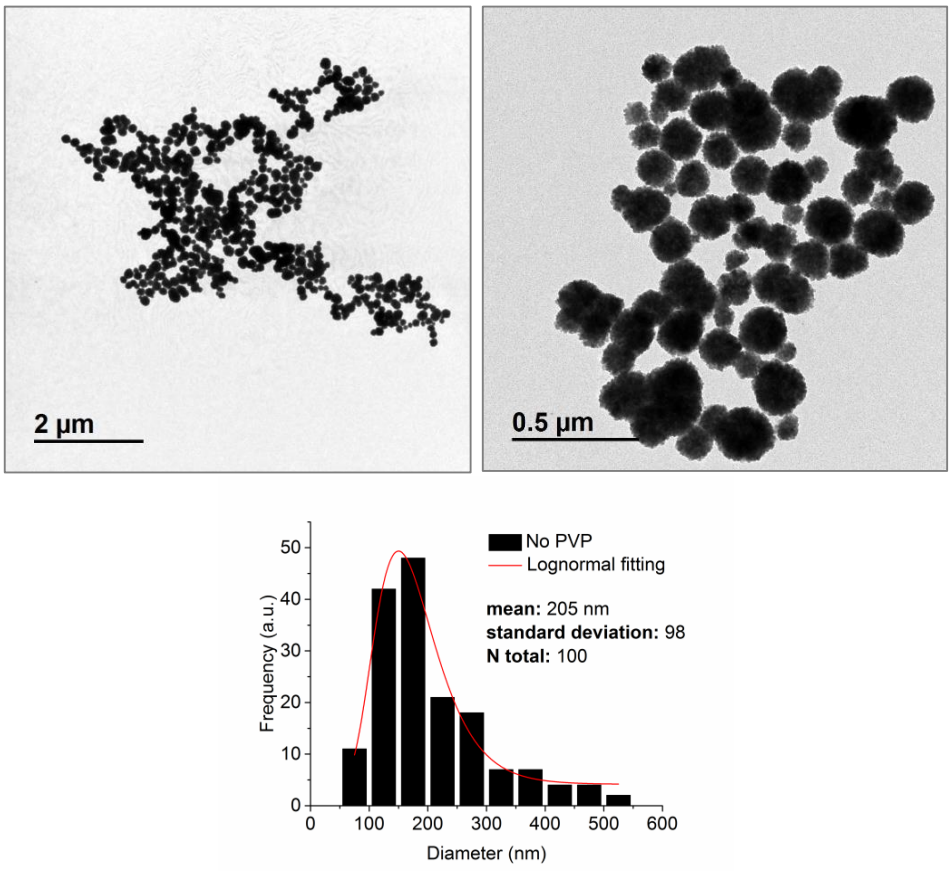

Figure S1. TEM Images of the particles obtained in the absence of PVP. Below, particle size distribution log-normal fitted. The standard deviation (S.D) is more than twice than for the rest of the samples.

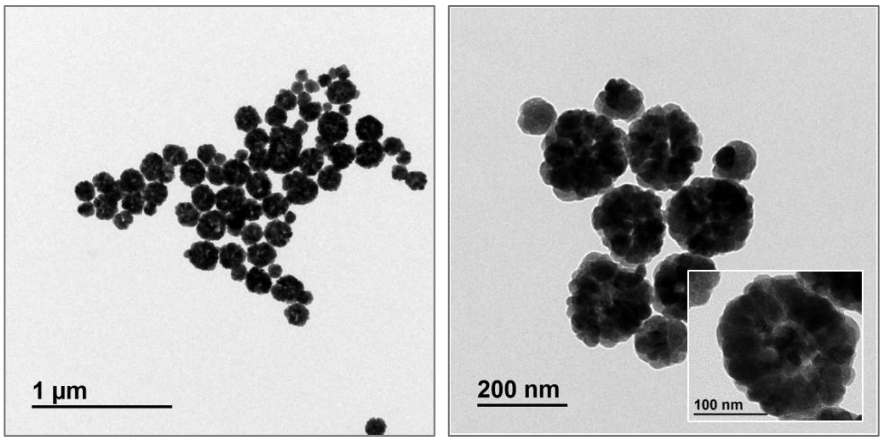

Figure S2. TEM Image of sample HS.

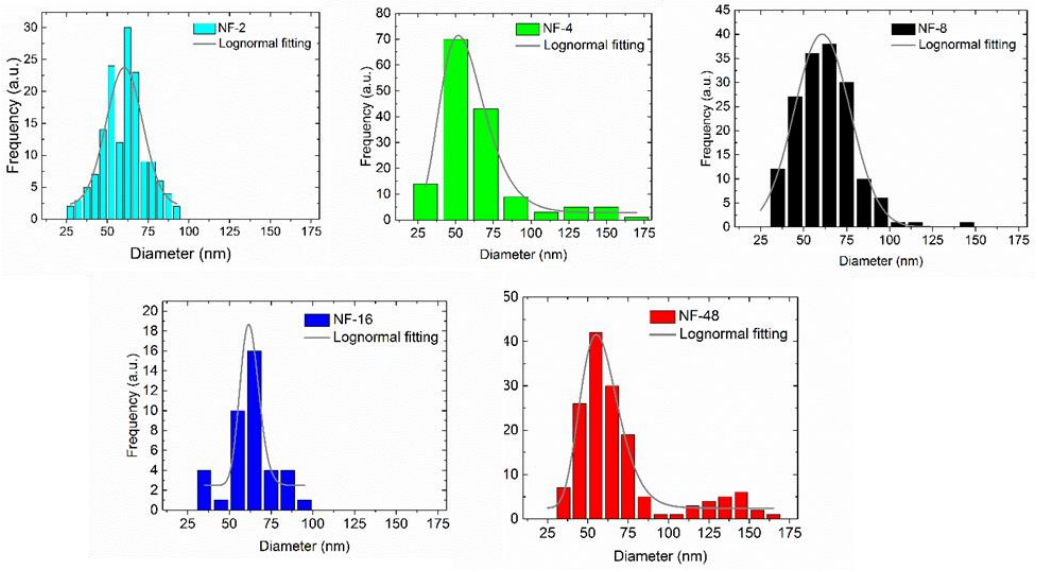

Figure S3. Histograms resulting from the frequency counts conducted through TEM measurements of the nanoflower diameter during the different heating times (2-48 h). Note that by mean Lognormal fitting a size distribution has been obtained.

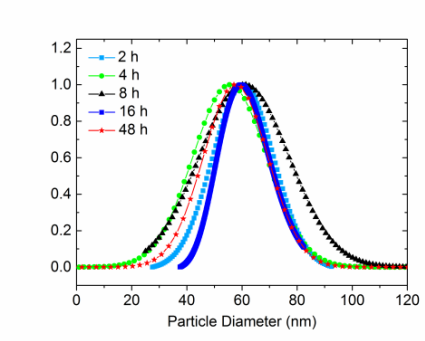

Figure S4. Log-normal size distributions fitted from the TEM measurements of the nanoflower diameter during the different heating times (2-48 h). Note that the measurements are number-weighted and normalized.

2. X-Ray Diffraction

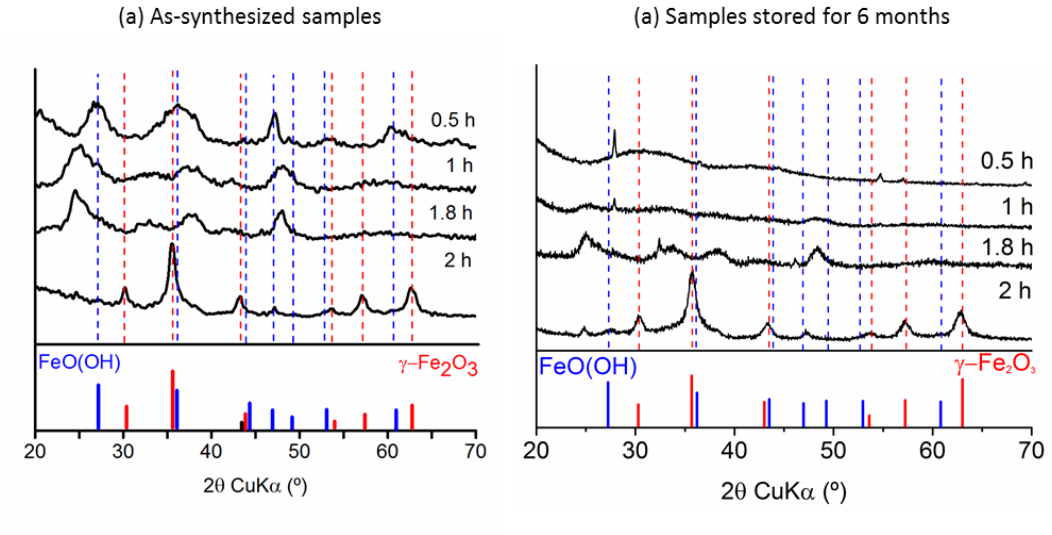

Figure S5. Formation mechanism of the Nanoflowers (NF-0.5-2). X-Ray diffraction patters collected for (a) the as-synthesized samples and (b) after being stored for six months.

3. Infrared Spectroscopy

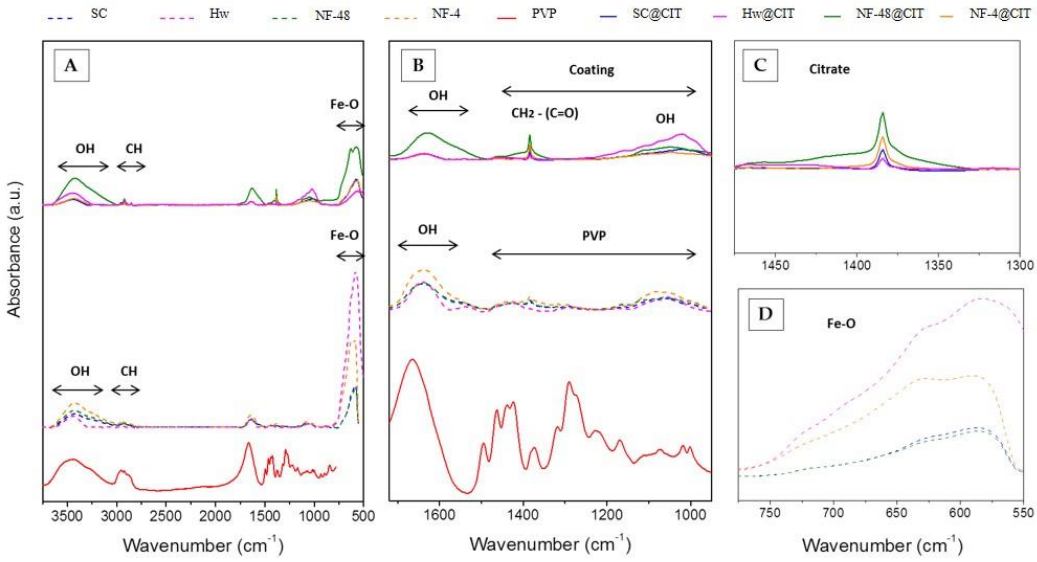

Figure S6. Infrared spectra of magnetite nanoparticles before and after coating process, and for PVP. a) Complete IR spectra, and expanded spectra between b) 1720 – 950 cm^{-1}, c) 1475 – 1300 cm^{-1} and d) 775–550 cm^{-1}.

4. Thermogravimetric analysis

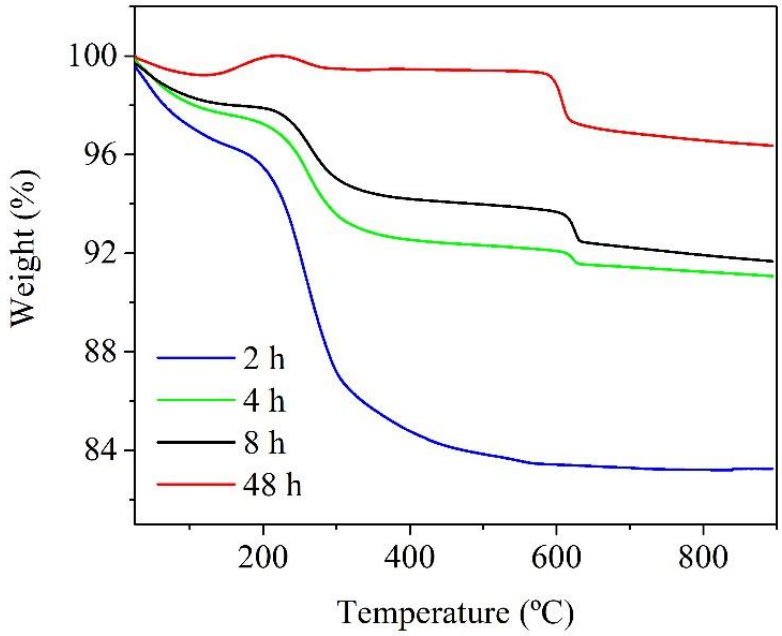

Figure S7. Thermogravimetric analysis for different periods of crystallization: 2, 4, 8 and 48 h.

5. Magnetic dynamics of low temperature anomalies in AC susceptibility measurements

In order to interpret the nature of the lower temperature anomalies we have tried to investigate their magnetic dynamics. To this end we have characterized the samples aged for 4 and 48 h by measuring their AC susceptibility at several frequencies (Figure S5). From the various methods traditionally employed to characterize the dynamics, we have chosen the determination of the preexponential factor τ_0 in the fit of the temperature of the maxima of the out of-phase susceptibility to an Arrhenius law $1/(2\pi f) = \tau_0 \cdot \exp(E/(k_B T))$, where f is the measuring frequency, E the activation energy and k_B the Boltzmann constant (see Table S1). At this point we like to draw the reader's attention to the strong similarity of our AC susceptibility results with those of colloidal maghemite nanoclusters[1] and iron oxide nanoparticles formed by means of dendrons.[2] In those articles the reported low temperature magnetic features behave according to τ_0 values in the range 10^{-8} –10^{-10} s, while the medium temperature ones offer values in the range 10^{-19} –10^{-23} s. Basic calculations on the dynamics of noninteracting magnetic particles[3,4] indicate that, for measuring frequencies below the megahertz range, the temperatures of the out-of-phase susceptibility maxima depend on frequency according to an Arrhenius law with preexponential factors in the range 10^{-9} –10^{-12} s, while for interacting assemblies attempts to use this law result in nonphysically much lower values. In our case, given their complex microstructure, it appears obvious that all the present magnetic entities are mutually interacting. In this sense, the obtained preexponential factors for the medium temperature anomaly will naturally be understood. The analysis of the low temperature peaks, on the contrary, resulted in preexponential factors consistent with the slow dynamics of noninteracting particles but we find this interpretation very unlikely.

Their relative sharpness, their regular dependence with the aging time, and the occurrence also in iron oxide nanoparticles prepared by completely different methods[1,2] point more to some phenomenon intrinsic to maghemite or to some usually appearing intermediate phase, although no rigorous interpretation of this phenomenon can be offered yet.

Table S1. Fit parameters obtained by analysing the temperature of the out-of-phase susceptibility maxima with an Arrhenius law.

	Low temperature (sharp) maximum		Medium temperature (rounded) maximum	
Sample	E/k_B (K)	τ_0 (s)	E/k_B (K)	τ_0 (s)
NF-8	516	4.3×10^{-8}	3860	1.7×10^{-15}
NF-48	418	8.4×10^{-10}	8686	1.6×10^{-31}

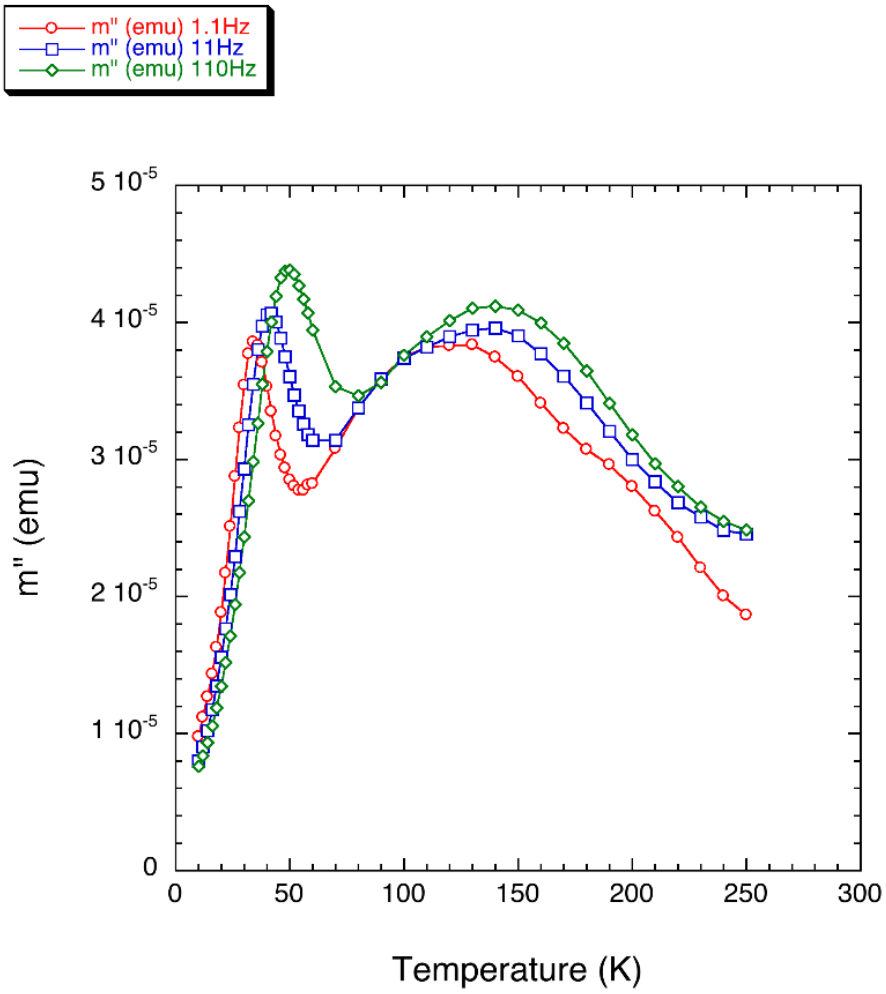

Figure S8. Out-of-phase AC susceptibility of sample NF-8at several frequencies: 1.1, 11 and 110 Hz.

References

1. Kostopoulou, A.; Brintakis, K.; Vasilakaki, M.; Trohidou, K.; Douvalis, A.; Lascialfari, A.; Manna, L.; Lappas, A., Assembly-mediated interplay of dipolar interactions and surface spin disorder in colloidal maghemite nanoclusters. Nanoscale **2014,** 6, (7), 3764-3776.
2. Kuchkina, N. V.; Morgan, D. G.; Kostopoulou, A.; Lappas, A.; Brintakis, K.; Boris, B. S.; Yuzik-Klimova, E. Y.; Stein, B. D.; Svergun, D. I.; Spilotros, A., Hydrophobic periphery tails of polyphenylenepyridyl dendrons control nanoparticle formation and catalytic properties. Chemistry of Materials **2014,** 26, (19), 5654-5663.
3. Shliomis, M.; Stepanov, V., Theory of the dynamic susceptibility of magnetic fluids. Advances in Chemical Physics **1994,** 87, (1), 32.
4. Garcia-Palacios, J., On the statics and dynamics of magnetoanisotropic nanoparticles. Adv. Chem. Phys. **2000,** 112, 1-210.

Part H

Resumen

Resumen

Introducción

En esta tesis, las nanoparticulas de óxidos de hierro han sido el caso del estudio (específicamente las fases magnetita y maghemita de los óxidos de hierro) ya que este nanomaterial presenta algunas características y ventajas interesantes, que surgen de su composición química y estructura atómica: pueden ser manipuladas por un gradiente de campo magnético externo y pueden responder a un campo magnético externo que cambia con el tiempo con resultados ventajosos relacionados con la transferencia energética de dicho campo de excitación a las nanopartículas.[1] Por último, las nanopartículas magnéticas afectan a la relaxividad de los protones circundantes. En base a estos atributos, las nanopartículas magnéticas son uno de los materiales funcionales emergentes tanto en la industria de la ciencia de materiales como en biomedicina.

En este trabajo, se han investigado sistemas de nanopartículas magnéticas ferrimagnéticas (FM) o superparamagnéticas (SP). El comportamiento magnético que enhiben va a ser modulado mediante la modificación de: su tamaño, forma o interacción. A continuación se describe como estos parámetros afectan a dicho comportamiento:

- Las partículas con un tamaño por debajo del valor crítico D_{SD} (diámetro de mono-dominio) la fuerza coercitiva disminuye al disminuir el tamaño. Cuando ésta alcanza el valor cero, la muestra se encuentra en el régimen superparamagnético. El superparamagnetismo es una forma de magnetismo que aparece en pequeñas nanopartículas ferromagneticas o ferrimagnéticas. Cuando el tamaño de nanoparticula es lo suficientemente pequeño, la magnetización puede cambiar al azar de dirección bajo la influencia de la temperatura y después de estar expuestas a un campo magnético externo, dado que su campo coercitivo es cero, la magnetización medida tendrá un valor promedio de cero. En este estado, un campo magnético externo es capaz de magnetizar

las nanopartículas, parecido a lo que ocurre con un imán paramagnético. Sin embargo, su susceptibilidad magnética es mucho mayor que en los imanes paramagnéticos. Es por esto por lo que este tipo de material magnético ha sido propuesto como material ideal para aplicaciones biomédicas.

- Las distorsiones en la forma de las partículas pueden provocar anisotropía adicional (que tiene una dependencia direccional con las propiedades magnéticas del material) estabilizando o desestabilizando el régimen de monodominio. Variaciones minúsculas en la uniformidad de la magnetización en las nanopartículas puede desempeñar un papel esencial para determinar sus propiedades magnéticas (susceptibilidad, anisotropía, los parámetros de histéresis, etc.).[2]

- En los materiales magnéticos nanoestructurados, las interacciones entre nanopartículas generalmente son claves, y dependen en gran medida de la distancia entre nanopartículas magnéticas. Así, para distancias grandes (asumiendo por lo tanto un sistema de nanopartículas que no interaccionan), el comportamiento magnético se define por el régimen superparamagnético (a valores finitos de temperatura). En cambio para casos con distancias pequeñas, el régimen superparamanético puede ser alterado por interacciones dipolares o por interacciones de canje.[3] Así, las interacciones dipolares modifican los entornos energéticos, alcanzando mínimos de energia[4] que llevan a coercitividad y remanencia reducidas. Por otra parte, las interacciones de canje en NPs superparamagnéticas pueden llevar a un comportamiento ferri/ferromagnético con histéresis.

De este modo, controlar dichos parámetros permite el diseño y fabricación de sistemas nanomagnéticos con propiedades magnéticas predefinidas.

En la literatura reciente, la estructura de las nanopartículas magnéticas se ha clasificado como mono-núcleo (con un solo núcleo magnético por partícula) o multi-núcleo (con numerosos núcleos magnéticos por partícula) (Figure 1). Las partículas mono-núcleo generalmente están recubiertas por una capa química o bioquímica activa que facilita el aislamiento de las mismas. Por el contrario las nanopartículas multi-núcleo tienen una matriz que une los núcleos magnéticos que forman la partícula final, la cual puede estar recubierta superficialmente. Además, por encima del régimen superparamagnético las nanopartículas tendrán momento magnético permanente incluso a temperatura ambiente, lo que generalmente implica cierto grado de aglomeración. Esta aglomeración, salvo en estructuras multi-núcleo, puede ser temporalmente revertida (mediante agitación o sonicación) y completamente anulada si se consigue la suficiente repulsión estérica o electrostática.

¿Cómo se pueden sintetizar específicamente sistemas mono- o multi-núcleo? De manera ideal, controlando el mecanismo de crecimiento y el proceso de recubrimiento de las nanopartículas magnéticas.

En este contexto, núcleos individuales sintetizados en un único paso se logran mediante la descomposición térmica a alta temperatura de precursores orgánicos y por el proceso mediado por polioles.

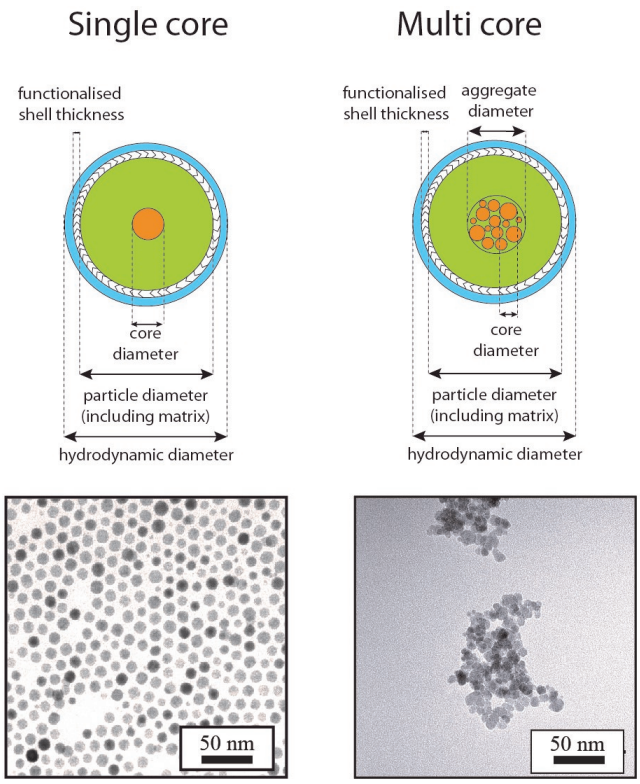

Figure 1: Estructura de coloides de nanoparticulas magnéticas y ejemplos representativos que se encuentran en la literatura: la estructura mono-núcleo está representada por nanopartículas de magnetita recubiertas con ácido oleico sintetizadas mediante descompsición térmica a altas temperaturas. La estructura multi-núcleo está representada por nanoparticulas sintetizadas por co-precipitación recubiertas posteriormente con ácido cítrico.

Es necesario que se de la nucleación homogénea en el punto de súper saturación crítica, generando núcleos primarios que crecen de manera controlada bajo el régimen de crecimiento por difusión.[5] Este modelo de nucleación está explicado por la teoría de LaMer.[6, 7] Así mismo, debe haber un reactivo (ácido oléico/oleilamina o un poliol con una determinada longitud de cadena, para el caso de la descomposición térmica de precursores orgánicos y la síntesis mediada por polioles, respectivamente) que actúe como surfactante, controlando la distancia entre los núcleos primarios y limitando su crecimiento. Hay muchos factores que están interrelacionados y son responsables de la formación de partículas mono-núcleo, y controlarlos manteniendo la monodispersidad es todo un reto. Sin embargo hay ciertas deficultades que se deben abordar en este tipo de partículas en referencia a su forma y a la toxicidad de los reactivos usados en su síntesis. Primero, atendiendo a la forma de las nanopartículas de magnetita obtenidas mediante las metodologías de síntesis directa, se han conseguido morfologías

esféricas, cúbicas y romboédricas. Sin embargo, de forma directa no se ha podido abarcar el resto de morfologías habituales. Una posible solución es la síntesis de un precursor y su transformación a la fase magnetita, que requiere mantener la morfología de la nanopartícula depué de la transformación y eso lo convierte en una difícil tarea. En segundo lugar, el uso de coloides magnéticos con fines biomédicos requiere que las nanopartículas estén dispersas en medio acuoso y los núcleos individuales logrados en medio orgánico necesitan etapas adicionales de transferencia al nuevo entorno.

Por otro lado, los sistemas multi-núcleo hasta el momento han sido obtenidos de dos maneras: por la adición in-situ de ciertos polímeros provocando la reducción en la densidad de carga superficial de los núcleos primarios en crecimiento favoreciendo su aproximación y posterior agrupación o logrando la agregación orientada de pequeñas subunidades en un proceso de ensamblado, basado en el modelo de crecimiento por adición de monómeros, [8] dirigido por la presencia de moléculas específicas o bajo la acción de un campo externo. No obstante, hay una carencia en el control del número de núcleos por partícula y la interacción entre ellos y por esto se persigue la obtención de estructuras altamente regulares.

Una vez diseñado el coloide magnético, ¿cuál es el siguiente paso para fabricar un material funcional? Normalmente, las nanopartículas magnéticas destinadas a una aplicación, deben estar compuestas, no exclusivamente de un núcleo magnético, si no que también necesitan un espaciador que proteja el núcleo, evitando que las nanopartículas se agreguen es suspensión.[9] Este espaciador generalmente actúa como plataforma para una funcionalidad extra en aplicaciones concretas, como se muestra en la Figure 2. Así, el espaciador puede tener naturaleza orgánica o inorgánica. Además, a fin de obtener un material funcional, se deben unir moléculas o biomoléculas más complejas que proporcionen una actividad determinada.

Por último, las nanopartículas magnéticas de óxido de hierro en forma de coloides abren un amplio e interesante abanico de posibilidades en biomedicina. Esto es el resultado directo de sus propiedades nanométricas porque: son lo suficientemente pequeñas para establecer una interacción con entidades biológicas tales como con receptores moleculares, etc., y a la vez son lo bastante grandes (manteniendo una alta relación superficie-volumen) como para transportar una carga de agente terapéutico o de contraste para imagen. Además, por su carácter magnético son capaces de i) establecer localmente un campo dipolar perturbador en presencia de un campo magnético, ii) experimentar una fuerza magnética que resulta en movilidad magnetoforética en presencia de un gradiente de campo magnético externo y iii) generar energía térmica cuando son expuestas a un campo magnético alterno. De todas estas notables ventajas derivan importantes aplicaciones biomédicas tales como agente de contraste en imagen por resonancia magn'etica (IRM), administración selectiva de fármacos, buscadores de dianas celulares e hipertermia magnética (aplicaciones in-vivo); y separación magnética (aplicaciones in-vitro). En particular, la posibilidad de tratar el cáncer mediante hipertermia inducida magnéticamente ha conducido al desarrollo de diferentes dispositivos diseñados para calentar células malignas dejando intacto el tejido sano.[10] En líneas generales, el procedimiento involucra la dispersión de partículas

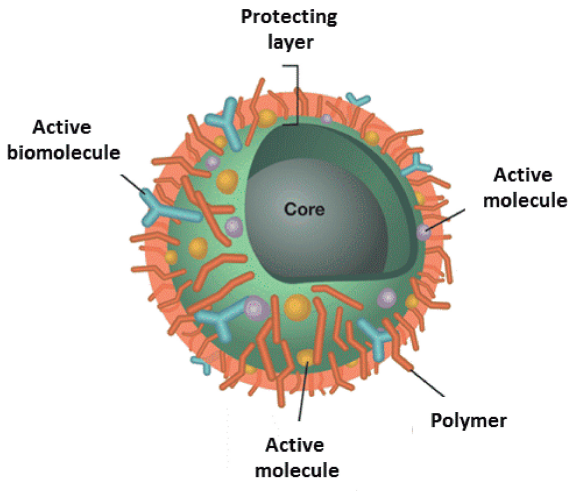

Figure 2: Estructura de una nanopartícula magnética funcional: compuesta por un núcleo magnético recubierto por una capa protectora. Generalmente, esta la capa protectora se funcionaliza con una molécula orgánica sobre la que se pueden hacer posteriores uniones de moléculas específicas que proporcionen cierta actividad.

magnéticas a través del tejido diana y aplicar después un campo magnético alterno de amplitud y frecuencia adecuadas como para causar el calentamiento de las nanopartículas. Este calor fluye inmediatamente al entorno del tejido enfermo en el cual, si la temperatura se mantiene por encima del umbral terapéutico de 42° C durante 30 min o más, la célula tumorosa es destruida.

Sin embargo, antes de usar las MNPs de óxidos de hierro en el campo de la biomedicina, hay una demanda en la estandarización de su síntesis y métodos de análisis. Esto aseguraría la reproducibilidad en su fabricación y serviría para definir y acotar características (de su estructura y naturaleza magnética) que son importantes para que se usen de forma segura en el campo de la biomedicina. Aparte de eso, es necesario también estudiar y evaluar la biotransformación y toxicidad de las IOMNPs en modelos animales. Si estas exigencias fuesen alcanzadas, las nanopartículas magnéticas producidas en los laboratorios podrían ser transferidad a clínica.

En conclusión, se han expuesto las ventajas de las nanopartículas magnéticas y por qué los óxidos de hierro se proponen como materiales ideales en diferentes aplicaciones biomédicas. Sus propiedades magnéticas dependen fuertemente de su tamaño, forma e interacción y en esta tesis se han modulado estos dos últimos parámetros, siempre manteniéndose dentro la escala nanométrica.

Objetivos

Este trabajo de tesis ha sido llevado a cabo en el marco del proyecto Europeo "NanoMag" (acuerdo de subvención n° 604448), cuyos objetivos son estandarizar, mejorar y redefinir los métodos de análisis de nanopartículas magnéticas y desarrollar muestras de referencia para aplicaciones biomédicas.

Para ello, este trabajo de Tesis ha sido orientado hacia diferentes tareas:

- Síntesis de nanopartículas uniformes de óxidos de hierro modulando el tamaño, forma, estructura interna, ensamblado y, en consecuencia, controlando sus características magnéticas.
- Caracterización completa de los materiales obtenidos aclarando la relación entre estructura y propiedades.
- Funcionalización con molécular/polímeros apropiados para la interacción con sistemas biológicos.
- Evaluación de la toxicidad de las nanopartículas magnéticas y cuantificación en sistemas biológicos.

Atendiendo a la estructura de las nanopartículas magnéticas (mono- y multi-núcleos), los abjetivos específicos de esta Tesis son:

- Optimización de la síntesis de nanopartículas magnéticas anisométricas mono-núcleo.
- Optimización y estudio de los procesos de auto-ensamblado para obtener nanopartículas magnéticas multi-núcleo en forma de flor. Análisis del efecto del tamaño (de núcleo y partícula) en las propiedades magnéticas.
- Estudio de la toxicidad, acumulación y detección de nanopartículas magnéticas mono- y multi-núcleo in-vitro y en un modelo animal simple y novedoso.

Resultados

Capítulo 2. Cómo la Forma y la Estructura Interna Afecta las Propiedades Magnéticas de Nanopartículas Anisométricas de Magnetita

Las aplicación de las nanopartículas magnéticas, mencionadas con anterioridad, requieren ciertas propiedades estructurales y magnéticas específicas, las cuales dependen fuertemente del tamaño y la forma.[11] En hipertermia magnética, se obtienen mayores tasas de calentamiento en nanopartículas en la transición entre el multidominio y el monodominio magnético, lo que ocurre en nanopartículas de aproximadamente 30 nm, aunque esto ocurre en un amplio rango de tamaño, transformando así la energía magnética en energía térmica (de Néel o Brown).[12] En segundo lugar, la forma de las nanopartículas puede tener un impacto significativo en el comportamiento magnético debido a la anisotropía de forma que modifica la orientación del momento magnético dentro de las nanopartículas. Por último, las interacciones dipolares entre nanopartículas dependen también de la forma de las mismas e influirán en la estructura del aglomerado que se forma, pudiendo dar lugar a configuraciones, como por ejemplo cadenas, que han demostrado biomimetizar los magnetosomas,[13] o o partículas huecas que consisten en nanocristales orientados.[14, 15].

En el capítulo 2, se describe una ruta alternativa de síntesis en medio acuoso de nanopartículas de magnetica anisométricas. Estas tienen por tanto diferentes morfologías y tamaños de núcleo por encima de 25 nm, y podrían ser producidas a gran escala. Nanobarras magnéticas de óxidos de hierro han sito obtenidas anteriormente mediante un método similar, y mostraron propiedades magnéticas interesantes y con una funcionalidad modulable en su superficie.[16]

Proponemos un proceso de tres pasos, a través de los cuales hemos obtenido partículas magnéticas alargadas, romboédricas y discos hexagonales con uniformidad en la nanoescala. Primero, se sigue una ruta de sínteis acuosa para obtener los correspondientes precursores antiferromagnéticos, como la fases de goetita o hematites, cuyo tamaño y forma se pueden modificar cambiando las condiciones de síntesis (se incluyen la temperatura, presión y naturaleza y concentración de las sales usadas[17]). A continuación, el precursor antiferromagnético se recubre con una capa de sílice que las previene la agregación.[18, 19] Finalmente, las nanopartículas antiferromagnéticas recubiertas se reducen a magnetita. Esto se lleva a cabo mediante una reducción seca (las nanopartículas están en forma de polvo) exponiéndolas a una atmósfera de gas de hidrógeno a una cierta presión parcial[20], o mediante reducción húmeda (las nanopartículas están dispersas en un disolvente orgánico) en presencia de ácido oleico.

Después de la síntesis de precursores y antes de que las nanopartículas fueron recubiertas, su morfología fue investigada por SEM. Las micrografías de SEM (Figura 3) muestran las tres morfologías obtenidas: (A) romboedros, (B) discos hexagonales y (C) agujas. Tanto el tamaño como la forma son altamente homogeneos.

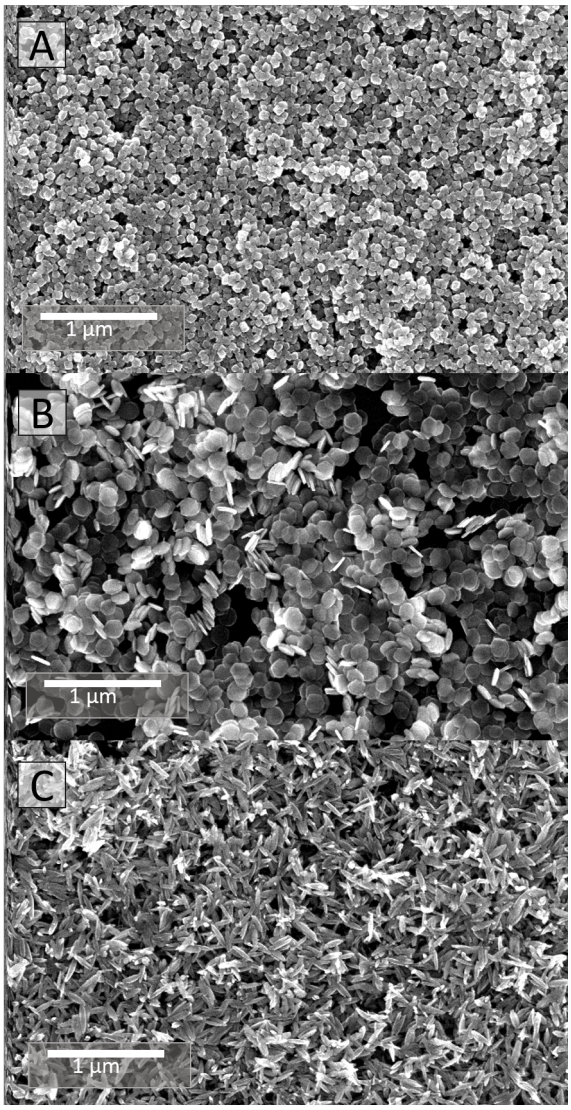

Figure 3: Imágenes de SEM del material precursor: (A) romboedros, (B) discos hexagonales y (C) agujas.

Después de la síntesis de precursores, las nanopartículas se recubren con sílice y se transforman a magnetita mediante reducción seca o húmeda. Como resultado, el precursor se recubrió con éxito alrededor de núcleos individuales o conjuntos de dos o tres núcleos ($\sim$ 75%), aunque una fracción de núcleos múltiples (5-10 núcleos recubiertos) ($\sim$ 25%) no se pueden descartar. La condensación de TEOS ocurre únicamente en la superficie de las NPs no se observó sílice coloidal.

Cuando se recubrieron con sílice las agujas de goetita (tanto en polvo como en solución) el sistema se calienta por encima de 350° C, y antes de la transformación a magnetita, sufren un proceso de deshidratación después del cual se transforman en hematites. Como consecuencia, las NPs desarrollan poros dentro de su estructura debido a la expulsión de agua,[17], a lo largo del eje central de la aguja, los cuales se unen con frecuencia a lo largo de la longitud del cristal.[21] Poros a lo largo del eje c, después de este tipo de tratamiento térmico, han sido reportados con anterioridad[22] de acuerdo connuestras observaciones. A pesar de la porosidad, las imágenes de HR-TEM sugieren que se genera una estructura monocristalina. Después de la deshidratación, las nanopartículas se reducen a magnetita y no se observa una sinterización entre partículas ni modificación de la forma gracias al recubrimiento con sílice y a las temperaturas suaves usadas para la reducción (por debajo de 600°C).

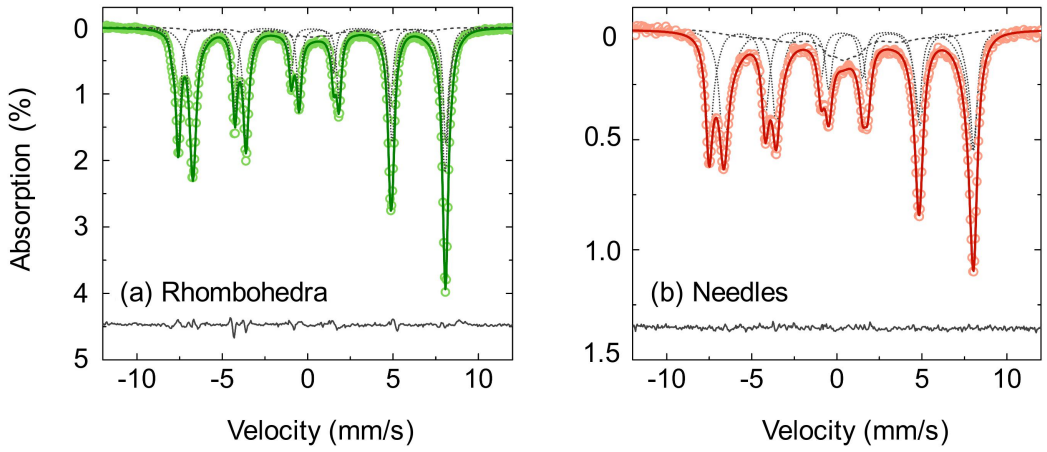

Figure 4: Comparación de los espectros de Mössbauer atemperatura ambiente de (a) romboedros y (b) agujas después de la reducción. Para cada uno, los puntos son las cuentas observadas, la línea continua es el mejr ajuste modelado de los resultados, y la línea de puntos son los sub-espectros vogtianos. La calidad del ajuste está indicada mediante χ^2 reducida y residual, dadas por la diferencia I_{obs}-I_{cal}.

Espectroscopía Mössbauer (Figure 4), junto con XRD y FTIR confirman la correcta transformación a magnetita pues los sitios octaédricos y tetraédricos del hierro se detectan.

Las curvas de magnetización de las muestras (Figure 5) muestran comportamientos similares para diferentes formas y técnicas de reducción. Las muestras exhiben un campo remanente diferente a cero

y coercitividad indicando que las nanopartículas están bloqueadas a temperatura ambiente o inferiores. Mirando en detalle, se puede observar que los romboedros y las agujas que se obtienen mediante una reducción húmeda presentan ciclos de histéresis con forma de "avispa", que no se observan en materiales obtenidos mediante reducción seca. Roberts et al. atribuyeron este hecho a una stado de remanescencia que es una mezcla de mono- y multi-dominio de las nanopartículas.[23]

Dado que las muestras preparadas por reducción seca no muestran ciclos de histéresis con forma de "avispa", esta técnica de reducción aparenta producir partículas con un estado de magnetización mas uniforme comparado con la reducción húmeda. Esto está de acuerdo con nuestros hallazgos en el tamaño cristalino calculado por XRD, porque los defectos y poros son responsables generalmente anclar y propagar dominios magnéticos, y obviamente estos poros y defectos son menos pronunciados en reducción en polvo.

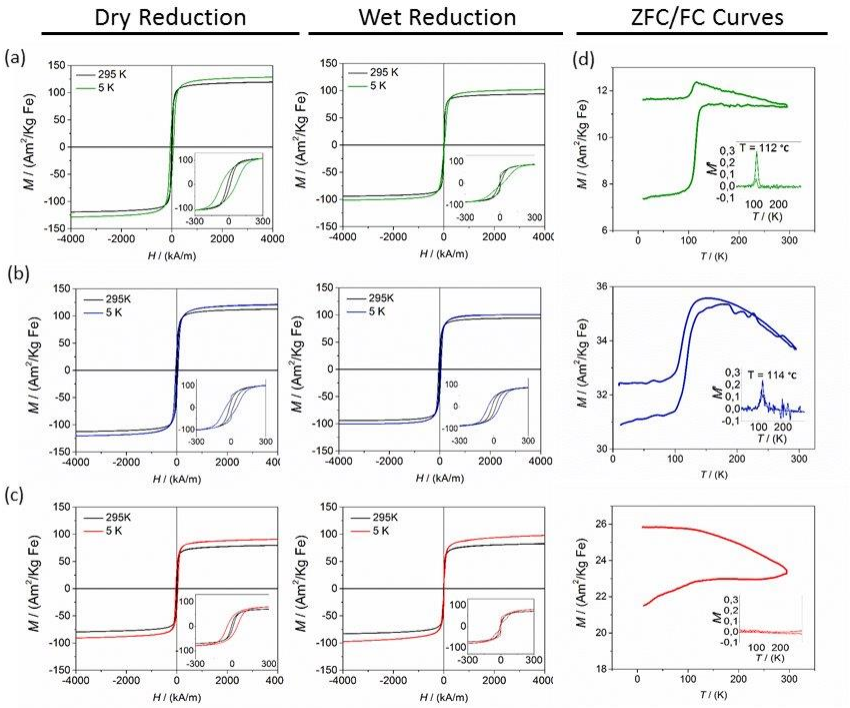

Figure 5: Ciclos de histéresis a 295 y 5 K de las nanopartículas con las diferentes morfologías. (verde=romboedros, azul=discos, rojo=agujas), comparando la reducción húmeda y seca. Insertado se muestran ciclos de histéresis en el régimen de campo bajo ($\pm$ 300 kA/m). Además, se muestran las curvas ZFC-FC (medidas a 5 mT) de las muestras obtenidas por reducción húmeda. Insertado se muestran la primera derivada de la magnetización respecto a la temperatura.

Los romboedros poseen el valor más alto de M_s, mientras que los discos exhiben el menor, lo cual

puede atribuirse a las diferencias de tamaño del eje menor. Es curioso el hecho de que los valores de M_s en el caso de las NPs obtenidas por reducción húmeda son considerablemente menores, indicando de nuevo la deferencia entre los métodos de reducción y la presencia de los poros, que tienen un efecto en las propiedades magnéticas. Para los discos, los valores de coercitividad son idénticos en ambos tipos de reducciones, mientras que para los romboedros y agujas no se puede comparar debido a la forma de "avispa" que tienen los ciclos de histéresis para el caso de la reducción húmeda.

Las curvas de magnetización dependientes del campo recogidas a mayoores velocidades de barrido de campos para los romboedros y las agujas se recogen en la Figura 5. Aquí, las curvas de histéresis con forma de "avispa" (observadas en las medidas de magnetización cuasiestáticas) se han desvanecido. El hecho de que la curva de histéresis dependa de la velocidad del barrido del campo confirman que dicha forma del ciclo se origina por la formación de dominios dentro de la partícula, dado que la nucleación y progación de paredes de dominio son dependientes del tiempo.[24].

Las curvas de magnetización ZFC-FC de todos los materiales obtenidos a partir de la reducción líquida se muestran en (Figura 5). Se observa una transición de Verwey[25] claramente en el caso de los romboedros y los discos (a 112-114 K) es decir, las NPs obtenidas a partir de los precursores de hematites. En el caso de las agujas, obtenidas a través de la goetita, esta transición es casi invisible. El hecho de que esta transición apenas se observe en el caso de las agujas puede estar relacionado con el tamaño de cristal determinado por XRD y podría estar asociada a la formación de una estructura porosa como se observa por HR-TEM. Los espectros de Mössbauer apoyan esta conclusión, mostranto lineas más anchas y un singlete central fere las agujas, sugiriendo una cristalinidad más reducida, lo cual podría explicar la perdida de la transición de Verwey. La forma de esta transición de Verwey para las diferentes morfologías, especialmente para la transición encubierta de los discos, que podría estar relacionado por la existencia de poros y por tanto a una estrucura cristalina con más defectos.

Capítulo 3. Nanopartículas Coloidales de óxido de Hierro en Forma de Flor: Estrategias de Síntesis y Recubrimiento

A pesar del progreso en auto-ensamblaje en coloides de unidades elementales orgánicas[26] e inorgánicas[27, 28] que actúan como "bloques de construcción" para formar estructuras más complejas, se han reportado pocos ejemplos donde se consiga el auto-ensamblaje ordenado y controlado de nanopartículas en suspensión.[29] Por otra parte, la agregación es un mecanismo general de formación de partículas, que recientemente se ha reconocido como un fenómeno de crecimiento común de partículas monodispersas,[30–34] a diferencia de procesos de crecimiento de adición de monómeros descrita en modelos clásicos. En el caso de nanopartículas magnéticas, estos procesos son - a priori - diferentes, debido a las fuerzas adicionales que surgen como consecuencia de su momento magnético. Estas interacciones pueden ser de tipo intraparticula (interacciones de canje) o interacciones dipolares magnetostácticas entre partículas, siendo este último tipo de interacción de largo alcance. Las interacciones de canje entre núcleos de una partícula multi-núcleo puede llevar al denominado carácter "superferrimagnético",[35] exhibiendo grandes momentos magnéticos y conservando un campo remanente débil a campo cero y por lo tanto, teniendo una baja tendencia a formar aglomerados. Por otra parte, las interacciones dipolares entre partículas con un momento magnético lo suficientemente alto dan lugar configuraciones, como cadenas, que pueden cambiar fuertemente las propiedades magnéticas de un coloide.[36]

Como consecuencia, el ensamblado de MNPs en estructuras multi-núcleo puede, en algunos casos, dar lugar a propiedades magnéticas "colectivas" que dan lugar a comportamientos magnéticos microscópicos muy diferentes a nanopartículas mono-núcleo o al material masivo.[37, 38] Dichas estructuras multi-núcleo han mostrado un gran interés en diferentes áreas como catálisis,[39] ferrofluidos y reología,[40] así como para bioaplicaciones, en las que se centran principalmente en nanopartículas multi-núcleo de maghemita y magnetita. Es este área han destacado por tener valores altos de relaxividad (r_2) en RMN,[9] señales altas en MPI (imagen por partículas magnéticas),citeic3a21 altas tasa de absorción específica bajo un campo AFM (valores de SAR),[41–43] alto momento magnético para su manipulación con un campo magnético externo[44] y una buen rendimiento como agentes teranósticos.[45–47]

En el capítulo 3, se han analizado los parámetros clave de la síntesis que dirigen el proceso de auto-ensamblado capaz de organizar núcleos magnéticos en nanopartículas multi-núcleo altamente regulares y reproducibles, que muestras dicho estado "superferrimagnético" debido a interacciones de canje. Para ello, se llevo a cabo una comparación de cuatro estrategias de síntesis diferentes para obtener nanopartículas coloidales de óxido de hierro con forma de flor (Figure 6).

Se llevo a cabo una caracterización estructural y magnética completa de los coloides y los polvos liofilizados siguiendo protocolos estandarizados para facilitar la comparación de estas estructuras.[48] Primero, se ha analizado el tamaño del núcleo mediante HR-TEM, XRD y curvas de M v H (a través

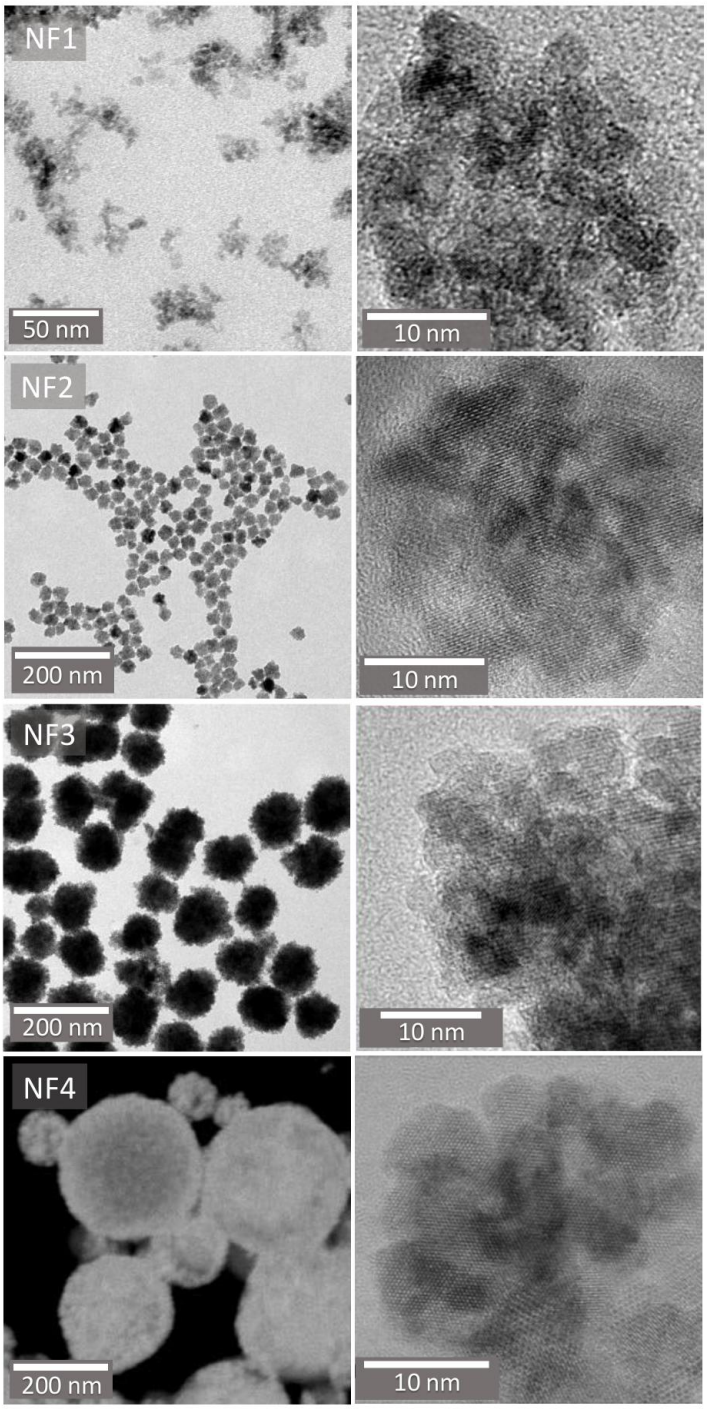

Figure 6: Imágenes de TEM (NF1-3), STEM (NF4) (izquierda), e imágenes HR-TEM (derecha) de las diferentes nanopartículas en forma de flor.

de la modelización mediante la función de Langevin). A continuación, se estudió el empaquetamiento y disposición de los núcleos formando las partículas multi-núcleo y investigaron las interacciones interpartículas. Para ello, el tamaño de partícula se calculo mediante TEM, DLS y susceptibilidad AC dependiente de la temperatura (mediante el modelo de Debye y el modelo extendido multi-núcleo). Cada técnica proporcionó un tamaño de núcleo o partícula característico que nos permitió determinar los parámetros estructurales claves que determinaban el comportamiento magnético, los cuales están recogidos en la Figura 7. El tamaño de los núcleos está en un rango entre los 8 y 15 nm y con un tamaño de partícula entre los 50 y 250 nm. Las diferencias encontradas en el tamaño determinado con diferentes técnicas de caracterización refleja la naturaleza compleja de estos materiales. En general, el tamaño calculado mediante XRD (D_{XRD}) es mayor al estimado mediante HR-TEM (D_{HRTEM}), lo que refleja que hay un cierto grado de fusión entre los núcleos formando las partículas finales.

En esos casos en los que se obtienen valores altos de $D_{XRD} \approx D_{HRTEM} > 10$ nm (NF2 and NF4), se detecta una coalescencia significativa de los núcleos, lo cual justifica los valores más altos de M_s que exhiben estas muestras. Para todas las muestras, el tamaño magnético modelado mediante la función de Langevin ($d_{c,2}$) es mayor que D_{HRTEM} y D_{XRD} sugiriendo la presencia de interacciones entre los núcleos y por lo tanto indicando in comportamiento colectivo de los mismos. De esto deducimos que en aquellos casos donde los núcleos tienen contacto directo y hay una continuidad en la orientación cristalina, se favorece el orden magnético en las interfases. Este es el caso de las nanoflores reportadas con anterioridad, las cuales reportaron tasas de absorción específicas (SAR) un orden de magnitud superiores a núcleos tradicionales de 11 nm de maghemita con las mismas condiciones de amplitud y frecuencia de campo.[49]

En relación al tamaño de partícula, las muestras en las que DLS $D_h \gg D_{TEM}$ o contienen un alto contenido de recubrimiento e hidratación en su superficie o tiene lugar un comportamiento colectivo entre las partículas (interacciones interpartículas, como por ejemplo las interacciones dipolares). El primero ha sido detectado mediante FTIR y TGA. El segundo fue detectado mediante susceptibilidad AC dependiente de la frecuencia. Los valores de tamaño hidrodinámico obtenidos mediante esta técnica ACS $D_{h,2}$ (mediante el modelo extendido de multi-núcleo) son comparables con DLS D_h, lo cual confirma que las interacciones dipolares entre las partículas han sido minimizadas en casi todos los casos, explicando la larga estabilidad de los coloides. En el caso de la muestra NF3, las interacciones dipolares detectadas por ACS podrían ser las causantes de la formación de cadenas y explicar el cambio en el espectro de AC dependiente de la dilución de la muestra.

Comparando los tamaños calculados mediante caracterización magnética,es decir, el tamaño magnético efectivo ($d_{c,2}$) y el tamaño hidrodinámico ACS $D_{h,2}$, hemos identificado 3 sistemas diferentes di nanopartículas multi-núcleo en forma de flor. Para NF2, el tamaño magnético efectivo tiende a aproximarse al tamaño de la nanoflor (ACS $D_{h,2}$ / $d_{c,2} \sim 1.8$) lo que indica que hay una interacción magnética fuerte entre los núcleos dentro de la partícula. Los núcleos no sólo están orientados si no que tienen también contacto estrecho llevando a interacciones intrapartícula de canje. Para NF1 y NF3, el tamaño

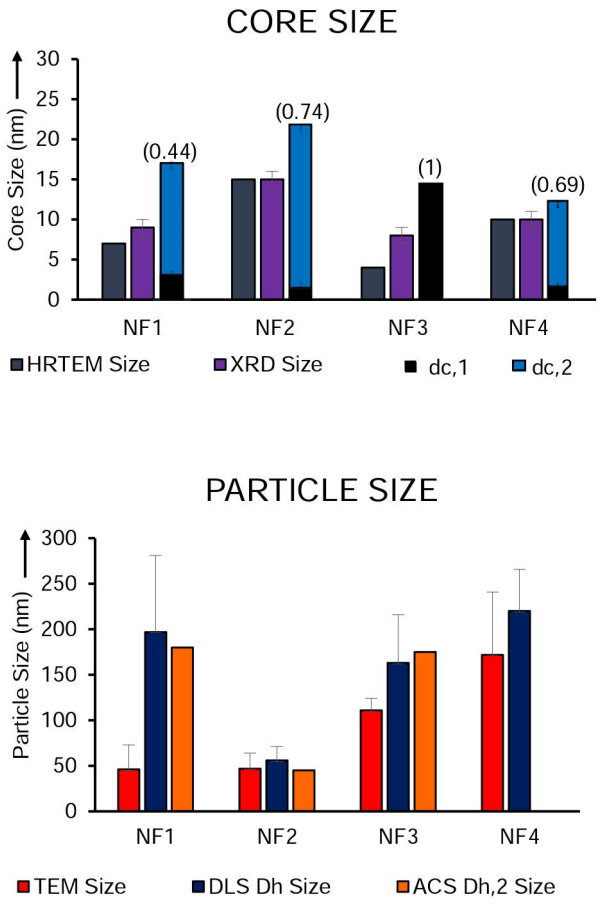

Figure 7: Núcleo (arriba) y tamaño de partícula (abajo) de las nanopartículas en forma de flor determinados mediante medidas estructurales y magnéticas. Entre paréntesis se incluye β, la fracción normalizada de la distribución de tamaño de determinada mediante las medidas de magntometría DC.

magnético efectivo es mucho menor al tamaño de la flor (ACS $D_{h,2}$ / $d_{c,2} \sim 10$) indicando un menor contacto entre núcleos, los cuales en el caso de NF1 están tan compactados. El caso de NF4 es más complicado, puesto que las nanoflores están embebidas en una esfera polimética creando una superestructura. El relativo pequeño tamaño de estas nanoflores, la alta constante de anisotropía pero la baja temperatura de bloqueo de NF4 sugiere que el tamaño finito de este sistema de nanoflor es uno de los parámetros clave que dicta sus propiedades de relajación de Néel.

Las diferencias encotradas entre NF1-4 están directamente relacionadas aspectos clave de sus rutas sintéticas (Estrategias 1-4, 8). NF1 ofrece la posibilidad de producción a gran escala en medio

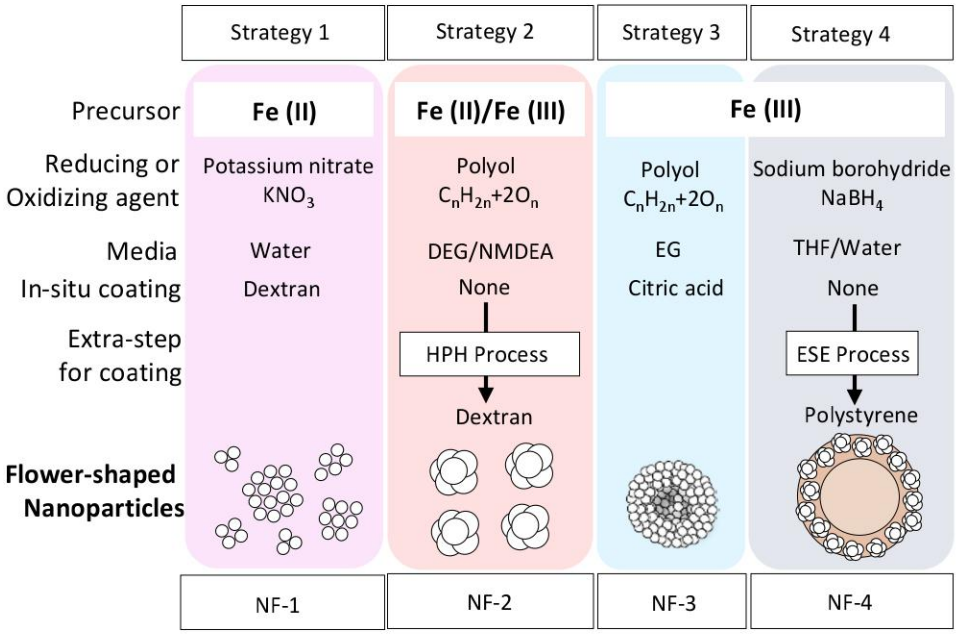

Figure 8: Estrategías seguidas para obtener las nanopartículas en forma de flor. NMDEA significa N-metil dietanolamina, el proceso HPH significa de recubrimiento por homogeneización a alta presión, y el ESE significa método de emulsión y evaporación de solvente.

acuoso. El uso de polioles como disolvente proporciona un gran control sobre la agregación de los núcleos, dando lugar a estructuras multi-nucleo regulares cuyos núcleos, dependiendo de las condiciones de síntesis, tienen mayor o menor contacto(NF2 y NF3). El uso de temperaturas más altas (200 °C) y tiempos de reacción largos lleva a la coalescencia de los núcleos (NF2), sin embargo, mediante la adición de un reactivo extra (citrato sódico) facilita la dispersión de las partículas en medio acuoso pero impide el contacto de los núcleos de una forma similar al dextrano en el caso de NF1. Sin embargo debe ser mencionado que, atendiendo al coste de las reacciones, NF2 y NF3 necesitan altas temperaturas y tiempos de reacción largos, lo que supone generalmente un consumo alto de energía. Además, las estrategias que requieren un único paso para la síntesis y recubrimiento (como es el caso de NF1 y NF3) son ventajosas en comparación con las estrategias paso a paso (NF2 y NF4).

Este es el primer paso hacia la estandarización de protocolos de síntesis y caracterización de nanopartículas en forma de flor.

Capítulo 4. Mecanismo de formación de nanoflores de maghemita sintetizadas mediante el proceso mediado por polioles

Mediante metodo de síntesis mediado por polioles, se han reportado estructuras de nanocrystales magnéticos ensamblados formando nanopartículas multi-núcleo con forma de flor en los últimos años.[50, 51] En comparación con núcleos individuales de los que parten, estas nanopartículas con estructura de flor han mostrado tener una mayor relaxividad longitudinal y transversal para imagen de resonancia magnética nuclear, para la generación de agentes de contraste,[52] y una mayor tasa de absorción específica (SAR) para hipertermia magnética debido a calentamiento por histéresis.[53]

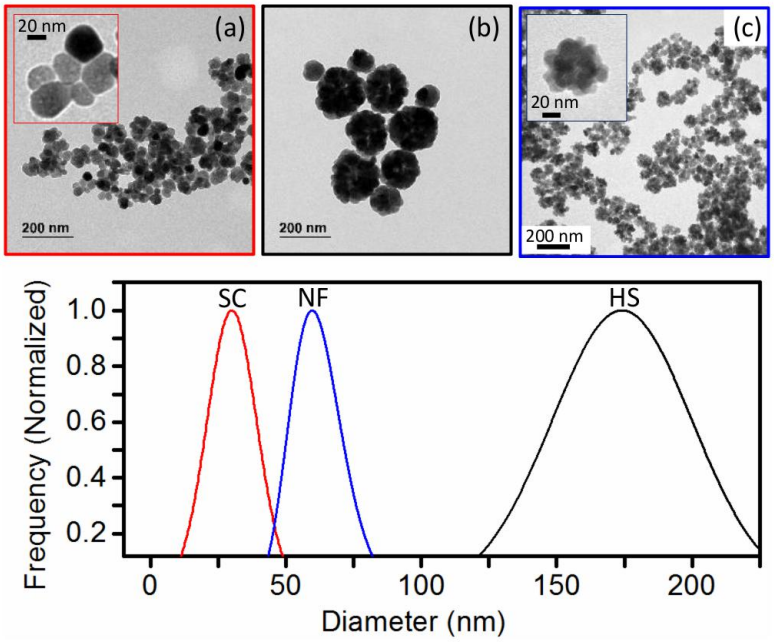

Figure 9: Imágenes de TEM de las diferentes estructuras obtenidas al variar la concentración de NaAc: (a) Partículas mono-núcleo (SC), 36.5 mmol, (b) esferas huecas (HS), 26.2 mmol, (c) nanoflores (NF), 15.8 mmol. Abajo, las distribuciones de tamaño log-normal calculadas mediante el análisis de TEM para las diferentes muestras.

El proceso de ensamblado y el tamaño del núcleo y la partículas son características cruciales que determinan las propiedades magnéticas del coloide y por ello, y en extensión define su uso óptimo para una cierta aplicación.[54, 55]

En el capítulo 4, se ha seleccionado el método de los polioles y se ha llevado a cabo el análisis de proceso de ensamblaje que lleva a la formación de nanopartículas mono-núcleo y multi-núcleo, habiendo obtenido dentro de este último tipo esferas huecas y nanoflores y se ha determinado que

parámetro define el tamaño de núcleo de la partícula en el caso de las nanoflores. Para ello, hemos análizado el efecto en la concentración de un precipitador (acetato sódico, NaAc), un estabilizante extra (polivinilpirrolidona, PVP) y el tiempo de calentamiento del sistema. A continuación se ha estudiado la consecuencias de dichas variaciones en la estructura en el comportamiento magnético colectivo. A través de la variación del tiempo de calentamiento se ha determinado el mecanismo de formación de las nanoflores. Por último, las muestras han sido recubiertas por ácido cítrico y su posible uso en aplicaciones de hipertermia magnética ha sido evaluado a través de la medida de la tasa de absorción específica (SAR).

Primero, la cantidad de $NaAc{\cdot}3H_2O$ se varió desde 15.8 to 36.5 mmol, manteniendo la concentración del resto de reactivos y las condiciones experimentales fijas. La figura 9 muestra las imágenes de TEM de cada muestra y sus correspondientes distribuciones de tamaño log-normal, obtenidas mediantela medida manual del diámetro de las partícula mediante el software Image J and análisis de datos mediante Origin.

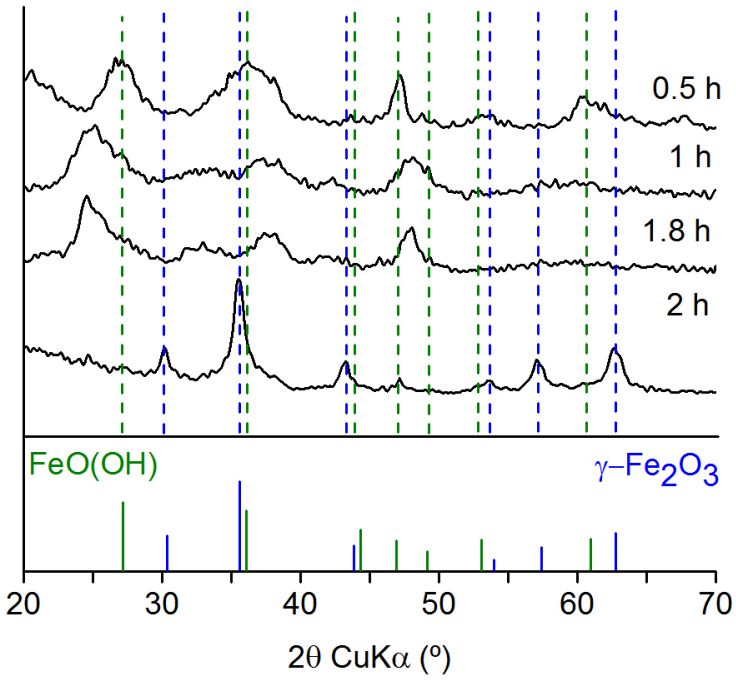

Figure 10: Mecanismo de formación de las nanoflores seguido a través de difracción de rayos-X de los polvos, recogidos después de tiempos de reacción 0,5, 1, 1,8 y 2 h. Abajo se muestran los patrones de difracción de la lepidocrocita (γ-FeOOH, verde) y maghemita (γ-$Fe_2 2O_3$, azul).

Se ha observado que la variación de la concentración de NaAc lleva a nanopartículas con diferente estructura (Figura 9). Para la concentración mayor de NaAc (36.5 mmol), se obtienen nanopartículas mono-núcleo de un tamaño de 35 nm (muestra SC, Figura 9 a). Sin embargo, al reducir la concentración de NaAc a 26.2 mmol, se obtienen nanopartículas multi-núcleo que forman esferas huecas de 170 nm en diámetro (muestra HS, Figura 9 b). Mediante la reducción de NaAc hasta 15.8 mmol se obtienen nanopartículas multi-nucleo con estructura de nanoflow (muestra NF, Figura 9 c). En este caso, los núcleos ($<$ 20 nm) forman una estructura altamente compacta y de tamaño uniforme con un diámetro de $\sim$ 60 nm.

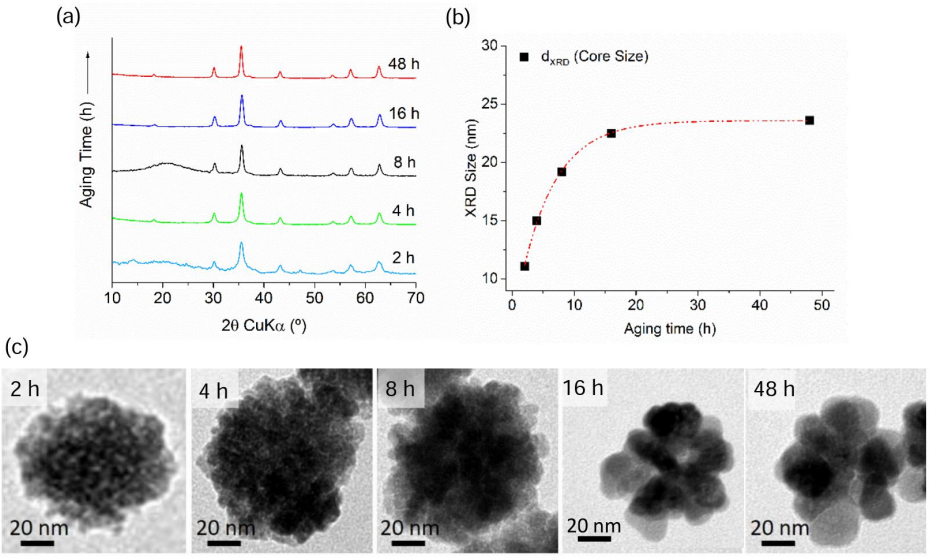

Figure 11: Estructura de las muestras NF a t=2-48 h: (a) patrones de difracción XRD, (b) tamaño de cristal calculado mediante la ecuación de Scherrer,(d) imágenes representativas de TEM de las respectivas muestras.

Para estudiar el mecanismo de formación y las propiedades magnéticas de las nanoflores, la concentración de NaAc se fijó (15,8 mmol) y el tiempo de calentamiento se varió desde 0,5 a 48 h. La Figura 10 muestra los patrones de difracción de rayos-X de las diferentes muestras. A un tiempo t=0,5 h, el patrón claramente se corresponde con lepicocrocita (γ-FeOOH) (2-θ angles of 27, 36, 47 and 60°). Sin embargo, el patrón de difracción cambia a t=1 y 1,8 h de tiempo de reacción. Estos patrones no se corresponde con ninguno de las fases conocidas de óxidos de hierro o oxihidróxidos de hierro. Dado que los patrones de difracción son diferentes, especulamos que se trata de una fase desconocida intermedia. A 2 h de tiempo de reacción, la mayoría de los máximos de Bragg pueden indexarse como maghemita (γ-$Fe_2 2O_3$), cuyo perfil típico de XRD se muestra en la Figura 10 marcado en rojo. Medidas de XRD realizadas meses después de la síntesis confirman que esta fase desconocida es metaestable.

Una vez que las nanoflores de maghemita se han formado, tras 2 h de tiempo de reacción, un proceso de envejecimiento comienta. Este proceso se estudió mediante microscpía electrónica, XRD y medidas magnéticas. La Figura 11 a muestra los difractogramas recogidos para las muestras NF-2-48 (el tiempo de reacción fue variado entre 2 y 48 h). Después de 4 h, la única fase detectada es maghemita. Los máximos de Bragg se van estrechando a lo largo del tiempo y el tamaño medio decristal obtenido de esta anchura (a través de la fórmula de Scherrer) muestra que las nanoflores sufren un proceso de recristalización, incrementando su tamaño medio de cristal d_{XRD} desde 11 hasta 23 nm (Figura 11 b). Una tendencia similar se observa en TEM, donde los núcleo están visiblemente creciendo a lo largo del tiempo (Figura 11 c) aparentemente por fusión dado que el tamaño general de la nanoflow no varía.

Las medidas de magnetometría DC se efectuaron sobre las nanoflores que habían sufrido el proceso de cristalización (a t superiores a 2 h). A tiempos prolongados (4, 8, 16 y 48 h) se observa que los valores de magnetización de saturación se han incrementado desde 48 a 90 Am^2/kg a 290 K (Figura 4.9 b), lo cual supone un aumento significativo. Las muestras también muestran un campo coercitivo creciente ($\sim$ 0,5-2 kA/m a temperatura ambiente y 8-19 kA/m a 5 K) con el envejecimiento de las mismas. El comportamiento magnético dinámico a tiempos de calentamiento prolongados fue estudiado a través de susceptibilidad AC dependiente de la temperatura. Estos resultados sugieren la contribución más importante procede de partículas bloqueadas magnéticamente por encima de la temperatura ambiente, pero a tiempos de envejecimiento prolongados, aparecen anomalías en la dinámica magnética de las nanopartículas a bajas temperaturas, las cuales se atribuyen a un fenómeno intrínseco de la maghemita o a alguna fase intermedia (sin embargo los difractogramas indican únicamente la fase de maghemita). Sin embargo, de mmomento no se puede ofrecer una interpretación rigurosa de este fenómeno.

Por último, en el Capítulo 4, la estabilidad coloidal y el potencial de calentamiento para hipertermia magnética se evaluó en muestras SC y MC, dentro de las MC, en las muestras con la morfología de esferas huecas y nanoflores, y en este último caso de las nanoflores se seleccionaron las muestras con un núcleo de 15 y 23 nm. Para ello, la carga superficial y la estabilidad coloidal se incrementada a través de un recubrimiento con ácido cítrico. Mediante FTIR, DLS, medidas de Potencial-Z y TGA, este recubrimiento se pudo confirmar la correcta funcionalización de las muestras.

Las nanoflores muestran en DLS una distribución monomodal estrecha centrada en $\sim$100 nm después del recubrimiento. Las muestras SC y HS muestra un tamaño hidrodinámico después del recubrimiento de 161 y 298 nm, respectivamente. La capacidad de calentamiento de los materiales recubiertos en medio acuoso y pH fisiológico fue evaluada con el fin de estudiar la diferencia en morfología y cristalinidad. Las nanoflores con un núcleo de 23 nm (NF-48) tienen el valor de SAR más alto, consiguiendo tasas de absorción de 1.131,2 W/g Fe para una freciencia y amplitud de campo de 710 KHz. y 24.8 kA/m, respectivamente. Esta muestra exhibe valores de SAR casi 5 veces superiores a las nanoflores con un tamaño de núcleo de 15 nm (NF-4), casi 4 veces superiores a las esferas hue-

cas y casi 1.5 veces superiores a las nanopartículas mono-núcleo de 35 nm, aunque estas muestras (SC y HS) posean mayores tamaños de núcleo (27 y 35 nm, respectivamente). Esto demuestra que tanto el tamaño cristalino como el empaquetamiento de los mismos son decisivos en la capacidad de calentamiento de estos materiales. Observamos que el caso específico de las nanoflores con tamaños de núcleo mayores (controlado mediante el envejecimiento de las muestras) ofrecen una capacidad de calentamiento mejorada en comparación con las nanoflores de tamaño critalino menor, las esferas huecos o nanopartículas mono-núcleo usadas en este trabajo.

Capítulo 5: Desvelando los mecanismos que determinan la absorción y la metabolización de nanopartículas magnéticas mono- y multi-núcleo in-vitro y en un modelo animal Xenopus Laevis

Una clave para la utilización segura en biomedicina de las nanopartículas magnéticas y su aprovación por agencias regulatorias yace en el estudio de su biotransformación y toxicidad. Por una parte, el curso y el destino de las nanopartículas una vez han complido su funciíon es todav ía un tema a estudiar. Por otra parte, la metabolización segura de los sub-productos debe ser evaluada y asegurada. Dado que el hierro está involucrado en diversos procesos vitales, los organismos exhiben mecanismo de transporte y almacenamiento de hierro en formas no-tóxica.[56] Por ello, se predice que las IOMNPs se incorporen de forma segura en sistemas biológicos. Hay evidencias crecientes que demuestran que las IOMNPs desencadenan mecanismos de asimilación de hierro en las células y que los productos de degradación son incorporados en rutas metabólicas normales del hierro.[57–63] Sin embargo, el recubrimiento de las nanopartículas ha demostrado ser determinante en la captación, degradación y destino de las nanopartículas.[64, 65] Para llegar a conclusiones sólidas acerca de la toxicidad y biodistribución de las IOMNPs sería ideal tener modelos biológicos pertinentes.

En el capítulo 5, se reporta el efecto de nanopartículas magnéticas de γ-Fe_2O_3 mono- y multi-núcleo, aptas para aplicaciones biológicas, en lineas celulares, de carcinoma hepatocelular (Hep G2) y adenocarcinoma colorectal (Caco-2), e in-vivo, en un modelo anfibio de Xenopus Laevis, ya que éste es ideal para estudiar el curso y destino de las nanopartículas, porque permite bioensayos flexibles para evaluar el desarrollo embrional en vertebrados, biología molecular y celular básica, genómica y estudios de neurobiología y toxicología.[66] Nanopartículas mono-núcleo (SC) fueron obtenidas mediante descomposición térmica del precursor de oleato de hierro (III) en 1-octadeceno (Figura 5.1 a-b). Las partículas tienen un diámetro de 13 $\pm$ 1 nm, tamaño y forma uniforme (Figura 12 c) y son relativamente esféricas y bien dispersas, devido a la presencia de ácido oleico alrededor de las partículas. A través de la ruta desíntesis mediada por polioles, se obtuvieron nanopartículas multi-núcleo (MC) a partir de cloruro de hierro (III). MC estsá compuesta de nanopartículas esféricasde 142 $\pm$ 23 nm con tamaño y forma uniforme. IOMNPs obtenidas por descomposición térmica son hidrofóbicas. Para hacerlas adecuadas para aplicaciones biológicas, el ácido oléico de la superficie fue intercambiado con ácido dimercaptosuccínico (DMSA) via reacción de intercambio de ligando (SC@DMSA). En el proceso mediado por los polioles, polivinilpirrolidona (PVP40) es adicionado con el fin de proporciona a las nanopartículas un recubrimiento hidrofílico. Sin embargo, se ha utilizado ácido cítrico como agente de recubrimiento extra con el que incrementar la carga superficial para facilitar la dispersión final de las partículas MC en medio acuoso (MC@Cit). Ambas muestras se recubren con polietilenglicol (PEG), aumentando el tamaño hidrodinámico y disminuyendo su carga superficial.La presencia del las moléculas o el polímero de recubrimiento se detectan a través de FTIR y TGA.

La Figura 12 muestra la caracterización toxicológica de las nanopartículas in-vitro, evaluadas me-

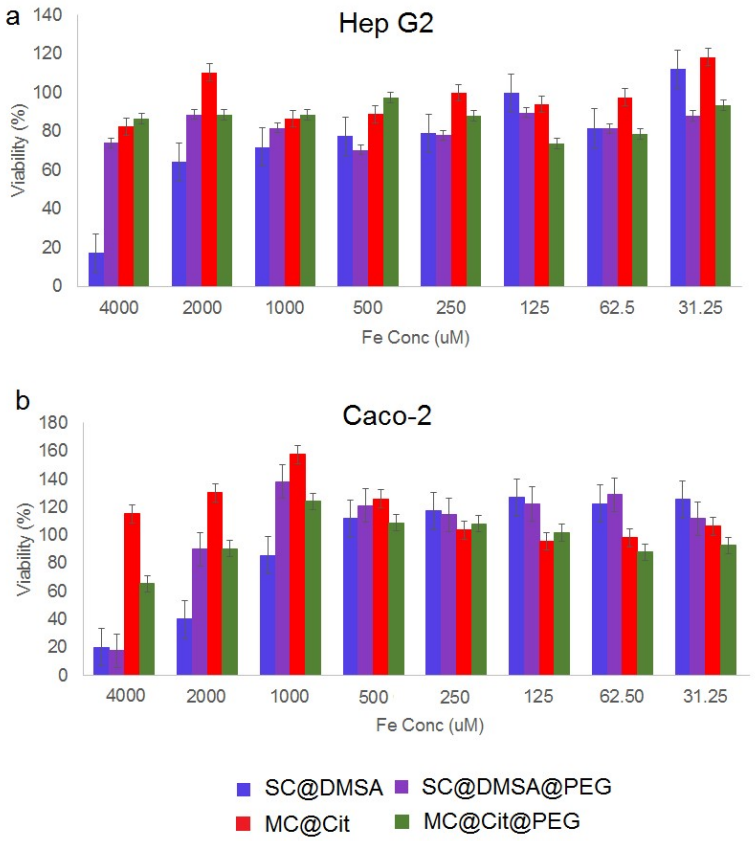

Figure 12: Evaluación de la viabilidad celular mediante el ensayo MTT de (a) lineas celulares Hep G2 (b) lineas celulares Caco-2, después de 24 h de tratamiento con las diferentes NPs. Los valores indican la media $\pm$ SD (n=3).

diante el grado de supervivencia a través del ensayo estándard de bromuro de metiltiazol tetrazolio (ensayo MTT). El ensayo de citotoxicidad después de incubar las células Hep G2 y Caco-2 con las nanopartículas muestran que la viabilidad de los cultivos no se altera significativamente con la presencia de las nanopartículas. hasta una concentración de 1000 μM Fe después de 24 h de tratamiento (80-100% viabilidad en comparación con el control). A concentraciones de hierro mayores de 1000 μM, SC disminuye el porcentaje de viabilidad en ambas lineas celulares hasta un 20%. En el caso de MC, el porcentaje de viabilidad en ambas lineas celulares está en el rango de 60-80%, indicando toxicidad baja incluso a concentraciones de hierro altas. Estas diferencias en el perfil de toxicidad a dosis altas podría estar relacionado con la diferente sensibilidad de ambas lineas celulares usadas en el tratamiento por las nanopartículas. El efecto de del recubrimiento con PEG no está muy claro a altas concentraciones. En el caso de la línea Hep G2, la funcionalización con PEG mejora la citotoxicidad

para SC mientras que en la línea Caco-2 no se observa tal efecto. Para MC, la funcionalización con PEG reduce la viabilidad a un 60% en la línea Caco-2.

El uso del modelo de Xenopus laevis tiene las ventajas de rápido desarrollo y crecimiento embrionario en 48 h, lo cual nos ha permitido estudiar el efecto de los diferentes tipo de IOMNPs en renacuajos con un conjunto completo de órganos funcionales. Los renacuajos fueron tratados con soluciones de nanopartículas a cuatro concentraciones diferentes de hierro, 0.25 mg/mL, 0.5 mg/mL, 0.75 mg/mL and 1 mg/mL. La segunda ventaja de este modelo es que nos ha permitido visualizar directamente las nanopartículas mientras los renacuajos las ingieren.

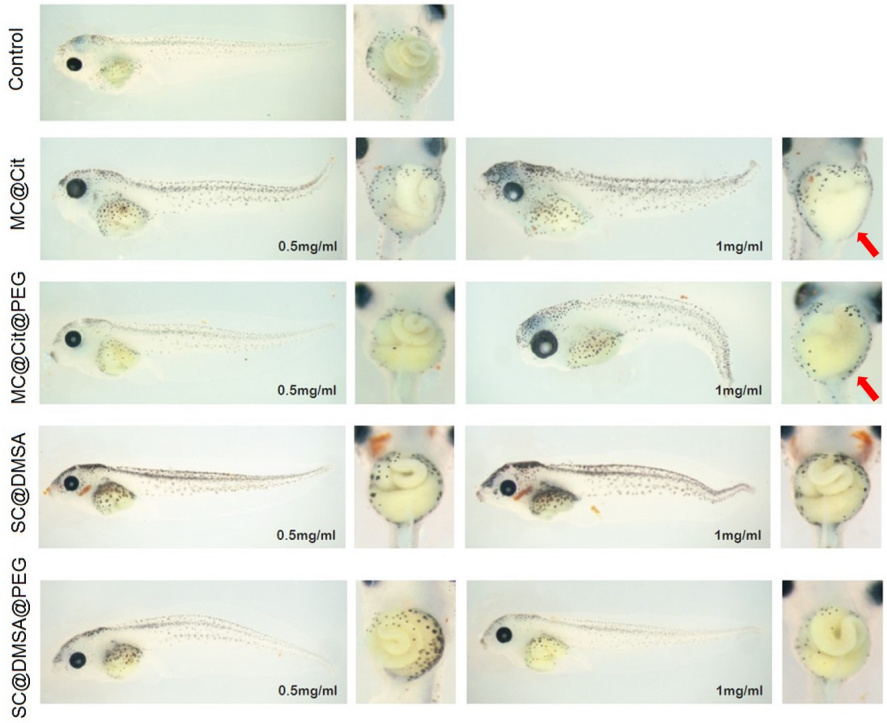

Figure 13: Imágenes representativas de X. laevis expuesto a soluciones de nanopartículas a concnetraciones de 0.5 y 1 mg/mL. (n=7 por grupo). Las flechas rojas destacan los intestinos en los que el efecto del tratamento ha sido dramático, modificando su estructura.

La toxicidad corporal de los renocuajos fue evaluada a concentraciones de 0.5 y 1 mg Fe/mL. La Figura 13 sugiere que la absorción de ha tenido lugar principalmente en el caso de SC@DMSA y que éstas han sido masivamente absorbidas por los organismos. Todos los embriones exhiben toxicidad corporal general por cuando son tratadas a una concentración de NPs de 1 mg Fe/mL. En este caso, los embriones muestran defectos en la forma corporal, la flexión de la cola y desarrollo tardío. En el caso de los embriones tratados con una concentración de de 0.5 mg/mL, los defectos son más sutiles

(Figura 13).

Por lo tanto, esto sugiere la absorción de los renacuajos dependende de la dosis de nanopartículas. Dado que los principales órganos involucrados en la absorción de nanopartículas son los intestinos y el hígado, se ha evaluado la morfología en dichos órganos. Para los renacuajos tratados con SC, la estructura con diferentes segmentos del intestino se conserva, aunque a concentraciones de hierro de 1 mg/mL se observa una inflamación de dichos segmentos. En los renacuajos tratados con MC los efectos son dramáticos en la morfología del intestino. El órgano no se forma correctamente, y como consecuencia, los diferentes segmentos no se diferencian (como se observa en las zonas destacadas con las flechas rojas en la Figura 13) en comparación con el órgano de los renacuajos control. A bajas concentraciones de SC o MC, donde los efectos de toxicidad corporal en los embriones se han reducido visiblemente, y en el caso de las muestras PEGiladas, no se observa daño ninguno en el intestino, en comparación con el resto de muestras.

La absorción de las nanopartículas se detecta claramente por SEM-EDS (en el espectro de dispersión de energía de rayos X se muestran las lineas de transición K-α and K-β del hierro, en contraste con los animales modelo), en cortes de la faringe. Sin embargo, para un análisis cuantitativo de la acumulación de las nanopartículas en los animales se recurre a caracterización magnética y análisis elemental.

Así, se estudió la susceptibilidad AC de pozos con 7 animales (Figura 14). La presencia de las nanopartículas magnéticas puede ser identificada a través de la susceptibilidad magnética en fase (χ'), acompañada por un máximo a una temperatura ligeramente más baja en la susceptibilidad fuera de fase (χ''). La temperatura y localización del máximo depende de las nanopartículas evaluadas (del material, su tamaño, grado de agregación, etc.). La altura de este máximo es una medida indirecta de la concentración de las nanopartículas. En nuestro caso, hemos observado una absorción dependiente de la dosis en los animales tratados con nanopartículas, a excepción de las muestras PEGiladas (Figura 14), independientemente de si son SC o MC. Estas muestras PEGiladas no se detectan en nigún caso, a menos que su concentración esté por debajo de los límites de detección de la técnica de ACS. La ausencia de una contribución sustancial de señal paramagnética, la cual se observa normalmente a más bajas temperaturas, indica que en los sujetos no hay presente átomos de hierro libre, de lo cual concluimos que el proceso de degradación es muy bajo.

Estos resultados están de acuerdo con lo que se observa por SEM-EDS, y la concentración de hierro determinada mediante análisis elemental (ICP-OES), que indica que se produce una absorción masiva de SC@DMSA. La absorción es de 2 a 5 veces superior, respectivamente, a la absorción de MC@Cit, teniendo en cuenta que los renacuajos son tratados con soluciones a dos concentraciones (0.5 y 1 mg Fe/mL). Mediante esta técnica, se confirma que los valores de contenido en hirro en el caso de los renacuajos tratados con muestras PEGiladas son comparables al control.

Una posible explicación para las alteraciones visibles del intestino, en el caso de los renacuajos tratados con la muestra MC@Cit@PEG, es que las nanopartículas son rápidamente excretadas por

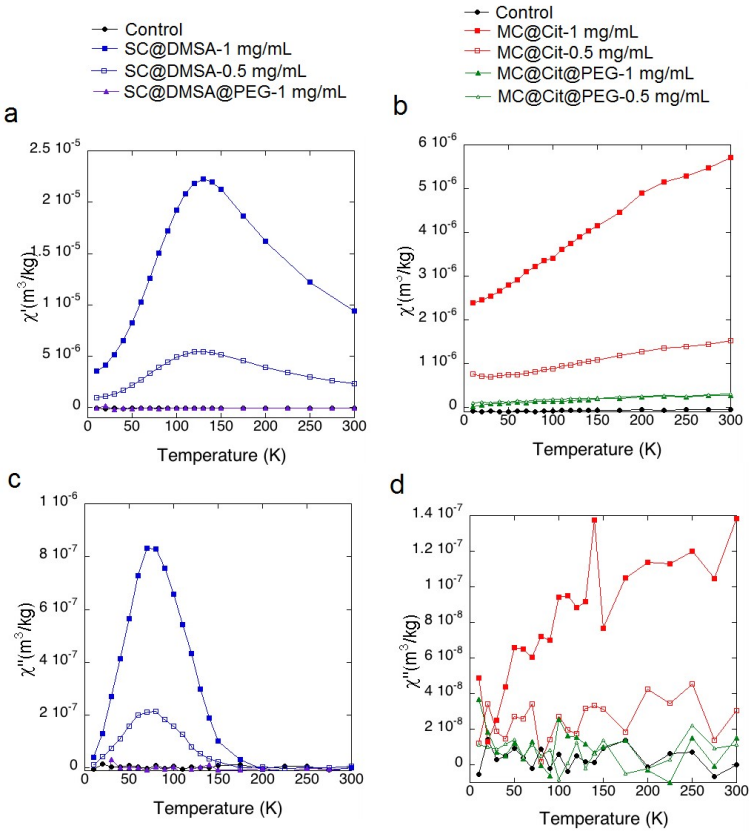

Figure 14: Caracterización del tejido mediante susceptibilidad magnética AC. Las componentes de susceptibilidad en fase (χ'(T)) y fuera de fase (χ''(T)) por masa de muestra, correspondientes a los tejidos liofilizados de los diferentes renacuajos (a,c) renacuajos expuestos a las muestras SC y (b, d) renacuajos expuestos a las muestras MC (n=7 por grupo).

el organismo y por eso el contenido de hierro en estas muestras es tan bajo. La funcionalización con PEG reduce la carga neta de la superficie de las partículs y este efecto podría reducir su absorción en el intestino, favoreciendo su excreción.

Dado que se predice que el hierro que resulta de la degradación de las nanopartículas se procese en las diferentes rutas metabólicas del hierro, a continuación, en el capítulo 5, se estudia la expresión de diferentes genes involucrados en la metabolización de hierro y el estrés oxidativo mediante PCR cuantitativa en tiempo real (RT-qPCR). Se detectaron incrementos en la ferritina, principal proteina de almacenamiento de hierro; dmt1, proteina a cargo de transportar cationes divalentes; y la hepcidina, que es la hormona reguladora central del metabolismo del hierro. Además, aumentaron los niveles de transferrina, proteína transportadora específica del hierro en el plasma.

Sin embargo, en el caso de los renacuajos tratados con MC@Cit no parece que haya un incremento en los niveles de dmt1 y transferrina. De estos resultados, se pueden describir diferencias en la velocidad del metabolización de nanopartículas SC o MC.

El incremento de los niveles de Fe^{2+} en los embriones 72 h después del tratamiento, activa la respuesta del hierro en su organismo, y se activa la traducción de proteínas involucradas en el metabolismo de hierro, como la ferritina. Por primera vez, hemos observado la activación in-vivo, a través de Hmox-1, de las proteinas reguladoras de hierro y su efecto en la transcripción de ferritina mRNA, asociada al tratamiento con las IOMNPs.

El resto de genes estudiados (superóxido dismutasa, sod; catalasa y la glutatión reductasa, gsr) mostraron un incremento en la expresión de las encimas involucradas en la atenuación del estrés oxidativo, en el caso de los renacuajos tratados con SC@DMSA y en menor medida en MC@Cit. Estos resultados sugieren que la activación de mecanismos protectores dependen de la absorción de las nanopartículas, pero en ningún caso estamos presenciando un caso agudo de estrés oxidativo cuando una disminución general de encimas antioxidantes tiene lugar.[67]

Conclusiones

Las conclusiones de esta tesis son:

- Mediante la síntesis de nanopartículas antiferromagnéticas, su recubrimiento con sílice y reducción a magnetita se han producido una librería de nanopartículas magnéticas de óxidos de hierro en un rango de tamaño de entre 50-100 nm (en su eje menor) y tres formas diferentes se ha demostrado poder obtener: romboedros, nanopartículas alargadas y discos hexagonales. Se ha obtenido una única fase de magnetita (verificado a través de las técnicas de difracción de rayos X, espectroscopía Mössbauer y curvas de magnetizaciíon ZFC/FC) y debido a la formación de poros y defectos en la estructura cristalina, inherentes a la transformación de fase, algunas muestras presentan una transición de Verwey a temperaturas ligeramente mas bajas o curvas de histéresis con forma de "avispa" y campos coercitivos bajos a temperatura ambiente.

- Se han podido sintetizar ensamblados de nanocristales de maghemita con diferente estructura mediante 4 estrategias. Las diferencias estructurales entre los ensamblados están diractamente relacionadas con el mecanismo de formación (aglomeración y fusión, aglomeración y recristalización o maduración de Ostwald), energía libre involucrada en el prceso de síntesis y condiciones experimentales (pH, carga superficial, temperatura, presión y tiempo). Mediante caracterización estructural y magnética se han descrito y modelado estas estructuras en forma de flor y se ha encontrado que los parámetros claves que llevan a propiedades magnéticas colectivas son: el contacto entre los núcleos dentro de una partícula y la continuidad de la orientación cristalina, lo cual favorece el orden magnético entre las interfases. Esto se refleja en unos efectos de relajación menos menos pronunciados (detectado mediante espectroscopía de Mössbauer) y una susceptibilidad inicial, χ_0, en la curva de magnatización. Las medidas de susceptibilidad magnética AC han permitido modelar el tamaño de partícula en solución de las nanoflores.

- En la síntesis de los polioles, la adición del acetato sódico es un parámetro clave que define el auto-ensamblado. En esta reacción, tiene un papel doble: la formación de las partículas y la nucleación y crecimiento. A concentraciones altas de acetato sódico se obtienen nanopartículas mono-núcleo. Al disminuir la concentración de acetato sódico, las subunidades nanocristalinas iniciales parecen crecer por agregación parcial, formando esferas huecas. Al seguir disminuyendo la concentración, los núcleos nanocristalinos iniciales están fuertemente agregados, produciendo las nanoflores finales. Para la síntesis de nanoflores, en los estadios iniciales de la reacción aparece Lepidocrocita, la cual sufre una dehidroxilación rápidamente, transformandose en una fase no descrita - posiblemente Lepidocrocita deshidroxilada - la cual evoluciona a nanoflores de maghemita. Este mecanismo de formación ha sido seguido mediante susceptibilidad magnética AC. Un tiempo de calentamiento prolongado, lleva a un tamaño creciente de núcleo. Como consecuencia, las muestras tienen una creciente magnetización de saturación,

coercitividad and exhiben crecientes valores de ILP.

- Se han estudiado la toxicidad in-vitro (en 2 líneas celulares) e in-vivo (en un modelo X. Laevis) en un sistema de nanopartículas MC (esferas huecas) y nanopartículas SC sintetizadas mediante descomposición térmica, recubiertas con diferentes moléculas y polímeros biocompatibles. La viabilidad de ambas lineas célulares se mantiene en todos los sujetos tratados con nanopartículas hasta una concentración de 1000 μM. En el caso de la viabilidad in-vivo, nigún sistema (mono-núcleo o multi-núcleo), independientemente del recubrimiento, era letal para embriones. Sin embargo, a altas concentraciones de hierro los embriones muestran defectos en la forma corporal, especialmente en el intestino, zona de flexión de la cola y retraso en el desarrollo del embrión. Las nanopartículas mono-núcleo son absorbidas de forma masiva en comparación con las multi-núcleo, y cuando la carga superficial de las nanopartículas es muy baja, como en el caso de las muestras pegiladas, no se observa una acumulación. Esto ha sido posible estudiarlo gracias a la susceptibilidad magnética AC. La degradación de las nanopartículas in-vitro e in-vivo y su biodisponibilidad para las células se traduce en un incremento de los niveles de ferritina, de acuerdo con una activación de las rutas metabólicas de hierro. Las observaciones de nano-biodegradación in-vitro e in-vivo están de acuerdo.

Contribuciones fundamentales de esta tesis

Esta Tesis presenta avances significativos en síntesis y ensamblado de nanopartículas, obteniendo diferentes nanoestructuras magnéticas con el potencial de ser utilizadas para aplicaciones biomédicas. Se ha modulado la forma y el ensamblado de los núcleos y se ha analizado como esto afecta a las propiedades magnéticas. La posibilidad de generar una estructura discontinua dentro de una nanopartícula mono-núcleo (Capítulo 2) podría ser una estrategia interesante para desarrollar nuevos materiales con propiedades magnéticas predefinidas. Además, la posibilidad de inducir interacciones magnéticas de canje a través del auto-ensamblaje y la aproximación de los núcleos magnéticos (Capítulo 3) lleva a estructuras multi-núcleo con propiedades colectivas y mejores propiedades de calentamiento para hipertermia magnética (Capítulo 4).

Como resultado, esta tesis proporciona una caracterización completa y detallada de las estructuras presentadas. Por lo tanto, este trabajo abre nuevas estrategias de síntesis controlada con tamaño y forma bien definida y propiedades magnéticas colectivas interesantes. Por lo tanto, las muestras que se presentan podrían servir como muestras de referencia de SC y MC y contribuirán como base para hacer comparaciones fiables de este tipo de materiales en el futuro.

Por último, se ha implementado el uso de la técnica de susceptibilidad magnética AC, haciendo uso de ella a lo largo de toda la Tesis con el fin de: i) modelar un parámetro estructural, el tamaño hidrodinámico (Capítulo 3), ii) seguir el mecanismo de formación de nanopartículas magnéticas (Capítulo 4)

y iii) seguir la acumulación y degradación de nanopartículas magnéticas in-vivo en matrices biológicas complejas).

Bibliography

[1] Pankhurst, Q. A., Connolly, J., Jones, S. & Dobson, J. Applications of magnetic nanoparticles in biomedicine. *Journal of physics D: Applied physics* **36**, R167 (2003).

[2] Cowburn, R. Property variation with shape in magnetic nanoelements. *Journal of Physics D: Applied Physics* **33**, R1 (2000).

[3] Mørup, S., Hansen, M. F. & Frandsen, C. Magnetic interactions between nanoparticles. *Beilstein journal of nanotechnology* **1**, 182 (2010).

[4] Grubbs, R. B. Nanoparticle assembly: solvent-tuned structures. *Nature materials* **6**, 553–555 (2007).

[5] Thanh, N. T., Maclean, N. & Mahiddine, S. Mechanisms of nucleation and growth of nanoparticles in solution. *Chemical reviews* **114**, 7610–7630 (2014).

[6] LaMer, V. K. & Dinegar, R. H. Theory, production and mechanism of formation of monodispersed hydrosols. *Journal of the American Chemical Society* **72**, 4847–4854 (1950).

[7] Mer, V. K. L. Nucleation in phase transitions. *Industrial & Engineering Chemistry* **44**, 1270–1277 (1952).

[8] De Yoreo, J. J. *et al.* Crystallization by particle attachment in synthetic, biogenic, and geologic environments. *Science* **349**, aaa6760 (2015).

[9] Laurent, S. *et al.* Magnetic iron oxide nanoparticles: synthesis, stabilization, vectorization, physicochemical characterizations, and biological applications. *Chemical reviews* **108**, 2064–2110 (2008).

[10] Van der Zee, J. Heating the patient: a promising approach? *Annals of oncology* **13**, 1173–1184 (2002).

[11] Hilger, I. & Kaiser, W. Iron oxide-based nanostructures for mri and magnetic hyperthermia. *Nanomedicine* **7**, 1443–1459 (2012).

[12] Dutz, S. & Hergt, R. Magnetic particle hyperthermia - a promising tumour therapy? *Nanotechnology* **25** (2014).

[13] Serantes, D. *et al.* Multiplying magnetic hyperthermia response by nanoparticle assembling. *Journal of Physical Chemistry C* **118**, 5927–5934 (2014).

[14] Guan, N., Wang, Y., Sun, D. & Xu, J. A simple one-pot synthesis of single-crystalline magnetite hollow spheres from a single iron precursor. *Nanotechnology* **20** (2009).

[15] Jia, B. & Gao, L. Morphological transformation of fe3o4 spherical aggregates from solid to hollow and their self-assembly under an external magnetic field. *Journal of Physical Chemistry C* **112**, 666–671 (2008).

[16] Rebolledo, A., Bomatí-Miguel, O., Marco, J. & Tartaj, P. A facile synthetic route for the preparation of superparamagnetic iron oxide nanorods and nanorices with tunable surface functionality. *Advanced Materials* **20**, 1760–1765 (2008).

[17] Cornell, R. & Schwertmann, U. *The Iron Oxides: Structure, Properties, Reactions, Occurrence and Uses* (1996).

[18] Graf, C., Vossen, D., Imhof, A. & Van Blaaderen, A. A general method to coat colloidal particles with silica. *Langmuir* **19**, 6693–6700 (2003).

[19] Stöber, W., Fink, A. & Bohn, E. Controlled growth of monodisperse silica spheres in the micron size range. *Journal of Colloid And Interface Science* **26**, 62–69 (1968).

[20] Morales, M., Pecharroman, C., Carreñ, T. & Serna, C. Structural characteristics of uniform γ-fe2o3 particles with different axial (length/width) ratios. *Journal of Solid State Chemistry* **108**, 158–163 (1994).

[21] Baker, A. *et al.* A structural study of haematite samples prepared from sulfated goethite precursors: The generation of axial mesoporous voids. *Journal of Materials Chemistry* **10**, 761–766 (2000).

[22] Morales, J., Tirado, J. & Macias, M. Changes in crystallite size and microstrains of hematite derived from the thermal decomposition of synthetic akaganeite. *Journal of Solid State Chemistry* **53**, 303–312 (1984).

[23] Roberts, A., Cui, Y. & Verosub, K. Wasp-waisted hysteresis loops: mineral magnetic characteristics and discrimination of components in mixed magnetic systems. *Journal of Geophysical Research* **100**, 17,909–17,924 (1995).

[24] Hillebrands, B. & Ounadjela, K. *Spin Dynamics in Confined Magnetic Structures* (2002).

[25] Goya, G., Berquó, T., Fonseca, F. & Morales, M. Static and dynamic magnetic properties of spherical magnetite nanoparticles. *Journal of Applied Physics* **94**, 3520–3528 (2003).

[26] Xing, P. & Zhao, Y. Multifunctional nanoparticles self-assembled from small organic building blocks for biomedicine. *Advanced Materials* (2016).

[27] Pan, S., He, L., Peng, J., Qiu, F. & Lin, Z. Chemical-bonding-directed hierarchical assembly of nanoribbon-shaped nanocomposites of gold nanorods and poly (3-hexylthiophene). *Angewandte Chemie* (2016).

[28] Volkmann, M., Meyns, M., Lesyuk, R., Lehmann, H. & Klinke, C. Attachment of colloidal nanoparticles to boron nitride nanotubes. *Chemistry of Materials* (2016).

[29] Stolarczyk, J. K., Deak, A. & Brougham, D. F. Nanoparticle clusters: Assembly and control over internal order, current capabilities, and future potential. *Advanced Materials* (2016).

[30] Ocaña, M., Rodriguez-Clemente, R. & Serna, C. J. Uniform colloidal particles in solution: Formation mechanisms. *Advanced Materials* **7**, 212–216 (1995).

[31] Raju, M., Van Duin, A. C. & Fichthorn, K. A. Mechanisms of oriented attachment of tio2 nanocrystals in vacuum and humid environments: reactive molecular dynamics. *Nano letters* **14**, 1836–1842 (2014).

[32] Frandsen, C. *et al.* Aggregation-induced growth and transformation of β-feooh nanorods to micron-sized α-fe2o3 spindles. *CrystEngComm* **16**, 1451–1458 (2014).

[33] Bannwarth, M. B. *et al.* Well-defined nanofibers with tunable morphology from spherical colloidal building blocks. *Angewandte Chemie International Edition* **52**, 10107–10111 (2013).

[34] Ingham, B. *et al.* How nanoparticles coalesce: an in situ study of au nanoparticle aggregation and grain growth. *Chemistry of Materials* **23**, 3312–3317 (2011).

[35] Dutz, S. Are magnetic multicore nanoparticles promising candidates for biomedical applications? *IEEE Transactions on Magnetics* **52**, 1–3 (2016).

[36] Serantes, D. *et al.* Multiplying magnetic hyperthermia response by nanoparticle assembling. *The Journal of Physical Chemistry C* **118**, 5927–5934 (2014).

[37] Jeong, U., Teng, X., Wang, Y., Yang, H. & Xia, Y. Superparamagnetic colloids: controlled synthesis and niche applications. *Advanced Materials* **19**, 33–60 (2007).

[38] Gutierrez, L. *et al.* Synthesis methods to prepare single-and multi-core iron oxide nanoparticles for biomedical applications. *Dalton Transactions* **44**, 2943–2952 (2015).

[39] Gijs, M. A., Lacharme, F. & Lehmann, U. Microfluidic applications of magnetic particles for biological analysis and catalysis. *Chemical reviews* **110**, 1518–1563 (2009).

[40] Nowak, J., Wiekhorst, F., Trahms, L. & Odenbach, S. The influence of hydrodynamic diameter and core composition on the magnetoviscous effect of biocompatible ferrofluids. *Journal of Physics: Condensed Matter* **26**, 176004 (2014). URL `http://stacks.iop.org/0953-8984/26/i=17/a=176004`.

[41] Grüttner, C., Müller, K., Teller, J. & Westphal, F. Synthesis and functionalisation of magnetic nanoparticles for hyperthermia applications. *International Journal of Hyperthermia* **29**, 777–789 (2013).

[42] Dutz, S., Kettering, M., Hilger, I., Müller, R. & Zeisberger, M. Magnetic multicore nanoparticles for hyperthermia—influence of particle immobilization in tumour tissue on magnetic properties. *Nanotechnology* **22**, 265102 (2011).

[43] Hugounenq, P. *et al.* Iron oxide monocrystalline nanoflowers for highly efficient magnetic hyperthermia. *The Journal of Physical Chemistry C* **116**, 15702–15712 (2012).

[44] Alexiou, C. *et al.* Locoregional cancer treatment with magnetic drug targeting. *Cancer research* **60**, 6641–6648 (2000).

[45] Bigall, N. C. *et al.* Colloidal ordered assemblies in a polymer shell: A novel type of magnetic nanobeads for theranostic applications. *Chemistry of Materials* **25**, 1055–1062 (2013).

[46] Zoppellaro, G. *et al.* Theranostics of epitaxially condensed colloidal nanocrystal clusters, through a soft biomineralization route. *Chemistry of Materials* **26**, 2062–2074 (2014).

[47] Mazuel, F. *et al.* Magneto-thermal metrics can mirror the long-term intracellular fate of magnetoplasmonic nanohybrids and reveal the remarkable shielding effect of gold. *Advanced Functional Materials* (2017).

[48] Ludwig, F. *et al.* Magnetic, structural, and particle size analysis of single-and multi-core magnetic nanoparticles. *IEEE Transactions on Magnetics* **50**, 1–4 (2014).

[49] Ge, J., Hu, Y., Biasini, M., Beyermann, W. P. & Yin, Y. Superparamagnetic magnetite colloidal nanocrystal clusters. *Angewandte Chemie International Edition* **46**, 4342–4345 (2007).

[50] Cheng, C., Xu, F. & Gu, H. Facile synthesis and morphology evolution of magnetic iron oxide nanoparticles in different polyol processes. *New Journal of Chemistry* **35**, 1072–1079 (2011).

[51] Caruntu, D. *et al.* Synthesis of variable-sized nanocrystals of fe3o4 with high surface reactivity. *Chemistry of materials* **16**, 5527–5534 (2004).

[52] Kim, B. H. *et al.* Large-scale synthesis of uniform and extremely small-sized iron oxide nanoparticles for high-resolution t 1 magnetic resonance imaging contrast agents. *Journal of the American Chemical Society* **133**, 12624–12631 (2011).

[53] Lartigue, L. *et al.* Cooperative organization in iron oxide multi-core nanoparticles potentiates their efficiency as heating mediators and mri contrast agents. *ACS Nano* **6**, 10935–10949 (2012).

[54] Gavilán, H. *et al.* Colloidal flower-shaped iron oxide nanoparticles: Synthesis strategies and coatings. *Particle & Particle Systems Characterization* (2017).

[55] Gavilán, H. *et al.* How shape and internal structure affect the magnetic properties of anisometric magnetite nanoparticles. *Acta Materialia* **125**, 416–424 (2017).

[56] Crichton, R. R. & Boelaert, J. R. *Inorganic biochemistry of iron metabolism: from molecular mechanisms to clinical consequences* (John Wiley & Sons, 2001).

[57] Balakumaran, A. *et al.* Superparamagnetic iron oxide nanoparticles labeling of bone marrow stromal (mesenchymal) cells does not affect their “stemness”. *PloS one* **5**, e11462 (2010).

[58] Geppert, M., Hohnholt, M. C., Nürnberger, S. & Dringen, R. Ferritin up-regulation and transient ros production in cultured brain astrocytes after loading with iron oxide nanoparticles. *Acta biomaterialia* **8**, 3832–3839 (2012).

[59] Hohnholt, M. C., Geppert, M. & Dringen, R. Treatment with iron oxide nanoparticles induces ferritin synthesis but not oxidative stress in oligodendroglial cells. *Acta biomaterialia* **7**, 3946–3954 (2011).

[60] Gu, J. *et al.* The internalization pathway, metabolic fate and biological effect of superparamagnetic iron oxide nanoparticles in the macrophage-like raw264. 7 cell. *Science China Life Sciences* **54**, 793–805 (2011).

[61] Rojas, J. M. *et al.* Superparamagnetic iron oxide nanoparticle uptake alters m2 macrophage phenotype, iron metabolism, migration and invasion. *Nanomedicine: Nanotechnology, Biology and Medicine* **12**, 1127–1138 (2016).

[62] Mulens-Arias, V., Rojas, J. M., Pérez-Yagüe, S., Morales, M. P. & Barber, D. F. Polyethylenimine-coated spions trigger macrophage activation through tlr-4 signaling and ros production and modulate podosome dynamics. *Biomaterials* **52**, 494–506 (2015).

[63] Mazuel, F. *et al.* Massive intracellular biodegradation of iron oxide nanoparticles evidenced magnetically at single-endosome and tissue levels. *ACS nano* **10**, 7627–7638 (2016).

[64] Rojas, J. M. *et al.* Time-course assessment of the aggregation and metabolization of magnetic nanoparticles. *Acta Biomaterialia (In Press* (2017).

[65] Ruiz, A. *et al.* Biotransformation of magnetic nanoparticles as a function of coating in a rat model. *Nanoscale* **7**, 16321–16329 (2015).

[66] James-Zorn, C. *et al.* Xenbase: Core features, data acquisition, and data processing. *genesis* **53**, 486–497 (2015).

[67] Radu, M. *et al.* Exposure to iron oxide nanoparticles coated with phospholipid-based polymeric micelles induces biochemical and histopathological pulmonary changes in mice. *International journal of molecular sciences* **16**, 29417–29435 (2015).

Part I

List of Publications

Publications included in this Thesis:

1. Gavilán, H.; Posth, O.; Bogart, L. K.; Steinhoff, U.; Gutiérrez, L.; Morales, M. P. How shape and internal structure affect the magnetic properties of anisometric magnetite nanoparticles, Acta Materialia **2017**, 125, 416-424.

2. Gavilán, H.; Kowalski, A.; Heinke, D.; Sugunan, A.; Sommertune, J.; Varón, M.; Bogart, L. K.; Posth, O.; Zeng, L.; González-Alonso, D.; Balceris, C.; Fock, J.; Wetterskog, E.; Frandsen, C.; Gehrke, N.; Grüttner, C.; Fornara, A.; Ludwig, F.; Veintemillas-Verdaguer, S.; Johansson, C.; Morales, M. P. Colloidal Flower-shaped Iron Oxide Nanoparticles: Synthesis Strategies and Coatings, Part. Part. Syst. Charact. **2017**, 1700094.

3. Gavilán, H.; Sánchez, E. H.; Brollo, M. E.; Asín, L.; Moerner, Katrine K.; Frandsen, C.; Lázaro, Francisco J.; Serna, C. J.; Veintemillas-Verdaguer, S.; Morales, M. P.; Gutiérrez, L. Formation mechanism of maghemite nanoflowers synthesized by polyol mediated process, **2017** (Submitted).

4. Marín-Barba, M.*; Gavilán, H.*; Gutiérrez, L.; Lozano-Velasco, E.; Rodríguez, I.; Wheeler, G.; Morris, C.; Morales, M. P.; Ruiz, A. Unravelling the mechanisms that determine absorption and metabolization of magnetic single and multi-core nanoparticles in-vitro and in a Xenopus laevis model, **2017** (Submitted).

5. Gavilán, H.; Brollo, M. E.; Gutiérrez, L.; Veintemillas-Verdaguer, S.; Morales, M. P. Controlling the size and the shape of uniform magnetic iron oxide nanoparticles for biomedical applications. Ed. N. T .K. Thanh, CRC Press, Taylor and Francis, Boca Raton London New York. **2017** (Accepted).

(*)These authors contributed equally to this work.

Other related Publications:

1. Vita, F,; Gavilán, H.; Rossi, F.; Fernández, J. C.; Secchi, A.; Arduini, A.; Albertini, F.; Morales, M. P. Tuning Morphology and Magnetism of Magnetite Nanoparticles by Calix[8]arene-Induced Oriented Aggregation, CrystEngComm **2016**, 18, 8591-8598.

2. Frank, L.; Balceris, C.; Viereck, T.; Posth, O.; Steinhoff, U.; Gavilán, H.; Costo, R.; Morales, M. P.; Zeng, L.; Olsson, E.; Johansson, C.; Johansson, C. Size analysis of single-core magnetic nanoparticles, J. Magn. Magn. Mater **2017**, 427, 19–24.

3. Bender, P.; Balceris, C.; Ludwig, F.; Posth, O.; Borgart, L. K.; Szezerba, W.; Castro, A.; Nilsson, L.; Costo, R.; Gavilán, H.; González-Alonso, D.; de Pedro, I. L.; Fernández-Barquín, L.; Johansson, C. Distribution functions of magnetic nanoparticles determined by a numerical inversion method, New Journal of Physics **2017** (Accepted).

4. Rojas, J. M.; Gavilán, H.; Del Dedo, V.; Lorente-Sorolla, E.; Sanz-Ortega, L.; Da Silva, G.; Costo, R.; Perez-Yagüe, S.; Talelli, M.; Marciello, M.; Morales, M. P.; Barber, D. F.; Gutiérrez, L. Time-course assessment of the aggregation and metabolization of magnetic nanoparticles, Acta Biomaterialia **2017** (In Press).

5. Serantes, D.; Chantrell, R. W.; Gavilán, H.; Morales, M. P.; Chubykalo-Fesenko, O.; Baldomir, D.; Satoh, A. Anisotropic magnetic nanoparticles for biomedicine: bridging frequency separated AC-field controlled domains of actuation, **2017** (Submitted).

Part J

Copy of Publications

Acta Materialia 125 (2017) 416–424

Contents lists available at ScienceDirect

Acta Materialia

journal homepage: www.elsevier.com/locate/actamat

Full length article

How shape and internal structure affect the magnetic properties of anisometric magnetite nanoparticles

Helena Gavilán [a, *], Oliver Posth [b], Lara K. Bogart [c], Uwe Steinhoff [b], Lucía Gutiérrez [a, d, **], M. Puerto Morales [a]

[a] Instituto de Ciencia de Materiales de Madrid, ICMM/CSIC, Cantoblanco, 28049 Madrid, Spain
[b] Physikalisch-Technische Bundesanstalt, 10587 Berlin, Germany
[c] UCL Healthcare Biomagnetics Laboratory, University College London, 21 Albemarle Street, London W1S 4BS, UK
[d] Dept. Química Analítica, Instituto de Nanociencia de Aragón, Universidad de Zaragoza, 50018 Zaragoza, Spain

ARTICLE INFO

Article history:
Received 27 September 2016
Received in revised form
9 December 2016
Accepted 11 December 2016

Keywords:
Nanoparticles
Magnetic properties
Size effects
Shape dependence
Structure properties relationship

ABSTRACT

A three-step aqueous approach to obtain large (>50 nm) magnetite single-core particles has been developed. The steps are a) synthesis of antiferromagnetic nanoparticles, b) particle coating and c) subsequent reduction of the core material to magnetite. By variation of precursor material and process conditions, the synthesis yielded rhombohedra, discs or needles below 200 nm. A combination of X-ray diffraction, ^{57}Fe Mössbauer spectroscopy and infrared spectroscopy confirmed magnetite to be the dominant final core material. From transmission electron microscopy, we identified porous structures after the reduction. Magnetic characterization of the different magnetic nanopaticles revealed strikingly different magnetic behaviour depending on their shape, internal structure and reduction process. We conclude that each of these parameters have to be considered in further characterization of large magnetite nanoparticles.

1. Introduction

In the last years, iron oxide magnetic nanoparticles (MNPs) have been widely used for biomedical applications. Examples of these applications include new ways of cancer treatment such as magnetic drug targeting [1] and magnetic hyperthermia [2], or the use of MNPs as contrast agents or tracers in Magnetic Resonance Imaging [3] and Magnetic Particle Imaging [4]. Each application requires MNPs with customized structural and magnetic properties, which are strongly dependent upon both particle size and shape [5]. As an example, ultra-small superparamagnetic MNPs with magnetic core sizes below 10 nm were suitable for the exploration of tumour permeability [6]. However, the uptake of MNPs by macrophages was most effective for MNPs with a core size of 10–30 nm, while for magnetic hyperthermia, maximum heating rate is obtained at the transition from multidomain to single domain magnetic behaviour occurring in a relatively broad size range at about 30 nm with a change of magnetic energy into thermal energy (Néel or Brown) [7]. Moreover, if collective magnetic behaviour of the cores exists, originated from interactions within a nanoparticle, heating rates can go up to one order of magnitude higher than for single-domain nanoparticles [8,9].

Nanoparticle shape can also have significant impact on the magnetic behaviour of MNPs in applications. Firstly, the magnetic shape anisotropy of the MNPs can assume much larger values than the magnetocrystalline anisotropy and thus can strongly affect the orientation of magnetic moments inside the particles. In addition, dipolar interactions between MNPs also depend on the particle shape and will influence the structural agglomerate formation leading to, for example, chain-like arrangements biomimicking magnetotactic bacteria [10] or hollow spheres consisting of oriented aggregates of nanocrystals [11,12].

One of the current challenges in nanoparticle research is the production of particles [13] comprising a large magnetite core that is well-controlled in size and shape, with a large magnetic moment and long term colloidal stability. Over the past decades, direct syntheses of magnetite NPs with different sizes and morphologies have been reported, including nano- spheres [13], cubes [14,15], wires [16], rods [17], octahedral [18], plates [19] and prisms [20].

* Corresponding author.
** Corresponding author. Instituto de Ciencia de Materiales de Madrid, ICMM/CSIC, Sor Juana Inés de la Cruz 3, Cantoblanco, 28049 Madrid, Spain.
E-mail address: helena_gr@icmm.csic.es (H. Gavilán).

http://dx.doi.org/10.1016/j.actamat.2016.12.016
1359-6454/

Synthesis of each of these shapes was performed out in organic media, so that, in general, nanocrystal shape control was achieved by selective adhesion of surfactant to a particular crystal facet and this subsequent slow growth along this direction. Without surfactants, nanoparticles can aggregate into dense or hollow micrometre spheres [11,12]. Synthesis in organic media is limited by the small particle batches that require further steps to be transferred to water, which results in low yields.

In the present paper, we describe an alternative aqueous-based approach to produce single-core magnetite MNPs with different morphologies and core sizes above 25 nm, which could be scalable for large production. Magnetic iron oxide nanorods were already produced by a similar method and showed interesting magnetic properties and tuneable surface functionality [21]. We propose a three-step process (Fig. 1) from which uniform rhombohedra, discs and elongated MNPs can easily be obtained. First, an aqueous synthesis route is followed to obtain uniform antiferromagnetic precursors such as goethite or hematite, whose size and shape can be tuned by changing the synthesis conditions including temperature, pressure, and nature and concentration of the salts used [22]. Then, the antiferromagnetic precursor particles are coated by a silica layer that prevents their aggregation [23,24]. Finally, the silica coated antiferromagnetic particles are reduced to magnetite. This is either performed on particles in powder form (dry-reduction), by exposing them to a hydrogen atmosphere at a certain partial pressure [25], or in liquid form, using oleic acid and an organic solvent (wet-reduction). In each process, the hydrogen and oleic acid act as the reducing agents [26,27]. Transformation of these antiferromagnetic phases into magnetite particles requires the full control of key parameters including temperature, atmosphere and pressure to produce pure single phases and avoid core sintering.

The products are physicochemically characterized by electron microscopy, X-ray diffraction, ^{57}Fe Mössbauer spectroscopy and infrared spectroscopy. Their magnetic behaviour is analysed by field and temperature dependent magnetization measurements. This characterization allows for comparing the products of dry reduction and wet reduction.

2. Experimental

2.1. Synthesis of the precursors

The preparation of uniform and nanometer precursor particles requires slight modifications of reported synthetic routes for hematite [26] and goethite [28] to obtain particle sizes below 200 nm and keep the uniformity.

(i) **Hematite:** The synthesis of hematite (α-Fe_2O_3) nano-sized rhombohedra and discs was carried out in a glass bottle dissolving $FeCl_3 \cdot 6H_2O$ in 50 mL of pure ethanol and 10 mL or 1 mL of water for rhombohedra or discs respectively under vigorous magnetic stirring. Then sodium acetate was added while magnetically stirring and the solution was homogenized by sonication for 10 min. The final solution had a concentration of $FeCl_3$ of 0.082 and 0.096 M for rhombohedra and discs, respectively. The concentration of sodium acetate was 0.49 and 0.58 M for rhombohedra and discs, respectively. The mixtures were sealed in a teflon-lined autoclave (125 mL) and maintained at 180 °C for 12 h for solvothermal crystallization. After natural cooling to ambient temperature, the resulting red solid product was washed with distilled water, filtered and finally dried overnight in an oven at 50 °C.

(ii) **Goethite:** The synthesis of goethite (α-FeOOH) nano-sized needles was performed by precipitation of a Fe(II) sulfate 0.15 M aqueous solution by the addition of a 0.225 M solution of sodium carbonate. The resulting dispersion was then oxidized at constant temperature. The concentration ratio of the reagents $[CO_3^{=}]/[Fe(II)]$ is 1.5. These processes were carried out according to the following procedure. Oxygen was first removed from the distilled water by N_2 bubbling to prevent Fe(II) oxidation during the dissolution of $FeSO_4$. The Fe(II) and sodium carbonate solutions 125 mL, each) were prepared with the desired concentrations. The sodium carbonate solution was then introduced into a thermostatic water bath at 44 °C under moderate stirring and the Fe(II) solution was added applying a constant air flow with a rate of 2 $Lmin^{-1}$ through the resulting suspension. Particles of goethite are then formed by aerial oxidation. After 180 min of reaction, the resulting precipitate was cooled, centrifuged and washed several times with distilled water. Finally, the powdered solid was collected by filtration and dried overnight at 50 °C.

2.2. Coating and reduction to magnetite

Silica coating and subsequent reduction of the precursor particles were carried out by optimizing procedures described elsewhere [25–27]. Silica coating ensures both, steric and electrostatic protection and it acts as dispersing agent of many electrostatic colloids. These advantages render silica an ideal, low-cost material to tailor surface properties. Additionally, this coating should endow the cores with several beneficial properties, such as the biocompatibility and the possibility of subsequent functionalization by connecting the silanol groups on the surface with other organic molecular agents [29].

For the silica coating, 100 mg of the precursor particles in powder form were dispersed in a 2-propanol/H_2O 2:1 v/v solution of 300 mL, NH_4OH 28% v/v and tetraethyl orthosilicate (TEOS) were added during sonication and the reaction was allowed to continue for 15 min. The final volume was 320.2 mL and the final concentration of the reagents was: $[NH_4OH] = 4.5 \times 10^{-4}$ M,

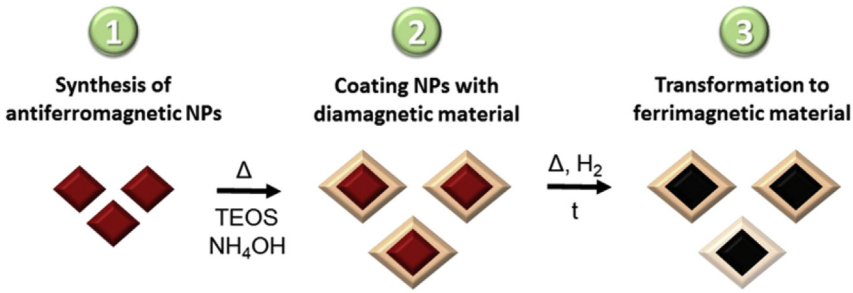

Fig. 1. General scheme for the synthesis of single-core MNPs.

[TEOS] = 2.8 × 10^{-6} M. The product was washed twice with 2-propanol. The solution was filtered and dried overnight at 50 °C.

(i) **Wet reduction:** For the reduction to magnetite in liquid, 50 mg of the silica coated precursor nanoparticles and 35 mL of trioctylamine were mixed by sonication for 30 min and subsequently 2.2 mL oleic acid were added. The mixture was transferred into a three-necked flask and heated at 350 °C under H_2 flow of 0.486 $Lmin^{-1}$ for 1 h until the colour changed to dark. After cooling to ambient temperature, the black product was collected by centrifugation and washed 3 times with toluene. Finally, the product was dried overnight at 50 °C.

(ii) **Dry reduction:** For dry reduction, 50 mg of the silica coated precursor nanoparticles in powder form were treated at 360 °C for 2 h in vacuum to remove moisture. The reduction was performed under H_2 atmosphere with a partial gas pressure of 61 kPa for 3.5 h refreshing the H_2 atmosphere after 1 h. The sample was then cooled down to ambient temperature.

2.3. Nanoparticle characterization

The size of the iron oxide cores in both the precursors and the final products was determined by transmission electron microscopy (TEM) with a JEM1010 microscope (JEOL, Peabody, USA) operating at 100 kV. TEM samples were prepared by placing a drop of the particles suspended in water onto a carbon coated copper grid and allowing it to dry at room temperature. The size distribution was determined by manual measurement of more than 100 particles using the public domain ImageJ software (http://imagej.nih.gov/). High-resolution TEM (HRTEM) was performed in a JEM-3100 F microscope (JEOL, Peabody, USA) operating at 300 kV. The particle morphology was determined from scanning electron microscopy (SEM) with a Philips XL30 microscope operating at 10 kV. The sample preparation is identical to the preparation for the TEM analysis.

The crystal structure of the antiferromagnetic precursors and the reduced particles was identified using a combination of X-ray diffraction (XRD), Fourier transform infra-red spectroscopy (FTIR) and room temperature ^{57}Fe Mossbauer spectroscopy. XRD was performed in a Bruker D8 Advance diffractometer with a graphite monochromator using CuK_α radiation (λ = 1.5406 Å). The patterns were collected within 10° and 70° in 2θ at a scan rate of 0.2 (2θ)/min. The core crystalline size was calculated via the Scherrer equation (XRD size) from the broadening (104) and (110) X-ray diffraction lines for the precursors, hematite and goethite, respectively and from (311) X-ray diffraction line for the resulting magnetite. FTIR was performed in a Bruker IFS 66V-S apparatus, in the range of 2000-250 cm^{-1}. The samples were prepared for FTIR by diluting the dried powder in KBr at 2% by weight and pressing it into a pellet.

Room temperature ^{57}Fe Mössbauer spectroscopy was used to determine the resulting iron oxide phase after reduction of the precursors. Approximately 50 mg of each sample was mixed with ca. 200 mg sucrose in a pestle and mortar to form a paste, and then flattened within a coin shaped absorber. Spectra were recorded at room temperature in transmission geometry using a ^{57}Co source in a Rh matrix, using a W302 spectrometer and W202 detector, both from SEECo (Minneapolis, USA).

For the magnetic characterization, the samples were measured in powder form after drying in an inox coated oven at 50 °C for 24 h. The powder was filled into polycarbonate capsules after accurately weighing. The sample mass was determined to be between 1 and 4 mg. Finally, the powder was immobilized in gelatin. The magnetization measurements have been performed in a Magnetic Property Measurement System (Quantum Design, USA) allowing the detection of the sample magnetic moment as a function of applied magnetic field and temperature.

In the field dependent measurements the magnetic field varied between -5 T and 5 T. The amplitude of consecutive field steps was changed logarithmically to ensure a sufficient number of measurements at low fields. The time between consecutive magnetization measurements was about 3 min to guarantee quasi-static conditions. Hysteresis loops were measured at 295 K and at 5 K. In the temperature dependent measurements the sample was first cooled down to 5 K in zero magnetic field (zero field cooling, ZFC). Then, a magnetic field of 5 mT was applied and the magnetic moment of the sample was measured with increasing temperature. After reaching 295 K, the magnetic moment was measured with decreasing temperature under the presence of the magnetic field of 5 mT (field cooling, FC).

Hysteresis loops were also measured in a vibrating sample magnetometer (MLVSM9, MagLab 9T, Oxford Instruments, UK) at room temperature and at 5 K after saturating the sample in a 5 T (−5 T) field and recording the complete magnetization curves at a field change rate of 0.3 T/min.

3. Results and discussion

3.1. Structural characterization of the precursors

A general scheme of the synthesis strategy followed in this work is presented in Fig. 1. After the synthesis of the precursors and before the particles were coated, their morphology has been investigated by SEM. The scanning electron micrographs of the precursors (Fig. 2) show the three different morphologies obtained: **(A)** rhombohedra, **(B)** hexagonal discs and **(C)** needles. Image S1 (Supporting Information) confirms the morphology of the rhombohedra, where the typical square bipyramids of this polyhedron are observed in any of the orthogonal orientations of the nanoparticle. Both the size and the shape of the nanoparticles are highly homogeneous.

3.2. Transformation of the precursors to magnetite

Fig. 3 shows TEM images of the precursor and the obtained MNPs where the core material has been transformed to magnetite by dry and wet reduction methods. The precursor has been successfully coated with a uniform silica shell around single cores or double-triple cores (~75%), although a fraction of multi-cores (5–10 cores coated) (~25%) cannot be discarded. TEOS condensation occurs only on the surface of the NPs and no colloidal silica nanoparticles have been observed.

The core size after reduction of the precursor was determined from the TEM images. The rhombohedra have an average core diameter of 67 nm, the discs are 140 nm in diameter and 22 nm thick, and finally the needles are 183 nm in length and 33 nm thick. All samples have a standard deviation lower than 20% (see Table 1). By comparing the images before and after reduction we see that the particle size and morphology are conserved which is due to the silica coating of approximately 10 nm. We also observe pores within the core structure after the reduction to magnetite, which is a consequence of the phase transformation from goethite in the case of the needles (Fig. 3 C), or hematite, in the case of the discs (Fig. 3B) and the rhombohedra (Fig. 3A).

When the silica coated goethite nanoparticles (either in powder or in solution) are heated up above 350 °C, dehydration firstly occurs forming directly hematite:

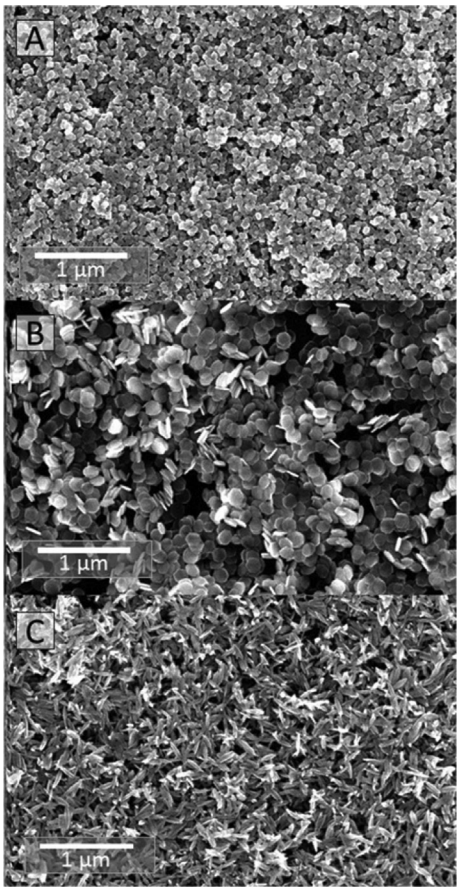

Fig. 2. SEM images of the precursors (A) rhombohedra, (B) discs and (C) needles.

$$2FeOOH \rightarrow Fe_2O_3 + H_2O$$

The conversion of goethite to hematite is facilitated by the common anion structure shared by these two compounds. Three unit cells of goethite form one unit cell of hematite leading to contraction of the volume by a fraction of 0.62 [30]. The nanoparticles develop porosities within the structure due to the expulsion of water [22], occurring along the central axis of the needles, often merging with a single, elongated defect running along the entire length of the crystallite [31]. Pores along the c-axis were also reported [32] in good agreement with our observations. High resolution TEM images of the needles after the dehydration show contrast differences. These might be explained by either discontinuities of the thickness along the nanoparticle (surface roughness) or by discontinuities in the density of the nanoparticle (internal cavities). In order to elucidate the structure of the needles, a combination of under, over and in-focus high resolution TEM images have been taken. In doing this we are able to observe a certain degree of surface roughness, but more interestingly a porous internal structure has been evidenced (Fig. 4). Despite such porosity, a continuous single-crystalline structure corresponding to a monocrystal has been demonstrated for the needles. After the dehydration, the nanoparticles are reduced to magnetite without interparticle sintering and this is because of both the silica shell and the mild temperatures used for reduction (below 600 °C).

TEM images obtained in this manner reveal the presence of pores for all particle morphologies, synthesised from both types of precursor. For hematite precursors, we observe pores in both the magnetite discs and rhombohedra that are randomly distributed within the structure (Fig. 3), as previously observed by Edwards et al. [33]. The reduction itself is associated with the formation of tunnels by the removal of oxygen. Magnetite is formed in the surrounding areas parallel to the tunnel generation, which yields an overall crystal structure of magnetite with such pores [34].

High-resolution TEM (HR-TEM) images of the needles and rhombohedra after both the wet and dry reduction are shown in Figs. S2–S4 (supporting information). For the rhombohedra, Fourier transformation of the HR-TEM image yields a diffraction pattern that corresponds to a monocrystal and demonstrates that even with such pores, each particle has a single crystal structure. It is particularly striking in the case of needles (Fig. S3, Supporting Information) after the dehydration and reduction process, that a continuous single-crystal structure corresponding to a monocrystal has been likewise demonstrated, despite the porosity along the c-axis. However, when lower reduction temperatures and shorter times were used, nanorods consisting of clusters of maghemite embedded in an aniferromagnetic hematite matrix were obtained [35].

3.3. Identification of iron oxide phase and measurement of core size

XRD patterns confirm that the precursor used to synthesize the rhombohedra and discs is indeed hematite, whilst the diffraction pattern of the precursor used to synthesize needles corresponds to goethite (Fig. 5). The X-ray diffractograms of nanoparticles produced via wet and dry reduction methods indicate a single iron oxide phase, which we attribute to the inverse spinel structure of either magnetite or maghemite. We have used the Scherrer equation on the most intense diffraction peak to calculate the average core crystalline size of each of the precursors; this corresponds to the (110) reflection for hematite and the (111) reflection for goethite. XRD patterns confirm that the cores of both the hematite rhombohedra and discs are single crystal structures and have similar average sizes, in good agreement with that measured *via* TEM. For the goethite needles, the core crystalline size obtained using the (111) reflection is closer to the smallest TEM dimension, and is in agreement with the goethite crystals being elongated along the (100) direction [22]. Table 1 shows core sizes determined by TEM and crystal sizes obtained by XRD measurements.

FTIR spectra of the hematite precursors (Fig. S5 in supporting information) show Fe-O bands at 355 cm^{-1} and 477 cm^{-1} which are attributed to the parallel and transverse vibrations (E_u), and bands at 575 cm^{-1} and 381 cm^{-1} attributed to the longitudinal vibration (A_{2u}). For the goethite precursor, a band at 409 cm^{-1} can be attributed to the Fe-O antisymmetric stretch parallel to the c-axis and bands at 628, 790, 886 cm^{-1} can be attributed to the Fe-O symmetric stretch parallel to the a-axis.

The transformation of the antiferromagnetic precursors to the magnetic phase was monitored using a combination of XRD - via the (311) reflection for the obtained magnetite nanoparticles - and FTIR. It should be mentioned that there are two main features contributing to the X-ray broadening, the crystal order and the particle shape, which makes such an analysis via XRD difficult.

The crystallite sizes obtained from the (311) reflection for the resulting magnetite needles, which is at 30° of the longest particle dimension, indicates a slightly increase with respect to the crystalline size calculated for the precursor, indicating a somewhat better crystal order after the reduction. By comparing XRD values for both reduction techniques, it seems that the dry reduction provides particles with a slightly larger crystallite size or less defects than the wet reduction.

Infra-red (IR) spectra measured after both wet and dry reduction, show bands that correspond to the silica coating of the nanoparticles and bands corresponding to magnetite, together with

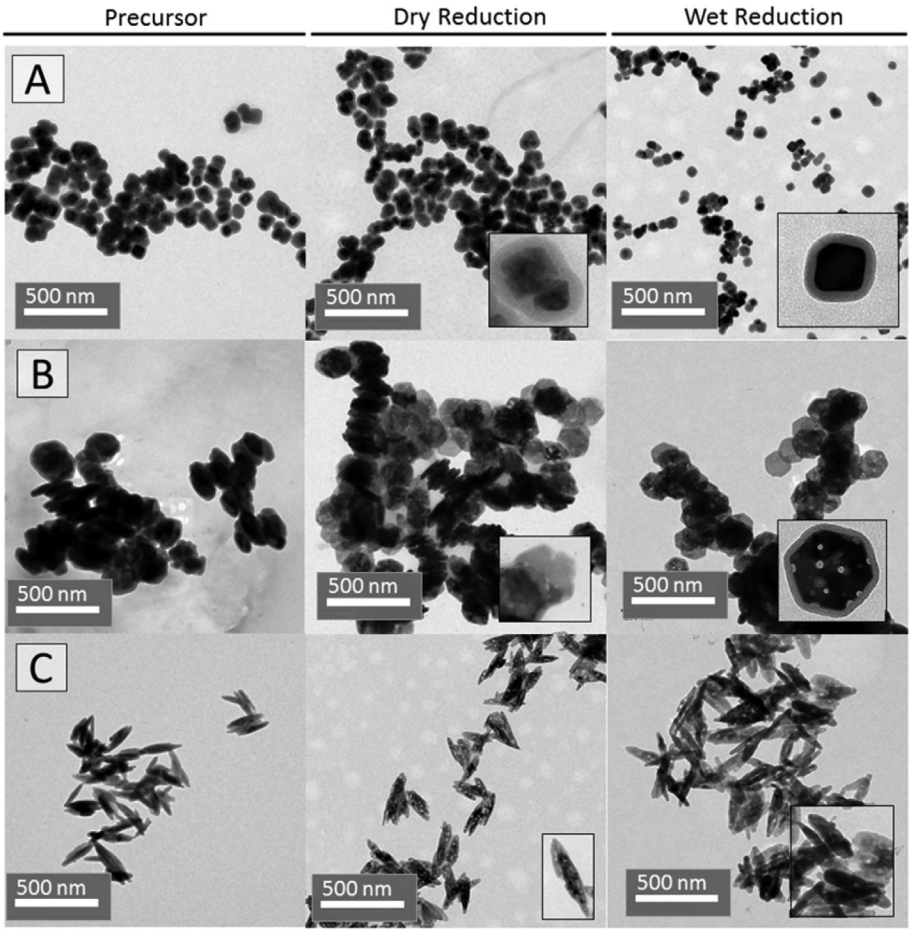

Fig. 3. TEM images of the precursors and the magnetic nanoparticles obtained by dry and wet reduction. (A) rhombohedra, (B) discs, (C) needles.

Table 1
TEM core size vs. X-ray crystallite size of the hematite/goethite precursor and the obtained MNPs by wet and dry reduction. P: Antiferromagnetic Precursor, Wet: Wet Reduction, Dry: Dry Reduction.

Sample	Antiferromagnetic precursors			After reduction		
	Iron Oxide	$\overline{D}_{TEM}$ (nm), σ (%)	$\overline{D}^{P}_{XRD}$ (nm)	Iron Oxide	$\overline{D}^{Wet}_{XRD}$ (nm)	$\overline{D}^{Dry}_{XRD}$ (nm)
Rhombohedra	α-Fe_2O_3	67 σ = 18	69	Fe_3O_4	47	48
Discs	α-Fe_2O_3	140 × 22 σ = 10,4	121	Fe_3O_4	34	42
Needles	α-FeO(OH)	183 × 33 σ = 18,7	17	Fe_3O_4	19	27

the band at 1632 cm^{-1} due to the stretching and bending vibration of H_2O molecules. The very strong and broad IR band at 1111 cm^{-1} with a shoulder at 1188 cm^{-1} is usually assigned to the transversal optical (TO) and longitudinal optical (LO) modes of the Si-O-Si asymmetric stretching vibrations, the band at 956 cm^{-1} is assigned to silanol groups and the one at 800 cm^{-1} is assigned to Si-O-Si symmetric stretching vibrations. Lastly, in the Fe-O range IR bands at 568 cm^{-1} and 357 cm^{-1} are attributable to magnetite [22], (Fig. S5). The presence of maghemite is not evident due to the absence of small shoulders around these two main bands in the low frequency range which are particularly sharp for the needles.

Room temperature Mössbauer spectra of rhombohedra and needles reduced via dry powder methods are shown in Fig. 6. For the rhombohedra, the spectrum is a sharp six-line pattern comprising two sub-spectra and is reminiscent of stoichiometric magnetite. The best fit spectra comprise a superposition of three Voigtian sextets, two of which have isomer shifts close to 0.26 mm/s and 0.67 mm/s, and associated hyperfine fields close to 49 T and 46 T, respectively, which are indicative of the tetra and octahedral sites within magnetite.

The third sub-component comprises less than 8% of the spectral area and is a broad sextet, with an isomer shift of 0.26 mm/s and is likely to come from Fe atoms around pore structures in the rhombohedra. We surmise that majority of the sample is well crystallised, stoichiometric magnetite.

Whilst we see that the Mössbauer spectrum of the needles (Fig. 6 (b)) also comprises a 6-line pattern, here we see that the absorption lines are broader and also slightly asymmetric. The best

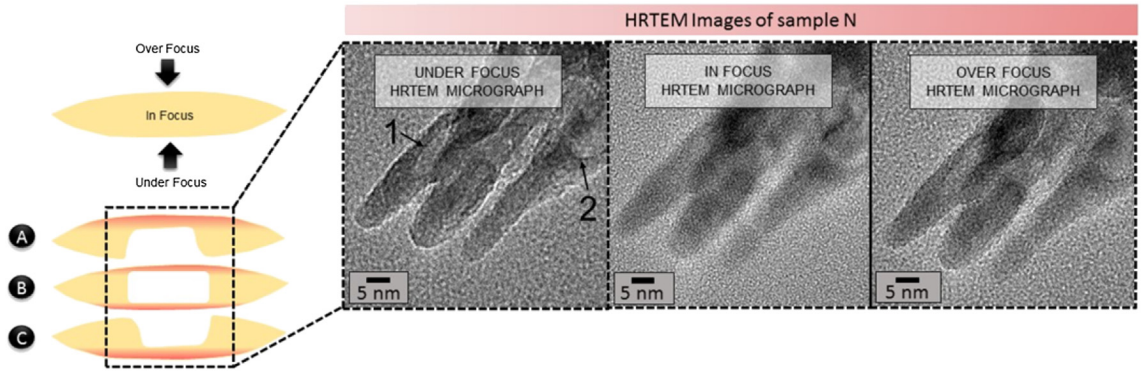

Fig. 4. Reconstruction of the internal structure of the needles after dehydration process. Dark contrast differences observed in TEM images might be explained by: (A), (C) External cavities/surface roughness/discontinuous thickness along the needle; (B) Internal cavities along the needle. The red areas on the left represent the observed areas when images are taken under, over and in-focus. (For interpretation of the references to colour in this figure legend, the reader is referred to the web version of this article.)

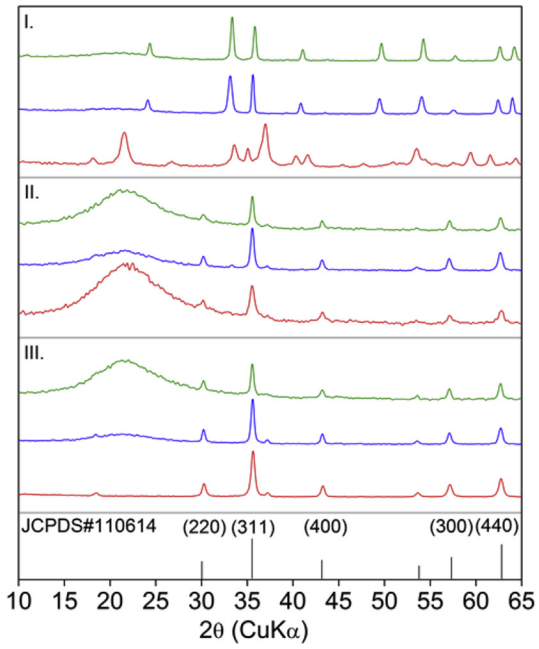

Fig. 5. X-ray powder diffractograms of the precursor (I) and products obtained by wet (II) and dry reduction (III). A single phase, whose Bragg peaks are attributed to magnetite or maghemite, is obtained through both reduction techniques for all morphologies: rhombohedra (green), discs (blue) and needles (red). (For interpretation of the references to colour in this figure legend, the reader is referred to the web version of this article.)

fit is also obtained using a superposition of three Voigtian sextets, two of which have isomer shifts and hyperfine fields reminiscent of magnetite as seen for the rhombohedra. The third sub-component comprises ca.18% of the spectral area and results in the slight 'hanging' of the spectra at v = 0. The isomer shift of this component is 0.41 mm/s and cannot be attributed to either Fe^{3+} on the A site of $Fe^{2+,3+}$ on the B site. We attribute this component to the highly porous structure disrupting the crystalline structure experienced by Fe nuclei in the needles. The mean isomer shift of the spectra is 0.48 mm/s and 0.49 mm/s, respectively, which are close to the value of 0.53 mm/s for stoichiometric magnetite [36,37].

3.4. Magnetic characterization of the magnetite particles

The field and temperature dependent magnetization measurements on all samples are shown in Fig. 7. For each sample system, the field dependent measurements performed at 5 K and 295 K are plotted in one graph. The insets show the magnetization behaviour in the low field regime at ±300 kA/m.

All magnetization curves show similar behaviour for different shapes and different reduction techniques. The samples exhibit non-zero remanence and coercivity indicating that the particles are magnetically blocked at room temperatures and below.

Looking into the details, it can be seen that the rhombohedra and needles obtained by wet reduction present a so-called wasp-waisted hysteresis loop, which is not observed in the materials produced by dry reduction. Roberts et al. explained the occurrence of a wasp-waisted hysteresis loop by a mixture of single- and multi-domain remanence states within the particles [38]. Since the samples prepared by dry reduction do not show the wasp-waisted hysteresis behaviour, it seems that this reduction technique produces particles with a more uniform magnetization state compared to the particles synthesised by wet reduction. This is in good agreement with the findings on the crystallite size measured by XRD, because defects and pores are usually responsible for the pinning and nucleation sites for magnetic domains, and obviously these defects and pores are less pronounced for dry reduced MNPs.

The saturation magnetization of the different samples is determined at 5 T where nearly all magnetic moments are aligned in field direction and thus dipolar interactions between the particle's magnetic moments are negligible. The saturation magnetization increases with decreasing temperature and the values of the saturation magnetization at room temperature are smaller than the 130 $Am^2/kg(Fe)$ found for bulk magnetite [39]. The reduced magnetization for fine-particle systems by finite-size effects is well known in literature [40]. Magnetite nanocrystals obtained directly by the polyol process and aggregated in dense or hollow spheres show similar saturation magnetization values (110 $Am^2/$ kg(Fe)) and a coercive field of (11 kA/m) at room temperature [11].

The saturation magnetization M_S and coercive field H_C have been extracted from the magnetization data and summarized in Table 2. The value of M_S is largest for the rhombohedra while the discs exhibit the lowest saturation magnetization and that can be traced back to influences of the particles size. Interestingly, the saturation magnetization is considerably lower for the wet reduced particles than for dry reduction indicating again a significant effect of the reduction process and the presence of pores on the magnetic properties of the material. For the disc shaped particles, the coercive field is identical in the wet and in the dry reduced samples. The coercivity of the rhombohedra and the needles cannot be compared due to the wasp-waisted hysteresis behaviour in case of wet reduction.

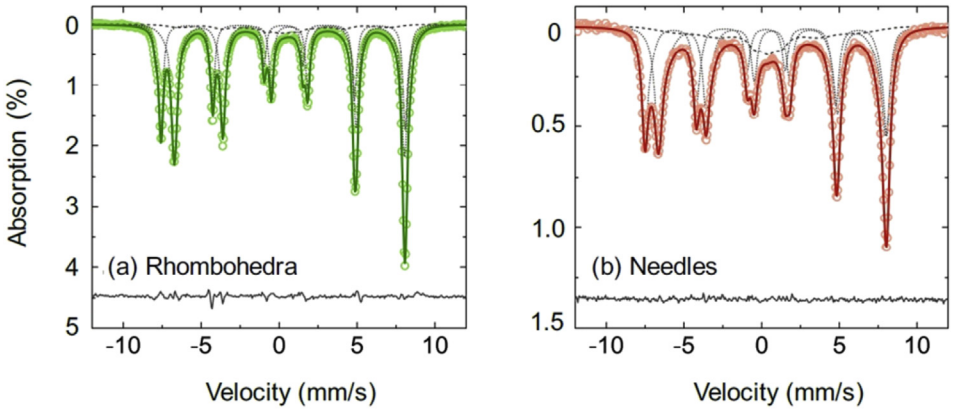

Fig. 6. Comparison of room temperature Mössbauer spectra for (a) rhombohedra and (b) needles after reduction. For each, points are the observed counts, the solid line is the modelled best fit to the data, and the dotted lines correspond to the Voigtian sub spectra. The quality of fit is indicated by the reduced χ^2 and the residual, given by $I_{obs} - I_{cal}$.

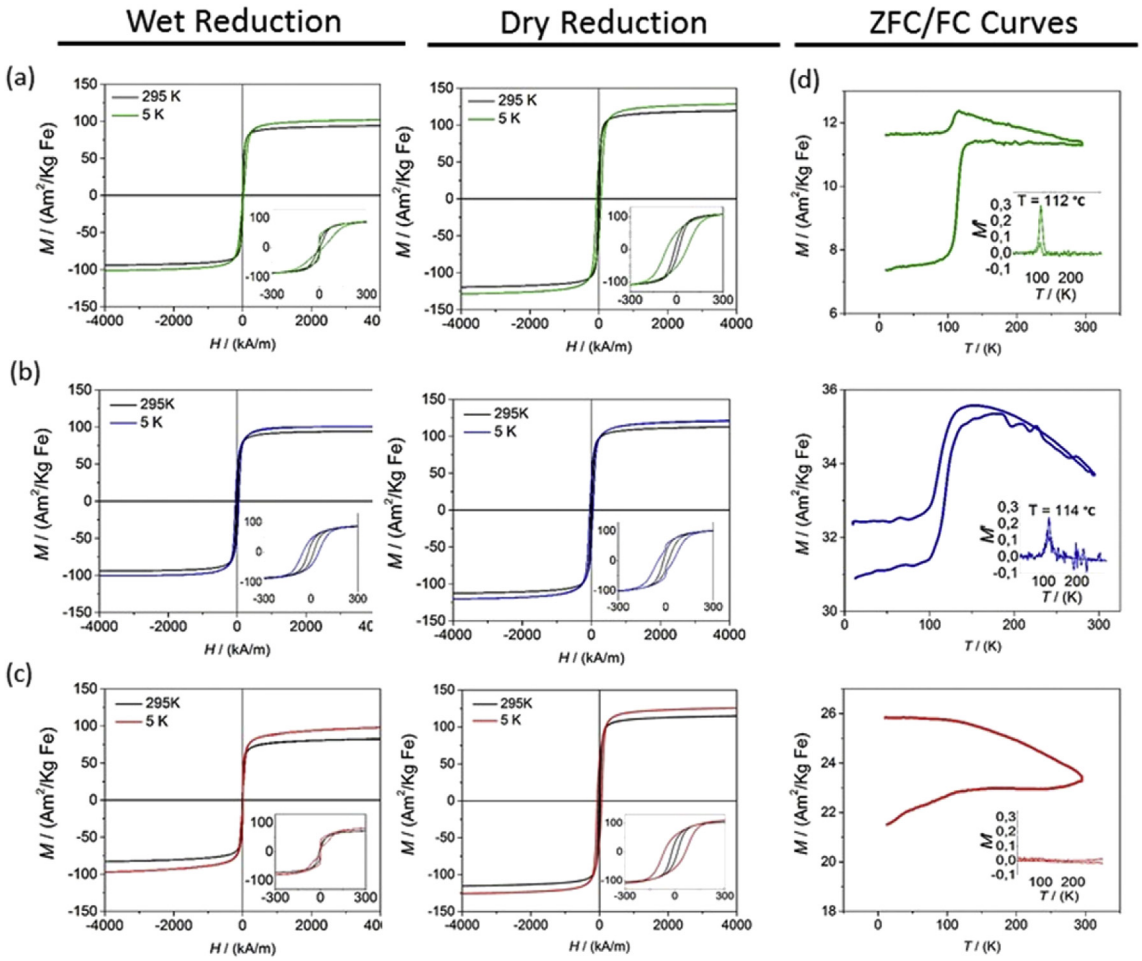

Fig. 7. Hysteresis cycles at 295 and 5 K for all particle morphologies (green = rhombohedra, blue = disks, red = needles), comparing wet and dry reduction. Inset: the hysteresis cycles at low field regime (±300 kA/m) are shown. In addition, ZFC/FC curves (measured at 5 mT) of samples reduced in liquid are presented with the inset showing the first derivative of the magnetization with respect to temperature. (For interpretation of the references to colour in this figure legend, the reader is referred to the web version of this article.)

Field dependent magnetization curves recorded at higher field sweeping rates for the rhombohedra and needles are shown in Fig. 8. Here the wasp-waisted hysteresis curve as observed in quasi-static magnetization measurements has vanished. The fact that the hysteresis curve depends on the field change rate indicates that the wasp-waisted hysteresis curves originate from domain formation within the particles, since the nucleation of domain wall and its movement are time dependent [41].

Zero-field cooled/field cooled (ZFC/FC) magnetization curves of all products obtained from wet reduction are shown in (Fig. 7). A

Table 2
Comparison of the values of saturation magnetization (MS) of magnetite particles after wet and dry reduction, and coercivity (HC) at 5 and 295 K. (R) indicates the rhombohedra, (D) the discs and (N) the needles particles.

Sample	Wet reduction				Dry reduction			
	M_S (Am^2/kg(Fe))		H_C (kA/m)		M_S (Am^2/kg(Fe))		H_C (kA/m)	
	5 K	295 K	5 K	295 K	5 K	295 K	5 K	295 K
Rhombohedra	102	94	11	4	128	119	62	12
Discs	100	94	50	17	121	113	50	15
Needles	98	83	0	4	126	115	62	16

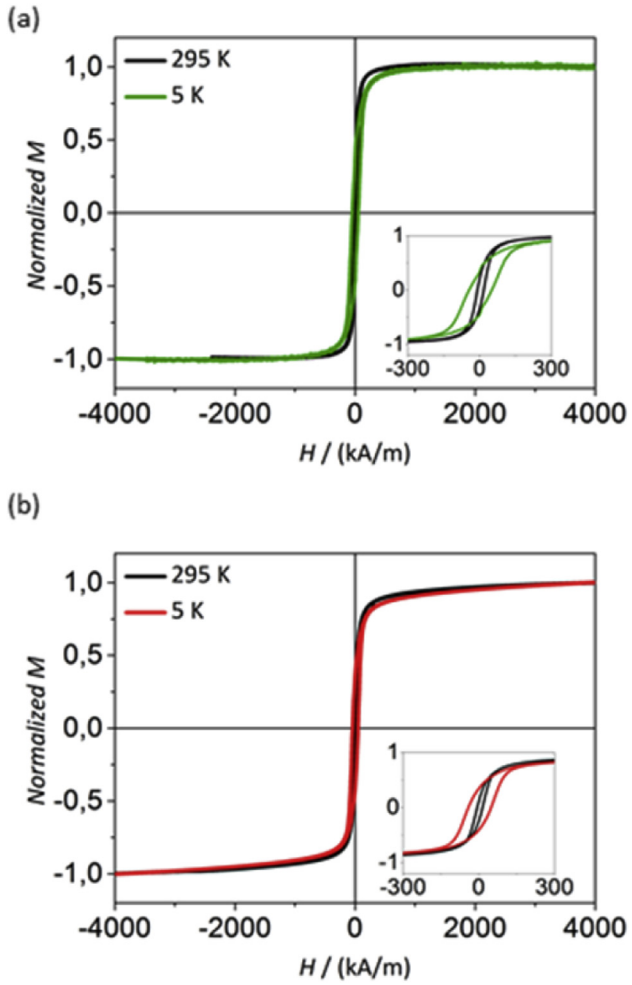

Fig. 8. Magnetization curves between ±5 T measured with a field sweep of 0.3 T/min for magnetite rhombohedra (green) and needles (red) obtained by wet reduction. (For interpretation of the references to colour in this figure legend, the reader is referred to the web version of this article.)

clear Verwey transition [42] is observed in the case of rhombohedra and discs at 112–114 K (obtained from a hematite precursor). However, the transition in case of the discs is less sharp than for the rhombohedra. In case of the needles (obtained from a goethite precursor) the Verwey transition is almost invisible.

Small degrees of non-stoichiometry or impurities in magnetite can reduce the Verwey transition temperature [43], located at 125 K for stoichiometric magnetite [44] and that could explain the different Verwey temperature observed for rhombohedra and discs. However, our XRD and Mössbauer studies confirm the magnetite nature of the particles. In fact, the reason for the shifted Verwey transition could be the crystal size, as discussed in Refs. [42], [45], where the state change during the transition and its temperature reduces with decreasing crystal size. The fact that almost no transition is observed in the needles could be associated to the smaller crystal size as determined by XRD for this sample (Table 1) and the observation of a porous structure within a single particle by HRTEM (Fig. 5 and Fig. S2 in supporting information). Mössbauer spectra support this conclusion showing broader lines and a central singlet for the needles suggesting poorer crystallinity, which would explain the loss of the Verwey transition, against sharp absorption lines for rhombohedra corresponding to pure stoichiometric magnetite.

The shape of the Verwey transition for the different morphologies, especially for the smeared out transition of the discs, could be traced back to the existence of pores inside the particles and therefore a less-ordered crystal structure.

4. Conclusions

In this work, an alternative route to produce a library of iron oxide magnetic nanoparticles in a core size range of 50–100 nm and three different shapes has been successfully demonstrated. Here the goethite and hematite precursors are coated with silica to avoid sintering and to conserve the particle shape in the subsequent reduction of the precursor material to magnetite. Two different reduction methods have been successfully applied yielding a single iron oxide phase of magnetite.

The magnetite phase has been verified by X-ray diffractograms, Mössbauer spectra and ZFC/FC magnetization curves. Magnetite nanoparticles coming from hematite precursor show a very clear Verwey transition at slightly lower temperatures than the reported ones for pure magnetite, probably due to small impurities or pores in the particles. The hysteresis parameters revealed that there is a difference between the magnetic material obtained by wet and dry reduction with higher values of saturation magnetization after dry reduction. However, rhombohedra and needle shaped samples show, in the case of the wet reduction, interesting magnetic properties with a wasp-shaped hysteresis curve and a very low coercive field at room temperature originated probably from the domain formation within the particles.

In addition, the approach for the reduction of the precursors has an influence on the magnetic behaviour of the final magnetite particles. MNPs that have been produced by dry reduction show fewer defects in the crystal structure. The possibility of generating a discontinuous structure within a particle by forcing the pore formation may be an interesting strategy to develop new materials with tuned magnetic properties for biomedical applications.

In conclusion, we demonstrate the production of large (>25 nm) magnetite MNPs where shape and internal structure could be varied by the synthesis parameters. We demonstrate that both MNPs shape and internal MNPs structure affect strongly the magnetic behaviour of the MNPs. In future characterization of magnetite MNPs systems these parameters should always be taken into account.

Supporting information description

Additional data on High-Resolution Transmission Electron Microscopy, Scanning Electron Microscopy and Infrared Spectroscopy are available.

Acknowledgements

We would like to thank Dr. Teresita González-Carreño for her lab experiment assistance. This work was supported by the EC FP-7

grant “NanoMag” (grant agreement no 604448) and the Spanish Government by MAGO project (MAT2014-52069-R). The magnetic characterization was supported by COST Action TD1402. LG acknowledges financial support from the Ramón y Cajal subprogram (RYC-2014-15512).

Appendix A. Supplementary data

Supplementary data related to this article can be found at http://dx.doi.org/10.1016/j.actamat.2016.12.016.

References

[1] R. Mejías, S. Pérez-Yagüe, L. Gutiérrez, L.I. Cabrera, R. Spada, P. Acedo, C.J. Serna, F.J. Lázaro, T. Villanueva, M.P. Morales, D.F. Barber, Dimercaptosuccinic acid-coated magnetite nanoparticles for magnetically guided in vivo delivery of interferon gamma for cancer immunotherapy, Biomaterials 32 (11) (2011) 2938–2952.
[2] K. Maier-Hauff, F. Ulrich, D. Nestler, H. Niehoff, P. Wust, B. Thiesen, H. Orawa, V. Budach, A. Jordan, Efficacy and safety of intratumoral thermotherapy using magnetic iron-oxide nanoparticles combined with external beam radiotherapy on patients with recurrent glioblastoma multiforme, J. Neuro-Oncology 103 (2) (2010) 317–324.
[3] T.-H. Shin, Y. Choi, S. Kim, J. Cheon, Recent advances in magnetic nanoparticle-based multi-modal imaging, Chem. Soc. Rev. 44 (14) (2015) 4501–4516.
[4] A.P. Khandhar, R.M. Ferguson, H. Arami, K.M. Krishnan, Monodisperse magnetite nanoparticle tracers for in vivo magnetic particle imaging, Biomaterials 34 (15) (2013) 3837–3845.
[5] I. Hilger, W.A. Kaiser, Iron oxide-based nanostructures for MRI and magnetic hyperthermia, Nanomedicine 7 (9) (2012) 1443–1459.
[6] Y.X.J. Wang, J.-M. Idee, C. Corot, Scientific and industrial challenges of developing nanoparticle-based theranostics and multiple-modality contrast agents for clinical application, Nanoscale 7 (39) (2015) 16146–16150.
[7] S. Dutz, H. Rudolf, Magnetic particle hyperthermia—a promising tumour therapy? Nanotechnology 25 (45) (2014) 452001.
[8] L.n. Lartigue, P. Hugounenq, D. Alloyeau, S.P. Clarke, M. Lévy, J.-C. Bacri, R. Bazzi, D.F. Brougham, C. Wilhelm, F. Gazeau, Cooperative organization in iron oxide multi-core nanoparticles potentiates their efficiency as heating mediators and MRI contrast agents, ACS Nano 6 (12) (2012) 10935–10949.
[9] S. Dutz, Are magnetic multicore nanoparticles promising candidates for biomedical applications? IEEE Trans. Magn. 52 (9) (2016) 1–3.
[10] D. Serantes, K. Simeonidis, M. Angelakeris, O. Chubykalo-Fesenko, M. Marciello, M.P. Morales, D. Baldomir, C. Martinez-Boubeta, Multiplying magnetic hyperthermia response by nanoparticle assembling, J. Phys. Chem. C 118 (11) (2014) 5927–5934.
[11] N. Guan, Y. Wang, D. Sun, J. Xu, A simple one-pot synthesis of single-crystalline magnetite hollow spheres from a single iron precursor, Nanotechnology 20 (10) (2009) 105603.
[12] B. Jia, L. Gao, Morphological transformation of Fe_3O_4 spherical aggregates from solid to hollow and their self-assembly under an external magnetic field, J. Phys. Chem. C 112 (3) (2008) 666–671.
[13] G. Salas, C. Casado, F.J. Teran, R. Miranda, C.J. Serna, M.P. Morales, Controlled synthesis of uniform magnetite nanocrystals with high-quality properties for biomedical applications, J. Mater. Chem. 22 (39) (2012) 21065–21075.
[14] D. Kim, N. Lee, M. Park, B.H. Kim, K. An, T. Hyeon, Synthesis of uniform ferrimagnetic magnetite nanocubes, JACS 131 (2) (2009) 454–455.
[15] M.V. Kovalenko, M.I. Bodnarchuk, R.T. Lechner, G. Hesser, F. Schäffler, W. Heiss, Fatty acid salts as stabilizers in size- and shape-controlled nanocrystal Synthesis: the case of inverse spinel iron oxide, JACS 129 (20) (2007) 6352–6353.
[16] S. Palchoudhury, W. An, Y. Xu, Y. Qin, Z. Zhang, N. Chopra, R.A. Holler, C.H. Turner, Y. Bao, Synthesis and growth mechanism of iron oxide nanowhiskers, Nano Lett. 11 (3) (2011) 1141–1146.
[17] H. Sun, B. Chen, X. Jiao, Z. Jiang, Z. Qin, D. Chen, Solvothermal synthesis of tunable Electroactive magnetite nanorods by controlling the side reaction, J. Phys. Chem. C 116 (9) (2012) 5476–5481.
[18] L. Zhang, J. Wu, H. Liao, Y. Hou, S. Gao, Octahedral Fe3O4nanoparticles and their assembled structures, Chem. Commun. (29) (2009) 4378–4380.
[19] J. Lu, X. Jiao, D. Chen, W. Li, Solvothermal synthesis and characterization of Fe_3O_4 and γ-Fe_2O_3 nanoplates, J. Phys. Chem. C 113 (10) (2009) 4012–4017.
[20] Y. Zeng, R. Hao, B. Xing, Y. Hou, Z. Xu, One-pot synthesis of Fe3O4 nanoprisms with controlled electrochemical properties, Chem. Commun. 46 (22) (2010) 3920–3922.
[21] A.F. Rebolledo, O. Bomatí-Miguel, J.F. Marco, P. Tartaj, A facile synthetic route for the preparation of superparamagnetic iron oxide nanorods and nanorices with tunable surface functionality, Adv. Mater 20 (9) (2008) 1760–1765.
[22] R.M. Cornell, U. Schwertmann, The Iron Oxides: Structure, Properties, Reactions, Occurrences and Uses, John Wiley & Sons, 2003.
[23] C. Graf, D.L.J. Vossen, A. Imhof, A. van Blaaderen, A general method to coat colloidal particles with silica, Langmuir 19 (17) (2003) 6693–6700.
[24] W. Stöber, A. Fink, E. Bohn, Controlled growth of monodisperse silica spheres in the micron size range, J. Colloid Interface Sci. 26 (1) (1968) 62–69.
[25] M.P. Morales, C. Pecharroman, T.G. Carreño, C.J. Serna, Structural characteristics of uniform γ-Fe_2O_3 particles with different axial (Length/Width) ratios, J. Solid State Chem. 108 (1) (1994) 158–163.
[26] Y. Yang, X. Liu, Y. Lv, T.S. Herng, X. Xu, W. Xia, T. Zhang, J. Fang, W. Xiao, J. Ding, Orientation mediated enhancement on magnetic hyperthermia of Fe_3O_4 nanodisc, Adv. Funct. Mater 25 (5) (2015) 812–820.
[27] Y. Yang, X. Liu, J. Ding, Synthesis of α-Fe_2O_3 templates via Hydrothermal route and Fe_3O_4 particles through subsequent chemical reduction, Sci. Adv. Mater. 5 (9) (2013) 1199–1207.
[28] R. Pozas, M. Ocaña, M.P. Morales, C.J. Serna, Uniform nanosized goethite particles obtained by aerial oxidation in the $FeSO_4$–Na_2CO_3 system, J. Colloid Interface Sci. 254 (1) (2002) 87–94.
[29] L.M. Liz-Marzán, P. Mulvaney, The assembly of coated nanocrystals, J. Phys. Chem. B 107 (30) (2003) 7312–7326.
[30] H. Naono, K. Nakai, T. Sueyoshi, H. Yagi, Porous texture in hematite derived from goethite: mechanism of thermal decomposition of geothite, J. Colloid Interface Sci. 120 (2) (1987) 439–450.
[31] A.S.J. Baker, A.S.C. Brown, M.A. Edwards, J.S.J. Hargreaves, C.J. Kiely, A. Meagher, Q.A. Pankhurst, A structural study of haematite samples prepared from sulfated goethite precursors: the generation of axial mesoporous voids,, J. Mater. Chem. 10 (3) (2000) 761–766.
[32] J. Morales, J.L. Tirado, M. Macias, Changes in crystallite size and microstrains of hematite derived from the thermal decomposition of synthetic akaganeite, J. Solid State Chem. 53 (3) (1984) 303–312.
[33] H. Brill-Edwards, B.L. Daniell, R.L. Samuel, Structural changes accompanying the reduction of polycrystalline haematite, J. Iron Steel Inst. 203 (1965) 361–368.
[34] P. Swann, N. Tighe, High voltage microscopy of the reduction of hematite to magnetite, Metall. Trans. B 8 (2) (1977) 479–487.
[35] A.F. Rebolledo, S. Laurent, M. Calero, A. Villanueva, M. Knobel, J.F. Marco, P. Tartaj, Iron oxide nanosized clusters embedded in porous nanorods: a new colloidal Design to Enhance capabilities of MRI contrast agents, ACS Nano 4 (4) (2010) 2095–2103.
[36] G.M. da Costa, C. Blanco-Andujar, E. De Grave, Q.A. Pankhurst, Magnetic nanoparticles for in vivo use: a critical assessment of their composition, J. Phys. Chem. B. 118 (40) (2014) 11738–11746.
[37] J. Santoyo Salazar, L. Perez, O. de Abril, L. Truong Phuoc, D. Ihiawakrim, M. Vazquez, J.-M. Greneche, S. Begin-Colin, G. Pourroy, Magnetic iron oxide nanoparticles in 10–40 nm range: composition in terms of magnetite/maghemite ratio and effect on the magnetic properties, Chem. Mater 23 (6) (2011) 1379–1386.
[38] A.P. Roberts, Y. Cui, K.L. Verosub, Wasp-waisted hysteresis loops: mineral magnetic characteristics and discrimination of components in mixed magnetic systems, J. Geophys. Res. Solid Earth 100 (B9) (1995) 17909–17924.
[39] R.C. O'Handley, Modern Magnetic Materials: Principles and Applications, Wiley New York, 2000.
[40] X. Batlle, A. Labarta, Finite-size effects in fine particles: magnetic and transport properties, J. Phys. D. Appl. Phys. 35 (6) (2002). R15.
[41] B. Hillebrands, K. Ounadjela, Spin Dynamics in Confined Magnetic Structures I, Springer, 2001.
[42] G. Goya, T. Berquo, F. Fonseca, M.P. Morales, Static and dynamic magnetic properties of spherical magnetite nanoparticles, J. Appl. Phys. 94 (5) (2003) 3520–3528.
[43] R. Aragón, D.J. Buttrey, J.P. Shepherd, J.M. Honig, Influence of nonstoichiometry on the Verwey transition, Phys. Rev. B 31 (1) (1985) 430–436.
[44] W. Friedrich, The Verwey transition - a topical review, J. Phys. Condens. Matter 14 (12) (2002). R285.
[45] C.L. Snow, Q. Shi, J. Boerio-Goates, B.F. Woodfield, Heat capacity studies of nanocrystalline magnetite (Fe_3O_4), J. Phys. Chem. C 114 (49) (2010) 21100–21108.

Particle & Particle Systems Characterization

www.particle-journal.com

Colloidal Flower-Shaped Iron Oxide Nanoparticles: Synthesis Strategies and Coatings

Helena Gavilán, Anja Kowalski, David Heinke, Abhilash Sugunan, Jens Sommertune, Miriam Varón, Lara K. Bogart, Oliver Posth, Lunjie Zeng, David González-Alonso, Christoph Balceris, Jeppe Fock, Erik Wetterskog, Cathrine Frandsen, Nicole Gehrke, Cordula Grüttner, Andrea Fornara, Frank Ludwig, Sabino Veintemillas-Verdaguer, Christer Johansson, and M. Puerto Morales**

The assembly of magnetic cores into regular structures may notably influence the properties displayed by a magnetic colloid. Here, key synthesis parameters driving the self-assembly process capable of organizing colloidal magnetic cores into highly regular and reproducible multi-core nanoparticles are determined. In addition, a self-consistent picture that explains the collective magnetic properties exhibited by these complex assemblies is achieved through structural, colloidal, and magnetic means. For this purpose, different strategies to obtain flower-shaped iron oxide assemblies in the size range 25–100 nm are examined. The routes are based on the partial oxidation of $Fe(OH)_2$, polyol-mediated synthesis or the reduction of iron acetylacetonate. The nanoparticles are functionalized either with dextran, citric acid, or alternatively embedded in polystyrene and their long-term stability is assessed. The core size is measured, calculated, and modeled using both structural and magnetic means, while the Debye model and multi-core extended model are used to study interparticle interactions. This is the first step toward standardized protocols of synthesis and characterization of flower-shaped nanoparticles.

1. Introduction

Despite the progress in colloidal self-assembly of organic[1] or inorganic[2,3] building blocks to form close-packed structures such as colloidal crystals,[4] there are only a few reports of controlled assembly of ordered nanoparticles in suspension.[5] In this matter, many fundamental aspects remain unknown and often, there is no predictive description of the ensemble behaviour or the origin of the forces driving aggregation.[6,7] Nonetheless, aggregation is a general mechanism of particle formation now recognized as a common growth phenomenon for many different monodisperse nanoparticles,[8–12] in contrast to the monomer by monomer addition that is described in classical models.

H. Gavilán, Dr. M. P. Morales
Department of Energy, Environment and Health
Instituto de Ciencia de Materiales de Madrid, ICMM/CSIC
Sor Juana Inés de la Cruz 3, 28049 Madrid, Spain
E-mail: helena_gr@icmm.csic.es; puerto@icmm.csic.es

A. Kowalski, Dr. C. Grüttner
Micromod Partikeltechnologie GmbH
Friedrich-Barnewitz-Str. 4, D-18119 Rostock, Germany

D. Heinke, Dr. N. Gehrke
NanoPET Pharma GmbH
D-10115 Berlin, Germany

Dr. A. Sugunan, Dr. J. Sommertune, Prof. A. Fornara
The Swedish Research Institute
Box 5607, SE-114 86 Stockholm, Sweden

Dr. M. Varón, Prof. C. Frandsen
Department of Physics
Technical University of Denmark
Fysikvej, 2800 Kongens Lyngby, Denmark

Dr. L. K. Bogart
Healthcare Biomagnetics Laboratory
University College of London
21 Albemarle Street, London W1S 4BS, UK

DOI: 10.1002/ppsc.201700094

Dr. O. Posth
Physikalisch-Technische Bundesanstalt
Abbestr. 2–12, 10587 Berlin, Germany

Dr. L. Zeng
Department of Applied Physics
Chalmers University of Technology
SE-41296 Gothenburg, Sweden

Dr. D. González-Alonso
Department of CITIMAC
University of Cantabria
39005 Santander, Spain

C. Balceris, Dr. F. Ludwig
Institute of Electrical Measurement and Fundamental Electrical Engineering
TU Braunschweig, 38106 Braunschweig, Germany

Dr. J. Fock
Department of Micro- and Nanotechnology
Technical University of Denmark
DK-2800 Kongens Lyngby, Denmark

Dr. E. Wetterskog
Department of Engineering Sciences
Ångström Laboratory
Uppsala University
SE-75121 Uppsala, Sweden

In absence of templates, interfaces or external fields, the self-assembly process in solution is governed by the balance of attractive and repulsive forces. Magnetic nanoparticles (MNPs) are – a priori – different due to additional forces that arise as a consequence of their magnetic moment. These interactions can be either intraparticle exchange interactions, or long-range magnetostatic dipolar forces between particles. Exchange interactions between cores of a multi-core particle may lead to the so-called "superferrimagnetic" behaviour,[13] exhibiting large magnetic moment and weak remanence in zero field, and thus, having low tendency to form agglomerates. On the other hand, dipolar interactions between particles with sufficient high moment account for the formation of configurations such as chains, which may change strongly the magnetic properties of the colloid.[14] As a consequence, the assembly of MNPs in multi-core structures can, in some cases, give rise to collective magnetic properties, which yields microscopic magnetic behaviour that is very different from single-core nanoparticles or bulk materials.[15,16] Such multi-core nanoparticles are currently of great interest in many different areas such as catalysis,[17] ferrofluids and rheology,[18] as well as bioapplications, which are mainly focused on iron oxide nanoparticles (magnetite or maghemite) because of their low toxicity.[19] Colloids made of magnetic multi-core nanoparticles show high nuclear magnetic resonance (NMR) relaxivity (r_2),[20] high magnetic particle imaging (MPI) signals,[21] high specific absorption rate of AC field (SAR),[22–24] high magnetic moment when manipulated with an external magnet[25] and enhanced performance as theranostic agents.[26–28]

Herein, we analyze the key synthesis parameters driving the self-assembly process capable of organizing colloidal magnetic cores into highly regular and reproducible multi-core nanoparticles showing the so called "superferrimagnetic state" due to exchange interactions. For that purpose we have conducted a comparison of four different synthesis of colloidal magnetic multi-core structures called flower-shaped nanoparticles (**Scheme 1**), consisting of iron oxide cores that are aggregated to form isometric 3D arrangements. Out of the numerous synthesis strategies reported in the literature,[5] we have focused our investigation on those that either produce multi-core particles in the single-domain region, i.e. smaller than 50 nm, or above the multi-domain limit, i.e. larger than 100 nm. In this work, some used approaches describe the in situ formation of MNPs and assembly in the presence of molecules or polymers, while others describe first the assembly of the formed MNPs and its further polymer coating, encapsulation or embedding. By comparing synthesis approaches we have been able to gain a better understanding into the nature of this self-assembly process that lead to multi-core magnetic nanoparticles with controllable size, shape and collective behaviour. Moreover, we have been able to determine to which extent the systems can be tuned by choice of synthesis conditions yielding core aggregation and colloidal stability.

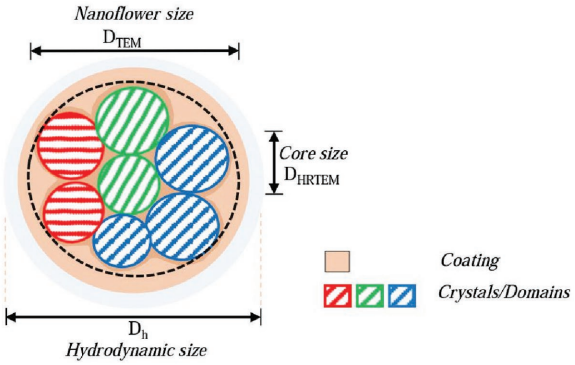

Scheme 1. Flower-shaped multi-core nanoparticle: Nanoflower and core size have been determined through TEM and HRTEM, respectively, and has a final hydrodynamic size in solution. The term crystal/domain is designated as cores that share crystal alignment.

Comprehensive structural and magnetic characterization of colloidal dispersions and freeze-dried powders has been performed following standardized protocols to facilitate comparison of these structures.[29] This is the first step toward standardization of synthesis and characterization of these nanoparticles, which is an important concern and demand nowadays.[30] First, we analyze the core arrangement within the particle and intraparticle interactions. A key parameter to understand the behaviour of the colloid is the degree of fusion of the cores within the nanoflowers, specifically whether they are in direct contact and if so, if they share crystalline alignment.[31] Secondly, we analyze the interparticle interactions,[32] which are minimized by steric and/or electrostatic repulsion due to the surface coatings (dextran, citric acid) or alternatively by embedding the cores on surfactant stabilized polystyrene beads. Surface modification of the flower-shaped nanoparticles provides colloidal stability in water and specific functionalization, which is of utmost importance for their successful application in the nano-bio area.[33]

2. Results and Discussion

2.1. Key Parameters Controlling Self-Assembly

Strategy 1 (**Scheme 2**) involves the oxidative aging of an $Fe(OH)_2$ intermediate in water in the presence of dextran (90 °C/4 h), to yield NF1. **Table 1** includes the mean size of the particle and core determined through transmission electron microscopy (TEM) and high-resolution transmission electron microscopy (HRTEM), respectively. Nanoflowers produced in this way have a mean diameter of 46 nm and they are composed of 7 nm cores that are loosely packed together (**Figure 1**). HRTEM images suggest that the cores share the same crystallographic orientation in some areas of the particle but not throughout the whole particle. It has previously been reported that for this reaction the excess of OH^- or Fe^{2+} in the media

Dr. S. Veintemillas-Verdaguer
Instituto de Ciencia de Materiales de Madrid
ICMM/CSIC
Sor Juana Inés de la Cruz 3, 28049 Madrid, Spain
Prof. C. Johansson
RISE Acreo
P.O. Box 53071, SE-40014 Göteborg, Sweden
The ORCID identification number(s) for the author(s) of this article can be found under https://doi.org/10.1002/ppsc.201700094.

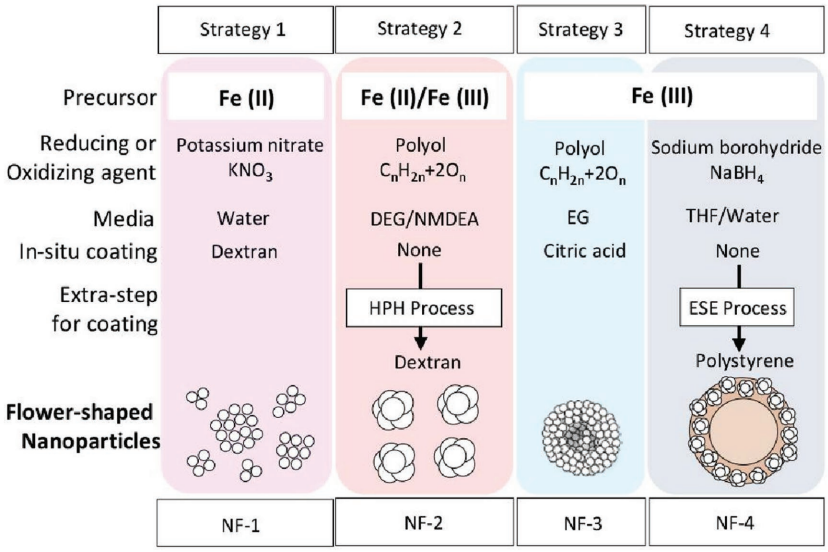

Scheme 2. Strategies followed to obtain flower-shaped nanoparticles. NMDEA stands for N-methyl diethanolamine, HPH process stands for high-pressure homogenization coating, and ESE process stands for emulsion solvent evaporation.

defines the mechanism of particle growth and therefore the formation of single or multi-core particles.[34,35] In our approach, an excess of OH^- was used to move the pH away from the magnetite isoelectric point (≈6.5),[36] thus charging the surface of the initial growing nuclei keeping them apart and resulting in single-core particles.[35,37,38] The use of in situ dextran coating, however, causes a reduction in surface charge density of the growing nuclei promoting its approach and aggregation. We observe that flower-shaped nanoparticles produced in this way have a poorly defined size, shape and broad size distribution (relative standard deviation >50%), probably due to the poor capping effect of dextran hydroxyl groups, which are attached through hydrogen bonds to the iron oxide particle surface.[39]

Samples NF2 and NF3 were obtained using polyol media (Scheme 2) at elevated temperatures (220 °C/12 h and 200 °C/10 h, respectively) and while NF2 is coated with dextran in a second step, NF3 is in situ coated with citric acid. Figure 1 shows that NF2 is composed of monodisperse 47 nm nanoflowers with a well defined size (Table 1) and shape.

Table 1. Flower-shaped nanoparticles (D_{TEM}), core (D_{HRTEM}), crystal (D_{XRD}) and hydrodynamic (D_h, DLS) sizes estimated through structural characterization.

Sample	D_{TEM} [nm]	D_{HRTEM} [nm]	D_{XRD} [nm]	D_h, DLS [nm]
NF1	46 ± 27	7	9 ± 1	192 ± 84
NF2	47 ± 17	15	15 ± 1	51 ± 15
NF3	110 ± 13	4	8 ± 1	158 ± 53
NF4	24 ± 7[a)]			
	172 ± 70	10[b)]	10 ± 1	250 ± 46

[a)]TEM size in this system means size of the nanoflower, and the polymer sphere embedding the flowers; [b)]HRTEM size in this system means core size of the nanoflower.

HRTEM images reveal cores of approximately 15 nm that are densely packed with essentially the same crystal orientation across the entire particle. Similarly, nanoflowers in NF3 are composed of spherical 110 nm nanoparticles (more than twice that of NF2) with a well-defined size and shape. HRTEM reveals that NF3 consists of very small randomly orientated cores of approximately 4 nm. It has been reported that polyols play an important role in the reaction and act as solvent, surfactant and reductant.[40] Here, we have used polyols of short chain length (diethylene glycol (DEG) in NF2 and ethylene glycol (EG) in NF3), which enable clustering of the cores to obtain desired multi-core structures. For NF2, sodium hydroxide was added to a stoichiometric mixture of iron (II) and iron (III) salts to control the precursor hydrolysis,[41] initiating a burst nucleation followed by the uniform growth of the single cores (LaMer growth). Also, the heating was prolonged for 12 h to promote clustering and subsequent coalescence of the cores leading to flower-shaped nanoparticles.[42,43] Interestingly, if either the heating time is limited to 2–3 h under these conditions, or if polyols of longer chain length are used, such as triethylene glycol[44] or 1,2-hexadecanediol,[45] then, only single-core nanoparticles are obtained. Regarding NF3, we observe three key parameters that allow the formation of the multi-core structure: the control of temperature and pressure by using an autoclave as reactor, the concentration of the precipitator (sodium acetate, NaAc) that promotes the hydrolysis of the Fe^{3+} ions and thereby controlling the phase transformation and the particle morphology, and finally, the addition of an extra stabilizer (sodium citrate, Na_3Cit) that acts as capping agent. High concentrations of NaAc, as those used in NF3, led to flower-shaped nanoparticles composed of uniform cores in size that self-assemble into solid spheres to reduce the surface energy and suffer the so-called recrystallization process.[46] Lower concentrations of NaAc led to the formation of 200 nm magnetite hollow spheres composed of cores with different sizes. The dissolution of inner small cores and growth of the larger ones on the surface, leads to the formation of such voids that are not observed in this work, by the Ostwald ripening process.[47] NF3 have such small core size of 4 nm (Figure 1), due to the presence of sodium citrate (Na_3Cit). This extra stabilizer acts as capping agent, significantly suppresses the nuclei growth (in a comparable way to the dextran in NF1 synthesis) and facilitates the final dispersion of the flower-shaped nanoparticles in aqueous media. Carboxyl groups of citric acid coordinate to the iron oxide particle surface via one or two of the carboxylate functionalities, depending upon steric necessity and the curvature of the surface.[48] Alternatively, the use of other additives such as poly(acrylic acid) (PAA) or poly(vinylpyrrolidone) (PVP) instead of Na_3Cit have been reported to account for different particle size (30–250 nm).[47,49,50]

As HRTEM images of NF2 and NF3 reveal a different degree of crystallographic orientation texture between the cores (also

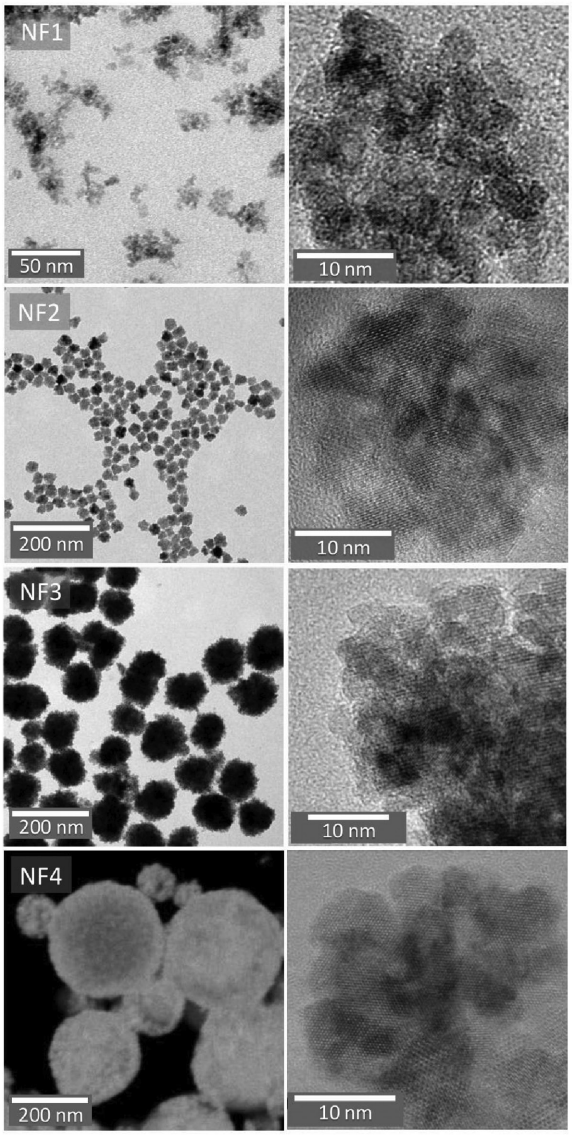

Figure 1. TEM (NF1-NF3) and scanning transmission electron microscopy (STEM) images (NF4) (left), and HRTEM images (right) of the different flower-shaped nanoparticles.

termed "domains") we have used dark field (DF) imaging analysis to further investigate the nature of the alignment, as is summarized in **Figure 2**. The bright areas in the DF images contribute to the diffraction spots marked by white arrows in the corresponding selected area electron diffraction (SAED) patterns. In all acquired DF images only part of the nanoflower becomes bright, which clearly illustrates that there is no obvious common crystallographic orientation of the cores. In the case of NF2, for example, we observe that a much larger area becomes bright, indicating orientated assembly of the cores forming the nanoflowers. Interestingly, we observe in the case of NF3 that these domains are much smaller than for NF2.

Finally, in strategy 4 (Scheme 2) nanoflowers were obtained by means of sodium borohydride, which acts as reducing agent and iron (III) acetylacetonate ($Fe(acac)_3$), which acts as an iron source.[51,52] In this case we obtain monodisperse 24 nm nanoflowers composed of cores of approximately 10 nm (Figure 1 right). HRTEM imaging suggests that there is a continuous crystallinity through the nanoflower, although contrast differences within a single nanoflower were also clearly visible (Figure S1, Supporting Information). For this reduction reaction, it was reported that higher $NaBH_4/Fe(acac)_3$ molar ratios lead to smaller particles. Molar ratios of 10, 25 and 40 yielded 8, 6 and 5 nm single-core particles respectively, since $NaBH_4$ increases burst nucleation and decreases the diffusional growth.[52] It was also reported that by elevating the temperature, the crystal size increased.[53] We propose that the key parameter governing the formation of complex nanoflower structures is the molar ratio of $NaBH_4$ to iron precursor; we selected a ratio of around 5, which is relatively low in comparison to other reports.[52] Additionally, the use of prolonged time period (overnight) for the synthesis, also contributes to the formation of this multi-core structure. Nanoflowers synthesized by this route were embedded on polystyrene spheres (Figure S2, Supporting Information) via the emulsion solvent evaporation (ESE) process, described in detail elsewhere.[51,52] The final NF4 samples has an average diameter of 172 nm and a standard deviation of 69 nm, as observed in the scanning transmission electron microscopy (STEM) image at low magnification (Figure 1).

2.2. Long-Term Stability of The Colloids

Hydrodynamic size (D_h) was measured using dynamic light scattering (DLS) (Table 1). Whilst D_h varies between 50 nm (NF2) and 250 nm (NF4), colloidal stability was maintained for more than 200 days for samples NF1, 2 and 3 (**Figure 3**). There are mainly two mechanisms for colloidal stability: electrostatic repulsion (if zeta-potential values at a given pH are higher than 20 mV or lower than –20 mV) and steric repulsion (for the cases where polymeric or macromolecular surfactants and molecules, i.e. dextran or polystyrene coating). NF1 shows a nearly neutral surface (+2.9 mV), whilst NF2 is highly positively charged (+23 mV) and NF3 is highly negatively charged (–40 mV). Although NF4 has a surface charge of –62 mV we observe an increase in its hydrodynamic size overtime (Figure 3), which is probably due to aggregation phenomena because of its large particle size.

2.3. Core Arrangement within the Nanoflower and Interparticle Interactions

The crystal structure of all nanoflowers was identified as a mixture of magnetite (Fe_3O_4) and maghemite (γ-Fe_2O_3) using X-ray diffraction (XRD) and ^{57}Fe Mössbauer spectroscopy (**Figure 4** and **5**, respectively). The acquired XRD data were analyzed through the Rietveld refinement method (Figure S3, Supporting Information). All the reflections were accounted with the *Fd-3m* space group with no sign of any spurious phase within the (<5%) uncertainty inherent in XRD. Calculated values of lattice parameters are in the range of 8.35–8.37 Å, which lie between the bulk value reported ≈8.39 Å and ≈8.34 Å for magnetite[54] and maghemite,[55] respectively (Table S1 and S2,

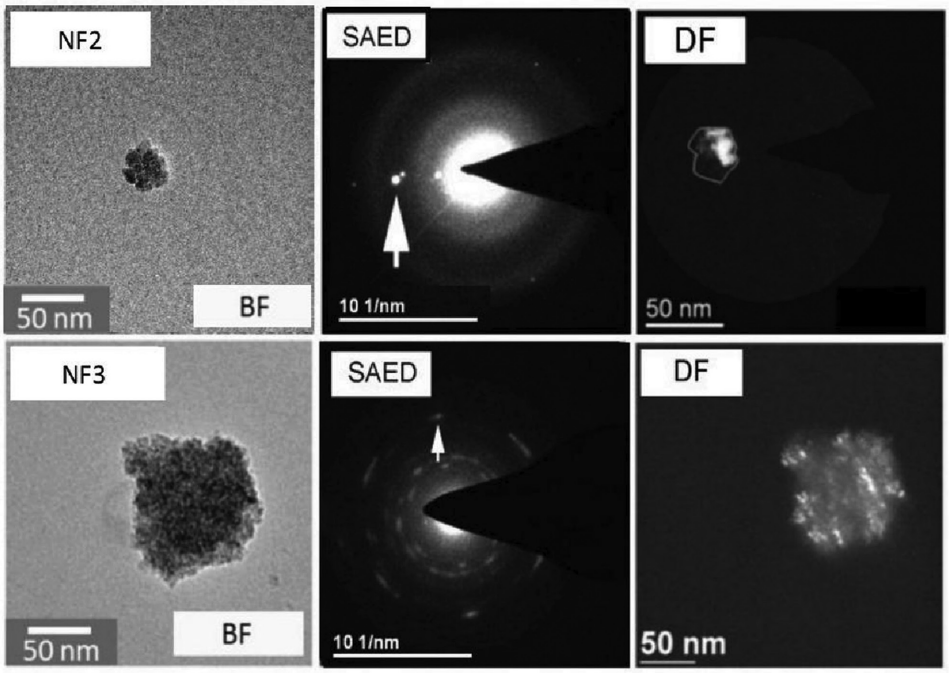

Figure 2. Bright-field (BF) analysis, selected area electron diffraction (SAED) patterns and dark-field (DF) analysis of samples NF2 and NF3.

Supporting Information). This indicates that all samples are at least partially oxidized to maghemite; this is in particularly notable for NF2, which was subjected to an oxidation treatment with iron nitrate prior to dextran coating. Bulk magnetite and maghemite can be distinguished by their different lattice parameter, but in nanosized materials, the combination of peak broadening and variation of the lattice parameters make this challenging. In addition, whereas the space group of magnetite is well established to be *Fd-3m*, maghemite may be present in different space groups depending of the vacancy ordering, *Fd-3m* being one of the possibilities.[56] The crystal sizes, previously described (Scheme 1), were calculated from the XRD data and are summarized in Table 1, along with core sizes measured by HRTEM (the term core is likewise described in Scheme 1). XRD sizes range from 8 (1) to 15 (1) nm. Differences in terms of crystal size allow us to categorize the nanoflowers into three regimes, that is below, equal or larger than 10 nm. NF3 has the largest nanoflower size (110 nm) and is composed of crystals of less than 8 nm, whereas NF2 with much smaller nanoflowers (47 nm), has crystals of 15 nm, the largest in this series of nanoflowers. These results are in very good agreement with the observations in both, HRTEM and DF images. Lastly, both NF1 and NF4 are intermediate systems with crystal sizes of 9 and 10 nm, respectively.

^{57}Fe Mössbauer spectroscopy measurements highlight their crystalline nature and shed light on the influence of the size and structural arrangement of the cores on the magnetic

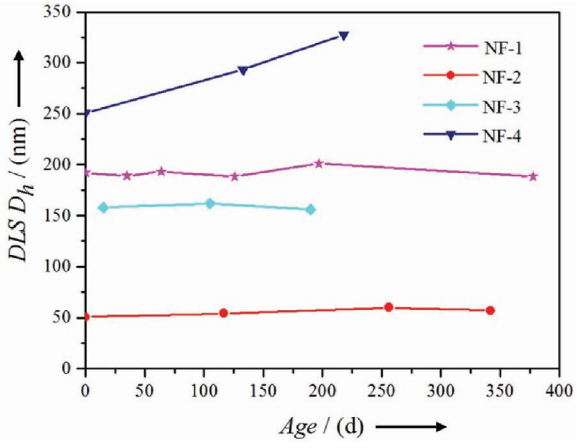

Figure 3. Hydrodynamic size (D_h) measured by DLS throughout time for the different flower-shaped nanoparticles.

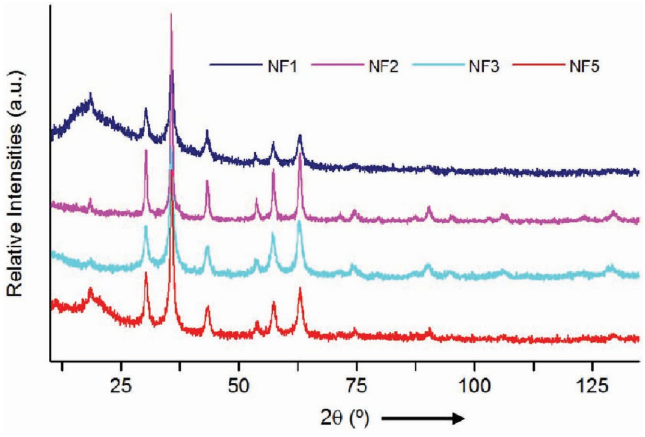

Figure 4. Room-temperature X-ray diffraction patterns of the different flower-shaped nanoparticles. The hump observed at low angles (below 25°) in NF1 and NF4 samples results from their amorphous organic content.

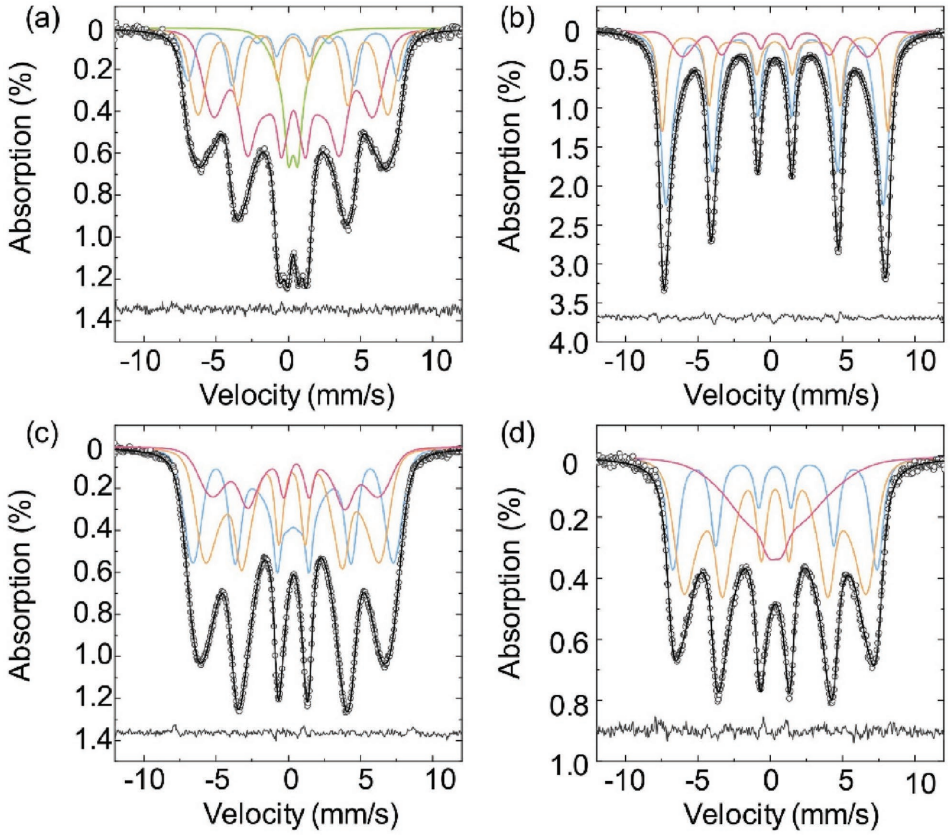

Figure 5. Room-temperature ^{57}Fe Mössbauer Spectroscopy spectra of: a) NF1, b) NF2, c) NF3 and d) NF4. All spectra have been fitted according to Fock et al. 2016 using Voigtian line shapes. The total fit is shown by solid black line (Voigtian sub-spectra in gray). The quality of each fit is indicated by the residual – the difference between observed and fitted intensities – shown beneath each spectrum.

properties. Room-temperature (RT) spectra are shown in Figure 5. All four samples comprise magnetically split spectra but with different degrees of magnetic relaxation due to their crystallinity (seen as line broadening, and partially collapsed or "hanging" sextets). In all four spectra, more than half of the spectral area is magnetically split and we surmise that, despite such relaxation effects, the samples are all below their superparamagnetic blocking temperature at room temperature on the time scale of Mössbauer spectroscopy (≈1 ns). Magnetic relaxation effects are most pronounced in the NF1-spectrum (Figure 5a), which is a superposition of a superparamagnetic doublet (13%) and a sextet with broad lines. Relaxation effects are least pronounced in the NF2-spectrum (Figure 5b), which features a sextet with relatively sharp lines. It is noticeable that samples NF1 and NF2, which have similar TEM particle sizes, show very different magnetic relaxation. The longer magnetic relaxation times of NF2 are likely to be a consequence of the core arrangement within the nanoflowers (showing crystalline correlation length of ca. XRD size = 15 nm) compared to NF1 (9 nm) and is in agreement with previous observations that exchange interaction between surface atoms of aggregated nanoscale cores tends to suppress superparamagnetic relaxation.[56] NF3 and NF4 display almost identical relaxation (Figure 5c,d), which is especially interesting as they are comprised of quite different core and nanoflower sizes. This suggests the presence of much stronger interactions between the cores in the particle in NF3 compared to the larger polystyrene-embedded NF4 nanoflowers. Furthermore, the smaller cores in NF3 seem to interact more strongly than the larger cores in NF1. These results perfectly match our previous observations by HRTEM of cores densely packed in a solid sphere in NF3, compared to the loosely packed cores in NF1 (Figure 1). RT Mössbauer spectra support the hypothesis that flower-shaped nanoparticles of larger core size show reduced relaxation, and that an increased density of cores within the nanoflowers suppresses magnetic relaxation.

The mean isomer shift ("center") of the Mössbauer spectra relative to α-Fe is sensitive to the oxidation state of iron and allows for the quantification of the magnetite-maghemite content in the samples via the method described by Fock, Bogart et al.[57] The method is applicable to room-temperature spectra, but in case of spectra obtained at low temperature (18 and 80 K) (see Figure S4, Supporting Information), where relaxation effects are negligible and hence spectral lines sharper, the mean isomer shift can be obtained with less uncertainty (see Table S3, Supporting Information).[57] From this, we find that the percentages of Fe atoms in the form of magnetite in the samples are, 9 ± 2, 5 ± 3, 5 ± 2, and 3 ± 2 for NF1, NF2, NF3 and NF4 respectively, i.e. the samples are essentially maghemite. This means that the differences found in XRD lattice parameters are related to differences in the degree of structural order rather than to variation in magnetite/maghemite content.

Indeed, the largest lattice parameters correspond to NF1 and NF3, which also have the smallest core sizes and therefore larger fraction of surface atoms. Samples NF1 and NF3 were synthesized in the presence of dextran and citric acid that absorb on the core surface hampering the contact between adjacent cores.

The static magnetic properties were evaluated for all samples in liquid suspensions by DC magnetometry measurements at 300 K (**Figure 6**a). The effective magnetic size of the nanoflowers was obtained by modeling the $M(H)$ curve using the classical superparamagnetic Langevin function (see Supporting Information). These results are presented in **Table 2**. The magnetization curve of NF3 was fitted by a monomodal size distribution indicating that the cores have a uniform size with a single effective magnetic diameter of 16 nm. In the case of NF2, we observe a better fit to the experimentally measured $M(H)$ curve when our Langevin fit uses a bimodal size distribution. This gives two effective magnetic sizes; the first size of 25 nm has a very narrow size distribution of 0.1 while the second distribution has a much smaller size of 2 nm. In addition, this sample has high saturation-magnetization value and high initial susceptibility, both of which are due to the high fraction of particles with large magnetic sizes. Likewise, for NF1 and NF4, the $M(H)$ curves are better fitted with a bimodal size distribution. Both samples consist magnetically of two particle fractions with different magnetic diameters although inspection of the initial magnetization slope at low fields suggests that NF4 contains a larger fraction of larger sizes, which justifies the larger saturation magnetization. It should be noted that in many cases the derived effective magnetic sizes cannot directly be compared with the particle size determined by TEM or the crystal sizes determined by XRD.

The effective magnetic size modeled by the Langevin function is further a distribution of magnetic moments projected on a sphere. This sphere is usually smaller than the TEM size due to the surface dead layer.[58] For the special case of flower-shaped nanoparticles consisting of packed cores forming a multi-core structure, this sphere is smaller than the flower TEM sizes but larger than the core size for all the systems in this work. The interactions between the cores can lead to magnetic sizes that are larger than the crystal sizes measured by XRD. DC magnetometry data indicates that the nanoflowers are, in general, better fitted using a bimodal size distribution and indicates that size and shape of the cores varies across the nanoflower, as revealed by DF images (Figure 2). However, for NF3, whose cores are smaller and randomly distributed, the best fit of the magnetization curve is with a monomodal distribution.

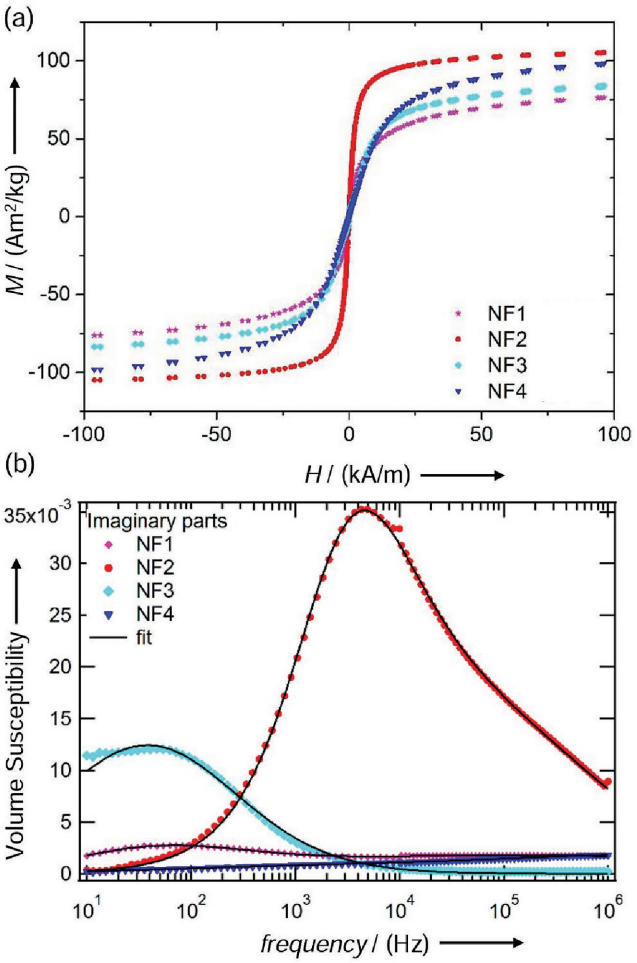

Figure 6. Magnetic characterization at 300 K. (a) DC magnetization curves and (b) AC susceptibility vs frequency (imaginary part) of all flower-shaped nanoparticles in suspension (The solid line shows best fit with generalized Debye model).

Dynamic magnetic properties of the nanoflowers were characterized by AC susceptibility (ACS) vs frequency and temperature. These measurements were conducted on samples in both dispersed and immobilized states (See Figure 6b

Table 2. Parameters determined through magnetic characterization: saturation magnetization (M_s) and magnetic size ($d_{c,1}$ and $d_{c,2}$) by DC magnetometry,[a)] hydrodynamic size (ACS $D_{h,1}$ and ACS $D_{h,2}$) by ACS versus frequency (Debye model and multi-core extended model, respectively),[b)] and anisotropy constant (K_{ACvT}) by ACS versus temperature.[c)]

Sample	M_s (σ) [A m^2 (kg Fe)$^{-1}$]	$d_{c,1}$ (σ) [nm]	$d_{c,2}$ (σ) [nm]	β[d)]	ACS $D_{h,1}$ (σ) [nm]	ACS $D_{h,2}$ [nm]	K_{ACvT} [x 10^4 J m^{-3}]
NF1	93 (3)	4.3 (0.52)	18.7 (0.24)	0.44	251 (116)	180	2.5 (2)
NF2	112 (3)	2 (0.8)	24.7 (0.08)	0.74	54 (11)	45	2.3 (2)
NF3	103 (3)	–	16 (0.1)	–	247 (5)	175	1.8 (2)
NF4	119 (4)	2.5 (0.56)	13.6 (0.03)	0.69	–	–	4.0 (3)

[a)]Measurements performed in the dried samples (powder form); [b)]Measurements performed in both colloidal dispersion and immobilized samples; [c)]Measurements performed in the colloidal dispersion; [d)]β is the normalized fraction of the larger particle size distribution.

and Supporting Information). An ACS hydrodynamic diameter was calculated using the generalized Debye model (ACS $D_{h,1}$)[59] and the multi-core extended model (ACS $D_{h,2}$)[60] as summarized in Table 2. NF1 shows a weak maximum of the imaginary part at ≈80 Hz caused by Brownian rotation. The gradual decay of the real part of both dispersed and immobilized particles (Figure S5, Supporting Information) indicates a wide distribution of relaxation times. This is further supported by the constant imaginary part of the sample with immobilized nanoparticles, which is superimposed by the weak Brownian relaxation peak for the dispersed sample, which indicates that the majority of particles relax via the internal Néel mechanism. Using the generalized Debye model we obtain an average hydrodynamic diameter of 251 nm whilst this value decreases to 180 nm using the multi-core extended model, which is comparable to the value measured by DLS (192 nm). However, for NF2, a pronounced peak in the imaginary part at 5 kHz clearly indicates Brownian rotation with a Néel contribution of 10–20%. The linear decay of the real part of the immobilized sample when plotted vs. ln(f) indicates a wide distribution of Néel relaxation times, i.e. anisotropy energies.[61] Modeling these data using the generalized Debye model yields a mean hydrodynamic diameter of 54 nm and 45 nm using the Debye and multi-core extended model, respectively, both of which are in good agreement with the value measured in DLS measurements (51 nm). For NF3, the Brownian relaxation peak in the out-of-phase component of the AC susceptibility is at about 50 Hz with a shallow shoulder toward low frequencies indicating agglomeration. The low-frequency relaxation disappears when the nanoparticles are diluted. The real part levels off at high frequencies together with a nearly zero imaginary part which can be caused by intra-potential-well contributions[62–64] and by nanoparticles that follow the excitation field via the internal Néel mechanism with relaxation times well below 1 μs, i.e. moments can follow the sinusoidal excitation field without phase lag up to at least 1 MHz frequency. In this case, the values of average hydrodynamic diameters are 247 nm using the generalized Debye model and 175 nm using the multi-core model, the latter being more comparable to the value measured by DLS (158 nm). Interestingly, for NF4, we observed almost no difference between immobilized and dispersed particles (Figure S5, Supporting Information), which is typical for a nanoparticle system that undergoes 100% Néel relaxation. The Néel relaxation peak in the out-of-phase component is in the range of several MHz, i.e. outside the measurement window, since the MNP dynamics are dominated by the Néel mechanism, no information can be obtained on their hydrodynamic size.

ACS vs temperature was performed at low temperature (5–260 K) to derive an effective anisotropy constant (K) for the nanoflowers that is presented in Table 2. The in-phase component (χ') of the AC susceptibility approaches a frequency independent value as $T \rightarrow 0$, corresponding to the intra-potential-well response of the particle moments.[64] Using the low-T χ'-values, we determined the effective anisotropy constant values (K) of: 2.5 (2), 2.3 (2), 1.8 (2) and 4.0 (3) ($\times 10^4$ J m^{-3}) for NF1, 2, 3 and 4 respectively (see Figure S6 and Table S6 in the Supporting Information for details). Interestingly, we find that the nanoflower system with the largest anisotropy constant (NF4), is also the only system for which blocking temperature is close to room temperature (see Figure S6b Supporting Information). This implies that the embedded nanoflowers might also display some order on the polystyrene sphere, as described for some magnetic nanocrystals forming close-packed structures, which showed an increase in anisotropy.[65] Conversely, NF1-3 are clearly blocked in the temperature range 5–390 K for $f < 1000$ Hz.

2.4. Description of the Structure of a Nanoflower

The results obtained for the core and particle size for each flower-shaped system through different characterization techniques are summarized in **Figure 7**. The size of the cores range from 4 to 15 nm and the size of the particle range from 50 to 250 nm. Differences in both, core and particle size reflect the complicated nature of these materials. In general, the size calculated via XRD (D_{XRD}) is larger than that estimated via HRTEM (D_{HRTEM}). This reflects the multi-core nature of the samples, whose cores are fused to a greater or lesser degree to form flower-shaped structures.

In those cases with high values of $D_{XRD} \approx D_{HRTEM} > 10$ nm (NF2 and NF4), significant coalescence of the cores is detected, which justifies the highest M_s values displayed by those

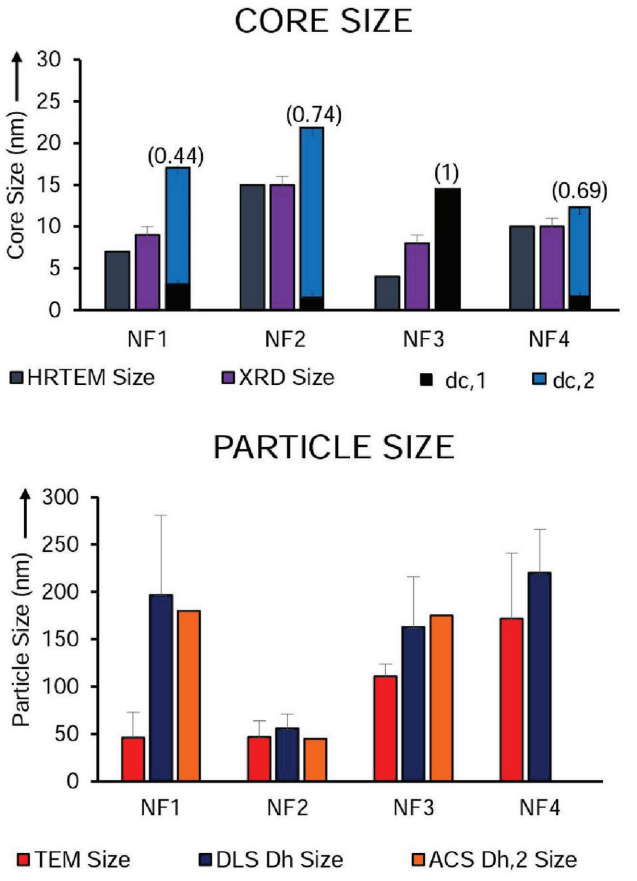

Figure 7. Core (above) and particle size (below) of the flower-shaped nanoparticles as determined by structural and magnetic means, according to Table 1 and 2. Between brackets, β is included, the normalized fraction of the larger particle size distribution as determined by DC magnetometry.

samples. For all cases, the magnetic size deduced from our Langevin based modeling ($d_{c,2}$) is larger than both D_{HRTEM} and D_{XRD} suggesting the presence of interactions between cores and thus shedding light on the collective behaviour within the nanoflowers. For samples that possess larger effective magnetic size, such as NF2, we observe both an increase in χ_0 in the RT magnetization curve and an increase in magnetic relaxation times, as demonstrated by a ^{57}Fe Mössbauer spectrum sextet with relatively sharp lines at RT. Samples with a more reduced effective magnetic size (NF1, NF3, and NF4) have a visibly smaller χ_0 in the magnetization curve and also have reduced relaxation, i.e. less Mössbauer spectral area within the sextet. We surmise that when there is a close contact between cores within a particle, the continuity of the crystal orientation is ensured favoring magnetic ordering across the interfaces. This is indeed the case of the structures previously called nanoflower that showed one order of magnitude higher heating rates than the specific absorption rate (SAR) reported for conventional 11 nm maghemite nanoparticles in the same field exposure conditions.[42]

Regarding the particle size, samples in which DLS $D_h \gg D_{TEM}$ either contain a large amount of coating and water hydration on their surface or have collective behaviour between the particles (interparticle interactions, i.e. dipolar interactions). The former can be detected by IR spectroscopy and quantified by thermogravimetric analysis (see Figure S7, Supporting Information). This is the case of NF1 and NF2 that have similar D_{TEM} particles sizes and therefore similar surface-area-to-volume ratios but they have very different organic content (80% for NF1 and 20% for NF2). Consequently, DLS D_h size of NF1 is much larger than D_{TEM} and hence indicates a larger amount of dextran present on the nanoparticles surface compared to NF2. The existence of organic component is already supported by the XRD data displayed in Figure 4, where the hump that appears for NF1 at low angles (below 25°) is consequence of such contribution.

The collective behaviour that is related to interparticle interactions can be detected by AC susceptibility. All samples have comparable hydrodynamic sizes obtained by both DLS D_h and ACS $D_{h,2}$ (modeled by the extended multi-core function), confirming that dipolar interactions between particles are minimized in these colloids and explaining the observed long-term stability. In the case of NF3, dipolar interactions between particles may cause the formation of chains and explain the observed change in AC susceptibility spectrum with sample dilution.

Comparing core and particle size from the magnetic measurements, i.e. effective magnetic size ($d_{c,2}$) and hydrodynamic size ACS $D_{h,2}$, we have identified three different flower-shaped multi-core systems. For NF2, the effective magnetic size tends to approach the nanoflower size (ACS $D_{h,2}/d_{c,2} \approx 1.8$) indicating strong magnetic interactions between cores within a particle. Cores inside the nanoflower are not only oriented but also in close contact leading to exchange interactions, and therefore collective magnetic behaviour. For NF1 and NF3, the effective magnetic size is much smaller than the flower size (ACS $D_{h,2}/d_{c,2} \approx 10$) indicating less contact between cores, which in NF1 may be loosely packed within the flower. Much more complicated is the case of NF4, where nanoflowers were embedded onto polymeric spheres creating a superstructure. The relatively small nanoflower size, high anisotropy constant, but low blocking temperature of NF4 suggests that the finite size of the nanoflower systems is one of the key parameters that dictates their Néel relaxation properties.

2.5. Toward the Standardization: Comparison of the Nanoflower Synthesis

Differences between the systems (NF1-4) are directly related to the various synthetic routes (Strategy 1–4), in terms of formation mechanism (clustering and coalescence, clustering and recrystallization or Ostwald ripening) and free energy involved in the process and experimental conditions (pH, surface charge, temperature, pressure and time). **Table 3** provides a comparison of the key parameters determining the core assembly and their implication on the resulting unique colloidal and

Table 3. Comparison resulting from the analysis of the synthesis and characterization of the flower-shaped iron oxide nanoparticles.

General comparison		NF1	NF2	NF3	NF4
Synthesis strategies	Reaction	One step	Multistep	One step	Multistep
	Production Yield	Large	Moderate	Moderate	Low
	Mechanism	Clustering	Clustering + Recrystallization	Clustering + Coalescence	Clustering + Coalescence + Embedding
Colloids Flower-shaped magnetic nanoparticles	Interaction between cores	Low	High	Moderate-high	Moderate
	Interaction between particles	Low	Low	Moderate	High
Advantages		Long-term colloidal stability	Large saturation magnetization and large susceptibility	Large magnetic moment per particle	Magnetic superstructure with high anisotropy
Disadvantages		Wide particle size distribution	High-energy-consuming synthesis		Reduced long-term colloidal stability

magnetic properties. Additionally, from the synthesis standardization point of view, the advantages and disadvantages of each strategy are highlighted. NF1 offers the possibility of large production and allows the synthesis of larger batches in aqueous media. The nanoflowers are directly stabilized by the presence of dextran in the reaction media and present long-term stability for at least 500 days (Figure 3). The use of polyol media provides great control over core aggregation, which yields multicore structures that consist of cores in more or less contact (NF2 and NF3) depending on the synthesis conditions. Furthermore, polyol media allows the use of higher reaction temperatures (200 °C) leading to fused cores within a particle e.g. NF2. However, in NF3, the use of an extra additive (sodium citrate) facilitates the final dispersion of the particles in aqueous media and hampers the aggregation of the cores in a similar way to dextran in the synthesis of NF1. Aqueous suspensions of these systems present long-term stability for at least 200 days (Figure 3). However, it should be taken into account that high temperatures over long time as applied in the synthesis of NF2 and NF3 (10–12 h) generally lead to high-energy consumption (costs). Moreover, one-pot syntheses such as those followed to obtain NF1 and NF3 have advantages compared to the conventional step-wise reactions as used for NF2 and NF4.

3. Conclusion

Analysis of the self-assembly process conducted in this work leads to the formation of flower-shaped nanoparticles with properties and possible applications that differ strongly from single-core particles of similar size and corresponding bulk material. Synthesis reagents and experimental conditions are key factors to control the core and particle sizes, as well as intra- and interparticle interactions, i.e. between cores and particles in suspensions. The results obtained from different characterization techniques have been brought together to obtain a self-consistent picture that describes how structural and magnetic properties are interrelated in those systems. Controlling self-assembly of magnetic multi-core nanoparticles allow the design of optimal magnetic properties of the colloids as a function of its specific application.

4. Experimental Section

Synthesis of Flower-Shaped Nanoparticles—Sample NF1: Dextran coated iron oxide nanoparticles were synthesized by partial oxidation of $Fe(OH)_2$ and green rust. Typically, KNO_3 2 M, NaOH 2 M and dextran solution (5 mL) were added to MilliQ water (25 mL) and degassed by bubbling with nitrogen.[66] Under stirring, $FeSO_4{\cdot}7H_2O$ 0.3 M (8.3 mL) were slowly added to the initial solution resulting in the precipitation of gel-like $Fe(OH)_2$ and green rust. To accelerate the oxidation process the solution was heated to 90 °C for 4 h. Finally, the particles were purified by dialysis and centrifugation resulting in a stable colloidal dispersion.

Synthesis of Flower-Shaped Nanoparticles—Sample NF2: Dextran coated γ-Fe_2O_3 NPs were synthesized by a polyol method adapted from Lartigue et al.[24] In a typical procedure of $FeCl_3{\cdot}6H_2O$ (4 mmol) and $FeCl_2{\cdot}4H_2O$ (2 mmol) were dissolved in diethylene glycol (DEG) and N-methyldiethanolamine (NMDEA) (1:1 v/v, 80 g) at room temperature. The solution was stirred for 1 h. Separately, NaOH (16 mmol) was dissolved in the polyol mixture (40 g) and subsequently added to the iron chlorides solution. The mixture was then stirred for 3 h at room temperature. The temperature of the solution was then elevated to 210 °C using a ramp temperature of 2 °C min^{-1}. Once the temperature reached 210 °C, the solution was stirred for 12 h at the same conditions. Then the mixture was cooled down to room temperature. The nanoparticles were separated magnetically and washed four times with a mixture of ethanol and ethyl acetate (1:1, v/v) and once with 10% nitric acid. Then, a, aqueous solution (20 mL) containing iron (III) nitrate (8.25 g) was added to the NPs, and the mixture was heated to 80 °C for 45 min. After cooling down to room temperature, the nanoparticles were washed again, once with 10% nitric acid, once with ethanol and once with acetone. The sediment was dried for 2 h at 40 °C. Finally, the particles were re-dispersed in water (20 mL). Coating with dextran was carried out by high-pressure homogenization process.[67]

Synthesis of Flower-Shaped Nanoparticles—Sample NF3: γ-Fe_2O_3 NPs were synthesized by a polyol-mediated method previously reported by Liu J et al.[46] Typically, iron chloride (2.702 g) was dissolved in ethylene glycol (EG) (47 mL) under magnetic stirring. Then trisodium citrate (Na_3Cit) and sodium acetate (NaAc) was gradually added under mild heating and magnetic stirring. The final concentration of the reagents is: [$FeCl_3$] = 0.21 M, [Na_3Cit] = 0.05 M, and [NaAc] = 0.76 M. The mixture was stirred vigorously for 30 min and then sealed in a Teflon-lined Aluminum autoclave (125 mL capacity) and maintained at 200 °C for 10 h. After cooling down to room temperature, the black product was washed 3 times with distilled water by centrifugation.

Synthesis of Flower-Shaped Nanoparticles—Sample NF4: Iron oxide nanoparticles were produced by a reduction method that was based on reports in the literature.[51,52] In brief, iron acetylacetonate (9.43 g) and sodium borohydride (5.04 g) were added to a mixture of H_2O and THF (400 mL), as detailed in the literature report. The mixture was stirred overnight at 150 rpm. The black precipitates were collected by centrifugation and rinsed with deionized water. A solution consisting oleic acid (67 mL) in THF (533 mL) was added to the suspension and shaken for 2 h. The nanoparticles were precipitated with ethanol and collected by centrifugation, followed by redispersion in chloroform (10 mL). In solution 1, the particle solution (6.25 mL) was added gently to chloroform (20.25 g). In the case of sample NF4, poly (styrene) (500 mg) is previously dissolved in the chloroform) in a 25 ml glass vial; In solution 2, poly(styrene-*alt*-maleic acid)-sodium salt solution (13.96 g) and sodium lauryl sulphate (3.35 g) solution is added to DIW (1 L). Solution 1 is added to solution 2 (53 mL) in a 100 mL Erlenmeyer flask by ultra sonication for 15 min with ultrasonic probe Amplitude 40% in an ice bath. Chloroform was evaporated under reduced pressure. The solution is centrifuged 2000 rpm for 5 min. The supernatant is collected and the precipitate is discarded.

Characterization—TEM Analysis: An FEI Tecani G2 T20 transmission electron microscope (TEM) equipped with LaB_6 electron gun and operated at 200 kV was used in this study. TEM sample preparation was done by putting a droplet of the diluted suspension in water on holey carbon film coated TEM Cu grid, and then letting it dry in air at room temperature. Images were acquired in bright field (BF) imaging mode and evaluated using DigtalMicrograph software. The method used for measuring the diameter of both the multi-core particles and iron oxide nanocrystals is described as follows. First, a circle was drawn on the image in DigitalMicrograph. Then the circle was adjusted so that its size is as small as possible but still covers a single particle or nanocrystal to be measured. The diameter of this circle is subsequently taken as the diameter of the particle. Structure of individual flower particles were also analyzed by selected area electron diffraction (SAED), bright field and dark field (DF) imaging and high-resolution transmission electron microscopy (HRTEM) imaging.

Characterization—X-Ray Powder Diffraction Analysis: Chemical composition and core crystal structure were confirmed along with the determination of crystal size by X-ray powder diffraction (XRD) experiments performed at room temperature (RT) in a D8 Advance diffractometer, using a Cu Kα radiation with Bragg–Brentano geometry. The samples in solution were freeze-dried for the subsequent XRD measurement, which were placed on a Si single-crystal low-background

sample holder that was rotated at 15 rpm to improve random orientation of crystallites, while minimizing the effect of preferred orientations within the sample. The acquired data were analyzed through the Rietveld refinement method using the FullProf Suite software.[68] To describe the peak profiles, a Thompson–Cox–Hastings function was chosen to guarantee a good description of the width excess to extract the average crystal size of the samples. The figures of merit are acceptable for fine particle systems. To fully account for peak broadening, it is necessary to include some lattice strain contribution (ε). These ε values lie around 50 ‰ and it is a sign of crystal defects, especially on particle surfaces.

Characterization—Mössbauer Spectroscopy: The iron oxide phase was identified using room temperature ^{57}Fe Mössbauer spectroscopy. Approximately 50 mg of each sample was mixed with ca. 200 mg sucrose in a pestle and mortar to form a paste, and then flattened within a coin shaped absorber. Spectra were recorded at room temperature in transmission geometry using a ^{57}Co source in a Rh matrix, using a W302 spectrometer and W202 detector, both from SEECo (Minneapolis, USA). Low-temperature Mössbauer measurements were recorded also in transmission geometry with a source of ^{57}Co in Rh, but using a close cycle helium refrigerator from APD Cryogenics and a spectrometer from Wissel GmbH operated in the constant acceleration mode. Best fits to the spectra have been obtained using a model independent analysis to obtain the best fit (lowest χ^2) to the observed spectra as described by Fock et al.[57,69] In this way, spectra have been fit using Voigtian lineshapes to represent a Gaussian distribution of Lorentzian hyperfine fields, which we have used to account for a distribution of particle volumes and shapes as well as reduced hyperfine fields related to relaxation effects.

Characterization—Infrared Spectroscopy: FTIR was used to detect and identify the presence of coating on the nanoparticle surface using a Bruker IFS 66V-S in the range of 2000–250 cm^{-1}. The samples were prepared by diluting the dried powder in KBr at 2% by weight and pressing it into a pellet.

Characterization—DLS Analysis: Colloidal properties were analyzed by DLS. Measurements were carried out in an instrument NICOMP Submicron Particle Sizer Model 370. The measured angle was 90°, a wavelength of 632.8 nm was used, the temperature was set to 30 °C and the sample was diluted with MilliQ water to 5×10^{-3} M iron. Then, 300 µL of the diluted sample were measured three times using a run time of 5 min each. The data analysis was performed with the 2nd cumulant method, and the Gaussian distributions are intensity-weighted. For the *Z*-potential measurements, a Zetasizernano ZS, Malvern instrument was used and data were evaluated by the Smoluchowski model. The measurements were recorded at 25 °C. 700 µL of each dilution (which was likewise diluted to 5×10^{-3} M iron with MilliQ water) was pipetted into a folded capillary cell (DTS 1062) and then measured two times with 20 runs per measurement.

Characterization—DC Magnetometry Measurements: DC magnetization measurements have been performed at 300 K on liquid samples using a Magnetic Property Measurement System (MPMS)-XL from Quantum Design (USA). 30 µL of the suspensions were filled into a polycarbonate (PC) capsule. The measurement system was demagnetized before measurement and the magnetic moment was recorded within a magnetic field range of ± 4.9 T. Data evaluation was performed by subtracting the empty sample holder signal (measured in a previous measurement) and the water contribution (using the susceptibility $\chi_{water} = -9 \times 10^{-6}$). The sample magnetization M' was calculated using the measured magnetic moment and the suspension volume $M' = Magn.moment/V$, and with the iron concentration c_{Fe}, the magnetization $M = M/c_{Fe}$ in terms of A m^2 (kg Fe)$^{-1}$ was obtained. Fitting the virgin curve by a bimodal model (see Section 4 of the Supporting Information) provides magnetic core size.

Characterization—AC Susceptibility Measurements: The altering current susceptibility (ACS) measurements on nanoflower samples were performed at room temperature utilizing two custom-built susceptometers by TU Braunschweig.[70] The frequency was swept from 10 Hz–10 kHz and from 200 Hz–1 MHz in logarithmical steps. The amplitudes of the excitation field amounted to 567 µT and 90 µT, respectively. Measurements have been carried out on suspensions of original and 10-fold diluted concentration and on freeze-dried reference samples, i.e. samples with immobilized nanoparticles of original concentration with a sample volume of 150 µL each. A blank measurement was performed prior to the sample measurement and subtracted from the acquired spectra of the sample. The systems are calibrated with a Dy_2O_3 powder sample with defined volume susceptibility. We also used two AC susceptometers at Acreo, the first one is the commercially available DynoMag system with excitation frequencies up to 500 kHz and a prototype high-frequency AC susceptometer with excitation frequencies up to 10 MHz. In the DynoMag system the excitation field is 5 mT and 30 µT in the high-frequency AC susceptometer. Also in these AC susceptometers the calibration was performed using the paramagnetic Dy_2O_3 material.

Supporting Information

Supporting Information is available from the Wiley Online Library or from the author.

Acknowledgements

This work was partially supported by the European Commission Framework Program 7 (NanoMag project, NO 604448) and by the Spanish Ministry of Economy and Competitiveness (Mago project, No. MAT2014-52069-R). H.G. has carried out this work while undertaking a doctoral programme on Advanced Chemistry at the Complutense University of Madrid.

Conflict of Interest

The authors declare no conflict of interest.

Keywords

colloids, magnetic properties, magnetite, nanoflowers, self-assembly

Received: March 9, 2017
Revised: April 4, 2017
Published online:

[1] P. Xing, Y. Zhao, *Adv. Mater.* **2016**, *28*, 73049.
[2] S. Pan, L. He, J. Peng, F. Qiu, Z. Lin, *Angew. Chem.* **2016**, *30*, 8459.
[3] M. Volkmann, M. Meyns, R. Lesyuk, H. Lehmann, C. Klinke, *Chem. Mater.* **2016**, *29*, 726.
[4] V. Sayevich, B. Cai, A. Benad, D. Haubold, L. Sonntag, N. Gaponik, V. Lesnyak, A. Eychmüller, *Angew. Chem., Int. Ed.* **2016**, *55*, 6334.
[5] J. K. Stolarczyk, A. Deak, D. F. Brougham, *Adv. Mater.* **2016**, *28*, 5400.
[6] Z. Nie, A. Petukhova, E. Kumacheva, *Nat. Nanotechnol.* **2010**, *5*, 15.
[7] J. J. De Yoreo, P. U. Gilbert, N. A. Sommerdijk, R. L. Penn, S. Whitelam, D. Joester, H. Zhang, J. D. Rimer, A. Navrotsky, J. F. Banfield, *Science* **2015**, *349*, aaa6760.
[8] M. Ocaña, R. Rodríguez-Clemente, C. J. Serna, *Adv. Mater.* **1995**, *7*, 212.
[9] M. Raju, A. C. Van Duin, K. A. Fichthorn, *Nano letters* **2014**, *14*, 1836.
[10] C. Frandsen, B. A. Legg, L. R. Comolli, H. Zhang, B. Gilbert, E. Johnson, J. F. Banfield, *CrystEngComm* **2014**, *16*, 1451.
[11] M. B. Bannwarth, S. W. Kazer, S. Ulrich, G. Glasser, D. Crespy, K. Landfester, *Angew. Chem., Int. Ed.* **2013**, *52*, 10107.

[12] B. Ingham, T. H. Lim, C. J. Dotzler, A. Henning, M. F. Toney, R. D. Tilley, *Chem. Mater.* **2011**, *23*, 3312.
[13] S. Dutz, *IEEE Trans. Magn.* **2016**, *52*, 1.
[14] D. Serantes, K. Simeonidis, M. Angelakeris, O. Chubykalo-Fesenko, M. Marciello, M. P. Morales, D. Baldomir, C. Martinez-Boubeta, *J. Phys. Chem. C* **2014**, *118*, 5927.
[15] U. Jeong, X. Teng, Y. Wang, H. Yang, Y. Xia, *Adv. Mater.* **2007**, *19*, 33.
[16] L. Gutiérrez, R. Costo, C. Grüttner, F. Westphal, N. Gehrke, D. Heinke, A. Fornara, Q. Pankhurst, C. Johansson, S. Veintemillas-Verdaguer, M. P. Morales, *Dalton Trans.* **2015**, *44*, 2943.
[17] M. A. Gijs, F. Lacharme, U. Lehmann, *Chem. Rev.* **2009**, *110*, 1518.
[18] J. Nowak, F. Wiekhorst, L. Trahms, S. Odenbach, *J. Phys.: Condens. Matter* **2014**, *26*, 176004.
[19] M. Mahmoudi, H. Hofmann, B. Rothen-Rutishauser, A. Petri-Fink, *Chem. Rev.* **2011**, *112*, 2323.
[20] S. Laurent, D. Forge, M. Port, A. Roch, C. Robic, L. Vander Elst, R. N. Muller, *Chem. Rev.* **2008**, *108*, 2064.
[21] D. Eberbeck, C. L. Dennis, N. F. Huls, K. L. Krycka, C. Gruttner, F. Westphal, *IEEE Trans. Magn.* **2013**, *49*, 269.
[22] C. Grüttner, K. Müller, J. Teller, F. Westphal, *Int. J. Hyperthermia* **2013**, *29*, 777.
[23] S. Dutz, M. Kettering, I. Hilger, R. Müller, M. Zeisberger, *Nanotechnology* **2011**, *22*, 265102.
[24] L. Lartigue, P. Hugounenq, D. Alloyeau, S. P. Clarke, M. Lévy, J.-C. Bacri, R. Bazzi, D. F. Brougham, C. Wilhelm, F. Gazeau, *ACS Nano* **2012**, *6*, 10935.
[25] C. Alexiou, W. Arnold, R. J. Klein, F. G. Parak, P. Hulin, C. Bergemann, W. Erhardt, S. Wagenpfeil, A. S. Luebbe, *Cancer Red.* **2000**, *60*, 6641.
[26] N. C. Bigall, C. Wilhelm, M.-L. Beoutis, M. García-Hernandez, A. A. Khan, C. Giannini, A. Sánchez-Ferrer, R. Mezzenga, M. E. Materia, M. A. Garcia, *Chem. Mater.* **2013**, *25*, 1055.
[27] G. Zoppellaro, A. Kolokithas-Ntoukas, K. Polakova, J. Tucek, R. Zboril, G. Loudos, E. Fragogeorgi, C. Diwoky, K. Tomankova, K. Avgoustakis, *Chem. Mater.* **2014**, *26*, 2062.
[28] F. Mazuel, A. Espinosa, G. Radtke, M. Bugnet, S. Neveu, Y. Lalatonne, G. A. Botton, A. Abou-Hassan, C. Wilhelm, *Adv. Funct. Mater.* **2017**, *27*, 1605997.
[29] F. Ludwig, O. Kazakova, L. F. Barquín, A. Fornara, L. Trahms, U. Steinhoff, P. Svedlindh, E. Wetterskog, Q. A. Pankhurst, P. Southern, M. P. Morales, M. F. Hansen, C. Frandsen, E. Olsson, S. Gustafsson, N. Gehrke, K. Lüdtke-Buzug, C. Grüttner, C. Jonasson, C. Johansson, *IEEE Trans. Magn.* **2014**, *50*, 5300204.
[30] P. Mulvaney, W. J. Parak, F. Caruso, P. S. Weiss, *ACS Nano* **2016**, *10*, 9763.
[31] V. Schaller, G. Wahnström, A. Sanz-Velasco, P. Enoksson, C. Johansson, *AIP Conf. Proc.* **2010**, *1311*, 42.
[32] B. L. Frankamp, A. K. Boal, M. T. Tuominen, V. M. Rotello, *J. Am. Chem. Soc.* **2005**, *127*, 9731.
[33] R. A. Bohara, N. D. Thorat, S. H. Pawar, *RSC Adv.* **2016**, *6*, 43989.
[34] T. Sugimoto, E. Matijević, *J. Colloid Interface Sci.* **1980**, *74*, 227.
[35] F. Vereda, J. de Vicente, M. P. Morales, F. Rull, R. Hidalgo-Álvarez, *J. Phys. Chem. C* **2008**, *112*, 5843.
[36] G. A. Parks, *Chem. Rev.* **1965**, *65*, 177.
[37] M. A. Vergés, R. Costo, A. Roca, J. Marco, G. Goya, C. Serna, M. P. Morales, *J. Phys. D: Appl. Phys.* **2008**, *41*, 134003.
[38] Y. Luengo, M. P. Morales, L. Gutiérrez, S. Veintemillas-Verdaguer, *J. Mater. Chem. C* **2016**, *4*, 9482.
[39] M. Bautista, O. Bomati-Miguel, X. Zhao, M. P. Morales, T. Gonzalez-Carreño, R. P. de Alejo, J. Ruiz-Cabello, S. Veintemillas-Verdaguer, *Nanotechnology* **2004**, *15*, S154.
[40] H. Dong, Y.-C. Chen, C. Feldmann, *Green Chem.* **2015**, *17*, 4107.
[41] D. Caruntu, G. Caruntu, C. J. O'Connor, *J. Phys. D: Appl. Phys.* **2007**, *40*, 5801.
[42] J. Ge, Y. Hu, M. Biasini, W. P. Beyermann, Y. Yin, *Angew. Chem., Int. Ed.* **2007**, *46*, 4342.
[43] P. Hugounenq, M. Levy, D. Alloyeau, L. Lartigue, E. Dubois, V. r. Cabuil, C. Ricolleau, S. p. Roux, C. Wilhelm, F. Gazeau, *J. Phys. Chem. C* **2012**, *116*, 15702.
[44] W. Cai, J. Wan, *J. Colloid Interface Sci.* **2007**, *305*, 366.
[45] H.-L. Liu, S. P. Ko, J.-H. Wu, M.-H. Jung, J. H. Min, J. H. Lee, B. H. An, Y. K. Kim, *J. Magn. Magn. Mater.* **2007**, *310*, 815.
[46] J. Liu, Z. Sun, Y. Deng, Y. Zou, C. Li, X. Guo, L. Xiong, Y. Gao, F. Li, D. Zhao, *Angew. Chem.* **2009**, *121*, 5989.
[47] Q. Sun, Z. Ren, R. Wang, W. Chen, C. Chen, *J. Nanopart. Res.* **2011**, *13*, 213.
[48] Y. Sahoo, A. Goodarzi, M. T. Swihart, T. Y. Ohulchanskyy, N. Kaur, E. P. Furlani, P. N. Prasad, *J. Phys. Chem. B* **2005**, *109*, 3879.
[49] F. Vereda, M. P. Morales, B. Rodríguez-González, J. de Vicente, R. Hidalgo-Alvarez, *CrystEngComm* **2013**, *15*, 5236.
[50] C. Cheng, F. Xu, H. Gu, *New J. Chem.* **2011**, *35*, 1072.
[51] J. Sommertune, A. Sugunan, A. Ahniyaz, R. S. Bejhed, A. Sarwe, C. Johansson, C. Balceris, F. Ludwig, O. Posth, A. Fornara, *Int. J. Mol. Sci.* **2015**, *16*, 19752.
[52] V. Yathindranath, L. Rebbouh, D. F. Moore, D. W. Miller, J. van Lierop, T. Hegmann, *Adv. Funct. Mater.* **2011**, *21*, 1457.
[53] T. Yonezawa, K. Kamoshita, M. Tanaka, T. Kinoshita, *Jpn. J. Appl. Phys.* **2008**, *47*, 1389.
[54] H. Okudera, K. Kihara, T. Matsumoto, *Acta Crystallogr. Sect. B: Struct. Sci.* **1996**, *52*, 450.
[55] C. Pecharromán, T. Gonzalez-Carreno, J. E. Iglesias, *Phys. Chem. Miner.* **1995**, *22*, 21.
[56] C. Frandsen, S. Mørup, *Phys. Rev. Lett.* **2005**, *94*, 027202.
[57] J. Fock, L. K. Bogart, O. Posth, M. F. Hansen, Q. A. Pankhurst, C. Frandsen, *Hyperfine Interactions* **2016**, *237*, 1.
[58] M. P. Morales, S. Veintemillas-Verdaguer, M. Montero, C. Serna, A. Roig, L. Casas, B. Martínez, F. Sandiumenge, *Chem. Mater.* **1999**, *11*, 3058.
[59] S.-H. Chung, A. Hoffmann, K. Guslienko, S. Bader, C. Liu, B. Kay, L. Makowski, L. Chen, *J. Appl. Phys.* **2005**, *97*, 10R101.
[60] S. Bogren, A. Fornara, F. Ludwig, M. P. Morales, U. Steinhoff, M. F. Hansen, O. Kazakova, C. Johansson, *Int. J. Mol. Sci.* **2015**, *16*, 20308.
[61] F. Ludwig, T. Wawrzik, T. Yoshida, N. Gehrke, A. Briel, D. Eberbeck, M. Schilling, *IEEE Trans. Magn.* **2012**, *48*, 3780.
[62] M. Shliomis, V. Stepanov, *Adv. Chem. Phys.* **1994**, *87*, 1.
[63] F. Ahrentorp, A. P. Astalan, C. Jonasson, J. Blomgren, O. T. Mefford, M. Yan, J. Cuortais, J. F. Berret, J. Fresnais, O. Sandre, S. Dutz, R. Müller, C. Johansson, in *AIP Conf. Proc.* **2010**, *1311*, 213.
[64] P. Svedlindh, T. Jonsson, J. García-Palacios, *J. Magn. Magn. Mater.* **1997**, *169*, 323.
[65] D. Parker, I. Lisiecki, M. Pileni, *J. Phys. Chem. Lett.* **2010**, *1*, 1139.
[66] N. Gehrke, D. Heinke, D. Eberbeck, F. Ludwig, T. Wawrzik, C. Kuhlmann, A. Briel, *IEEE Trans. Magn.* **2015**, *51*, 1.
[67] M. Wabler, W. Zhu, M. Hedayati, A. Attaluri, H. Zhou, J. Mihalic, A. Geyh, T. L. DeWeese, R. Ivkov, D. Artemov, *Int. J. Hyperthermia* **2014**, *30*, 192.
[68] J. Rodríguez-Carvajal, *Comm. Powder Diffr. (IUCr). Newsletter* **2001**, *26*, 12.
[69] J. Fock, L. K. Bogart, D. Gonzalez-Alonzo, J. I. E. Martinez, M. F. Hansen, M. Varon, C. Frandsen, Q. A. Pankhurst, *Unpublished*.
[70] F. Ludwig, A. Guillaume, M. Schilling, N. Frickel, A. Schmidt, *J. Appl. Phys.* **2010**, *108*, 033918.

Formation mechanism of maghemite nanoflowers synthesized by polyol mediated process

Helena Gavilán*[†], Elena H. Sánchez[†], María E. F. Brollo[†], Laura Asín[‡], Katrine K. Moerner[§], Cathrine Frandsen[§], Francisco J. Lázaro[||], Carlos J. Serna[†], Sabino Veintemillas-Verdaguer[†], M. Puerto Morales[†] and Lucía Gutiérrez*[⊥].

[†]Department of Energy, Environment and Health, Instituto de Ciencia de Materiales de Madrid / CSIC (ICMM-CSIC), Madrid, Spain.

[‡]Institute of Materials Science of Aragón, Universidad de Zaragoza / CSIC and CIBER-BBN, Zaragoza, Spain.

[§] Department of Physics, Technical University of Denmark, 2800 Kongens Lyngby, Denmark.

[||]Departamento de Ciencia y Tecnología de Materiales y Fluidos, Universidad de Zaragoza, Zaragoza, Spain.

[⊥]Department of Analytical Chemistry, Fundación Instituto Universitario de Nanociencia de Aragón (INA), Universidad de Zaragoza and CIBER-BBN, Zaragoza, Spain.

KEYWORDS: Self-assembly, maghemite, multi-core particles, nanoflowers, magnetic hyperthermia, iron oxides.

ABSTRACT: Magnetic nanoparticles are being developed as structural and functional materials for use in diverse areas, including biomedical applications. Here, we report the synthesis of maghemite (γFe_2O_3) nanoparticles with distinct morphologies: single-core and multi-core, including hollow spheres and nanoflowers, prepared by the polyol process. We have used sodium acetate (NaAc) to control the nucleation and assembly process to obtain the different particle morphologies. Moreover, from samples obtained at different time steps during the synthesis, we have elucidated the formation mechanism of the nanoflowers: The initial phases of the reaction present a lepidocrocite (γFeOOH) structure, which suffers a fast dehydroxylation, transforming to an intermediate "undescribed" phase - possibly partly dehydroxylated lepidocrocite - that after some incubation time evolves to maghemite nanoflowers. Once the nanoflowers have been formed, a crystallization process takes place where the γFe_2O_3 crystallites within the nanoflowers grow in size (from ~11 to 23 nm), but the particle size of the flower remains essentially unchanged (~60 nm). Samples with different morphologies were coated with citric acid and their heating capacity in an alternating magnetic field was evaluated. We observe that nanoflowers with large cores (23 nm, controlled by annealing) densely packed (tuned by low NaAc concentration) offer five times enhanced heating capacity compared to the nanoflowers with smaller core sizes (15 nm), 4 times heating effect compared to the hollow spheres and 1.5 times compared to single-core nanoparticles (36 nm) used in this work.

INTRODUCTION

Through the polyol-mediated synthesis developed by F. Fievet, Lagier and Figlarz,[1] the formation of both noble metals and metal oxide nanocrystals has been widely reported, obtaining monodisperse systems thanks to the polyol acting as the surfactant of the as-synthesized particles, reducer and reaction media.[2] The first advantage of this procedure is that it allows the synthesis of hydrophilic particles that remain stable in aqueous media[3] and other polar solvents within one-step,[4] avoiding further coating steps required by other synthesis routes such us thermal decomposition of organometallic precursors. In addition, owing to the high dielectric constants of the polyols,[5] they are able to dissolve inorganic compounds used as reactants, and due to their relatively high boiling points, great crystallinity of the particles can be achieved.

Several examples of the synthesis of metal nanoparticles achieved by this procedure exist in the literature. Among others, functional materials such as Au–Pd colloidal nanoparticles for catalysis purposes[6] and Co nanorods for the development of new permanent magnets[7] have been recently synthetized. Besides noble metals, both the synthesis of single-core and multi-core magnetic nanoparticles[8] have been reported through polyol reduction, organizing colloidal magnetic cores into highly regular nanoparticles with tuned properties. Of special interest are iron oxide multi-core nanoparticles assembled in flower-shaped structures synthesized by polyols.[9] In comparison with the single-core counterparts, these flower-like nanoparticles have shown enhanced longitudinal and transverse relaxivities for magnetic resonance imaging (MRI) contrast generation[10] and enhanced specific absorption rate (SAR) values for magnetic hyperthermia due to hysteresis heating.[11] The interest on magnetite (Fe_3O_4) and maghemite (γ-Fe_2O_3) nanoparticles for biomedical applications,

both in diagnosis[12] and therapy,[13,14] relies on its biocompatibility[15,10] and non-toxicity,[16] its chemical stability, and the strong response when exposed to an external magnetic field.[17]

Assembly process and particle and core sizes are crucial characteristics that determine the magnetic properties of the colloid and therefore its optimal use for a given application.[18,19] In the present work, we have analysed the assembly process that leads to the formation of single-core and multi-core hollow and flower-like maghemite nanoparticles through the polyol process. We have also determined the experimental parameters that allow control of the core sizes within the nanoflowers. In detail, we have analysed the role of specific experimental conditions in the synthesis such as the presence of a precipitator (sodium acetate, NaAc) and an extra stabilizer (polyvinylpyrrolidone, PVP), and the aging time. Then, the consequences of the different morphologies and core sizes on the magnetic cooperative behaviour have been studied. Finally, some selected samples were coated with citric acid and the possible use of these particles for magnetic hyperthermia applications has been evaluated through specific loss power (SLP) measurements.

▪ EXPERIMENTAL SECTION

Materials. Ferric chloride hexahydrate ($FeCl_3 \cdot 6H_2O$, ≥ 98%, Sigma Aldrich), polyvinylpyrrolidone (PVP40, Sigma Aldrich), sodium acetate trihydrate ($NaAc \cdot 3H_2O$, ≥ 99%, Sigma Aldrich), ethylene glycol (EG, ≥ 99.5 %, Fluka) and citric acid ($C_6H_8O_7$, ≥ 99.5%, Sigma Aldrich) were obtained and used without any further treatment.

Synthesis of nanoparticles. The synthesis of iron oxide nanoparticles has been based on a previous work described in the literature,[13] but the experimental procedure and the concentration of NaAc and PVP have been varied. Typically, 2.62 mmol $FeCl_3 \cdot 6H_2O$ were dissolved with ultrasound in 109 mL ethylene glycol. Then, 140 mmol PVP40 were added slowly under vigorously magnetic stirring (>1000 rpm) and mild heating until completely dissolved. Then, 15.8–36.5 mmol of $NaAc \cdot 3H_2O$ were added to the solution. The mixture was sealed in a Teflon-lined autoclave (125 mL) and maintained at 200 °C for 0.5 – 48 h for solvothermal crystallization, following cooling inside oven. The precipitated solid product was washed with ethanol and distilled water through centrifugation several times.

Surface coating. For citric acid coating a standard procedure was used.[8,20] First, sample volume equivalent to 20 mg of Fe was adjusted to pH 2 and then dispersed in 13 mL of a solution of citric acid 0.1 M. Afterwards, the mixture was heated at 80 °C for 30 min. The solution was centrifuged and washed with distilled water. Finally the pH was adjusted first to 11 with KOH 1M and then to 7 with HNO_3 0.01 M.

Characterization. The particle sizes and morphologies were determined by transmission electron microscopy (TEM) with a JEM1010 microscope (JEOL, Peabody, USA) operating at 100 kV. Samples were prepared by placing a drop of the uncoated particles suspended in water onto a carbon coated copper grid and allowing it to dry at room temperature. The size distributions were determined by manual measurement of more than 100 particles using the public domain software ImageJ.

The crystal structure was identified by X-ray diffraction (XRD) performed on freeze-dried powders in an X'pert PRO diffractometer from Panalytical with a Johansson monochromator and using Cu K_α radiation (λ= 1.5406 Å). The patterns were collected within a 2θ range of 10°-90° at a scan rate of 0.04°/min. The crystallite size, d_{XRD}, of the maghemite samples was determined by Scherrer's formula, using the (311) diffraction line. The presence of the coating and the phase evolution was also confirmed by Fourier transform infrared spectroscopy (FTIR) in the range of 4000-250 cm^{-1} by use of a Bruker (USA) IFS 66VS. The samples for FTIR were prepared diluting the dried powder in KBr at 2% by weight and pressing it into a pellet.

Colloidal properties were studied in a Zetasizer Nano S, from Malvern Instruments (UK). The hydrodynamic size, D_h, was determined by Dynamic Light Scattering (DLS) and the zeta potential was measured as a function of pH at 25 °C, using HNO_3 and KOH to change the pH of the suspensions. D_h is given as the intensity-weighted and number-weighted mean values to compare to the TEM mean values.

For the magnetic characterization, the samples were measured in powder form after drying in an inox-coated oven at 50 °C. After accurately weighing a mass of ≈10 mg, the powder was filled into polycarbonate capsules and immobilized with cotton wool. Hysteresis loops were measured in a Vibrating Sample Magnetometer (MLVSM9, MagLab 9T, Oxford Instruments, UK) at 5 and 290 K in fields up to 4000 kA/m at a field change rate of 240 kA/(m·min) after saturating the sample in a 4000 kA/m field. AC susceptibility measurements were performed in a Quantum Design (USA) MPMS-XL SQUID magnetometer using the same capsules described above. Data was collected in the temperature range between 2 and 300 K using magnetic field amplitude of 0.41 mT and frequency of 11 Hz. Additional measurements at 0.11 and 110 Hz were performed in selected samples.

In order to further elucidate the composition of the samples and their magnetic properties, ^{57}Fe Mössbauer spectra were obtained in transmission geometry on freeze-dried samples at 18, 80 and 295 K, using a constant acceleration spectrometer from Wissel GmbH and a flux-closed helium refrigerator from APD Cryogenics. Spectra have been fit using Lorentzian-shaped lines. Isomer shifts are given relative to that of α-Fe.

The evaluation of heat generation was determined by a commercial AC-field applicator (DM100, Nanoscale Biomagnetics, Spain). 1 ml of sample was placed in a closed container centered in the inductive coil and the AC-field was applied for 5 minutes. The applied field amplitude was H = 24 kA/m and the applied frequencies were 419, 542 and 710 kHz. The temperature of the sample was recorded by an optic fiber sensor incorporated in the equipment.

▪ RESULTS AND DISCUSSION

Some relevant parameters were initially fixed to assure the formation of monodispersed colloids with particle sizes below 200 nm, which is a key issue to guarantee colloidal stability and to make this suspension potentially more suitable for biomedical applications. The first parameter is the choice of polyol and especially its length, which has been shown to influence the size and the assembly of the magnetic cores.[21] In this work, ethylene glycol (EG) has been selected, as it is a short polyol that allows clustering such that multi-core particles can be obtained. Polyols with longer chains generally lead to single-core nanoparticles[4,22] (depending on the rest of the reagents present in the reaction vessel). The second parameter is the addition of PVP, which has been shown to provide extra stability, since it acts as capping agent. The third parameter is the iron/PVP concentration, which determines the particle size. Polyol-based synthesis of iron (III) salts in an autoclave using polyols of short chain and stabilizers such as PVP or polyethylene glycol (PEG) usually leads to uniform particles of around 300 nm.[13,23] The use of a base, namely sodium hydroxide (NaOH)[24] or urea[25] has accounted for a further reduction of size. In this work, the iron/PVP concentration was fixed to achieve particles smaller than 200 nm.

This section is divided in three parts. First, the role of NaAc on the growth and assembly process is evaluated. Then, the formation mechanism of the nanoflowers is analysed. Last, four samples with different morphologies (different assembly configurations) and crystallite sizes are selected and functionalized with citric acid, such that they form stable magnetic colloids, and their different potential for magnetic hyperthermia treatments is evaluated.

The Role of Sodium Acetate on the Assembly Process. The amount of NaAc·3H_2O was varied from 15.8 to 36.5 mmol (Table 1), while maintaining the rest of the reactants and conditions. Fig. 1 shows the normalized log-normal size distributions of the samples, obtained by manual measurement of the particle diameter through Image J software and further data fitting using Origin software. In all cases monodisperse systems with narrow size distributions were achieved thanks to the presence of PVP (the standard deviation was below 25 %). Figure S1 shows the particles obtained in the absence of PVP with irregular morphology (means size of 200 nm and standard deviation of 48 %). We found that the variation of NaAc concentration leads to nanoparticles with distinctly different structures (Fig. 1). The highest concentration of NaAc (36.5 mmol) produced single-core nanoparticles of 35 nm (sample SC, Figure 1a). These particles appear under the TEM randomly distributed and somewhat aggregated (possibly as a consequence of their magnetic character and the drying process on the TEM grid), but no specific assembly of the single-core particles was observed. However, when decreasing the NaAc concentration to 26.2 mmol, spherical hollow multi-core nanoparticles about 170 nm in diameter were formed (sample HS, Figure 1b). TEM images reveals lower material density in the inner part which is attributed to hollow structure.[13] Figure S2 further supports the existence of voids within the spheres (again due to contrast between the darker edges of the particle and the brighter centers). The lowest amount of NaAc (15.8 mmol) yielded multi-core particles with flower-like structure (sample NF, Figure 1c). In this case, the cores (<20 nm) are densely packed forming a nanoflower particle with a characteristic size of ~60 nm.

Figure 2 shows the XRD patterns of samples SC, HS and NF, which correspond to a ferrite spinel structure attributed to γ-Fe_2O_3 (JCPDS#110614). An increase in the broadening of the Bragg peaks, which indicates a decreasing crystallite size, is observed from SC, to HS, and again to NF. The crystal sizes d_{XRD} (Table 1) determined by Scherrer's equation agrees well with d_{TEM} in the case of single-core particles (SC) (d_{XRD} = 36 nm), but in case of NF and HS, d_{XRD} is significantly smaller d_{TEM}. This discrepancy reflects the multi-core nature of these samples.[18] From TEM and XRD, it is clear that decreasing the amount of NaAc leads to more densely packed assemblies with smaller core sizes.

Fig. 3 shows the field dependence of magnetization of the three different particle morphologies: SC, HS and NF, at 290 K and 5 K. The insets in Fig. 3 show the hysteresis loops in the low field regime, and Table 2 summarizes the saturation magnetization (M_s), initial mass susceptibility at low fields (χ_0), squareness (M_r/M_s ratio) and coercivity (H_c).

Table 1. Sodium acetate optimization: Experimental conditions, TEM size distribution and XRD size of maghemite nanoparticles with different morphologies including single-core (SC), hollow spheres (HS) and nanoflowers (NF).

Sample	[NaAc] (mmol)	Time (h)	d_{TEM} (nm)	d_{XRD} (nm)
SC	36.5	16	35 ± 8	36.2 ± 0.1
HS	26.2	16	170 ± 30	27.4 ± 0.2
NF	15.8	16	63 ± 13	22.9 ± 0.2

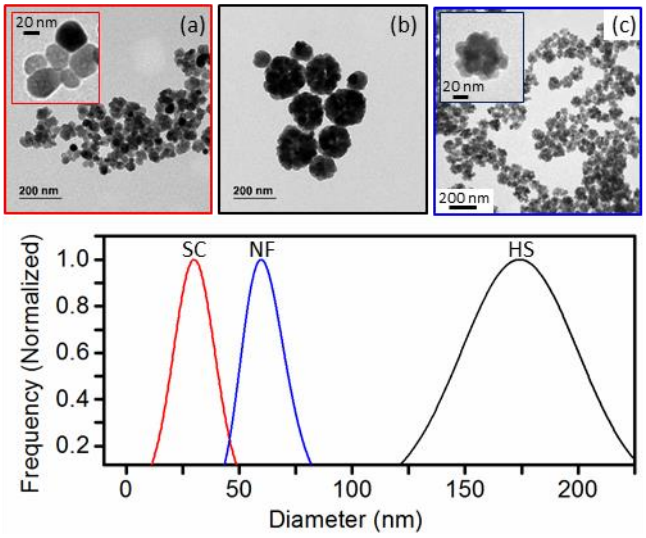

Figure 1. TEM images of the different structures obtained when varying the NaAc amount: (a) Single-core particles (SC), 36.5 mmol, (b) hollow spheres (HS), 26.2 mmol, (c) nanoflowers (NF), 15.8 mmol. Below, normalized log-normal TEM size distributions of the samples.

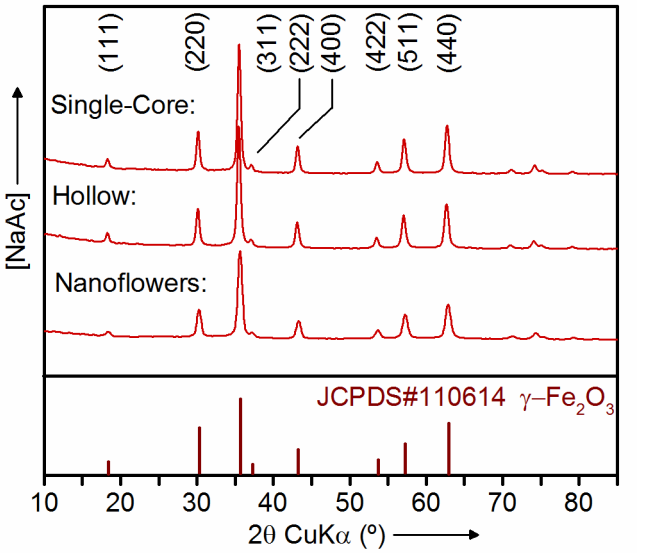

Figure 2. X-Ray Diffractogram of single-core particles (SC), hollow spheres (HS) and nanoflowers (NF).

Please, note that M_s obtained in this work is formally the magnetic moment per unit mass (the volume magnetization is divided by the samples mass, which is equal to the density. This is generally termed as the specific magnetization, σ) and that χ_0 is calculated through the numerical field derivative of M. The samples have M_s values between 80–90 Am^2/kg at room temperature and go up to 100 Am^2/kg at 5 K. As with XRD, saturation magnetisation is larger for sample SC, than samples HS and NF. Enlargement of the low field sections of the curves are shown in the insets, in order to get a more accurate view of hysteresis effects. Samples SC and HS show larger coercivity values of 4.5 and 4 kA/m, respectively, at 290 K, in contrast to sample NF that shows nearly zero coercivity and remanence at 290 K. All samples, regardless of their structure, have coercivity values between

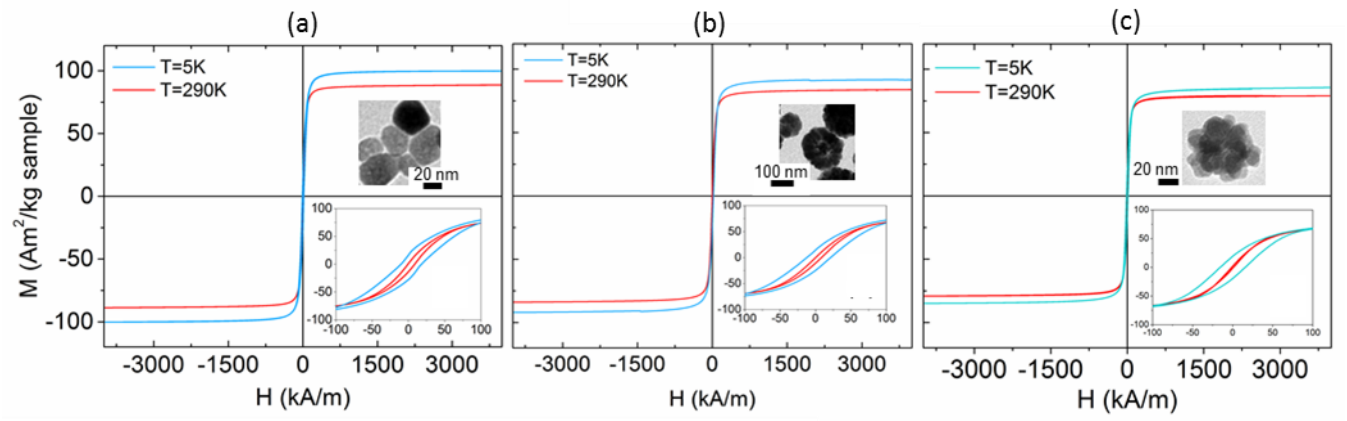

Figure 3. Magnetization curves for single-core particles (SC) (a), hollow spheres (HS) (b) and nanoflowers (NF) (c) at 5 and 290 K.

Table 2. Hysteresis parameters at room temperature and 5 K for samples SC, HS, and NF.

Sample	RT			5 K		
	M_s (Am^2/kg)	H_C (kA/m)	χ_0 (m^3/kg)	M_S (Am^2/kg sample)	M_r/M_s	H_C (kA/m)
SC	90.2± 0.1	4	1.70 ± 0.02	100.3 ± 0.1	0.23 ± 0.1	14
HS	84.3 ± 0.1	4	1.31 ± 0.01	92.5 ± 0.1	0.21 ± 0.1	17
NF	79.7 ± 0.1	1	1.60 ± 0.02	85.5 ± 0.1	0.22 ± 0.1	16

14 and 17 kA/m at low temperature, which is of the same order of magnitude that the coercivity reported for magnetite-maghemite nanoparticles with only magnetocrystalline anisotropy.[26] Also, the initial mass susceptibility (1.31–1.70 m^3/kg) at room temperature and the low squareness ratio (0.21–0.23) at 5 K are comparable for the three materials.

The above results show the fundamental role of NaAc in this synthesis route, since it directly defines the core size and morphology of the samples, and in turn leads to nanoparticles with different magnetic behavior. The reason underlies in the chemical process taking place. It is known that both NaAc and water need to be present in the reaction to modify the reduction potential of the polyol, that otherwise is not able to reduce the iron reactants.[27] Moreover, its concentration defines the self-assembly process. Thus, for the highest acetate concentration (0.3 M), massive nucleation and uniform growth by diffusion takes place, resulting in single-core particles. When the amount of acetate is reduced (~ 0.25 M), the initial nuclei seem to grow by partial aggregation in hollow spheres.

Other studies have reported the formation of similar hollow spheres by dissolution of inner small cores and growth of the larger ones on the surface by Ostwald ripening process.[13] Further reduction in acetate (< 0.2 M) leads to smaller nuclei that strongly aggregate to produce the final flower-like particles. In absence of NaAc, no precipitation occurred, as previously reported.[28]

Formation Mechanism of Multi-Core Nanoflowers. In order to study the formation mechanism and magnetic properties of multi-core nanoflowers, the NaAc concentration (15.8 mmol) was fixed and the heating time was varied from 0.5 to 48 h. All NF samples are named according to their heating time (measured in hours). For this series of samples, NF–16 is equivalent to sample NF studied above. First, electron microscopy was used to study the evolution of nanoflower formation. Figure 4 shows the as-synthesized product at the different reaction times. At short reaction times (< 30 min), a reddish colloidal suspension is observed, consisting of primary nuclei of 2–3 nm unstable under the TEM electron beam. After 1.8 h, there is a reddish-brown precipitate, which corresponds with nuclei that rarely approach and form aggregates poorly defined (as distinctly observed in the inset image of Figure 4). After 2 h of aging time, the primary nuclei seem to be transformed into a material with a laminar habit (sheets that have lower contrast than the nanoflowers) and the first nanoflowers (60 nm in size) are observed. The laminar phase disappears after 4 h. The nanoflower size is preserved (d_{TEM} ≈ 60 nm) between 2 and 48 h, see Table 3, but a clear increase of the core size is observed over time. Thus, TEM images reveal two different stages in the mechanism of flower formation. The first one is an initial stage (< 2 h of heating time) where several intermediate phases may coexist. The second one (2 – 48 h) comprises the growth of the cores within a nanoflower, which does not change in its total size (≈ 60 nm). Figure S3 shows the histograms obtained from TEM measurements of the nanoflower sizes. This data was fitted to a log-normal size distribution (Figure S4) and it seems that the size distribution gets narrower after longer periods of heating time. This is in good agreement with a two-stage mechanism of nanoparticle formation by self-assembly of diffusing aggregating nanocrystalline subunits, which are in turn formed by burst nucleation in a supersaturated solution, followed by coarsening.[29] A detailed analysis of both stages is provided in the following sections.

Initial stages of the flower formation (<2 h). In order to identify the different phases that appear during these initial stages, the composition of samples NF–0.5–2 were evaluated by XRD

Table 3. TEM and XRD sizes during the formation of nanoflower particles. For all these syntheses, [NaAc] was kept at 15.8 mmol.

Sample	Time (h)	d_{TEM} (nm)	d_{XRD} (nm)
NF-0.5	0.5	-	-
NF-1	1	-	-
NF-1.8	1.8	-	-
NF-2	2	60 ± 11	11.3 ± 0.3
NF-4	4	56 ± 13	14.8 ± 0.3
NF-8	8	61 ± 16	19.2 ± 0.2
NF-16	16	63 ± 13	22.9 ± 0.2
NF-48	48	58 ± 11	23.7 ± 0.2

(Table 3). For all these syntheses, [NaAc] was kept at 15.8 mmol. Figure 5 shows the X-ray diffraction pattern of the NF samples. At t = 0.5 h, the pattern clearly matches that of lepidocrocite (γ-FeOOH) (2-theta angles of 27, 36, 47 and 60°). A different pattern is observed at 1 and 1.8 h reaction time. These patterns do not correspond with any of the well-known iron oxide or oxyhydroxide phases. As the patterns are quite distinct we speculate that they may represent the formation of an unknown intermediate phase. At 2 h of reaction time, most of the XRD peaks can be indexed to maghemite (γ-Fe_2O_3), whose typical XRD profile is shown in red below the diffractograms). Additionally, there are two small and narrow peaks (at 24.6° and 47.2°) that reveal some remain of the intermediated phase (in correspondence with the observations by TEM). Figure S5 shows the XRD patters of those samples collected after 6 months of storage. It is noteworthy that while sample NF-0.5 is unstable and tends to evolve to ferroxyhyte (FeOOH JCPDS#220353) and that the unknown intermediate phase (NF–1 and NF–1.8) remains stable after 6 months.

Figure 6 shows the Mössbauer spectra of NF powders in the initial stages, t = 0.5–2 h. The spectra of all four samples are magnetically split at 18 K and have been fitted with 2 or 3 sextets with an isomer shift, δ, around 0.50 mm/s, indicating that the samples consist of ferric phases. At 80 K and room temperature, doublets dominate the spectra. Again, the isomer shift of the doublets (~ 0.45 mm/s at 80 K and ~ 0.37 mm/s at room temperature) as well as their quadrupole splittings (ε ~ 0.6 mm/s), indicate only ferric phases in all four powder samples. The spectrum of NF–0.5 obtained at 18 K has been fitted with 3 sextets. The most dominating sextet (shown in dark blue color) has broad lines, a hyperfine field, B_{hf}, around 45 T, and ε around 0.0 mm/s.

This sextet is most likely due to the presence of lepidocrocite, in agreement with the XRD and TEM results. The Neel temperature of lepidocrocite is 77 K,[30] but there appears to be quite a lot of magnetic relaxation of lepidocrocite already at low temperature, indicated by the broad lines and the blue sextet with lower hyperfine field. At 80 K and room temperature, lepidocrocite is paramagnetic and hence seen as a doublet. The third sextet (orange) in the spectrum of sample NF–0.5 has sharp lines, a hyperfine field B_{hf} of ~50.6 T and a quadrupole shift, ε, of -0.13 mm/s. The hyperfine parameters of this component match those of goethite, although this (probably nanocrystalline) phase was not detected by X-ray. At 80 K a ferric (goethite) sextet (B_{hf} =48.0 T, ε = 0.12 mm/s)

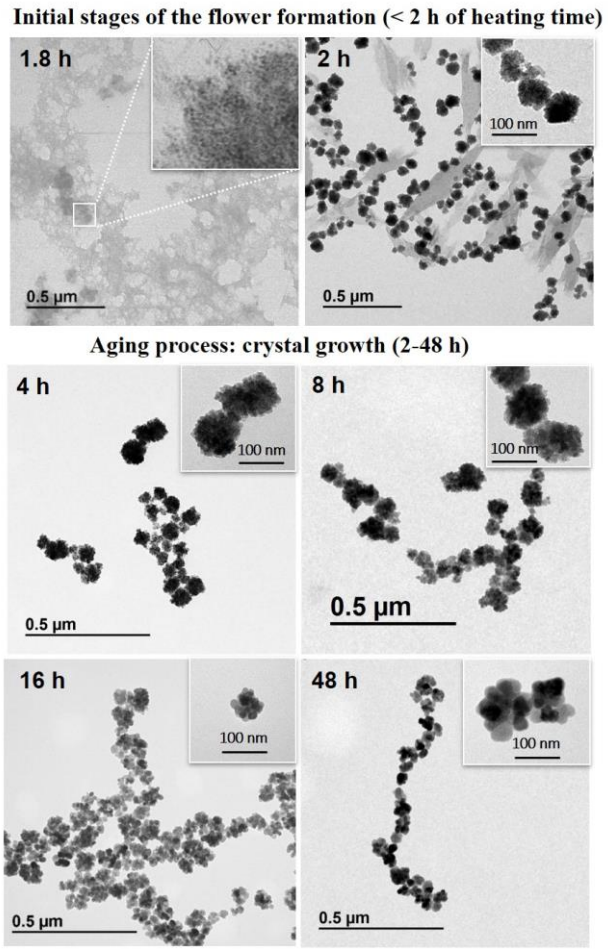

Figure 4. TEM images of NF samples prepared with 15.8 mmol of NaAc at different reaction times: 1.8, 2, 4, 8, 16 and 48 h. Insets show a detailed image of a single nanoflower.

with broad lines remains, while the room temperature spectrum features no goethite sextet, presumably due to superparamagnetic relaxation.This goethite component occupies about 7 % of the spectral area of NF–0.5 and is not seen in the other samples.

The Mössbauer spectra of NF-1 and NF–1.5 are very similar to each other (in agreement with the XRD patterns of NF-1 and NF-1.8). These Mossbauer spectra, where the outer sextets have B_{hf} ~ 46.2-49.6 T, δ ~ 0.5 mm/s, ε ~ 0.0 mm/s, could be assigned to ferrihydrite, or magnetically relaxing maghemite, but such assignment does not match the XRD patterns, whose main peaks are not found to match an existing phase (explicitly not ferrihydrite or maghemite). The Mössbauer parameters match well with a (new) undescribed intemediate phase in-between that of lepidocrocite and maghemite, i.e. a phase that is dehydroxylated lepidocrocite (or "maghemite with hydroxylgroups"). Mössbauer spectra obtained at 80 K in an applied field of 0.5 T show no magnetic splitting, indicating that this phase is paramagnetic at 80 K. Recent studies have shown the presence of new intermediate phases that occur during the transformation between iron oxides/oxyhydroxides that may not be stable enough to be easily characterised. For example, an intermediate phase has been identified in the transformation between 2-line ferrihydrite and hematite, which was termed as "hydromaghemite" or "ferriferrihydrite".[31]

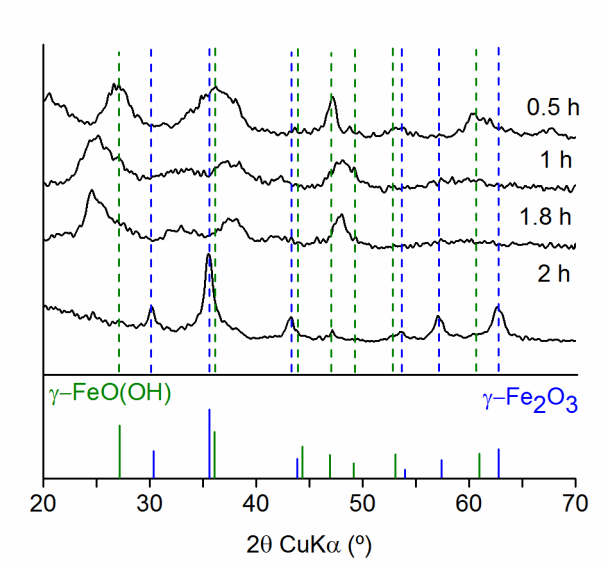

Figure 5. Formation mechanism of nanoflowers followed by X-ray diffraction of the powders collected after 0.5, 1, 1.8 and 2 h of aging time. Expected peak positions of lepidocrocite (γ-FeOOH, green) and maghemite (γ-Fe_2O_3, blue) are shown.

Although this phase has similar B_{hf} and δ values to the intermediate phase observed in this work, the X-ray patterns do not mach, which means that we have captured a different "intermediate" phase.

The 18 K spectrum of NF-2 is dominated by a maghemite sextet (shown in wine red) with B_{hf} =52.6.0 T, ε=0.01 mm/s, δ ~0.5 mm/s. The asymmetry of this sextet (between lines 1 and 6) and its isomer shift strongly indicate that it is ferric, i.e. almost pure maghemite.[32] At 80 K, part of the spectrum (~20 %) is relaxed into a doublet, but the majority of the spectrum is a sextet with relatively sharp lines. Measurements obtained within an applied field (data not shown), show that the relaxed part is paramagnetic, i.e presumably due to the lepidocrocite or the "intermediate" phase. At room temperature, the sextet contribution remains most of its spectral area but has very broad lines. From this relaxation behavior, a mixture of phases is assumed (in agreement with XRD), i.e. part of the sample is paramagnetic already at 80 K (lepidocrocite), while the remaining part of the sample (maghemite) show slow relaxation even at room temperature.

AC magnetic measurements have been performed in order to follow the particle formation especially at the initial stage of 0.5 h, where sample is unstable under the TEM beam. For NF–0.5, the in-phase susceptibility presents Curie-like behaviour down to 25 K, with a magnetic effective moment of about 2.6 μ_B (Bohr magnetons), calculated by assuming, e.g., the formula of lepidocrocite. The deviation of the in-phase susceptibility from the Curie law behaviour at low temperatures, together with the rise of the out-of-phase component suggests that magnetic blocking of very small nanoparticles takes place below ~ 20 K. For NF–1.8, the maximum of the in-phase component together with the out-of-phase component step at ~ 150 K indicates magnetic blocking of nanoparticles up to this temperature. The location of these maxima, which are at higher temperatures than in the case of NF–0.5 h, indicates the growth of the nanoparticles at these early stages. Given that at this temperature lepidocrocite

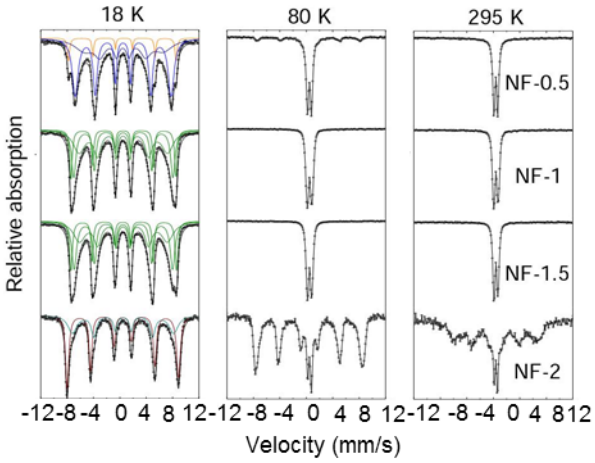

Figure 6. Formation mechanism of nanoflowers followed by Mössbauer spectroscopy at 18, 80 and 295 K for samples collected after 0.5, 1, 1.5 and 2 h of aging time.

(and the "intermediate" phase of NF–1 and NF–1.5 should be paramagnetic, this feature may be caused by particles with considerable magnetisation, possibly being made of the undescribed intermediate phase in its advance stage (1.8 h). For NF–2, the appearance of both components of the AC susceptibility is typical of particles magnetically blocked well above room temperature, displaying susceptibility maxima at temperatures above the measured range, in agreement with the observation of maghemite flowers (~ 60 nm) by TEM.The results of TEM, XRD, Mössbauer spectroscopy and AC susceptibility support that, prior to formation of maghemite nanoflowers, lepidocrocite with laminar habit is formed which transforms to maghemite through an intermediate phase, probably dehydroxylated lepidocrocite.

Consequently, the formation mechanism can occur as follows at this initial stage:

$$COO^- + H_2O \rightarrow CH_3COOH + OH^- \text{ (Eq. 1)}$$
$$Fe^{3+} + 3OH^- \rightarrow Fe(OH)_3 \text{ (Eq. 2)}$$
$$2Fe(OH)_3 \rightarrow 2\,\gamma - FeOOH + H_2O \text{ (Eq. 3)}$$
$$CH_2OH - CH_2OH \rightarrow CH_2OH - CHO + H_2O \text{ (Eq. 4)}$$

First, NaAc causes a weak hydrolyzation (Eq. 1), which controls the release rate of OH^-. It has been reported that iron ions could coordinate to the acetate anion (CH_3COO^-) forming a coordination compound that could evolve to magnetite directly in the presence of EG that is oxidized to glycolaldehyde (Eq. 4), a reductant capable of reducing most noble metal ions.[33] However, in our case, since lepidocrocite and dehydroxylated lepidocrocite have been suggested through XRD and Mössbauer spectroscopy as intermediate phases (samples NF–0.5, 1 and 1.8), we propose that the mechanism follows a sol-gel reaction, where the initial γ-FeOOH nuclei are formed thanks to the sodium acetate releasing OH^- (Eq. 2-3).

The high temperatures, pressure and the action of sodium acetate allows the formation of lepidocrocite by a burst type nucleation,[34,35] which in this case seems to occur rapidly (< 0.5 h). After nucleation, there is phase transformation (via dehydrolyzation) and aggregation leading to maghemite nanoflowers with

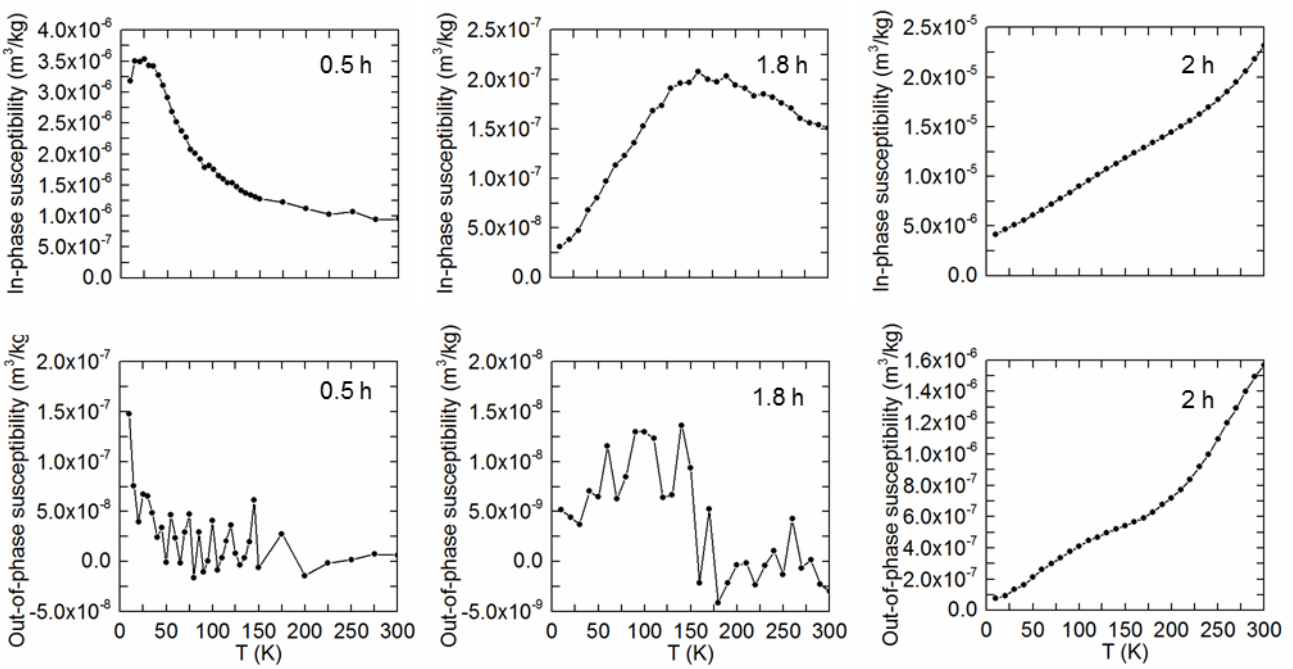

Figure. 7 Temperature dependence of the low field mass AC susceptibility at 11 Hz, for the initial stages (heating times 0.5, 1.45 and 2 hours) of the nanoflower formation. Please, note the different susceptibility scales in each plot.

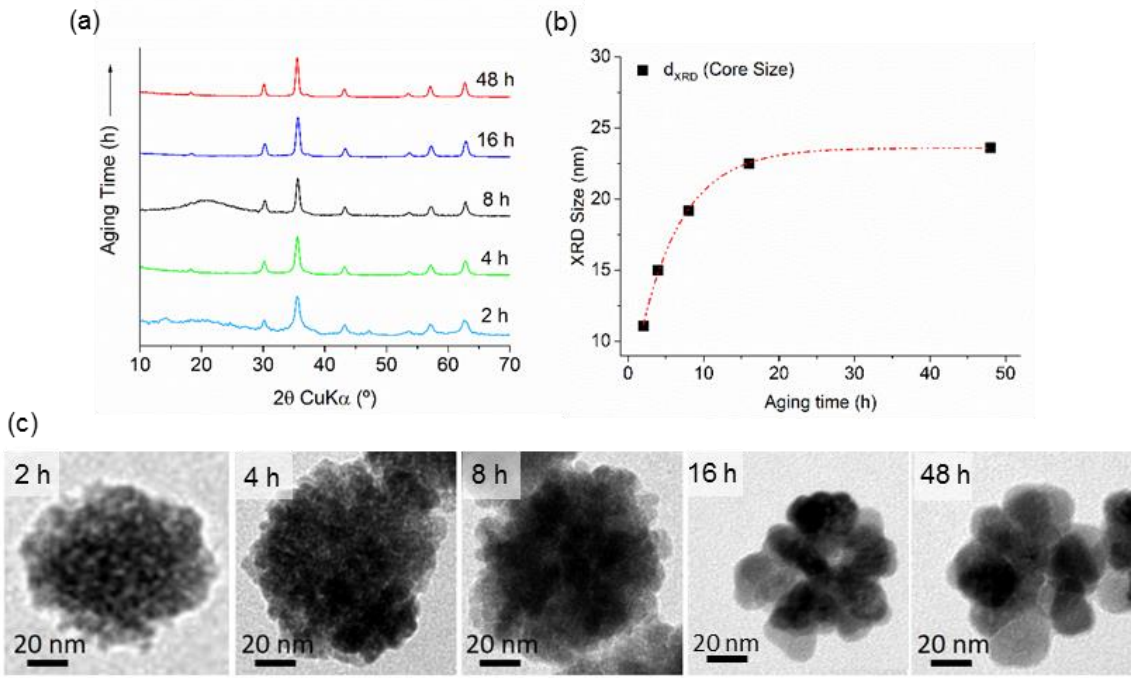

Figure. 8 Structure of the NF along at t = 2-48 h: (a) XRD patters. (b) Crystallite size calculated by Scherrer's equation. (d) Representative TEM images of the growing cores.

a fixed size. To figure out whether the immediate product is magnetite or maghemite is by no means a trivial issue. On the one hand, a reduction process (Eq. 4) can occur during the solvent mediated transformation to magnetite[2] ($2FeO(OH) + Fe(OH)_2 \rightarrow Fe_3O_4 + 2\,H_2O$), which is easily oxidized maghemite. On the other hand, it has been demonstrated by Navrotsky et al. [36] that a direct size driven transformation of lepidrocrocite to maghemite is thermodinamically possible ($2FeO(OH) \rightarrow \gamma - Fe_2O_3 + H_2O$). Our results seem to support the thermodynamic considerations stated by Navrotsky and we conclude that this oxy-hydroxide transforms directly to

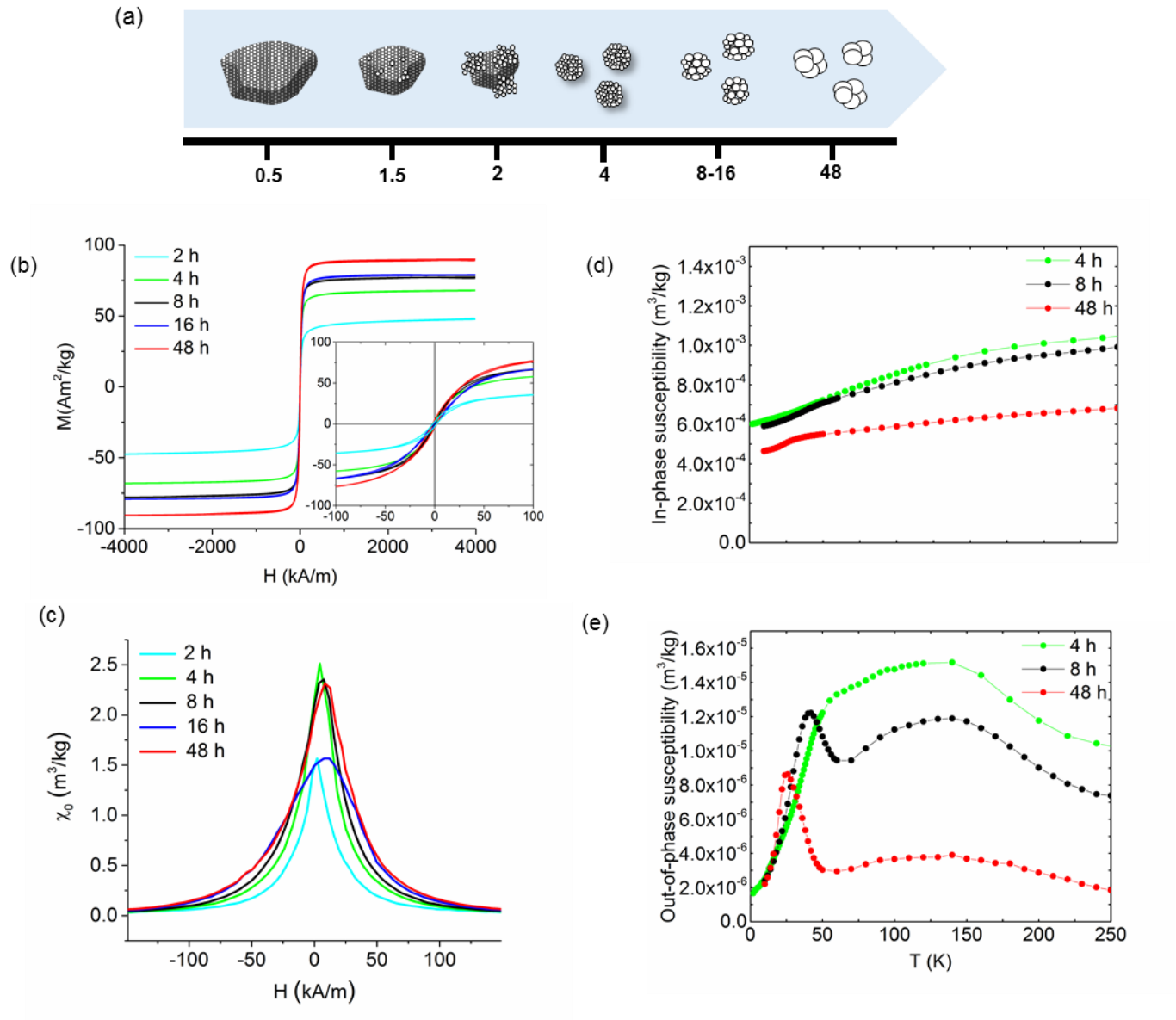

Figure. 9 Formation mechanism of maghemite nanoflowers: (a) Sketch of particle evolution thoughout the aging process. (b) DC magnetization curves at 290 K of samples NF–2–48, (c) mass initial susceptibility (χ_0) of samples NF–2–48 and (d-e) Temperature dependence of the low field AC susceptibility at 11 Hz, along the formation of nanoflowers at 4, 8 and 48 hours of aging time.

maghemite,[37] but we could not exclude the initial presence of small amounts of Fe^{+2} in our samples that will remain undetectable by further oxidation during the characterisation process.

Aging process: crystal growth (2–48 h). Once the maghemite nanoflowers have formed, after 2 h of reaction time, an aging process starts. This process has been studied through TEM, XRD and magnetic measurements. Fig. 8a shows the XRD patterns collected for NF–2–48. After 4 h, only maghemite is detected. The diffraction peaks become narrower throughout the aging process and the crystal size obtained from the width of the diffraction peaks by use of the Scherrer's formula show that the nanoflowers undertake a crystallization process, increasing its mean crystal size d_{XRD} from 11 to 23 nm (Fig. 8b). Similar trend is observed by TEM, where the cores of the particles are seen to grow over time (Figure 8c). Throughout time the organic content of the samples is reduced, as seen in the thermogravimetric analyses (TGA) in Figure S7), from 12 to 4%.

Figure 9a illustrates the whole progress of formation mechanism and crystallization of NF samples, which can be linked to Eq. 1-4, where laminar lepidocrocite is formed and then transformed to maghemite nanoflowers.

The magnetic properties of the flowers during the aging steps 2–48 h were evaluated in detail (Figure 9b-e). By prolonging the aging time (4, 8, 16 and 48 h), the nanoflowers saturation magnetization is increased from 48 to 90 Am^2/kg at 290 K (Figure 9b), which implies quite a significant enhancement. The samples also show increasing coercivity values (~0.5–2 kA/m at RT and 8-19 kA/m at 5 K) with aging. The initial mass susceptibility at low fields (χ_0) was calculated for all samples through DC magnetometry from the numerical field derivative of the magnetization (Figure 9c) (as χ_0 calculated in Table 2). Samples NF-4, NF–8 and NF–48 have χ_0 values of 2.3–2.5 m^3/kg, which is higher than SC and HS nanoparticles (χ_0 for these samples is 1.7 and 1.35 m^3/kg, respectively). This enhancement on the magnetic susceptibility has been previously linked to a

Table 4. Colloidal properties of maghemite nanoparticles with the different morphologies: Single-core (SC), hollow spheres (HS) and nanoflowers at different aging time (NF-4 and NF-28) coated with citric acid (CIT).

	As-synthesized			Citric acid coating		
Sample	D_h (nm)	PdI	IEP	D_h (nm)	PdI	IEP
SC-CIT	896	0.28	5.5	161	0.26	5.0
HS-CIT	705	0.31	5.7	298	0.25	5.1
NF-4-CIT	331	0.27	6.6	109	0.14	4.9
NF-48-CIT	965	0.23	6.0	102	0.11	4.0

magnetic cooperative effect due to aggregation of cores forming densely packed nanoflowers.[11] The magnetic behaviour of the progressively aged nanoflowers has also been investigated by means of AC susceptibility (see Fig. 9 d-e). The results can be interpreted by considering three contributions: i) a positive in-phase susceptibility level at room temperature due to the presence of rather large magnetic entities with permanent magnetism, ii) a wide and rounded out-of-phase maximum very likely indicating the blocking of magnetic entities of intermediate size and iii) a low temperature step in the in-phase component accompanied by a rather sharp peak in the out-of-phase below ~ 50 K. The major contribution corresponds to the particles magnetically blocked well above room temperature, already detected in sample NF–2, although from t = 4 h up to t = 48 h the magnitude of the resulting in-phase susceptibility is significantly higher since paramagnetic lepidocrocite dissolves in favour of other strongly magnetic phases. These samples present much higher signal per mass of sample than NF–2 (Fig. 7) in agreement with the disappearance of the lepidocrocite or the intermediate phases observed by TEM and XRD at the longest reaction times. For NF–4, NF–8 and NF–48, the magnitude of the room temperature in-phase component decreases for increasing aging time. This result well agrees with the field derivative of magnetization shown in Fig 9c. We believe this value mostly results from the contribution of the large magnetic entities. The magnetic dynamics of the lower temperature anomalies have been investigated to interpret their nature (detailed discussion, Fig. S8 and table S1 from the Supporting Information). The relative sharpness of the lowest temperature peaks, their pre-exponential factors of the Arrhenius law, their regular dependence with the aging time, and the occurrence also in iron oxide nanoparticles prepared by completely different methods[38,39] point to some phenomenon intrinsic to maghemite or to some usually appearing intermediate phase, although no rigorous interpretation of this phenomenon can be offered yet.

In summary, the analysis of the samples with longest reaction times indicates that lepidocrocite and the "undescribed" intermediate phase have disappeared. Interestingly, increasing reaction times give rise to a significant increase of the core sizes but not of the flower size.

Biomedical Applications. We here evaluate aspects relevant for biomedical applicability (especially colloidal stability and heating potential for magnetic hyperthermia) of four selected samples: SC, HS and NF–4 and NF–48, as these samples represent distinct different morphologies (tuned by the NaAc concentration) and hold different core sizes. The surface charge

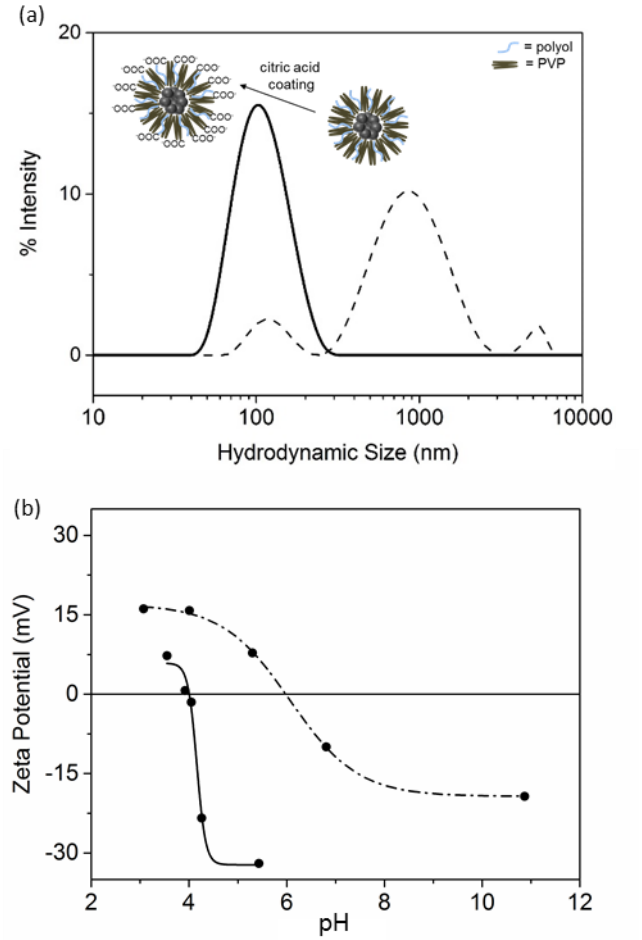

Figure. 10 Effect of the citric acid coating on sample NF–4: (a) DLS measurement and inset scheme of the coating and (b) Zeta Potential curves fitted to a Boltzmann sigmoidal function. Dashed line connects data points for as-synthesized sample. Continuous line connects data points for citric acid coating.

and the colloidal stability of samples SC, HS, NF-4 and NF-48 were enhanced by citric acid coating. Infrared spectroscopy confirms the successful citric acid coating from the absorption bands typical of the carboxyl at 1384 and 1022 cm^{-1} (Figure S6 of SI). The hydrodynamic size (D_h), polydispersity index (PdI) and isoelectric point (IEP) of as-synthesized and coated particles are summarized in Table 4. The hydrodynamic sizes are smaller for the coated samples than for the as-synthesized particles due to an increase in the surface charge, as the shift of the IEP to lower pHs confirms (the NPs have increased surface charge at pH 7). Figure 10a shows the change in hydrodynamic size after the coating for sample NF-4. D_h for NF–4 changes from a polydisperse distribution to a narrow monomodal distribution centered at ~100 nm after the coating, which is closer to the average particle size determined by TEM (Table 1). Furthermore, number-weighted D_h values for NF samples (50-70 nm) do approach d_{TEM}, as this is number weighted. Similarly, a change to a more well-dispersed system is also seen for sample NF-48 when coated with citric acid. For samples SC and HS the hydrodynamic size after coating is 161 and 298 nm, respectively, which is much larger than d_{TEM} for sample SC and relatively larger than d_{TEM} for sample HS suggesting a certain degree of agglomeration of the particles in suspension.

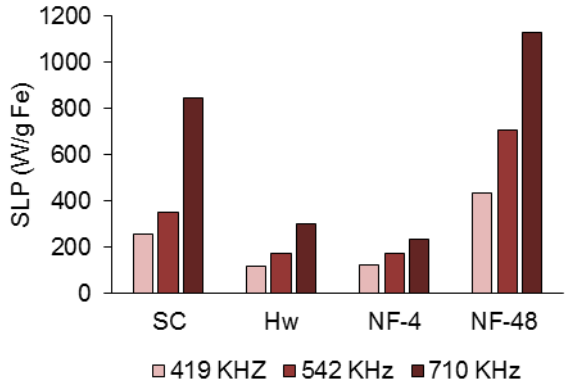

Figure 11. SLP values of samples SC, HS, NF-4 and NF-48. SLP values of different samples calculated by the "slope method". Field amplitud was 23.8 kA/m and three different frequencies were applied: 419, 542 and 710 KHz.

Figure 10b shows the measured zeta potential curve for sample NF-4. The citric acid coating promotes the stabilization by repulsive forces,[40] since there is an increase of the surface charge from -10 mV up to -40 mV at pH 7, assuring long-term stability at physiological pH. We observe a similar increase of surface charge for samples SC, HS and NF–48. Moreover, there is, for all samples, a shift of the isoelectric point (zero zeta potential) to lower pH values that confirms the successful coating with carboxyl groups for sample NF–4. This shift is larger in the nanoflowers, probably due to the higher surface-to-volume ratio in comparison with the single-core particles (SC) and the hollow spheres (HS).

The heating capacity of the coated materials in water at physiological pH was evaluated in order to study the differences in terms of sample morphology and crystallinity. Figure 11 shows the different specific loss power (SLP) values calculated through "the slope method" (change of temperature over time $\Delta T/\Delta t$) for different frequencies: 419, 542 and 710 KHz, for samples SC, HS, NF–4 and NF–48. The specific loss power is found as:

$$SLP\left({}^{W}/_{g_{Fe}}\right) = c \times \frac{Mass_{sample}}{Mass_{Fe}} \times \frac{\Delta T}{\Delta t} \textbf{ (Eq. 5)}$$

where c is the capacity of the suspension (typically assumed to be the heat capacity of the suspension medium for low concentrations of MNPs).[41] Nanoflowers with a core size of 23 nm (NF-48) have the highest SLP values e.g. yielding 1131.2 W/g Fe for a frequency of 710 KHz. This sample displays SLP values nearly 5 times larger than nanoflowers with crystal size of 15 nm (NF-4), nearly 4 times larger than hollow spheres and 1.5 times larger than single-core nanoparticles, although these two latter samples (HS and SC) have bigger core sizes of 27 and 36 nm, respectively. This demonstrates that both core sizes and the packing of the cores have decisive influence on the heating capacity. Specifically, we observe that nanoflowers with large cores (controlled by annealing) and densely packed cores (tuned by NaAc concentration) offer enhanced heating capacity compared with nanoflowers with smaller crystallite sizes, hollow spheres, and single-core nanoparticles used in this work.

Given the heterogeneity in the conditions (field and frequency) used to measure SLP by different research groups, and the multiple possibilities of the materials characterized (with different particle size, shape, structure (single-core or multi-core), crystalline structure, composition, etc.), it is complicated to find the most appropriate examples in the literature to compare our data. For example, 30 nm single-core magnetite nanoparticles, obtained by $FeSO_4$ precipitation and subsequent ageing had a SLP value of 95 W/g (field amplitude 10 kA/m and frequency of 249 kHz).[42] Our SC sample, with similar particle size, presents a higher SLP value (257 W/g) with the lowest amplitude and frequency (22.8 kA/m and 419 kHz, respectively), however, the measurement conditions are not exactly the same. Regarding hollow structures, liposomes (120 nm) encapsulating magnetite particles (10 nm core size) presented a SLP value of 210 W/g.[14] With the same conditions, sample HS has a similar SLP value of 301 W/g, although the core size and the particle size are not exactly the same. In the frame of multi-core structures, materials obtained by coprecipitation of ferric and ferrous chloride in a microwave, with crystal size of 13 nm and hydrodynamic sizes of 123 nm, similar to sample NF–4, had a SLP value of 190 W/g (field amplitude 10.5 kA/m and frequency of 950 kHz).[43] These values are similar to the ones obtained for sample NF–4 at the most similar conditions measured in our case (232 W/g with field amplitude 24 kA/m and frequency of 700 kHz). Measurements in the same field and frequency conditions for a material similar to sample NF–48 (magnetite nanoflowers of 22 nm obtained by the polyol-mediated synthesis) yielded similar SLP data (1130 W/g for NF-48 and 1180 W/g for the 22 nm nanoflowers). The obtained SLP data for our materials envisages a possible use for magnetic fluid hyperthermia treatment of cancer, however, the lack of standardized measurement conditions makes complicated to compare the data with other existing materials.

The intrinsic loss power (ILP) of the samples was calculated from Eq. 6:

$$ILP\left({}^{nHm^2}/_{kg}\right) = \frac{SLP}{H^2 f} \textbf{ (Eq. 6)}$$

It ranges from 0.5–0.6 (in the case of samples NF–4 and HS, respectively), 1.9 (sample SC) up to 2.6 (sample NF–48). Lastly, it must be noted that the product of H·f was kept for all combinations below 4.85×10^8 kA/m·s, which is mandatory for avoiding nonspecific eddy heating in tissues.[44]

CONCLUSIONS

The polyol-mediated synthesis has been explored and developed for the preparation of well-controlled magnetic nanoparticles with different core size and arrangement to form the final single-core and multi-core particles. The particles are formed by burst nucleation and growth processes that determine the final nanostructure going from single-core to hollow spheres and nanoflowers, with high crystallinity, due to the selected polyol synthesis route that uses high temperature over long periods of times.

Sodium acetate is found to be a key parameter governing theself-assembly process. In this reaction, it has a double role: the particle formation, and the nucleation and growth. For higher acetate concentration, massive nucleation and growth by diffusion takes place, resulting in single-core particles. As the amount of acetate is reduced, the initial nanocrystalline subunits seem to grow by partial aggregation in hollow spheres. Further reduction in acetate leads to initial nanocrystalline nuclei that strongly aggregate to produce the final flower-like particles. The synthesis of magnetic nanoflowers occurs via burst nucleation, growth by aggregation and recrystallization that takes

place over time. The initial stages of the reaction are composed of lepidocrocite, which suffers a fast dehydroxylation, transforming to an intermediate "undescribed" phase – possibly a partly dehydroxylated lepidocrocite – that evolves to maghemite nanoflowers. A prolonged heating of the flowers leads to nanoflower particles with larger cores with interesting magnetic and colloidal properties and consequently high heating capacities, being sample NF–48 the one that displays the highest ILP value.

In the future, the transferred energy from an exciting magnetic field to nanoparticles, leading to a dissipation of heat in targeted bodies such as tumors, is likely to be explored much further. Taking advantage of this physical phenomenon, magnetic nanoparticles are by many also considered as potential chemotherapy and radiotherapy enhancement agents, where a limited heat dissipation dose increases the effectiveness in cell destruction. Our studies have outlined possible ways to control the formation of distinct structures *via* polyol synthesis, specifically core sizes and arrangement have been tuned. This indicates ways to tailor and optimize magnetic properties for specific applications. On the one hand, the most well-crystalline nanoflowers (NF-48) has the highest heating capacity. On the other hand, nanoflowers with core size above 15 nm (NF-4) combine high saturation magnetization and initial susceptibility, while conserving low remanence at room temperature, which can be suitable for specific biomedical applications and also applications such as magnetic separation.

ASSOCIATED CONTENT

Supporting Information

The Supporting Information is available free of charge on the ACS Publications website.

Transmission Electron Microscopy images of hollow particles, the nanoparticles obtained in the absence of PVP and log-normal size distributions of samples (NF–4–48).

Infrared spectra of magnetite nanoparticles before and after coating process.

Thermogravimetric analysis for different periods of crystallization: 2, 4, 8 and 48 h.

AC magnetic susceptibility analysis of the magnetic dynamics of samples above 2 h.

AUTHOR INFORMATION

Corresponding Author

* H. Gavilán: Email: helena_gr@icmm.csic.es.
* M.P. Morales: Email: puerto@icmm.csic.es
* L. Gutiérrez: Email: lu@unizar.es.

Author Contributions

The manuscript was written through contributions of all authors. All authors have given approval to the final version of the manuscript.

Funding Sources

This work was supported by the EC FP-7 grant "NanoMag" (grant agreement no 604448) and the Spanish Government by MAGO project (MAT2014-52069-R).

ACKNOWLEDGMENT

LG acknowledges financial support from the Ramón y Cajal subprogram (RYC-2014-15512) and MEFB acknowledges financial support from the Brazilian agency CNPq grant [232947/2014-7]. Servicio General de Apoyo a la Investigación-SAI, Universidad de Zaragoza is acknowledged. Support Laboratories at ICMM, microscopy service at CNB and Servicio Interdepartamental de Investigación (Sidi), Universidad Autonoma de Madrid, are also acknowledged.

ABBREVIATIONS

NaAc, sodium acetate; PVP, polyvinylpyrrolidone; EG, ethylene glycol; NaOH, sodium hydroxide; PEG, polyethylene glycol; SC, single-core; HS, hollow spheres; NF, nanoflowers; TEM, Transmission Electron Microscopy; XRD, X-Ray diffraction; DLS, Dynamic Light Scattering; FTIR, Fourier transform infrared spectroscopy; TGA, thermogravimetric analysis; SAR, specific absorption rate; SLP, specific loss power; ILP, intrinsic loss power; MRI, magnetic resonance imaging; M_s, saturation magnetization; χ_i, initial mass susceptibility at low fields; H_c, coercivity; M_r, remanence.

REFERENCES

1. Fievet, F.; Lagier, J.; Blin, B.; Beaudoin, B.; Figlarz, M., Homogeneous and heterogeneous nucleations in the polyol process for the preparation of micron and submicron size metal particles. *Solid State Ionics* **1989,** 32, 198-205.

2. Dong, H.; Chen, Y.-C.; Feldmann, C., Polyol synthesis of nanoparticles: status and options regarding metals, oxides, chalcogenides, and non-metal elements. *Green Chemistry* **2015,** 17, (8), 4107-4132.

3. Qu, H.; Caruntu, D.; Liu, H.; O'Connor, C. J., Water-dispersible iron oxide magnetic nanoparticles with versatile surface functionalities. *Langmuir* **2011,** 27, (6), 2271-2278.

4. Cai, W.; Wan, J., Facile synthesis of superparamagnetic magnetite nanoparticles in liquid polyols. *Journal of colloid and interface science* **2007,** 305, (2), 366-370.

5. Haynes, W., the CRC Handbook of Chemistry and Physics 93RD Edition, 2012. *Chemical Rubber Company*.

6. Zhang, H.; Watanabe, T.; Okumura, M.; Haruta, M.; Toshima, N., Catalytically highly active top gold atom on palladium nanocluster. *Nat Mater* **2012,** 11, (1), 49-52.

7. Soumare, Y.; Garcia, C.; Maurer, T.; Chaboussant, G.; Ott, F.; Fiévet, F.; Piquemal, J. Y.; Viau, G., Kinetically Controlled Synthesis of Hexagonally Close-Packed Cobalt Nanorods with High Magnetic Coercivity. *Advanced Functional Materials* **2009,** 19, (12), 1971-1977.

8. Gutiérrez, L.; Costo, R.; Grüttner, C.; Westphal, F.; Gehrke, N.; Heinke, D.; Fornara, A.; Pankhurst, Q.; Johansson, C.; Veintemillas-Verdaguer, S., Synthesis methods to prepare single-and multi-core iron oxide nanoparticles for biomedical applications. *Dalton Transactions* **2015,** 44, (7), 2943-2952.

9. Cheng, C.; Xu, F.; Gu, H., Facile synthesis and morphology evolution of magnetic iron oxide nanoparticles in different polyol processes. *New Journal of Chemistry* **2011,** 35, (5), 1072-1079.

10. Laurent, S.; Forge, D.; Port, M.; Roch, A.; Robic, C.; Vander Elst, L.; Muller, R. N., Magnetic iron oxide nanoparticles: synthesis, stabilization, vectorization, physicochemical characterizations, and biological applications. *Chemical reviews* **2008,** 108, (6), 2064-2110.

11. Lartigue, L. n.; Hugounenq, P.; Alloyeau, D.; Clarke, S. P.; Lévy, M.; Bacri, J.-C.; Bazzi, R.; Brougham, D. F.; Wilhelm, C.; Gazeau, F., Cooperative organization in iron oxide multi-core nanoparticles potentiates their efficiency as heating mediators and MRI contrast agents. *ACS nano* **2012,** 6, (12), 10935-10949.
12. Kim, B. H.; Lee, N.; Kim, H.; An, K.; Park, Y. I.; Choi, Y.; Shin, K.; Lee, Y.; Kwon, S. G.; Na, H. B., Large-scale synthesis of uniform and extremely small-sized iron oxide nanoparticles for high-resolution T 1 magnetic resonance imaging contrast agents. *Journal of the American Chemical Society* **2011,** 133, (32), 12624-12631.
13. Sun, Q.; Ren, Z.; Wang, R.; Chen, W.; Chen, C., Magnetite hollow spheres: solution synthesis, phase formation and magnetic property. *Journal of Nanoparticle Research* **2011,** 13, (1), 213-220.
14. Di Corato, R.; Espinosa, A.; Lartigue, L.; Tharaud, M.; Chat, S.; Pellegrino, T.; Ménager, C.; Gazeau, F.; Wilhelm, C., Magnetic hyperthermia efficiency in the cellular environment for different nanoparticle designs. *Biomaterials* **2014,** 35, (24), 6400-6411.
15. Mahmoudi, M.; Hofmann, H.; Rothen-Rutishauser, B.; Petri-Fink, A., Assessing the in vitro and in vivo toxicity of superparamagnetic iron oxide nanoparticles. *Chemical reviews* **2011,** 112, (4), 2323-2338.
16. Weissleder, R. a.; Stark, D. D.; Engelstad, B. L.; Bacon, B. R.; Compton, C. C.; White, D. L.; Jacobs, P.; Lewis, J., Superparamagnetic iron oxide: pharmacokinetics and toxicity. *American Journal of Roentgenology* **1989,** 152, (1), 167-173.
17. Pankhurst, Q. A.; Connolly, J.; Jones, S. K.; Dobson, J., Applications of magnetic nanoparticles in biomedicine. *Journal of physics D: Applied physics* **2003,** 36, (13), R167.
18. Gavilán, H.; Kowalski, A.; Heinke, D.; Sugunan, A.; Sommertune, J.; Varón, M.; Bogart, L. K.; Posth, O.; Zeng, L.; González-Alonso, D.; Balceris, C.; Fock, J.; Wetterskog, E.; Frandsen, C.; Gehrke, N.; Grüttner, C.; Fornara, A.; Ludwig, F.; Veintemillas-Verdaguer, S.; Johansson, C.; Morales, M. P., Colloidal Flower-shaped Iron Oxide Nanoparticles: Synthesis Strategies and Coatings. *Particle and Particle Systems Characterization* **2017,** (In Press).
19. Gavilán, H.; Posth, O.; Bogart, L. K.; Steinhoff, U.; Gutiérrez, L.; Morales, M. P., How shape and internal structure affect the magnetic properties of anisometric magnetite nanoparticles. *Acta Materialia* **2017,** 125, 416-424.
20. Martina, M.-S.; Fortin, J.-P.; Ménager, C.; Clément, O.; Barratt, G.; Grabielle-Madelmont, C.; Gazeau, F.; Cabuil, V.; Lesieur, S., Generation of superparamagnetic liposomes revealed as highly efficient MRI contrast agents for in vivo imaging. *Journal of the American Chemical Society* **2005,** 127, (30), 10676-10685.
21. Hachani, R.; Lowdell, M.; Birchall, M.; Hervault, A.; Mertz, D.; Begin-Colin, S.; Thanh, N. T. K., Polyol synthesis, functionalisation, and biocompatibility studies of superparamagnetic iron oxide nanoparticles as potential MRI contrast agents. *Nanoscale* **2016,** 8, (6), 3278-3287.
22. Caruntu, D.; Caruntu, G.; O'Connor, C. J., Magnetic properties of variable-sized Fe3O4 nanoparticles synthesized from non-aqueous homogeneous solutions of polyols. *Journal of physics D: Applied physics* **2007,** 40, (19), 5801.
23. Jia, B.; Gao, L., Morphological transformation of Fe3O4 spherical aggregates from solid to hollow and their self-assembly under an external magnetic field. *The Journal of Physical Chemistry C* **2008,** 112, (3), 666-671.
24. Ge, J.; Hu, Y.; Biasini, M.; Beyermann, W. P.; Yin, Y., Superparamagnetic magnetite colloidal nanocrystal clusters. *Angewandte Chemie International Edition* **2007,** 46, (23), 4342-4345.
25. Xu, F.; Cheng, C.; Chen, D. X.; Gu, H., Magnetite nanocrystal clusters with ultra-high sensitivity in magnetic resonance imaging. *ChemPhysChem* **2012,** 13, (1), 336-341.
26. Cullity, B. D.; Graham, C. D., *Introduction to magnetic materials*. John Wiley & Sons: 2011.
27. Gerischer, H., Elektrodenpotentiale: Tables of Standard Electrode Potentials. Hrsg. von G. Milazzo und S. Caroli. John Wiley & Sons, Chichester, New York 1978. *Nachrichten aus der Chemie* **1978,** 26, (10), 661-661.
28. Poul, L.; Ammar, S.; Jouini, N.; Fievet, F.; Villain, F., Synthesis of inorganic compounds (metal, oxide and hydroxide) in polyol medium: A versatile route related to the sol-gel process. *Journal of Sol-Gel Science and Technology* **2003,** 26, (1-3), 261-265.
29. Privman, V., Diffusional nucleation of nanocrystals and their self-assembly into uniform colloids. *arXiv preprint arXiv:0806.4644* **2008**.
30. Cornell, R. M.; Schwertmann, U., *The iron oxides: structure, properties, reactions, occurrences and uses*. John Wiley & Sons: 2003.
31. Barrón, V.; Torrent, J.; De Grave, E., Hydromaghemite, an intermediate in the hydrothermal transformation of 2-line ferrihydrite into hematite. *American Mineralogist* **2003,** 88, (11-12), 1679-1688.
32. Fock, J.; Bogart, L. K.; Gonzalez-Alonzo, D.; Martinez, J. I. E.; Hansen, M. F.; Varon, M.; Frandsen, C.; Pankhurst, Q. A., On the 'center of gravity' method for measuring the composition of magnetite/maghemite mixtures, or the stoichiometry of magnetite-maghemite solid solutions, via 57Fe Mössbauer spectroscopy In preparation. *(In preparation)*.
33. Skrabalak, S. E.; Wiley, B. J.; Kim, M.; Formo, E. V.; Xia, Y., On the polyol synthesis of silver nanostructures: glycolaldehyde as a reducing agent. *Nano letters* **2008,** 8, (7), 2077-2081.
34. Baronov, A.; Bufkin, K.; Shaw, D. W.; Johnson, B. L.; Patrick, D. L., A simple model of burst nucleation. *Physical Chemistry Chemical Physics* **2015,** 17, (32), 20846-20852.
35. Thanh, N. T.; Maclean, N.; Mahiddine, S., Mechanisms of nucleation and growth of nanoparticles in solution. *Chemical Reviews* **2014,** 114, (15), 7610-7630.
36. Navrotsky, A.; Mazeina, L.; Majzlan, J., Size-driven structural and thermodynamic complexity in iron oxides. *Science* **2008,** 319, (5870), 1635-1638.
37. Serna, C.; Morales, M., Maghemite (γ-Fe 2 O 3): a versatile magnetic colloidal material. *Surface and colloid science* **2004**, 27-81.
38. Kostopoulou, A.; Brintakis, K.; Vasilakaki, M.; Trohidou, K.; Douvalis, A.; Lascialfari, A.; Manna, L.; Lappas, A., Assembly-mediated interplay of dipolar interactions and surface spin disorder in colloidal maghemite nanoclusters. *Nanoscale* **2014,** 6, (7), 3764-3776.

39. Kuchkina, N. V.; Morgan, D. G.; Kostopoulou, A.; Lappas, A.; Brintakis, K.; Boris, B. S.; Yuzik-Klimova, E. Y.; Stein, B. D.; Svergun, D. I.; Spilotros, A., Hydrophobic periphery tails of polyphenylenepyridyl dendrons control nanoparticle formation and catalytic properties. *Chemistry of Materials* **2014,** 26, (19), 5654-5663.
40. Liu, J.; Sun, Z.; Deng, Y.; Zou, Y.; Li, C.; Guo, X.; Xiong, L.; Gao, Y.; Li, F.; Zhao, D., Highly Water-Dispersible Biocompatible Magnetite Particles with Low Cytotoxicity Stabilized by Citrate Groups. *Angewandte Chemie* **2009,** 121, (32), 5989-5993.
41. Kozissnik, B.; Bohorquez, A. C.; Dobson, J.; Rinaldi, C., Magnetic fluid hyperthermia: advances, challenges, and opportunity. *International Journal of Hyperthermia* **2013,** 29, (8), 706-714.
42. Vergés, M. A.; Costo, R.; Roca, A.; Marco, J.; Goya, G.; Serna, C.; Morales, M., Uniform and water stable magnetite nanoparticles with diameters around the monodomain–multidomain limit. *Journal of Physics D: Applied Physics* **2008,** 41, (13), 134003.
43. Blanco-Andujar, C.; Ortega, D.; Southern, P.; Pankhurst, Q.; Thanh, N., High performance multi-core iron oxide nanoparticles for magnetic hyperthermia: microwave synthesis, and the role of core-to-core interactions. *Nanoscale* **2015,** 7, (5), 1768-1775.
44. Atkinson, W. J.; Brezovich, I. A.; Chakraborty, D. P., Usable frequencies in hyperthermia with thermal seeds. *IEEE Transactions on Biomedical Engineering* **1984,** (1), 70-75.

Insert Table of Contents artwork here

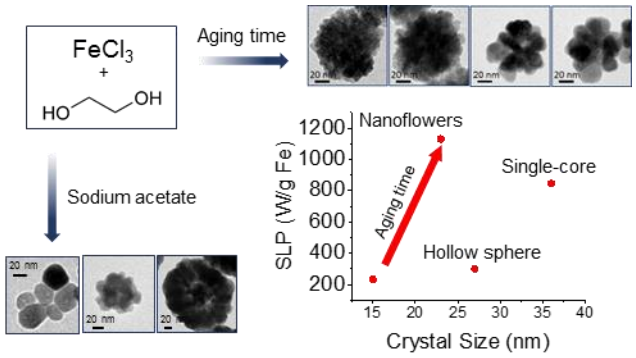

Unravelling the mechanisms that determine absorption and metabolization of magnetic single and multi-core nanoparticles in-vitro and in a Xenopus laevis model

M. Marín-Barba[1⊥], H. Gavilán[2⊥], L. Gutiérrez[3], E. Lozano-Velasco[1], I. Rodríguez[4], G. Wheeler[1], C. Morris[1], M.P. Morales[2] and A. Ruiz[1*]

[1]University of East Anglia, Norwich Research Park, Norwich, Norfolk, NR4 7TJ, UK.

[2]Instituto de Ciencia de Materiales de Madrid, Sor Juana Inés de la Cruz 3, 28049 Madrid, Spain.

[3]Dept. Química Analítica, Instituto de Nanociencia de Aragón, Universidad de Zaragoza, 50018 Zaragoza, Spain.

[4]Dept. of Nutrition, School of Medicine, Norwich Research Park, Norwich, Norfolk, NR4 7TJ, UK.

[⊥]These authors contributed equally to this work

Abstract

Multi-core superparamagnetic nanoparticles have been proposed as ideal tools for some biomedical applications because of its high magnetic moment per particle, high specific surface area and long term colloidal stability. Controlling aggregation and packing of the cores it is possible to obtain not only single-core but also multi-core and hollow spheres having internal voids. In this work we compare toxicological properties of single and multi-core nanoparticles. Both types of particles showed moderate *in vitro* toxicity (MTT assay) tested in Hep G2 (human hepatocellular carcinoma) and Caco-2 (human colorectal adenocarcinoma) cells. The influence of surface chemistry in their biological behaviour was also studied after functionalization with O,O′-bis(2-aminoethyl) PEG (2000 Da). For the first time, these nanoparticles were evaluated in a *Xenopus laevis* model, studied their toxicity and described how they trigger iron metabolism. The results also highlight the potential of *Xenopus laevis* model bridging the gap between in vitro cell-based assays and rodent models for toxicity assessment to develop effective nanoparticles for biomedical applications.

1. Introduction

Iron oxide magnetic nanoparticles (IOMNPs) are extensibily studied nowadays for its potential for biomedical applications.[1],[2] Their surface chemistry can be modified, adding functionality to the material and enabling their use for gene therapy, tissue regeneration and drug delivery, to specifically target tumors using external magnetic fields. Their magnetic properties can be exploited for magnetic resonance imaging and magnetic-fluid hyperthermia, which raised hope for improved imaging techniques[3] and cancer treatment.[4],[5] However, in spite of their potential, few of these biomaterials have reached the clinical practice[6].

A crucial issue for magnetic nanoparticle safe utilization in biomedicine and their approval by regulatory agencies lies in their biotransformation and toxicity. On one hand, the course and fate of the nanoparticles once they fullfil their mission needs to be studied. On the other hand, the safety metabolization of the by-products must be assessed and assured. Since iron is involved in diverse vital processes[7], organisms display mechanisms to transport and store

iron in non-toxic forms.[7] Therefore, IOMNPs are predicted to be safely incorporated in biological systems. Increasing evidence demonstrates that IOMNPs trigger iron-coping mechanisms in cells and that the degradation products of these materials are incorporated into normal iron metabolic routes.[8],[9],[10],[11],[12],[13],[14] However, nanoparticle coating has been shown to be determinant on the IOMNPs uptake, degradation and fate.[15],[16] In order to stablish solid conclusions about IOMNPs toxicity and biodistribution and its cellular effects, it would be ideal to have biologically pertinent models.

In this sense, *Xenopus laevis* is an amphibian model ideal to study the course and fate of the nanoparticles since it allows flexible bioassay for evaluating vertebrate embryology development, basic cell and molecular biology, genomics, neurobiology and toxicology.[17] Though this model, the risk of exposure to contaminated water was reported. The contaminants were metal oxide-based nanomaterials (γ-Fe_2O_3, TiO_2, ZnO and CuO) and the mortality, malformations and growth inhibition were studied,[18] confirming that γ-Fe_2O_3 did not pose risks to amphibian populations. Furthermore, it was pointed that NPs sizes above 200 nm had toxic effects.[19] Despite this, literature available on the effects of many compounds on the larval development of *X. laevis* in environmental studies, there are no reports evaluating nanoparticles designed for bioapplications bridging the safety assessment of NPs in cell-based assays with data generated from rodent *in vivo* systems. Rat animal models have proven to be suitable models for the study of anaemia oral treatment with IOMNPs.[20]

In this work, we report the effect of γ-Fe_2O_3 magnetic single and multi-core nanoparticles suitable for bioapplications on *X. laevis* embryos. The particles have uniform size in the nanoscale and are coated with biocompatible shells. IOMNPs colloids used in this work can be classified as single-core (with only one magnetic core per particle) and multi-core (with several magnetic cores per particle).[21] While single-core superparamagnetic nanoparticles have been proposed as ideal tools in biomedicine, since they circulate longer after injection in an animal,[22] which may favour their uptake in leaky vasculature regions such as tumors,[23] for some medical applications, such as bioseparation or magnetic fluid hyperthermia, it can be advantageous to use larger multi-core particles that have a large magnetic moment per particle.[24] However, few *in vitro* and *in vivo* studies have been dedicated to the comparison of single-core and multi-core nanoparticles [REF Claire Wilheml acs nano 2016] and there is a lack of knowledge still on how the aggregation of magnetic cores forming multi-core nanoparticles affects the nanoparticle uptake and transformation, and thus its toxicity and biodistribution.

AC magnetic susceptibility measurements will be used here to characterize the IOMNPs once they are internalised in biological systems. This technique has proven to be an excellent tool to study magnetic nanoparticles in complex matrices, since the diamagnetic signal coming from tissues does not interfere with the superparamagnetic signal of the NPs. [25] This way it was possible to follow the signal of the magnetic nanoparticles in animal models[26],[27] and to quantify the iron content. This is one of the greatest challenges in the nanomaterials area nowadays, i.e. determining how best to characterize the nanopaticles and follow its transformation/degradation,[28]The study of *in vivo* fate of IOMNPs is imperative to develop successful biomedical applications. In this paper, it is presented for the first time, the study, by means of AC magnetic susceptibility measurements, of the intake of iron-containing particles in *X. laevis* embryos.

2. Materials and Methods

2.1 Materials

Commercial products: iron(III) chloride hexahydrate ($FeCl_3 \cdot 6H_2O$, >98%, Sigma-Aldrich), sodium oleate (>82%, Riedel-de Haen), oleic acid (90%, Aldrich), oleylamine (70%, Aldrich), meso-2,3-dimercaptosuccinic acid (DMSA, 98% Aldrich), 1-octadecene (90%, Aldrich), n-hexane (99%, Scharlau), toluene (99.8%, Sigma-Aldrich), dimethyl sulfoxide (>99.5%, Sigma-Aldrich), O,O′-bis(2-aminoethyl)PEG, 2000 Da (Sigma Aldrich), ethyl-3-(3-dimethylaminopropyl)-carbodiimide (≥ 98 %, Fluka, EDS) polyvinylpyrrolidone (PVP40, Sigma Aldrich), sodium acetate trihydrated ($NaAc \cdot 3H_2O$, ≥ 99%, Sigma Aldrich), ethylene glycol (EG, ≥ 99.5 %, Fluka), citric acid ($C_6H_8O_7$, ≥ 99.5%, Sigma Aldrich) and ethanol (96%, Panreac). Dialysis tubing cellulose membranes were purchased from Sigma and washed prior to use.

2.2 Nanoparticles synthesis

Synthesis of iron oxide single-core nanoparticles (SC). The synthesis of iron oxide nanoparticles has been based on a previous work described in the literature.[29] The reaction was carried out under nitrogen. In a round-bottomed flask (500 mL), equipped with a mechanical stirrer (glass stirrer shaft) thermometer, entry for nitrogen flow and reflux condenser, iron(III) oleate (4.54 g, 5 mmol) was mixed with oleic acid (0.724 g, 2.6 mmol) in 1-octadecene (50 mL). The mixture was stirred (100 rpm) and slowly heated (5 $^{o}C \cdot min^{-1}$ for T< 100ºC, and 2$^{o}C \cdot min^{-1}$ for T> 100ºC) until reflux (325ºC) with a heating mantle. The heating mantle was withdrawn and the system was allowed to cool down to room temperature. The resulting black mixture was washed with ethanol several times by centrifugation (RCF = 7500) and magnetic decantation (the particles were separated with the aid of a magnet). The resulting dried black solid (the solid was dried under nitrogen flux) was redispersed in hexane. The as-synthesized nanoparticles are coated with oleic acid.

Synthesis of iron oxide multi-core nanoparticles (MC). The synthesis of iron oxide nanoparticles has been based on a previous work described in the literature[30] but the experimental procedure and the concentration of NaAc have been varied. Typically, 2.62 mmol iron(III) chloride were dissolved with ultrasound in 109 mL of ethylene glycol. Then, 140 mmol PVP40 were added slowly under vigorously magnetic stirring (>1000 rpm) and mild heating until completely dissolved. Then, 26.2 mmol of $NaAc \cdot 3H_2O$ were added to the solution. The mixture was sealed in a Teflon-lined autoclave (125 mL) and maintained at 200 °C for 16 h for solvothermal crystallization, following cooling inside oven. The precipitated solid product was washed with ethanol and distilled water through centrifugation (RCF = 7500) several times. The as-synthesized nanoparticles are coated with the polyol and the PVP.

2.3 Surface modification

Ligand exchange with dimercaptosuccinic acid on single-core NPs (SC@DMSA). For DMSA ligand exchange, a standard procedure was used.[31] In a typical experiment, ethanol (20 mL) was added to a volume of SC dispersed in hexane containing a mass of Fe_3O_4 of 50 mg. The mixture was sonicated and then placed on a magnet to separate the liquid from the black solid residue of nanoparticles. The residue was washed with more ethanol (5 X 10 mL) following the same procedure, until the discarded liquid had a clean appearance. The remaining black residue was dispersed in toluene (20 mL) and the dispersion added to a solution of DMSA (90 mg) in dimethyl sulfoxide (5 mL). The resulting black suspension was then shaken in a laboratory tube rotator. After 2 days, SC@DMSA nanoparticles were precipitated as a black powder stuck to the glass tube and the liquid phase was transparent and pale yellow. The liquid was discarded and the nanoparticles were washed with ethanol (4 X 10 mL), sonicating and centrifuging (RCF = 7500). The final black solid was air dried and redispersed in distilled water. KOH 1 M was added to increase the pH to 10 and HNO_3 0.01 M was used to lower the pH to 7. The dispersion was then placed in a cellulose membrane and dialyzed for 5 days in distilled water, to remove any excess of unreacted DMSA and any

other small impurities that may be present in the dispersion without being attached to the nanoparticles.

Surface coating with citric acid on multi-core NPs (MC@CIT). For citric acid coating a standard procedure was used.[21],[32] First, sample volume equivalent to 20 mg of Fe was adjusted to pH 2 and then dispersed in 13 mL of a solution of citric acid 0.1 M. Afterwards, the mixture was heated at 80 °C for 30 min. The solution was centrifuged and washed with distilled water. Finally the pH was adjusted first to 11 with KOH 1M and then to 7 with HNO_3 0.01 M.

Surface coating with polyethylene glycol (SC@DMSA@PEG and MC@CIT@PEG). PEG conjugation reaction has been based on a previous work described in the literature.[33] Amine-functionalized PEG was attached to SC@DMSA or MC@CIT via an ethyl-3-(3-dimethylaminopropyl)-carbodiimide (EDC)-mediated coupling reaction using the polymer O,O′-bis(2-aminoethyl)PEG, 2000 Da. PEGylation reaction was carried out in a refrigerated ultrasonic bath; an aqueous solution containing 10 mg SC@DMSA or MC@CIT was mixed with the PEG derivative (4 mg). The total amount of EDC (1 mg) was divided into five aliquots, one of which was added every 1 h, and the fifth 4 h after the previous addition. The molar ratio of COOH groups/amine groups/EDC was 1:1.5:1; pH was adjusted to 6, and the mixture was sonicated (4 h, 25 °C), followed by extensive dialysis.

2.4 Nanoparticle structural characterization

The particle sizes and morphologies were determined by transmission electron microscopy (TEM) with a JEM1010 microscope (JEOL, Peabody, USA) operating at 100 kV. Samples were prepared by placing a drop of the uncoated particles suspended in water onto a carbon coated copper grid and allowing it to dry at room temperature. The size distributions were determined by manual measurement of more than 100 particles using the public domain software ImageJ. The presence of the coating and the washing process was also confirmed and studied by Fourier transform infrared spectroscopy (FTIR) in the range of 4000-250 cm^{-1} by use of a Bruker (USA) IFS 66VS. The samples for FTIR were prepared diluting the dried powder in KBr at 2% by weight and pressing it into a pellet. The presence of the coating was also studied by thermogravimetric analyses (TGA). They were performed in a Seiko TG/DTA 320U thermobalance, whose temperature scanning range is from room temperature up to 900 °C. For this work, samples were heated from room temperature to 700 °C at 10 °C/min under an air flow of 100 $mL \cdot min^{-1}$. Platinum pans were used and α-Al2O3 was used as reference. Colloidal properties were studied in a Zetasizer Nano S, from Malvern Instruments (UK). The hydrodynamic size was determined by Dynamic Light Scattering (DLS) and the zeta potential was measured as a function of pH at 25 °C, using HNO_3 and KOH to change the pH of the suspensions. Hydrodynamic size is given as the intensity-weighted mean.

2.5 Cell culture

Hep G2 (human hepatocellular carcinoma) and Caco-2 (human colorectal adenocarcinoma) cells were cultured as mono-layers in Dulbecco's modified Eagle medium supplemented with 2% penicillin-streptomycin and 10% fetal bovine serum, in a humidified incubator (37°C, 5% CO_2). For toxicity experiments, cells were seeded in 96-well plates at 50,000 cells/cm^2 (approximately 1.6 x 10^4 cells/well, 150 µL/well). For iron uptake experiments, Caco-2 cells between passages 30-36 were seeded onto collagen-coated 12-well plates (Bio-Greiner, UK) at a density of 2 x 10^5 cells/well suspended in 1 mL of supplemented DMEM which was replaced every 2 days. Cells were used on confluence at days 13-15 post-seeding. In order to ensure a low basal media iron levels, 24 hours prior to the initiation of the nanoparticles treatments, the DMEM medium was replaced by Eagle's minimum essential medium (MEM)

without foetal bovine serum supplemented with 10 mmol/L PIPES [piperazine-N, N' –bis-(2-ethanesulfonic acid)], 26.1 mM $NaHCO_3$, 19.4 mmol/L glucose, 1% antibiotic-antimycotic solution, 11 µmol/L hydrocortisone, 0.87 µmol/L insulin, 0.02 µmol/L sodium selenite (Na_2SeO_3), 0.05 µmol/L triiodothyronine and 20 µg/L epidermal growth factor.[34] The day of the experiment, the nanoparticles were diluted in the low-iron MEM to obtain a 250 µM final iron concentration and subsequently Caco-2 cells were exposed for 24 hours with the treatments.

2.6 Cytotoxicity assay (MTT)

Cell viability was determined using the standard 3-(4,5-dimethylthiazol-2-yl)-2,5-diphenyl tetrazolium bromide (MTT) assay 24 h after exposure to NP. Cells were seeded in 96-well plates at 50,000 cells/cm^2 (approximately 1.6 x 10^4 cells/well, 150 µL/well). In total 60 wells were seeded per plate (6 rows x 10 columns) as the outer wells were left empty to avoid errors due to evaporation. Each row was used as a replicate (3 wells/condition) and serial dilutions went across the columns of the plate. Cells were left to grow until 70-80 % confluency. NP-containing medium was removed after 24 h, cells were rinsed three times with PBS, and MTT solution in medium (final MTT concentration 50 µg ml^{-1}) was added and incubated (2 h, 37 °C). The MTT solution was removed without disturbing cells, 0.2 mL $well^{-1}$ of DMSO and 0.025 mL $well^{-1}$ of Sorensen buffer were added, the plates were shaken gently to dissolve formazan crystals, and the absorbance was read on a microplate reader at 550 nm. Cell viability (%) was calculated as [(A − B)/A × 100], where A and B are the absorbance of control and treated cells, respectively. Values represent mean ± SD (n = 3).

2.7 *In vivo* test

For the *Xenopus laevis* embryo toxicity model, adult females were primed with PMSG (Pregnant Mare's Serum Gonadotropin) four days before the experiment and induced with Chorulon (contains Human Chorionic Gonadotrophin, HCG) the day before. Eggs were obtained by squeeze and fertilized in a petri dish by adding male sperm (male testis incubated with 2ml 1xMMR (Marc's modified ringers) + 8ml FBS). Then the eggs were washed with 0.1xMMR to remove the sperm (20min) and left 7 min in L-cysteine (10g into 500mL 1xMMR pH 8.0). Finally 2 washes were performed with 1xMMR, and the eggs were plated in BSA-coated petri dishes covered with 0.1xMMR. Embryos were left at 23ºC until they reached stage 38, and then plated at 24-well plates (7 embryos/well) in 0.1xMMR media containing the nanoparticles and incubated at 23ºC. Non-treated embryos were used as control. The mortality and the morphological changes of the embryos were recorded every 24h until embryos reached stage 45.

2.8 Histological evaluation

When the embryos reach the appropiate stage, they where fixed in MEMFA (3.7% Formaldehyde, 1X MEM salts and DEPC H_2O) overnight at 4ºC. Samples were washed in PBS, dehydratated and kept in 100% ethanol. To embeed embryos in wax, they were directly washed in histoclear, 1:1 histoclear:wax and finally wax and placed in moulds. Embryos were sectioned using a microtome generating 10um slices. Slices were then hydrated and dryed to be analysed by Scanning electron microscopy.

2.9 Iron content analysis

Groups of 7 embryos were pooled. Animals were weighed and lyophilized 72 hours in a Telstar lyoquest lyophilizer (Spain), and the iron content was measured by Inductively Coupled Plasma-Optical Emission Spectrometry (ICP-OES) in an Optima 2100 DV from PerkinElmer, after acid digestion, with concentrated HNO_3 during 1 h; or kept freeze dried for magnetic characterization, respectively. The sample manipulation was performed using disposable plastic material to avoid ferromagnetic contamination.

2.10. Magnetic characterization

The resulting freeze-dried samples were placed into gelatin capsules for their magnetic characterization in a Quantum Design MPMS-XL SQUID magnetometer with an AC susceptibility option. The measurements were performed with AC amplitude of 0.41 Oe, in the temperature range between 1.8 and 300 K and at a frequency of 11 Hz.

2.11 RNA extraction and quantitative PCR

Gropus of 7 embryos were snap frozen in liquid nitrogen. RNA was extracted using High Pure RNA isolation kit (Roche) and 1 ug of RNA was taken to synthetise cDNA using Maxima First Strand cDNA synthesis kit (Thermofisher). RT-PCR was perfored using SYBER Green detection method. Primers were designed targeting both copies of *X.laevis* genes. Dmt1_F: cagaggatgaaacgcactca, Dmn1_R: atcctgccactgatccagac; Fth1_F: tggagtaacaccctggaagc, Fth1_R: aggatcaaccttgtcggatg; Tf_F: agaaagggcaagtgggtttt, Tf_R: tctggcaaagtgacaacagc; hepcidin_F: aaatcaaccccaatctgctg, hepcidin_R: gtttgttgattgccgaaggt; hmox1_F: ggagacctctcaggtggaca, hmox1_R: atggagttcatacgggaacg; gpx1_F: ttccccctctttgagaaggt, gpx1_R: atgatgctcttgggatcctg; sod2_F: tgtgcaggctcagtgtttgt, sod2_R: gctgcagagcaccataatca; gsr_F: gcaaagaggagaaggtggtg, gsr_R: cggaggaagtcggatgaata.

3. Results and Discussion

3.1. Nanoparticles synthesis and characterization

Two different types of iron oxide nanoparticles were synthesized in this work. Single core nanoparticles (SC) were obtained by thermal decomposition of the iron(III) oleate precursor in 1-octadecene (Fig 1 a-b). Particles were 13 nm (± 1 nm) in diameter, uniform in size (Fig 1 c), relatively spherical and well dispersed, owing to the presence of oleic acid around the particles. In a different approach multi-core nanoparticles (MC) were obtained by polyol mediated reduction of iron(III) chloride. MC are composed of spherical 142 nm (± 23 nm) nanoparticles with a well-defined size and shape. These MC nanoparticles consist of smaller cores of approximately 10 nm. HRTEM and X-ray diffraction patterns have already been reported.[35] Particle structure and size were selected intentionally, since they are two key parameters that directly influence *in vivo* biological behaviour. The size of intravenously injected nanoparticles greatly affects their *in vivo* biodistribution, *e.g.* particles from 60 to 150 nm in size are taken up by the reticuloendothelial system leading to rapid uptake in the liver and spleen. Intravenously injected nanoparticles with diameters of 10–40 nm allow longer blood circulation and can cross capillary walls, and they are often phagocytosed by macrophages which traffic to lymph nodes and bone marrow.[36] However, how these

parameters affect the greater picture of toxicity and biodegradability mechanisms is still poorly understood.

Iron oxide nanoparticles obtained by thermal decomposition are hydrophobic. To make them suitable for biological applications, oleic acid on the surface of the nanoparticle was removed with DMSA via ligand exchange reaction (SC@DMSA). Polyol mediated process render hydrophilic nanoparticles along with polyvinylpyrrolidone (PVP40), present in the reaction, however an extra capping agent like citric acid enhance the electrostatic repulsion and facilitates the final dispersion of the MC nanoparticles in aqueous media (MC@Cit). Hydrodynamic sizes are always higher than sizes measured by TEM, indicating the presence of the coating or some degree of agglomeration after surface modification, but both types of particles remains below 200 nm (34 and 181 nm were obtained for SC@DMSA and MC@Cit), an important requirement for biomedical applications. Both particles have high negative surface charge at pH 7 (Z-potential equal to −38 and −25 mV for SC@DMSA and MC@Cit, respectively). In order to evaluate the influence of the surface charge in particle absorption and biodegradation we conjugated covalently a diamine PEG derivative to the carboxylic groups (from both DMSA and citric acid) in the surface of the nanoparticles. After PEG conjugation, average hydrodynamic size at pH 7 increased from 34 to 65 nm and from 181 to 183 nm for SC@DMSA and MC@CIT, respectively (SC@DMSA@PEG and MC@Cit@PEG) and net surface charge decreased from approximately −38 to -24 mV for SC@DMSA@PEG samples and from -25 to -18 mV for MC@Cit@PEG . Colloidal properties of aqueous suspensions of the nanoparticles at pH 7 are summarized in Table 1.

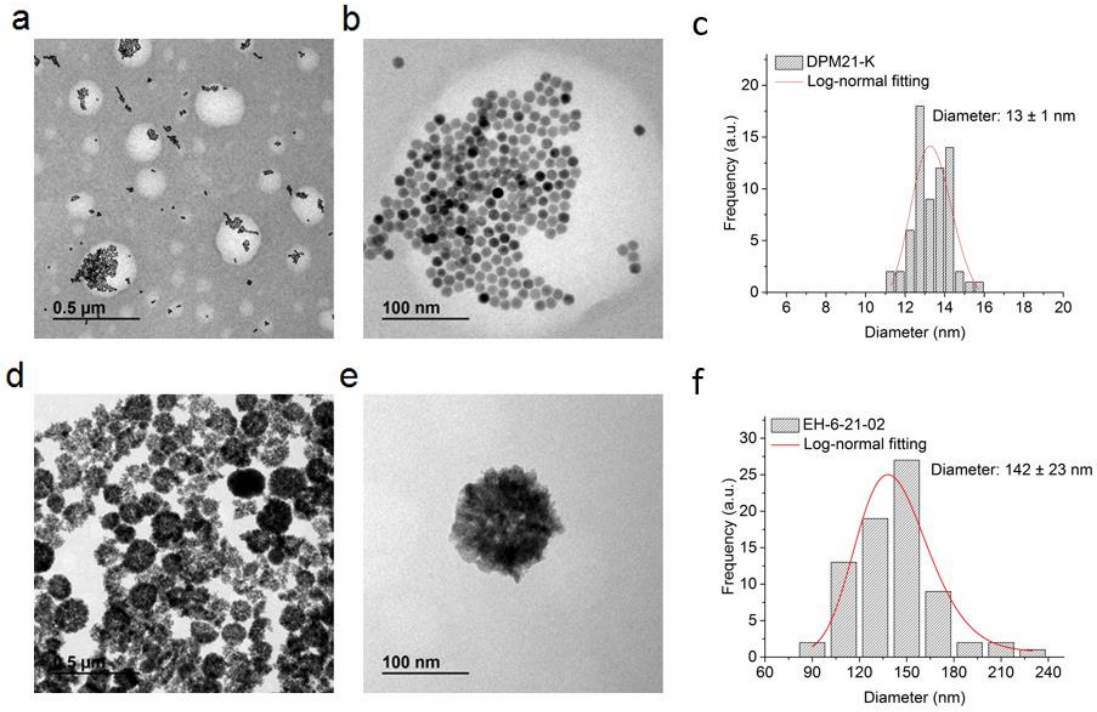

Fig 1. Transmission electron microscopy (TEM) images of single and multi-core nanoparticles. (a,b) SC@DMSA; (d,e) MC@Cit; (c,f) Size distribution histograms. Red lines indicate the log-normal fitting function of TEM particle size data.

Table 1. Colloidal properties of aqueous suspensions of the nanoparticles at pH 7. Hydrodynamic sizes, PDI (= standard deviation/mean size) and surface charge of single and multi-core nanoparticles after PEG conjugation.

Sample	Hydrodynamic size (nm)	PDI	ζ-Potential (mV)
SC@DMSA	34.2	0.054	-38 ± 12
SC@DMSA@PEG	65.2	0.084	-24 ± 7
MC@CiT	181.0	0.201	-25 ± 9
MC@CiT@PEG	183.1	0.225	-18 ± 9

Nanoparticle surface modification was also confirmed by FTIR (Fig 2 a, b). For all the samples the typical bands of metal skeleton vibration (Fe–O) in the region of 550–600 cm^{-1} and a broad peak between 3000 and 3500 cm^{-1} due to surface −OH groups are observed. After PEG conjugation, some peaks appeared at 1354 and 1102 cm^{-1}, indicating asymmetric and symmetric stretching of C–O–C, and out-of-plane bending of the –CH of the PEG chains at 956 cm^{-1}. TGA of the unconjugated nanoparticles reveals a weight loss of ∼15% and 8% for SC@DMSA and MC@CIT respectively, due to the removal of physical and chemical water and capping molecules (DMSA or citric acid). Particles modified with diamine PEG nonetheless showed a larger amount of conjugated polymer (∼20% in the case of SC@DMSA@PEG and 13% for MC@Cit@PEG) which indicates greater reaction efficiency. In all cases, weight loss took place between 200 and 400°C, associated with polymer burning.

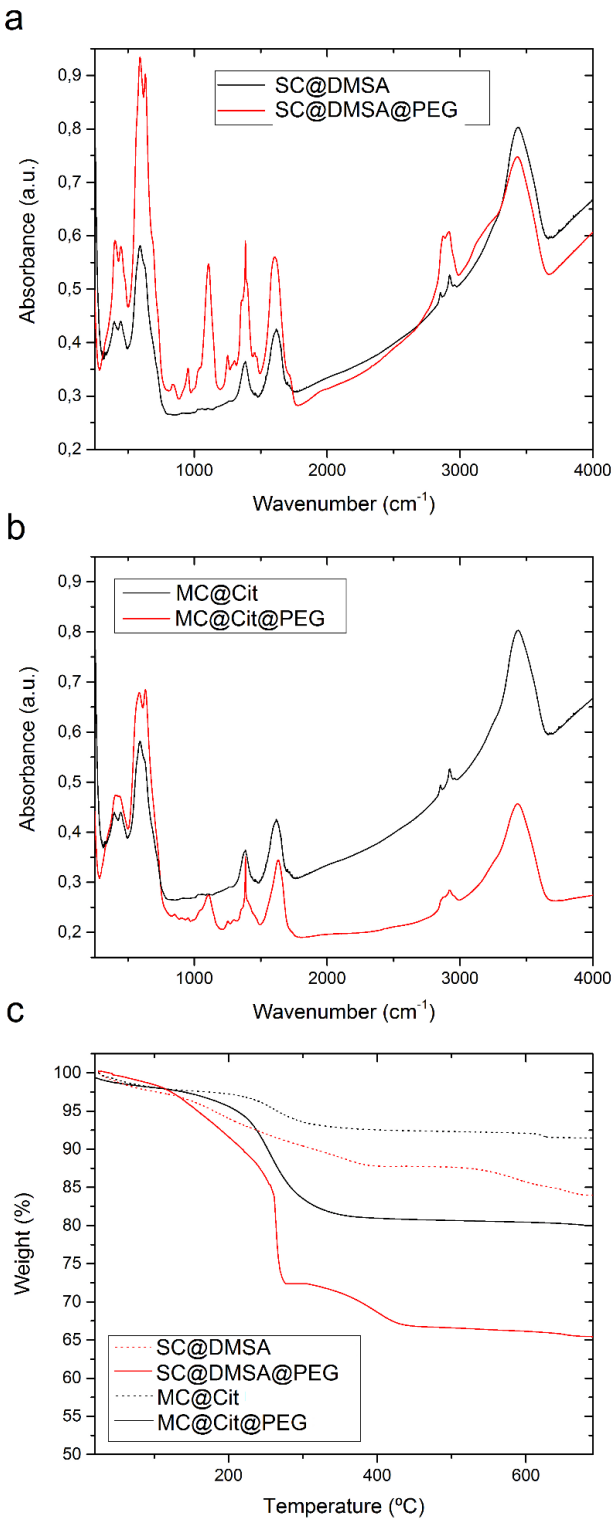

Fig 2. FTIR spectra of uncoated/coated with PEG nanoparticles (a) Single-core nanoparticles; (b); Multi-core nanoparticles (c) TGA curves.

3.2. Toxicity *in vitro*

In vitro toxicological characterization of the nanoparticles was evaluated through the degree of cell survival by means of the standard methyl thiazol tetrazolium bromide (MTT assay). The analysis of cytotoxicity after incubation with Hep G2 and Caco-2 cells with the nanoparticles showed that viability of cell culture is not significantly affected by the presence of the nanoparticles up to 1000 µM Fe concentration after 24 h of treatment (80–100% viability compared with the control). At iron concentrations higher than 1000 µM, SC decrease the viability of both cell lines down to values of 20 %. In the case of MC, viability percentage of both cell lines is in the range of 60-80 %, indicating lower toxicity even at high iron concentrations. Differences in toxicity profile at higher doses could be related to different sensitivity of both cell lines used in the treatment with nanoparticles. The effect of PEG coating is not very clear at high iron concentration. In the case of Hep G2 cells, PEG functionalization improves the cytotoxicity for SC while in Caco-2 has no effect. For MC, PEG functionalization reduces the viability down to 60 % in Caco-2 cells. Even when this method needs further refinement and standardization for toxicity evaluation of nanoparticles it offers an inexpensive and high-throughput alternative to perform *in vitro* cytotoxicity screenings.[37]

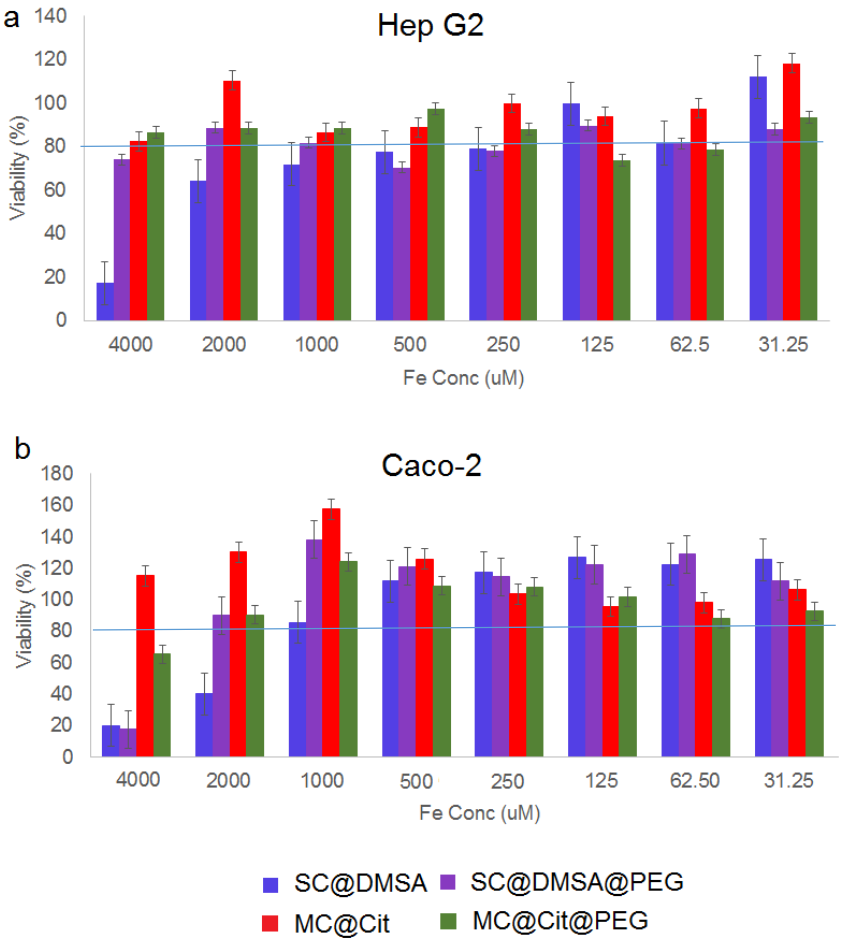

Fig 3. Evaluation of cell viability by MTT assay of (a) Hep G2 cells and (b) Caco-2 cells after 24 h treatment with the nanoparticles. Values indicated mean ± SD (n = 3).

3.3. *In vivo* iron evaluation of nanoparticles

The use of this model has advantages with respect to other animal models. First, embryos develop externally, allowing experiments to be performed prior to, or directly following fertilization. They have a rapid embryo growth and development within 48 hours (Fig 4), a tadpole has a fully functional set of organs, and it can be examined to determine if any experimental intervention (in this case a solution containing nanoparticles) has had an effect. In this experiment, nanoparticles were added at stage 38 (late tailbud) and survival was evaluated every 24 h until embryos reach stage 45 (tadpole), approximately 72 h of exposure. In order to optimise the dose for the following experiments, embryos were treated with four different concentrations, 0.25 mg/mL, 0.5 mg/mL, 0.75 mg/mL and 1 mg/mL. None of the conditions were found lethal for the embryos (Fig 5), therefore we decided to perform the rest of the experiments comparing a low and a high dose of nanoparticles (0.5 and 1 mg/mL).

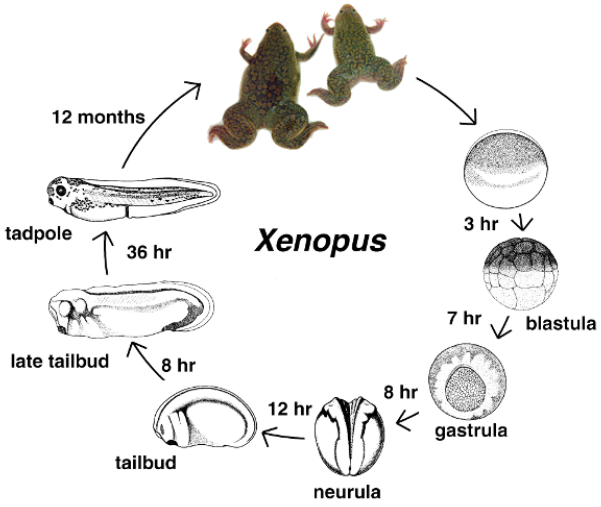

Fig 4. Life cycle of X. laevis. Frog embryos develop externally. The embryo growth takes place fast and a tadpole with fully functional set of organs is formed within 48 h. The growth to adult takes place within 12 months. Image from http://www.xenbase.org/anatomy/intro.do.

The transparency of *Xenopus* embryos allows the visualization of the nanoparticles as they are being swallowed, which takes place mainly for the SC@DMSA, suggesting that this nanoparticles are massively absorbed by the organisms.

All embryos displayed a general body toxicity when treated with NPs at 1 mg/mL characterised by defects in embryo body shape, tail bending and developmental delay. In the case of embryos treated with 0.5 mg/mL, defects were more subtile (Fig 6). This result suggested a dose-dependant uptake of the NPs by the embryos. As the main organs involved in NPs' absorption and biotransformation are the gut and liver, we evaluate the morphology of these organs. For SC-treated embryos, the intestine coiled structure is preserved although is visible enlarged when embryos are treated at 1 mg/mL.

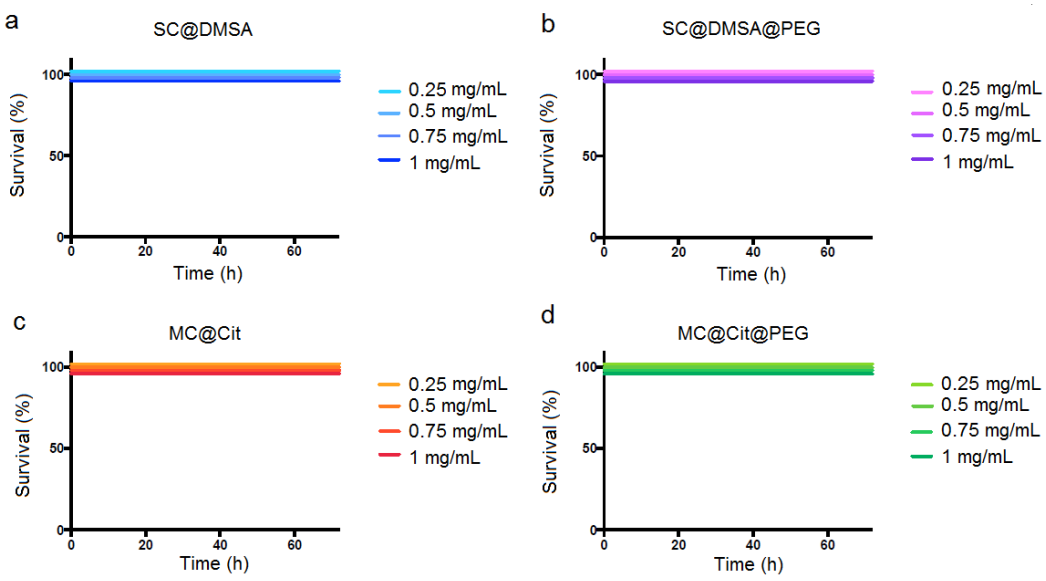

Fig 5. Survival curves of *X. laevis* exposed to different particle concentrations (n=7 per group).

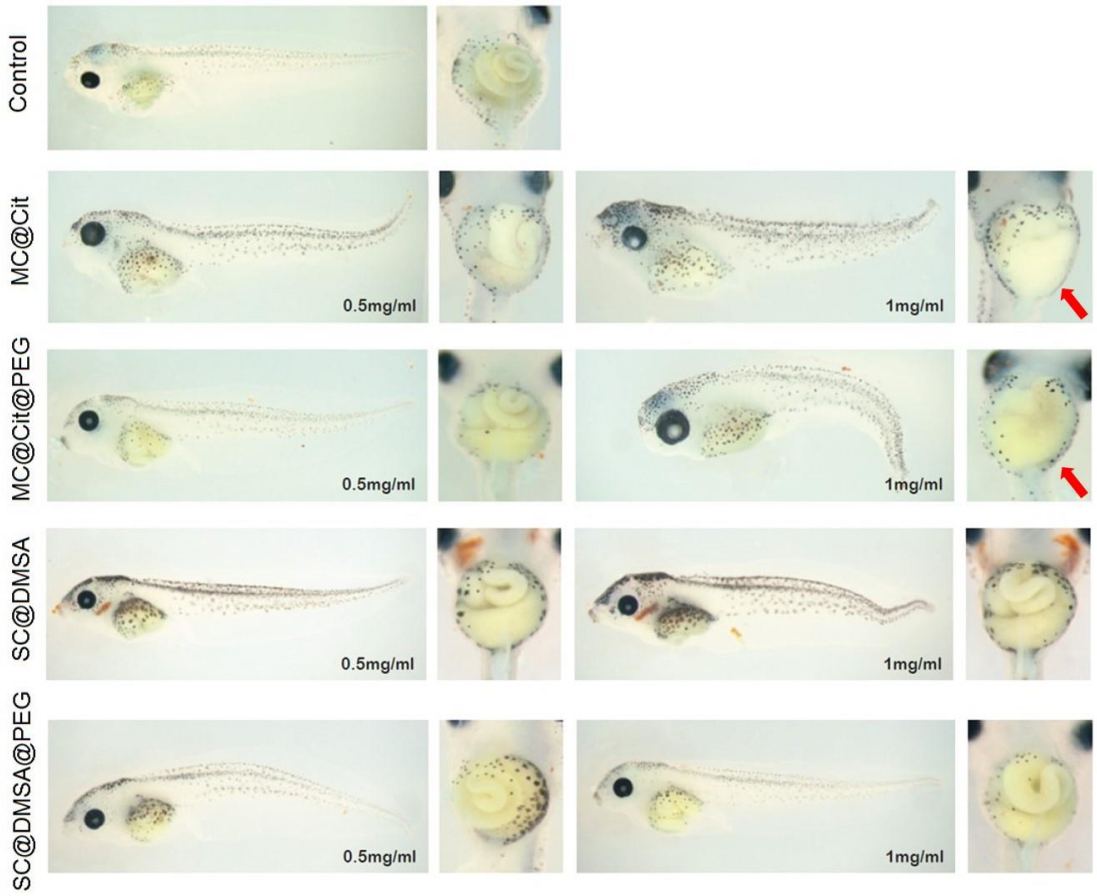

Fig 6. Representative images from *X. laevis* exposed to 0.5 and 1 mg/mL of nanoparticles. (n=7 per group). Red arrows highlight those intestines in which the effect of treatment was dramatic, modifying their coiled structure.

The MC-treated embryos displayed a dramatic effect in the morphology of the intestine. The organ is not mantained or not well formed, as we are unable to see the intestine loops. Interestingly, at lower dosis of SC or MC, where the general toxic effects of the embryo are visibly reduced, the damage in the gut is absent in the treatment with PEG functionalized nanoparticles compared with the uncoated ones.

Electron microscopy images of pharynx sections (Fig 7), taken from different embryos, have allowed us to localize the particles in the organisms. The presence of the NPs in the tissue sample is evidenced by the Energy Dispersive X-ray (EDS) elemental mapping. Those spots with brighter contrast, due to the higher Z atomic number of iron, confirmed that only at the dose of 1 mg/mL, SC@DMSA and MC@Cit, could be detected in the upper body tissue sections, in contrast with the control. PEGylated nanoparticles (SC or MC) were no detected in any sample.

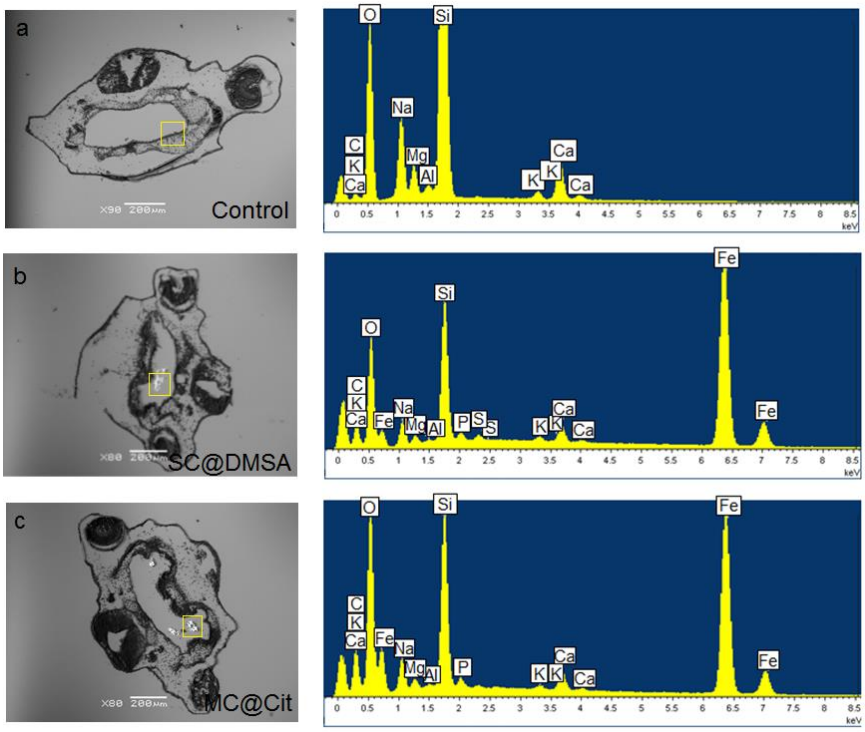

Fig 7. Scanning electron microscopy (SEM) images of pharynx sections from different embryos: (a) Control, (b) Embryos exposed to SC@DMSA nanoparticles, (c) Embryos exposed to MC@Cit nanoparticles. Right panel shows elemental analysis of selected areas in the images obtained by Energy Dispersive X-ray Spectrometry (SEM-EDS).

3.4. Iron quantification – AC magnetic susceptibility and ICP-OES

IOMNPs intake is visibly detected in the images of pharynx sections of the embryos because the EDS spectra clearly showed K electron shell (K-α and K-β lines) of iron, whereas in the case of control these peaks are absent. In order to quantify the iron present in the samples through these technique, the application of quantitative correction procedures are needed, which are sometimes referred to as matrix corrections.[38] As SEM only provides local information, the quantitative analysis of nanoparticles' intake, was performed through magnetic characterization and iron elemental analysis. Moreover, these techniques allow the comparison of the accumulation depending on the coating and the surface charge (DMSA, citric acid, and PEG functionalization).

In order to evaluate the accumulation of the nanoparticles in the animals, we performed AC susceptibility of pools of seven animals. Magnetic measurements, especially AC magnetic susceptibility, are extremely sensitive being able to distinguish the contribution from the magnetic nanoparticles from that of other endogenous iron-containing species, usually present in a bigger concentration but with weaker magnetic signal than the nanoparticles. The presence of magnetic nanoparticles can be identified by a maximum in the in-phase magnetic susceptibility (χ') accompanied by a maximum at slightly lower temperatures in the out-of-phase susceptibility (χ''). The temperature location of the maxima depends on the nanoparticle (material, size, aggregation degree, etc). The height of the maxima is a surrogate measurement of the concentration of nanoparticles.

In our case, a dose-dependent amount of nanoparticles is observed in the animals treated with particles without PEG coating (Fig 7), independently if they are SC or MC. Interestingly PEG coated nanoparticles, both SC and MC, were not detected, or at least they are under the detection limits of the technique. These results are in agreement with what we observed by EDX-SEM. In this work, the presence of ferritin, the iron storage protein with an out-of-phase susceptibility maxima located at around 10 K,[16] has not been observed. The absence of a substantial paramagnetic contribution, usually observed at the lowest temperatures, indicates that the presence of free iron atoms that could come from a degradation process is very low.

Thought AC magnetic susceptibility, dose-dependent amount of nanoparticles (SC@DMSA and MC@Cit) has been detected. However, a quantitative analysis of NPs' intake was performed by ICP-OES. Data is summarized in Figure 8. Elemental analysis results are in agreement with the iron content detected by AC magnetic susceptibility, observing a dose-dependent iron absorption. The massive absorption of SC@DMSA detected in the embryos has been confirmed by ICP-OES, a two or five-fold increase in comparison with MC@Cit for iron concentrations of 0.5 and 1 mg/mL, respectively. Interestingly, the iron content in the animals treated with PEGylated NPs is comparable to the control.

One possible explanation for the visual disturbance of the intestine structure of the embryos treated with MC@Cit@PEG, could be that the particles are rapidly excreted by the organism and therefore the iron content in these animals is so low. PEG functionalization reduces net surface charge of the particles and this effect could reduce the absorption of the particles in the gut favouring their excretion. Another possible explanation for the morphological alterations observed at higher doses in the treatment with the nanoparticles could be the presence of residual chemicals used during the MC synthesis non-associated to the iron cores.

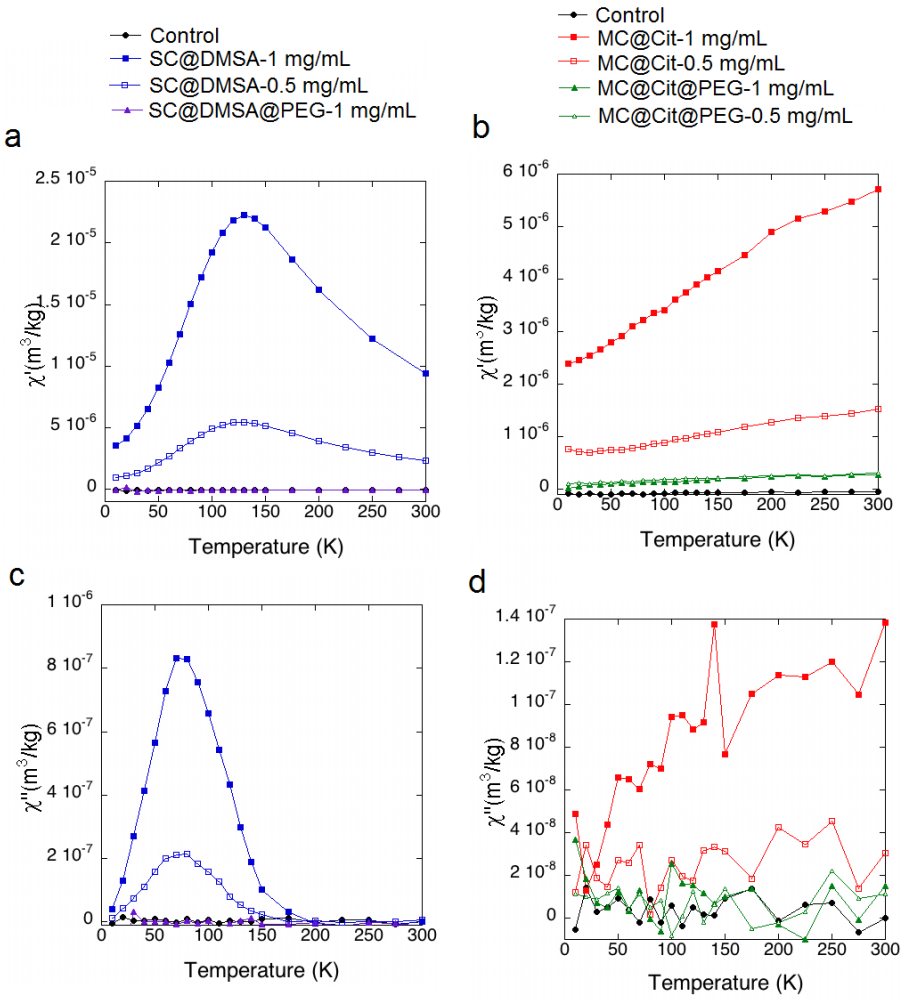

Fig 7. Tissue characterization by AC magnetic susceptibility. In-phase (χ′(T)) and out-of-phase (χ′′(T)) components of the magnetic susceptibility, per mass of sample, corresponding to freeze-dried tissues from different embryos: (a, c) Embryos exposed to SC nanoparticles, (b, d) Embryos exposed to MC nanoparticles. (n = 7 per group).

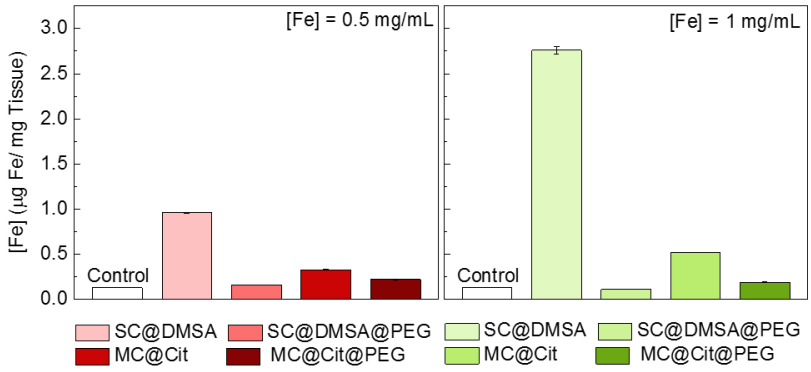

Fig 8. Iron quantification though ICP-OES of the freeze-dried tissues from different embryos: On the left treated an iron concentrations of 0.5 mg/ml, and on the right of 1 mg/mL.

3.5. Iron metabolism

The study of *in vivo* fate of NPs is imperative to develop successful biomedical applications. The safety assessment of nanoparticles should include different nanotoxicological tests after nanoparticles exposure, but also monitoring the material biodegradation and integration in the metabolic pathways. Since iron resulting from NPs' degradation is predicted to be processed by iron metabolic pathways, we next studied the expression of different genes involved in iron metabolism and oxidative stress. The expression of genes linked to iron metabolism was assessed by real-time quantitative PCR (RT-qPCR) in embryos treated with SC@DMSA and MC@Cit after 72 h of treatment with the nanoparticles at 1 mg/mL.

In the SC@DMSA treated embryos, there is an increase of dmt1 1.9 times higher than the control coupled with a downregulation of hepcidin of 0.3 times. The levels of transferrin are also increased 2.6 compared with the control. Contrary, the MC@Cit treated embryos do not seem to have an increase in the levels of dmt1 and transferrin. In both cases the expression of ferritin is increased after nanoparticle treatment, 2.9 fold change for SC@DMSA and 1.9 fold change for MC@Cit treated embryos.

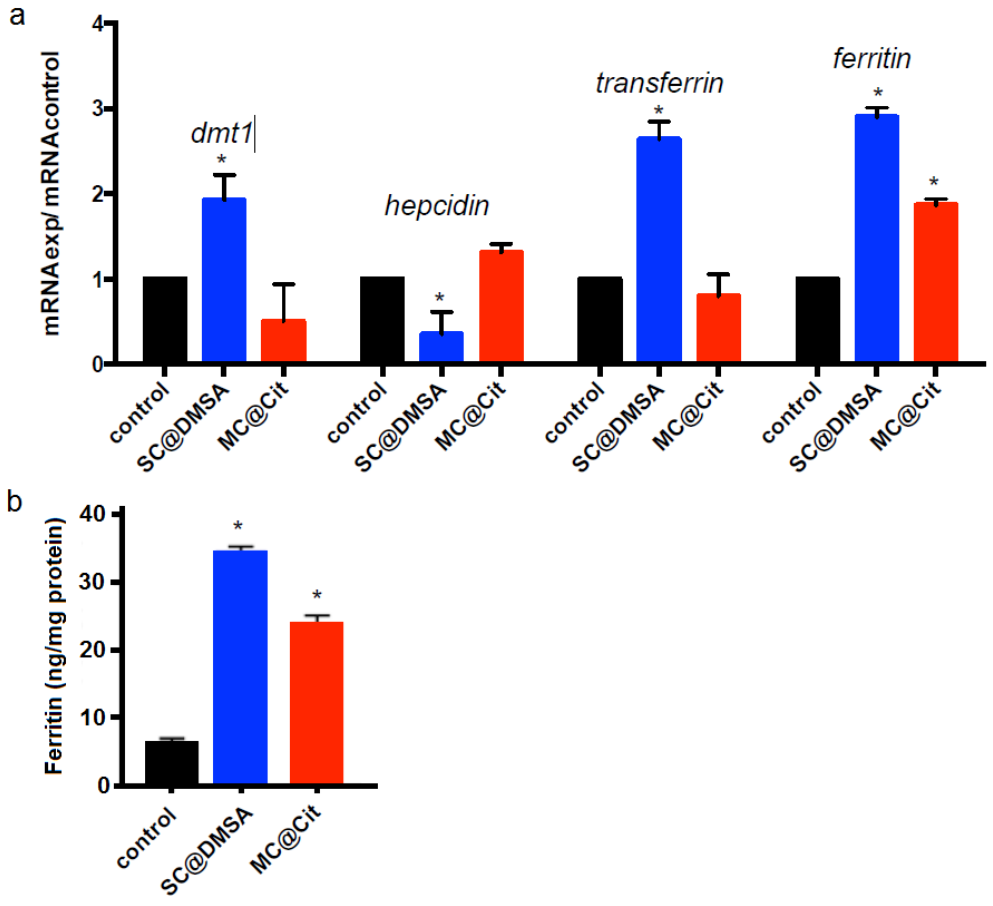

Fig 9. (a) Effect on the expression of different genes involved in iron metabolism in *X. laevis* embryos exposed to SC@DMSA or MC@Cit. (n=7 per group). * shows statistically-significance compared with the control ($p<0.05$) (b) Ferritin formation in Caco-2 cells exposed to 250 µM of single or multi-core nanoparticles. Cells were exposed for 24 hours with the different nanoparticles treatments. Data represent means ± SD (n = 3).

From this data we can describe differences in the metabolization speed of single core or multicore nanoparticles. After iron ingestion, ferrous ions (Fe^{2+}) are absorbed in the enterocytes through the divalent metal transporter-1 (DMT1). In the apical membrane of the enterocytes, the duodenal cytochrome B (Dcytb) facilitates the reduction of ferric to ferrous ions enabling the absorption of iron. In the basolateral membrane of the enterocytes the ferroportin transporter is located together with hepcidin, which regulates the entry of iron into circulation through inhibiting ferroportin. In the bloodstream, transferrin is capable to bind iron exported by ferroportin and carry it through the different organs. Ferritin is the most important protein involved in iron storage within cells, and the levels of Fe^{2+} present in the organism regulates its expression.[39]

From magnetic measurements and elemental analysis we detected a higher absorption of SC@DMSA compared with MC@Cit. Depending on the amount of internalized particles, the embryos will trigger iron metabolic pathway with different speed. In the case of SC@DMSA treated embryos; dmt-1, transferrin and ferritin have the highest levels of expression. Hepcidin is already downregulated, which implies a saturation of the metabolic pathway of iron. In the case of MC@Cit only ferritin and hepcidin are upregulated corroborating a slower activation of the iron metabolic pathway depending on the amount of internalized particles after 72 h of treatment.

Although when in cell culture experiments we cannot observe the complex interactions around the mechanism of NPs' degradation, we can describe some cellular aspects. In order to determine whether the iron released by the nanoparticles is bioavailable to the cells, we analysed ferritin formation in Caco-2 cells as a measure of cell iron uptake. Single core nanoparticles seems to be internalized by the cells more efficiently than multicore nanoparticles. This increase in the content of ferritin in the cells, measured by ELISA, is in agreement with the increase in the gene expression observed in *Xenopus*.

3.6. Oxidative stress

It has been described in macrophages treated with iron oxide hybrids nanomaterials, an increase in transcript levels of hmox1.[40] Hmox1 is induced after oxidative stress, reactive oxygen species or heavy metals, thus degrading haem group to form biliverdin and Fe^{2+}. The production of Fe^{2+} leads to the activation of iron regulatory protein (IRP) which is able to control the translation of iron sensitive protein like ferritin. In the absence of iron, IRP binds to ferritin mRNA and inhibits its translation. However, when iron ions are available, they bind to IRP and release it from ferritin mRNA, thus allowing its translation.[41] The increase in Fe^{2+} in the embryos 72 h after the treatment, activates iron response proteins, which activates the translation of proteins involved in iron metabolism such as ferritin. For the first time we are observing *in vivo* the activation by Hmox-1 of iron regulatory proteins and their effect in the transcription of ferritin mRNA associated to the treatment with iron oxide nanoparticles.

The rest of the genes studied (sod, catalase and gsr) showed an increase in the expression of enzymes involved in the attenuation of oxidative stress in the case of embryos treated with SC@DMSA compared with MC@Cit. These results suggest the activation of protective mechanisms depending on NPs' intake in order to reduce reactive oxygen species (ROS) generated during the biodegradation process. This is the early response of the organism when nanoparticle clearance induces the formation of ROS. However, we are not in the presence of an acute state of oxidative stress when a general decrease of antioxidant enzymes takes place. [42]

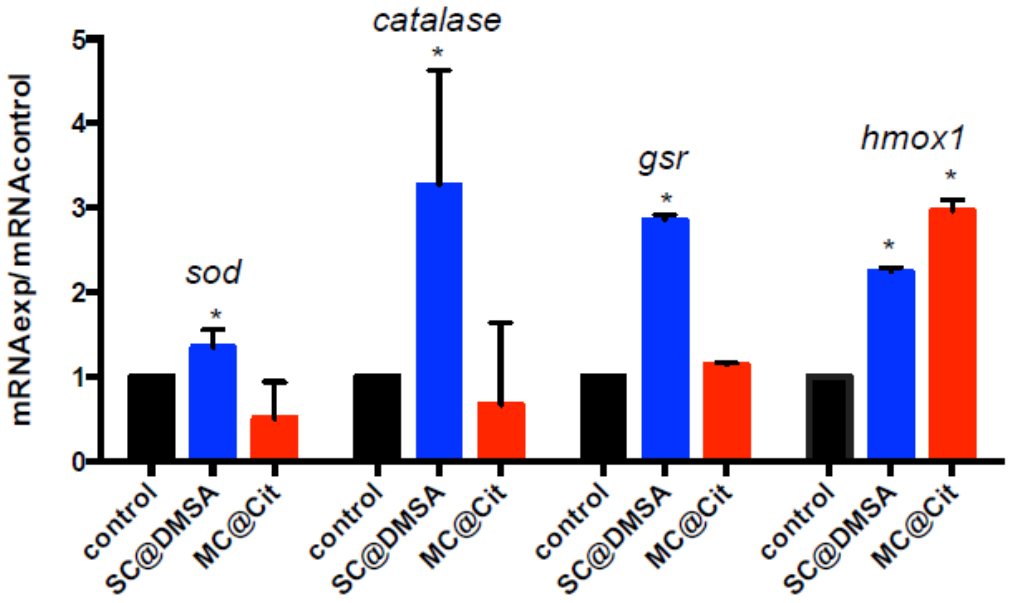

Fig 10. Effect on the expression of different genes involved in oxidative stress in *X. laevis* embryos exposed to single or multi-core nanoparticles. (n=7 per group). * shows statistically-significance compared with the control ($p<0.05$)

4. Conclusions

In this work, the toxicity and biodistribution of DMSA, citric acid and PEG coated single-core and multi-core iron oxide magnetic nanoparticles has been studied in Hep G2 (human hepatocellular carcinoma) and Caco-2 (human colorectal adenocarcinoma) cell lines and in an amphibian animal model during its embryo development.

The viability of both cell lines is preserved in all cases when treated with the nanoparticles up to an iron concentration of 1000 µM. Above that concentration, DMSA and PEGylated nanoparticles caused toxicity on HepG2 and Caco-2 cell lines, respectively. In the case of the in-vivo viability, none of the single-core nor multi-core coated nanoparticles were found lethal for the embryos. However, at high iron concentration (1 mg/mL) the embryos showed defects in their body shape, especially in the intestine, tail bending and developmental delay. Furthermore, single-core nanoparticles are massively absorbed in comparison with multi-core nanoparticles. Non-accumulation of the NPs occurs when the surface charge is lower, *i.e*. in the case of PEGylated nanoparticles. For this system, the nanoparticles seem to be excreted. In order to confirm this, the iron content of the animal's faeces and the medium should be analysed.

With the rise in production of nanoparticles for diagnostic or therapeutic purposes, the only way to reach the clinical practice is understanding the nano-biodegration of the particles.[43] Besides, at the present a dedicated regulatory framework for testing nanomedicines does not yet exist and cell based assays are the most current method of choice to describe nanomaterial biotransformation.[44],[15] With all these results, we provide evidence that an early

developmental vertebrate models such as *Xenopus laevis* is a rapid and inexpensive systems for NPs toxicity assessment, compared with adult mammalian models. Because most theranostic applications need nanoparticles to be taken up by the cells, intracellular nano-biodegradation in an *in vitro* model needs to correlate with *in vivo* observations. In the case of IONPs degradation *in vitro* and their biodisponibility by the cells traduced in the increase of ferritin levels, should correlate with the corresponding activation of the iron metabolic pathway like we observed in this work.

Here, we demonstrated for the first time, the study, by means of AC magnetic susceptibility measurements, of the intake of iron-containing particles in *X. laevis* embryos. We can consider *Xenopus* as the bridge between cell-based assays and mammalian models taking into account that the activation of the iron metabolic pathway, especially with SC@DMSA, correlates with the previous results of the group in different murine models tracking IONPs biodegradation.[16],[45]

5. References

[1] J. Roger, J. Pons, R. Massart, A. Halbreich, J. Bacri, *The European Physical Journal Applied Physics* **1999**, *5*, 321-325.

[2] W. Schütt, C. Grüttner, U. Häfeli, M. Zborowski, J. Teller, H. Putzar, C. Schümichen, *Hybridoma* **1997**, *16*, 109-117.

[3] S. Laurent, D. Forge, M. Port, A. Roch, C. Robic, L. Vander Elst, R. N. Muller, *Chemical Reviews* **2008**, *108*, 2064-2110.

[4] C. Alexiou, W. Arnold, R. J. Klein, F. G. Parak, P. Hulin, C. Bergemann, W. Erhardt, S. Wagenpfeil, A. S. Luebbe, *Cancer research* **2000**, *60*, 6641-6648.

[5] A. Jordan, R. Scholz, P. Wust, H. Fähling, R. Felix, *Journal of Magnetism and Magnetic Materials* **1999**, *201*, 413-419.

[6] R. Weissleder, M. Nahrendorf, M. J. Pittet, *Nature materials* **2014**, *13*, 125-138.

[7] R. R. Crichton, J. R. Boelaert, *Inorganic biochemistry of iron metabolism: from molecular mechanisms to clinical consequences*, John Wiley & Sons, **2001**.

[8] A. Balakumaran, E. Pawelczyk, J. Ren, B. Sworder, A. Chaudhry, M. Sabatino, D. Stroncek, J. A. Frank, P. G. Robey, *PloS one* **2010**, *5*, e11462.

[9] M. Geppert, M. C. Hohnholt, S. Nürnberger, R. Dringen, *Acta biomaterialia* **2012**, *8*, 3832-3839.

[10] M. C. Hohnholt, M. Geppert, R. Dringen, *Acta biomaterialia* **2011**, *7*, 3946-3954.

[11] J. Gu, H. Xu, Y. Han, W. Dai, W. Hao, C. Wang, N. Gu, H. Xu, J. Cao, *Science China Life Sciences* **2011**, *54*, 793-805.

[12] J. M. Rojas, L. Sanz-Ortega, V. Mulens-Arias, L. Gutiérrez, S. Pérez-Yagüe, D. F. Barber, *Nanomedicine: Nanotechnology, Biology and Medicine* **2016**, *12*, 1127-1138.

[13] V. Mulens-Arias, J. M. Rojas, S. Pérez-Yagüe, M. P. Morales, D. F. Barber, *Biomaterials* **2015**, *52*, 494-506.

[14] F. Mazuel, A. Espinosa, N. Luciani, M. Reffay, R. Le Borgne, L. Motte, K. Desboeufs, A. Michel, T. Pellegrino, Y. Lalatonne, C. Wilhelm, *ACS Nano* **2016**, *10*, 7627-7638.

[15] J. M. Rojas, H. Gavilán, V. d. Dedo, E. Lorente-Sorolla, L. Sanz-Ortega, G. B. d. Silva, R. Costo, S. Perez-Yagüea, M. Talellia, M. Marciello, M. P. Morales, D. F. Barbera, L. Gutiérrez, *Acta biomaterialia* **2017**.

[16] A. Ruiz, L. Gutiérrez, P. Cáceres-Vélez, D. Santos, S. Chaves, M. Fascineli, M. Garcia, R. Azevedo, M. Morales, *Nanoscale* **2015**, *7*, 16321-16329.

[17] C. James-Zorn, V. G. Ponferrada, K. A. Burns, J. D. Fortriede, V. S. Lotay, Y. Liu, J. Brad Karpinka, K. Karimi, A. M. Zorn, P. D. Vize, *genesis* **2015**, *53*, 486-497.

[18] S. Nations, M. Wages, J. E. Cañas, J. Maul, C. Theodorakis, G. P. Cobb, *Chemosphere* **2011**, *83*, 1053-1061.
[19] S. Nations, M. Long, M. Wages, J. Canas, J. D. Maul, C. Theodorakis, G. P. Cobb, *Ecotoxicology and environmental safety* **2011**, *74*, 203-210.
[20] M. Martín, A. Rodríguez-Nogales, V. Garcés, N. Gálvez, L. Gutiérrez, J. Gálvez, D. Rondón, M. Olivares, J. M. Dominguez-Vera, *Nanoscale* **2016**, *8*, 15041-15047.
[21] L. Gutiérrez, R. Costo, C. Grüttner, F. Westphal, N. Gehrke, D. Heinke, A. Fornara, Q. Pankhurst, C. Johansson, S. Veintemillas-Verdaguer, *Dalton Transactions* **2015**, *44*, 2943-2952.
[22] D. Faivre, *Iron Oxides: From Nature to Applications*, John Wiley & Sons, **2016**.
[23] V. Torchilin, *Advanced drug delivery reviews* **2011**, *63*, 131-135.
[24] S. Dutz, M. Kettering, I. Hilger, R. Müller, M. Zeisberger, *Nanotechnology* **2011**, *22*, 265102.
[25] F. J. Lázaro, L. Gutiérrez, A. R. Abadía, M. S. Romero, A. López, *Journal of magnetism and magnetic materials* **2007**, *316*, 126-131.
[26] L. Gutiérrez, F. J. Lázaro, A. R. Abadía, M. S. Romero, C. Quintana, M. P. Morales, C. Patiño, R. Arranz, *Journal of inorganic biochemistry* **2006**, *100*, 1790-1799.
[27] F. J. Lázaro, L. Gutiérrez, A. R. Abadía, M. S. Romero, A. López, M. J. Muñoz, *Journal of Magnetism and Magnetic Materials* **2007**, *311*, 460-463.
[28] P. Mulvaney, W. J. Parak, F. Caruso, P. S. Weiss, ACS Publications, **2016**.
[29] G. Salas, C. Casado, F. J. Teran, R. Miranda, C. J. Serna, M. P. Morales, *Journal of Materials Chemistry* **2012**, *22*, 21065-21075.
[30] Q. Sun, Z. Ren, R. Wang, W. Chen, C. Chen, *Journal of Nanoparticle Research* **2011**, *13*, 213-220.
[31] Y.-w. Jun, Y.-M. Huh, J.-s. Choi, J.-H. Lee, H.-T. Song, S. Kim, S. Kim, S. Yoon, K.-S. Kim, J.-S. Shin, *Journal of the American Chemical Society* **2005**, *127*, 5732-5733.
[32] M.-S. Martina, J.-P. Fortin, C. Ménager, O. Clément, G. Barratt, C. Grabielle-Madelmont, F. Gazeau, V. Cabuil, S. Lesieur, *Journal of the American Chemical Society* **2005**, *127*, 10676-10685.
[33] A. Ruiz, G. Salas, M. Calero, Y. Hernández, A. Villanueva, F. Herranz, S. Veintemillas-Verdaguer, E. Martínez, D. Barber, M. Morales, *Acta biomaterialia* **2013**, *9*, 6421-6430.
[34] R. P. Glahn, O. A. Lee, A. Yeung, M. I. Goldman, D. D. Miller, *The Journal of nutrition* **1998**, *128*, 1555-1561.
[35] B. Jia, L. Gao, *The Journal of Physical Chemistry C* **2008**, *112*, 666-671.
[36] C. Corot, P. Robert, J.-M. Idée, M. Port, *Advanced drug delivery reviews* **2006**, *58*, 1471-1504.
[37] M. Mahmoudi, H. Hofmann, B. Rothen-Rutishauser, A. Petri-Fink, *Chemical reviews* **2011**, *112*, 2323-2338.
[38] J. Goldstein, D. E. Newbury, P. Echlin, D. C. Joy, A. D. Romig Jr, C. E. Lyman, C. Fiori, E. Lifshin, *Scanning electron microscopy and X-ray microanalysis: a text for biologists, materials scientists, and geologists*, Springer Science & Business Media, **2012**.
[39] S. Waldvogel-Abramowski, G. Waeber, C. Gassner, A. Buser, B. M. Frey, B. Favrat, J.-D. Tissot, *Transfusion Medicine and Hemotherapy* **2014**, *41*, 213-221.
[40] D. Elgrabli, W. Dachraoui, H. De Marmier, C. Ménard-Moyon, D. Bégin, S. Bégin-Colin, A. Bianco, D. Alloyeau, F. Gazeau, *Scientific reports* **2017**, *7*.
[41] R. Eisenstein, H. Munro, *Enzyme* **1990**, *44*, 42-58.
[42] M. Radu, I. M. Din, A. Hermenean, O. L. Cinteză, R. Burlacu, A. Ardelean, A. Dinischiotu, *International journal of molecular sciences* **2015**, *16*, 29417-29435.
[43] H. Bouwmeester, I. Lynch, H. J. Marvin, K. A. Dawson, M. Berges, D. Braguer, H. J. Byrne, A. Casey, G. Chambers, M. J. Clift, *Nanotoxicology* **2011**, *5*, 1-11.
[44] F. Mazuel, A. Espinosa, N. Luciani, M. Reffay, R. Le Borgne, L. Motte, K. Desboeufs, A. Michel, T. Pellegrino, Y. Lalatonne, *ACS nano* **2016**, *10*, 7627-7638.

[45] R. Mejías, L. Gutiérrez, G. Salas, S. Pérez-Yagüe, T. M. Zotes, F. J. Lázaro, M. P. Morales, D. F. Barber, *Journal of controlled release* **2013**, *171*, 225-233.